DISCOVERY OF POTENT INHIBITORS OF HUMAN β-TRYPTASE BY PROTEIN SURFACE RECOGNITION

Dissertation

zur Erlangung des akademischen Grades eines Doktors der Naturwissenschaften

– Dr. rer. nat. –

vorgelegt von

Qian-Qian Jiang

geboren in Shandong, China

Institut für Organische Chemie

der

Universität Duisburg-Essen

2013

This work was performed during the period from May 2009 to August 2013 at the Institute of Organic Chemistry, Department of Chemistry, University of Duisburg-Essen, under the supervision of Prof. Dr. Carsten Schmuck.

Approved by the examining committee on: 15.10.2013

Chair:	Prof. Dr. Maik Walpuski
Advisor:	Prof. Dr. Carsten Schmuck
Reviewer:	Prof. Dr. Stephan Barcikowski

I declare that this dissertation represents my own work, except where due acknowledgement is made.

Essen, August 2013

.....

Qian-Qian Jiang

Acknowledgements

At the very first, I would like to express my deepest gratitude to my supervisor, Prof. Dr. Carsten Schmuck for the supervision and support. Thanks for giving me the opportunity to do the research in the field of bioorganic chemistry. With his constructive guidance and significant contribution I could have worked out this dissertation. He has offered me not only a lot of valuable ideas and suggestions with his profound knowledge and research experiences, but also helpful feedbacks and advisions to help me improving in doing scientific work and presentation. I would also like to express my thanks to him for listening to new ideas and giving me large freedom in handling my project. Moreover, I am grateful for his respectable personality, friendly style and warm concerns.

I would like to express my great thanks to my previous supervisor Prof. Dr. Yun-Bao Jiang for his kind recommenditon and suggestions.

I would like to thank CSC (China Scholarship Council) for providing me the scholarship to support my PhD study in Germany. I am greatly grateful to Consuls Lin Wang and Xia Lu for the help of scholarship arrangement and extension.

I would like to thank Prof. Dr. Stephan Barcikowski, Dr. Christoph Rehbock and Lisa Gamrad for the fruitful and pleasant collaboration and sharing valuble ideas and vast expertise.

I am also grateful to our cooperative partner, Prof. Dr. Daniel Hoffmann and Dr. Dominik Heider for the statistical analysis and docking studies.

I would like to thank Wilhelm Sicking for the molecular modeling calculations and Martin Ehlers for the docking studies.

I would like to thank Dr. Torsten Schaller and Heinz Bandmann for the NMR measurements and Werner Karow for recording the mass spectra.

I would like to thank all students for their dedication and contribution to this thesis.

I would like to give great thanks to all my colleagues of our research group for all the help and the beautiful and funny moments. They were always helpful and kind to me. They have made my life much easier and happier in Germany. Special thanks go to my laboratory colleagues, Hannes Kuchelmeister, Tassilo Fenske, Pia Mereu and Sandra Jungh änel for the collaborative and positive working atmosphere. Great thanks go to Dr.

Supratim Banerjee for reviewing the thesis and the helpful suggestions. For reviewing the manuscript, Lina Bartch and Dr. Christoph Hirschhäuser are greatly thanked. Great thanks also go to Dr. Junchen Wu, Ute Michels, Barbara Geibel, Michael Merschky and Sebastian Langolf for all the help. I am also grateful to Christine Cangemi for helping me going through all the documents. Special thanks also go to Johannes Hofmann for all the help, concerns and happy moments.

I would like to thank my friend Jing for her help and support, especially in the difficult moments of my work. Mao, Dongxu, Haofei, Zhaoqing, Qian, Wenbin and Miao are thanked for the friendship, support and happy times we have had.

At last, I would love to express my special thanks to my parents and my sisters for their deepest love, understanding and support, during my entire studies. Best thanks are also given to Mingbo who is always there for me even in the difficult moments of my work. Thanks for his selfless support, understanding and encouragement.

Table of Contents

1. INTRODUCTION

1.1 Enzymes

Enzymes are protein molecules whose roles are to catalyze and control thousands of chemical reactions that take place in living organisms. They can be produced from any living organism and are essential to sustain life. Life depends on a complex network of chemical reactions catalyzed by specific enzymes, and any modification of enzyme pattern may result in far-reaching consequences for the living organism.[1]

Enzymes are most often globular proteins which assume an approximately spherical conformation in solution. Their molecular weights vary from ten thousand to millions. Over 5000 enzymes have been identified and they can be classified according to their functions into six major classes: (1) Oxido-reductases (transfer hydride between two substrates), (2) Transferases (transfer groups other than hydrogen), (3) Hydrolases (hydrolytic cleavage enzymes, substrate cleaved by water), (4) Lyases (removing or adding groups to double bonds), (5) Isomerases (catalyze structural or geometric changes within their single substrate molecules), (6) Ligases (synthetases joining two groups together, coupled with the breakdown of ATP or a similar triphosphate).[2]

Proteases, also known as peptidases or proteinases, are globular, water-soluble enzymes which regulate many physiological processes. They are biology's version of Swiss army knives, cutting long sequences of peptides into fragments which can fold into proteins.[3] They belong to the family of hydrolases and play an essential role in the hydrolysis of the peptide bonds. More than 500 proteases (accounting for approximately 2 % of human genes) with different functions and tasks have been identified.[4] Proteases have adapted to a wide range of conditions (e.g. pH, reductive environment, *etc*.) through the evolutionary development. Moreover, different catalytic mechanisms have been identified for substrate hydrolysis. According to the catalytic residue in their active site which effects enzymatic hydrolysis, proteases can be classified into six different classes: serine, cysteine, threonine, aspartate, glutamic and metallo-proteases. Proteases are very selective for the cleavage of specific substrates, each of which is responsible for cutting the specific amino acid sequences under preferred environmental conditions.

Proteases regulate numerous vital physiological processes (e.g. activation, synthesis

and turnover of all proteins) and hence play a key role in signaling pathways in all living organisms. They are consequently essential regulators related to all stages of a life cycle, namely, from conception, birth through growth, maturation and aging to diseases and death of all organisms. In general, proteases act reasonable if they are regulated and tightly controlled. However, endogenous and exogenous factors can disturb the balance of proteolysis processes, resulting in abnormal development, thus leading to diseases and death. Due to the importance of proteases in health and disease, the substances that interact with them thus decrease their activity, which are called inhibitors have been developed to shut down the enzymes, thus preventing the excessive proteolysis processes.[5]

1.2 Serine Protease β-Tryptase

Serine proteases are one of the most abundant groups of proteolytic enzymes in the human genome which play crucial roles in health and disease.[6-8] Over one-third of all known proteases are serine protease. Their members are essential to a variety of biological activities, including digestion, blood clotting, immune response and inflammation, as well as reproduction. Among these, human β-tryptase is the predominant serine protease in human mast cells and is known to be involved in the pathogenesis of asthma and other allergic and inflammatory diseases.[9-11] The x-ray structure of β-tryptase (Figure 1.1, left) is known since 1998 and has revealed unique and interesting structural features that distinguish it from other serine proteases.[12] It is a tetramer consisting of four monomers pointing towards a central pore and the four active sites are buried deep inside of the hollow structure. Due to its unique structure β-tryptase is resistant to nearly all known standard endogenous proteinase inhibitors. Therefore, a number of small synthetic inhibitors of β-tryptase have been reported.[8] Likewise in our working group, a focused combinatorial library of 216 tetravalent peptide ligands (**1**) obtained by using six amino acids (Arg, Lys, Glu, Phe, Ala, Trp) in the variable positions to ensure a sufficient degree of structural and chemical diversity within the library (Figure 1.1, right) were synthesized and screened to identify potent inhibitors of β-tryptase. By taking the advantage of multivalent interaction, the tetravalent peptide ligands were shown to bind to β-tryptase through electrostatic interactions between the positively charged residues of the ligands and the anionic hotspots on the surface of the enzyme, sterically blocking access of the substrate to the active site thus shutting down the enzyme in a reversible and noncompetitive way with nanomolar affinity.[13]

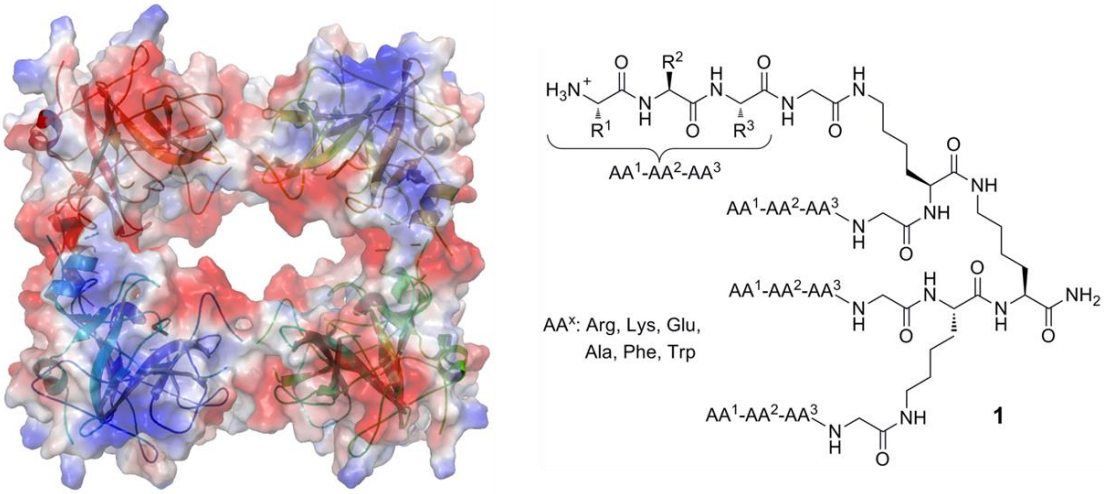

Figure 1.1 *Left:* Cartoon and surface representation of the β-tryptase tetramer. *Right:* Schematic representation of combinatorial library of 216 tetravalent peptide ligands.

For the protein surface recognition, besides the multivalency effects, the artificial binding motifs featuring more than one possible interaction means (e.g. electrostatic interaction plus hydrogen bonding) also play a crucial role in stabilizing the host-guest complex as well as increasing the binding affinity and specificity. For example, in our working group, a guanidiniocarbonyl pyrrole (GCP) binding motif was developed for efficient binding of carboxylates and anionic biomolecules such as oligopeptides or proteins.[14-15] This artificial arginine analog GCP as a tailor-made binding motif can be incorporated to the natural peptide sequence to improve the binding affinity and specificity, which is very interesting not only for understanding the interaction events but also for the development of new therapeutics or drug candidates.

The present work focuses on the design of novel and efficient inhibitors of the serine protease β-tryptase. A docking study is performed to have a better understanding of the possible binding sites on the protein surface. Within this work novel peptide ligands containing the artificial arginine analog GCP as a tailor-made binding motif in the peptide arms are developed for the inhibition of β-tryptase through the binding to the anionic hotspots on the surface of the enzyme. Furthermore, dynamic combinatorial libraries are used to identify new and potent inhibitors of β-tryptase by selecting the active building blocks featuring recognition units as well as the multivalent scaffolds. A new approach is also developed by using gold nanoparticle as the scaffold which is functionalized by the peptide ligands featuring inhibitory potentials. Both the inhibitory properties of the inhibitors and the inhibition mode to shut down the enzyme are investigated. The results are a valuable proof for the possibility of using these inhibitors and methods to the field of drug discovery.

2. BACKGROUND INFORMATION

2.1 Enzyme Inhibition

Enzymes are powerful biological catalysts that are essential in physiological processes, leading to the acceleration of the reaction rates by more than millions of times relative to the corresponding reactions without catalysts. Enzymes are not only efficient catalysts but with also high specificity. They are highly specific for catalyzing certain definite chemical reactions as well as the substrates which are involved in the reactions. Due to these properties, enzymes are candidates as therapeutic targets to combat diseases by modulating their activities with inhibitors or activators which can either decrease or increase enzyme activities. Therefore, the processes of the development and characterization of inhibitors or activators to regulate the enzyme activity are very important. This chapter will introduce the approaches used to the study of the enzyme kinetics and enzyme assays.

2.1.1 Enzyme Kinetics

Enzyme kinetics is the branch of enzymology that deals with the factors affecting the rates of enzyme-catalyzed reactions. The first general rate reaction equation for reactions involving enzymes was proposed by *Henri* in 1903.[16] Based on *Henri*'s experimental work, *Michaelis* and *Menten* presented the simplest and best known *Michaelis-Menten* model of enzyme kinetics in 1913.[17] It describes the rate of enzyme-catalyzed reactions by relating the reaction rate to the concentration of the substrate. The simplest reaction involves one substrate and one enzyme featuring one catalytic site. In this process the enzyme (E) and substrate (S) participate in an equilibrium with the enzyme-substrate complex (ES), which can then subsequently dissociate to the substrate and enzyme again, or can lead to catalysis and form the product (P) of the reaction and release enzyme again. The equilibrium is assumed to be not disturbed by product formation during the period initial rate of reaction is measured.

$$\mathrm{E + S} \underset{k_{-1}}{\overset{k_1}{\rightleftharpoons}} \mathrm{ES} \xrightarrow{k_2} \mathrm{P + E} \qquad (1)$$

The rate constants for the individual steps are depicted with k_1, k_{-1} and k_2 which are

used for the definition of *Michaelis* constant K_m:

$$K_m = \frac{k_{-1} + k_2}{k_1} \tag{2}$$

Assuming that the enzyme-substrate complex is in rapid equilibrium with the reactants enzyme and substrate, which means that the equilibrium takes place on a much faster time-scale than the product is formed, the *Michaelis-Menten* equation (3) is obtained as follows:

$$v_0 = \frac{V_{max}[S]}{K_m + [S]} \tag{3}$$

In this equation, the initial reaction rate v_0 relates to the substrate concentration [S] and the maximum rate of the reaction V_{max}.

The plot of the reaction rate and the substrate concentration in the enzyme-catalyzed reaction is a hyperbolic curve (Figure 2.1, left) and from this the K_m value is described as the substrate concentration when the reaction rate is the half of V_{max}. The parameters can be obtained as well by linearizing the *Michaelis-Menten* equation, which can be done by taking the reciprocal of both sides of the equation to give *Lineweaver-Burk* equation (4):

$$\frac{1}{v_0} = \left(\frac{K_m}{V_{max}}\right)\frac{1}{[S]} + \frac{1}{V_{max}} \tag{4}$$

The parameters V_{max} and K_m can be determined directly from this representation by checking the intercept on the y axis and the slope of the plot (Figure 2.1, right).

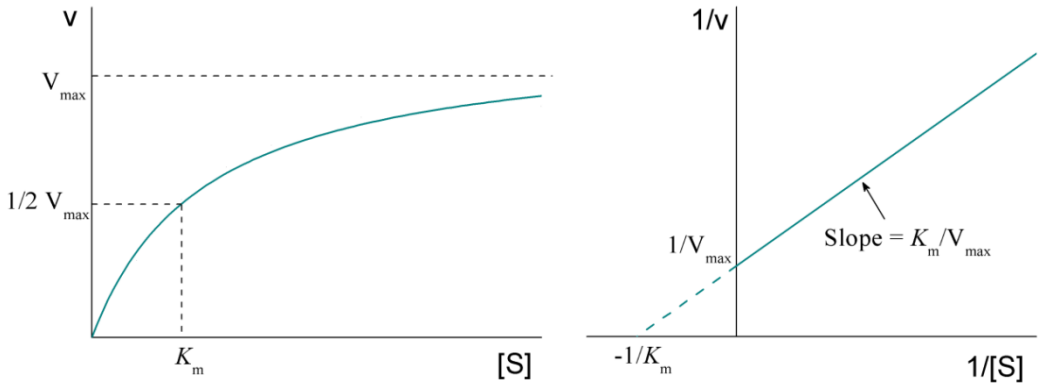

Figure 2.1 *Left:* Graphical plot of reaction rate v against substrate concentration [S] according to *Michaelis-Menten* equation. The enzyme concentration is fixed. *Right: Lineweaver-Burk* plots of 1/v against 1/[S]. K_m and V_{max} can be determined directly by the intersection on the x- and y-axis.

As already described above, an inhibitor can reduce the velocity of enzyme-catalyzed reaction and thus can be used as candidates for drugs, antibiotics and toxins, *etc*. The studies of enzyme inhibition most often bring us the knowledge about the enzyme

specificity, the properties of the enzyme active site and the kinetic mechanism of the enzyme-catalyzed reaction. According to the nature of the inhibitors binding to the enzymes, two types of inhibitors are described: reversible and irreversible inhibitors. Irreversible inhibitors usually bind to the enzyme in a covalent way and change it chemically via covalent bond formation. These inhibitors most often modify the side chains of key amino acid residues that are needed for enzymatic activity and cannot be easily removed afterwards. In contrast, reversible inhibitors often bind to the enzyme with non-covalent interactions, e.g. hydrogen bonding, electrostatic and hydrophobic interactions. These inhibitors generally do not undergo chemical reactions upon interaction with the enzyme and can be easily removed by dilution, dialysis, ultrafiltration, centrifugation or replacement processes. Reversible inhibitors can be classified as competitive, uncompetitive or noncompetitive inhibitors depending on whether the inhibitors bind to the enzyme, the enzyme-substrate complex or both of them.

A competitive inhibitor is a compound that combines with the free enzyme and competes with the substrate for the same binding site of the enzyme. Most often the competitive inhibitor resembles the substrate structurally and geometrically. It could be a nonmetabolizable analog or derivative of the substrate, or an alternate substrate of the enzyme, or the product of the enzyme-catalyzed reaction. The effect of a competitive inhibitor on the kinetics of an enzyme-catalyzed reaction is illustrated in Figure 2.2 (left). The inhibitor concentration [I] is arbitrarily chosen as K_i for comparison with the equilibrium in the absence of an inhibitor. It shows that the rate of the reaction rises more slowly in the presence of inhibitor but will ultimately reach the same V_{max} at a higher substrate concentration and the K_m value is increased. The *Lineweaver-Burk* plots which have the intersection on the y-axis and the increased slope confirm that the V_{max} is unaffected by a competitive inhibitor but the K_m value is increased.

A noncompetitive inhibitor can bind to both the enzyme and the enzyme-substrate complex and has no effect on substrate binding and *vice versa* because inhibitor and substrate do not compete for the same binding site. As shown in Figure 2.2 (middle), the inhibitor and substrate bind randomly and independently at different sites. Namely, I binds to E and ES, S binds to E and EI. The binding of one ligand has no effect on the dissociation of the other. Most often the noncompetitive inhibitor changes the enzyme conformation sufficiently to prevent the proper positioning of the catalytic center which has no effect on substrate binding but the ESI complex is nonproductive. The effect of a noncompetitive inhibitor on the enzyme kinetics shows that the V_{max} cannot be reached in the presence of a noncompetitive inhibitor even at an infinitely high substrate concentration. This can be explained by the equilibria shown: no matter how high amount of substrate is added, as long as the inhibitor exists, a portion of the enzyme will remain as the nonproductive ESI complex. Because at any inhibitor concentration the enzyme forms (E and EI) have equal affinities for the substrate, the K_m value should be constant.

The *Lineweaver-Burk* plots also show clearly a constant intersection on the x-axis which means the K_m value is unchanged by a noncompetitive inhibitor but the V_{max} is decreased.

An uncompetitive inhibitor binds to the enzyme-substrate complex. It does not bind to the free enzyme, so it does not compete with the substrate for the same binding site. In this inhibition mode, most often the free enzyme has an inappropriate binding site for the inhibitor but when the substrate binds to the active site of the enzyme, a conformational change occurs in the enzyme which makes the binding site accessible to the inhibitor, yielding a catalytically inactive ESI complex. The effect of an uncompetitive inhibitor on the enzyme kinetics (Figure 2.2, right) shows that the V_{max} cannot be reached in the presence of an uncompetitive inhibitor because at any inhibitor concentration an infinitely high substrate concentration will not drive the entire enzyme to the ES form. However, unlike the noncompetitive inhibitor, the *Lineweaver-Burk* plots show that the intersection on the x-axis changes but the slope remains the same which means the K_m value is decreased as well and in the same extent as the V_{max}.

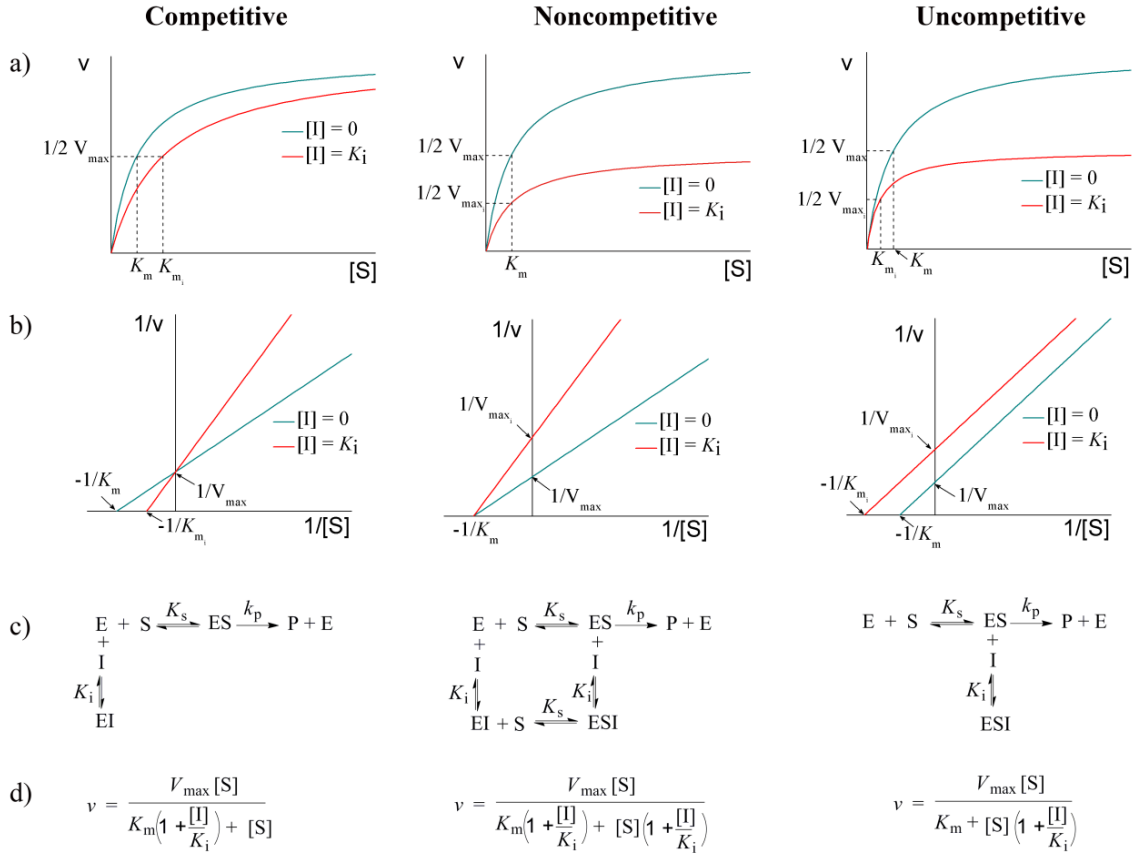

Figure 2.2 Enzyme kinetics of three different types of inhibitions, namely competitive (*left*), noncompetitive (*middle*) and uncompetitive inhibition (*right*).[18] a) The plots of reaction rate v against substrate concentration [S] according to the velocity equation in the absence and in the presence of a fixed concentration of an inhibitor. b) *Lineweaver-Burk* plots of 1/v against 1/[S] in the absence and in the presence of an inhibitor. c) Schematic representation of the reaction equilibria of the enzyme (E), substrate (S), inhibitor (I) and the complexes (ES, EI and ESI) between them as well as the product (P). d) The velocity equations in the presence of an inhibitor.

Although the *Lineweaver-Burk* plot has been widely used as a linear transformation method to determine kinetic parameters and different types of enzyme inhibitors, it has one major limitation. As the line of the plot is primarily defined by the data points at low substrate concentration, which is liable to cause big errors, the kinetic parameters determined from linear fitting curve may not accurately reflect the true values. Some other linear plots derived from the rearrangement of the *Michaelis-Menten* equation or the *Lineweaver-Burk* equation are also used for the determination of kinetic parameters. For example, the *Hanes-Woolf* plot is obtained by multiplying the *Lineweaver-Burk* equation by [S] yields a function that relates [S]/v linearly with [S] and the *Eadie-Hofstee* plot is derived from the *Michaelis-Menten* equation to yield a linear relation between v and v/[S]. However, with these two methods small deviation can cause large errors as well. Therefore, nowadays the nonlinear regression based on computational analysis is preferred which can lead to more accurate results.[19]

2.1.2 Enzyme Assays

Enzyme assays are methods to study enzyme activities. They are used to determine the rates of enzyme-catalyzed reactions and play a vital role in enzyme kinetics and enzyme inhibition studies. They are of considerable importance, not just for the detection of enzyme activities, but in regards to the search for novel enzymes and specifically cleaved substrates as well. Enzyme assays are very important for bio-engineering, drug discovery and medical diagnostics which are used as essential tools for the understanding of the functions and actions of different enzymes in biological systems.

Enzyme activity measures the amounts of active enzyme present in a reaction. The measurement of enzyme catalytic activity is mainly based on two ways by quantifying either the concentration of substrate consumed ([S]) or that of product produced ([P]) during the course of the experiment. Measuring the production of the product is usually more accurate because detecting small changes in [P] (initially [P] = 0) is easier than detecting small changes in large amounts of substrate [S].

At present, two major types of methods are used to measure the rates of enzymatic reactions: a continuous assay by *Tian* and *Tsou*[20] and a discontinuous (dilution) assay by *Kitz* and *Wilson*.[21] In both cases, it is important to have steady-state conditions which mean that the concentrations of substrate and inhibitor are much larger than the enzyme concentration ([S] >> [E], [I] >> [E]) to result in a steady concentration of enzyme-substrate complex during the reaction.

The discontinuous (dilution) assay measures enzyme activity in a fixed period of time. In this assay, the enzyme and inhibitor are first incubated under steady-state conditions. To this sample the substrate is added and aliquots are then taken from the enzyme reaction at intervals and the residual enzyme activities in these reaction samples are measured. The reaction aliquots are known as the time points of the reaction and the amount of product production at each time point can be determined by UV/Visible (UV/Vis) or fluorescence spectroscopy. Then the initial rate of the reaction can be determined from the slope within the linear region of the curve by plotting the formed product concentration against time. This assay is very useful in the chemical reactions yielding products that are not spectroscopically distinct from the substrate. The product should be rapidly converted into a chromophore or a fluorophore that can be quantified by the related spectroscopy.

The more convenient and simple method to monitor enzyme kinetics is the continuous assay. It has been widely used, allowing measuring the rate of reaction in one single experiment as compared to the discontinuous assay. The continuous assay often uses spectroscopic techniques to measure the production of product, or consumption of substrate *in situ*, which resemble the more accurate situations *in vivo* where the modification of the enzyme and the turnover of the substrate take place simultaneously. In this assay, the enzyme is mixed with the substrate and inhibitor to start the reaction, the

concentration of the product formed from the substrate hydrolysis is then determined as a function of time. There are many different methods of detection in the continuous assays. Some of the more common techniques used to quantitatively distinguish product from substrate include the UV/Vis spectroscopy and fluorescence spectroscopy. These spectra measure the absorbance or fluorescence changes of the substrate or product at a specific wavelength over time. Then the reaction rate can be observed as a function of time. Due to the linear correlation of the observed spectra signals with the concentration of the compound, the rates of the absorbance or fluorescence changes can be converted to the rates of substrate consumed or product yielded. Due to the high relevance for this thesis, the following description will focus on the continuous assay.

The spectrophotometric assay is the most common method of detection in enzyme assays due to its simplicity, non-destructivity, selectivity, and sensitivity. The increase of the fluorescence due to the production of the product can be measured during the assay. The recorded fluorescence increase over time yields linear curves with different slopes. One thing to pay attention to is that the enzyme assay should be done at the beginning of the experiment to make sure it is in the initial velocity range (linear range) of the enzyme-catalyzed reaction.[20]

In order to measure the efficiency of the inhibitor to inhibit the enzyme activity, normally two experiments should be performed. In the first experiment the K_m and V_{max} of the enzyme-catalyzed reaction alone (without inhibitor) can be determined as described in Chapter 2.1.1. The second experiment can be done similarly in the presence of an inhibitor. It is also possible to determine the binding mode of the inhibitor. Therefore, by measuring the velocity slopes in the presence of inhibitors at different concentrations (v_i), which are smaller than the initial velocity in the absence of inhibitor (v_0), the dissociation constant (K_i) of the inhibitor can be determined according to the *Dixon* equation (5).[22]

$$v_i = \frac{v_0}{1 + \frac{[I]}{K_i}} \tag{5}$$

Linear plots can be obtained by the rearrangement of this equation, resulting in a function that relates $1/v$ linearly with [I]. The K_i value as well as the inhibition mode can be determined by plotting $1/v$ against [I] at different substrate concentrations. The *Dixon* plots are shown in Figure 2.3. The intersection on the x-axis indicates the half maximal inhibitory concentration (IC_{50}) while the intersection of the curves at different substrate concentrations reveals the K_i value. For noncompetitive inhibition, the IC_{50} value is independent of the substrate concentration and is equal to the K_i value. For competitive and uncompetitive inhibition, the IC_{50} value is varied with different substrate concentrations and the substrate concentration has to be considered for the calculation of the K_i value.

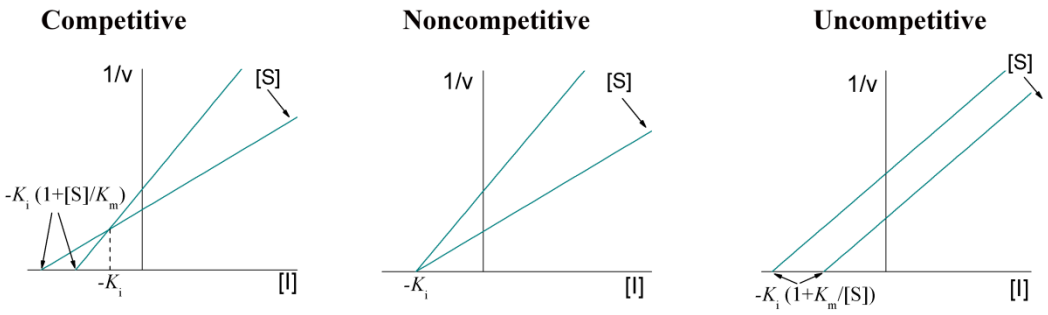

Figure 2.3 *Dixon* plots (1/*v* against [I]) for the determination of K_i values of three different types of inhibition at different fixed substrate concentrations: competitive (*left*), noncompetitive (*middle*) and uncompetitive inhibition (*right*).[23] The intersection points in the *Dixon* plot of the competitive and noncompetitive inhibitions resulting from different substrate concentrations indicate the K_i value, whereas the intersection point of the uncompetitive inhibition provides the K_i value when the substrate concentration is infinitely high.

Normally, the K_i value can be calculated from the IC_{50} value corrected by the K_m and substrate concentration. For example, the IC_{50} value can be determined by using the direct nonlinear regression analysis with the program GraFit and the K_i value can then be calculated from that. For a competitive inhibitor, the apparent K_{iapp} value is first calculated by nonlinear regression analysis, then with the known or determined K_m value of the enzyme-substrate complex the concentration independent K_i value can be determined with the following equation (6):

$$K_i = \frac{K_{iapp}}{1 + \frac{[S]}{K_m}} \tag{6}$$

Similarly, for the uncompetitive inhibitor, the true K_i value can be determined with following equation (7):

$$K_i = \frac{K_{iapp}}{1 + \frac{K_m}{[S]}} \tag{7}$$

The calculated dissociation constant K_i is then independent of the substrate concentration and its affinity to the enzyme, so it is possible to compare it accurately with literature known inhibitors.

Since the suitable measurement methods are necessary to measure the product production of the enzymes, a large variety of different enzyme assays has been developed. Therefore, the following part describes some common methods for enzyme assays which make it possible to determine the production of the product by testing natural or artificial substrates and inhibitors.

As mentioned above, the simplest and most practical way is based on a chromogenic or fluorogenic substrate whose absorbance or fluorescence properties changes during the enzyme-catalyzed reactions, e.g. releasing a colored or fluorescent product upon enzyme cleavage or inducing a directly detectable change upon reaction (e.g. a precipitation). Therefore, most often the enzyme assays is based on direct fluorescence or absorbance readout in 96-well microtiter plates either in solution or in culture suspensions.[24] However, in many enzyme reactions, changes in substrates or products are not observable by spectrophotometric methods because they do not absorb light. This kind of enzyme reactions can be detected with the help of indicators which respond directly to substrate consumption or product formation. A number of assays have been established as well by using other different analytical instruments such as HPLC, GC, MS, NMR and IR besides fluorescent and UV/Vis spectrometers.

Since enzymes are often specific for substrates, different chromogenic or fluorogenic substrates are necessary for each of the enzyme assays. A large variety of examples focuses on a small family of chromophores or fluorophores which are incorporated into different synthetic substrates to provide the spectral signal during the enzyme reactions. An example is indican which is a chromogenic substrate belonging to the family of glycosides. It is present in plants such as Woad (*Isatis tinctoria*, the root of which is used as a traditional Chinese medicine herb) and *Polygonum tincorum*. The glycosidic bond of the indican (**2**) can be cleaved by a glycosidase, resulting in an indoxyl (**3**) and glucose as the product. The indoxyl is unstable and then oxidized by a mild oxidizing agent such as atmospheric oxygen to form the blue indigo dye (**4**, Figure 2.4).[25]

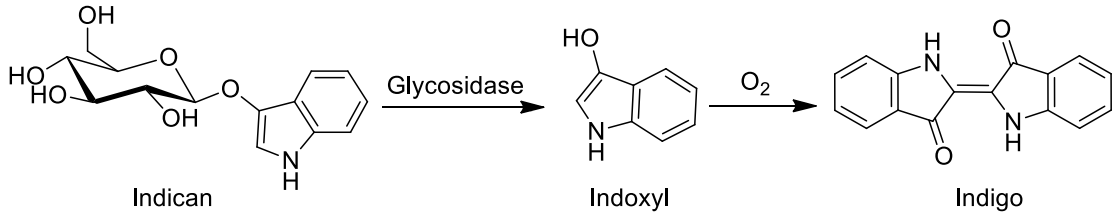

Figure 2.4 Cleavage of chromogenic substrate by a glycosidase-catalyzed reaction. Indican (**2**) is hydrolyzed by the enzyme followed by the oxidation with oxygen to form the dimer indigo (**4**).

This natural product example is used as a model following which a wide range of artificial enzyme substrates have been designed. For example, nitrophenyl β-galactoside (**5**), in which *p*-nitrophenol is linked to β-galactose, can also be used to detect the activity of β-galactosidase by releasing a yellow nitrophenolate (λ_{max} = 405 nm) at alkaline pH which can be easily measured in a spectrophotometer.[26] Similarly, *p*-nitrophenyl caproate (**6**)[27] and *p*-nitrophenyl octyl ether (**7**) are used as chromogenic substrates for lipase and cytochrome P450,[28-29] respectively, releasing the nitrophenolate (**8**) for detection (Figure 2.5).

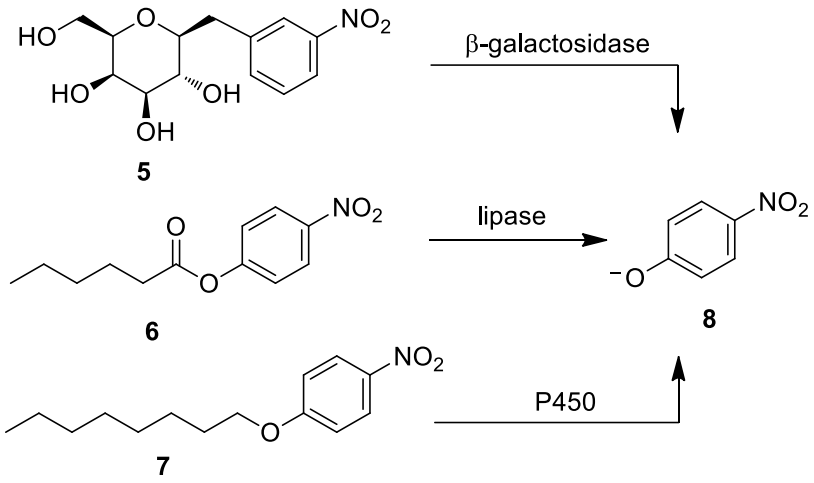

Figure 2.5 Cleavage of chromogenic *p*-nitrophenyl substrates by enzyme-catalyzed reactions, releasing a yellow nitrophenolate which can be measured in a spectrophotometer.

Another example reported by *Wang* is using a synthetic fluorogenic substrate carrying a morpholinecarbonyl-derived rhodamine 110 (MC-R110) as the detectable species.[30] The substrate Ac-Asp-Glu-Val-Asp-MC-R110 (**9**) was used for determining the activity of caspase-3. Before cleavage, the substrate is non-fluorescent in buffer solution. Upon the enzyme cleavage, *N*-MC-R110 (**11**) is formed which has a high fluorescence emission at 525 nm (485 nm excitation) and can be detected directly by the luminoscope (Figure 2.6).

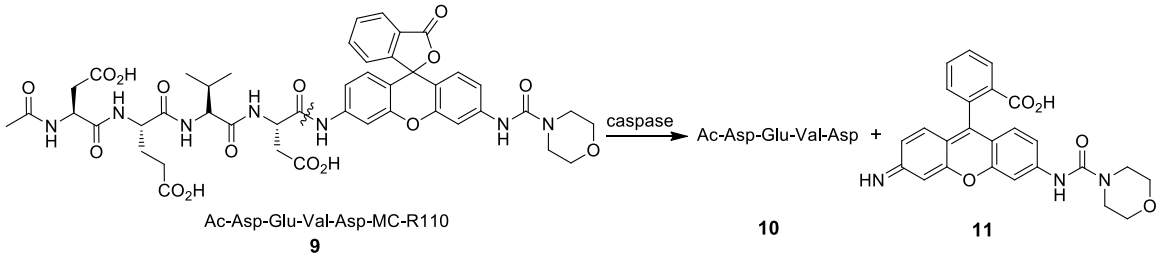

Figure 2.6 Cleavage of fluorogenic substrate by the enzyme-catalyzed reactions. The product formation can be determined by the fluorescent emission at a wavelength of 525 nm resulted from the released MC-R110 (**11**).

Additionally, indirect release mechanisms have been used as well for a number of substrates. For example, *Reymond* and co-workers reported a fluorogenic assay (Figure 2.7) based on the detection of carbonyl oxidation product (**16**), which undergoes a β-elimination reaction catalysed by bovine serum albumin (BSA) to form the fluorescent product umbelliferone anion (**17**).[31] This method is very useful for the detection of precursors (substrates) that are resistant to oxidation. As shown in Figure 2.7, the substrates bis-phosphate (**12**) for phosphatases, diester (**13**) for lipases and esterases, and expoxide (**14**) for epoxide hydrolases are hydrolyzed by the specific hydrolytic enzymes to form 1,2-diol (**15**). The diol (**15**) was rapidly and quantitatively oxidized to aldehyde

(**16**) in the presence of sodium periodate ($NaIO_4$), which is transformed into a blue fluorescent product **17** (λ_{ex} = 360 nm, λ_{em} = 440 nm) by a β-elimination reaction. By using this method, the enzyme reactive moieties of the substrate can be separated from the fluorophore, thus the large aromatic group will have no effect on the binding properties.

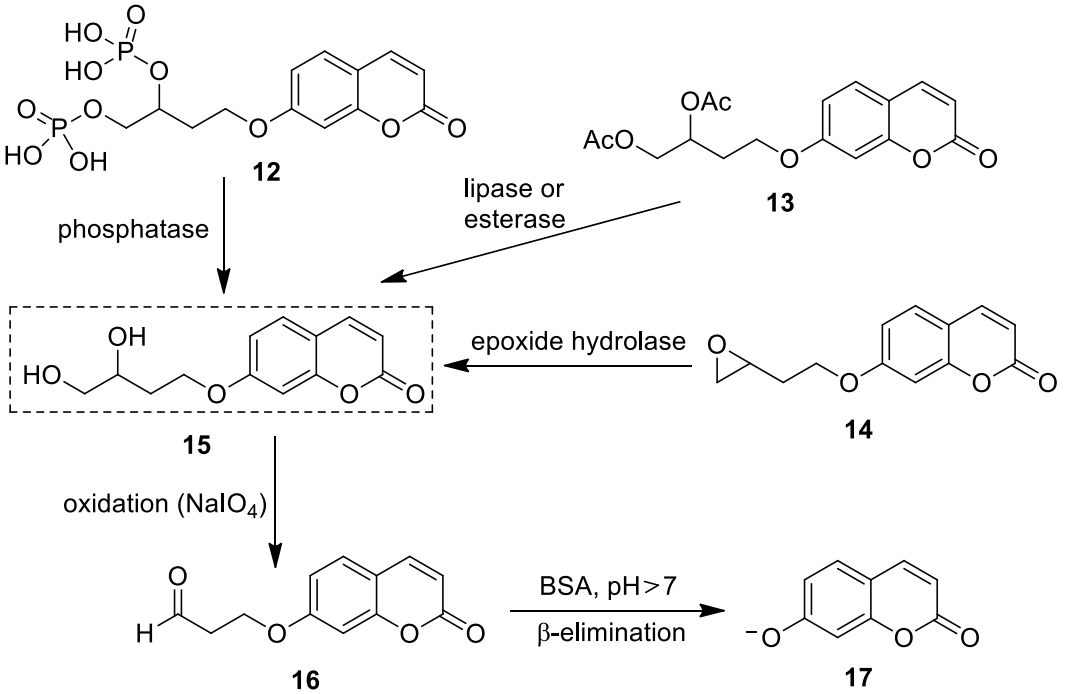

Figure 2.7 Periodate-coupled fluorogenic enzyme assays for phosphatase, lipases and esterases, and epoxide hydrolases with indirect release of umbelliferone (**17**).

Besides nitrophenols, rhodamines and umbelliferones, fluoresceins[32] and BODIPY[33] dyes are also well established to incorporate into substrates. All of these agents have rather large aromatic groups that have the tendency to influence the solubility of the substrate and the binding behavior of the substrate compared to the non-labeled substrates. Therefore, one must be careful when using such large chromophores or fluorophores.[24] Alternatively *Nau* and co-workers reported recently that new types of assay based on fluorescence resonance energy transfer (FRET) by using new and non-aromatic fluorophores are possible.[34-35]

FRET is a distance-dependent transfer of excited state energy from an initially excited donor to an acceptor. Typical effective distances between the donor and acceptor molecules are within 10-100 Å. Another requirement is that the fluorescence emission spectrum of the donor must overlap with the absorption spectrum of the acceptor. The FRET efficiency is dependent on both the donor-acceptor distance and the spectral overlap. Normally the donor molecule is a fluorophore while the acceptor molecule can be either another fluorophore or a non-fluorescent molecule (quencher). Most often a fluorescent donor and an acceptor are located on opposite sides of the substrates in an appropriate distance to ensure the intramolecular FRET. Before enzyme cleavage, because

the emission of the donor is absorbed by the acceptor, only the emission of the acceptor or no fluorescence (when the acceptor is a quencher) can be observed. Upon enzyme cleavage at a protease cleavage site between donor and acceptor, the double-labeled substrate is separated into two single-labeled fragments, resulting in the recovery of the fluorescence of the donor due to the increase in the donor-acceptor distance which causes the decrease of the FRET efficiency (Figure 2.8).

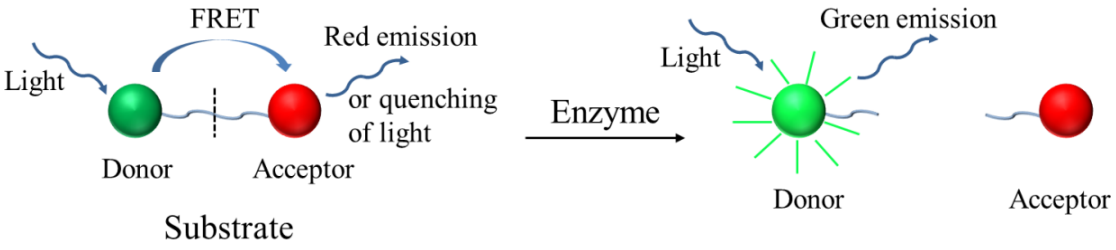

Figure 2.8 Principle of enzyme assays based on FRET between the labeled donor and acceptor on the substrates.

A lot of enzyme assays are based on the mechanism of FRET. For example, *Nagano et al.* developed a fluorescent substrate for detecting the activity of phosphodiesterase based on FRET mechanism (Figure 2.9).[36] A coumarin group was used as the donor and the fluorescein group as the acceptor. The artificial substrate (**18**) was designed by attaching both of the donor and acceptor to two phenyl linkers to prevent the dye-to-dye close contact[37] with the phosphodiester moiety situated in the middle. In aqueous buffer solution, when excited at 370 nm, the emission of the coumarin donor was strongly absorbed by the fluorescein acceptor and the emission of the acceptor (λ_{em} = 515 nm) was observed due to the FRET from the donor to the acceptor. Upon the hydrolysis of the phosphodiester group by the phosphodiesterase, the donor (**19**) and acceptor (**20**) were separated, resulting in an increase in the donor fluorescence (λ_{em} = 450 nm) and a decrease in the acceptor fluorescence. The enzyme activity can then be detected by the changes of the fluorescence. Recently, they designed a different FRET method using the coumarin-fluorescein as the donor-acceptor pair as well. Upon changing the two isomeric forms of fluorescein (from lactone form to quinoid form) by enzyme hydrolysis reaction, resulting in the dramatically changes in absorption properties, the intramolecular FRET occurred and thus the enzyme activity can be determined by the ratiometric fluorescent detection method.[38]

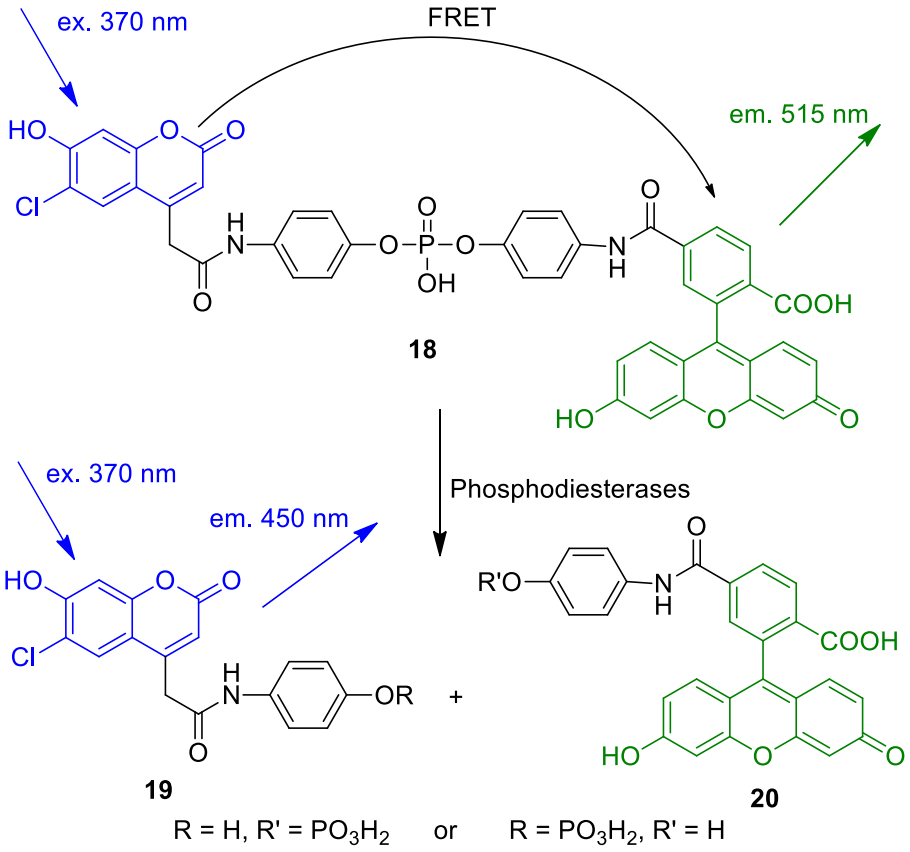

Figure 2.9 The FRET-based enzyme assay mechanism for phosphodiesterases.

A number of FRET substrates based on the fluorophore-quencher (donor-acceptor) systems to measure the enzyme hydrolytic reactions have been also developed.[39-42] In most of these systems, the substrates have no fluorescence before the enzyme reaction because of the intramolecular quenching FRET effect. However, the fluorescence of the donor is increased after the enzyme-catalyzed reaction due to the diminishment of the intramolecular quenching effect which can then be detected to determine the enzyme activity.

The above described enzyme assays are based on chromogenic and fluorogenic substrates which result in a direct change in the absorbance of light or the emission of light. However, for some specific reactions with unlabeled substrates, the enzyme-catalyzed reactions do not result in detectable light signals. In this case, the indicator assays can be used to detect such reactions. One of the most straightforward methods is the enzyme-coupled assay. It is based on using the product of one reaction as the substrate of a second enzyme, converting it to a second product and so on, until one of these following reactions produces the detectable signal. For example, the reduction of hydrogen peroxide to water catalyzed by peroxidases occurs with the concomitant oxidation of various chromogenic dyes, such as 2,2'-azino-di-(3-ethyl-benzthiazoline-6-sulphonic acid) (ABTS).[43] In a recent report, *Turner* and co-workers

have designed a novel high throughput screening (HTS) method to detect both the activity and enantioselectivity of asymmetric ketone reduction by ketoreductases (KRED) in the presence of an *R*-selective alcohol oxidase, and horseradish (HRP) and ABTS for monitoring the precise amount of concomitant production of H_2O_2 and hence *R*-alcohol.[44]

Some indicator assays are based on functional group selective reagents. For example, pH indicators have been used to monitor enzyme-catalyzed reactions which release or consume protons. An early example is the characterization of serine proteases by using the simple ester substrates to monitor their esterase activity.[45] This method can reduce the reagent costs and shorten analysis time compared with the conventional techniques and substrates. pH indicators have also been used for the development of a colorimetric assay to screen the enantioselectivity of hydrolases by using the fact that ester hydrolysis lowers the pH of the reaction medium.[46-47] Selective chromogenic or fluorogenic reagents with functional groups have also been used to measure enzyme activities. For example, the only well-known fluorescence assay for aminopeptidase is based on a fluorescence off-on chemosensor for amino acids which can be used to monitor the proteolytic activity of proteases on whole protein substrates in real time by using the released amino acids for displacement of Cu(II) from calcein, thus turn on the green fluorescence.[48]

The main drawback of the indicator assays is that they are often sensitive to interferences, for example, a signal may be produced by other events rather than catalytic turnover or by which the catalytic turnover may be masked. It may require narrow assay conditions which might be incompatible with specific enzymes. Therefore, in order to overcome the drawbacks, a HTS application with the help of proper controls should be used. This is a very useful and necessary assay whenever a very specific reaction is to be optimized.

In order to obtain more information in less time, the fingerprinting method has been developed which is based on measuring and analyzing multiple substrates simultaneously. Enzyme fingerprinting focuses the analysis on a single enzyme by using a series of structurally related substrates to detect its selectivity.[49] The screening data may be used to identify reactive substrates, or for classification of the enzymes.[50] Selectivity for structures or solvents can be performed either by parallel assays in microtiter plates[51] or by on-bead assays which are based on the identification of protease substrates created on beads with the help of combinatorial chemistry.[52]

The combinatorial chemistry is a useful technology that allows the simultaneous and fast synthesis of large libraries containing a large numbers of different but related compounds. Recently, the more sophisticated and faster technique such as ‘split and mix’ synthesis[53] have been used. The output of the ‘split and mix’ synthesis is multiple compounds attached to the synthesis beads, each bead having one type of compound bound to its surface. Therefore, by using this method, it is possible to synthesize the ‘one-bead-one-compound’ combinatorial libraries.[54-55] To know which compound is

bound to which bead, either the compound itself needs to be identified by appropriate analytical tools, or the bead needs to be encoded.[56] Such method can then be used to synthesize substrates and inhibitors. In order to screen such a large number of compounds in the libraries, a reliable high-throughput assay is essential. The commonly used assays for such combinatorial library methods are the on-bead assays without the cleavage step to avoid the complicated purification steps. Methods have been developed for the on-bead screening, including either the commonly used direct binding of fluorescence-labeled target molecule to the on-bead library and visually identification of beads that display compounds able to bind to the target,[57-58] or detection of functional properties of the on-bead compound such as identifying phosphorylation[59] or proteolytic substrates.[60]

Because the compounds are still covalently attached to the solid support in the on-bead assay, in order to perform the biological assays in aqueous media, the solid support has to be biocompatible. Therefore, the resin beads should have good swelling properties in both organic and aqueous solvents. Ideally, the beads should be uniform in both size and loading. Furthermore, the resin must be inert towards the tested enzymes. The most common used resin for on-bead screening of enzymes is the PEGA resin which is based on solely hydrophilic polyethylene glycol (PEG) chains and shows excellent swelling properties in aqueous buffers. This resin has been widely used in solid phase peptide synthesis (SPPS) for the synthesis of ‘one-bead-one-compound’ combinatorial libraries, following which the on-bead screening can be performed.[61-63]

In summary, a considerable number of enzyme-catalyzed reactions can be analyzed by direct or indirect assays through monitoring fluorescence or absorbance readout in microtiter plates where the enzymes, substrates and inhibitors are mixed in aqueous buffer solution. Moreover, the enzyme assays for the on-bead screening of combinatorial libraries allow easy, fast and quantitative analysis of all the library members with less effort.

2.2 Serine Protease β-Tryptase

Human β-tryptase belongs to the family of serine proteases and is the predominant protein released from most human mast cell secretory granules. Serine proteases adopt two principle structure folds: trypsin-like (chymotrypsin-like) and subtilisin-like structure. Most members have the trypsin-like structure, e.g. trypsin, chymotrypsin, tryptase, elastase, plasmin and thrombin, *etc*. The trypsin-like structure consists of two β-barrels with the catalytic amino acids located at the interface of the two domains.[64] The shape and properties of the enzymes' binding pockets account for their substrate specificities. For example, for the three digestive enzymes, trypsin cleaves peptide bonds located on the C-terminal side positively charged residues (Lys/Arg preferred at P1 position), chymotrypsin prefers large hydrophobic residues such as Phe/Tyr/Trp at P1 position while elastase prefers small hydrophobic residues such as Gly/Ala/Val.[65] Like trypsin, tryptase has a preference for positively charged lysine or arginine (Arg > Lys) at the P1 position of the substrate.[66] Here the nomenclature is defined by *Schechter* and *Berger*.[67] Nomenclature for the substrate amino acid residues from N-terminus to C-terminus is defined as Pn, . . . P2, P1, P1', P2', . . . Pn', where P1-P1' denotes the cleaved peptide bond. In other words, the amino acid residues from the position of the hydrolyzed bond to the N-terminus are referred as Pn and those to the C-terminus are referred as Pn'. Accordingly, the adjacent binding sites of the enzyme called 'subsites' are numbered as Sn and Sn' (n = 1, 2, 3…). They are located on both sides of the catalytic site of the enzyme and the cleavage site is between S1 and S1' pocket.

Serine proteases are named after the nucleophilic serine residue at the active site. The unusual reactivity of serine is due to a charge relay system, known as the so-called catalytic triad which is located in the active site of the enzyme and is directly involved in the catalytic reactions. For tryptase, the triad consists of three amino acid residues: aspartic acid (Asp-102), histidine (His-57) and serine (Ser-195). As shown in Figure 2.10, with the help of the proton-withdrawing oxyanion of Asp-102 binding to His-57, the histidine acts as a better proton acceptor and deprotonates the hydroxyl group of Ser-195, allowing it as a powerful nucleophile to attack the carbonyl group of the substrate. Another important characteristic feature of serine protease is the so-called oxyanion hole. In the case of tryptase, the oxyanion hole is formed by the backbone NHs of Gly-193 and Ser-195. These atoms form a pocket of partial positive charge that activates the carbonyl group of the scissile peptide bond and stabilizes the tetrahedral intermediate state.[68]

The generally accepted mechanism for trypsin-like serine proteases is shown in Figure 2.11.[7] On binding of the substrate, His-57 as a base attracts the proton from the hydroxyl group of Ser-195 while it attacks the carbonyl carbon of the peptide substrate, to yield a tetrahedral intermediate which is stabilized by H-bond from backbone NHs of Ser-195 and Gly-193 in the oxyanion hole. The resulting H^+ of His-57 is stabilized by the H-bond

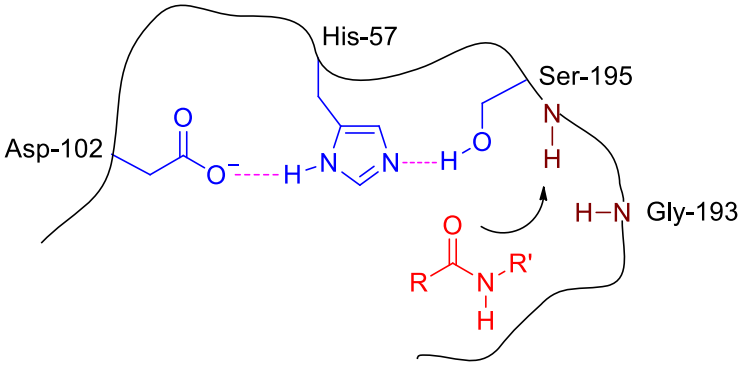

Figure 2.10 The catalytic triad (Asp-102, His-57 and Ser-195) and the oxyanion hole (formed by the backbone NHs of Ser-195 and Gly-193) of trypsin-like serine proteases.

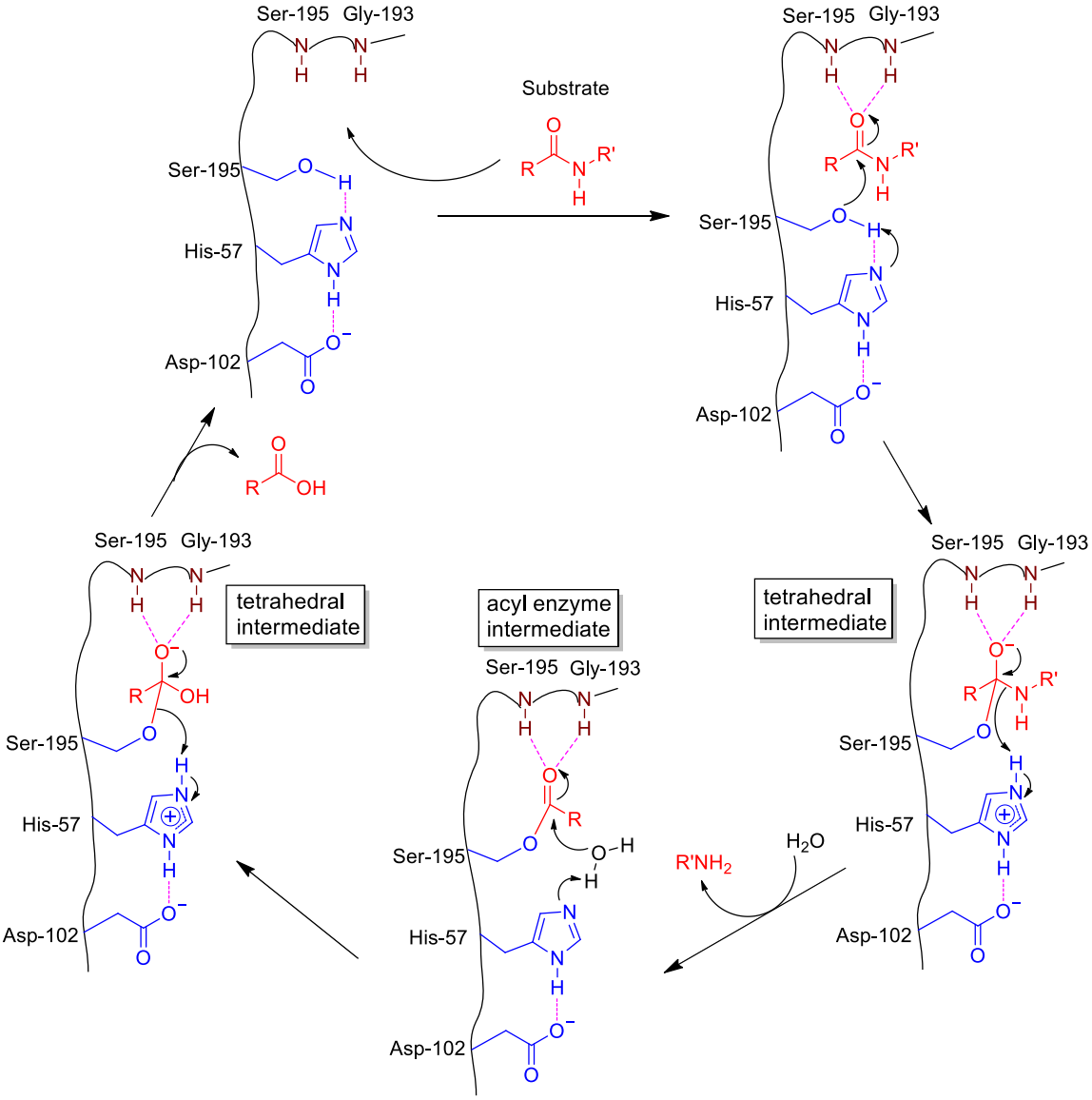

Figure 2.11 The catalytic cleavage mechanism for trypsin-like serine proteases by the catalytic components (triad and the oxyanion hole).[7]

with the side chain of Asp-102. The next step is the reconstruction of the carbonyl group with expulsion of the leaving group, assisted by proton donation by His-57, resulting in the breakdown of the peptide bond to release the first product-the free amine, and the formation of the acylenzyme intermediate. Then a water molecule protonates His-57, and the resulting hydroxyl ion attacks the carbonyl carbon atom of the acyl enzyme, yielding a second tetrahedral intermediate. This intermediate collapses, assisted by protonated His-57 acting as an acid, releasing the second peptide fragment with free C-terminus and the catalytic triad is restored.

Tryptase was found in mast cells more than 50 years ago.[69] With an amount of 10-35 pg per mast cell, tryptases represent up to one fourth of the total protein content of the cell, and even 90 % are stored in the secretory granules.[70-71] Human tryptase comprises several isoenzymes (α_1, α_2, β_{1a}, β_{1b}, β_2, β_3, mMCP-7-like-1, mMCP-7-like-2) derived from human lung and skin tissues.[72-73] β-tryptases are the main isoenzymes isolated from lung and skin mast cells whereas α-tryptases are mainly expressed in basophils,[74] both of which are granulated cells rich in histamine and heparin. Mast cells play an important role in the immune system. When stimulated with antigens or allergens (proteins or polysaccharides), mast cell degranulation can be induced, for example with the aid of receptor FcεRI-bound antigen-coated immunoglobulin E (IgE), resulting in the extracellular release of inflammatory mediators such as histamine, tryptase, *etc*.[75-77] Assessment of the increase in tryptase levels has been used as a specific mast cell activation marker and mediator for the diagnosis of anaphylaxis and even a greater specificity could be obtained from selective measurement of the increase of β-tryptase.[78-79] A number of studies have demonstrated that tryptase participates in allergic and inflammatory processes, causing bronchoconstriction and airway hyperresponsiveness, which is the key characteristic of asthma.[80-83] Furthermore, tryptase acts as a neuropeptidase, cleaving the bronchodilating neuropeptides vasoactive intestinal peptide (VIP) and peptide histinine methionine (PHM), as well as the vasodilator/bronchoconstrictor neuropeptide calcitonin gene-related peptide (CGRP). Tryptase also activates prekallikrein and generates kinins,[84-85] which has been suggested as a mechanism by which tryptase enhances bronchoconstriction in asthmatic patients.[86] Tryptase stimulates cellular response through activation of protease-activated receptor-2 (PAR-2), a G-protein-coupled receptor, which is related to the increased collagen deposition in the asthmatic airway.[83, 87] For these reasons, tryptase has become an interesting target for studies of therapeutic agents for asthma and other allergic and inflammatory disorders. Therefore, to identify potential inhibitors for tryptase, the enzyme structure, catalytic site and the interaction with inhibitors should be studied.

Specificity of trypsin-like serine proteases is usually categorized in terms of P1-S1 interaction. The active site of the tryptase monomer is structurally quite similar to trypsin. In particular, the S1 specificity pockets of both enzymes are nearly identical and well suited to accommodate Arg or Lys at P1 position. The combination of Asp-189, Gly-216

and Gly-226 create a negatively charged S1 pocket that accounts for their specificity. The S2 subsite of tryptase monomer is open and larger than that of trypsin, and the S3/S4 subsite is fully blocked. Even though β-tryptase has significant sequence similarity with other trypsin-like serine proteases, it has unique properties. For example, human β-tryptase is resistant to most of the endogenous proteinase inhibitors. The well-known proteinaceous inhibitors are the leech-derived tryptase inhibitor (LDTI)[88] and tick-derived protease inhibitor (TdPI).[89] Tryptase has highly preference for small peptide substrates to larger proteins. To understand the unique behaviour of β-tryptase and obtain a reliable model for drug design, its structure is analyzed.

The x-ray structure of human β-tryptase[12, 90] revealed that it has a tetrameric structure composed of four quasi-equivalent monomers which are arranged in two different orientations within the tetramer. The tetramer has a molecular weight of approximately 134 kDa. Four monomers A, B, C and D are arranged in a flat rectangular frame with each monomer sitting in the corner and facing to a central pore (Figure 2.12). The tetramer shows almost perfect 222 symmetry and the three 2-fold axes are arranged nearly perpendicular. The quasi-symmetry is due to the different conformations of Tyr-75 residues located in the monomer-monomer interfaces. Therefore, only two pairs of monomers (A and C, B and D) are equivalent in the tetramer structure. Each monomer contains one active site and the four active sites are directed towards a central oval pore measuring approximately 50 × 30 Å. Within the central pore, the four negatively charged S1 binding pockets (containing residue Asp-189) are shown in defined distances.

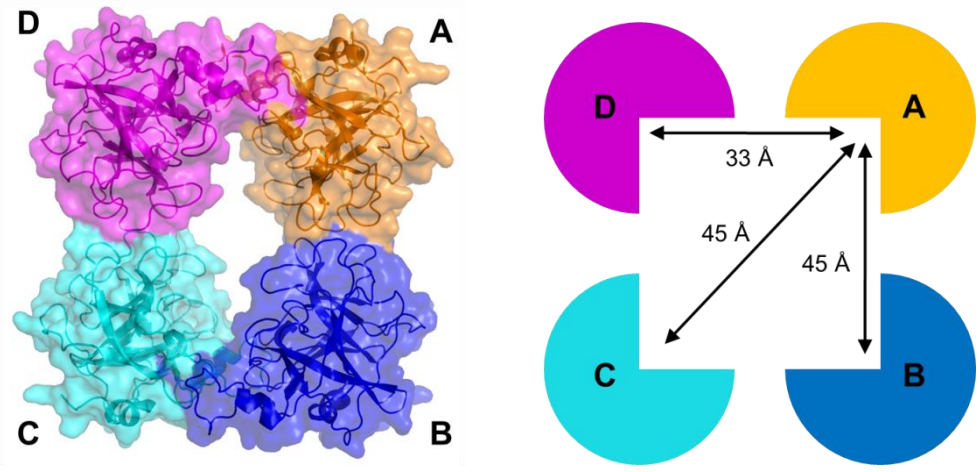

Figure 2.12 *Left:* Tetrameric structure of β-tryptase tetramer (PDB code: 1A0L). The four monomers (A, B, C, D) are shown as ribbons surrounded by semitransparent surfaces. Two monomers each (A and C, B and D) are arranged in the same orientation. *Right:* Schematic representation of the β-tryptase tetramer with the inter-S1 subsite distances. Residue Asp-189 is at the bottom of each S1 pocket.[91-92]

Tryptase monomers connect with their neighbours through different interactions. Monomers A and D (Figure 2.13, left) interact with each other through hydrophobic contacts, salt bridges as well as hydrogen bonding interactions. The surface area size of

the A-D interface (and the equivalent B-C interface) is 1075 Å, which is almost twice as large as the A-B interface (and the equivalent C-D interface) with a size of 540 Å connecting only via hydrophobic interactions.[86] The tetrameric structure of β-tryptase is stabilized *in vivo* by heparin, a negatively charged polysaccharide, which can interact with a number of positively charged amino acid residues on both sides of the interfaces of the monomers (Figure 2.13, right). β-tryptase is only enzymatically active in the form of this non-covalently linked tetramer and it dissociates into inactive monomers in the absence of heparin or high salt concentrations.[93]

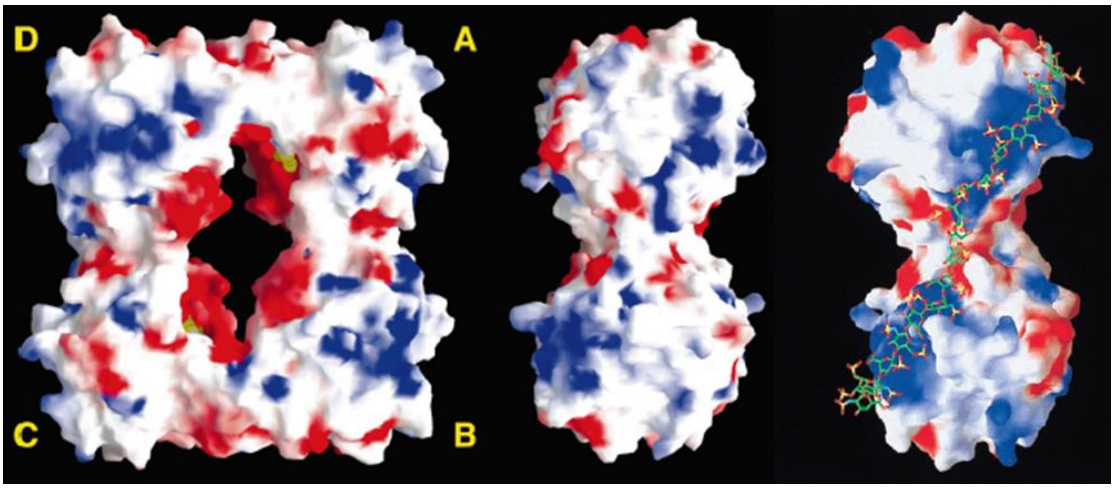

Figure 2.13 Solid-surface structure of human β-tryptase. The blue and red colors indicate positive and negative electrostatic potentials, respectively. *Left:* Front view onto the four monomers. The four monomers (A, B, C, D) are arranged at the corners of a frame-like structure towards to a central pore. A cluster of negatively charged residues is centred at the entrance to the central pore. *Middle:* Side view towards the AB homodimer. The positively charged patches on the periphery of the AB dimer (and CD dimer) extend towards the front side of monomer B and the back side of A. *Right:* Binding model of heparin chain along the A-B edge of the tetramer. Heparin can bind to the positively charged patches, thus spanning and stabilizing the monomer-monomer interface. *(Reprinted with permission from C. P. Sommerhoff, W. Bode, G. Matschiner, A. Bergner, H. Fritz, Biochim. Biophys. Acta **2000**, 1477, 75-89. Copyright 2000 Elsevier).*[86]

As shown in Figure 2.13, the four active sites of β-tryptase are buried inside the central pore which is surrounded by a number of negatively charged amino acid residues such as glutamate and aspartate, thereby attracting the positively charged substances. However, the access to the active sites is significantly limited by the two narrow openings of the pore. This pore displays a rectangular cross-section but twisted by approximately 30° about the tetramer axis. It has an inner pore size of approximately 50 × 25 Å but two openings of the pore are much narrower (approximately 40 × 15 Å). Even though the entrances of the pore are just large enough for elongated peptides of the diameter of an α-helix to thread through and to interact with the active sites,[90] the narrow pore restricts the size of accessible substrates and inhibitors to the active sites and that is why most of proteinaceous inhibitors fail for tryptase.

2.3 Inhibitors of Serine Protease β-Tryptase

Since tryptase was found in pathophysiologic conditions responsible for asthma and other allergic and inflammatory disorders, it has become an attractive drug target and a number of efficient inhibitors have been reported. In terms of different inhibition mechanisms, the reported inhibitors can be classified into three types: heparin antagonists, active site inhibitors and protein surface binding inhibitors.

2.3.1 Heparin Antagonists

As mentioned above, β-tryptase is only enzymatically active in the tetrameric form. Thus, it is not surprising that compounds which can bind to heparin have the capability to inhibit tryptase. Heparin antagonists are defined as compounds that compete with β-tryptase to bind heparin, resulting in the denaturation of β-tryptase into four inactive monomers by the removal of heparin from the tetramer.

In an earlier study, antithrombin III, a small protein known as the thrombin inhibitor, was reported to partially compete with tryptase for heparin binding, accelerating the loss of tryptase activity *in vivo*.[94] Various kinds of cationic molecules have been reported as heparin antagonists and represent an interesting type of inhibitors. For example, lactoferrin, a cationic 78 kDa protein released from activated neutrophils, was reported as a potent (IC_{50} = 24 nM) and selective inhibitor for tryptase.[95] Myeloperoxidase (MPO), a 118 kDa cationic protein released from primary neutrophil granules, was shown to be efficient and selective tryptase inhibitor with an IC_{50} value of 16 nM.[96] The inhibition is prevented by the presence of an excess amount of heparin. Other smaller tryptase inhibitors are the arginine-rich 4.5 kDa protein protamine (IC_{50} = 65 nM), and nonprotein polybrene (hexadimethrine bromide, 5-10 kDa) (IC_{50} = 3.6 nM), two polycationic compounds which are commonly used clinically as heparin antagonists for neutralization of the anti-clotting effect of injected heparin during surgery.[97] The inhibition modes of these two inhibitors are different. Protamine appears to be a reversible inhibitor indicated by the reactivation of the enzyme by addition of excess heparin whereas polybrene seems to be an irreversible inhibitor as excess heparin failed to reactivate the enzyme. Recently, synthetic polycationic heparin inhibitors based on a calix[8]arene scaffold have shown competitive inhibition of human tryptase with a very high specificity and affinity towards heparin neutralization. However, the inhibitory effect, e.g. the IC_{50} value has not been determined in detail in this report.[98]

2.3.2 Active Site Inhibitors

The classical active site inhibitors of β-tryptase are able to enter the entrance of the central pore and interact with the active sites in a competitive way. They normally have small molecular weight due to the pore size and geometry restriction of β-tryptase and

represent the biggest group of tryptase inhibitors so far. Some small proteins can also inhibit tryptase acting as active site inhibitors. For example, the well-known atypical Kazal-type proteinaceous inhibitor LDTI, a small protein isolated from the medical leech *Hirudo medicinalis* consisting of 46 amino acid residues, was shown to bind to two of the four active sites of tryptase due to the steric hindrance and thus only inhibiting the enzyme activity by approximately 50 %.[88] Even though it inhibits the tryptase with high affinity (K_i = 1.4 nM), it lacks selectivity relative to other related serine proteases such as trypsin (K_i = 0.9 nM) and chymotrypsin (K_i = 20 nM). TdPI, a Kunitz/BPTI (bovine pancreatic trypsin inhibitor)-related protein found in *Rhipicephalus appendiculatus* consisting of 97 amino acid residues, was shown to inhibit β-tryptase in the nanomolar range.[89] In the inhibition course (Figure 2.14), a first TdPI molecule was cleaved by tryptase and fits into two diagonal active sites, followed by the second molecule binding to another active site from behind, resulting in blockage of three of catalytic sites and thus 75 % inhibition was reached.

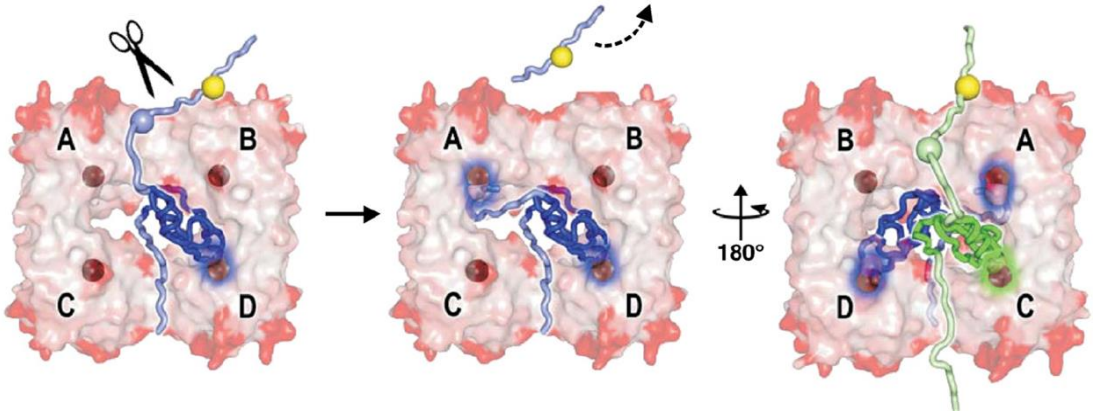

Figure 2.14 Binding model of the TdPI to β-tryptase. The first TdPI molecule binds to the active site D and A after the cleavage by tryptase. The second molecule binds from the behind side to active site C. *(Reprinted with permission from G. C. Paesen, C. Siebold, K. Harlos, M. F. Peacey, P. A. Nuttall, D. I. Stuart, J. Mol. Biol.* ***2007****, 368, 1172-1186. Copyright 2007 Elsevier).*[89]

Recently, MCoTI-II, a member of a class of microproteins known as cyclotides that possess a macrolactam-cystine knot scaffold, isolated from the seeds of *Momordica cochinchinensis*, was reported to inhibit tryptase with some sequence modifications with nanomolar affinity (K_i = 9 nM) but also has no selectivity relative to trypsin (K_i = 2.6 nM).[99] Other efficient proteinaceous inhibitors derived from a linear variant of the cyclic cysteine knot miniprotein MCoTI-II, with 28 amino acid residues, belong to the smallest serine proteinase inhibitors. They were reported to bind all the four active sites of β-tryptase with four miniprotein inhibitors and completely inhibit the enzyme activity with a K_i value of 1 nM but also lack selectivity to trypsin.[100]

There are a number of synthetic small molecules that can efficiently inhibit β-tryptase by binding to the active sites. Normally they are derived from non-reactive substrate analogues which bind in the active site but cannot be processed by the enzyme and thus

competitively prevent the substrate from binding. For example, one of the first tryptase monovalent inhibitors was APC-366 (**21**), an active site-directed competitive inhibitor which went into the clinical trial for treatment of asthma (Figure 2.15).[9] However, it only underwent phase II clinical trials and was discontinued due to the only small beneficial effect. This might be because of the poor efficiency (K_i = 0.33–450 μM) and selectivity relative to other serine proteases.[101-103] Other inhibitors such as Babim (**22**)[101, 104] and RWJ-56423 (**23**)[103] have been used for testing the role of tryptase. They are potent inhibitors binding to the active sites with K_i values of 5 nM and 10 nM, respectively but still have low selectivity against other serine proteases. The trypsin-like serine proteases inhibitors leupeptin (**24**) and *p*-aminobenzamidine (pAb, **25**) can inhibit β-tryptase as well. They act as competitive inhibitors with K_i values of 1.0 μM and 65 μM, respectively.[105] However, due to the lack of selectivity of these monovalent inhibitors, it is not possible to determine if their effect *in vivo* is because of the inhibition of mast cell tryptase or other target proteases. Therefore, more selective inhibitors of tryptase need to be designed.

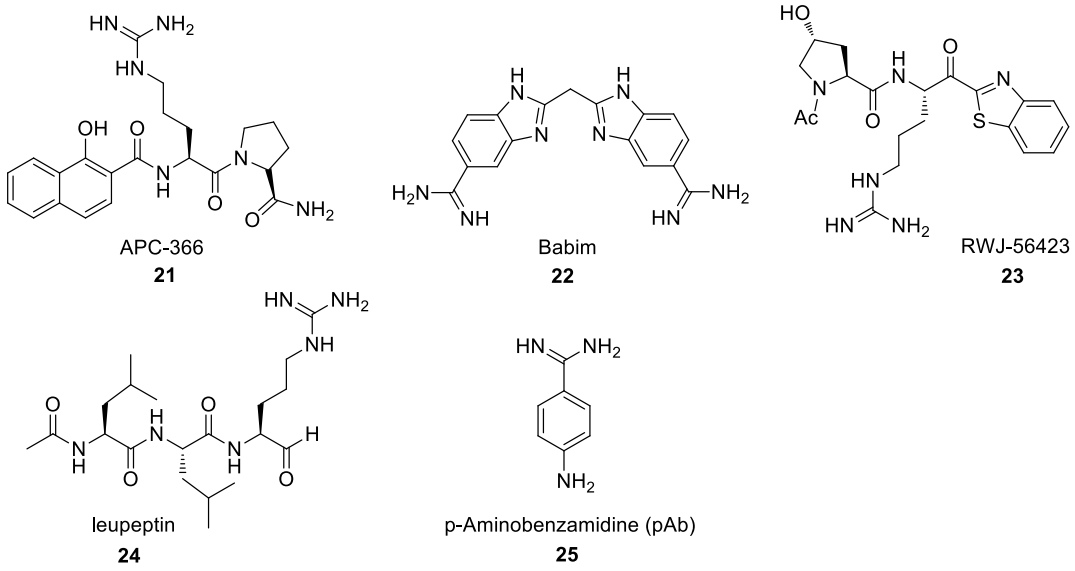

Figure 2.15 Chemical structures of monovalent inhibitors of β-tryptase.

The crystal structure of β-tryptase led to the design of new inhibitors, such as bivalent inhibitors. By playing around with the spacer length between two functional groups, this type of inhibitors can interact simultaneously with two active sites as they are relatively spatially close to each other within the central pore. This may allow the discovery of more potent and selective inhibitors by using the advantage of the multivalent effect by bridging two active sites.[106-108] For example, AMG-126737 (**26**) has been shown to be a potent (K_i = 90 nM) and selective dibasic inhibitor of tryptase to block the development of airway hyperrespinsiveness in allergen-challenged guinea pigs (Figure 2.16).[109] By testing different substitution positions of the amidine group and changing $–SO_2$ to –CO, an even more potent inhibitor (**27**) was discovered to inhibit tryptase by bridging two adjacent active sites with a K_i value lower than 0.01 nM.[110] This inhibitor also showed excellent

selectivity over other serine proteases such as trypsin and plasmin.

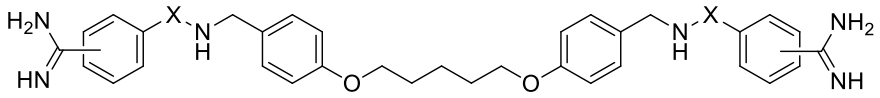

Figure 2.16 Chemical structures of bivalent inhibitors of β-tryptase.

APC-2095 (**28**) is an active site inhibitor of tryptase which showed not only high inhibition efficiency (K_i = 0.1 nM) but also good selectivity against other serine proteases (Figure 2.17).[108] It has shown to block late phase bronchoconstriction and airway hyper-responsiveness in allergic sheep and has been tested in phase II clinical trials for the treatment of both psoriasis and ulcerative colitis.[111] Another example is MOL-6131 (**29**), a reversible and competitive bivalent inhibitor of tryptase (K_i = 45 nM), which showed effects on airway inflammation and hyper-reactivity in a mouse model of asthma.[112] Dibasic inhibitors based on deketopiperazine templates and *m*-aminomethyl-phenylalanine as arginine mimetic were investigated by *Schaschke et al*.[91] By varying spacer length, compound (**30**) was found to span the distance between the active sites of two neighboring subunits of tryptase tetramer and thus inhibiting β-tryptase with a K_i = value of 10 nM. Based on the same scaffold, a combinatorial library of dibasic compounds featuring guanidine or amidine functional groups were designed to identify inhibitors of β-tryptase with a micromolar affinity.[113]

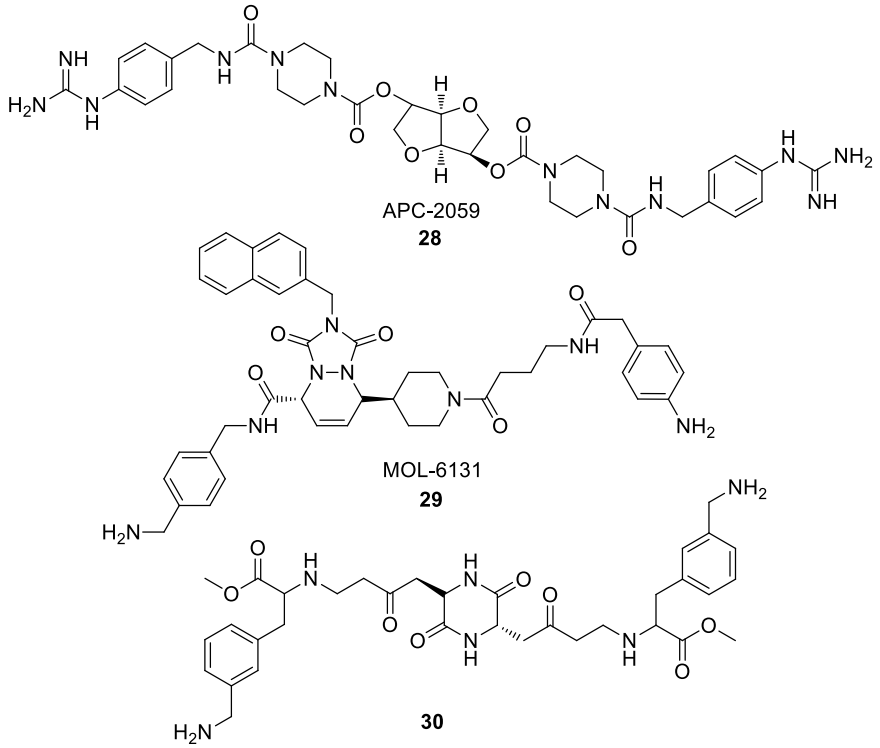

Figure 2.17 Chemical structures of bivalent inhibitors (**28**–**30**) of β-tryptase.

In addition to the bivalent inhibitors featuring flexible spacers, *Schaschke et al*. also reported an efficient inhibitor (**31**) based on the rigid cyclodextrin template to which two 3-(aminomethyl)benzenesulfonyl-glycine groups were attached.[92] The template has the appropriate size to bridge the space between two active sites of tryptase with 3-(aminomethyl)benzene as a functional group occupying the specific S1 subsites (Figure 2.18). It was shown to have a high inhibition efficiency to β-tryptase (K_i = 0.6 nM) and selectivity over other serine proteases such as trypsin (K_i = 4.8 μM) and thrombin (K_i > 160 μM).

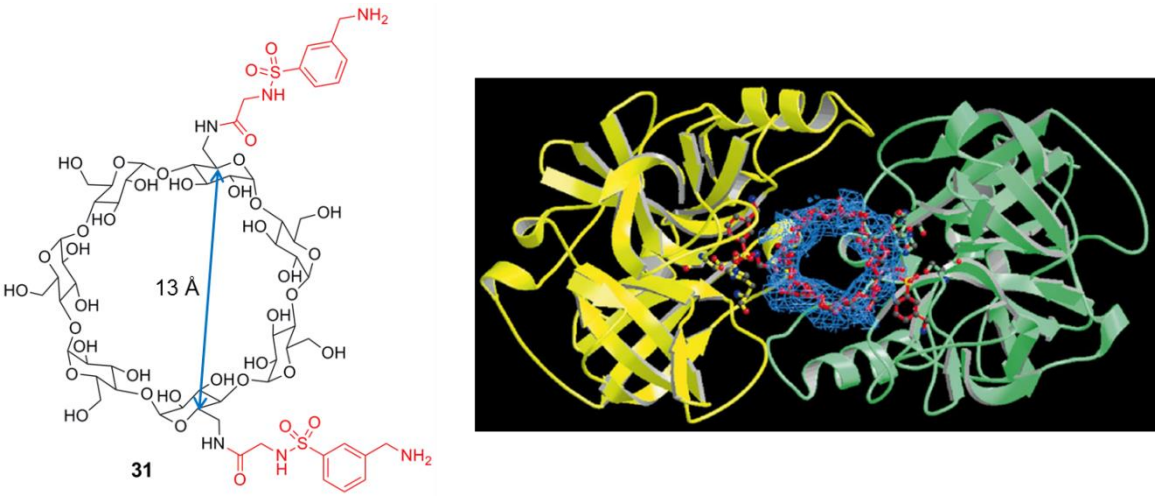

Figure 2.18 *Left:* Chemical structure of inhibitor (**31**) for β-tryptase based on β-cyclodextrin. The functional groups are colored red. *Right*: The x-ray structure of β-tryptase with the bivalent inhibitor **31**. It binds to the two shortest active sites of the tetramer. The two related tryptase subunits A and D (cf. Figure 2.12) are shown as green and yellow ribbons with the catalytic triad as stick and ball models. The inhibitor is shown in stick and ball representation in red color. *(The modeling image is reprinted with permission from N. Schaschke, G. Matschiner, F. Zettl, U. Marquardt, A. Bergner, W. Bode, C. P. Sommerhoff, L. Moroder, Chem. Biol.* ***2001****, 8, 313-327. Copyright 2001 Elsevier).*[92]

Leatherbarrow et al. reported a series of peptides based on the sequence SCTKSIPPQCY derived from the solvent exposed loop of the so-called Bowman-Birk inhibitor (BBI), which are potent inhibitors of chymotrypsin-like proteases but do not inhibit human β-tryptase. This type of tri-functional inhibitors can inhibit β-tryptase with a K_i value as low as 1 nM.[114]

Based on the natural product cyclotheonamide E4, which was modified by replacing the S1 ligand with basic β-homoamino acids derived from arginine and implementing a basic P3 residue that determines the extended substrate specificity of β-tryptase, a highly efficient and selective inhibitor (**32**) of β-tryptase was obtained with a K_i value of 7 nM (Figure 2.19).[115] Furthermore, by using the arginine mimic β-homoaminomethyl-phenylalanine as a privileged S1 ligand, compound (**33**) was shown to be a potent inhibitor of β-tryptase as well with a K_i value of 25 nM. It showed excellent selectivity over other serine proteases and stability in human plasma and serum.[116]

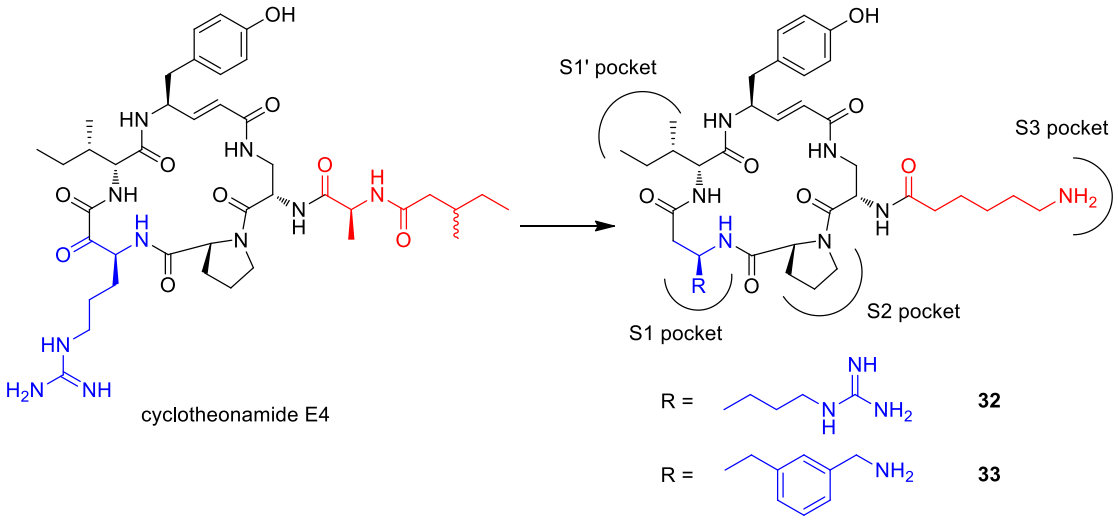

Figure 2.19 Chemical structures of cyclotheonamide E4 based inhibitors (**32**–**33**) of β-tryptase.

The above mentioned bivalent inhibitors of β-tryptase were all based on basic P1 groups which are favored by the acidic S1 pocket. Neutral P1 inhibitors have not been reported for β-tryptase, even though they have been identified for trypsin-like serine proteases containing Ala-190, such as factor Xa (fXa) and thrombin.[117-118] Recently, *Liang et al.* investigated whether dimeric inhibitors with two neutral P1 moieties from a known fXa inhibitor could offer potent inhibition of tryptase. The S1 pocket of β-tryptase is identical to that of fXa or thrombin except it contains Ser-190 instead of Ala-190. The mutation from Ala-190 to Ser-190 shrinks the binding space for inhibitor and decreases the hydrophobic interaction between the inhibitor and the residue. However, no detectable binding was obtained, which revealed the importance of Ala-190 for the binding of neutral P1 inhibitor and casted doubt on the possibility of developing neutral P1 inhibitors of β-tryptase.[119] This example clearly demonstrated the necessity of the basic P1 groups for the design of the efficient active site inhibitors of β-tryptase.

2.3.3 Protein Surface Binding Inhibitors

A new approach developed recently to inhibit the human β-tryptase is based on the binding to the surface of the protein. Most likely this type of inhibitors binds to the entrance of the negatively charged central pore of β-tryptase, blocking the access of the substrate to the active sites and thus preventing it from binding.

Calix[8]arene based receptors with different basic amino acids (Figure 2.20) were designed and synthesized for tryptase surface binding by *Cunsolo et al.*[120] The inhibitors have K_i values between 2 and 80 nM and had selectivity over trypsine, but the inhibition mode is unclear. On one hand, tryptase was indirectly inhibited due to the interaction of the inhibitor with heparin. On the other hand, competitive inhibition was also obtained. However, the exact binding site is still unknown. Only the surface interaction between the inhibitor and the acidic area close to the enzymatic active sites was proposed.

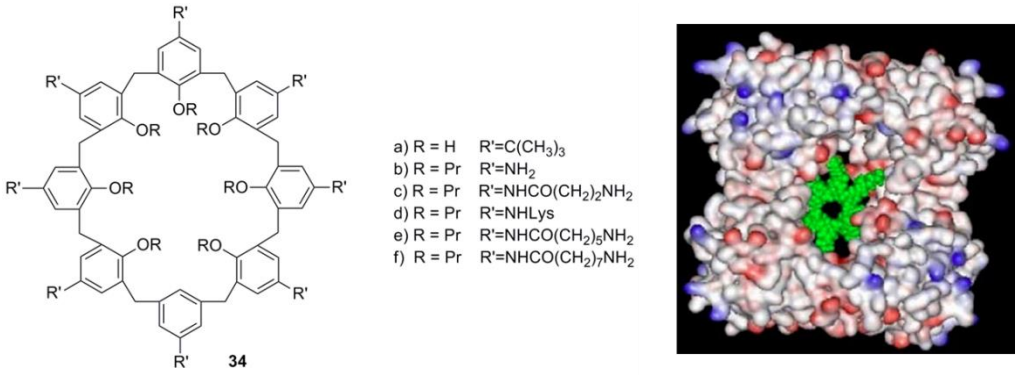

Figure 2.20 *Left:* Chemical structures of calix[8]arene based inhibitors (**34**) of β-tryptase. *Right:* Proposed representation for the complex between tryptase and inhibitor **34d** (green CPK model). *(The image of the proposed binding mode is reprinted with permission from T. Mecca, G. M. L. Consoli, C. Geraci, F. Cunsolo, Bioorg. Med. Chem.* ***2004****, 12, 5057-5062. Copyright 2004 Elsevier).*[120]

Schmuck et al. recently designed a type of ligand which can bind to the surface of the protein, close to the entrance of the central pore. Most likely this ligand acts as a 'molecular plug' upon binding, blocking the access to the active sites and thus preventing the substrate from binding.[13] To identify the most efficient ligands a focused combinatorial library of 216 tetravalent peptide ligands with four identical arms was designed (**1**, see page 3, figure 1.1). Six amino acids (Arg, Lys, Glu, Ala, Phe, Trp) were used in the variable positions to cover a wide range of characteristics, such as basic, acidic, aliphatic and aromatic properties. The most efficient ligands combined basic and aromatic amino acids in the arms and inhibit the enzyme with nanomolar affinity in a reversible and noncompetitive way. For example, the best ligand $(RWKG)_4$ (**35**) was shown to inhibit β-tryptase with a K_i value of 170 nM (Figure 2.21). Ligands with negative charges in their arms showed only weak or no inhibition confirming that binding to the negatively charged surface around the pore is crucial. Force field calculations confirmed that the ligands have indeed the correct molecular size to span the central pore upon protein surface binding even though no structural proof for this binding mode could be obtained.

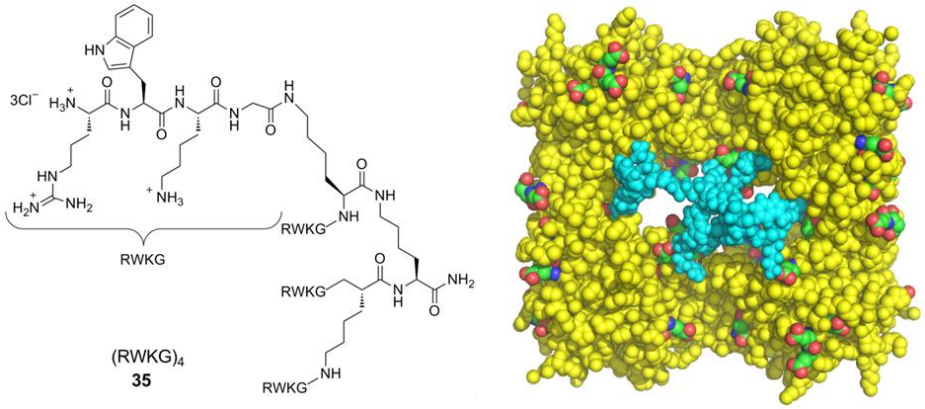

Figure 2.21 *Left:* Chemical structure of the best peptide inhibitor $(RWKG)_4$ (**35**) of β-tryptase obtained from the combinatorial library. *Right:* Force field calculations confirm that the ligand (**35**) can bind to the protein surface, closing the central pore and thus preventing the substrate from binding to the active sites.

2.4 Protein Surface Binding

In general, a protein has a folded conformation featuring a solvent-exposed (exterior) surface and a solvent-excluded (interior) surface (Figure 2.22).[121] Most often concave and well-defined enzyme active sites are situated at the interior of proteins, containing convergent functional groups that are shielded from solvents and solutes. Therefore, the corresponding highly functionalized small molecules can efficiently inhibit their action. By contrast, the exterior surfaces are flat and most often in direct contact with water and solutes. Functional groups on the protein exterior surface are in general divergent. In comparison to the well-defined pockets in the active sites of enzymes, exterior protein surfaces are more challenging targets due to the relatively large solvated surfaces (500-2000 $Å^2$). Most often protein binding areas are focused on critical hot spot of ca. 600 $Å^2$ size with a predominance of Try, Tyr and Arg residues as shown in Figure 2.22.[122] Hence, binding to the protein surface by designed molecules must account for the extensive solvation of the exterior surface of a protein, as well as the topology of the recognized surface.[123-125] Tight binding of protein surfaces based on non-covalent interactions requires the involvement of large surface areas and multiple points of functionality. Therefore, in order to achieve the sufficient binding affinity to protein surface, the multivalent interaction between the protein surface and the designed molecule is important and necessary. The advantages of the multivalency were described by *Wich* in his PhD thesis.[126]

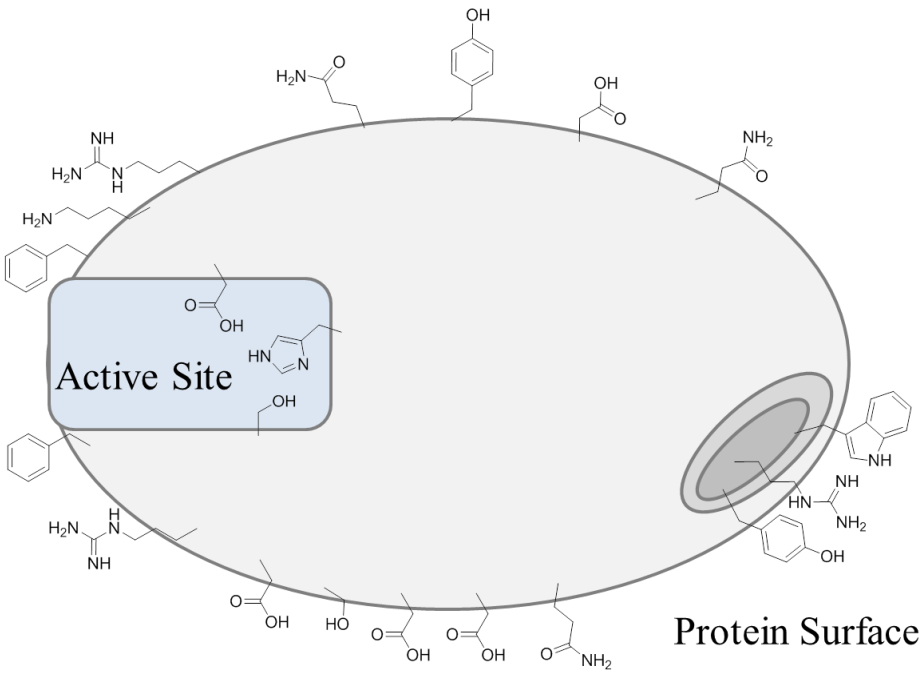

Figure 2.22 Schematic illustration of a protein (enzyme) interior, exterior, and hot spot.[121]

There are a number of biomolecules and synthetic ligands that can interact with the protein surface. Protein surface interactions contribute to study or disrupt protein-protein interactions which are of crucial importance in many biological processes, such as cellular communication, immune response, signal transduction, enzyme inhibitions, apoptosis, *etc*.[127-129] The protein surface interaction between yeast iso-1-cytochrome *c* and yeast cytochrome *c* peroxidase was one of the first examples illustrated by the crystallographic investigation.[130] Cytochrome *c* is a small heme protein with a highly basic surface (12 kDa, pI ≈ 10) and plays key roles in electron transfer and apoptosis. This crystal structure reveals that a specific electron transfer pathway occurred within this complex. The interaction areas are between a hydrophobic patch centered on the solvent exposed heme region of cytochrome *c* surrounded by a number of positively charged basic lysine and arginine residues and a complementary hydrophobic patch surrounded by negatively charged residues on the cytochrome *c* peroxidase (Figure 2.23, left). This conformation of the protein complex was observed in solution as well as determined by paramagnetic NMR.[131] Calorimetric data indicated that the binding depends on ionic strength, which is based on the structural information involving desolvation of charged residues to form salt bridges.[132] Another example is the interaction between the tumor suppressor p53 and the cellular oncoprotein MDM2 (also known as HDM2). They were found to form a negative feedback loop which contributes to limit the growth of the suppressing activity of p53.[133] The crystal structure of the transactivation domain of the protein p53 forms an amphipathic α-helix conformation, binding to a deep hydrophobic cleft on the MDM2 protein surface (Figure 2.23, right).[134] In particular, only three key residues (Phe-19, Trp-23 and Leu-26) of p53 are essential for binding by inserting deep into the MDM2 cleft due to the steric complementarity between the hydrophobic face of the p53 α-helix and the cleft of the MDM2.

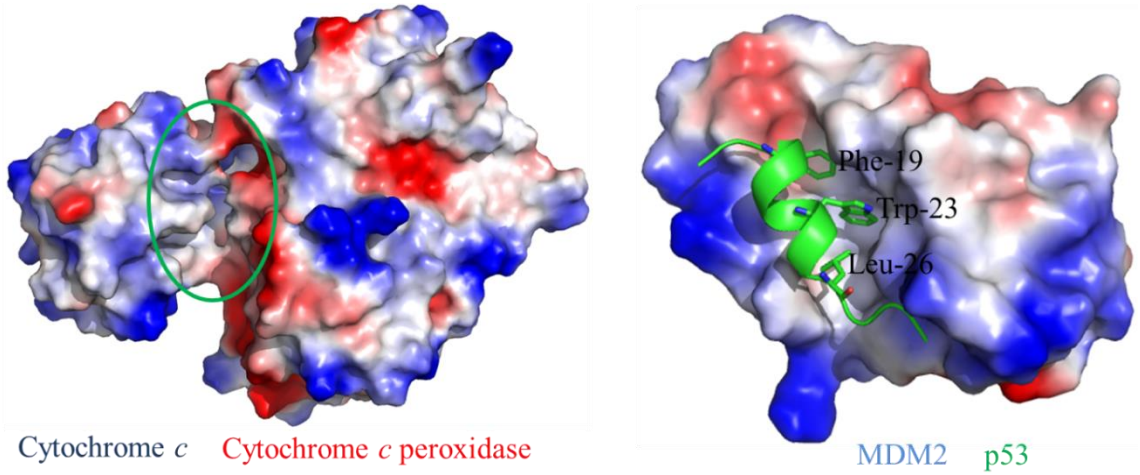

Figure 2.23 *Left:* The interaction between yeast iso-1-cytochrome *c* and yeast cytochrome *c* peroxidase with recognition domains highlighted by a green circle (PDB code: 2PCB). *Right:* The interaction of the MDM2 oncoprotein with the p53 tumor suppressor. The three key amino acid residues of p53 are shown as sticks. (PDB code: 1YCR).

Protein surface binding by artificial molecules that can lead to protein modification/modulation or the inhibition of protein-protein interaction has become an interest of current research in recent years.[135-136] In comparison to the recognition of proteins by biomolecules such as antibodies, recognition by synthetic molecules has higher chemical stability but lower selectivity and specificity. The key issue of the design of artificial molecules which can bind to a relatively large surface area of a protein is the development of supramolecular or multivalent ligands based on different scaffolding structures for the presentation of related binding functional groups in a specific orientation.[137-138] The design feature of ligand functionalities should match the hydrophobic and charged domains on the protein surface with complementary regions on the synthetic ligands. Most often so far the designed multivalent ligands were based on calixarene, porphyrin, G-quadruplex, anthracene, or gold nanoparticles as scaffolds and were developed by using both rational design and combinatorial approaches (Figure 2.24).

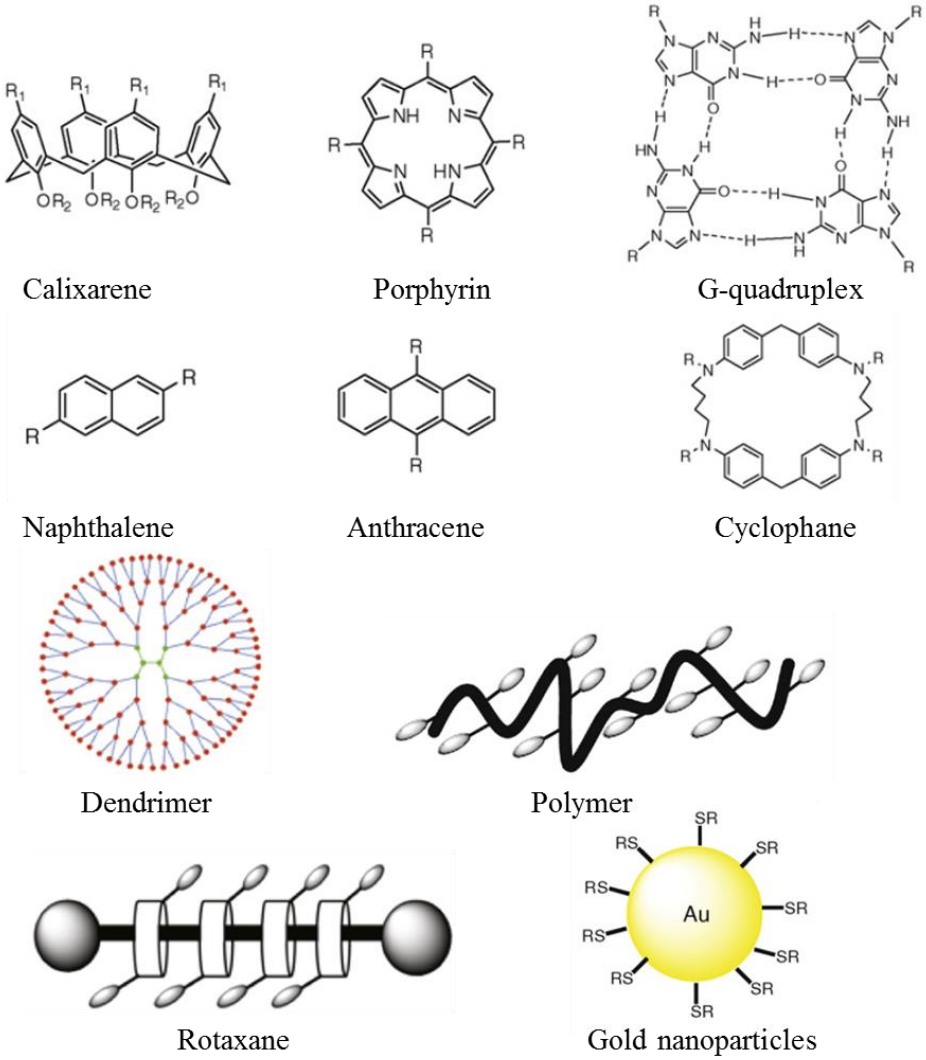

Figure 2.24 Schematic representation of the various multivalent scaffolds. *(Reprinted with permission from V. Martos, P. Castreño, J. Valero, J. de Mendoza, Curr. Opin. Chem. Biol.* ***2008****, 12, 698-706. Copyright 2008 Elsevier).*[137]

Calixarenes are cavity-shaped cyclic oligomers formed by formaldehyde with *p*-alkylphenols under alkaline conditions. The valence of these oligomers can vary from 1 to 8, depending on the reaction conditions. They have a semirigid cone structure with a hydrophobic cavity, a wider upper rim and a relative narrow lower rim. Calixarenes have been used as one of the most common scaffolds for preparing host molecules in host-guest chemistry due to their attractive architecture.[139-140] Their derivatives can bear a variety of functional groups for molecular recognition. In particular, water-soluble calixarene derivatives have great potential for binding to proteins or other biomolecules.[141-142]

For example, *Neri* and co-workers developed a surface recognition of tissue and microbial transglutaminases (tTG and mTG) by peptidocalix[4]arene diversomers. TG is an enzyme that catalyzes the posttranslational modification of proteins by transamidation of available glutamine residues.[143] Calix[4]arene was used as scaffold in a locked cone conformation, bearing tetrapeptide chains linked to the upper rim by their N-terminus. Derivatives bearing a Gly-Phe-Gly-Tyr tetrapeptide sequence (**36**) showed the most effective inhibition towards both TG isomers. Most likely these inhibitors bind to a specific surface of TG on a region noncomprising the enzyme active site (hot spot). Consequently, a conformational rearrangement of the active form occurred by the enzyme-inhibitor interaction which leads to the enzyme inhibition.[144] The same group also investigated the use of this calixarene scaffold to construct inhibitors (**37**) of histone deacetylase enzymes (HDACs) which play key role in removing acetyl groups from ε-N-acetyl lysine residues on histone, allowing histones to wrap DNA more tightly. Based on the measured affinity it was possible to show that the K_i values are strictly dependent on the size of the hydrophobic arms on the upper rim of calixarene. The most efficient candidate **37i** (IC_{50} = 0.14 μM) was shown to bind to the surface of the protein via occupying the hydrophobic pockets by the aromatic arms mainly through hydrophobic or aromatic stacking interactions, as well as interacting with the Zn^{II} ion at the bottom of the channel by carboxylate moieties (Figure 2.25, Right).[145]

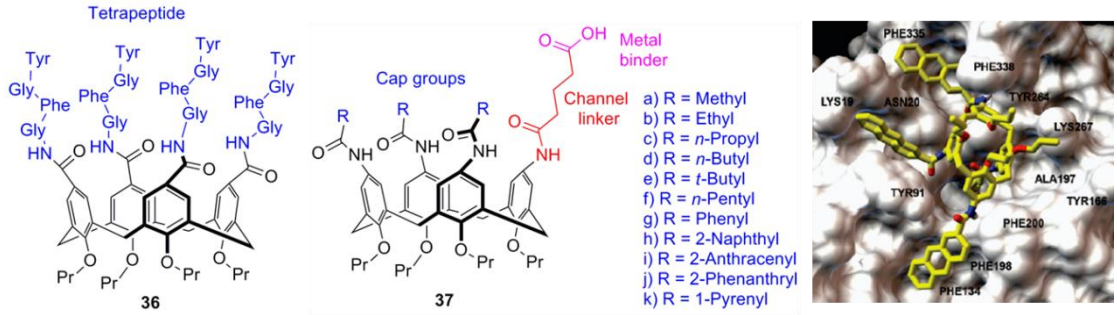

Figure 2.25 *Left:* Calixarene based receptor for transglutaminase inhibition.[144] *Middle:* Structural features of calixarene derivatives for HDAC inhibition. *Right:* 3D model of the putative binding mode of the most efficient candidate **37i** to the surface of the histone deacetylase like protein (HDLP, PDB code: 1C3R). *(The modeling image is reprinted with permission from M. G. Chini, S. Terracciano, R. Riccio, G. Bifulco, R. Ciao, C. Gaeta, F. Troisi, P. Neri, Org. Lett.* ***2010****, 12, 5382-5385. Copyright 2010 American Chemical Society).*[145]

Hamilton et al. reported a synthetic protein surface binding ligand (**38**) as an antibody mimic bearing four peptide loops linked to a central core of a calix[4]arene scaffold (Figure 2.26). The loops contained negatively charged peptide sequence Gly-Asp-Gly-Asp with a prepared surface area of approximately 450 $Å^2$ to recognize the cationic surface of the protein. The ligand showed a competitive inhibition of the serine protease α-chymotrypsin with a K_i value of 0.81 μM by binding close to the active site cleft of the enzyme and blocking the access of the substrate. It showed slow binding kinetics in an analogous manner to natural protein proteinase inhibitors.[146] Furthermore, by binding to the exterior surface of chymotrypsin, it was able to disrupt the interaction between the serine protease and its proteinaceous inhibitors, particularly in blocking the chymotrypsin-soybean trypsin inhibitor complex.[147] This ligand also showed strong binding to the complementary cationic regions on the surface of cytochrome *c*, forming a 1:1 complex with a binding constant of 3×10^8 M^{-1}. The surface binding to cytochrome *c* is very efficient so that it could disrupt the protein-protein interactions and displace its natural high affinity protein partner, cytochrome *c* peroxidase (see Figure 2.23), which indicated that it binds close to its heme region as its natural protein partner. The ligand could inhibit the reduction of the Fe (III)-cytochrome *c* by ascorbate by binding to the protein surface and preventing the approach of ascorbate to the heme edge.[148-149]

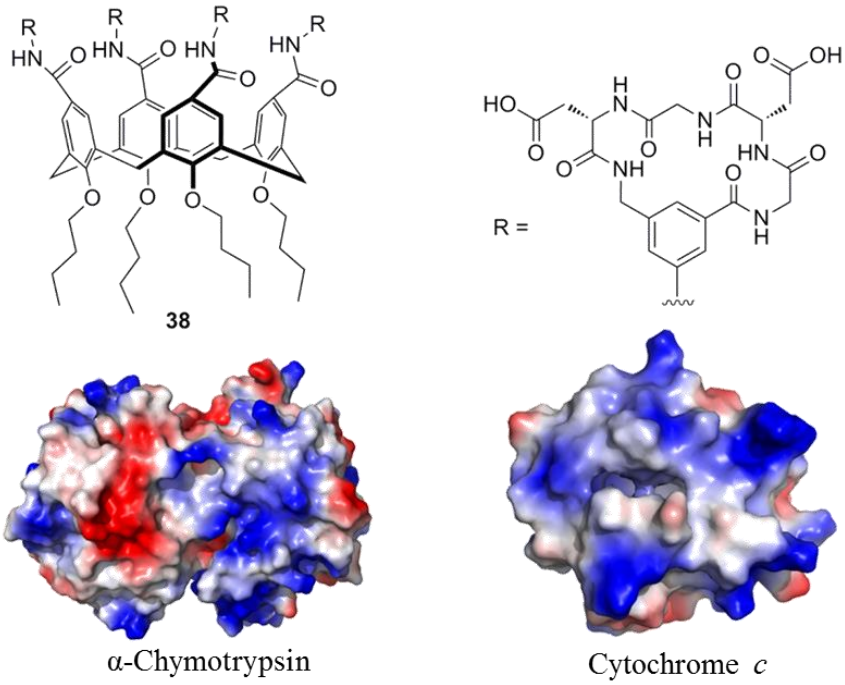

Figure 2.26 *Top:* Artificial receptor base on calix[4]arene scaffold for the recognition of protein surface. *Bottom:* Presentation of protein surfaces of α-chymotrypsin and cytochrome *c*.

Giralt and *Mendoza* recently designed a ligand (**39**) based on a calix[4]arene scaffold with four cationic guanidiniomethyl groups at the upper rim and hydrophobic loops at the lower rim. It can stabilize the tetrameric structure of the tumor suppressor protein p53 by

fitting into the hydrophobic clefts between two of the monomers at each side of the protein through both electrostatic and hydrophobic interactions. Two molecules of this calixarene can bind to the protein sequentially in a cooperative manner with dissociation constants of $K_{D1} \approx 130$ μM and $K_{D2} \approx 65$ μM for both binding events (Figure 2.27).[150]

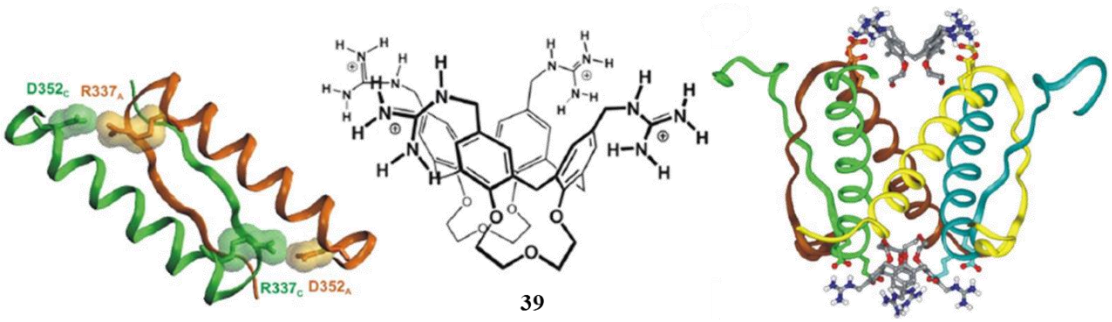

Figure 2.27 *Left:* Primary p53 dimer showing the major Arg-Asp interactions that stabilize the tetramer. *Middle:* Structure of calixarene based ligand **39** for tetramerization domain of p53. *Right:* The 2:1 complex between ligand **39** and p53 is formed through electrostatic and hydrophobic interactions. *(Reprinted with permission from S. Gordo, V. Martos, E. Santos, M. Menendez, C. Bo, E. Giralt, J. de Mendoza, Proc. Natl. Acad. Sci. USA **2008**, 105, 16426-16431. Copyright 2008 National Academy of Sciences, U.S.A.).*[150]

A recently reported crystal structure of a calixarene-protein complex by *Crowley* and co-workers provides solid evidence and allows a better understanding of the interaction between ligand and a protein surface. The complex formation between the anionic tetra-sulfonato-calix[4]arene and cytochrome *c* was investigated by using both NMR spectroscopy and x-ray crystallography. The crystal structure revealed that the ligand explores several binding sites on large surfaces of cytochrome *c* through weakly non-covalent interactions, each of which involves one lysine side chain trapped inside the cavity of calixarene, and one or more neighboring lysine residues providing additional electrostatic interactions. This study provided important structural information on a typical multivalent ligand that does not bind to the active site, but to the protein exterior surface with hydrophobic or charged areas. It is a valuable model for future scaffold-based design of artificial ligands targeting protein surfaces.[151]

Porphyrins are also very attractive for preparation of receptors for protein surface recognition because of their unique structural features, such as rigid structures, multifunctionality, diagnostic photophysical properties, easy synthetic manipulation, and large aromatic surfaces allowing hydrophobic and π-π stacking interactions. The charge, hydrophobicity, size, and symmetry of the functionalities at the periphery of porphyrin derivatives can be used as binding characteristics to target various proteins. Most often porphyrin derivatives are highly fluorescent and show changes in emission intensity upon binding to the target protein. This fluorescent readout has been used for the detection of the protein surface binding receptors.

Cytochrome *c* is an attractive target because the unpaired electrons in the ferro form

could quench fluorescence upon binding to the receptor. *Hamilton et al.* have designed receptors based on a tetraphenylporphyrin scaffold bearing various anionic and hydrophobic groups at the periphery for the surface recognition of cytochrome *c*. The tetraphenylporphyrin scaffold could closely match the arrangement of the hydrophobic and basic domain in the heme edge surface of cytochrome *c*. The derivative bearing Tyr-Asp residues (**40**), which contain a combination of eight phenyl groups and eight carboxylate groups (Figure 2.28), was identified to be the strongest receptor for cytochrome *c* with a dissociation constant (K_D) of 20 nM.[152] Metalloporphyrin derivatives have also been investigated by this group for complexation with cytochrome *c*, which resulted in selective denaturation and acceleration of proteolysis with dimeric Cu (II)-porphyrins, and proteolysis of cytochrome *c* by trypsin.[153-154]

Several other metal-containing proteins with unpaired electrons could also quench the porphyrin fluorescence upon binding due to the proximity of the metal to the porphyrin ring in the complex. This has been used for the design of an array of porphyrin derivatives for protein fingerprinting. For example, *Hamilton et al.* developed an porphyrin array system which can detect various metal-containing proteins based on their distinct fluorescent quenching patterns upon binding to protein surfaces, providing a characteristic fingerprint for a specific protein.[155] Furthermore, a more comprehensive identification of both metal- and nonmetal-containing proteins and protein mixtures has been demonstrated by using porphyrin array combined with pattern recognition techniques.[156]

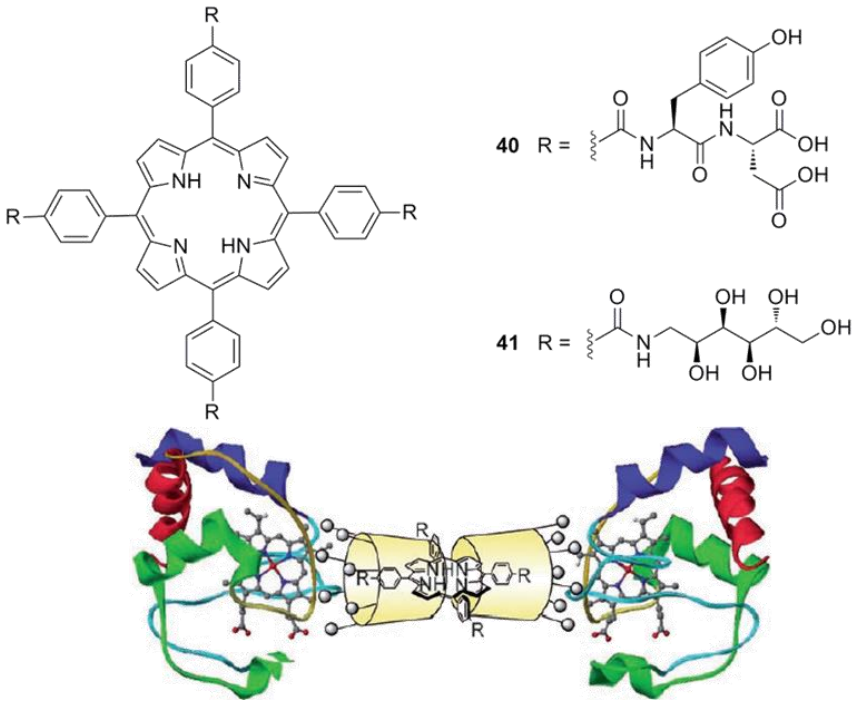

Figure 2.28 *Top:* Porphyrin based receptors for the surface binding of cytochrome *c*. *Bottom:* A structure of the ternary complex of cytochrome *c*, CDM-β-CD, and TGPP. *(The bottom image is reprinted with permission from K. Kano, Y. Ishida, Angew. Chem. Int. Ed.* ***2007****, 46, 727-730. Copyright 2007 John Wiley and Sons).*[157]

Porphyrin based compounds could also be used as a guest molecule which is not involved in the direct binding to the protein surface, but plays a key role in selectively controlling the protein functions. For example, *Kano et al.* recently developed a ternary complex consisting of a target protein, a supramolecular receptor and an additional guest that is bound to the receptor. This supramolecular complex consists of a tetrakis(4-glucaminocarbonylphenyl) porphyrin (**41**), tethered by two polyanionic heptakis(6-*O*-carboxymethyl-2,3-di-*O*-methyl)-β-cyclodextrin (CDM-β-CD), which could recognize the surface of cytochrome *c* (Figure 2.28, bottom) through the electrostatic interactions.[157]

A smaller aromatic compound anthracene was also used as a fluorescent hydrophobic scaffold for the design of receptors for protein surface binding by *Hamilton et al.* The anthracene core was functionalized by hydrophobic and acidic groups for the hydrophobic and electrostatic interactions with the surface of cytochrome *c* and lysozyme. Receptors **42** (Figure 2.29) with eight appropriately spaced carboxylate groups showed efficient binding in a cooperative manner over a large surface area. Receptors **42a** and **42b** bind to cytochrome *c* with low micromolar affinity of 0.66 μM and 0.30 μM, respectively. Further investigations of **42a** revealed that the binding to the surface of cytochrome *c* and lysozyme is selective against some other proteins, like cytochrome c551, myoglobin, α-lactalbumin which showed an order of magnitude lower affinity.[158]

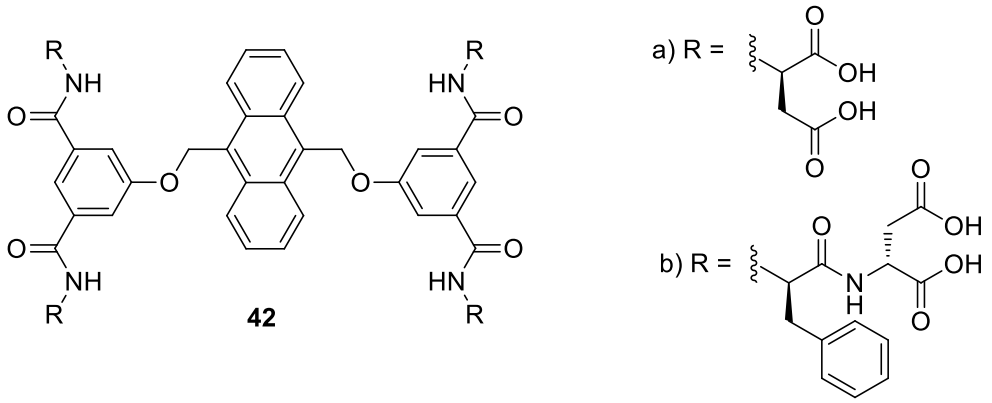

Figure 2.29 Structures of receptors based on anthracene scaffold for the surface recognition of cytochrome *c*.

Recently, molecular self-assembly based on non-covalent interactions by small molecular components was used to generate versatile scaffolds providing sufficient multivalency and surface area for protein surface recognition. *Hamilton et al.* have reported that functionalized G-quartets (Figure 2.30) are capable of binding to the surface of cytochrome *c*. G-quardruplexes are formed from the π stacking of G-quartets by intra- or inter-molecular *Hoogsteen* base-pair associations in parallel or antiparallel orientations. The 5′-end of the assembled G-quartet was functionalized with peptide binding groups that can bind to both hydrophobic patch and acidic residues near the heme edge surface of

cytochrome *c* as used for the porphyrin derivative (**40**, see Figure 2.28). The oligoanionic-functionalized G-quadruplex (**43**) was shown to bind to the protein surface through hydrophobic and electrostatic interactions, leading to the denaturation and acceleration of proteolysis of cytochrome *c*. The binding of **43** to cytochrome *c* was demonstrated to be selective when compared to RNAseA, α-lactalbumin and cytochrome c551.[159]

Another receptor (**44**) based on a G-quadruplex scaffold with peptide loops functionalized on the 5′-end of the assembled G-quartet for the protein surface binding was developed by the same group as well. Receptor **44** displayed efficient inhibition of α-chymotrypsin with the apparent dissociation constant (K_i^{app}) of 0.33 μM. It is at least four times more potent than the earlier reported calixarene derivative **38** (see Figure 2.26, K_i^{app} = 1.4 μM) bearing the same peptide loops. The improvement of the efficiency might be due to the flexible alkyl linker to allow the delivery of the peptide loops to a larger protein surface area and the additional electrostatic interaction contributed by the negatively charged oligophosphate scaffold.[160]

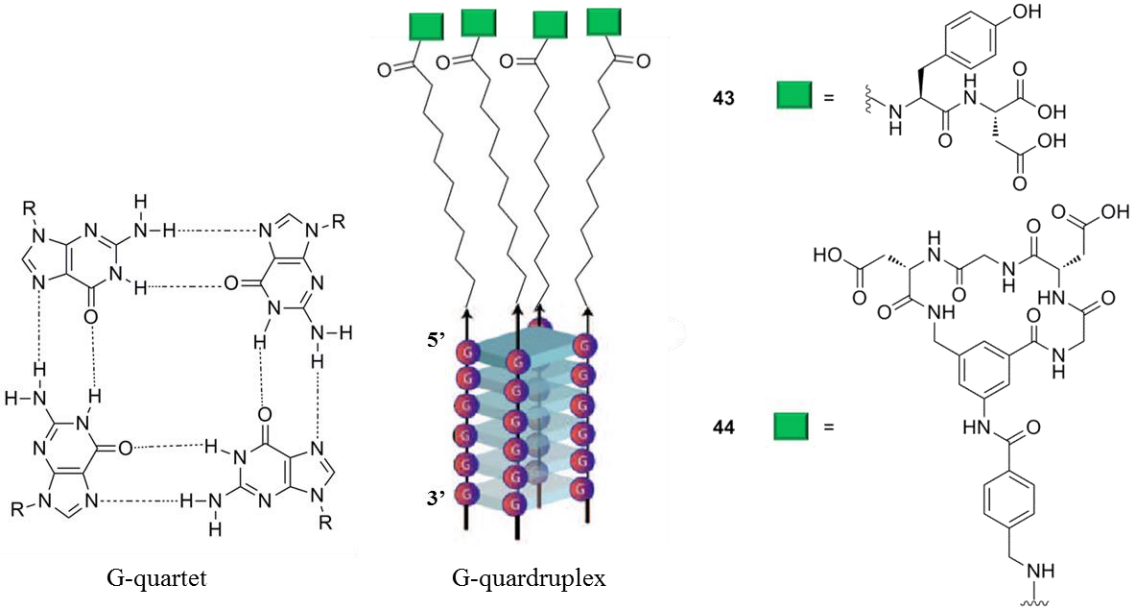

Figure 2.30 Representation of the structure of G-quartet and the functionalized parallel G-quardruplex with different artificial fragments for the self-assembly. Functionalized G-quardruplexes **43** and **44** are used for the surface recognition of cytochrome *c* and α-chymotrypsin, respectively.

Several alternative scaffolds such as polymers,[161] ruthenium trisbipyridine complexes,[162-163] and gold nanoparticles[164] have been used to develop efficient protein surface binders. The latter scaffold is promising due to their large surface area, the tunable size (1.5 nm to > 10 nm, comparable to proteins),[165] the ability to cover the surface with a wide range of desirable functionalities,[166] and the scaffolding properties for preparing the multivalent receptors.[167] Furthermore, the inherent physical properties such as optical, electronic and magnetic properties of the metal core of nanoparticles provide unique

opportunities to create biosensors, diagnostic agents and to control the interactions of the surface.[168] Monolayer-protected clusters (MPCs) and mixed monolayer-protected clusters (MMPCs) have been used as promising candidates for the creation of bimolecular receptors.[169-171] Further, MPCs and MMPCs using functional organic groups on the nanoparticle surface can be used as multivalent recognition elements for targeting the surfaces of biomolecules, allowing comparisons of biological complex formation such as protein-protein interactions based on surface complementarity.[172]

Rotello and co-workers have demonstrated that functionalized gold nanoparticles have great potential for binding to the protein surfaces. For example, they used mercaptoundecanoic acid (MUA) functionalized gold nanoparticles (**45**, Figure 2.31) to bind to α-chymotrypsin (ChT) by electrostatic interactions between the anionic particle surface and the cationic 'hot spot' around the ChT active site, resulting in the inhibition of enzyme activity through a two-step mechanism with a fast reversible inhibition followed by a slower irreversible denaturation process. The highly efficient binding led to a K_i^{app} of approximately 10 nM and a binding stoichiometry of five protein molecules to one nanoparticle.[173] Here the molar concentration of gold nanoparticles can be calculated by expressing the nanoparticles in moles. The volume of a particle can be predicted from its size by assuming it as a sphere. By using density equivalent to that of bulk gold (19.3 g/cm^3), an average particle mass can be calculated, as well as the molar mass. Then the molar concentration can be calculated from the number of moles and the volume.[174] The molar concentration is not often used because most particles have size distributions and only using the mean size for calculating the molar mass does not really reflect the nature of the colloids. The denaturation of ChT at the interface was ascribed to the hydrophobic interactions with the alkyl chains of the monolayer. A certain level of selectivity was revealed through this electrostatic complementarity, as elastase, β-galactosidase (β-Gal) and cellular retinoic acid binding protein showed no significant interaction with MMPC **45**. Importantly in their subsequent studies the binding of MMPC **45** to ChT was found to be tuned by the ionic strength of the solution due to the nature of electrostatic interactions.[175] Further efforts were put to disrupt this irreversible inhibition of ChT through the modification of the nanoparticle surface using cationic surfactants. The release of the ChT molecules from the nanoparticle surface with up to 50 % restoration of their activity were demonstrated by using DLS and enzyme activity assays. Two prevailing mechanisms by which this recovery is accomplished were illustrated based on different surfactants. The thiol- and hydroxyl-teminated surfactants directly modify the monolayer by intercalation and/or chain displacement resulting in diminishing the surface charge and release of the protein. Alkyl surfactant could liberate the protein by the formation of a bilayer-type structure, as indicated by the approximately 4.5 nm increase in hydrodynamic radius (Figure 2.31).[176]

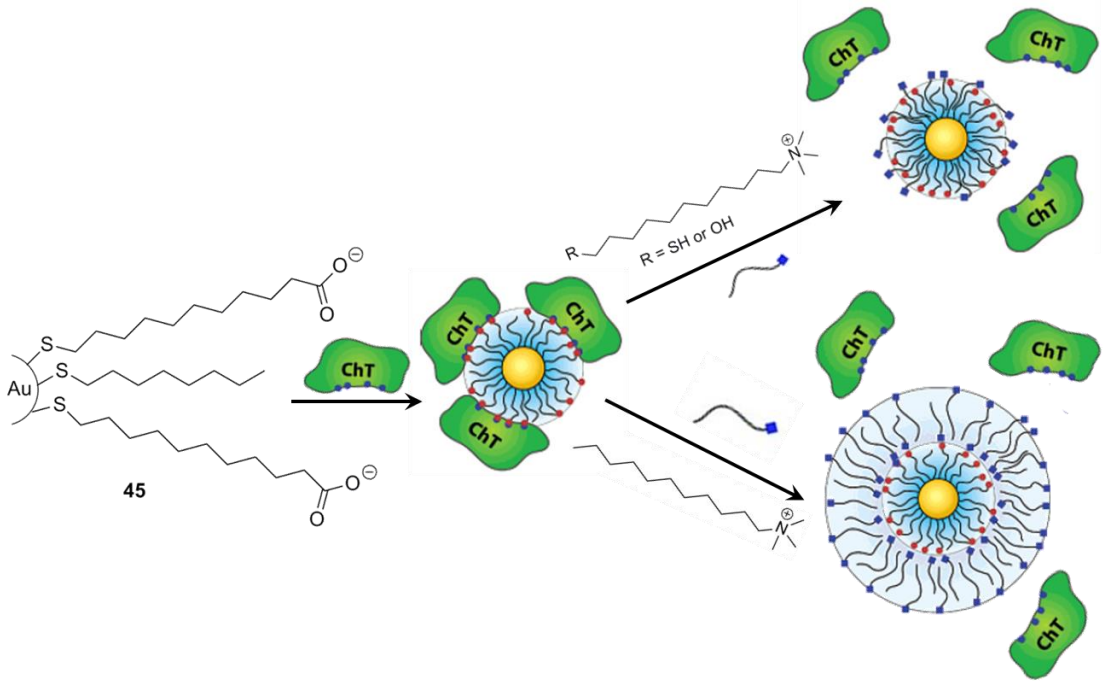

Figure 2.31 Schematic representation of ChT surface binding by MMPC **45** and monolayer modification upon addition of various surfactants, leading to the release of ChT from the surface of MMPC. *(Reprinted with permission from N. O. Fischer, A. Verma, C. M. Goodman, J. M. Simard, V. M. Rotello, J. Am. Chem. Soc.* ***2003****, 125, 13387-13391. Copyright 2003 American Chemical Society).*[176]

The example described above revealed that MMPCs can be used as an effective tool for the modification/modulation of enzyme activity. The interaction of ChT with MMPC **45** resulted in protein denaturation. However, the native structure of a protein is required to retain upon binding in many biological applications such as *in vivo* protein delivery and *in vitro* enzyme stabilization. To achieve this goal, oligo(ethylene glycol) (OEG) was often introduced as spacer between thioalkyl chain and the terminal functionality to prevent both nonspecific binding to protein surface and denaturation by shielding of the hydrophobic interior of the monolayer from the protein surface.[177] Water soluble CdSe nanoparticles **46** and **47** featuring OEG spacers were fabricated by *Rotello* and co-workers to improve the stability of ChT at the interface of nanoparticles (Figure 2.32). Nanoparticles containing the carboxylate-terminated ligands (**46**) were demonstrated to bind to the protein surface through spatial blocking of the active site via electrostatic interactions, resulting in a reversible inhibition without protein denaturation. Circular dichroism (CD) and fluorescence studies showed that the structure of ChT upon binding to the nanoparticles is retained. The enzyme activity can be completely restored through disruption of the electrostatic interactions with an increase in ionic strength of the solution. In contrast to the complexation between anionic **46** and ChT, no interaction was observed with **47** which terminated with hydroxyl groups. This study demonstrated that both protein activity and structure can be modulated by functionalized nanoparticles.[178]

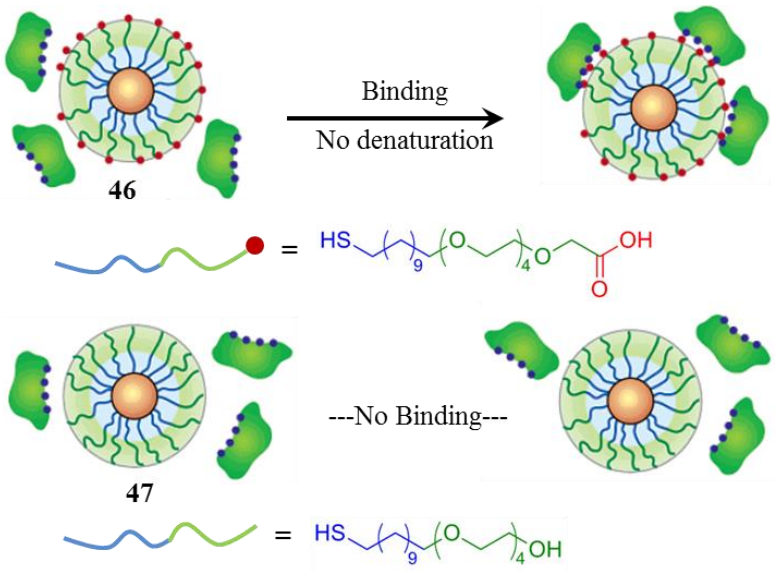

Figure 2.32 Schematic depiction of control of ChT structure and function through protein surface binding by CdSe nanoparticles **46** and **47**. *(Reprinted with permission from R. Hong, N. O. Fischer, A. Verma, C. M. Goodman, T. Emrick, V. M. Rotello, J. Am. Chem. Soc.* ***2004****, 126, 739-743. Copyright 2004 American Chemical Society).*[178]

Further studies to tune the interaction and structure of protein upon the binding of functionalized nanoparticles were investigated by using more elaborate monolayers. For example, *Rotello* and co-workers reported that functionalized gold nanoparticles with different surface charges can bind selectively to cytochrome c or cytochrome c peroxidase, thus disrupting the protein-protein interaction.[179] They also systematically investigated the interaction of protein surfaces with a series of amino acid-functionalized gold nanoparticles. Both electrostatic and hydrophobic interactions between the hydrophobic patches of receptors and protein were shown to contribute to the complex stability. ITC measurements revealed that the enthalpy and entropy changes for the complex formation depend on the functionality of nanoparticles and the surface characteristics of proteins, e.g. distributions of charged and hydrophobic residues on the protein surface.[180-181]

Array-based sensing, the so-called "chemical nose/tongue" strategies have been successfully applied for protein detections, such as the use of porphyrins as described above. It uses selective interactions with analytes to generate patterns that can be used for identifying different targets, as well as the analysis of changes in complex mixtures. Recently, *Rotello et al.* have developed a protein sensor array using chemical nose technology. The sensor array was generated using six cationic gold nanoparticles (**48**) featuring different ligand structures and a highly fluorescent anionic poly(p-phenyleneethynylene) (PPE) polymer PPE-CO_2 as a fluorescence indicator. These nanoparticles (**48**) were used as both selective binding elements and fluorescence quenchers for the polymer. The binding of the anionic polymer to the cationic surface of nanoparticles through electrostatic interactions resulted in fluorescence quenching of the

polymer (fluorescence "OFF") through energy transfer. The subsequent addition of proteins displaced the polymer bounded to the surface of the gold nanoparticles, leading to the fluorescence recovery of the polymer (fluorescence "ON"). A fingerprint fluorescence response pattern for individual proteins was then generated based on the different protein-nanoparticle interactions (Figure 2.33) that was characterized using linear discriminate analysis (LDA).[182] By using the same strategy, they reported a sensor generated by using arrays of gold nanoparticle and green fluorescent protein (GFP) to detect and identify proteins in both buffer and human serum. Distinct and reproducible fluorescence response patterns were obtained from five serum proteins including human serum albumin, immunoglobulin G, transferrin, fibrinogen and α-antitrypsin with high sensitivity (500 nM).[183]

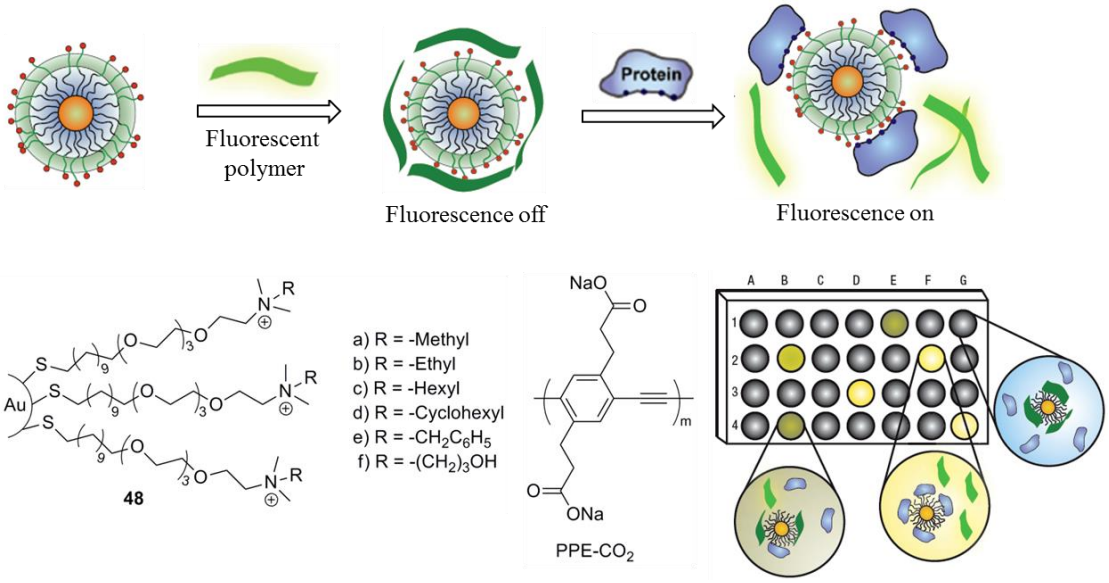

Figure 2.33 Schematic representation of 'chemical nose' sensor array based on gold nanoparticle-fluorescent polymer conjugates. *Top*: The competitive binding between protein and the quenched gold nanoparticle-polymer complexes leads to the restoration of fluorescence. *Bottom*: The combination of an array of sensors generates fingerprint response patterns for individual proteins through different release of fluorescent polymers from nanoparticle surfaces. *(Reprinted with permission from C. C. You, O. R. Miranda, B. Gider, P. S. Ghosh, I. B. Kim, B. Erdogan, S. A. Krovi, U. H. F. Bunz, V. M. Rotello, Nat. Nanotechnol.* ***2007****, 2, 318-323. Copyright 2007 Nature Publishing Group).*[182]

Rotello et al. have also reported an enzyme-nanoparticle sensor array for detecting proteins in which the sensitivity is amplified via enzymatic catalysis. In this approach, cationic gold nanoparticles (**49**) can bind to the surface of β-galactosidase (β-Gal) through electrostatic interaction, resulting in the inhibition of the enzyme activity. The release of β-Gal from gold nanoparticle surface with restoration of their enzymatic activity was observed upon addition of analyte proteins through competitive binding, providing an amplified readout of the binding event (Figure 2.34). The enzyme-amplified array sensing approach increased the sensitivity of the array, allowing the detection of a range of

biomedical relevant proteins at a concentration of 1 nM in both phosphate buffer and desalted human urine.[184] By using a similar strategy, a colorimetric test-strip sensor was developed for identifying E. coli with high sensitivity (10^4 bacteria/mL).[185]

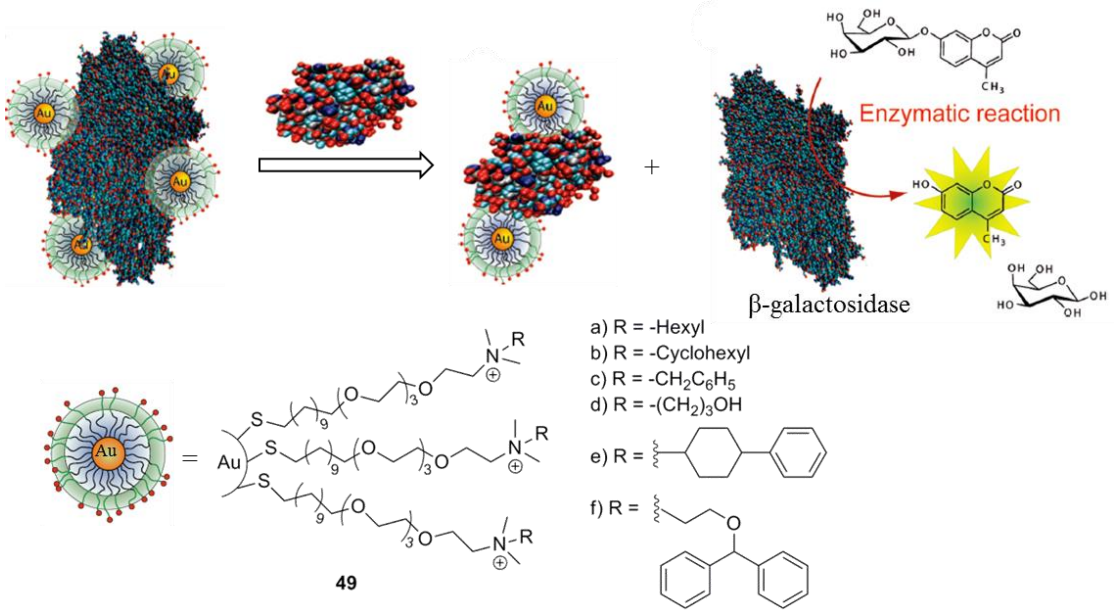

Figure 2.34 Schematic representation of sensor system comprised of β-galactosidase and cationic gold nanoparticles. β-Gal is displaced by protein analytes, restoring the enzyme catalytic activity toward the fluorogenic substrate 4-methylumbelliferyl-β-D-galactopyranoside. *(Reprinted with permission from O. R. Miranda, H. T. Chen, C. C. You, D. E. Mortenson, X. C. Yang, U. H. F. Bunz, V. M. Rotello, J. Am. Chem. Soc.* ***2010****, 132, 5285-5289. Copyright 2010 American Chemical Society).*[184]

The above examples illustrate the successful strategies in the design of synthetic small molecules and functionalized nanoparticles that have potentials for the protein surface recognition. It is well established that multivalent interactions are essential to achieve high affinity protein surface binding with some selectivity. Protein surface binding is often driven by a combination of electrostatic and hydrophobic or aromatic interactions by multivalent ligands based on a variety of scaffolds. The scaffolds play a key role in providing a variety of functionalities in a specific geometrical configuration and large surface area to complement the surface characteristics. For example, gold nanoparticles have been demonstrated to be attractive scaffolds providing large surface area and easy access to the attachment of different functional groups. However, even though ligand multivalency can provide high affinity to the target protein, selectively binding to a specific protein is still difficult to achieve. The development of new scaffolds and recognition elements to provide the multivalent, complementary interaction with the target protein is still of current interest. The selection of efficient binding elements and scaffolds simultaneously to provide efficient recognition can be achieved with less effort by using a new approach-dynamic combinatorial chemistry. The following chapter will present the principles and applications of this approach.

2.5 Dynamic Combinatorial Chemistry

Dynamic combinatorial chemistry is a concept that developed in the mid-1990s.[186-189] It uses reversible covalent or non-covalent interactions between a set of building blocks to generate a mixture of all possible combinations of the available components under thermodynamic control. It is assumed that all the components in the mixture continuously interconvert. The composition of this mixture at equilibrium is referred to as a dynamic combinatorial library (DCL). The thermodynamic nature of DCL allows changes in the library composition upon external stimuli. It can respond to various external influences including the change of pH, temperature, pressure, concentration and addition of a guest molecule or template, which can drive the constituents to reorganize to reach the minimal total free energy of the system under the new conditions. Chemical template was the most used stimuli for the identification of receptors or ligands in DCLs. By adding a target to the DCL, the composition of the DCL will adjust to form good binders for the target to minimize the free energy of the overall system, resulting in the selection and amplification of the strong binding compounds at the expense of the weak ones.[190-191]

In comparison with traditional combinatorial chemistry, dynamic combinatorial chemistry has several unique features.[192-193] As depicted in Figure 2.35, the reversibility of the formation of library constituents is an essential feature. It allows a continuous interchange of building blocks between all possible constituents in the library. Whereas traditional combinatorial chemistry is static as the library mixture consists of non-interconverting library members. The composition of a DCL is governed by thermodynamics rather than kinetics, which give it the access to respond to external influences. The dynamic process is conducted in the presence of the target, leading to the shift of the equilibrium towards formation of library members which can strongly bind to the target. Thus, the desired compounds are amplified in the library mixture at the expense of undesired ones that contain the same building blocks. Furthermore, the amplification of the desired compounds can be efficient enough to allow isolation of the molecule directly from the library. In contrast, the members of traditional combinatorial library are constructed by synthesis with a defined variety of components. The composition of the library is fixed and the addition of a target will not lead to any rearrangement of molecular fragments into more favorable library members. Additionally, complex topologies and sometimes unpredictable structures can be obtained from DCL by the self-assembly of building blocks around a target molecule or a template. In addition to the differences in composition, both approaches also have different requirements on screening of the library members. A traditional combinatorial library often requires high throughput screening (HTS) method due to the large number of individual library members. Whereas the library members of a DCL can be reduced to a few or ideally a single one, allowing easily identification of the active compounds.

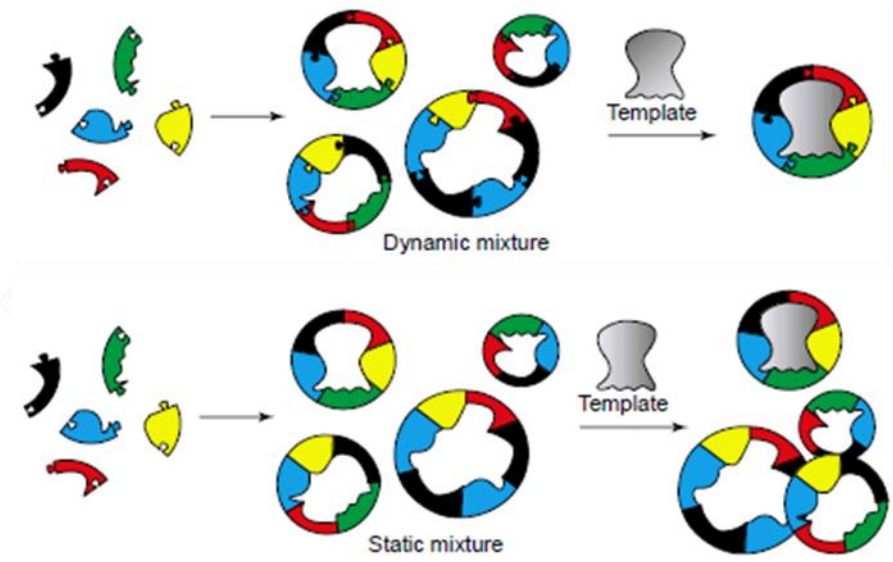

Figure 2.35 Schematic illustrations of the principles of dynamic combinatorial chemistry (*top*) and traditional combinatorial chemistry (*bottom*). *(Reprinted with permission from S. Otto, R. L. E. Furlan, J. K. M. Sanders, Drug Discovery Today **2002**, 7, 117-125. Copyright 2002 Elsevier).*[193]

Besides the described advantage of dynamic combinatorial chemistry, some limitations should be considered as well when preparing the dynamic combinatorial libraries. The most important constraint is that every single building block and library member should be sufficiently soluble during the equilibration. The insolubility of one or more components in the library will affect all members of the library that contain any of the involved building blocks. This is because the re-dissolving rate of the precipitated compound is very often slow enough to effectively trap it in the solid form, thus resulting in an equilibrium shift towards this kinetic trap which leads to wrong result. Furthermore, the mandatory use of reversible linkage between building blocks is also a limitation, as the number of chemical reactions that are appropriate to use for the construction of DCLs is limited. In addition, in contrast to traditional combinatorial libraries where all chemical bonds are formed fixed and unaffected by subsequent reactions, the control of the DCL is difficult due to the reversible reactions, since all library constituents are in equilibrium and no bond is fixed unless the exchange is switched off to prevent any further equilibrium. Thus, many techniques developed in traditional combinatorial chemistry (such as split and mix method) are not suitable to use in dynamic combinatorial chemistry.

Despite these drawbacks, the unique advantages of DCL make it an attractive and powerful technique, in particular in the field where molecular recognition can be implemented through the interaction with a template and thus leading to the selection, stabilization and amplification of active library members.[194] The facilitated characterizations of the constituents of a DCL by using efficient analytical methods such as HPLC, capillary electrophoresis, NMR and mass spectrometry make it even a more useful tool in the fields of molecular recognition, enzyme inhibition, drug delivery, and

functional material and devices.[195-200] Due to the relevance for this thesis, the following description will focus on its application to host-guest interactions, especially the identification of ligands for biomolecules.

The use of DCL technique requires appropriate reversible reactions that can proceed rapidly under mild conditions and are compatible with a wide range of functional groups and the recognition events. Additionally, the exchange process should be possible to be tuned (switch on or off) as required, which is often achieved by oxidation, reduction, pH and temperature changes, *etc*. The resulting characteristic of the library members should not be affected by the switching-off process, as this may change the binding properties of the active compounds. Since the introduction of this concept, a number of reversible covalent and non-covalent exchange reactions (Table 2.1) have been developed for construction of DCLs including the most exploited disulfide, imine and hydrazone exchange.[191-193] The selection of suitable reaction for DCL is very important to fulfill the needs of the reaction conditions and the target. In particular, the use of DCL in biological systems is tremendously challenging because it must proceed under physiological conditions required by the biomolecule target as well as satisfying the thermodynamic conditions of the suitable reversible reactions due to the requirement of the dynamic process. So it is not surprising that the reversible reactions to generate adaptive DCLs which can be applied to biological systems are limited. So far disulfide, imine and hydrazone exchanges have been extensively used in DCL with success in biological systems. Due to their suitability for biological systems and the relevance of this work, the following text describes some applications of DCL based on these three reactions for identifying synthetic receptors, ligands for biomolecules and inhibitors of enzymes.

The disulfide exchange reaction is widely used in biology and plays a key role in the folding of proteins,[201] the maintenance of the redox state of cells and the protection the organism from oxidative stress,[202] *etc*. The mechanism involves the displacement of a thiolate anion from the disulfide through a nucleophilic attack by the thiolate anion and the liberated thiolate anion can attack another disulfide (Figure 2.36, left).[203] The exchange requires deprotonated thiol and thus is highly dependent on the pH. At near neutral conditions (pH 7-9) it is possible to generate a sufficient amount of thiolate anion to enable an exchange. The exchange can be easily switched off by adjusting the pH value to slightly acidic conditions (pH $\leq$ 5). On the basis of their biological compatibility as well as the mechanistic reversibility, disulfide exchange has been developed as one of the most widely used reactions in DCL. Normally two different starting points are possible for the generation of DCLs by using this reaction: either from thiols or from disulfides (Figure 2.36, right). In solution, thiols are readily oxidized to disulfides upon exposure to air, which are immediately subject to exchange reaction mediated by residual thiolate. The exchange can also start from disulfides under mild conditions in the presence of a catalytic amount of reducing agent such as dithiothreitol (DTT) or ‘free thiol’. Both

Table 2.1 Examples of reversible processes that are used in dynamic combinatorial chemistry. Different building blocks are colored as red and blue.

Reversible Covalent Reactions	
Ester Exchange	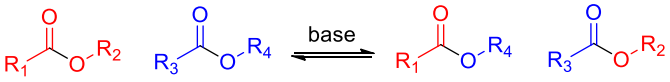
Amide Exchange	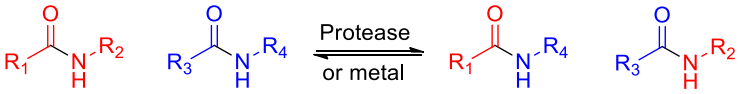
Acetal Exchange	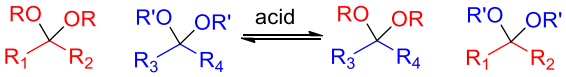
Michael Reaction	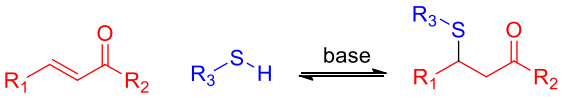
Diels-Alder Reaction	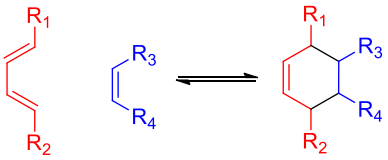
Imine Exchange	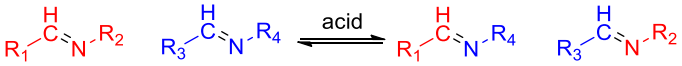
Oxime Exchange	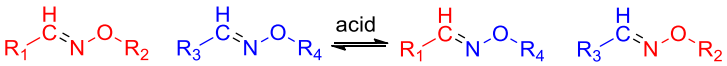
Hydrazone Exchange	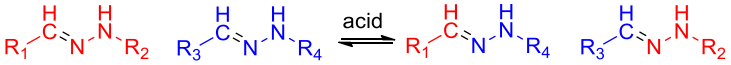
Disulfide Exchange	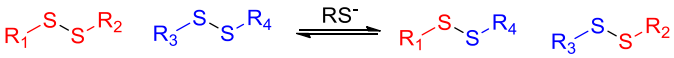
Alkene Metathesis	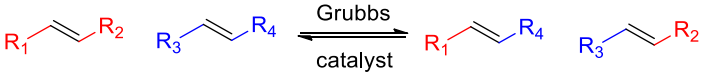
Non-covalent interactions	
Metal-Ligand Coordination	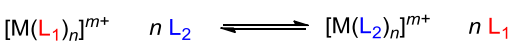
Hydrogen Bonding	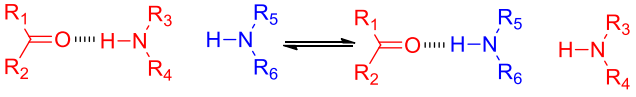

approaches can lead to the same library composition. The disulfide exchange reaction ends if insufficient thiolate anion is available.

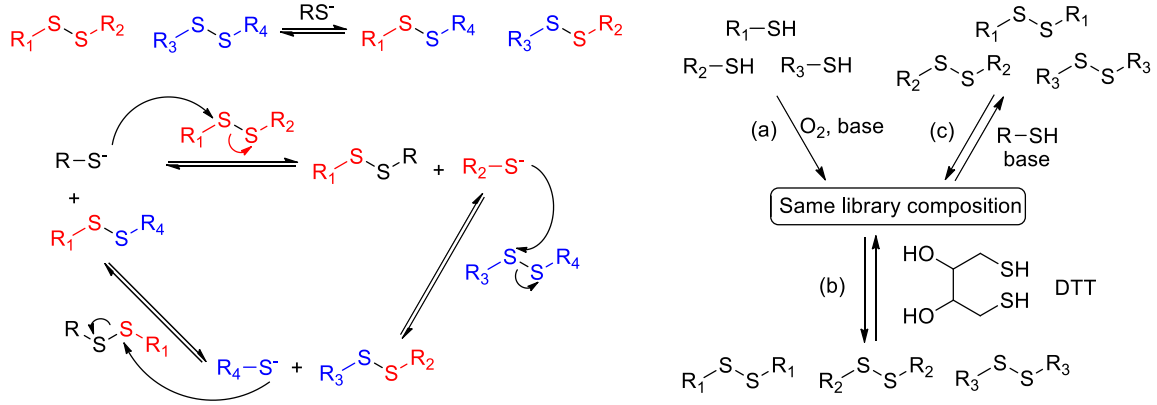

Figure 2.36 *Left*: Mechanism of disulfide exchange reaction. *Right*: Different approaches to DCLs of disulfide from two starting positions, (a) air oxidation, (b) reducing agent, (c) 'free thiol'.

Otto and *Sanders* have established that disulfide exchange can be used to generate diverse DCLs of macrocyclic disulfides formed by a series of structurally diverse dithiol building blocks, including carbohydrate and α-amino acid.[204] Later on, many efforts were put to identify new receptors from larger libraries based on useful changes in library composition induced by molecular recognition as a driving force. Inspired by a family of cyclophane receptors of general architecture **50** developed by *Dougherty*,[205] *Otto et al.* synthesized three dithiol building blocks **51-53**, which formed a DCL containing a large number of macrocyclic receptors upon oxidation (Figure 2.37). The amplification of DCL was then analyzed by HPLC upon addition of different ammonium guests (**54-56**). Surprisingly, guest **54**, which is one of the best guests for the *Dougherty*'s receptor (**50**), resulted in the amplification of cyclic heterotrimer **57**, instead of the analogue of *Dougherty*'s receptor (**50**). Binding studies revealed that the affinity of **57** (K_a = 2.5 × 10^5 M^{-1}) is in the same range as **50** even though they feature different structures. Moreover, addition of a larger guest (quaternized morphine **55**) induced the amplification of a bigger trimer **58** with a binding constant of 7.1 × 10^5 M^{-1}, whereas surprisingly the amplification of an even larger tetramer **59** was found by addition of a smaller guest (tetramethylammonium iodide **56**) with higher binding affinity (4 × 10^6 M^{-1}).[206-207] These results demonstrated that DCL can be used as a powerful and practical method for the discovery and synthesis of new unexpected receptors.[208] One single library with sufficient diversity is possible to identify more than one receptor by addition of different guests. The difference in binding affinity allows the selective amplification of the active compounds from a large number of similar structures. In addition to the application in molecular recognition field, DCLs based on this kind of dithiols were also developed for the discovery of receptors with catalytic activities.[209-210]

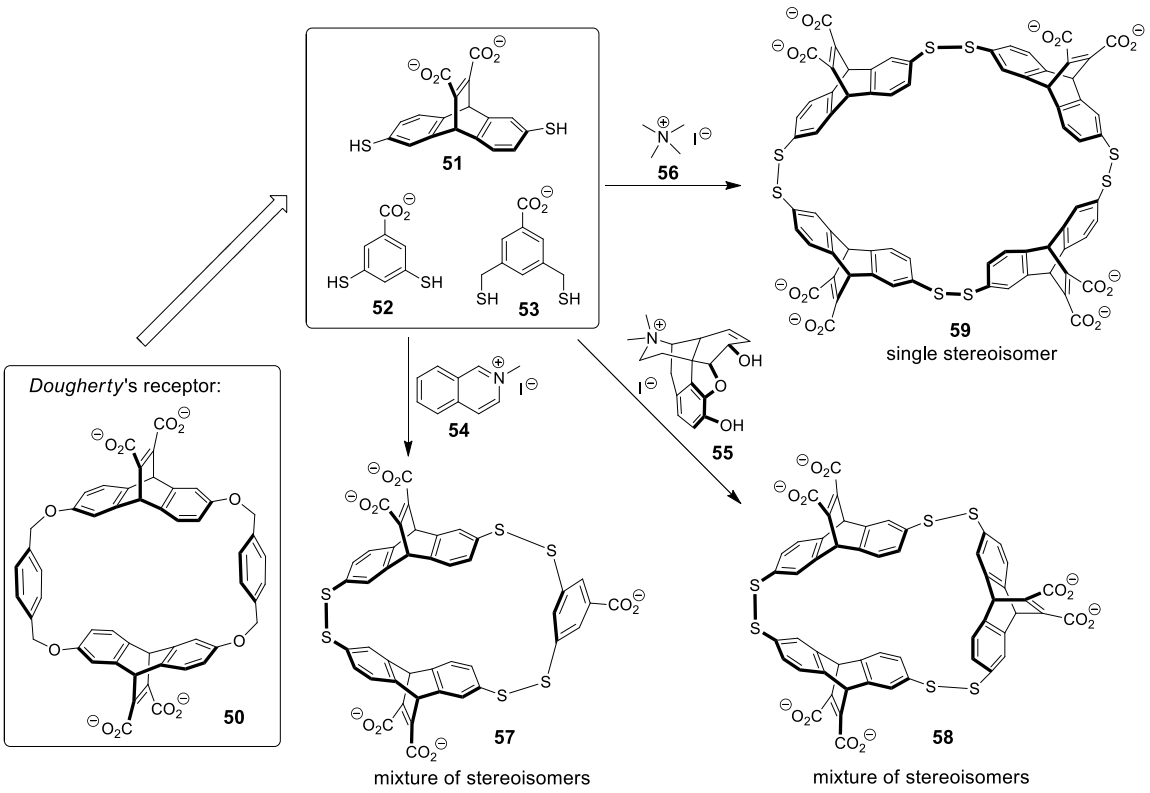

Figure 2.37 Dithiol building blocks **51**-**53** for constructing DCL inspired by *Dougherty*'s receptor **50**. Amplification of three different active compounds **57**-**58** was achieved in the presence of three different guest molecules **54**-**56**.

Disulfide exchange reactions have also been successfully applied in discovery of ligands for biomolecules. For example, *Ravoo et al.* recently developed DCLs of tripeptides by using disulfide exchange for the identification of biomimetic carbohydrate receptors.[211] *Balasubramanian et al.* reported that assembly of molecules that bind to DNA quadruplex can be templated from a small DCL of nine different species for the generation of G-quadruplex ligands.[212] A small disulfide DCL formed by three polyamide building blocks was also applied by them to the selection and discrimination of ligands that bind to DNA secondary structures (duplex or quadruplex) specifically.[213] Inspired by a set of quadruplex-binding ligands based on an oxazole-peptide macrocycle,[214] they recently investigated a higher level of discrimination in G-quadruplex binding by using disulfide libraries (Figure 2.38) containing thiol analogue of oxazole-peptide macrocycle (**60**) and two sets of different side-chain motifs based on *para*-benzylic thiols (**61a-e** and **61f-i**). The DCLs generated from **L1** and **L2** were screened against two intramolecular quadruplex-forming sequences (c-Kit21, c-Myc22) and a 22-mer duplex DNA for comparison. In the **L1** library in the presence of the quadruplex, the two guanidinium disulfides **60**-**61a** and **60**-**61e** were amplified, whereas no amplification was observed when the same library was equilibrated with duplex DNA. In the case of **L2** library, **60**-**61f** were most strongly amplified. All the amplified compounds were found with higher binding affinities (4- to 12-fold) to be superior to the analogue macrocycle (**60**).

This example demonstrated that by exploring the effect of chemical modifications, different amplified ligands in the libraries can be identified.[215] However, these libraries have relatively modest sizes; a similar level of discrimination could be achieved with the help of regular parallel synthesis. Moreover, larger DCLs have a higher potential of containing stronger binders, although the concentration of the strong binders decrease due to spreading the building blocks out over an increasing number of library members which can lead to detection problems but to a lesser extent. Furthermore, larger DCLs have a smaller probability of failing to show any amplification than smaller DCLs. Therefore, the generation of DCLs with large size has become a topic of major interest.[216]

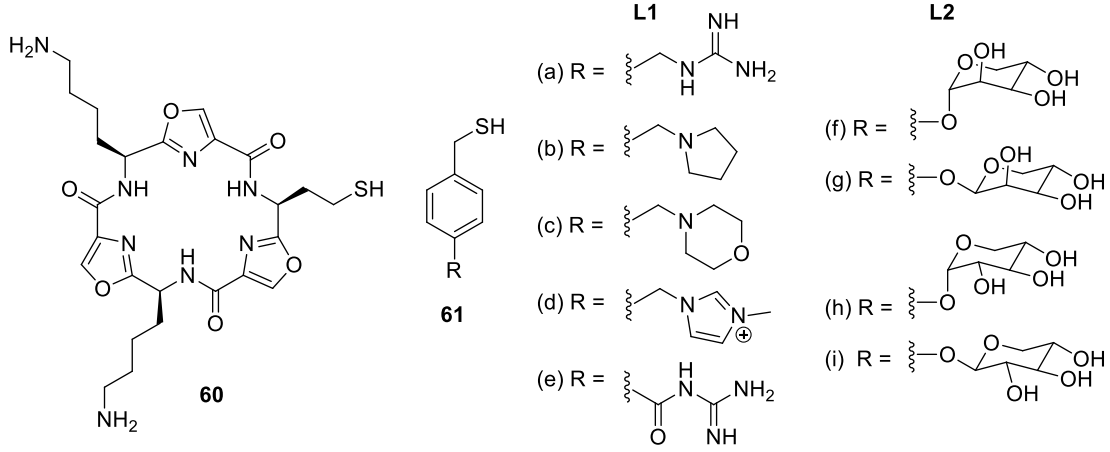

Figure 2.38 Structures of building blocks used to generate two DCLs based on oxazole-based peptide macrocycle **60** and side chains that cationic (**61a**-**e**) and neutral (**61f-i**) through disulfide exchange.

The imine formation discovered by *Schiff*,[217] is most often generated from the reaction of aldehydes or ketones with amine derivatives. This reversible imine reaction has been widely used in DCLs which are often generated at mildly acidic and even basic pH (aqueous buffer between 5.0 and 8.5 or weak acids in organic media) at room temperature, preventing aldol side reactions. The imine formation and interchange process is dependent on pH value, allowing the control of the reaction rate and efficiency by adjusting the pH value which is very important in the subsequent equilibrium for the generation of DCLs. The reaction is most often carried out under slightly acidic conditions as well as at neutral conditions with a slower rate (Scheme 2.1). However, the pH value must not be too high or too low, because the leaving group (OH) is not sufficiently protonated at higher pH and the amine is protonated at lower pH. Because of the inherent thermodynamic instability in aqueous media, it may cause screening and isolation problems. Analysis usually relies on NMR analysis of the complete mixture. A subsequent reduction process to convert the hydrolytically sensitive imines into amines by using selective reducing agents such as sodium cyanoborohydride ($NaBH_3CN$) or tetrabutylammonium cyanoborohydride (TBC) is required in imine exchange DCLs. This reduction facilitates the isolation and analysis of the final equilibrated mixture and allows a subsequent HPLC or LC-MS analysis. It is very important to make sure different library members have similar reactivity in the

reduction process, so that the amine product distribution indeed reflects the imine distribution in the library.[189] However, care has to be taken to ensure that the structurally similar amines maintain the binding properties of the selected imines.

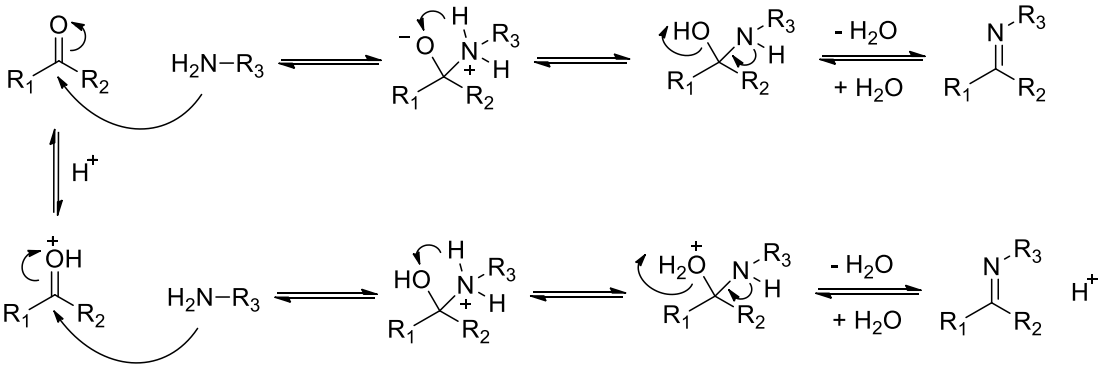

Scheme 2.1 *Left*: Mechanism of imine formation at neutral (top) and acidic (bottom) conditions.

Due to the imine formation at or near physiological conditions, this reaction has been used in DCC for identification of ligands for biomolecules and enzyme inhibitors.[218-219] The first example reported by *Lehn et al.* has clearly described the characteristic and potential of DCLs interacting with biomolecules.[189] Three aldehydes and four amines were used as building blocks to generate 12 imine-linked library members for identifying carbonic anhydrase inhibitors. The imines were reduced to the corresponding amines to allow a subsequent HPLC analysis. Several library species were amplified in the presence of carbonic anhydrase template. They pointed out that it is important to use an excess of amine building blocks to avoid unwanted imine reactions on the amine groups of biomolecules such as proteins or peptides. A recent study was based on *N*-acetyl-D-glucosamine, a low affinity inhibitor (K_i = 20-50 mM) for hen egg-white lysozyme (HEWL), an enzyme that cleaves oligomers of *N*-acetyl-D-glucosamine.[220] Two amines (**62** and **63**) with *N*-acetyl-D-glucosamine and D-glucose motifs and six aromatic aldehydes (**64**-**69**) were used as building blocks to create the imine-based DCL for the discovery of HEWL inhibitors (Figure 2.39). A 4-methylumbelliferyl chromophore was connected to the carbohydrate group to allow comparable HPLC detection of different adducts. After the equilibration and reduction, amplification of two adducts (**70** and **71**) was found in the presence of HEWL by using HPLC-MS analysis. The most amplified compound **70** was shown to inhibit HEWL in a competitive way with much higher affinity (K_i = 0.6 mM) than *N*-acetyl-D-glucosamine, and was able to compete with chitobiose (K_i = 0.2 mM), a known successful inhibitor of the enzyme. This example showed the capacity of imine-based DCL to discover efficient inhibitor of enzyme and discriminate subtle affinity variations induced by the different substitution on the structure.

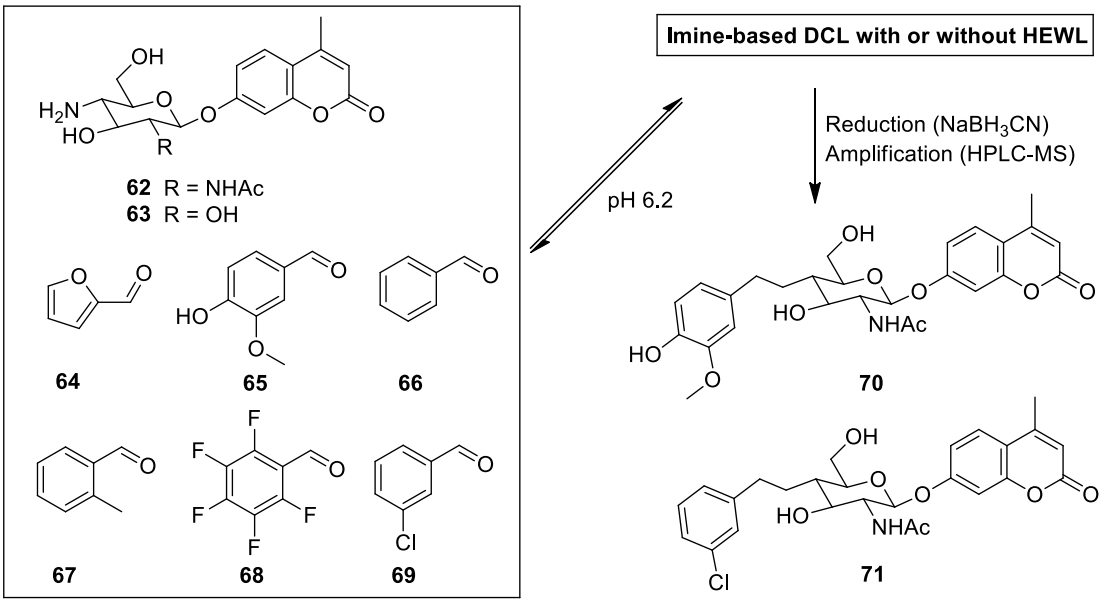

Figure 2.39 Structures of amine (**62**-**63**) and aldehyde (**64**-**69**) building blocks used to generate imine-based DCL. After reduction, amplification of two adducts (**70**-**71**) were found in the presence of HEWL.

The mechanism of hydrazone formation is similar to that of imine formation. Unlike imines that condense and hydrolyze quickly at neutral to acidic conditions but are unstable in the presence of water, hydrazones formed from hydrazines and aldehydes are thermodynamically stable even at low pH while they tend to be kinetically inert under neutral conditions. This is because the mesomeric effect decreases the electrophilicity of hydrazone, slowing down the hydrolysis and exchange rate. The hydrazone formation and exchange can be carried out only under acidic conditions (pH ≤ 4) or at high temperatures. Most often acyl hydrazones which are formed by hydrazides and aldehydes (Scheme 2.2) are used in DCL. The acyl group is introduced to moderate the stabilizing effect of the amine subunit in C=N-NRR′. Without the acyl group or similar other electron withdrawing groups hydrazones are probably too stable to be used in DCLs, because the reversible exchange would be very slow.[191] The acyl hydrazone exchange reaction enables rapid library generation in which dynamic properties can be easily controlled by adjusting pH value. The formation and component interchange processes take place at lower pH (≤ 4) and can be essentially stopped at high pH (> 7). Furthermore, acyl hydrazone libraries are compatible with a wide range of solvents and functional groups due to the orthogonal nature of the different components (hydrazides and aldehydes).

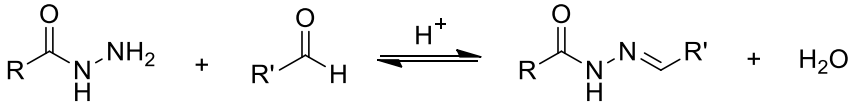

Scheme 2.2 Reversible acyl hydrazone formation under acidic conditions.

DCLs based on acyl hydrazone exchange have been used for identifying new receptors

for metal ions or small guest molecules. For example, *Sanders et al.* investigated an acyl hydrazone DCL based on the pseudo-dipeptide building block *p*PFm (**72**), containing L-proline (P), L-phenylalanine (F), and a *p*-substituted (*p*) aromatic linker (Figure 2.40). DCLs of this building block without template contained a series of macrocycles (**73**-**76**) of different ring sizes. Addition of LiI, as well as NaI, to a lesser extent, induced the amplification of the cyclic trimer (**74**). The amplified trimer **74** accounts for 98 % of the overall peptide material in the library in the presence of Li^+, allowing isolation of the receptor. The subsequent analysis demonstrated that the trimer is a good receptor for Li^+, with a binding constant of 4×10^4 M^{-1} as estimated by ^1H NMR titration. FT-IR and NMR studies revealed significant signal shifts of the carbonyl group of the receptor indicating that there is a conformational change upon Li^+ binding. This indicated that macrocycles can fold in a suitable conformation to optimize their binding to the guest molecule.[221] The replacement of the phenyl group of phenylalanine unit in *p*PFm by a cyclohexyl group to give an analogous building block *p*PCm led to a very similar library, from which similar results were obtained, indicating the aromatic side chain is not essential for the binding.[222]

The other remarkable and unexpected result achieved from this acyl hydrazone DCL is the generation of a catenane receptor that strongly binds to the neurotransmitter acetylcholine.[223] The DCL generated from the same pseudo-dipeptide building block (**72**) dramatically shifted the equilibrium to the formation of a new product **77** at the expense of all the other library members by the addition of acetylcholine chloride (Figure 2.40). In the presence of acetylcholine, the new library member **77** appeared within an hour. It was found to be an isomer of the cyclic hexamer but with different retention time revealed by HPLC-MS analysis. The two isomers showed distinct electrospray MS/MS fragmentation behavior: the simple hexamer fragmented into a pentamer and successively smaller components, whereas the new product fragmented directly to the trimer. This fragmentation behavior is typical of a [2]-catenane and indicates that the new library member consisted of two identical interlocked cyclic trimers. Due to the chiral nature of each ring, there are two possible diastereomers of the [2]-catenane. However, NMR studies confirmed that only one of two possible diastereomers is amplified. The DCL took an unusually long time to equilibrate, and eventually after 44 days the catenane reached its maximum concentration, accounting for 70 % of the total material in the library. It is most likely that the catenane formation pathway is inherently not favored, but it can effectively be captured and stabilized by the template acetylcholine as soon as it is formed. The catenane **77** is shown to be a good receptor for acetylcholine with a binding constant of 1.4×10^7 M^{-1} as determined by ITC. Whereas binding affinity of acetylcholine to the trimer **74** ($K_a = 1.5 \times 10^3$ M^{-1}) and the tetramer **75** ($K_a = 5.7 \times 10^3$ M^{-1}) were much weaker. This example further demonstrated the great power of DCC for identification and synthesis of unexpected receptors, in particular a catenane receptor would have been more difficult to prepare without the template.[224]

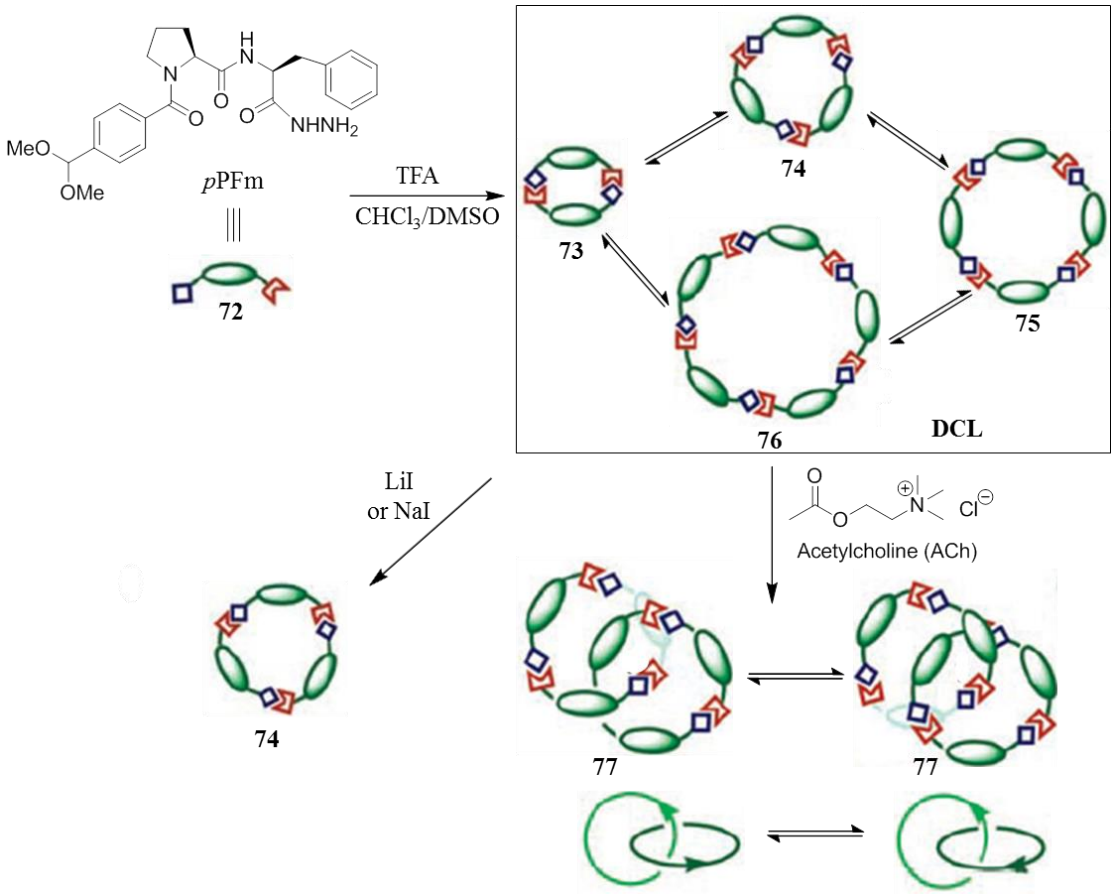

Figure 2.40 An acyl hydrazone DCL based on the pseudo-dipeptide building block *p*PFm for identifying different synthetic receptors by using different guest molecules as templates. *(Reprinted with permission from R. T. S. Lam, A. Belenguer, S. L. Roberts, C. Naumann, T. Jarrosson, S. Otto, J. K. M. Sanders, Science **2005**, 308, 667-669. Copyright 2005 The American Association for the Advancement of Science).*[223]

In contrast to imines, hydrazones are stable to analysis and isolation in aqueous solution, but their formation and exchange generally requires acidic conditions (pH 4 or below) which are not compatible with most biomolecules. *Lehn et al.* have developed pre-equilibrated DCLs based on reversible hydrazone formation to identify efficient binders for biomolecules by using a dynamic deconvolution process.[225-227] In this pre-equilibrated DCL protocol, the equilibration of the library has to be carried out in the absence of the biological target. For target screening the used conditions are then adjusted to the required physiological pH based on the enzymatic assays freezing-out the library composition. In order to identify the active components of the libraries, a "dynamic" deconvolution strategy can be utilized (Figure 2.41). In this approach, a full library is prepared by using all the building blocks. In addition, a set of different sub-libraries is prepared under similar conditions, in which one building block each is missing. The removal of a single building block from the full library results in the redistribution of the remaining constituents, and thus all constituents containing this building block will be eliminated from the library. To this aim, for each building block contained within the DCL,

a sub-library is prepared from which all library constituents based on this unit are removed. All the libraries are then subjected to enzyme screening. By comparison of the screening results of the full library with different sub-libraries, it is often possible to deduce which building blocks are necessary for high activity. Namely, a decrease in inhibitory effect or an increase in enzyme activity of the sub-library indicates the importance of the removed building blocks in the formation of active compounds in the dynamic library. Thus the best library members can be identified by the construction from two active components with orthogonal functional groups.

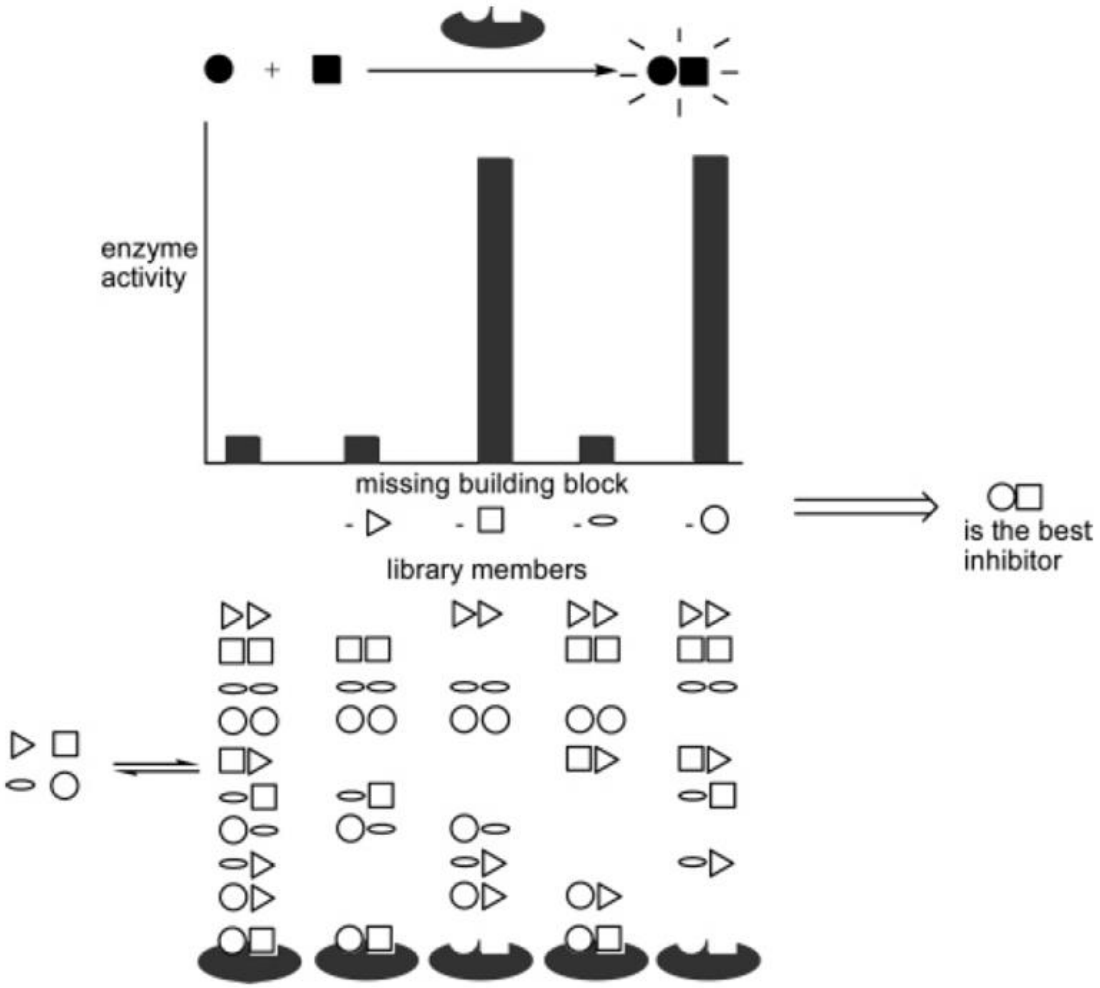

Figure 2.41 Cartoon representation of the principle of dynamic deconvolution. *(Reprinted with permission from P. T. Corbett, J. Leclaire, L. Vial, K. R. West, J. L. Wietor, J. K. M. Sanders, S. Otto, Chem. Rev.* ***2006****, 106, 3652-3711. Copyright 2006 American Chemical Society).*[191]

By using the dynamic deconvolution strategy, DCLs for targeting acetylcholinesterase,[225] HPr kinase/phosphatase,[226] and the plant lectin concanavalin A (Con A)[227] have been successfully established by *Lehn et al.* For example, in the recent study targeting the plant lectin Con A, acyl hydrazone DCLs were prepared by mixing a series of six carbohydrates functionalized benzaldehydes (**78**-**83**) and a set of oligohydrazide (**84**-**92**) core building blocks (Figure 2.42).[227] The structural core building

blocks were chosen as scaffolds bearing one, two or three hydrazide groups, onto which the carbohydrate binding units can be attached and arranged in a given geometry to construct multivalent library constituents. The deconvolution strategy was pursued, generating one large full library and 15 sub-libraries in which one specific aldehyde or hydrazide building block is missing. The full library formed from all of the 15 components is capable of containing 474 different library species. It was found to efficiently inhibit the binding of Con A, determined with the help of an enzyme-linked lectin assay. A series of sub-libraries was then screened, and those lacking the mannose unit **83**, and trihydrazides **90**, **92** were found to have a significantly increase in enzyme activity. Clearly component **83** is essential for inhibition to occur. In order to further probe the individual effects of the hydrazide components, a reduced library containing only one aldehyde unit **83** and all of the scaffolds, as well as 10 corresponding sub-libraries were prepared and profiled, showing significantly reduced inhibition in the library without **90**. The compound **93** was then synthesized separately by connecting the most active components **83** and **90** from the library and its inhibitory effects further evaluated. It was shown to have an IC_{50} of 22 μM, which is 36-fold better than the reference compound, methyl-α-D-mannoside (IC_{50} = 0.8 mM).

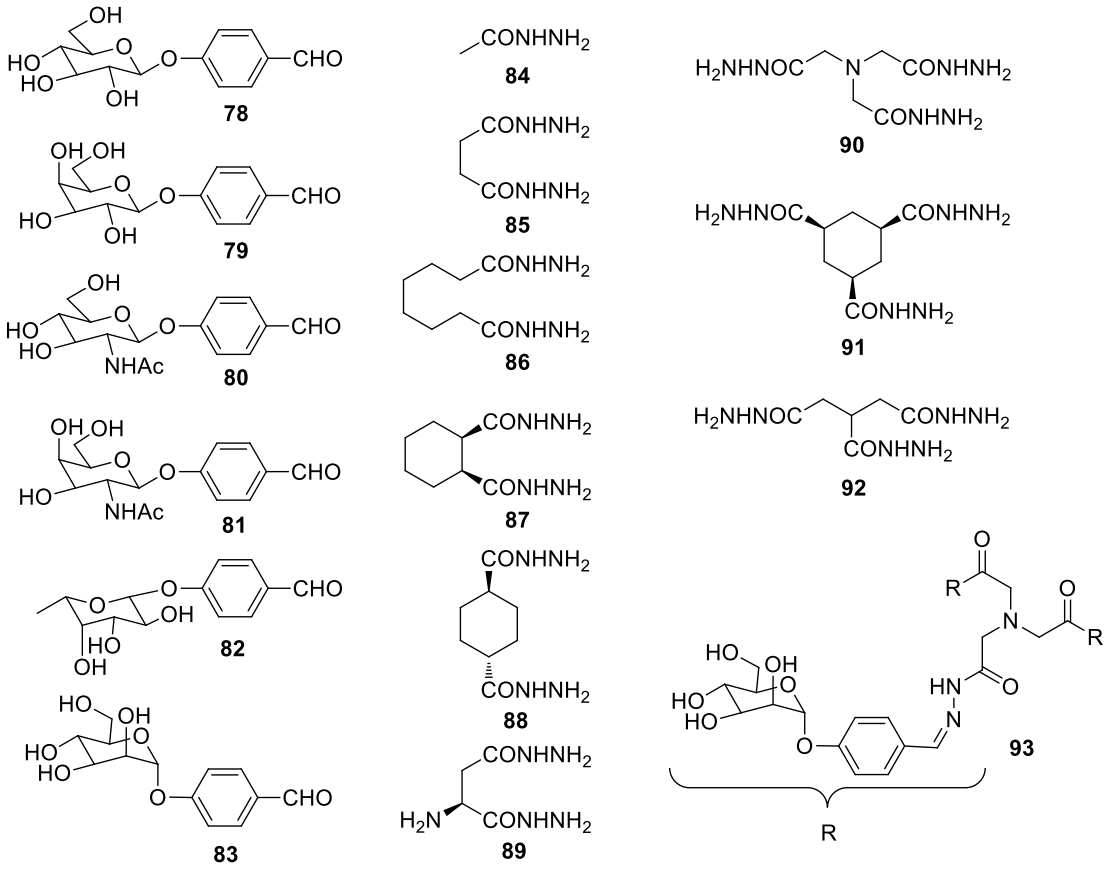

Figure 2.42 Structures of aldehyde (**78**-**83**) and hydrazide (**84**-**92**) building blocks for hydrazone libraries, and the best library member (**93**) was selected from DCL targeting concanavalin A using a dynamic deconvolution strategy.

Recent studies have shown that the equilibration of hydrazones can be accelerated at weak acidic conditions close to physiological pH by using aniline as nucleophilic catalyst (Scheme 2.3).[228] In the presence of aniline catalyst, equilibration of the hydrazone library can be rapidly complete within one day at room temperature under weak acidic conditions, which would take weeks in the absence of aniline. Due to the inherent instability of imines in water, the catalyst can be used in a high concentration to accelerate the exchange process. Moreover, aniline, being a mild nucleophile, has good solubility in a variety of solvents and is compatible with many functional groups. This strategy allows the application of DCL based on acyl hydrazone exchange in identifying ligands for biological target.

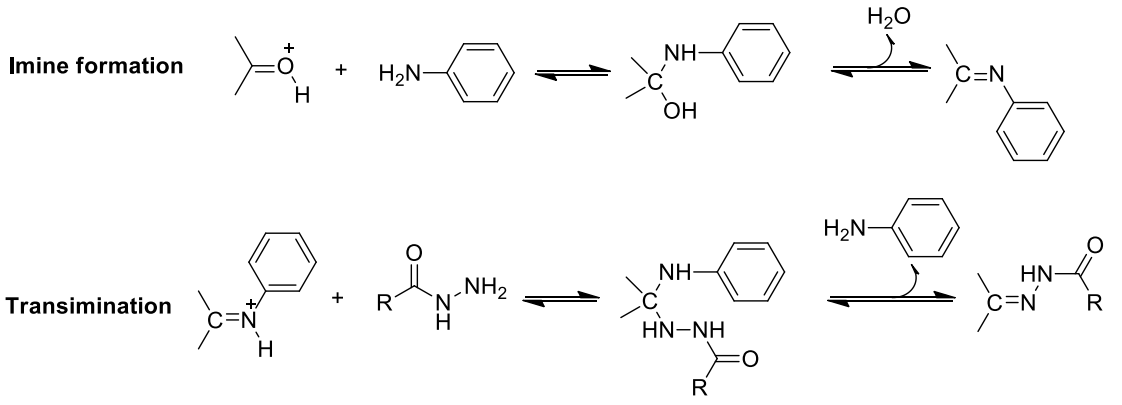

Scheme 2.3 Mechanisms of imine formation (top) and transimination (bottom) under acidic conditions.[229]

Recently, *Greaney et al.* developed a hydrazone DCL in the presence of aniline catalyst for the discovery of Glutahione S-Transferase (GST) inhibitors. One reactive aldehyde **94a**, related to the known GST substrate chlorodinitrobenzene (CDNB), and ten aryl hydrazides (**95a**-**j**) were used as building blocks for the generation of DCL (Figure 2.43). The equilibration of the library was complete after 6 h in the presence of aniline at pH 6.2. Two active compounds were amplified in the presence of recombinant GST isomers hGST P1-1 and SjGST. However, due to the poor solubility of the resulting library members, further binding studies were not possible. Therefore, the solubility of the library members was enhanced by replacing the -Cl with a glutathione moiety to get aldehyde **94b**. The DCL generated from **94b** led to the amplification of compounds **96c** and **96g** from the DCL templated by recombinant GST isomer hGST P1-1 or SjGST, respectively. Subsequent studies confirmed that the amplified compounds have efficient inhibitory effects by binding to the GST H-site. By extending the inhibitor structure, **96c** (IC_{50} = 57 μM) was found to have six-fold higher affinity for hGST P1-1 than the precursor **96b** (IC_{50} = 331 μM), while **96g** (IC_{50} = 22 μM) had over one order of magnitude higher affinity for SjGST, relative to **96b** (IC_{50} = 279 μM). **96g** also showed selectivity for SjGST against all the other library members in accordance with the screening results. However, unlike the screening results, both of the compounds showed similar affinity to

hGST P1-1 (57 μM and 50 μM).[230] Recently, bivalent GST inhibitors were identified by using the similar approach.[231]

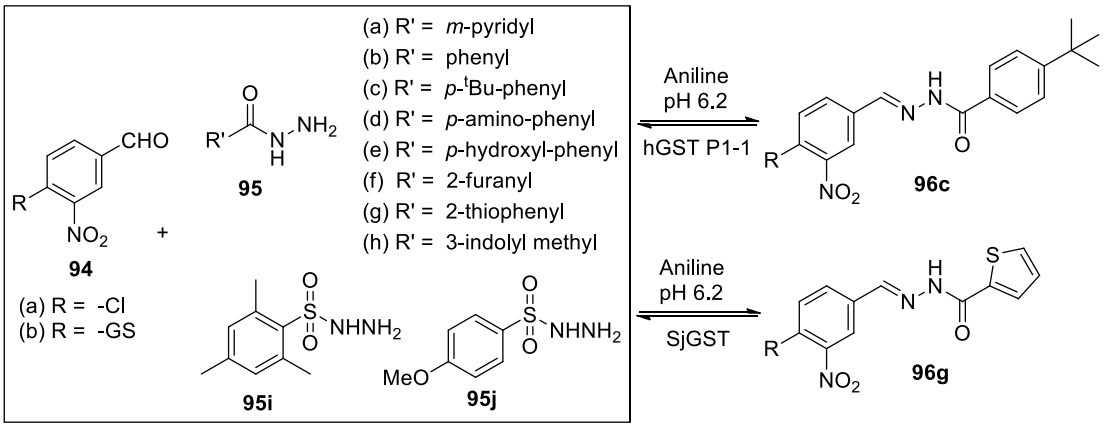

Figure 2.43 Building blocks for aniline-catalyzed acyl hydrazone DCL and the amplification of two active compounds in the presence of protein targets.

The above examples demonstrate that dynamic combinatorial chemistry has great power and practicality in identifying synthetic receptors for small guest molecules and ligands for biological targets. DCC is also a useful tool to identify molecules with unusual structures and binding properties. It provides an attractive synthetic route to complex molecules that are more challenging to obtain through the normal synthetic method. However, although strong amplification of the selected library members has been observed in many cases, it is not always in good correlation with the binding affinity. *Severin et al.* revealed that this correlation could break down, or even reverse depending on the template concentration. It was shown that a high concentration of template could lead false positive results as the amplification of the weaker binders may compete with that of stronger ones. In particular, small oligomers and hetero-compounds are favored to be amplified over larger ones and homo-compounds respectively, even though they have similar binding affinity or even reverse as the amplification results showed.[232-233] These predictions were also confirmed by simulated lager complex DCLs[234] and the experimental work.[235] Even though the false results can be avoided by using low template concentration, DCL system seems not as simple as we initially thought. However, these effects are not a significant limitation to the DCL approach, because even if the most amplified library member may not have the strongest binding affinity to the target, it is most likely to be one of the better binders in the dynamic libraries. In particular, the use of DCLs combined with the dynamic deconvolution strategy to identify potent enzyme inhibitors is of major interest in this work.

3. PROJECT AND OBJECTIVES

This dissertation is focused on the discovery of novel and potent inhibitors with high affinity for the serine protease β-tryptase. The aim of this work is to identify new peptide structures containing the tailor-made binding motif for binding to the surface of the enzyme. New approaches for inhibitor identification will also be developed. Moreover, various scaffolds ranging from rational designed scaffolds with diverse structure, flexibility and valency to nanoparticles scaffolds with large surface area and tunable functionalities will be used to build up multivalent inhibitors. The tetrameric structure of β-tryptase has A_2B_2 arrangement with two pairs of monomers equivalent (Figure 3.1, left). The protein surface of β-tryptase has a pI value around 5.0 to 6.6, indicating only a slightly negatively charged surface.[236] However, the surface features some highly acidic "hot spots" with clusters of negatively charged amino acids (e.g. glutamic acids and aspartic acids) which are mainly located at the entrance to the central pore and around the catalytic active sites of β-tryptase buried within this cavity (Figure 3.1, right). Therefore, the blocking of the entrance to the central pore would prevent the access of substrate to the active sites thus inhibiting the enzyme activity.

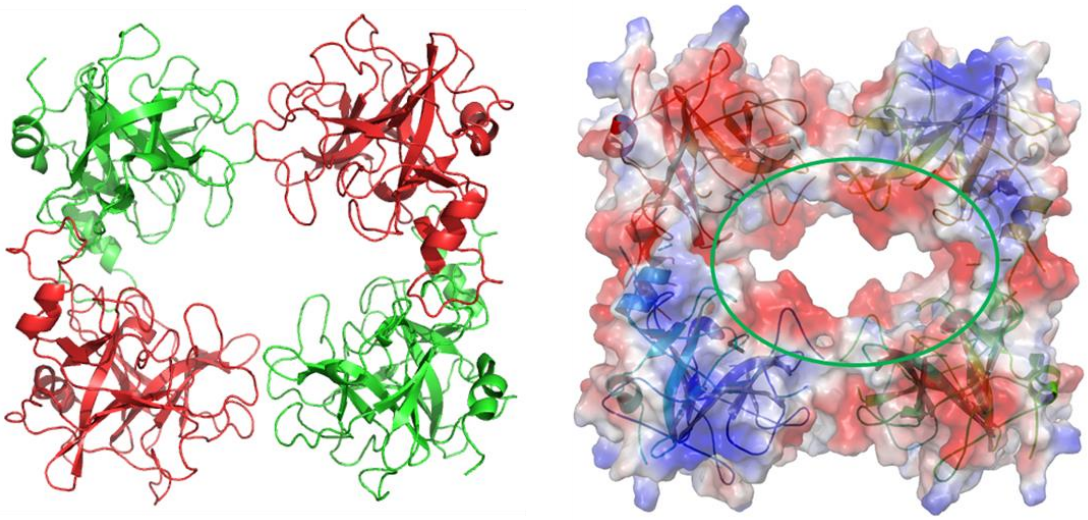

Figure 3.1 *Left:* Tetrameric structure of β-tryptase (PDB code: 1A0L). Two pairs of equivalent monomers (coloured as red and green) are arranged in the same orientation. *Right:* Surface of the β-tryptase features some highly acidic "hot spots" around the central pore. The colors indicate positive (blue) and negative (red) electrostatic potential on the surface of β-tryptase

3.1 Design of Tetravalent Peptide Ligands with Two Different Sets of Arms as Potent Enzyme Inhibitors

The first project of this thesis is based on the previous work concerning the enzyme inhibition by designing a new class of inhibitors. In the previous work, a type of inhibitors of β-tryptase with four identical arms was identified from a focused combinatorial library of 216 tetravalent peptide ligands (**1**) which bind to the surface of β-tryptase, sterically blocking access of the substrate to the active site thus shutting down the enzyme in a reversible and noncompetitive way. Inspired by the structure of β-tryptase with its A_2B_2 arrangement of the four monomers and a docking study suggesting that the enzyme has at least two different binding sites for cationic peptide ligands, ligands with two different sets of arms should be even more promising candidates for the inhibition of β-tryptase. Therefore, this project is now to design new tetravalent ligands **97** by incorporating two different types of arms instead of the four identical arms into the tetrapeptides in order to improve the binding affinity to β-tryptase (Figure 3.2). Furthermore, besides proteinogenic amino acids, the artificial arginine analogue, the guanidiniocarbonyl pyrrole unit (GCP) should be incorporated in the arms to improve the binding affinity to β-tryptase. To further test how the artificial GCP group influences the inhibition of β-tryptase, the ligands **98** with four identical arms tailored with GCP groups were designed to compare them with the previous ligands.

The combinations of cationic and aromatic amino acids will be chosen to build up the arms based on the previous findings that these combinations provides most efficient inhibitors for β-tryptase. Therefore, ligands **97** could be identified that contain the original best sequence RWKG as the first set of arms and a different second sequence for the other set of arms. Ligand **98** with four identical arms will carry three or four amino acids, ending with the GCP group in each arm. The basic residues (lysine, arginine, GCP) should allow for the binding of the acidic area that mainly bearing carboxylates from side chains of aspartic and glutamic acid residues at the entrance to the central pore and around the active cleavage sites of β-tryptase. The inhibition properties of these ligands towards β-tryptase will be studied by enzyme assay.

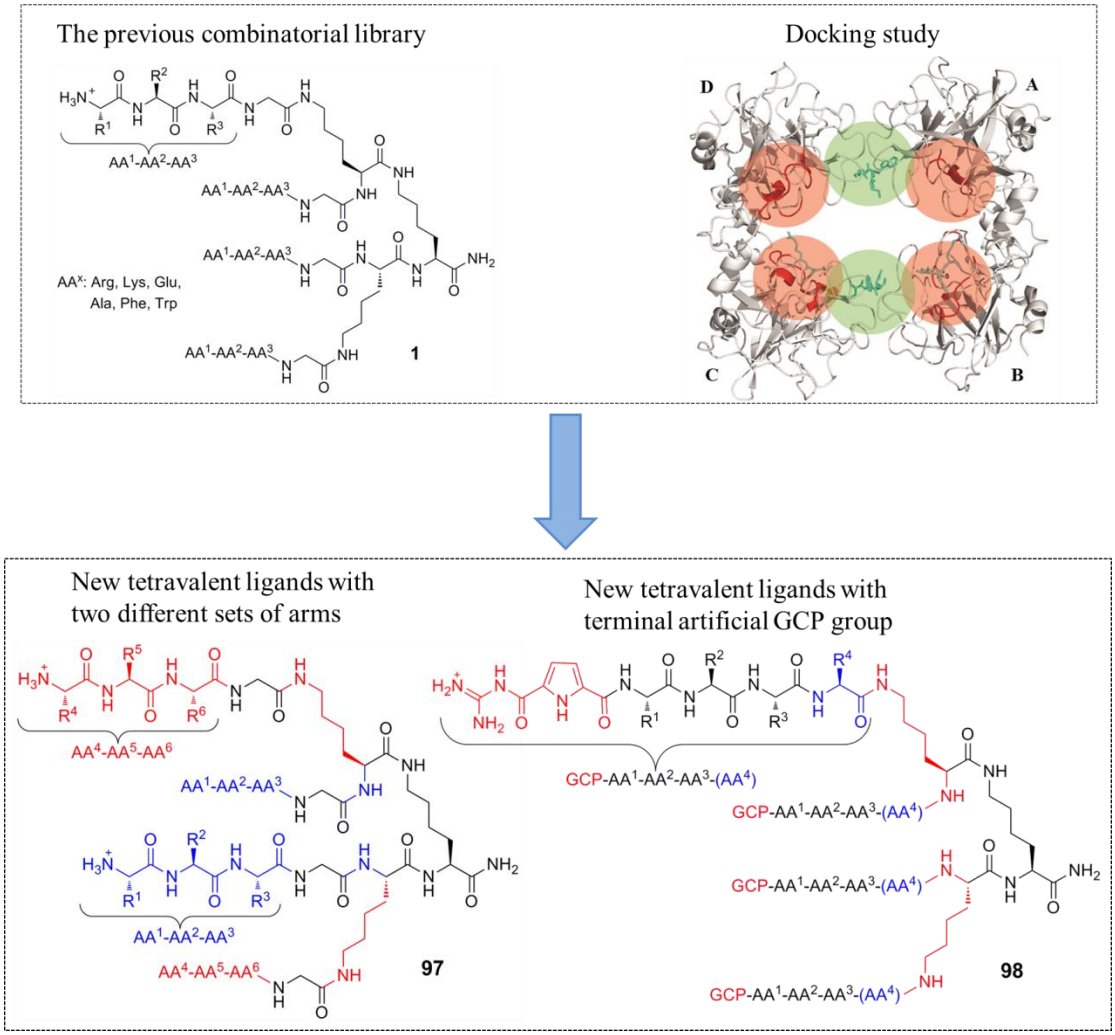

Figure 3.2 Tetravalent ligands (**97**) with two different sets of arms (colored in red and blue, respectively) and four-armed ligands (**98**) with four identical arms terminating with the GCP units. The design was inspired by the previous findings from the combinatorial library and now the docking studies.

3.2 Dynamic Combinatorial Chemistry: New Method for the Discovery of Inhibitors of β-Tryptase

In this project, dynamic combinatorial chemistry will be used as a new method for the identification of inhibitors of β-tryptase. The pre-equilibrated DCLs based on the reversible acyl hydrazone formation reaction will be used for the discovery of new and potent inhibitors of β-tryptase with the help of a dynamic deconvolution strategy (Figure 3.3). The hydrazide will carry different peptide arms featuring the recognition elements binding to the enzyme. The aldehydes with diverse spacer, flexibility and valency can be chosen as scaffolds to build up multivalent library species. The formation of hydrazones can be monitored by HPLC, MS and NMR. The full library and different sub-libraries in which one specific building block is removed can be

prepared. By using a deconvolution strategy to compare the enzyme screening results for different sub-libraries with the full library, the active building blocks will be selected and this way the influence of the peptide sequence on the enzyme inhibition can be studied as well as the influence of the scaffolds.

The next step will be the synthesis of the active library members by the construction of the selected active building blocks featuring orthogonal functional groups. Then the individual acyl hydrazones can be subjected to independent enzyme assays to investigate the inhibitory properties. Such a method could give new insight to the discovery of potent enzyme inhibitors with less effort than the traditional combinatorial library.

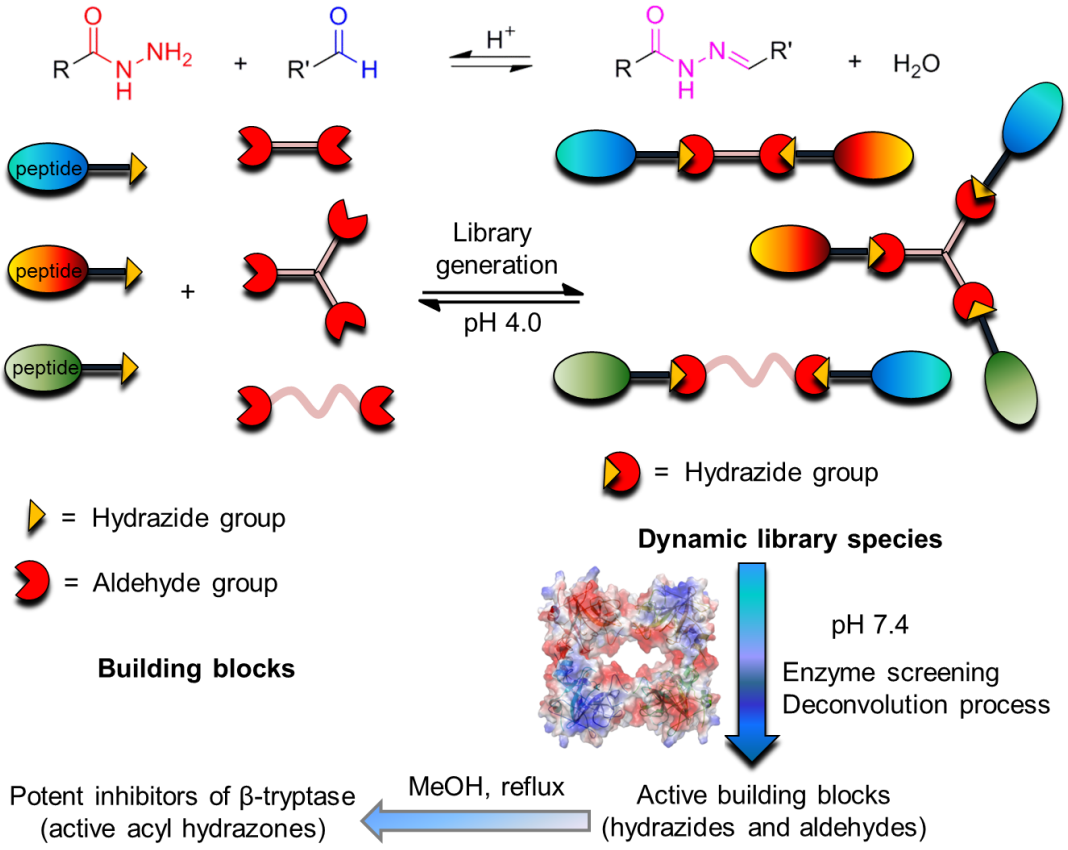

Figure 3.3 Schematic representation of the acyl hydrazone based DCL for identifying inhibitors of β-tryptase.

3.3 Gold Nanoparticles: Promising Scaffold for Protein Surface Recognition

The aim of this project is to take advantage of the gold nanoparticles (Au NPs) as attractive scaffold due to their large surface area, tunable size and the ability to feature the surface with a wide range of desirable functionalities to design multivalent ligands for the protein surface binding. To achieve this goal, the surface of the functionalized

gold nanoparticles should present complementary recognition elements that are required for the interaction with the surface of protein. Therefore, the peptide ligands with basic amino acids should be used to bind to the acidic hot spots of β-tryptase. The peptide ligands (**99**) shown in Figure 3.4 will contain three subunits: the thioalkyl chain to stabilize the gold core, the triethylene glycol as a linker to improve the solubility and prevent both nonspecific interactions with enzyme and protein denaturation, and the positively charged peptide chain to bind to the enzyme. Neutral ligand **100** with the terminal hydroxyl is used to compare the binding affinities with the peptide ligand. The Au NPs (**101**) featuring the peptide ligands will be prepared by laser ablation which will be done together with our cooperation partner, the working group of *Prof. Stephan Barcikowski* in the Institute of Technical Chemistry at the University of Duisburg-Essen.

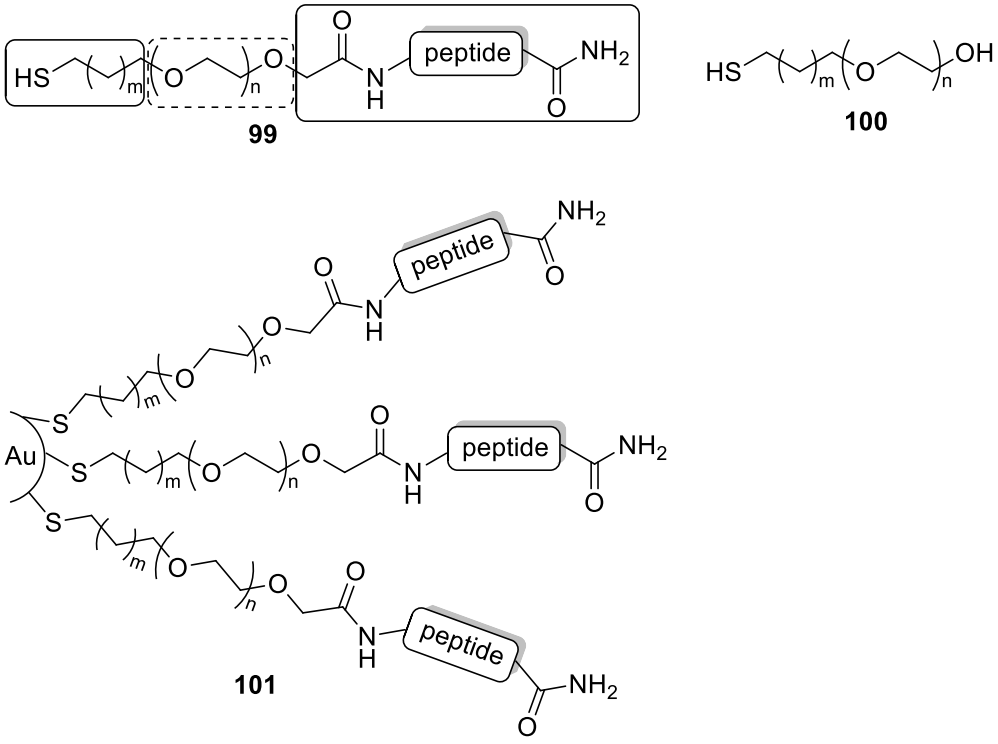

Figure 3.4 Schematic representation of the structure of the ligands **99**, **100** and the functionalized gold nanoparticles **101** featuring peptide ligand **99**.

The monovalent and bivalent conjugated Au NPs will be generated to investigate their enzyme inhibitory properties. The functionalized gold nanoparticles should be characterized by NMR, IR, UV/Vis, disc centrifugation, DLS and TEM to verify and determine the functionality on the surface, as well as the particle size. The influence of the amino acid composition of the peptide chain, the functionalization degree, as well as the gold concentration on the enzyme inhibition will be studied.

4. RESULTS AND DISCUSSIONS

4.1 Design of Tetravalent Peptide Ligands with Two Different Sets of Arms as Potent Enzyme Inhibitors

The first project of this thesis is based on the previous work from *Peter Wich* concerning the discovery of a new class of inhibitors of β-tryptase by using tetravalent peptide ligands with two different sets of arms. The previous work revealed a protein surface binding approach to shut down the enzyme through the interaction of a tetravalent peptide ligand with the entrance to the central pore of β-tryptase sterically blocks access of the substrate to the active site thus inhibiting the enzyme in a reversible and noncompetitive way.[13] The best ligand $(RWKG)_4$ (K_i = 0.17 μM) containing basic and aromatic amino acids in their arms was chosen from the combinatorial library of 216 tetravalent peptide ligands (**1**) with four identical arms attached to a lysine dendrimer scaffold (Figure 4.1). Most likely this ligand acts as a 'molecular plug' upon binding to the central pore of the enzyme thus preventing the substrate from binding. The structure of the enzyme with the A_2B_2 arrangement of the four monomers (see Figure 3.1) and a docking study (see Figure 4.3) suggest that the enzyme has at least two different binding sites for cationic peptide ligands and hence ligands with two different types of arms might also be promising candidates for inhibiting tryptase giving access to an even higher structural diversity. Therefore, the first project of this thesis is focused on the discovery of novel and potent inhibitors with high affinity for serine protease β-tryptase by design and synthesis of tetravalent ligands with two different sets of arms. In addition, the artificial GCP group was also incorporated into the arms to test its effects on the enzyme inhibition.

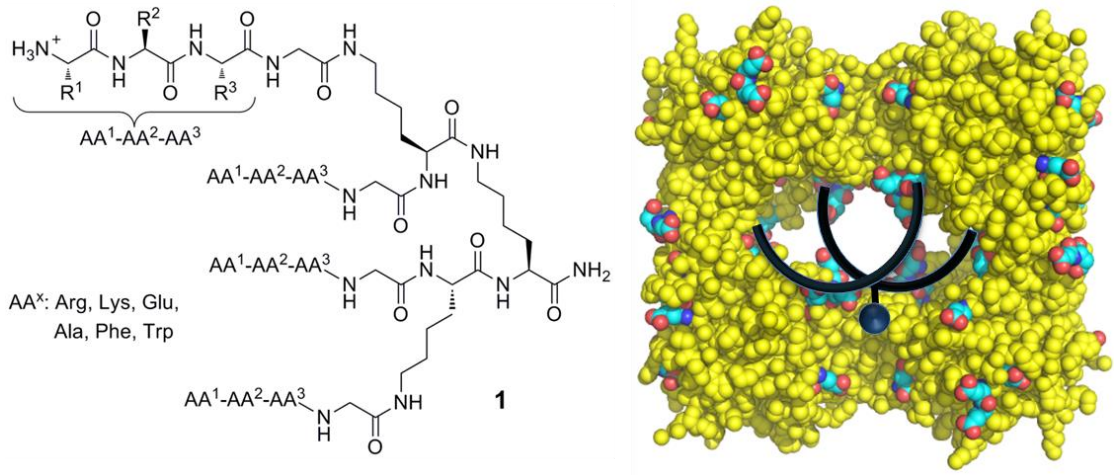

Figure 4.1 *Left:* The structure of the combinatorial library of 216 tetravalent peptide inhibitors. *Right:* The illustration of the interaction between the best ligand $(RWKG)_4$ and β-tryptase: The inhibitor can bind to the surface of the protein acting as a tight "molecular plug" closing the central pore and thus blocking access to the active sites.

4.1.1 Statistical Analysis of the Inhibition Data and Docking Studies

The statistical analysis and docking studies were performed by *Dr. Dominik Heider* in the working group of *Prof. Daniel Hoffmann* from the Institute of Bioinformatics at the University of Duisburg-Essen. In the previous work a focused combinatorial library of 216 tetravalent peptide ligands with four identical arms on a lysine dendrimer had been screened for inhibition of β-tryptase. These ligands varied in the composition of the tripeptide unit within their arms. A quantitative on-bead screening had been performed so that a set of inhibition data from 216 ligands was available.[13] The data was now used to perform a statistical analysis to identify which is the most important position of the variable tripeptide part in the arms and what kind of properties of the respective amino acids in the arms are beneficial for the inhibition. Therefore, the amino acids of the tripeptide sequences were numerically encoded using two scales, namely the hydropathy index of *Kyte* and *Doolittle*[237] normalized to range 0 to 1, and the net charge in unit of elementary charge. In this way, every tripeptide sequence from the previous combinatorial library was now translated into a vector of six numerical values. The hydropathy and charge vectors were plotted separately using the R-package rgl[238-239] for the 25 % strongest and weakest inhibitors, respectively (Figure 4.2). The linear and nonlinear correlation of inhibition with the six descriptors was evaluated computationally with the statistics software "R",[238] and nonlinear regression was performed with random forests as implemented in R.[240] The results showed that enzyme inhibition by the tetravalent ligands was clearly correlated with the amino acid composition of the tripeptide sequences as expressed by charge and hydropathy: An adjusted $R^2 = 0.63$ for multiple linear correlation and only marginally higher values with nonlinear regression were found. The linear

correlation of highest significance was found for the charge of the first variable position ($p < 2e\text{-}16$) with a positive charge leading to stronger inhibition. Positive charges are favored as well at the other two positions but to a lesser extent. This is in agreement with the negative correlation of inhibition with hydropathy as the favored amino acids arginine and lysine have the lowest values of hydropathy.[237] Figure 4.2 shows that the 25 % strongest and 25 % weakest inhibitors can be well separated in the space of the chosen physico-chemical descriptors hydropathy and charge, with the first amino acid having the greatest impact on enzyme inhibition: low hydropathy and positive charge at this position result in strong inhibitors, while high hydropathy and negative charge at this position are characteristic of weak inhibitors.

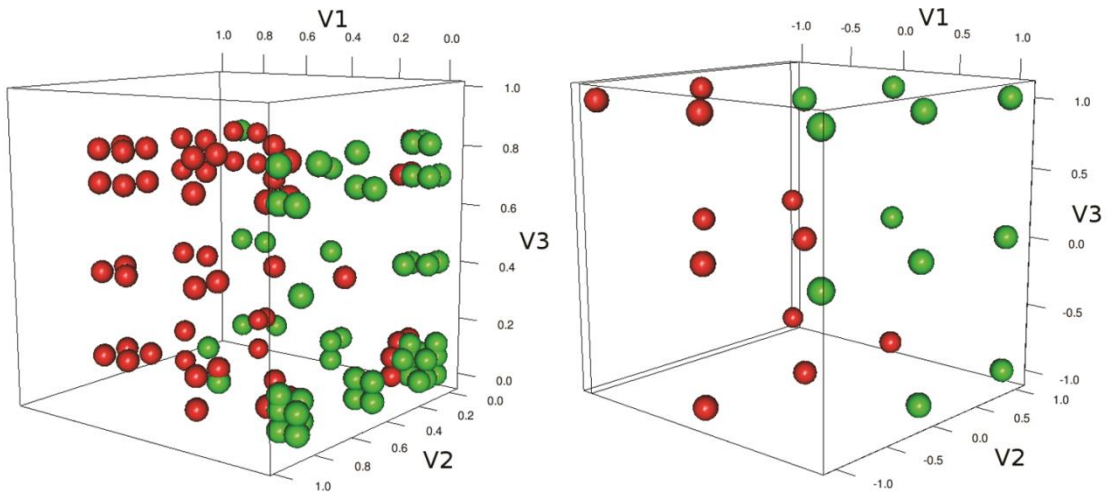

Figure 4.2 The distribution of tripeptide sequences of the 25 % strongest (green) and 25 % weakest inhibitors (red) from the previous combinatorial library in the space of the described hydropathy *(left*) and charge (*right*) vectors. The three dimensions V1, V2, V3 correspond to the three amino acid positions in the tripeptide sequences. Note that in the right every position marked by a ball is occupied by several superimposed balls.

Besides the studies on the correlation of enzyme inhibition with the amino acid composition of the tripeptide sequences, we were also interested in identifying possible binding sites for this kind of ligands on the protein surface. Therefore, docking studies with the simple tripeptide sequence KWR derived from the strongest inhibitor $(RWKG)_4$ in the previous combinatorial library were performed. We wanted to see to which position of the enzyme this tripeptide can bind and hopefully this binding sites information could help us in the development of improved inhibitors. The tripeptide was modeled with Yasara[241] and WhatIF[242] and then docked with Autodock Vina[243] into the crystal structure of human β-tryptase (PDB code: 1A0L). Water molecules within the crystal structure as well as the bounded ligand in this structure were removed. In the docking process, the tripeptide was flexible and the enzyme conformation was retained, and the whole surface of the enzyme was scanned. With the help of computational docking, we identified four

potential binding sites of the tripeptide KWR on the enzyme. Two predicted binding sites are located at the interfaces of two monomers within the tryptase tetramer (green in Figure 4.3). These two binding sites are predicted to bind to the peptide with the highest affinities. Two peptides bound at these two binding sites would have a distance between 26-27 Å. This distance could just be bridged easily by the tetravalent ligands that we used in our previous study. The other two predicted binding sites are located around the catalytic centers within the monomers (red in Figure 4.3). Because of the symmetry of the enzyme, there should be potentially four of these binding sites in the tetramer. The six ligand poses with the highest affinities (out of nine best obtained from AutoDock vina) are all located at the monomer-monomer interfaces; they have significantly higher affinities than poses located round the catalytic centers. The minimum distance between peptides docked at the two different binding sites is 16-17 Å, which means that the tetravalent ligand could in principle easily bind to both types of binding sites at the same time. This docking study therefore nicely confirms the previous experimental results:[13] The monovalent peptide RWKG is indeed a competitive inhibitor of β-tryptase but only with moderate affinity (K_i = 306 μM). This result is in agreement with the now predicted binding sites around the catalytic active centers. The binding at the interface of two monomers is preferred as well for the monovalent ligand. However, binding of just one linear peptide at this binding site is not enough to inhibit the enzyme. Obviously substrate access to the active sites is not blocked. This only occurs when both binding sites at the monomer-monomer interfaces are occupied by one ligand which binds across the central pore of the enzyme.

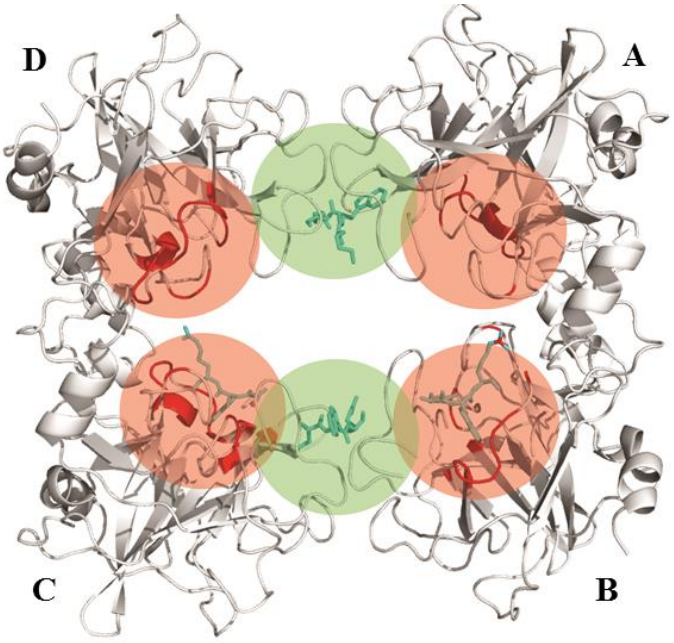

Figure 4.3 Potential binding sites of β-tryptase derived from a computational docking study with the tripeptide KWR. The four monomers of the enzyme are named A, B, C and D. Two types of binding sites were found, one with higher affinity at the two monomer-monomer interfaces (green), and one around the four catalytic centers (red).

Therefore, the statistical analysis confirmed that peptide sequences with a combination of cationic and aromatic amino acids are preferred. Moreover, low hydropathy and positive charge at the first position of the peptide sequence has the greatest positive impact on the enzyme inhibition. Docking study indicated that multivalent ligands should be superior to monovalent ones for enzyme inhibition. The size of the multivalent ligands should span the distance between the binding sites at the monomer-monomer interfaces or the binding sites around the catalytic centers. This way the central pore of the enzyme can be blocked and access of the substrate to the active site is prevented.

4.1.2 Synthesis of the Guanidiniocarbonyl Pyrrole Moiety (GCP) as Tailor Made Binding Motif

The basic GCP motif has been demonstrated by our working group to be an efficient binding site for oxoanions and had already been used for the design of artificial receptors for amino acids, oligopeptides or oligonucleotides and found to be an efficient artificial transfection vector for gene delivery.[14-15] We know that this binding motif in its protonated form has superior anion binding affinities compared to the natural basic amino acids lysine and arginine used for this purpose. So it is used as an artificial arginine analogue and can be incorporated into the peptide ligands to test how this motif affects the enzyme inhibitory properties. Because the synthesis of the GCP group has been reported in the literature and is well known and frequently used in our working group, it is described only briefly in a short overview (Scheme 4.1).

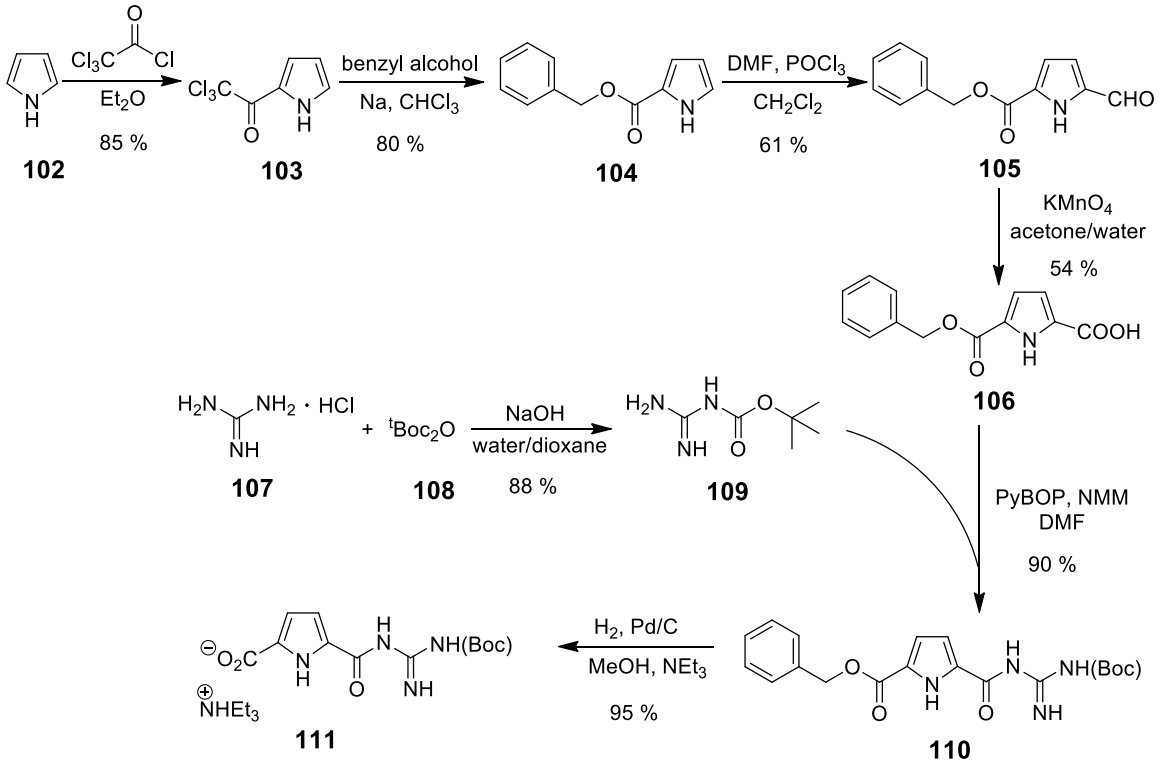

Scheme 4.1 Synthesis of the guanidiniocarbonyl pyrrole (GCP) binding motif.

The synthesis of the GCP started with commercially available pyrrole (**102**) which was acylated with trichloroacetyl chloride in diethylether through an electrophilic aromatic substitution reaction to give trichloroacetyl pyrrole (**103**). This compound was then subjected to a haloform reaction with benzyl alcohol in the presence of a small amount of sodium to give the benzyl ester (**104**) which was purified by a flash column chromatography. In the following *Vilsmeier-Haack* formylation, the *Vilsmeier* reagent, produced by adding phosphoryl chloride to dimethylformamide (DMF) was added to the benzyl ester solution to give the 5-formyl pyrrole-2-carboxylate acid benzyl ester (**105**). In this step a byproduct 4-formyl pyrrole-2-carboxylate acid benzyl ester was formed as well but in a lower amount which can be easily separated by chromatography. The aldehyde (**105**) was then oxidized to the carboxylic acid (**106**) with potassium permanganate in a mixture of acetone and water. In the next coupling reaction, the *N*-Boc-guanidine (**109**) which was obtained from the reaction of guanidinium chloride (**107**) with Boc_2O (**108**) was reacted with the acid (**106**) by using PyBOP as the coupling reagent and *N*-methylmorpholine (NMM) as a base to give **110**. In the last step, the benzyl ester group was cleaved off by hydrogenation with a catalytic amount of palladium on activated charcoal in methanol in the presence of triethylamine to give Boc-protected guanidinocarbonyl pyrole (**111**).

4.1.3 Solid Phase Peptide Synthesis of Tetravalent Peptide Ligands

The peptide ligands were synthesized with 9-fluorenylmethyloxycarbonyl (Fmoc) solid phase peptide synthesis (SPPS).[244-246] By using this method, the peptide ligands can be easily prepared on a solid support in a high yield and purity. The principle of this method is to attach the first amino acid via a linker to a polymeric solid support and then grow the desired peptide sequence which can be cleaved from the solid support under appropriate acidic conditions. Generally, the syntheses take place from C- to N-terminus and the amino acids which are temporarily protected via base labile Fmoc protecting group at their N-termini are attached to the free N-terminus of the growing peptide chain by activating the C-termini with a coupling reagent. In the Fmoc strategy the side chains of the amino acids have to be protected to avoid the cross-reaction, most commonly with acid-labile protecting groups, e.g. *tert*-butyloxycarbonyl (Boc), *tert*-butyl (*t*Bu) and 2,2,4,6,7-pentamethyldihydro- benzofuran-5-sulfonyl (Pbf) groups.[247] These protecting groups on the side chains need to be stable during the syntheses and should be easy to remove in the end. The amino acids and the protecting groups used for the SPPS in this project are shown in Figure 4.4. Generally the coupling reactions are carried out by using an excess of amino acids and coupling reagents with respect to the resin-bound functional groups to ensure complete conversion. One advantage of solid phase peptide synthesis is the easy removal of byproducts or coupling reagents from the resin by filtration and washing steps during the synthesis so that no purification steps are needed in between the synthetic steps. The purification is needed only after the cleavage of the product from the

resin under acidic conditions. Therefore, as a convenient method for peptide synthesis, SPPS is adapted to various conditions and requirements of the preparation of oligopeptides with high yields and purities.

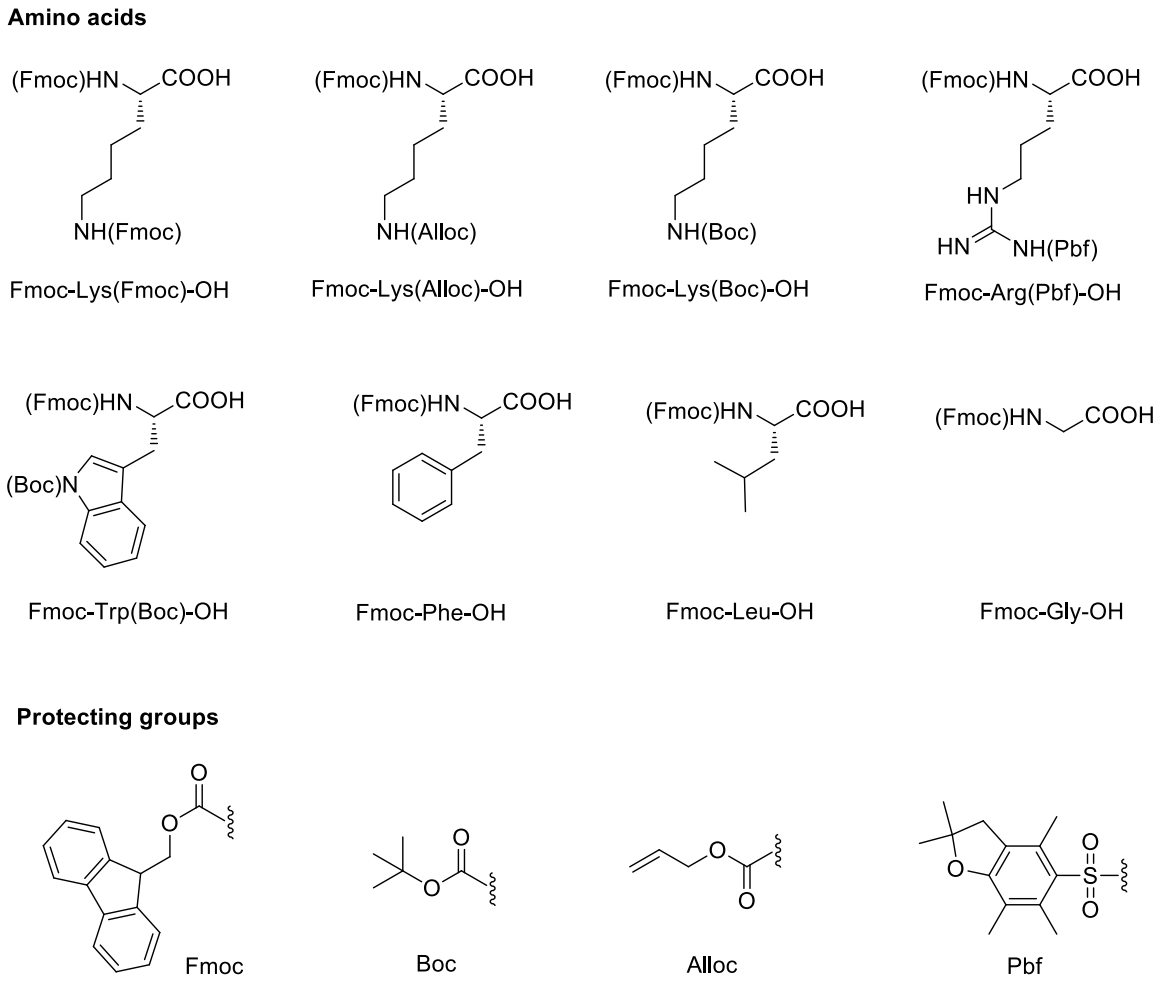

Figure 4.4 The amino acids and the protecting groups used for the Fmoc-SPPS in this project.

The peptides in this work were synthesized with either the acid-labile modified Rink amide linker (Rink amide MBHA resin) or an equivalent linker directly linked to a polystyrene base matrix (Rink amide resin) via the formation of peptide C-terminal amides. The polymer matrix is 1 % divinylbenzene (DVB) cross-linked polystyrene, 100-200 mesh. Because attachment of the peptide to amine supports is made via an amide bond, coupling of the first amino acid can be achieved using normal methods of amide bond formation. Since 4-dimethylaminopyridine (DMAP) is not required for this step, there is no risk of racemization or dipeptide formation. Cleavage of the peptide amide from the solid supports can be done in a single step by treatment with 95 % trifluoroacetic (TFA). Figure 4.5 showed the Rink amide linker and Rink amide MBHA linker both with Fmoc-protected amine.[248-249] The linker used for the resin is to provide the reversible linkage between the solid support and the growing peptide chain, and to protect the C-terminal α-carboxyl group during the process of peptide chain extension. It is also

important for the cleavage of the peptide from the solid support. Both of the resin linkers are designed to release peptide amides upon treatment with TFA. The Rink amide resin is more acid sensitive than the Rink amide MBHA resin. Cleavage with high concentration of TFA can lead to the breakdown of the linker, with the concomitant formation of byproducts that are hard to remove by simple washing steps. However, these problems can be minimized by the use of low concentration of TFA or by the addition of trialkylsilanes to the cleavage mixture. Rink amide MBHA resin consists of the modified Rink amide linker attached to MBHA resin via an unusual amino acid norleucine which is less acid sensitive.[249-250] Both of them are used very often in Fmoc-strategy by providing peptide C-terminal amides in high yields and purities.

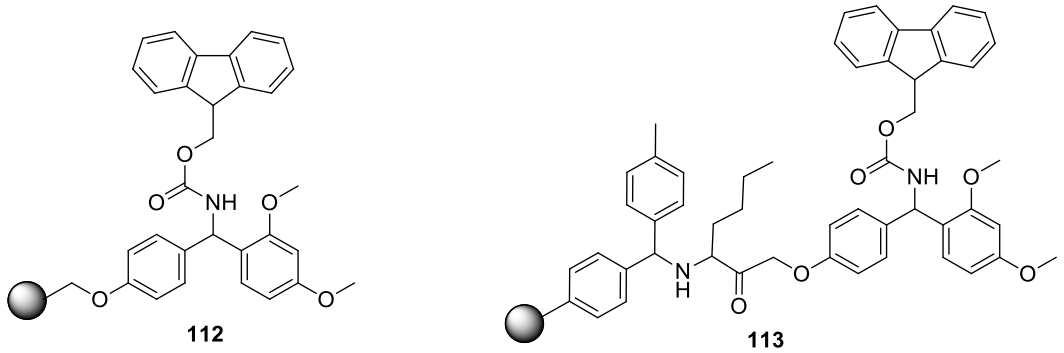

Figure 4.5 Rink amide resin (*left*) and Rink amide MBHA resin (*right*).

Determination of the Loading Values of Rink Amide Resin and Rink Amide MBHA Resin

Since the Rink amide resin and Rink amide MBHA resin were used most commonly in this work for the SPPS. The loading of these two resins was determined to test the amount of coupling positions on the resin. Each of the resins was weighed into a vessel. After the resins were allowed to swell in dichloromethane (DCM) for 1 hour, the Fmoc protecting group attached to the linker was removed by using 20 % piperidine/DMF, the solutions were filtered and collected and combined with the washing solutions as well to ensure the complete collection of the removed Fmoc groups. The dibenzofulvene-piperidine adduct (**114**) formed during the Fmoc deprotection could be detected with the help of its absorption at 301 nm by monitoring the UV/Vis spectrum between 250 and 350nm (Figure 4.6).[251]

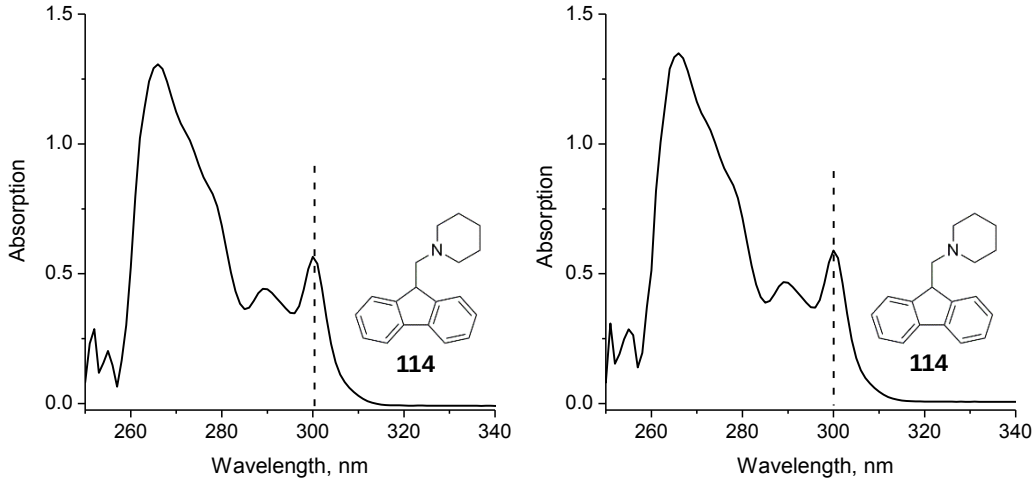

Figure 4.6 UV/Vis absorption spectra of dibenzofulvene-piperidine adduct (**114**) formed by the Fmoc deprotection from Rink amide resin (*left*) and Rink amide MBHA resin (*right*).

The concentration c of this adduct can be calculated by the measured absorption A at 301 nm with the help of *Lambert-Beer* Law (A = εbc). The specific absorption coefficient ε of this adduct[251] is 7800 L mol $^{-1}$ cm^{-1} and with the cuvette of width b = 1 cm, the loading L in mmol/g can be calculated using the following equation (8):

$$L = \underbrace{\frac{A}{b\,\varepsilon}}_{c} \frac{D\,V}{m} \qquad (8)$$

Where D is the dilution factor, V is the total volume of the collected solution, and m is the mass of the weighed resin beads.

Therefore, the amount of available coupling position is determined from the amount of cleaved Fmoc groups. For both resins the loading concentration was calculated via equation 8. The calculated loading value of the Rink amide MBHA resin is 0.67 mmol/g, which is in the range of the given value of the manufacturer (0.5-0.8 mmol/g). The calculated loading of Rink amide resin is 0.99 mmol/g which is a bit less than the given value (1.29 mmol/g). This could be due to the adsorption of moisture so that the real loading of the resin is less because the amount of resin contains some water due to a long time storage and use. Another possible reason could be due to the damage of some resin beads after a long storage time because the materials of the resin are somewhat friable and have a tendency to degrade over the course of long storage. The obtained loading values were used to calculate the amounts of the reactants for the couplings and the yields in the end.

Fmoc-SPPS of Tetravalent Peptide Ligands with Two Different Sets of Arms

For designing the tetravalent ligands **115-120** (Figure 4.7) with two different sets of arms, the best peptide sequence RWKG obtained from the previous library was always

chosen for the first set of arms except for ligand **116** which contained peptide sequence KWKG to allow a comparison of lysine and arginine at the first place. The basic amino acids lysine, arginine or its artificial analog GCP moiety and hydrophobic amino acid leucine and aromatic amino acids phenylalanine or tryptophan were selected to construct the second set of arms to test the influence of the new combination of different types of amino acids on the enzyme inhibition. The choice of these amino acids was based on the previous results obtained from the focused combinatorial library, now confirmed by the above discussed statistical analysis in chapter 4.1.1. These findings demonstrated that the combinations of cationic and aromatic amino acids provided the most efficient inhibitors of β-tryptase. Ligand **120** was designed by incorporating the artificial arginine analog GCP (**111**) into the first place of one set of arms replacing either arginine (**115**) or lysine (**116**) at this position in order to test how the artificial GCP moiety influence the enzyme inhibition. We chose again a second generation lysine dendrimer as a scaffold to build up the new type of tetravalent ligands. However, in order to attach two different sets of peptide arms two orthogonal protecting groups on the scaffold were needed. The Fmoc and allyloxycarbonyl (Alloc) groups were then chosen as the two orthogonal protecting groups for the lysine scaffold so that we can use standard Fmoc solid phase peptide synthesis. The Fmoc and Alloc protecting groups were used for the α-amino groups and the amino groups on the lysine side chains, respectively. The correspondingly protected lysine is commercially available. The Fmoc protecting group can be removed by using 20 % piperidine/DMF which is compatible with acid-labile side chain protecting groups. The Alloc group is fully compatible with the conditions encountered during solid phase peptide synthesis and can be removed with the well-established palladium-catalyzed hydrosilylolysis procedure without affecting the other acid labile protecting groups on the side chains of the used amino acids.[252-253]

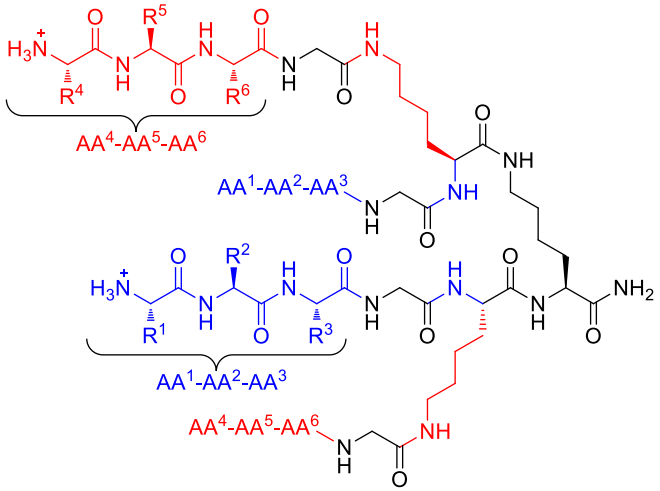

	AA^1	AA^2	AA^3	AA^4	AA^5	AA^6
115	Arg	Trp	Lys	Arg	Leu	Phe
116	Lys	Trp	Lys	Lys	Leu	Phe
117	Arg	Trp	Lys	Lys	Leu	Phe
118	Arg	Trp	Lys	Lys	Trp	Lys
119	Arg	Trp	Lys	Phe	Arg	Lys
120	Arg	Trp	Lys	GCP	Leu	Phe

Figure 4.7 Schematic representation of variations on the two different sets of arms of the tetravalent peptide ligands (**115-120**) for enzyme inhibition. The three positions on the two different arms are varied with cationic and aromatic amino acids, as well as the artificial arginine analog GCP moiety. The two different sets of peptide arms are colored in blue and red, respectively.

The synthesis of peptide ligand **115** was performed according to a standard Fmoc solid phase peptide synthesis (Scheme 4.2). Completion of each coupling and deprotecting step were monitored by a *Kaiser* test,[254] a color test for the detection of free amines which shows positive if free amines are present on the solid support most often after Fmoc deprotection while negative if all amines have been converted to amides after a quantitative coupling reaction. The synthesis was started on Fmoc-protected Rink amide resin (loading value: 0.99 mmol/g). After the resin was swollen in DCM for 1h to increase the accessibility of the Fmoc-amino groups inside the resin, the removal of Fmoc protecting group was achieved by treatment with 20 % piperidine/DMF for 20 min (2 times). The resin was thoroughly washed with DMF. The first coupling reaction using Fmoc-Lys(Fmoc)-OH and benzotriazol-1-yl-N-oxy-tris(pyrrolidino)phosphonium hexafluorophosphate (PyBOP) as coupling reagent in 4 % *N*,*N*´-diisopropylethylamine (DIPEA) in DMF with 2.5 equivalents of each reactant was achieved by shaking the mixture for 6-12 h under argon (Ar) atmosphere. Since very often the first coupling step of the solid phase peptide synthesis is rather difficult, resulting in incomplete conversions and thus in low yields and purities, this step was repeated to ensure a complete reaction of all free amino groups on the resin. A negative *Kaiser* test indicated the complete reaction. After the removal of Fmoc groups from both the α-amino group and the side chain amino group of lysine, the orthogonally protected amino acid Fmoc-Lys(Alloc)-OH was attached similarly by using 5 equivalents of each reactant to obtain the orthogonally protected lysine scaffold (**122**) with two sets of different protecting groups on the α-amino groups and the amino groups of the side chains. After removing Fmoc groups, the first two arms consisting of four amino acids: Fmoc-Gly-OH, Fmoc-Lys(Boc)-OH, Fmoc-Trp(Boc)-OH and Boc-Arg(Pbf)-OH were attached similarly to obtain **123** by using standard conditions according to Fmoc-SPPS. If necessary, the coupling step was repeated as indicated by the *Kaiser* test. Then the removal of the Alloc protecting group was achieved under neutral conditions with catalytic amount of tetrakis(triphenylphosphine) palladium(0) ($Pd(PPh_3)_4$) in the presence of phenylsilane ($PhSiH_3$) as a scavenger for the allyl unit.[252-253] After thoroughly washing with DCM and DMF, the second two arms consisting of four amino acids: Fmoc-Gly-OH, Fmoc-Phe-OH, Fmoc-Leu-OH and Boc-Arg(Pbf)-OH were attached to the resin, again using standard conditions for Fmoc-SPPS. After successful completion of all the couplings as indicated by the *Kaiser* test, the resin was washed extensively with DCM, methanol (MeOH) and DCM again. Then the resin was dried for 1 h and treated with a mixture of TFA/TIS/H_2O (95:2.5:2.5) for 3 h which led to the cleavage of the product from the Rink amide resin and the simultaneous removal of all the side chain protecting groups. Triisopropylsilane (TIS) and water are necessary as nucleophilic scavenger to intercept reactive cationic species which are formed from the protecting groups under these harsh conditions, e.g. *t*-butyl cationic species from the Boc deprotection.[255-256] The cationic species could be subject to the addition of the liberated amino acids containing electron-rich functional groups, e.g. tryptophan, tyrosine, *etc*. thus

reducing the yield and purity. After precipitation from diethyl ether the crude product was purified by reversed phase medium-pressure liquid chromatography (RP18-MPLC) using appropriate conditions (H_2O/MeOH + 0.1 % TFA). Pure product was transferred into its hydrochloride salt by dissolving in water with hydrochloric acid and lyophilizing several times. The product was obtained with > 95 % purity according to analytical high performance liquid chromatography (HPLC) analysis. The other ligands **116**-**120** were synthesized accordingly.

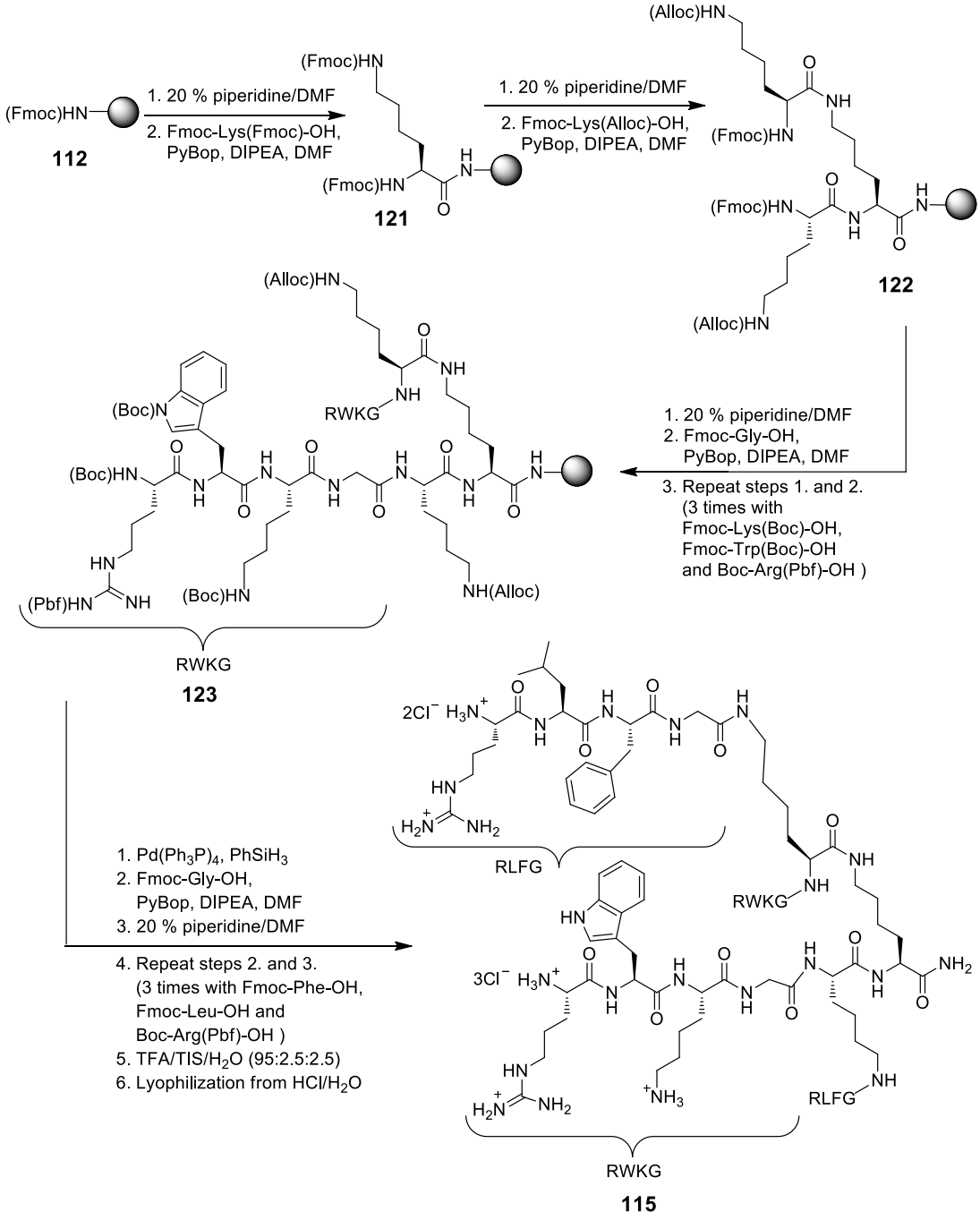

Scheme 4.2 Solid phase peptide synthesis of the peptide ligand **115** with two different sets of arms.

Syntheses of Tetravalent Peptide Ligands with Four Identical Arms Terminating with GCP Groups via Microwave-Assisted SPPS

As mentioned above, the GCP group was demonstrated by us to be an efficient anion binding motif which has superior binding affinities compared to both lysine and arginine. However, compared to side chain amino groups of lysine (pK_s ca. 10.5) and arginine (pK_s ca. 12.5), this GCP group is only partially protonated at neutral pH because of the reduced basicity (pK_s ca. 6.5). So it is unclear whether the use of this group can indeed improve the enzyme inhibitory efficiency under the physiological assay conditions. Therefore, in order to study the influence of this artificial arginine analog on the inhibitory properties compared to our previous results in more detail, the ligands **124**-**125** (Figure 4.8) with four identical arms ending with GCP groups were synthesized and tested for their inhibition of β-tryptase. A number of reports have advocated that the use of microwave-assisted solid phase peptide synthesis to obtain peptides represents a very efficient way not only accelerating both the coupling and deprotection reactions by increasing the temperature which is uniform in the whole reaction mixture volume in contrast to the oil bath, but also improving the purity and yield of difficult peptide sequences via the avoidance of aggregation as well as incomplete reactions as compared to the conventionally room temperature SPPS.[257-259] Traditionally, the heating method utilized by organic synthesis is carried out by conductive heating with an external heat source such as an oil bath or electric plate heater. This is comparatively slow and inefficient way for transferring energy into the reaction system since it depends on convection currents and the thermal conductivity of the various materials that have to be penetrated. In addition, a temperature gradient can develop within the sample and local overheating can lead to the formation of unwanted byproduct. In comparison, microwave technology uses electromagnetic waves that pass through material and cause the molecules in the material to oscillate, thus generating heat. The heat is generated mainly by dipolar polarization through the interaction of the polar molecules with the microwave irradiation. Generally, irradiation of microwave can heat the reaction mixture in a homogeneous and very efficient way. Since the preceding vessels are typically made out of microwave-transparent materials the radiation passes through the walls of the vessel directly into the whole reaction mixture volume, this way all reactants have the same energy and any temperature or energy gradient are avoided.

Therefore, we also tested microwave-assisted SPPS to synthesize ligands **124**-**125**. Again a second generation poly-lysine dendrimer was chosen as the scaffold to attach four identical arms consisting of a tri- ro tetra-peptide and the terminal GCP group. Ligand $(GCP\text{-}RWKG)_4$ (**124**) is derived from the best sequence $(RWKG)_4$ obtained from our previous work containing the same tetrapeptide sequence but with an additional GCP group at the end. Ligand $(GCP\text{-}RWK)_4$ (**125**) contains the terminal GCP group as well, but in contrast to **124**, the glycine was removed from the sequence. Initially, glycine was

added to the sequence as an invariable amino acid to increase the flexibility and the length of the arms allowing better interaction with the enzyme. However, it is not clear whether the glycine is necessary for the enzyme inhibition. Hence, both the influence of the glycine and the effect of the artificial GCP group on β-tryptase inhibition can be examined with these two ligands **124** and **125**.

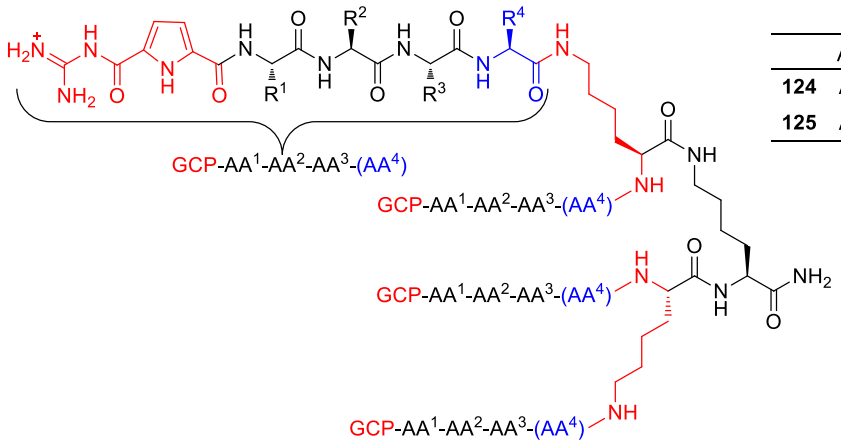

	AA^1	AA^2	AA^3	AA^4
124	Arg	Trp	Lys	Gly
125	Arg	Trp	Lys	—

Figure 4.8 Schematic representation of the structure of tetravalent peptide ligands (**124-125**) with four identical arms terminating with the GCP groups.

Ligand **124** was synthesized using microwave-assisted Fmoc solid phase peptide synthesis (Scheme 4.3). The microwave conditions (power, temperature and reaction time) were tested before starting the synthesis. Different power and temperature were tested by *Kuchelmeister* in his PhD thesis.[260] It was shown that variation of the power (10-100 W) did not cause big differences in the yields. Therefore, 20 W was chosen for the reactions. It has been reported that the microwave-assisted coupling reaction could be done without racemization at a temperature of 80 °C.[258] Therefore, 60 °C was used for the coupling and Fmoc deprotection reactions which worked very well with good yields. The next step was testing the time of the coupling and Fmoc deprotection reactions. The results showed that the coupling reaction was almost quantitative after 20 minutes. Therefore, the reaction conditions at 20 W with maximum temperature of 60 °C for 20 min were chosen for the coupling steps. If the *Kaiser* test was positive after the first coupling, 30 min was used for the second run. The Fmoc deprotection time was rather shorter, almost all the Fmoc groups were removed after 1.5 min, but to ensure quantitative deprotection, this reaction was repeated twice at 20 W with maximum temperature of 60 °C for 1.5 min and 5 min respectively. The synthesis was started from Fmoc-protected Rink amide MBHA resin (loading value: 0.67 mmol/g), which was swollen in DCM for 1 h at ambient temperature under Ar, followed by the Fmoc removal by treatment with 20 % piperidine in DMF first for 1.5 min and then for 5 min (20 W, T_{max} = 60 °C, ΔT = ± 5 °C). Afterwards the first amino acid Fmoc-Lys(Fmoc)-OH was attached using PyBOP as coupling reagent in 4 % DIPEA/DMF with 2.5 equivalents of each reactant. The reaction mixture was irradiated for 20 min (20 W, T_{max} = 60 °C, ΔT = ± 5 °C). The first coupling step was repeated to

ensure the complete conversion of all accessible amino groups on the resin. After Fmoc deprotection, Fmoc-Lys(Fmoc)-OH was attached again similarly using 5 equivalents of each reactant to obtain the lysine scaffold (**126**) with four identical branches featuring Fmoc protected amino groups. Then after removing all the four Fmoc groups on the lysine scaffold with the help of microwave irradiation, the following four amino acids: Fmoc-Gly-OH, Fmoc-Lys(Boc)-OH, Fmoc-Trp(Boc)-OH, and Fmoc-Arg(Pbf)-OH, as well as the Boc-protected GCP group (**111**) were attached similarly using 10 equivalents of each reactant to build up the four identical arms. Completion of each coupling and deprotecting step was monitored by *Kaiser* test. After the last coupling step, the resin was thoroughly washed with DCM, MeOH and DCM again, then the resin was dried for 1 h and treated with a mixture of TFA/TIS/H_2O (95:2.5:2.5) for 3 h at room temperature without microwave irradiation which led to the cleavage of the product from the resin and the simultaneous removal of all protecting groups. After precipitation from diethyl ether, the crude product was purified by RP18-MPLC using appropriate conditions (H_2O/MeOH + 0.1 % TFA). Pure product was transferred into its hydrochloride salt by dissolving in water with hydrochloric acid and lyophilizing several times. The product was then obtained with > 95 % purity according to analytical HPLC analysis. The other ligand **125** with four identical arms and tailor-made GCP groups were synthesized accordingly.

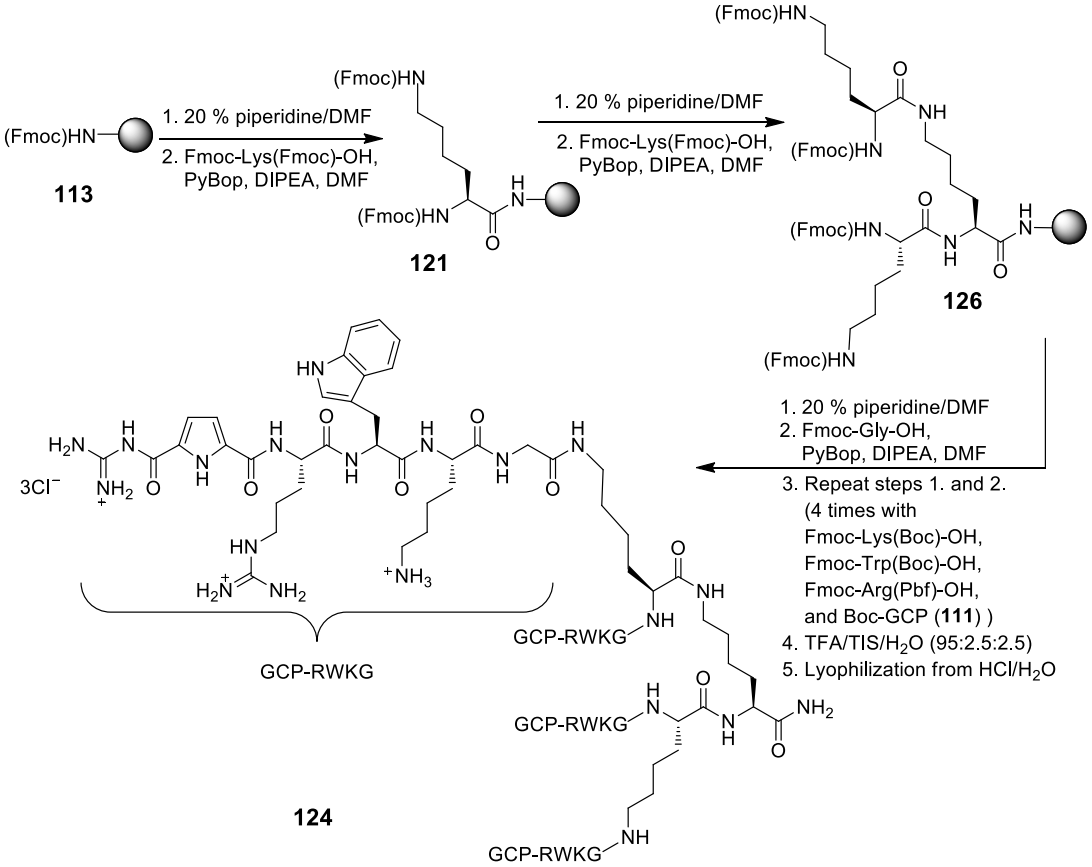

Scheme 4.3 Microwave-assisted solid phase peptide synthesis of the peptide ligand **124** with four identical arms and tailor-made GCP groups.

4.1.4 Enzyme Assay

The enzyme activity is regularly examined by fluorescence measurements which measure the fluorescence change of the cleaved product over time, resulting in linear curves with varying slopes depending on different enzyme activities. The theoretical background information about the principles of the enzyme assays has been already described in Chapter 2.1.2. The specific procedures according to literature known procedures,[13, 114, 120] but with some modifications applied to the serine protease β-tryptase used in this project will be explained in the following section.

As described in Chapter 2.2, the tetrameric structure of β-tryptase is stabilized by heparin, and in the absence of heparin β-tryptase dissociates into monomers and is not enzymatically active anymore. Therefore, the heparin-stabilized Skin β Tryptase, Human, Recombinant (rhSkin β-tryptase) was used in this work. The enzyme was commercially available in aqueous solution at a mass concentration of 200 μg/mL. For easier use the enzyme (0.5 mL) was separated into aliquots in 50 vials, so that it was available in single vials each containing 2 μg of the enzyme in 10 μL solution at the same concentration of 200 μg/mL.

Tryptase is known to cleave peptides on the C-terminal side of lysine and arginine amino acid residues. Therefore, the fluorogenic substrate N-*p*-Tosyl-Gly-Pro-Arg 7-amido-4-methylcoumarin hydrochloride (Tos-Gly-Pro-Arg-AMC, **127**) can be used for determining the enzymatic activity of β-tryptase. Upon cleavage by the enzyme a strong increase of fluorescence emission at 460 nm (380 nm excitation) occurs due to the release of the free 7-amino-4-methylcoumarin (AMC, **129**) which can be used to monitor the kinetics of the enzymatic cleavage (Figure 4.9).

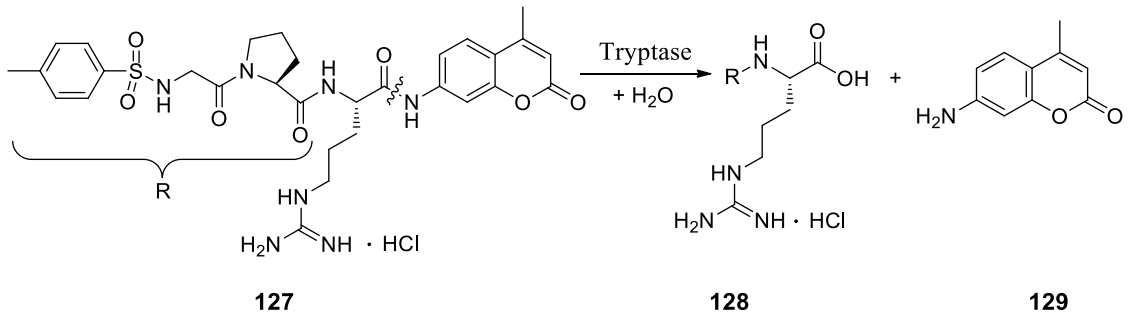

Figure 4.9 Hydrolysis of the fluorogenic substrate Tos-Gly-Pro-Arg-AMC (**127**) by β-tryptase. The fluorescence active AMC (**129**) was released upon enzyme cleavage.

Enzyme Kinetic Assay Method

In order to measure the kinetic parameters for the hydrolysis of the fluorogenic substrate Tos-Gly-Pro-Arg-AMC by rhSkin β-tryptase, the experiments were performed in a high throughput kinetic assay using a fluorescence spectrophotometer with a microplate reader unit and white 96 well plates. The assay was carried out in a 50 mM Tris-HCl

buffer at pH 7.4, containing additional 50 µg/mL heparin (to stabilize the enzyme), 0.02 % Triton-X (to minimize aggregation) and 100 mM NaCl. The enzyme was prepared in assay buffer and the final concentration of the enzyme used in the assay had to be determined prior the tests. In order to avoid the detection problems, the appropriate concentration of the enzyme should be tested to make the slope of the linear graph (the product conversion over time) between 15 and 30 by measuring the enzyme at different dilutions in the absence of inhibitor. The stock solution of substrate was prepared in dimethyl sulfoxide (DMSO) at a concentration of 2 mM. All the inhibitors were prepared as a stock solution of 1 mM in DMSO. The kinetic assays (at 25 ^{o}C) were carried out in a final volume of 200 µL in assay buffer (165 µL) wherein the enzyme (10 µL, final concentration 0.25 nM) was incubated with various concentrations of inhibitors (20 µL) and finally the substrate (5 µL, final concentration 50 µM) was added. All the solutions were thoroughly mixed and finally the increase of fluorescence activity was measured at 460 nm emission (380 nm excitation) over the time of 15 min.

The inhibitory activities (in %) of all the inhibitors was first determined four-fold at an inhibitor concentration of 100 µM. If the enzyme inhibition was higher than 80 % also the half maximal inhibitory concentration (IC_{50}) was determined at varying inhibitor concentrations and the enzyme inhibition constant (K_i) can be calculated from the IC_{50} depending on the binding mechanism to the enzyme. For this purpose the assay was done by measuring a dilution series of the stock solution of inhibitors in DMSO resulting in the following final concentrations: 100 µM, 80 µM, 60 µM, 40 µM, 20 µM, 10 µM, 8 µM, 6 µM, 4 µM, 2 µM, 1 µM, 0.1 µM. Depending on the inhibition activity, sometimes bigger and smaller concentrations had to be prepared (1000-0.01 µM). Figure 4.10 shows the inhibition profile for the rate of hydrolysis in the presence of different concentrations of inhibitor **115** as a representative example. The resulting data were processed with the Excel and GraFit program to obtain the kinetic parameters and the IC_{50} value was determined by nonlinear regression analysis.

The *Michaelis* constant (K_m) for the combination of β-tryptase and the substrate Tos-Gly-Pro-Arg-AMC was determined by measuring the reaction rate with different substrate concentrations but the same enzyme concentration in the absence of any inhibitors by *Wich*.[126] The K_m value was obtained as 368 µM.

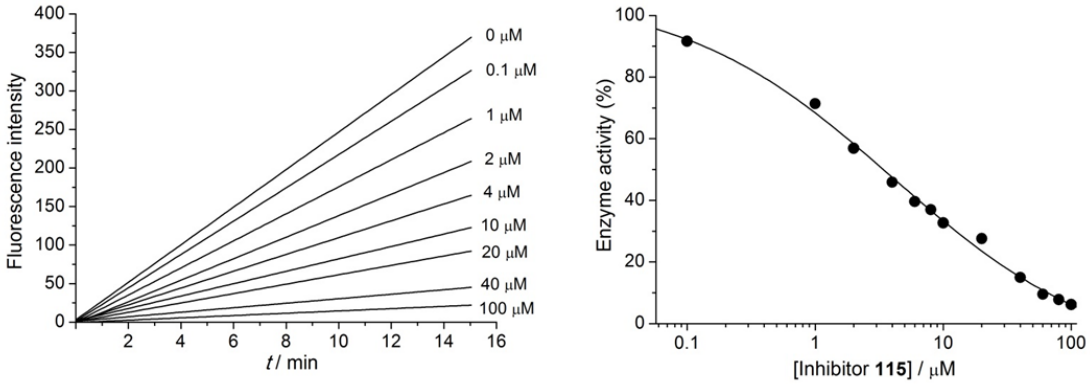

Figure 4.10 *Left:* Product conversion over time at different concentrations of inhibitor **115**. *Right:* Nonlinear regression analysis of the residual enzyme activity versus the inhibitor concentration for the determination of the IC_{50} value.

Enzyme Inhibition Results

The six peptide ligands with two different sets of arms and the two tetrapeptide ligands with four identical arms were tested for the enzyme inhibition. All structures are shown in Figure 4.11 and Figure 4.12. The inhibitory activities (in %) of all the ligands was first determined at the ligand concentration of 100 μM. All the ligands showed inhibition of more than 80 % at this concentration (Table 4.1 and Table 4.2). We then determined the IC_{50} value and from this the K_i value can be evaluated. A 4-parameter equation (9) was used to calculate the IC_{50} values of the inhibitors with the help of GraFit program.

$$y = \frac{Range}{1 + \left(\frac{x}{IC_{50}} \right)^{s}} + \text{Background} \qquad (9)$$

x is the concentration of the inhibitor, *y* is the enzyme activity, *Range* is the fitted uninhibited value minus the Background, and *s* is a slope factor. The equation assumes that *y* falls with increasing *x*.

Since this type of ligands binds to the enzyme noncompetitively (see page 89), IC_{50} and K_i values are identical in this case.[261] The K_i values of all ligands are summarized in Table 4.1 and Table 4.2.

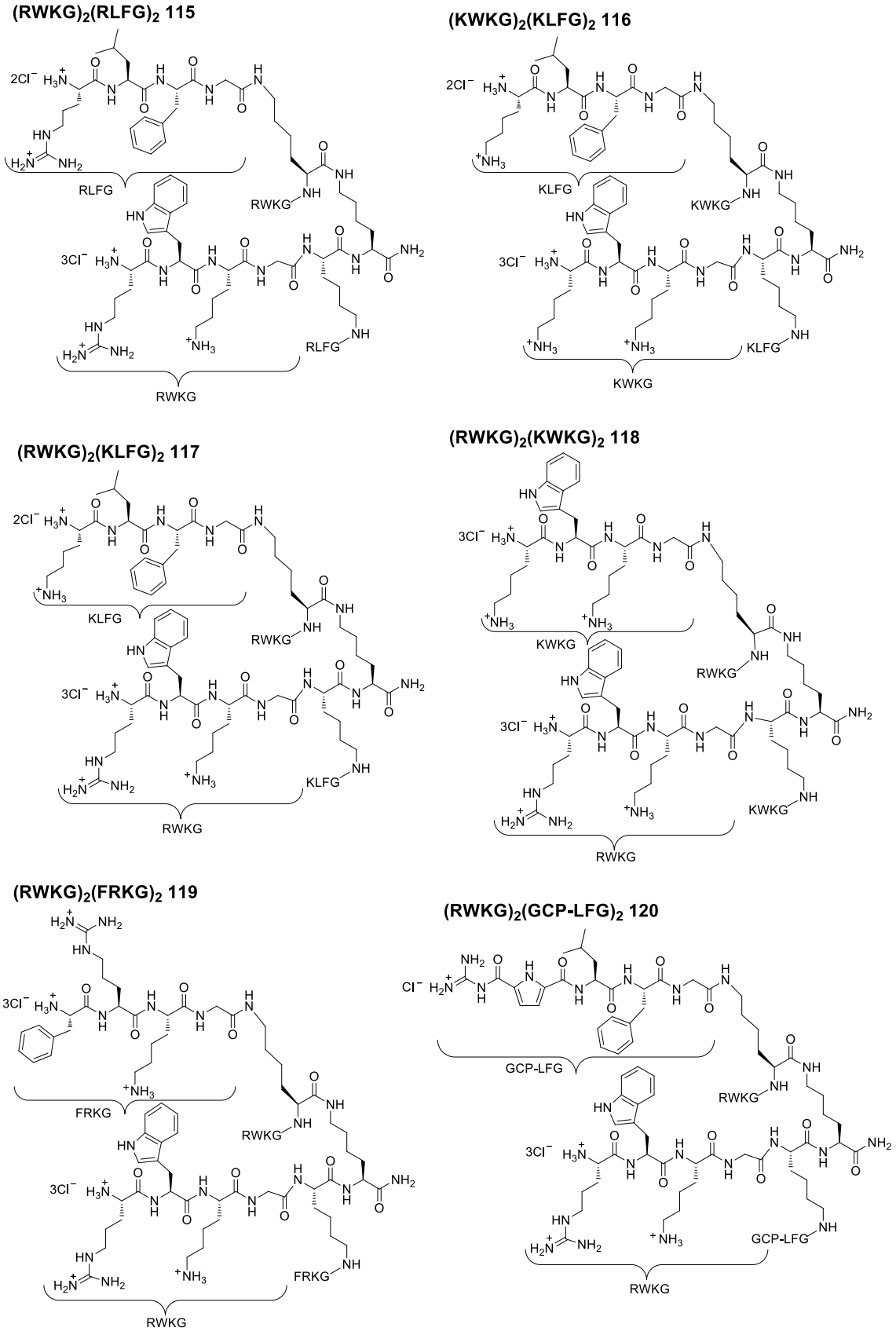

Figure 4.11 Structures of the ligands (**115**-**120**) with two different sets of arms tested for the enzyme inhibition (including short form of the names for easy comparison with the inhibition results).

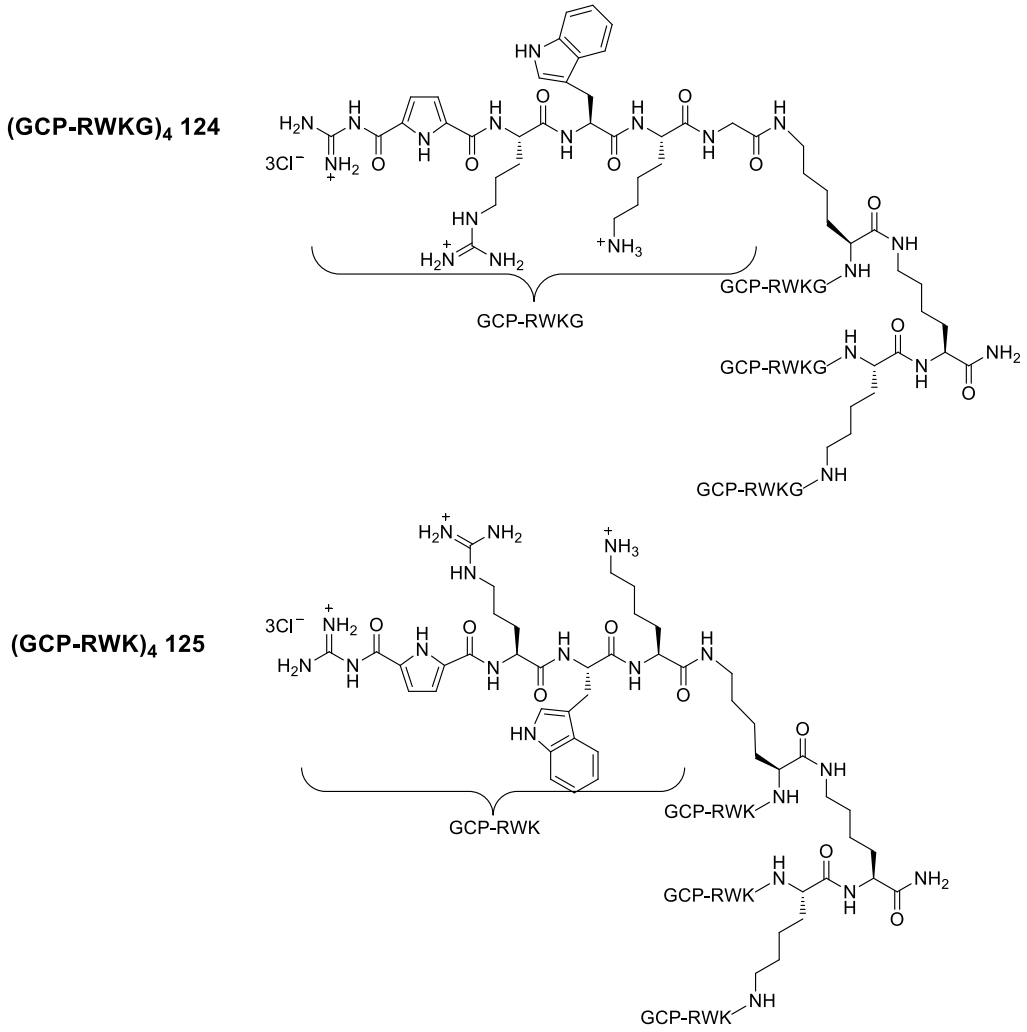

Figure 4.12 Structures of the ligands (**124**-**125**) with four identical arms and terminal GCP groups in all four arms tested for the enzyme inhibition and the influence of the artificial GCP units (including short form of the names for easy comparison with the inhibition results).

The results of the enzyme screening assay (Table 4.1) clearly showed that the tetravalent peptide ligands (**115**-**120**) with two different sets of arms based on the orthogonally protected lysine scaffold efficiently inhibit β-tryptase. Ligands **115**-**119** show similar enzyme inhibitory potency in a lower micromolar range. The similar K_i values of ligands **115** and **117**, as well as **116** and **117** revealed that there are no significant differences of enzyme inhibitory efficiency upon varying the first amino acid arginine or lysine of one pair of arms. Furthermore, most of these combinations of two different arms tested so far are not superior to the original best tetravalent peptide ligand $(RWKG)_4$ (K_i = 0.17 μM) obtained from the initial focused combinatorial library. However, ligand **120** containing the artificial GCP groups in one set of arms is the most effective ligand in this series. This ligand is approximately two orders of magnitude more potent than ligands **115**-**119**, which consist of similar peptide sequences but without the artificial GCP groups. More interestingly ligand **120** is even more efficient than the best original ligand

$(RWKG)_4$ as the apparent K_i value of ligand **120** calculated from a monophasic inhibition profile is 0.067 μM. Obviously the presence of the GCP group has a significant influence on the inhibition properties of this kind of peptide ligands. For example, the comparison of ligand **120** with its analogs **115** and **117** revealed that the artificial GCP group can significantly improve the inhibition of β-tryptase: replacing the amino acid arginine in ligand **115** with the GCP group increases the affinity by a factor of 60 whereas the replacement of lysine in ligand **117** with the GCP group increases the affinity by a factor of 200.

Table 4.1 Enzyme inhibitory activities of peptide ligands **115-120** with two different sets of arms at a concentration of 100 μM and their corresponding K_i values.

Ligands	Inhibition	K_i [μM] [a]		
		rhSkin β-tryptase	Trypsin	α-Chymotrypsin
$(RWKG)_2(RLFG)_2$ **(115)**	94 %	4.04 ± 0.81	> 100	> 100
$(KWKG)_2(KLFG)_2$ **(116)**	94 %	12.77 ± 3.77	> 100	> 100
$(RWKG)_2(KLFG)_2$ **(117)**	97 %	13.37 ± 2.45	> 100	> 100
$(RWKG)_2(KWKG)_2$ **(118)**	98 %	10.37 ± 1.64	> 100	> 100
$(RWKG)_2(FRKG)_2$ **(119)**	98 %	8.16 ± 1.14	> 100	> 100
$(RWKG)_2$(GCP-LFG)$_2$ **(120)**	96 %	0.067 ± 0.024 [b]	> 100	> 100

[a] K_i values were calculated by fitting the inhibition data to a 4-parameter equation. [b] Apparent K_i value for a monophasic inhibition profile. The more detailed biphasic analysis provides a high and a low affinity binding mode (see Figure 4.13).

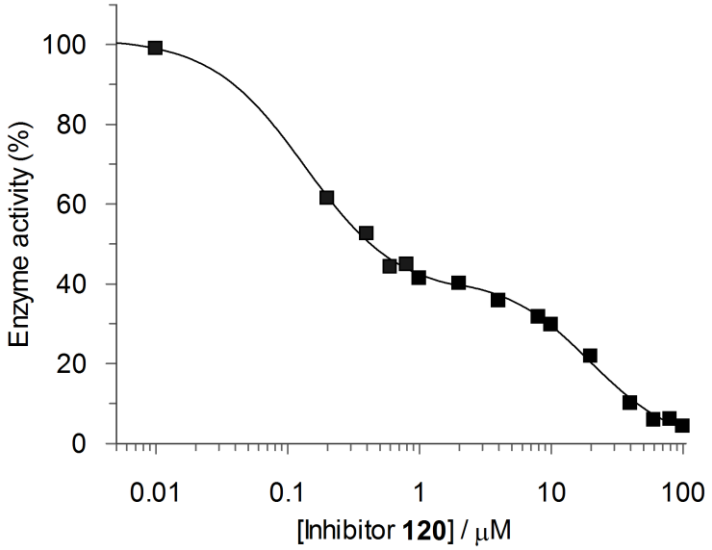

Figure 4.13 Biphasic inhibition curve of β-tryptase by inhibitor **120**. The plot represents the sum of two overlapping sigmoid curves separated by a plateau. The IC_{50} values for the high affinity (0.056 ± 0.026 μM) and low affinity (19.59 ± 2.63 μM) binding processes were estimated by GraFit program.

If we take a closer look on the inhibition profile of ligand **120**, it is found that the behavior of this ligand is even more complex. Instead of fitting well to a monophasic inhibition profile, the inhibition data (Figure 4.13) can be fitted best to biphasic kinetics,[262-263] showing two modes of inhibition with different binding affinities: one with high affinity (K_i = 0.056 ± 0.026 μM) and the other one with low affinity (K_i = 19.59 ± 2.63 μM). The biphasic inhibition profile illustrates the sum of two overlapping sigmoid curves which is separated by a plateau. Most likely this reflects the two different sets of binding sites on the surface of β-tryptase, with one being favored and the other one being less favored. This is consistent with the results identified from the docking study as described in Chapter 4.1.1 (Figure 4.3). The two different sets of arms of ligand **120** most likely bind to the two different binding sites of β-tryptase with different binding affinities. The reason why ligands **115-119** did not show similarly pronounced biphasic kinetics is unclear at this moment. Perhaps the binding affinity of ligands **115-119** to the two different sets of binding sites on the enzyme is not significantly different enough to lead to a biphasic inhibition mode. The artificial GCP group might also play an important role in the different inhibition behaviors which is the main difference between these two types of ligands. In ligand **120** the presence of GCP groups in one pair of arms instead of the proteinogenic amino acids changes the binding affinity to the anionic hot spots of the enzyme and differs much from the binding affinity of the other pair of arms. Whereas in ligands **115-119** the two different sets of arms contained only proteinogenic amino acids which perhaps do not allow discriminating significantly between the two sets of binding sites. Since the sequences of the two different arms in ligand **120** are yet to be optimized (e.g. using a combinatorial approach), the discovery of even more potent inhibitors based on this scaffold is possible.

Table 4.2 Enzyme inhibitory activities of peptide ligands **124-125** with four identical arms terminated with GCP groups at a concentration of 100 μM and their corresponding K_i values.

Ligands	Inhibition	K_i [μM] [a]		
		rhSkin β-tryptase	Trypsin	α-Chymotrypsin
$(GCP\text{-}RWKG)_4$ **(124)**	98 %	4.93 ± 0.96	>100	>100
$(GCP\text{-}RWK)_4$ **(125)**	96 %	10.67 ± 2.27	>100	>100

[a] K_i values were calculated by fitting the inhibition data to a 4-parameter equation.

The K_i values in Table 4.2 showed that ligands **124-125** featuring four identical arms terminating with GCP groups are also efficient inhibitors of β-tryptase. These two ligands show similar inhibitory properties for β-tryptase in a lower micromolar range. Initially, glycine as an invariable amino acid was added to the sequence to increase the flexibility

and the length of the linker, it was also interesting for us to vary the linker length but with exactly the same binding sequence in the arms to test how the linker length would affect enzyme inhibition. Hence, ligands **124** and **125** were designed with different linker lengths by incorporating the same binding sequence but with or without an additional glycine. The presence or absence of glycine has no significant influence on the K_i values, as identified by the comparison of ligand **124** with **125**, indicating that the tripeptide sequence plus the terminal artificial GCP group has the appropriate length to bind to the different binding sites on the surface of β-tryptase.

To obtain a better understanding of the interaction between the inhibitor and the enzyme, we then focused on the most potent inhibitor within this series (**120**), which has two different sets of arms and the artificial GCP group, to investigate the enzyme selectivity, the reversibility and the enzyme inhibition mode.

Enzyme Selectivity Assay

Human β-tryptase is from the family of serine protease but has a unique tetrameric structure. However, the other two archetypal serine proteases trypsin and α-chymotrypsin have significant sequence similarities with the corresponding β-tryptase monomer. Of the 245 residues of the tryptase monomer, 162 and 168 amino acid residues are topologically equivalent to chymotrypsin and trypsin, respectively, with an rms deviation of the α-carbon atoms of only 0.65 Å for both comparisons. Moreover, the active sites of the tryptase monomer and trypsin are quite similar in structure to each other. In particular, the S1 specificity pocket of tryptase is nearly identical to that of trypsin and it is well suited to accommodate P1 arginine and lysine side chains.[90]

Therefore, enzyme selectivity was tested against these two archetypal serine proteases trypsin and α-chymotrypsin. The enzyme assays with these two enzymes were performed in a 50 mM Tris-HCl buffer at pH 8.0, containing 5 mM EDTA and 100 mM NaCl according to the literature known procedure.[13] Fluorogenic substrates Z-Phe-Arg-AMC and Suc-Leu-Tyr-AMC were used for trypsin and α-chymotrypsin, respectively. However, our ligands showed no inhibition against either trypsin or α-chymotrypsin even at a concentration of 100 μM (Table 4.1 and Table 4.2). Hence the inhibitors seem to have no effect on the other two proteases, indicating our synthesized ligands are highly specific for β-tryptase compared to other closely related serine proteases. Also, these types of ligands might not bind to the active cleavage sites but interact with the entrance to the central pore or around the active catalytic center as identified by the docking studies in Chapter 4.1.1.

Reversibility of β-Tryptase Inhibition

The reversible binding between the inhibitors and the enzymes is based on rather weak non-covalent interactions and not the formation of chemical bonds or chemical reactions between inhibitors and enzymes. Therefore, the inhibitor-enzyme complex can rapidly dissociate with the recovery of the enzyme activity compared to an irreversible interaction. To verify that the enzyme inhibition in this work is rather caused by a reversible interaction than the decomposition of the enzyme, the reversibility of the β-tryptase inhibition was tested.

The first test on reversibility of β-tryptase inhibition was performed in a dialysis experiment. The principle of this experiment is that reversible inhibitors can be exchanged and washed away by buffer solution, thus the enzyme activity will be recovered over time. The Float-A-Lyzer G2 dialysis separation tubes (20 kDa) which contained a mixture (total volume of 800 µL) of assay buffer (Tris-HCl, 50 mM, pH 7.4), β-tryptase and inhibitor **120** in DMSO or pure DMSO (160 µL) as the reference were used. The dialysis tubes were floated vertically in the dialysate reservoir containing a stirring bar to adjust the stirring rate to form a gentle rotating current. The samples were dialyzed at room temperature and with 4 complete buffer changes (every 12 h) over a period of 48 h. The activity tests were done from time to time by taking a 100 µL sample from the dialysis tube, adding 95 µL assay buffer and the substrate (5 µL, final concentration 50 µM) before the mixtures were submitted to a fluorescence assay to determine the residual activity of the enzyme. With pure buffer even over a period of 48 h no significant recovery of enzyme activity was observed (the enzyme was reactivated only by 2 %). This is, however, not too surprising as it is well known that multivalent inhibitors with high binding affinity bind to the enzyme so tightly that they sometimes show kinetics similar to irreversible inhibitors.[264-265] Whereas the binding of a multivalent ligand to its target is similar to that of a monovalent ligand, the release of the ligand from the protein (the "off-rate") is extremely slow. This is the main reason for the multivalency effect, responsible for the significantly increased binding affinity of multivalent ligands compared to monovalent ones.

Therefore, a second experiment was performed to test the reversibility of enzyme inhibition. The inhibitor-enzyme complex was treated with the addition of excess heparin (a polyanion as a competing binding substrate for the ligand) in this test. If the inhibition is reversible, the cationic inhibitor should prefer to interact with heparin rather than the enzyme, which will lead to a recovery of the enzyme activity. In this experiment the enzyme was incubated with the inhibitor or blank DMSO in assay buffer (Tris-HCl, 50 mM, pH 7.4) for 5 minutes. Then in a parallel experiment, either heparin in buffer or buffer alone (5 µL) was added to the vials. All the vials were mixed and incubated for another 5 minutes, then the substrate was added and the residual activity of the enzyme was measured using the standard fluorescence assay.[266] 16 % recovery of tryptase activity

was observed, which confirms that the inhibition of β-tryptase by our tetravalent inhibitors is in principle reversible. Also, it indicated that the binding of the inhibitor to the enzyme does not damage the active tetrameric structure of β-tryptase.

Enzyme Inhibition Mode

The mode of enzyme inhibition was further determined in the following experiments to investigate how the inhibitors interact with the enzyme. The modes of inhibition are typically classified into three main types: competitive, uncompetitive, and noncompetitive inhibition. The theoretical background information of all these types of inhibition is described in Chapter 2.1.1. With the help of this determination, it is possible to test if the inhibitor binds into the active cleavage sites of the enzyme and where the inhibitor interacts with the β-tryptase.

Therefore, the rate of the enzyme reaction was measured at different substrate concentrations (10-600 μM) but always with a fixed enzyme concentration for different inhibitor concentrations (0, 5, 10 and 100 μM). The type of the inhibition was determined by interpretation of the nonlinear regression fits (Figure 4.14) as well as the linear *Lineweaver-Burk* plots (Figure 4.15). The analyses of both plots clearly indicate that the enzyme inhibition is noncompetitive. In the nonlinear representation, the maximum reaction velocity (V_{max}) is different for different inhibitor concentrations even at high substrate concentrations. In contrast, for competitive inhibition, increasing the substrate concentration would lead to the same maximum velocity independent of the inhibitor concentration. Furthermore, the half maximum reaction rate in each case is reached at similar substrate concentrations independent of the present amount of inhibitor, which confirms that the K_m value of the substrate is constant in the presence of different inhibitor concentrations. All the information is an indication for a noncompetitive inhibition. Moreover, the double-reciprocal *Lineweaver-Burk* representation shows that the plots for different inhibitor concentrations have no common interception on the y-axis which would be a sign for competitive inhibition. But they have a common intersection on the x-axis which indicates a noncompetitive inhibition. Hence, with the help of these experiments it is possible to prove that our tetravalent inhibitors do not compete with the substrate for the same binding site (active cleavage sites) and hence most likely interact with the surface of the enzyme. Therefore, these types of synthesized tetravalent ligands with tailor-made binding motifs are the reversible and noncompetitive inhibitors of β-tryptase.

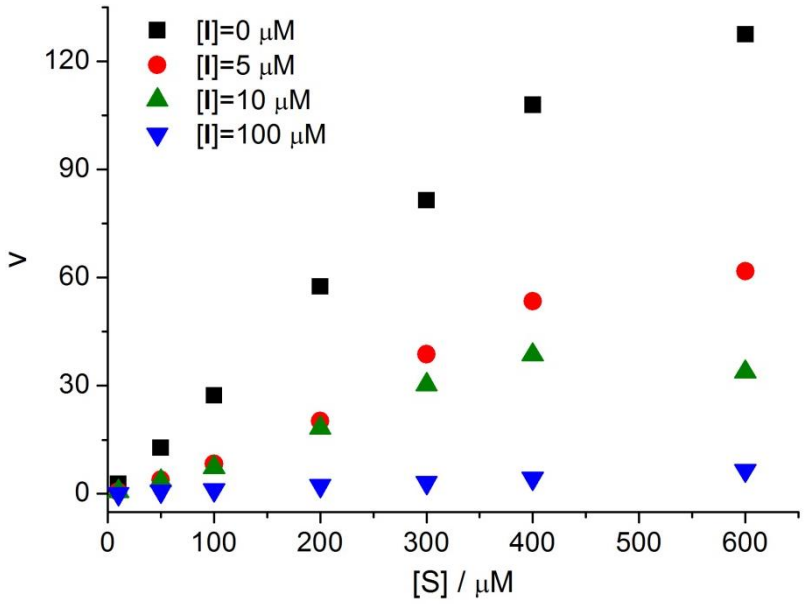

Figure 4.14 Nonlinear representation of reaction velocity against total substrate concentration according to the *Michaelis-Menten* equation. With increasing inhibitor (**120**) concentration, the K_m values are constant but the maximum reaction velocity decreases even for high substrate concentration which indicates noncompetitive inhibition.

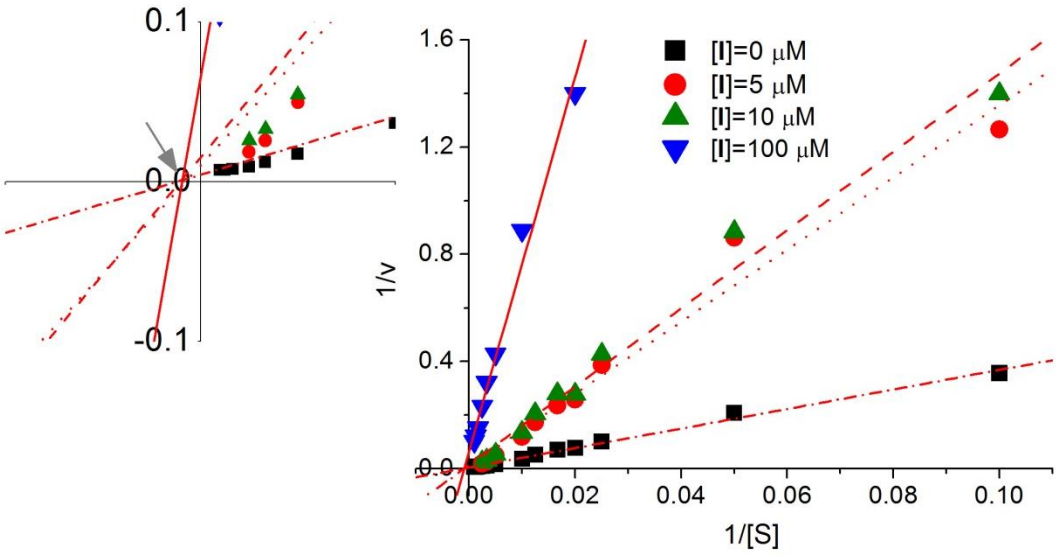

Figure 4.15 *Lineweaver-Burk* plots of 1/v against 1/[S] for inhibitor **120**. The plots at different inhibitor concentrations have a common intersection on the x-axis but not on the y-axis, which again indicates a noncompetitive inhibition.

4.1.5 Molecular Modeling Studies

The findings in the above chapters led to the most likely conclusion that the inhibitor rather blocks the accessibility to the active sites than binding directly to the active catalytic sites buried inside of the tryptase. To further verify how the inhibitor might inhibit β-tryptase, force field calculations were used to visualize possible binding modes between the inhibitor and β-tryptase. The central pore of β-tryptase features many negatively charged amino acid residues such as aspartic acids or glutamic acids and the synthesised inhibitors bear complementary charged amino acids in their side chains such as the basic lysine, arginine and the artificial GCP groups. Thereby most likely the calculations should demonstrate the ability of such inhibitors blocking the acidic pore of β-tryptase by building salt bridges via electrostatic interaction and hydrogen bonding. The calculations were performed by *Wilhelm Sicking* in our working group using the software Schrödinger MacroModel Version 9.6 with the optimized potential for liquid simulation (OPLS) 2005 force field choosing water as solvent. The enzyme input is based on the reported crystal structure of β-tryptase from the RCSB Protein Data Bank (PDB code: 1A0L). All water molecules and substrates within the PDB crystal structure were removed from the binding pore.

In order to start the calculation a start conformation of the inhibitor connecting to the acidic pore of β-tryptase was chosen. The structure of the enzyme was retained during the conformational search while the inhibitor was flexible. Therefore, the calculations began at the potential energy of the start conformation and by simulating new conformations a minimal potential was searched. The resulting structure was obtained from the result of 1000 calculation cycles.

The calculated binding mode of inhibitor **120** to the surface of β-tryptase is shown in Figure 4.16. A cluster of acidic amino acids accumulates at the entrance to the central pore and around the active cleavage sites of β-tryptase and thus attracts the basic amino acids of the inhibitor. The four arms of the inhibitor **120** can bind to these anionic residues around the entrance to the central pore via complementary electrostatic interactions and thus spread out across the pore of the enzyme, blocking the access of the substrate to the active cleavage sites.

Ribbon cartoon of the crystal structure of β-tryptase showed more clearly how the inhibitor binds to the central pore of the enzyme (Figure 4.17). The four monomers of the β-tryptase are named A, B, C and D. Key residues that interact with the inhibitor are displayed as sticks and numbered according to the protein sequence and monomers, respectively. The calculations reveal a number of key interactions for this inhibitor binding to the entrance of the central pore. Namely, the inhibitor is bound to the surface of β-tryptase by 14 hydrogen bonds. The side chains of arginine and lysine from one arm of the ligand bind to the interface of two monomers (A and D) of the enzyme mainly through the electrostatic interactions with Asp-145A, Asp-147A and Glu-149A. The lysine side

chain from the other arm of the ligand can bind to the interface area of the other two monomers (B and C) of β-tryptase by interacting with Glu-149C while the guanidinium group from the side chain of arginine forms a hydrogen bonded ion pair with Asp-145C from monomer C. Two GCP groups from the other two set of arms form hydrogen-bonding networks with Glu-217C and Gln-221C, Glu-217A and Asp-60B, respectively.

Figure 4.18 illustrates the schematic representation of the interactions between the ligand and the residues around the entrance to the central pore of β-tryptase. Only two different arms of the ligand are shown according to the symmetry of the molecule. As shown clearly, the basic arms of the ligand can indeed interact with the glutamic acids and the aspartic acids around the anionic hot spots of the enzyme. Note that one guanidinio group of GCP can form ion pairs with two residues of the enzyme at the same time. These modeling results agree very well with the findings from the docking studies (Figure 4.3) which showed that the two interfaces between the two sets of monomers within the tetramer are favored binding sites for this type of ligands. Therefore, the modeling also confirms that tetravalent peptide inhibitors with two different sets of arms can bind to the entrance to the central pore of β-tryptase as required for blocking access of substrate to the active sites of the enzyme.

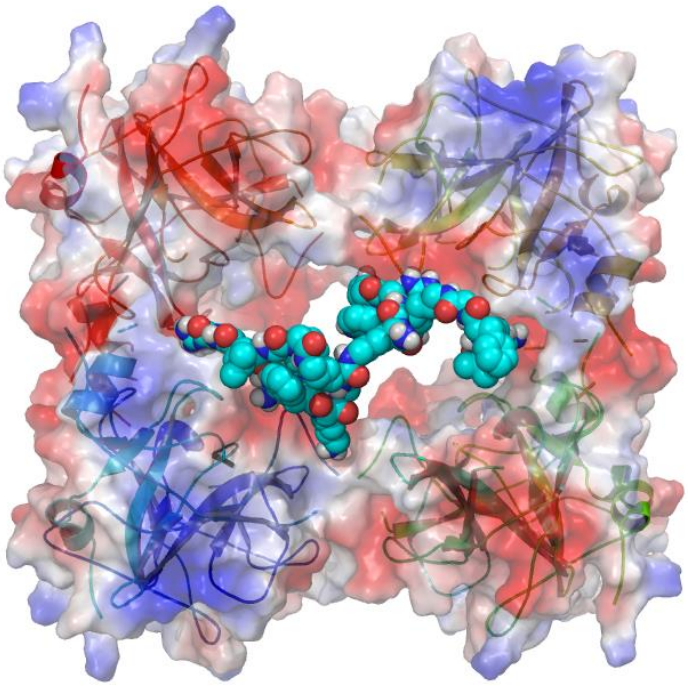

Figure 4.16 Calculated structure of a possible binding mode of the inhibitor **120** (shown as spheres with carbon atoms colored cyan) to the surface of β-tryptase (PDB code: 1A0L). Nonpolar hydrogens of the inhibitor were removed for clarity. The colors indicate positive (blue) and negative (red) electrostatic potential on the molecular surface of β-tryptase. A cluster of acidic amino acids is centered on the entrance to the central pore in which the active sites are buried. The inhibitor interacts with these acidic residues and spans over the central pore, thus blocking the access to the active sites.

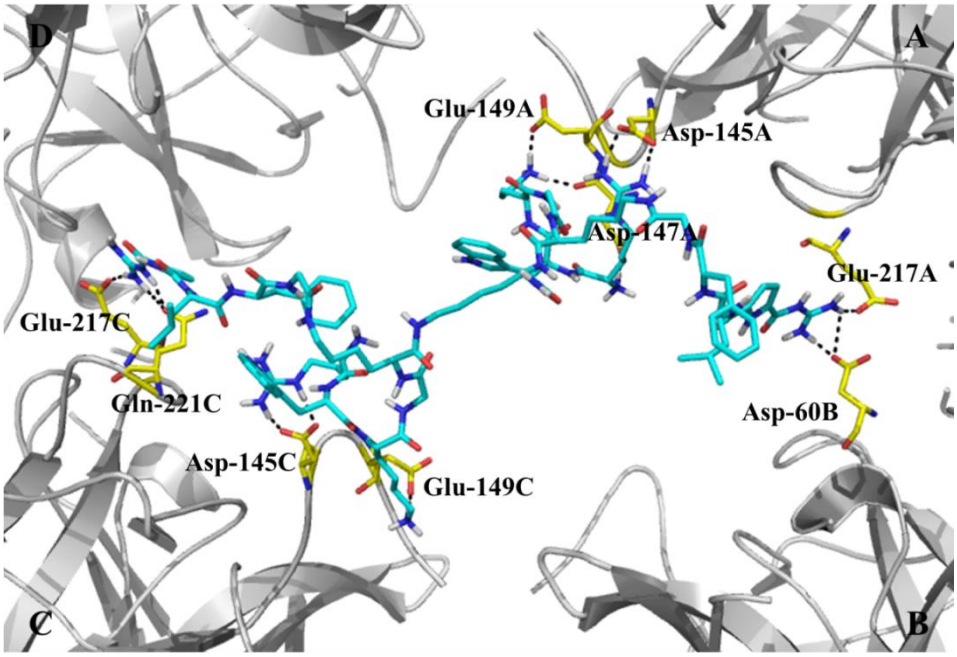

Figure 4.17 A close-up view of the binding region on the surface of β-tryptase. Inhibitor **120** is shown as sticks with carbon atoms colored cyan. The four monomers of the enzyme are named A, B, C and D. Key residues that interact with the inhibitor are displayed as sticks (carbon atoms colored yellow) and numbered according to the protein sequence and monomers, respectively. Binding interactions in the enzyme-inhibitor complex are shown as black dashed lines.

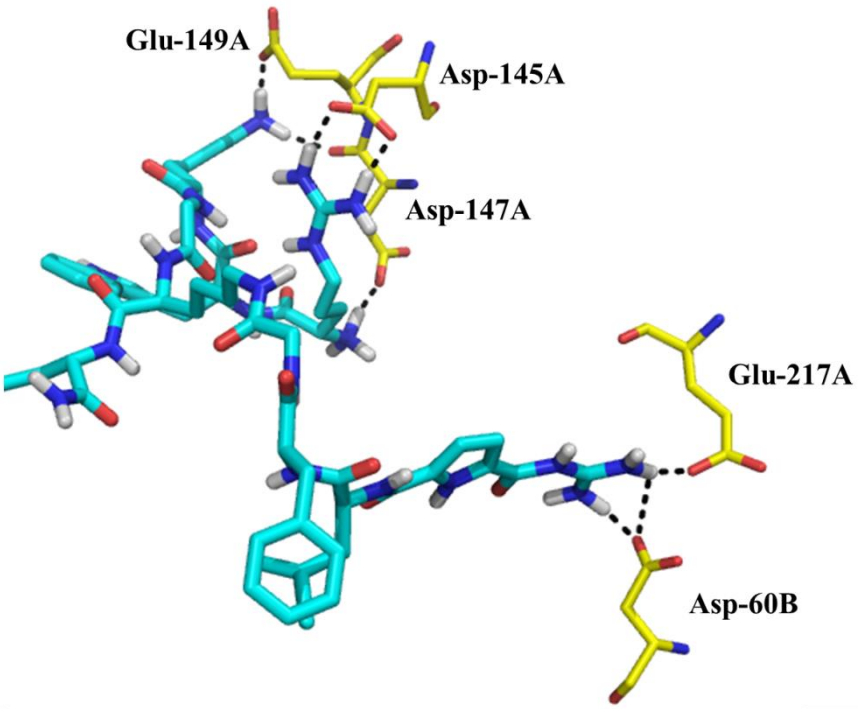

Figure 4.18 Schematic representation of the interaction between the ligand and the protein residues. Only two different arms of the inhibitor are shown according to the symmetry of the molecule. Non-polar hydrogen atoms have been omitted. The hydrogen bonds are presented as black dashed lines.

In conclusion, the first part of this thesis focused on the synthesis and evaluation of a series of tetravalent ligands featuring two different sets of arms and also containing the artificial arginine analog GCP as a tailor-made binding motif. Tetravalent ligands with four identical arms with the terminal GCP group were also investigated. They can bind to anionic hotspots on the surface of the enzyme near the entrance to the central pore, blocking the access to the active sites and thus inhibit β-tryptase in a reversible and noncompetitive way. All ligands efficiently inhibit β-tryptase with lower micromolar to nanomolar affinity and are highly selectivity for tryptase against other related serine proteases (e.g. trypsin, α-chymotrypsin). In collaboration with the group of *Prof. D. Hoffmann* and with the help of *W. Sicking*, we could demonstrate by docking studies and force field calculations that inhibition is most likely based on the complementary electrostatic interactions between the positively charged amino acids of the four-armed ligands and two kinds of favored anionic binding sites of the enzyme situated at the monomer-monomer interface (more favored) and around the active sites (less favored). The inhibition data show that the terminal artificial GCP groups can significantly improve the enzyme inhibitory activity compared to analogous ligands with only proteinogenic amino acids. The tripeptide arm plus the terminal GCP group on the lysine dedrimer scaffold is demonstrated to provide the appropriate length to bind to the different binding sites on the surface of the enzyme. Hence, we do not only demonstrate that multivalent ligands which can bind to the surface of the enzyme are efficient inhibitors but also that the design of tailor-made binding sites for specific amino acid residues is an attractive strategy for the design of high-affinity inhibitors. Because the peptide arms and the scaffolds are yet to be optimized, the discovery of more potent inhibitors by the combination of different peptide arms and scaffolds should be possible by using a dynamic combinatorial approach. Such an approach will be used to identify more efficient inhibitors of β-tryptase in the next chapter.

4.2 Discovery of Potent Inhibitors of Human β-Tryptase from Dynamic Combinatorial Libraries

We have successfully utilized the lysine dendrimer as scaffold for designing the tetravalent peptide ligands as the inhibitors of β-tryptase. It is also interesting for us to test other scaffold to build up the multivalent inhibitors, e.g. the scaffolds with various linker lengths, core flexibilities and functionalities. It has been demonstrated by the previous findings and the statistical analysis that the combinations of the cationic and aromatic amino acids in the binding arms provided the most efficient inhibitors of β-tryptase. More interestingly the artificial GCP group is demonstrated to have a beneficial effect on tryptase inhibition. Thus it is also interesting to utilize different potent combinations of the amino acid sequences and the artificial GCP group to provide the binding elements for inhibiting the enzyme. Therefore, in this project we describe a dynamic combinatorial approach to the discovery of new and potent inhibitors of β-tryptase with the help of dynamic deconvolution strategy. By using this approach it is possible to study various combinations of binding sequences and scaffolds for their inhibitory properties and hence to discover the efficient inhibitors of β-tryptase with less effort.

4.2.1 Design of Dynamic Combinatorial Libraries

As described in Chapter 2.5, the reversible acyl hydrazone formation by hydrazides and aldehydes in acidic aqueous media has been proven to be a highly suitable reaction for generating DCLs. Acyl hydrazone libraries are compatible with a wide range of solvents and functional groups. For example, the hydrazide functionality can be attached to the recognition elements and the aldehyde functionality can be reserved as the structural scaffolds (*vice versa*), leading to the formation of the multivalent ligands.

In this project, the dynamic combinatorial libraries were generated from the assembly of a series of peptide-derived hydrazide and aldehyde building blocks. In order to inhibit β-tryptase, the peptide sequences which have the capability of interacting with the enzyme were attached to the hydrazide moiety to form the peptide-derived hydrazides. The aldehyde building blocks were used as scaffolds to arrange the binding components in a given geometry and to provide the multivalent interactions. The aldehydes feature two or three aldehyde groups with various spacer distance and core rigidity to determine how these factors influence the inhibitory properties.

To identify the active compounds from such acyl hydrazone based DCLs, a dynamic deconvolution protocol was utilized.[225-227] The pre-equilibrated full library containing all the building blocks was prepared in the absence of the enzyme as well as different sub-libraries in which one specific building block is missing. By comparing the enzyme screening results for the full library with sub-libraries, the active building blocks can be selected from the libraries.

Design and Syntheses of Peptide-Derived Hydrazides

In order to use the Fmoc SPPS strategy to synthesize the peptide-derived hydrazides, the hydrazine should be modified with a dicarboxylic acid on one side to provide the hydrazide with one free carboxylate group to couple with the amino groups on the growing peptide arms. Therefore, the general strategy for this synthesis employed here was adapted from the literature with some modifications.[267-268] The synthesis (Scheme 4.4) started with commercially available hydrazine monohydrate (**130**) which was reacted with Boc anhydride (Boc_2O) to get the Boc-protected hydrazine (**131**). This compound was then reacted with succinic anhydride in water to give compound **132**. The reaction proceeded cleanly, and full conversion to **132** was confirmed by ESI-MS. The reaction mixture was lyophilized to obtain **132** which can be used in Fmoc SPPS without any further purification.

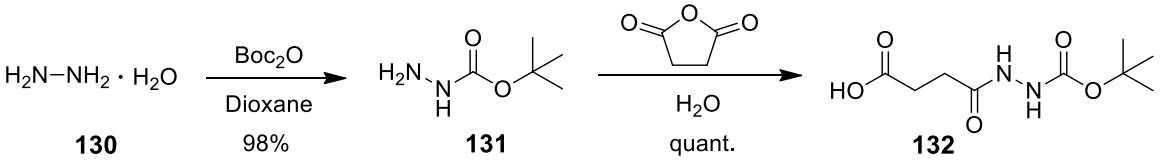

Scheme 4.4 Synthesis of the Boc protected butanedionic monohydrazide (**132**).

As depicted in Figure 4.19, the general design of the peptide-derived hydrazides (**133**) was to attach the various peptide sequences to the butanedionic monohydrazide part. The peptide chains are designed as the binding arms for β-tryptase. It has been demonstrated in the previous work that the combinations of cationic and aromatic amino acids in the peptide arms provide the highest affinity to inhibit β-tryptase whereas the introduction of anionic amino acids in their arms showed weak or no inhibition of β-tryptase. For example, *Wich* demonstrated that the best ligands $(RWKG)_4$ and $(KWKG)_4$ obtained from the screening results of the focused combinatorial library combined the positively charged and aromatic amino acids in their arms and showed efficient inhibition of the enzyme.[13] Therefore, in order to efficiently inhibit the enzyme, the same peptide sequences GKWR and GKWK were now chosen for the binding arms. I could also already confirm that the arginine analog GCP group has a beneficial effect on tryptase binding and inhibition. Therefore, this artificial GCP group was also incorporated into the peptide arm GKWK by attaching it to the different lysine side chains in the arm to test its influences on the inhibition of β-tryptase compared to the related natural peptide sequence GKWK. Furthermore, for comparison the negatively charged glutamic acid was introduced into one peptide arm as a negative control as the negative charge in the peptide chain is unfavorable for the inhibition of β-tryptase.

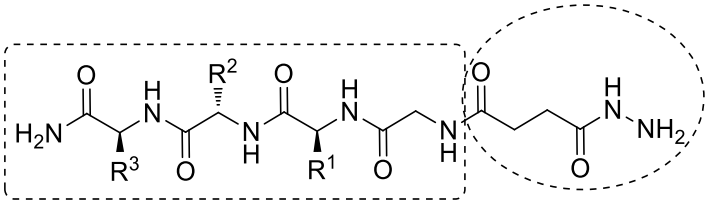

133

Figure 4.19 Schematic representation of the peptide-derived hydrazides (**133**) with variations on the peptide sequences for enzyme inhibition. The three positions on the peptide sequence are varied with cationic and aromatic amino acids, as well as the artificial GCP moiety.

Based on this design, the first peptide-derived hydrazide **135** was synthesized on the Rink amide MBHA resin using a microwave-assisted Fmoc SPPS procedure (see Chapter 4.1.3) as shown in Scheme 4.5. Because the resin was newly bought, so the loading value had to be tested before use. The determined loading value is 0.84 mmol/g, which is a bit higher than the resin used before (0.67 mmol/g). This is not hard to understand because the loading value of the resin that has been stored for a long time always decreases due to the adsorption of moisture or the damage of the resin beads. All the coupling and Fmoc deprotection steps were carried out under argon atmosphere. The resin was at first swollen in DCM for 2 h, followed by the Fmoc deprotection by treating the resin twice with 20 % piperidine/DMF under the standard microwave irradiation condition (20 W, T_{max} = 60 ℃, $\Delta T = \pm 5$ ℃, 1.5 + 5 min). Then the resin was thoroughly washed with DMF and the liberation of the free amino groups was confirmed by a positive *Kaiser* test. The first amino acid Fmoc-Arg(Pbf)-OH (3 eq) was attached to the resin with the help of the coupling reagent PyBOP (3 eq) and the base DIPEA (6 eq) in DMF by microwave irradiation for 20 min (20 W, T_{max} = 60 ℃, $\Delta T = \pm 5$ ℃). Then this coupling was repeated to ensure a complete reaction of all accessible amino groups on the resin. The successful quantitative coupling reactions were confirmed by a negative *Kaiser* test. Then after the Fmoc deprotection, the next three amino acids: Fmoc-Trp(Boc)-OH, Fmoc-Lys(Boc)-OH, Fmoc-Gly-OH and the Boc-butanedionic monohydrazide (**132**) were attached in the same manner. All the completion of the coupling steps were verified with the *Kaiser* test. If necessary, the coupling steps were repeated. Then the resin was thoroughly washed with 3 × DCM, 3 × MeOH, 3 × DCM and dried under vacuum for 1 h. To cleave the peptide, the resin was transferred to a glass peptide synthesis vessel and the product was cleaved from the resin by using a mixture of TFA/H_2O/TIS (95:2.5:2.5) for 3 h. Under these acidic conditions, all side-chain protecting groups were simultaneously removed. After precipitation from diethyl ether, the crude product was purified by RP18-MPLC using appropriate conditions (H_2O/MeOH + 0.1 % TFA). After the purification steps, the product was obtained with a purity of 99 % according to analytical HPLC analysis. Pure product was then transferred into its hydrochloride salt by dissolving it in water with hydrochloric acid and lyophilizing several times.

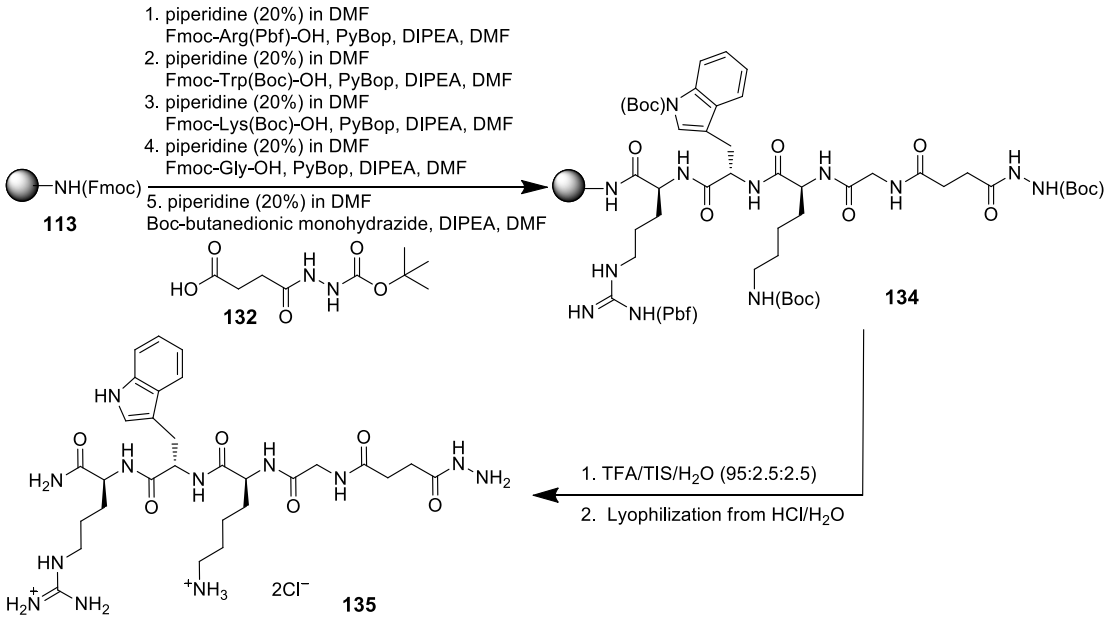

Scheme 4.5 Microwave-assisted Fmoc SPPS procedure for the peptide-derived hydrazide **135**.

The second peptide-derived hydrazide **136** was prepared according to the similar synthetic route of **135**. This compound **136** (Figure 4.20) contains the peptide sequence GKWK instead GKWR in hydrazide **135**. After the cleavage and purification steps, the product was obtained with 98 % purity according to analytical HPLC analysis.

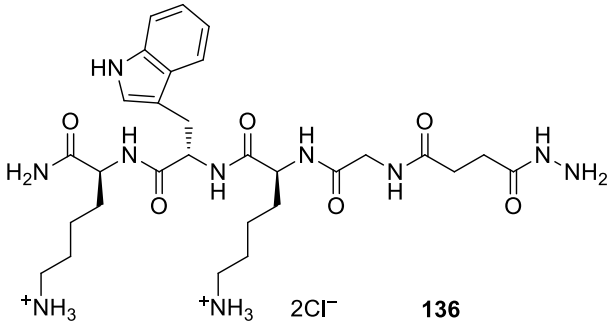

Figure 4.20 The peptide-derived hydrazide **136** was also prepared by using microwave-assisted SPPS.

The peptide-derived hydrazide **138** (Scheme 4.6) was synthesized under similar conditions as described for **135**. The Rink amide MBHA resin was swollen in DCM for 2 h, followed by the Fmoc deprotection by using 20 % piperidine/DMF. Then the first amino acid Fmoc-Lys(Alloc)-OH was attached to the resin with the help of PyBOP and DIPEA. Afterwards the three amino acids: Fmoc-Trp(Boc)-OH, Fmoc-Lys(Boc)-OH, Fmoc-Gly-OH and Boc-butanedionic monohydrazide (**132**) were attached to the resin accordingly. Then the Alloc protecting group was removed with $Pd(PPh_3)_4$ (0.1 eq) in the presence of $PhSiH_3$ (24 eq) in DCM for 10 min (20 W, T_{max} = 30 °C, $\Delta T = \pm 5$ °C). After washing with DCM and DMF, the Boc protected GCP unit (**111**) was attached to the lysine side chain by using the coupling reagent PyBOP and the base DIPEA. After the washing cycle, the product was cleaved from the resin using a mixture of TFA/H_2O/TIS

(95:2.5:2.5) for 3 h. After the purification and the counterion exchange steps, the product was obtained with 96 % purity according to the analytical HPLC analysis.

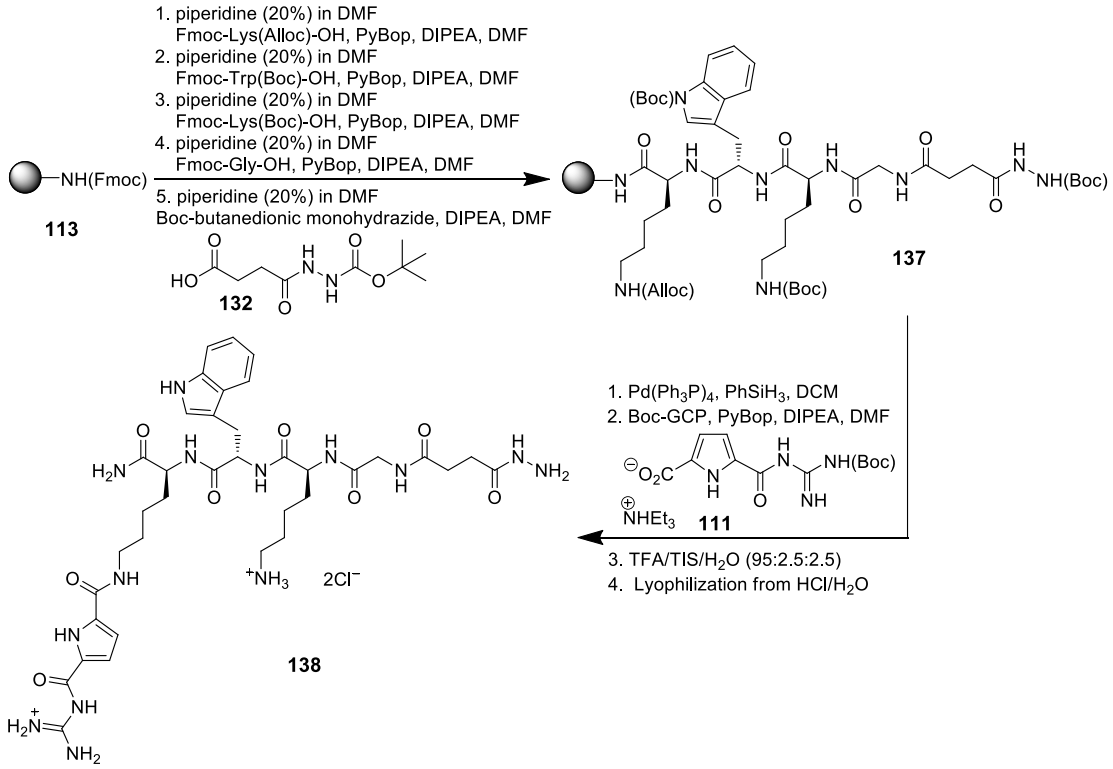

Scheme 4.6 Microwave-assisted Fmoc SPPS procedure of peptide-derived hydrazide **138**.

According to a similar synthetic route as depicted for **138** the peptide-derived hydrazide **139** (Figure 4.21) was prepared. Hydrazide **139** contains the same amino acid sequence GKWK and the artificial GCP group but featuring the GCP group at a different position. Hydrazide **139** was obtianed with a purity of 95 % as determined by analytical HPLC analysis. For comparison the peptide-derived hydrazide **140** with the peptide sequence GAFE was designed as a negative contol for the inhibition of β-tryptase. Hydrazide **140** was prepared according to the synthetic route as described for **135**. The product was obtained with a purity of 91 % according to analytical HPLC analysis.

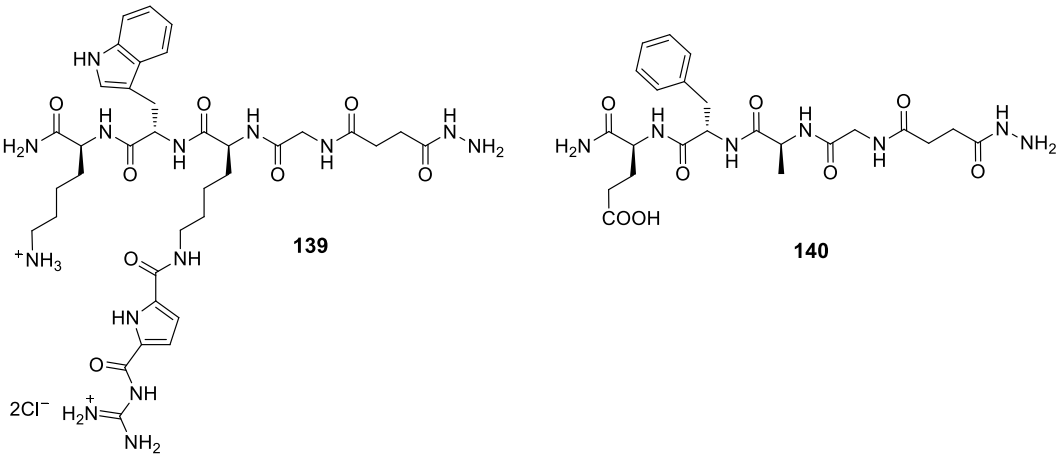

Figure 4.21 The hydrazides **139** and **140** were also prepared with the help of microwave-assisted SPPS.

4.2.2 Generation of Dynamic Combinatorial Libraries (DCLs)

The previous section has already described the design and synthesis of five different peptide-derived hydrazides (**135-136**, **138-140**) used in this project. Five different di- and tri-aldehydes (**A-E**) used here were commercially available. All the structures of these ten building blocks are depicted in Figure 4.22.

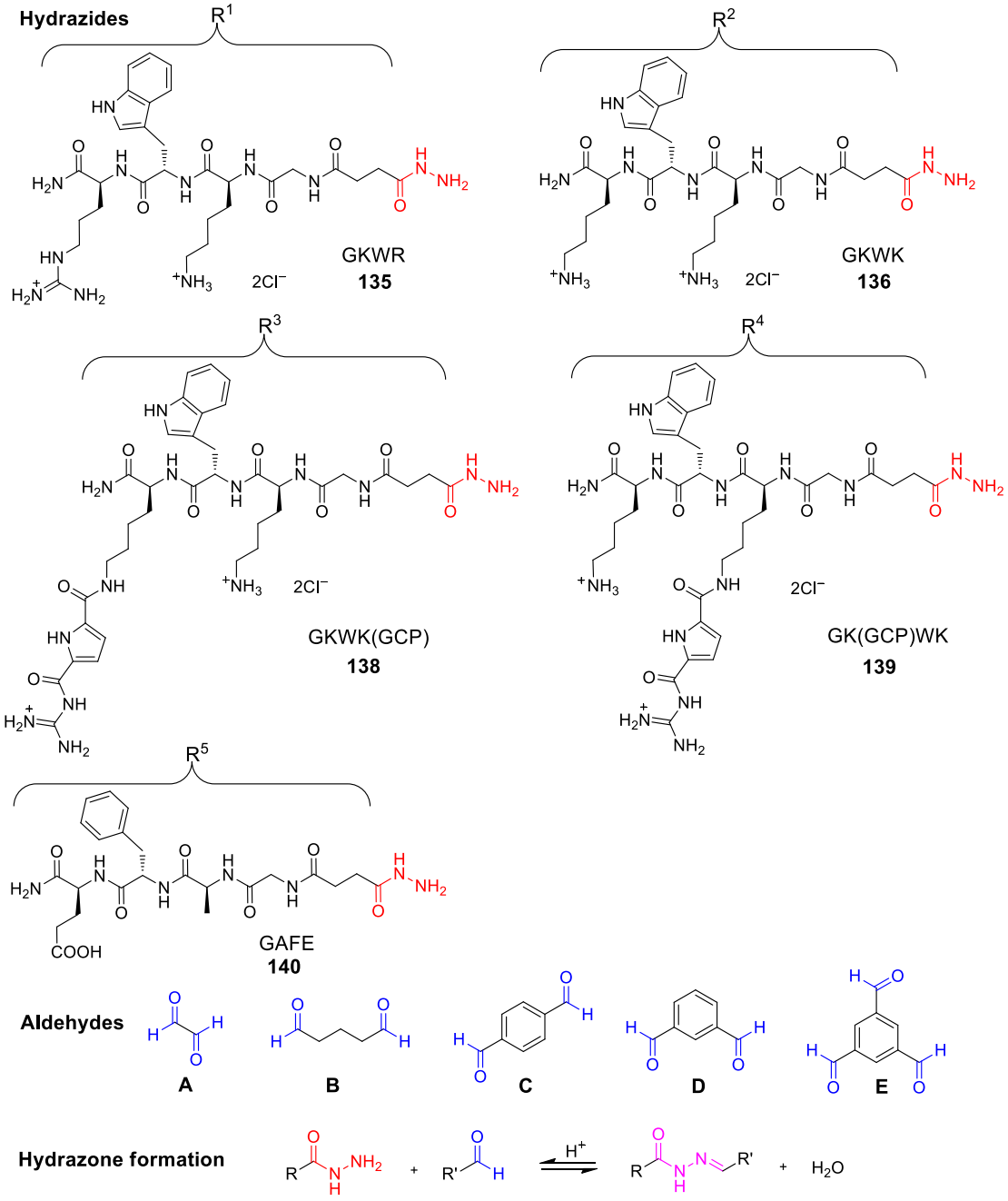

Figure 4.22 Structures of peptide-derived hydrazides (including short names of the peptide arms for easy comparison with the inhibition results) and aldehydes chosen as the building blocks of the DCLs. The headgroups of hydrazides and aldehydes which are subjected to the formation of the corresponding acyl hydrazones (colored purple) are colored red and blue, respectively. The structures of five quasi-peptide subunits are abbreviated as R with related numbers (R^1-R^5).

The IC_{50} values of all the ten building blocks were measured first to see how they alone can inhibit β-tryptase according to the described procedure in Chapter 4.1.4. As shown in Table 4.3, the four peptide-derived hydrazides (**135-136**, **138-139**) show some inhibitory activities for β-tryptase with IC_{50} values only in micromolar range. Hydrazide **135** containing the best peptide sequence GKWR from the previous combinatorial library shows the most efficient inhibition of the enzyme among all the five hydrazides. IC_{50} values of the two hydrazides (**138-139**) containing GCP groups are a bit lower than hydrazide **136** which consists of the same peptide sequence but with no GCP group attaching to the lysine side chain. As expected, hydrazide **140** with the negatively charged peptide arm shows no inhibition of the enzyme even at a high concentration of 1 mM. Moreover, all the aldehydes show no inhibition even at a very high concentration of 10 mM. Therefore, the aldehydes should rather provide the structural scaffold to build up the multivalent ligands than contribute to the enzyme inhibition.

Table 4.3 IC_{50} values [μM] for β-tryptase of the hydrazides and aldehydes used in the DCLs.

Hydrazides	IC_{50} [μM]	**Aldehydes**	IC_{50} [μM]
135	12.65 ± 0.61	**A**	> 10000
136	61.05 ± 3.97	**B**	> 10000
138	23.58 ± 1.17	**C**	> 10000
139	24.50 ± 2.87	**D**	> 10000
140	> 1000	**E**	> 10000

As described above, in order to identify the potent inhibitors from the libraries, a dynamic deconvolution strategy was utilized.[225-227] By removing a specific building block from the full library (containing all the ten building blocks), each sub-library can be built up, thus the importance of this missing component to form active compounds can be tested by comparing the activity of sub-library to that of the full library.

The maximum non-symmetrical library size N can be calculated by equation 10,[225] where n is the number of hydrazide and m_p is the number of aldehyde with different functionality degree p (e.g. p = 2 for di-aldehyde and p = 3 for tri-aldehyde). The library resulting from five hydrazides (n = 5), four di-aldehydes (m_2 = 4) and one tri-aldehyde (m_3 = 1) would contain 225 possible constituents (assuming all the aldehyde groups are reacted to form acyl hydrazones, not counting partially formed species).

$$N = \sum_p m_p n^p \tag{10}$$

However, since all the di- or tri-aldehydes are symmetrical, some of the combinations with hydrazides are identical, thus to remove the repetitive numbers the library size

number is reduced to N_{sym}, which is the symmetrical library not considering combination orders (equation 11).

$$N_{sym} = \sum_p \left[\frac{m_p}{p!}\prod_{i=0}^{p-1}(n+i)\right] \quad (11)$$

Therefore, on accounting for this symmetry effects, the full library number is reduced to contain 95 different library members. Upon the sub-libraries, the library sizes reduced differently depending on the removal of hydrazide or aldehyde with different functionality degree. For example, the library number reduced to 60 by removing one hydrazide whereas it reduced to 80 or 60 respectively by the removal of the di-aldehyde or tri-aldehyde. Thus, approximately 37 % or 16 % of the library constituents can be removed simultaneously from the full library by the removal of one component. Dynamic deconvolution strategy therefore provides a rapid way to identify the important components required for the activity of the library constituents.

In order to test the appropriate conditions for generating the DCLs, initial control experiment with one test library containing one hydrazide **136** and one aldehyde **E** was performed in 100 mM sodium acetate buffer at pH 4.0, upon agitation overnight. The resulting mixture was evaluated by analytical HPLC and electrospray ionization mass spectroscopy (ESI-MS). The HPLC runs (Figure 4.23) showed that at this conditions, this type of hydrazide and aldehyde do form a new compound. The ESI-MS verified that the new compound is the trivalent acyl hydrazone by assembly of hydrazide **136** and tri-aldehyde **E**. Thus, this condition can be used for the generation of DCLs.

Therefore, the dynamic libraries can be easily generated in sodium acetate buffer solutions at pH 4.0 containing 10 % DMSO (v/v) to help dissolve the aromatic aldehydes and the acyl hydrazones, upon gently agitation for three days. Normally the generation of acyl hydrazone libraries can be accomplished within a few minutes to a couple of hours, depending on the combination of hydrazide and aldehyde as well as the pH of the solution (e.g. a lower pH results in a faster reaction). However, in our case, to ensure the complete reaction, the reaction mixture was agitated for three days. Longer reaction times (five and ten days) were also tested, but did not show any different results, indicating the equilibration is complete after three days. The formation of acyl hydrazones was monitored by analytical HPLC and ESI-MS.

The full library was prepared by mixing all the ten building blocks (five hydrazides and five aldehydes) together in an aqueous acetate buffer solution (10 % DMSO) at room temperature. At the same time, 10 sub-libraries were generated under the same conditions by mixing all components except that one specific building block was omitted and replaced by the blank acetate buffer solution containing 10 % DMSO. Equilibration of all the libraries was carried out in the absence of the enzyme. The concentration of the hydrazide or aldehyde group of each building block was kept the same, e.g. stock solutions of the building blocks were prepared with 1 mM for monofunctional hydrazides,

0.5 mM for di-aldehydes and 0.33 mM for tri-aldehyde. The final concentration of the libraries amounted to 0.5 mM in total for both hydrazide and aldehyde groups. Together with a reference sample (acetate buffer containing 10 % DMSO) without any building blocks, this series of 12 samples was sufficient to screen the complete 95-membered library. After the resulting library mixtures were equilibrated for three days to ensure a complete equilibrium, the resulting acyl hydrazone libraries were adjusted to physiological conditions (pH 7.4) freezing-out the library composition. The libraries were then subsequently tested for inhibitory activity in the presence of β-tryptase.

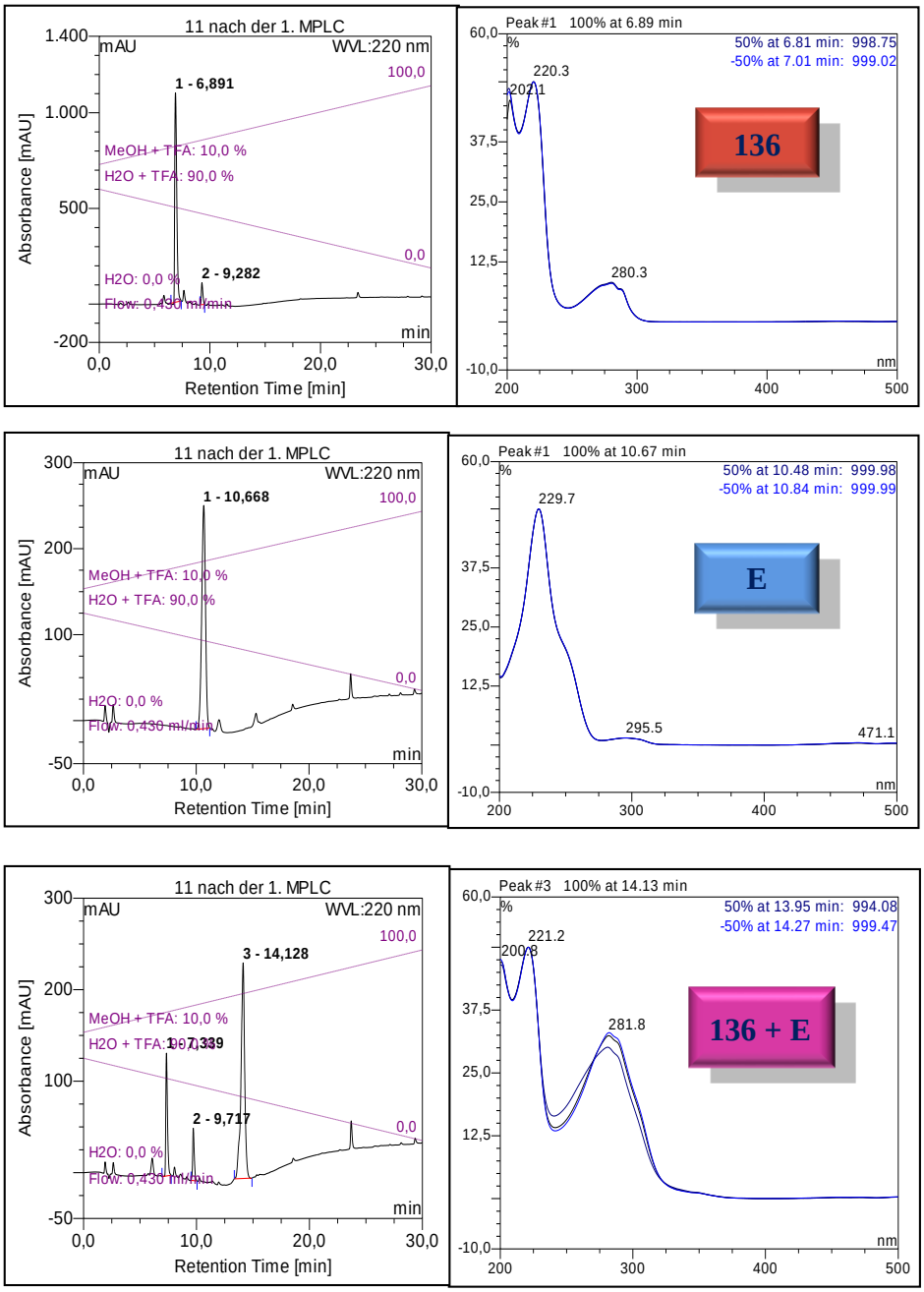

Figure 4.23 Analytical HPLC runs of peptide-derived hydrazide **136** (*top*), tri-aldehyde **E** (*middle*) and the resulting mixture with the formation of new acyl hydrazone (*bottom*).

4.2.3 Screening of DCLs by Dynamic Deconvolution Procedure

After the complete equilibration of all the libraries, the subsequent enzyme screening was performed under physiological conditions. The active inhibitors can then be identified by comparing the screening results of the ten sub-libraries with the full library. The decrease in inhibitory effect or the increase in enzyme activity would indicate the absence of important components for generating efficient inhibitors of β-tryptase. Inhibition experiments were performed in white 96 well microplate via a high throughput assay using a fluorescence spectrophotometer. The heparin-stabilized human rhSkin β-tryptase and the substrate Tos-Gly-Pro-Arg-AMC were used for the enzyme assay. All screening measurements of DCLs were performed in 50 mM Tris-HCl buffer solution at pH 7.4, containing enzyme stabilizer heparin, together with NaCl and Triton-X. In the enzyme screening measurement (at 25 ^{o}C), 10 μL of β-tryptase was added to 180 μL Tris-HCl buffer, in which the enzyme was incubated with various equilibrated library mixtures (5 μL) and finally the substrate (5 μL, final concentration 50 μM) was added. The solutions were thoroughly mixed and the rate of hydrolysis of the AMC substrate was determined by monitoring the fluorescence change at 460 nm for 15 min. Due to the high concentration of the initial libraries (the total concentration of hydrazides is 0.5 mM in the full library), the DCLs were diluted 5 to 50 times with acetate buffer solution containing 10 % DMSO accordingly for the enzyme assay in order to significantly discriminate the inhibitory potency among all the libraries. Thus, total concentrations of hydrazides in the full library were tested from 10 to 100 μM, resulting in the final hydrazide concentration of the full library from 0.25 to 2.5 μM in the enzyme screening mixtures. However, the dilution should not be too high or too low depending on the overall inhibition of the libraries. The overall inhibition of the full library should be approximately 60 %-90 % to ensure the optimal observable effects.

To identify the active components in the libraries, the dynamic deconvolution process was utilized. The enzyme screening results obtained from these libraries are shown in Figure 4.24, where the relative activities of the sub-libraries were normalized, compared to the full library. The full library tested here with final total concentration of hydrazides at 1.25 μM showed an inhibitory effect of 62 %. The inhibition of the enzyme activity by this library reveals the presence of at least one or more active species that are potent β-tryptase inhibitors in a given equilibrated library mixture. By determining the enzyme inhibitory effects of sub-libraries in which one individual building block each is missing, an increase in enzyme activity of the sub-libraries compared to full library indicates that the removed component has a significant contribution to the inhibitory effect, whereas a decrease in enzyme activity reveals that the omitted component hampered the inhibitory effect of more active species in the library mixture.

The data in Figure 4.24 clearly showed that several active components were present in this library. As expected, the recognition building blocks, hydrazides (**135-136**, **138-139**)

featuring peptide sequences with the combination of the basic and aromatic amino acids are necessary for the inhibition to occur. Hydrazide **138** (GKWK(GCP)) is the most active building block among all the five hydrazides. By removing **138** from the full library, the enzyme activity is restored by 47 % relative to the full library. Hydrazides **135** (GKWR) and **136** (GKWK) are less but similarly active with the restoration of enzyme activity of ca. 20-25 %. Hydrazide **139** (GK(GCP)WK) is the least active one in this set of positively charged peptide hydrazides with a recovery of 13 % enzyme activity. These results indicate that the artificial GCP group has significant influence on the inhibitory potency in either way (compare **136** with **138** and **139**). It can significantly increase the enzyme inhibitory activity compared to analogous peptide chain solely based on proteinogenic amino acids (compare **136** and **138**). However, this effect can be weakened depending on the position of the GCP group in the peptide chain (compare **138** and **139**). The removal of the negatively charged **140** (GAFE) from the full library slightly decreases the enzyme activity, indicating hydrazones containing the negatively charged peptide hydrazide are not necessary for the enzyme inhibition.

Similarly, for the scaffold building blocks, tri-aldehyde **E** is the most important component for providing multivalent ligands for the inhibition. Its removal restores 18 % of enzyme activity compared to the full library. Smaller effects were observed for the di-aldehydes **B**-**D** (ca. 5-10 % recovery) while **A** is the least active scaffold (nearly no recovery of the enzyme activity).

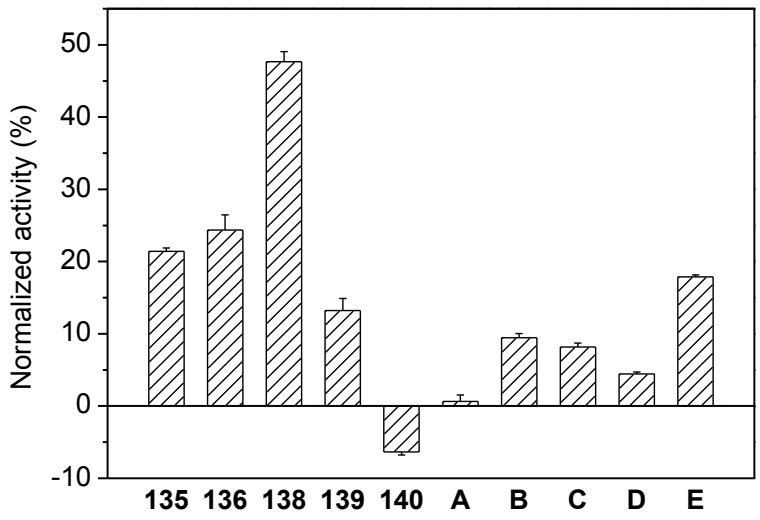

Figure 4.24 Dynamic deconvolution of dynamic combinatorial libraries of acyl hydrazones: DCL containing five peptide-derived hydrazide and five aldehyde building blocks, with normalized relative enzyme activity of all sub-libraries, compared to the full library. The individual columns represent the sub-libraries each lacking the specific building block below the column. The final total concentration of hydrazides in the full library is 1.25 μM. The y error bars represent the standard deviation.

To further investigate the individual effects of the aldehyde scaffolds, a second size-reduced library containing all the aldehydes (**A**-**E**) but only the most active hydrazide

138 was generated and analyzed in the same way. The size of this full library is reduced to five different acyl hydrazones (not counting the partially formed species). Six sub-libraries were prepared accordingly by removing one specific building block. All libraries were then subjected to the enzyme assays. Different dilutions (10 and 50 times) of the libraries were used for enzyme inhibition. The full library was first tested with the same concentration of hydrazides at 1.25 μM in the screening mixture, resulting in an inhibitory effect of 95 %. It is not surprising that the inhibitory effect is much higher than the first library containing all the five hydrazides (62 %) due to the replacement of the less active building blocks by the more efficient one. In order to better discriminate the efficiencies of these scaffolds, libraries with lower concentration (hydrazides concentration at 0.25 μM) were analyzed as well, showing approximately 52 % enzyme inhibition. The results in Figure 4.25 revealed that the aromatic and rigid scaffolds **E** and **C** are the most active building blocks for active inhibitors: tri-aldehyde **E** is the most active scaffold (ca. 30 % recovery) in the library, followed by di-aldehyde **C** with a bit smaller effect (ca. 16 % recovery). Furthermore, the results showed that the removal of component **138** leads to full recovery of the enzyme activity relative to the full library, confirming that the aldehydes themselves have no inhibitory effects. This result is also confirmed by the enzyme inhibition measurement of the individual aldehydes which showed no inhibition even at a concentration of 10 mM (Table 4.3). Hence, the aldehydes only provide the structural scaffold to build up the multivalent inhibitors but they do not contribute to the enzyme inhibition. Therefore, building blocks **135**-**136**, **138**-**139** as well as **E** and **C** are the most active components in this library. Consequently, the most active constituents are likely to be formed from the assembly of these hydrazides and aldehydes.

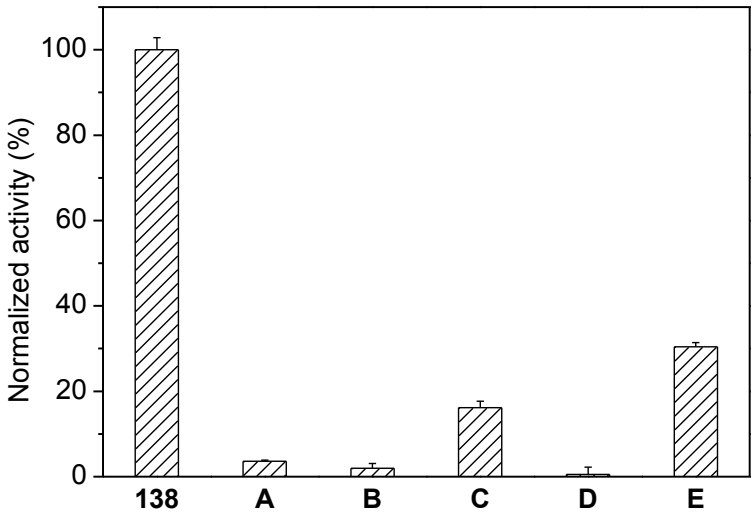

Figure 4.25 Dynamic deconvolution of dynamic combinatorial libraries of acyl hydrazones: DCL containing one peptide-derived hydrazide (**138**) and all five aldehyde building blocks, with normalized relative enzyme activity of all sub-libraries, compared to the full library. The individual columns represent the sub-libraries each lacking the specific building block below the column. The final total concentration of hydrazides in the full library is 0.25 μM. The y error bars represent the standard deviation.

4.2.4 Further Evaluation of Selected Species from DCLs

As soon as the active components were identified with the dynamic deconvolution process, a more detailed study of the inhibitory properties was performed. To this aim, a set of representative library members (Figure 4.26) based on these two scaffolds **E** and **C** were separately synthesized by the combination of the active hydrazides and aldehydes selected from the libraries to further identify their enzyme binding affinity and the inhibition mechanism for β-tryptase.

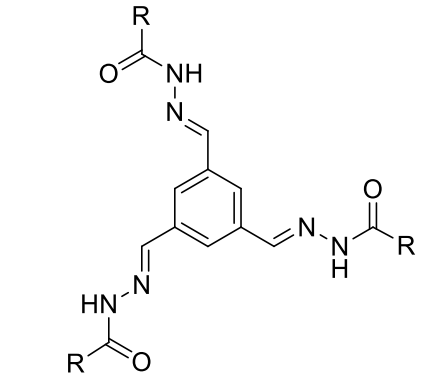

R = R^1 **141**
R^2 **142**
R^3 **143**
R^4 **144**
R^5 **145**

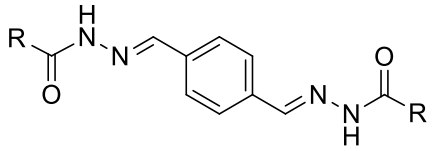

R = R^1 **146**
R^2 **147**
R^3 **148**

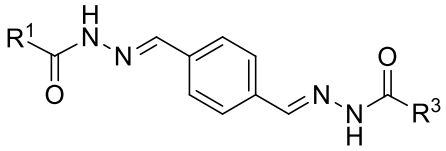

149

Figure 4.26 Schematic representation of individual acyl hydrazones **141**-**149**. Substituents R^1-R^5 represent the peptide subunits of the hydrazides (see Figure 4.22).

Syntheses of Acyl Hydrazones

The acyl hydrazone **141** was synthesized from peptide-derived hydrazide **135** (3.5 eq) and tri-aldehyde **E** (1 eq) with slightly excess of hydrazide compared to the amount of the aldehyde headgroups (Scheme 4.7). The hydrazide and aldehyde were dissolved in MeOH and the reaction mixture was refluxed overnight under Ar atmosphere. After the solvent was removed, the crude product was purified by RP18-MPLC using appropriate conditions (MeOH/H_2O + 0.1 % TFA). Pure product was transferred into its hydrochloride salt by dissolving it in water with hydrochloric acid and lyophilizing several times. The product was obtained as white solids with 93 % purity according to analytical HPLC analysis. The acyl hydrazones **141**-**149** were synthesized according to similar procedures.

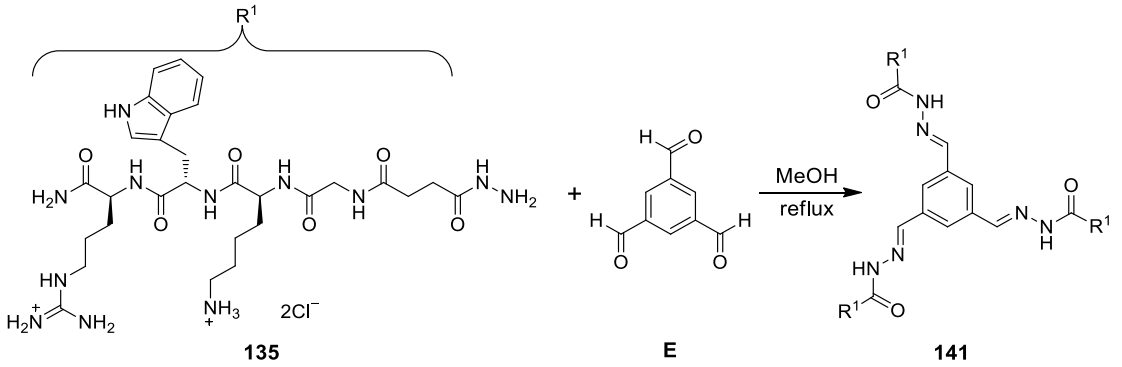

Scheme 4.7 Synthesis of individual acyl hydrazone **141** by assembly of active hydrazide **135** and tri-aldehyde **E** in solution.

All structures of acyl hydrazones **141**-**149** based on the tri-aldehyde **E** and di-aldehyde **C** are shown in Figure 4.27 and Figure 4.28, respectively. Compounds **141**-**144** were synthesized by the combination of the active hydrazides **135**-**136**, **138**-**139** and tri-aldehyde **E** to further identify their inhibitory properties to β-tryptase. The acyl hydrazone **145** was synthesized from the assembly of inactive hydrazide **140** and the tri-aldehyde **E** to further verify the screening results of the DCLs.

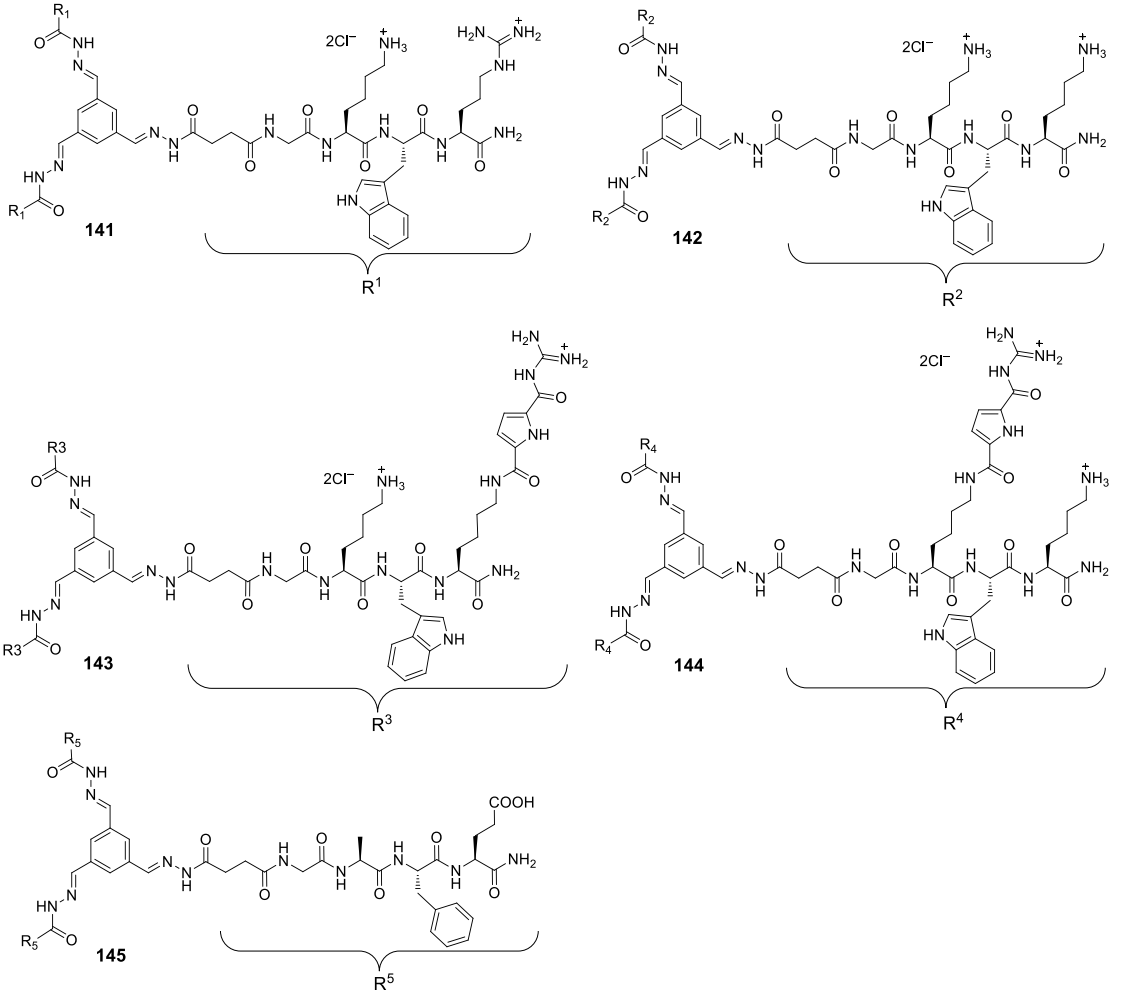

Figure 4.27 Structures of acyl hydrazones (**141**-**145**) based on the active tri-aldehyde scaffold **E**.

Compounds **146**-**148** were synthesized by the combination of active hydrazides **135**, **136**, **138** and di-aldehyde **C** to study the inhibitory properties and compare with the compounds derived from tri-aldehyde **E**. Due to the reversibility of the interconverting library constituents, the homo- and hetero- library members should exist simultaneously. Therefore, the heterodimeric compound **149** containing two different active hydrazides **135** and **138** was also synthesized to investigate the inhibitory activity compared to the homodimeric species **146** and **148** which contain only hydrazide **135** or **138**. The resulting acyl hydrazones were then subjected to independent enzyme assays to investigate their inhibitory properties.

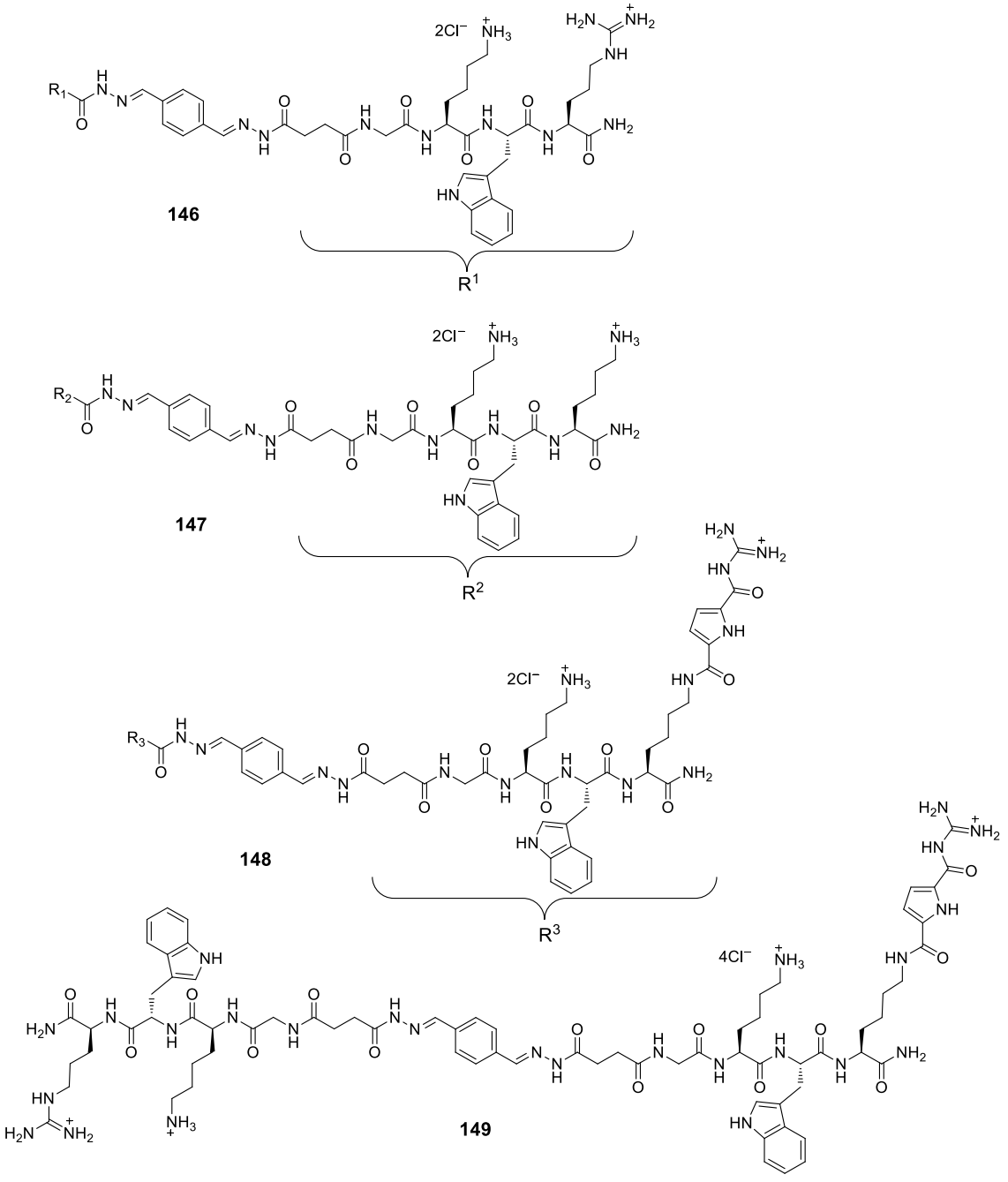

Figure 4.28 Structures of acyl hydrazones (**146**-**149**) based on the active di-aldehyde scaffold **C**.

Enzyme Inhibition Assay

As described in Chapter 4.1.4, in order to measure the kinetic parameters the hydrolysis of substrate Tos-Gly-Pro-Arg-AMC by rhSkin β-tryptase was determined using a fluorescence spectrophotometer. The enzyme assays were performed in white 96 well microplate in 50 mM Tris-HCl buffer at pH 7.4. The rate of hydrolysis in the presence of different concentrations of acyl hydrazones were measured at appropriate enzyme concentration and fixed substrate concentration (50 μM).

The inhibition data for the interaction of acyl hydrazones and β-tryptase are summarized in Table 4.4. Due to the fact that for this type of compounds the K_i and IC_{50} values are the same (see page 114), only the K_i values are displayed in the following table. The results showed that the compounds **141**-**143**, **146**-**148** derived from the combination of the most active hydrazides **135**-**136**, **138** and the aldehydes **E** or **C** have K_i values in the lower nanomolar range and are highly efficient inhibitors of β-tryptase. Compounds **143** and **148** containing the peptide sequence GKWK(GCP) with the artificial GCP groups are approximately 5 times more efficient than **142** and **147**, respectively, which consist of the same peptide sequence GKWK but without GCP groups. Obviously the attachment of GCP to the peptide side chain can improve the inhibition affinities of such peptide-derived acyl hydrazones. Moreover, the most potent trivalent inhibitors **141** (K_i = 12.5 nM) and **143** (K_i = 22.5 nM) derived from the tri-aldehyde **E** are 14-fold and 8-fold more efficient than the best tetravalent inhibitor $(RWKG)_4$ (K_i = 170 nM) from the previous combinatorial library, respectively. Even compounds **146** (K_i = 65.6 nM) and **148** (K_i = 78.0 nM) derived from di-aldehyde **C** are two times more efficient than $(RWKG)_4$ as well. Therefore, for this type of multivalent peptide ligands, they are indeed the best inhibitors of β-tryptase so far. More interesting, **141** and **146** even contain the same peptide sequence GKWR but with only three or two peptide arms attached to the aromatic rigid core instead a flexible lysine dendrimer, indicating the rigid scaffolds are superior to more flexible ones. These results suggest that multivalent ligands based on the rigid scaffolds could be more potent inhibitors of β-tryptase than that based on a flexible scaffold. Furthermore, the comparison of the multivalent acyl hydrazones with the monovalent peptide-derived hydrazides indicates a significant multivalency effect. For example, the trivalent compounds **141**-**143** derived from tri-aldehyde **E**, are three orders of magnitude more potent than the individual hydrazides **135**, **136** and **138** which have K_i values between 12 and 60 μM (Table 4.3). In the case of the bivalent compounds **146**-**148**, derived from di-aldehyde **C**, **146** and **147** are approximately 200 and 160 times more active than their monovalent analogs **135** and **136**, respectively, while **148** is 300 times better than its monovalent counterpart **138**. These results suggest that in contrast to the monovalent hydrazide which most likely binds to the active site of the enzyme, the inhibition mode of the multivalent acyl hydrazone might be due to a multivalent interaction based on preventing the entrance to the central pore of β-tryptase.

Table 4.4 K_i values [nM] of the compounds **141-149** for β-tryptase and the other two serine proteases trypsin and α-chymotrypsin (α-ChT).

Compounds	K_i [nM] [a]		
	β-Tryptase	Trypsin	α-Chymotrypsin
141 (135+E)	12.5 ± 0.8	> 100000	> 100000
142 (136+E)	104.9 ± 31.0	> 100000	> 100000
143 (138+E)	22.5 ± 2.1	> 100000	> 100000
144 (139+E)	114 and 29900 [b]	> 100000	> 100000
145 (140+E)	> 100000	> 100000	> 100000
146 (135+C)	65.6 ± 2.3	> 100000	> 100000
147 (136+C)	391.8 ± 24.4	> 100000	> 100000
148 (138+C)	78.0 ± 3.1	> 100000	> 100000
149 (135+C+138)	120.8 ± 3.9	> 100000	> 100000

[a] K_i values were calculated by fitting the inhibition data to a 4-parameter equation. [b] A biphasic behavior was observed with two inhibitory processes, showing high affinity (K_i = 114.0 ± 19.3 nM) and low affinity (K_i = 29.93 ± 1.44 μM) modes of inhibition, respectively. (see Figure 4.29).

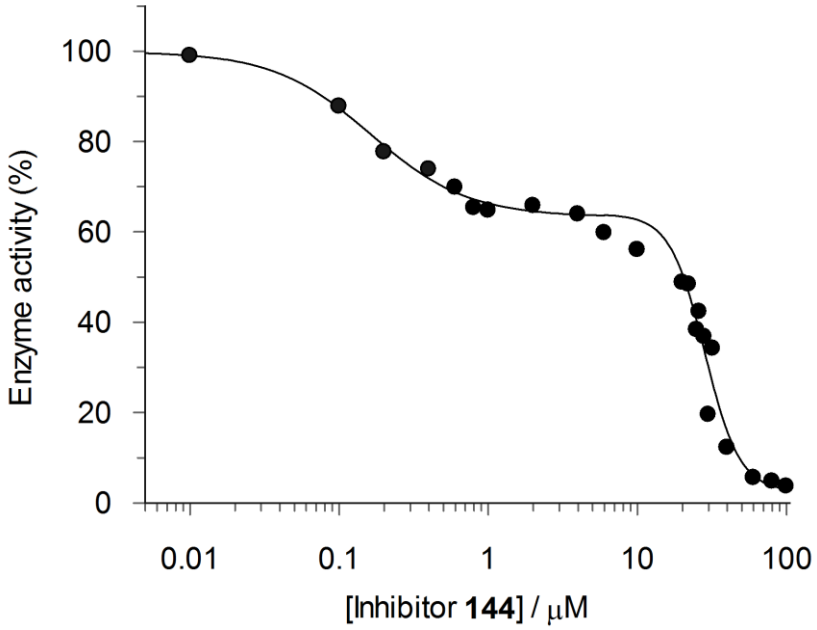

Figure 4.29 Biphasic inhibition curve of β-tryptase by compound **144**. The plot represents the sum of two overlapping sigmoid curves which is separated by the plateau. The IC_{50} values for the high affinity (114.0 ± 19.3 nM) and low affinity (29.93 ± 1.44 μM) binding were estimated by GraFit program.

Compound **144** derived from hydrazide **139** (GK(GCP)WK) and the scaffold **E** showed a different inhibition manner. The inhibition data can be fitted best to biphasic kinetics (Figure 4.29), indicating two modes of inhibition with different affinities: one with high affinity (114.0 ± 19.3 nM) and the other one with low affinity (29.93 ± 1.44 μM). Compound **144** is similarly active (K_i = 114 nM for the high affinity binding mode) as **142** (K_i = 105 nM) which contains hydrazide **136** (GKWK) but 5-fold less active than **143** (K_i = 22.5 nM) which contains hydrazide **138** (GKWK(GCP)). This result is in agreement with the deconvolution results of the DCLs, but it is surprising because hydrazides **138** and **139** are actually isomers, which consist of the same peptide sequence GKWK (as in **136**) attaching artificial GCP binding motif to lysine side chain but in a different position. These results suggest that the position of the GCP motif does significantly affect the inhibitory properties. Only when the GCP group is attached to the side chain of the lysine at the C-terminus of the hydrazide chain (as in **138**) it increased the inhibitory affinity. When it is attached to the lysine side chain in the middle part of the hydrazide (as in **139**) it is as active as lysine at this position (as in **136**). The interpretation of the different inhibitory activity of these two acyl hydrazides **143** and **144** can be explained by the calculation results discussed in Chapter 4.2.5.

To further verify the screening result of the DCLs, the unfavorable library member **145** was also synthesized from the assembly of inactive hydrazide **140** (GAFE) and scaffold **E**. As predicted by the screening results of DCLs, it showed no inhibition of β-tryptase. This result also demonstrates that the inhibitory activity rather stems from the peptide arms of the acyl hydrazones than from the aromatic core of the scaffold or the acyl hydrazone linkage. The K_i values (Table 4.3) of the individual hydrazide and aldehyde are in agreement with this conclusion.

Because of the reversibility of interconverting library constituents, the homo- and hetero- library members exist simultaneously. Therefore, the heterodimeric compound **149** containing two different hydrazides **135** (GKWR) and **138** (GKWK(GCP)) was synthesized and its inhibitory properties were investigated for comparison with the homodimeric species **146** and **148** containing one hydrazide **135** or **138** in the two arms, respectively. The K_i value of 120 nM showed that the inhibitory activity of **149** is in a similar range but slightly lower than the corresponding homodimeric species **146** (K_i = 65.6 nM) and **148** (K_i = 78 nM), which indicates that acyl hydrazones with identical peptide arms might be slightly favored for the inhibition of β-tryptase, at least for bivalent library species.

In order to better understand the interaction between these series of acyl hydrazone inhibitors and the enzyme, the following experiments were done to investigate the enzyme selectivity, the reversibility and the inhibition mode of β-tryptase.

Enzyme Selectivity

Enzyme selectivity was tested against the other two archetypal structurally similar serine proteases trypsin and α-chymotrypsin as mentioned in Chapter 4.1.4. However, none of the inhibitors showed any measureable inhibition of these two related enzymes even at a concentration of 100 μM (Table 4.4). Thus, these inhibitors seem to have no effect on these two related enzymes, indicating that this series of acyl hydrazones are highly specific for β-tryptase compared to other closely related serine proteases. This suggest that again most likely the compounds inhibit β-tryptase by protein surface binding to the negatively charged area around the entrance to the central pore of β-tryptase, as both enzymes are structurally rather similar to the tryptase monomer but without the acidic hot spots near the central pore of tryptase.

Reversibility of Inhibition

The tests on reversibility of β-tryptase inhibition were performed by two experiments according to similar procedure as described in Chapter 4.1.4. In the first dialysis experiment, 14 % recovery of tryptase activity was observed after 66 h which indicated that the interaction between the enzyme and the inhibitor are reversible. Additionally, the second experiment with addition of excess heparin to compete with β-tryptase for the interaction with the cationic ligand was done to verify the results. In this case, 16 % recovery of enzyme activity was observed. Hence, this test verified the results of dialysis experiment, showing that the activity of β-tryptase could be partially restored, thus indicating that the inhibition is in principle reversible. Also, it indicated that the binding of the inhibitor to the enzyme does not damage the active tetrameric structure of β-tryptase.

Identification of Enzyme Inhibition Mode

In order to further elucidate the mode of enzyme inhibition, the rate of enzyme reaction was measured at different inhibitor concentrations (0-0.1 μM) but always with a fixed enzyme concentration for different substrate concentrations (25, 50, 75, 100,150 and 200 μM). The inhibition mechanism of the acyl hydrazone for β-tryptase was then characterized by constructing the *Dixon* plots, a plot of reciprocal velocities against inhibitor concentrations at different substrate concentrations (Figure 4.30). The plots have a common intersection on the x-axis which reveals that the constant K_i value is not affected by increasing the substrate concentration, thus indicating a noncompetitive inhibition.[22-23]

In conclusion, it is possible to prove that the acyl hydrazone inhibitors do not compete with the substrate for the active cleavage sites and hence most likely bind to the anionic surface of β-tryptase through complementary electrostatic interactions. Therefore, this type of inhibitors from the combination of peptide-derived hydrazides and aromatic rigid

scaffold are reversible and noncompetitive inhibitors of β-tryptase.

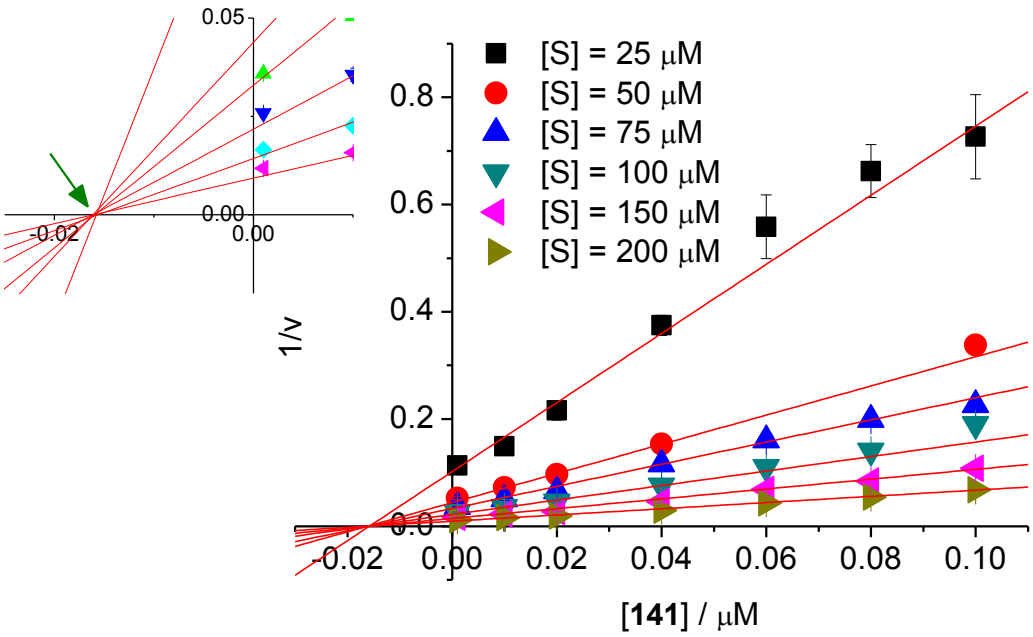

Figure 4.30 Relative *Dixon* plot of reciprocal velocities (1/v) against inhibitor concentrations at the following fixed substrate concentrations: [S] = 25, 50, 75, 100, 150 and 200 μM. The y error bars represent the standard deviation.

4.2.5 Molecular Mechanics Calculations

All the findings of the previous experiments suggest that the most likely interaction mode is that the inhibitors sterically block the access of substrate to the active cleavage sites. In order to further verify how the inhibitors bind to β-tryptase, force field calculations were used to visualize possible binding modes between the inhibitor and β-tryptase. Compound **143** which consists of three peptide arms with artificial GCP groups was then chosen as a representative inhibitor for the calculation. Compared to **143**, its isomer **144** contains similar peptide arms which differ only in the position of the artificial GCP binding motif attached to lysine side chain, resulting in significant difference in inhibitory activity. Therefore, to obtain further insight in their differences in inhibitory affinity to β-tryptase, molecular mechanics calculations of both **143** and **144** were studied.

The force field calculations were done by *Wilhelm Sicking* with the help of Schrödinger MacroModel Version 9.9 software. The enzyme input is based on the reported crystal structure of β-tryptase (PDB code: 1A0L). All water molecules and substrates of the PDB crystal structure were removed from the binding pore. The conformation of β-tryptase was fixed and the inhibitor was mobilized during the calculation. So the calculations began at a potential energy of the start conformation and a minimum potential was searched by simulating new conformations. The resulting structures were obtained from the result of

1000 calculation cycles.

The calculation confirmed that both molecules can indeed bind to the surface of β-tryptase. The calculated conformations of inhibitors (**143** and **144**) and β-tryptase are shown in Figure 4.31. The two inhibitors bind to the enzyme in similar manner by interacting with acidic amino acids around the entrance to the central pore through electrostatic interactions, thus limiting the accessibility of the substrate to the active sites. A closer look (Figure 4.32) on the binding interactions of **143** with β-tryptase shows that the inhibitor can bind to the entrance to the central pore of the enzyme through a number of key interactions with protein residues Glu, Asp and Gln. It is bound to the surface of β-tryptase by 14 hydrogen bonds through the interaction with the two binding sites (the monomer-monomer interface and the binding site close to the active site) as described by the docking studies (see Figure 4.3). The three GCP groups of **143** interact with a significant number of anionic residues around the central pore forming H-bond assisted ion pairs to Glu-217A, Gln-221A, Asp-60B, Glu-217C, Gln-221C and Asp-60D, respectively. Additionally side chains of the three lysines interact with Asp-145A, Asp-147A, Glu-149A and Glu-149C through electrostatic interactions.

The calculated binding modes and binding energies of **143** and **144** are quite similar, indicating that they bind to β-tryptase in principle in the same manner. However, in order to investigate why the inhibitory affinity to β-tryptase is so different between **143** and **144**, the optimized conformations of these two individual inhibitors were also calculated. Therefore, to obtain the energy-minimized structures of **143** and **144**, conformational searches were performed with 67000 and 76000 cycles, with resulting energies of -4336.5 kJ/mol and -4372.0 kJ/mol, respectively. After 1000 cycles, the resulting minimum structures of **143** and **144** were already found several times with energies of -4330 kJ/mol and -4361 kJ/mol, respectively, which confirmed that the additional subsequent calculations do not result in pronounced structure changes. Normally, the absolute interaction energies obtained from force field calculations are difficult to compare for different molecules due to the uncertainties and approximations in these calculations. However, in this case isomers **143** and **144** are compared and the data are more reliable.

The calculation studies of the individual molecules **143** and **144** showed that the energy of **144** is significantly lower by ca. 36 kJ/mol relative to its isomer **143** (Figure 4.33). The results suggest that **144** has more stabilizing intramolecular interactions compared to **143**. Hence, as both molecules bind to the enzyme with similar energies, the more stable isomer **144** is the less efficient inhibitor. Therefore, the calculations suggest that the improved inhibitory activity of **143** is not necessarily the result of stronger binding to the protein, but a less stable ground state conformation of the inhibitor itself.

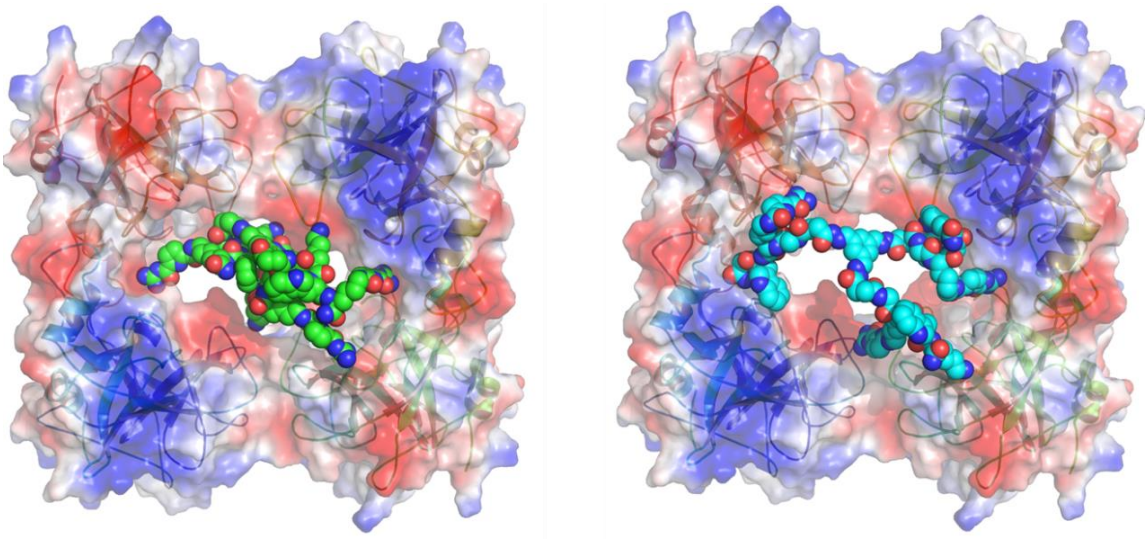

Figure 4.31 Calculated structures of possible binding modes of inhibitors **143** (*left*) and **144** (*right*) to β-tryptase. The inhibitors were shown as spheres with carbon atoms colored green and cyan, respectively. All the hydrogen atoms of the inhibitors were removed for clarity. The inhibitors bind to the entrance of the central pore, thus limiting the accessibility to the active sites. The binding energies of **143** and **144** were found to be -53819 kJ/mol and -53812 kJ/mol after 1000 calculation cycles, respectively.

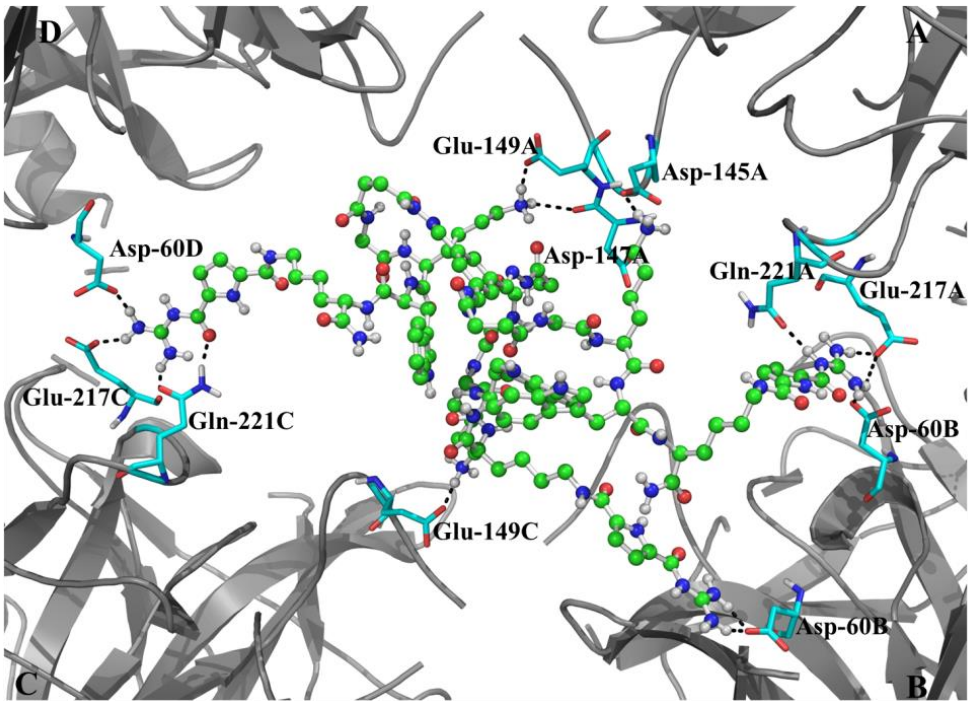

Figure 4.32 The binding region of inhibitor **143** (shown as balls and sticks with carbon atoms colored green) on the surface of β-tryptase (shown as ribbon cartoon). Four monomers of the enzyme are named A, B, C and D. Key protein residues (Glu, Asp and Gln) that interact with **143** are displayed as sticks with carbon atoms colored cyan and numbered according to the protein sequence and different monomers. Polar interactions among protein residues and inhibitor are presented as black dash lines.

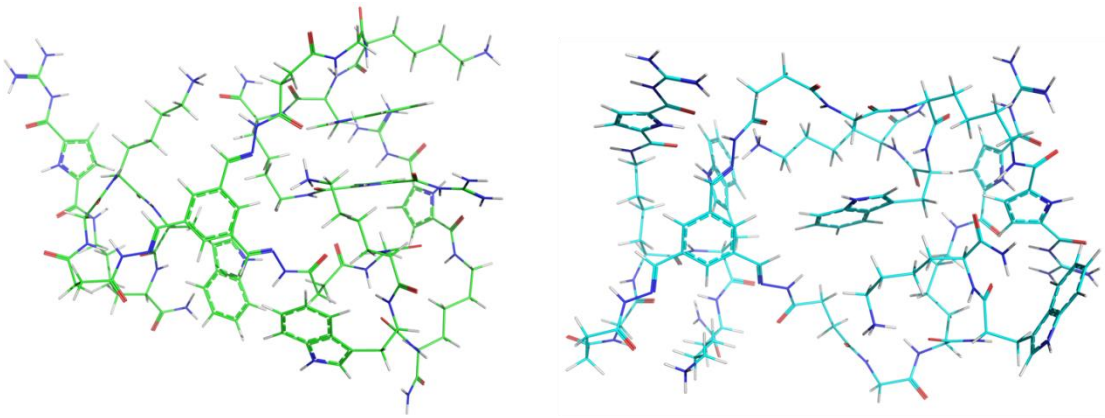

Figure 4.33 Calculated energy-minimized structures of **143** (*left*) and **144** (*right*). The structures are displayed as sticks with oxygen atoms colored red, nitrogen atoms colored blue, carbon atoms colored green and cyan, respectively. The minimal energies of **143** and **144** were found -4336.5 kJ/mol and -4372.0 kJ/mol after 67000 and 76000 calculation cycles, respectively.

In conclusion, the hydrazone-based dynamic combinatorial libraries from five peptide hydrazides and five aldehydes which could contain 95 different library constituents were generated and tested to identify high affinity inhibitors of β-tryptase by using a dynamic deconvolution approach. Both two- and three-armed peptide hydrazones with a rigid core inhibit β-tryptase with lower nanomolar affinity in a reversible and noncompetitive way and are highly selectivity for tryptase compared to other related serine proteases (e.g. trypsin, α-chymotrypsin). The most potent compound **141** based on the tri-armed rigid scaffold is one order of magnitude more efficient than the best tetravalent inhibitor $(RWKG)_4$ based on a flexible lysine dendrimer scaffold obtained from the previous combinatorial library. Small variations in the peptide arms induced by the artificial arginine analog GCP attached to the different position of the peptide arm lead to different binding affinities. The substitution of GCP at the C-terminal amino acid side chain can significantly improve the inhibitory activity of such inhibitors relative to only proteinogenic amino acids. Hence, it could be demonstrated here again that the use of tailor-made binding motifs such as the artificial arginine analog GCP can lead to more potent inhibitors. Additionally, due to the multivalency effect, more efficient inhibitors might be possible by using the scaffold with larger surface area, such as gold nanoparticles. In the next chapter, inhibitors based on such a scaffold will be prepared and investigate their inhibitory efficiency.

4.3 Surface Binding of Human β-Tryptase by Gold Nanoparticle-based Inhibitors

The recognition of protein surfaces is challenging due to their solvent-exposed large size and structural complexity (see chapter 2.4). For this reason, the use of scaffolds with large complementary surfaces offering multivalent interactions is of particular advantage for protein surface binding. In the last decades gold nanoparticles were of great interest in the application in biotechnology and catalysis as they present fascinating and versatile properties that differ from their bulk material, such as the size-related electronic, magnetic and optical properties (quantum size effect).[168] Gold nanoparticles (Au NPs) feature the surface plasmon resonance (SPR) due to the collective oscillation of the electron gas at the surface, which leads to an intense absorption band in the visible region around 520 nm, showing deep-red color and allowing easy detection by UV/Vis spectroscopy. Furthermore, gold nanoparticles feature large surface area, tunable size, and a wide series of functionalities such as thiol (through chemical bond) and amine (through physical bond) ligands. All these properties allow the possibility of using them as candidates for preparing receptors for protein surface recognition.[164] The theoretical background information of gold nanoparticles as promising scaffold for protein surface binding has been described in Chapter 2.4. With the help of the DCL approach presented in the previous chapter, the peptide sequences combining the basic and aromatic amino acids as well as the artificial GCP binding motif attached to a rigid core scaffold have been shown to inhibit β-tryptase with high affinity. In order to further test the efficiency of these peptide sequences and increase the multivalency effect, similar peptide arms will now be used to attach to the gold nanoparticle scaffold, providing as recognition elements binding to the acidic surface area of β-tryptase. Alkanethiol chains incorporated with triethylene glycol (TEG) to prevent nonspecific interaction and denaturation will be used as a linker to stabilize the gold core. The design of the functional peptide ligands is based on the attachment of the peptide recognition unit to this thioalkylated TEG chain. The peptide ligands can then be attached to the surface of the gold nanoparticle scaffold, resulting in the functionalized nanoparticles to target the surface of β-tryptase. A ligand containing the alkanethiol chain but with a terminal hydroxyl group is also synthesized as a surface blocker. In the following sections the synthetic route to the thioalkylated TEG chain and the peptide ligands as well as the functionalized gold nanoparticles will be described. The characterization and the results from the enzyme assays will be presented as well.

4.3.1 Synthesis of the Thioalkylated TEG Linker

In order to couple the thiolalkylatd TEG chain to a peptide on solid support, a carboxylic acid group should be introduced to the terminal TEG chain and a suitable protecting group should be used for the thiol group to allow the simultaneous deprotection

and cleavage of the product from the resin. The synthetic route to such a compound is adapted from the literature with some modifications.[269-271] As shown in Scheme 4.8, commercially available 5-Bromo-1-pentene (**150**) was reacted with excess triethylene glycol in the presence of sodium hydroxide as the base to give the monoether (**151**) which was purified by column chromatography to get rid of the diether. This compound was again alkylated with ethyl bromoacetate in the presence of the strong base sodium hydride to give the ester (**152**). The subsequent addition reaction of thioacetic acid to the terminal olefin of **152** (thiol ene reaction) was performed in the presence of a catalytic amount of azobis(isobutyronitrile) (AIBN) in THF under reflux to afford thioacetate (**153**). This reaction can be carried out either under UV light irradiation at room temperature or under reflux. Both these conditions lead to the decomposition of AIBN through elimination of nitrogen and generate radicals. They act as initiators to produce thiol radicals which subsequently add to the alkene. This thioacetate compound was then subjected to acidic hydrolysis to give the free thiol product (**154**), which was then directly protected by the trityl group to give trityl thioether (**155**). In the last step, saponification of the ethyl ester group with aqueous lithium hydroxide was carried out in the mixture of THF and MeOH (1:1, v/v) to afford the desired carboxylic acid (**156**).

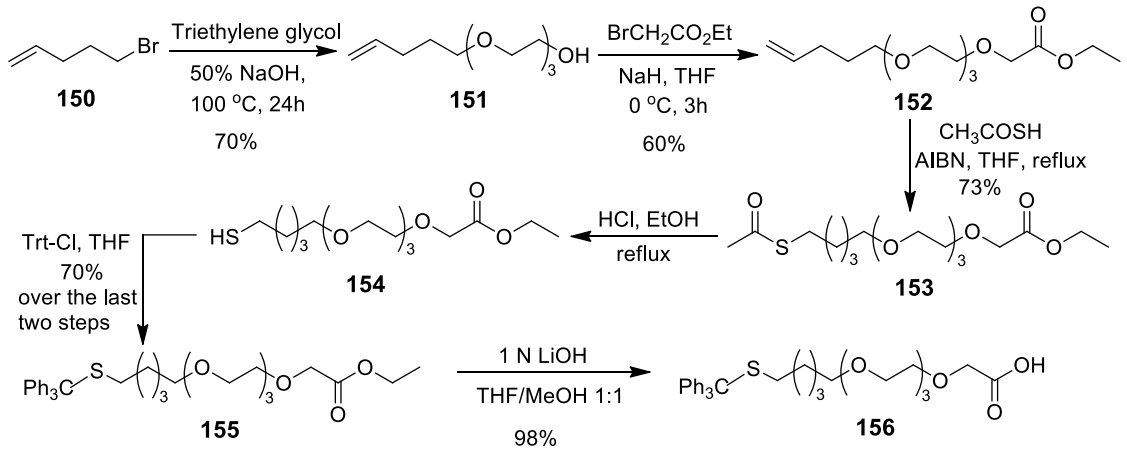

Scheme 4.8 Synthesis of the trityl protected thiolalkylatd TEG derived carboxylic acid (**156**) for the coupling with a peptide on solid support.

The thiolalkylatd TEG ligand with the terminal hydroxyl group is used as a control ligand to adjust the surface functionalities and charges. It was synthesized according to the similar procedure but without incorporating the carboxylic acid. As shown in Scheme 4.9, addition of thioacetic acid to the terminal olefin of the compound **151** afforded thioacetate (**157**), which was then subjected to acidic hydrolysis to give the ligand (**158**).

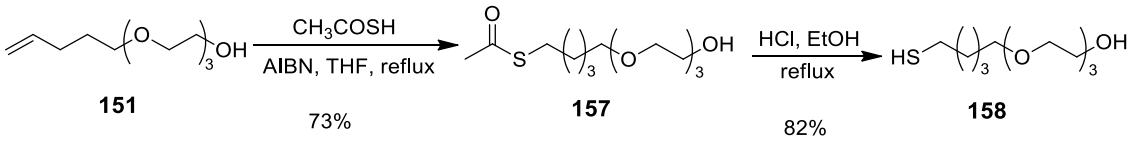

Scheme 4.9 Synthesis of the thiolalkylatd TEG ligand (**158**).

4.3.2 Microwave-Assisted SPPS of Thiolalkylated Peptide Ligands

As demonstrated in the last chapter, peptide sequences combining basic and aromatic amino acids as well as the artificial arginine analog GCP binding motif show efficient inhibitory affinity to β-tryptase. To further test their efficiency on the surface of gold nanoparticles, similar peptide sequences were used to incorporate with the linker (**156**) on the solid support, resulting in peptide-derived alkanethiols to attach to the surface of the gold nanoparticles. Because the length of the linker (**156**) is already long, tripeptide instead of tetrapeptide was used with the glycine missing.

The thiolalkylated peptide ligand **161** (KWK(GCP)) contains the peptide sequence KWK with the artificial GCP group attached to the side chain of the C-terminal lysine. This peptide arm has shown high inhibitory affinity to β-tryptase (see Chapter 4.2). Ligand **161** was synthesized on the Rink amide MBHA resin (0.84 mmol/g) using a standard microwave-assisted Fmoc SPPS procedure (see Chapter 4.1.3). As shown in Scheme 4.10, the resin was first swollen in DCM for 2 h, followed by the Fmoc deprotection by treating with 20 % piperidine/DMF under the standard microwave irradiation condition. After a washing cycle with DMF, the first amino acid Fmoc-Lys(Alloc)-OH (3 eq) was attached to the resin with the help of the coupling reagent PyBop (3 eq) and the base DIPEA (6 eq) in DMF under standard microwave irradiation condition for 20 min. The coupling was then repeated and the negative *Kaiser* test confirmed the complete coupling of the free amino groups. After the Fmoc deprotection, Fmoc-Trp(Boc)-OH (3 eq) and Fmoc-Lys(Boc)-OH (3 eq) were coupled using the same conditions to obtain **159**. After the Fmoc deprotection, the linker (**156**) was coupled to the resin with the help of HOBt (3.6 eq) and DIC (4.5 eq) to give **160**. The next step is the removal of Alloc protecting group with the help of $Pd(PPh_3)_4$ (0.1 eq) in the presence of $PhSiH_3$ (24 eq) in DCM, followed by the coupling of the Boc protected GCP unit (**111**) to the lysine side chain with the help of the coupling reagent PyBop (3 eq) and the base DIPEA (6 eq). Then the resin was thoroughly washed with 3 × DCM, 3 × MeOH, 3 × DCM and dried under vacuum for 1 h. To cleave the peptide, the resin was transferred to a glass peptide synthesis vessel and the product was cleaved from the resin by using a mixture of TFA/phenol/H_2O/TIS (90:5:2.5:2.5) for 3 h. Under this condition, all side-chain protecting groups were simultaneously removed. Phenol is necessary as scavenger to provide protection for aromatic residues. The crude product was purified by RP18-MPLC using appropriate conditions (H_2O/MeOH + 0.1 % TFA). After the purification steps, the product was obtained with a purity of 95 % according to analytical HPLC analysis. Pure product was then transferred into its hydrochloride salt by dissolving it in water with hydrochloric acid and lyophilizing several times.

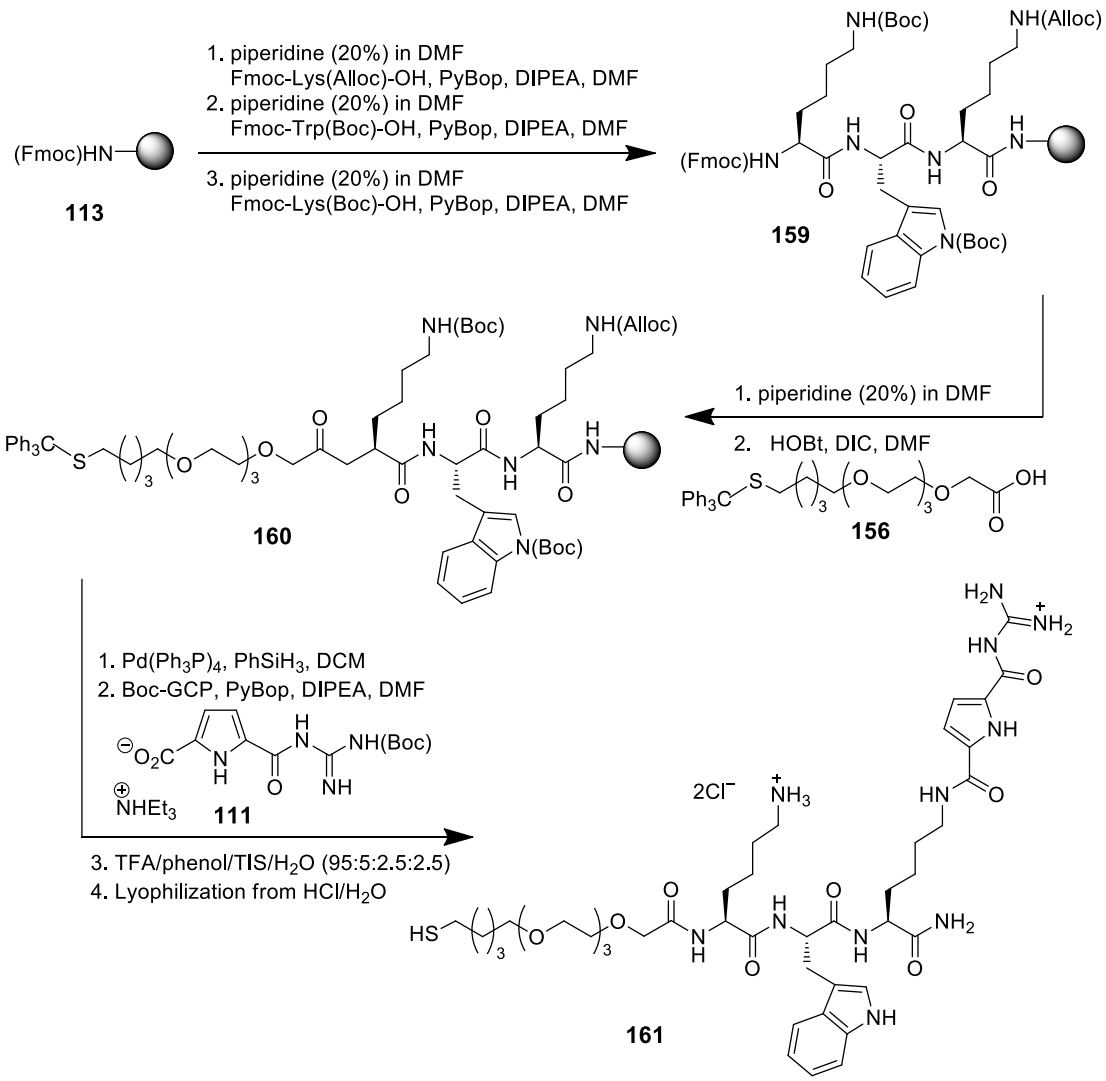

Scheme 4.10 Microwave-assisted Fmoc SPPS procedure of thiolalkylated peptide ligand **161**.

The second thiolalkylated peptide ligand **162** (K(GCP)WK) with the GCP group at a different position（the side chain of the other lysine) was synthesized according to the similar synthetic route. Accordingly, peptide ligands **163** and **164** containing only the proteinogetic amino acids were also prepared. Ligand **163** contains the peptide sequence KWK for comparison with ligands **161** and **162** featuring one artificial arginine analog GCP group at one of the two lysine side chains. To further compare with the arginine, the best peptide sequence KWR from the previous library was synthesized as well. Additionally, thiolalkylated peptide ligand **165** was prepared with the negatively charged peptide sequence EWE featuring two glutamic acids to compare with the positively charged ligands **161**-**164**. All the structures of these four ligands are depicted in Figure 4.34.

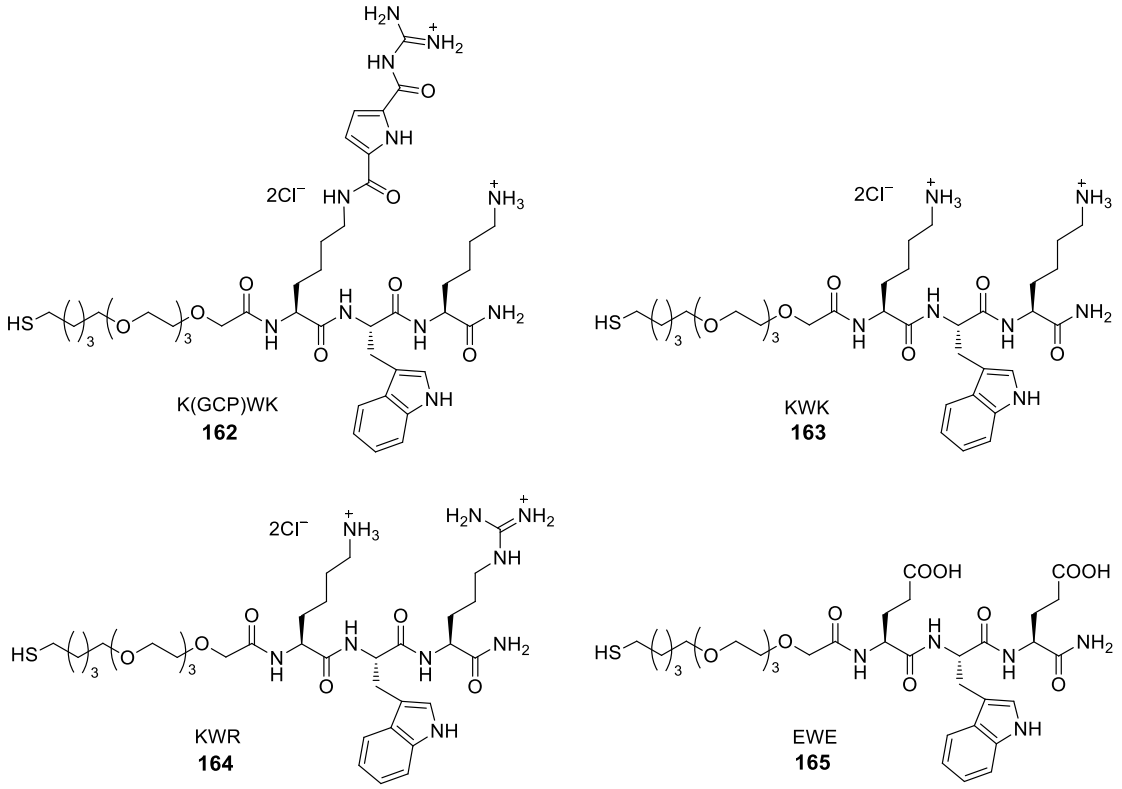

Figure 4.34 Four other thiolalkylated peptide ligands **162-165** (including short names of the peptide arms for easy comparison) were also prepared via microwave-assisted Fmoc SPPS.

4.3.3 Synthesis of Peptide Ligands as Control Molecules

The preparation of the gold nanoparticles will be first tested with the ligand **161** (KWK(GCP)) which features the efficient peptide sequence containing the artificial arginine analog GCP group and has been shown previously to be a potent binding unit to β-tryptase. In order to compare the enzyme inhibitory affinity of the functionalized gold nanoparticles with that of the free ligand, a model ligand with the same peptide sequence KWK(GCP) and a similar alkylated TEG linker but without the thiol group was synthesized (to prevent the possible formation of disulfide by the thiolalkylated peptide ligand **161**). As shown in Scheme 4.11, the terminal alkenyl group of compound **152** was reduced by hydrogenation with a catalytic amount of palladium on activated charcoal in methanol to give the saturated ester **166**, which was then subjected to saponification of the ethyl ester group with aqueous lithium hydroxide in the mixture of THF and MeOH (1:1, v/v) to afford the desired carboxylic acid (**167**).

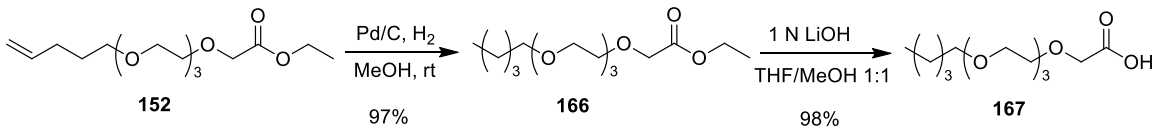

Scheme 4.11 Synthesis of the alkylated TEG derived carboxylic acid (**167**) for the coupling with a peptide sequence on solid support.

Then the peptide ligand **168** (Figure 4.35) was synthesized based on this alkylated TEG linker (**167**) by incorporating the same peptide sequence KWK(GCP) as ligand **161**. It was synthesized on the Rink amide MBHA resin (0.84 mmol/g) according to the standard microwave-assisted Fmoc SPPS procedure as described for ligand **161**. After the completion of all the coupling steps, the product was cleaved from the resin by using a mixture of TFA/H_2O/TIS (90:2.5:2.5) for 3 h. After the purification steps, the product was obtained with a purity of 95 % according to analytical HPLC analysis.

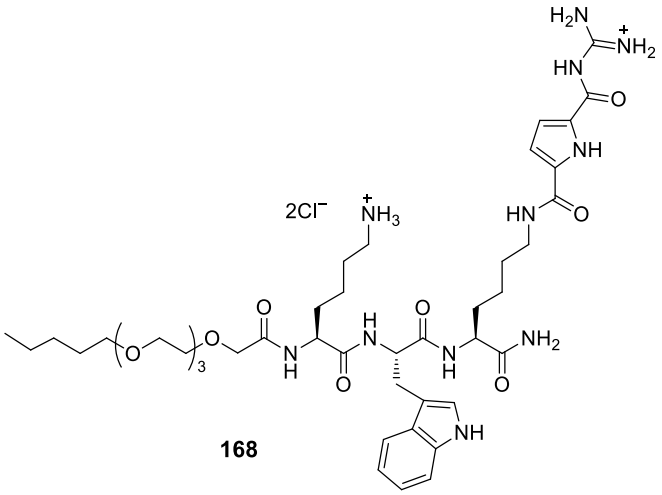

Figure 4.35 Structure of peptide ligand **168** containing the alkylated TEG chain.

The peptide ligand **170** containing the same peptide sequence KWK(GCP) as ligand **161** but without the alkylated TEG chain was also synthesized on the Rink amide MBHA resin (0.84 mmol/g) according to the standard microwave-assisted Fmoc SPPS procedure. As shown in Scheme 4.12, after the Fmoc deprotection, the amino acids Fmoc-Lys(Alloc)-OH, Fmoc-Trp(Boc)-OH and Ac-Lys(Boc)-OH were attached to the resin successively. After the removal of the Alloc protecting group, the Boc protected GCP moiety (**111**) was attached to the lysine side chain. Then the product was cleaved from the resin by using a mixture of TFA/ H_2O/TIS (90: 2.5:2.5) for 3 h. After the purification steps, the product was obtained with a purity of 95 % according to analytical HPLC analysis.

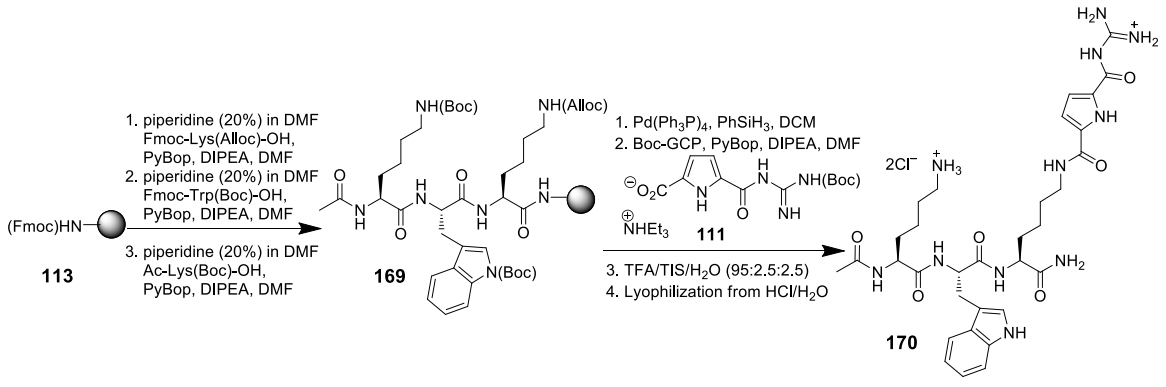

Scheme 4.12 Microwave-assisted Fmoc SPPS procedure of the peptide ligand **170**.

4.3.4 Preparation of Functionalized Gold Nanoparticles

A variety of methods for the preparation of gold colloids have been established. For example, the well-known *Brust-Schiffrin* method is based on the reduction of $HAuCl_4$ in the presence of reducing agent sodium borohydride and stabilizing ligands such as alkylthiols (Figure 4.36). Most often this reaction is carried out in unpolar solvent such as toluene with $HAuCl_4$ transferred to it by using a phase-transfer reagent such as tetraoctylammonium bromide. Thiol ligands can strongly bind to the gold surface due to the soft character of both sulfur and gold. Hence, the gold nanoparticle surface is stabilized by the long alkyl chains and prevented from aggregation in solution. The size of the particles can be controlled by the reaction conditions, such as temperature, the rate of the reduction and the thiol/gold ratio.[272-273] This method is often combined with a successive *Murray* place-exchange reaction[274] by using a wide range of functional thiols to obtain the functionalized gold nanoparticles for targeting biomolecules, cellular uptake, *etc*.

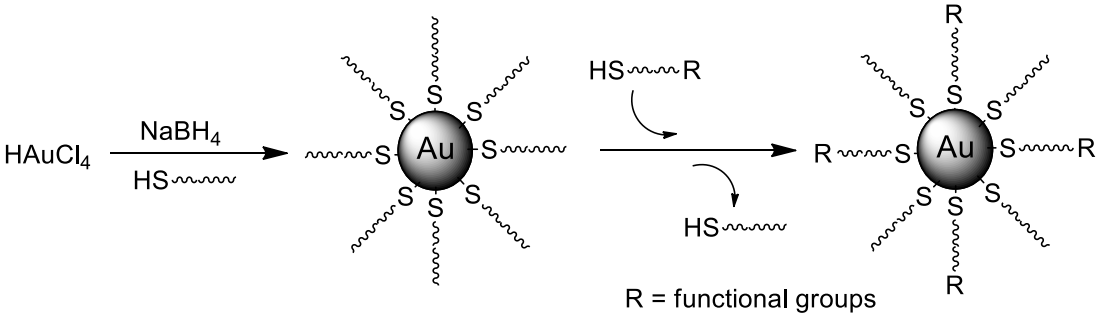

Figure 4.36 Schematic representation of the generation of functionalized gold nanoparticles by using *Brust-Schiffrin* method and *Murray* place-exchange reaction.

However, the biological application of the functionalized Au NPs requires the purification process to remove the remaining surfactants, reducing agents and the chemical precursors. In particular, the alkylthiol needs to be removed after the ligand exchange reaction to avoid biological toxicity because it might induce nonspecific hydrophobic interactions with the protein. Moreover, the initial hydrophobic alkylthiol ligands might cause solubility problems in the buffer solutions required for the biological applications and the difficulties in determining the ratio of different ligands on the surface of Au NPs.

Recently, an alternative method to obtain water-soluble gold nanoparticles in a one step process by laser ablation has been established.[275] In contrast to the bottom-up chemical method, this top-down physical approach can be used to produce metal nanoparticles with "bare" surfaces without the need of chemical precursors or reducing agents. Recently, *Amendola et al.* revealed the fundamental mechanisms of laser ablation in liquids and the parameters that influence the composition and the structure of the nanoparticles during the laser ablation.[276] Laser ablation of a bulk metal plate in liquids leads to the formation of

the nanoparticles during the condensation of a plasma plume. This process starts with the absorption of the laser pulse by the bulk metal plate, resulting in the detachment of the ablated material. Then the expansion of a plasma plume containing the ablated material into the surrounding liquid occurs, and the energy is quenched by the liquid solution, generating a cavitation bubble which expands in the liquid and then collapses, followed by the slow growth and agglomeration of the nanoparticles. Laser generated gold nanoparticles have been demonstrated to have a novel surface chemistry. The groups of *Meunier* and *Mafun é* have revealed that the nanoparticles were partially oxidized to Au^{+} and Au^{3+} by the oxygen present in aqueous media by X-ray photoelectron spectroscopy (XPS) and IR spectroscopy.[277-278] These Au-O compounds can be hydrolyzed to give a surface of Au-O^{-}, thus leading to a negatively charged surface of the nanoparticles. The oxidized surface can react efficiently with OH^{-} and Cl^{-} to produce the surface charge which avoids the aggregation and the broadening of the plasmon bands of the nanoparticles (Scheme 4.13). When the pH value is above 5.8, the oxygen atoms are negatively charged (Au-O^{-}) and show constant zeta potential value, resulting in smaller nanoparticles with high stability. However, Au-OH is dominant when the pH value is below 5.8 and the particles easily aggregate. Therefore, the size of the nanoparticles can be controlled by adjusting the pH value or using different salt concentrations. Recently, a report of *Cuenya et al.* confirmed these findings by investigating the formation and stability of the gold oxide on the surface of gold nanoparticles.[279] Due to this partial oxidation, laser ablated gold nanoparticles act as electron acceptors and thus are easily modified by molecules bearing electron donor moieties such as thiols, disulfides, amines and carboxylates through covalent or electrostatic interactions.

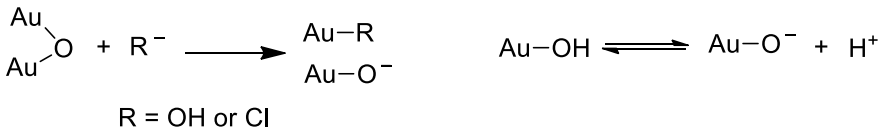

Scheme 4.13 Surface conversion of gold oxide compounds.

In comparison with the chemical synthetic routes for nanoparticle, laser ablation has several advantages.[280-281] Laser generated gold nanoparticles are negatively charged and thus have a high colloidal stability in aqueous solution or organic solvents. In contrast to the common chemical reduction routes which depend on the availability of reducing agents or the stabilizing ligands, laser ablation does not rely on chemical precursors, allowing the synthesis of ligand-free colloids and thus resulting in a high nanoparticle surface activity. This method is compatible with an almost unlimited variety of metals, surface functionalities and solvents. Furthermore, ligand-free nanoparticle surfaces allow a wide range of surface functionalities with higher conjugation efficiency and compatibility. In contrast, the place exchange reactions are limited with the type of the thiolated ligands. Moreover, the ligands around the nanoparticles are hardly to be entirely

replaced, resulting in the difficulties for quality and quantity analysis. However, besides these advantages, the limitations of laser ablation approach should be considered when preparing the nanoparticles by using this method. The major limitation of laser ablation is the control of the particle size, in particular when preparing ligand-free nanoparticles. The size distribution of the nanoparticles generated by laser ablation tends to be broadened due to the aggregation processes of the ablated atoms such as the post-ablation agglomeration of nanoclusters or the ejection of large fragments. It has been demonstrated that the decrease of diameter and a narrow size distribution can be obtained by selection of the laser fluence and the laser shots.[282-283] The use of surfactants,[284] cyclodextrins,[285-286] and biomolecules[287] has also been shown to reduce the nanoparticle sizes. Even though big particles can be generated during laser ablation, they can be removed with various methods, such as centrifugation, membrane filtration, dialysis and size exclusion chromatography, *etc*.

The generation of the functionalized gold nanoparticles can be achieved by either *ex situ* or *in situ* conjugation.[283, 288-289] As depicted in Figure 4.37, the *ex situ* conjugation is proceeded by adding the ligands after the laser ablation while the *in situ* conjugation is achieved by conjugating the ligands to the gold nanoparticles simultaneously with their generation. *Barcikowski et al.* have demonstrated that the conjugation efficiencies of both *ex situ* and *in situ* are very high with *in situ* conjugation showing four times higher efficiency. Laser ablated gold nanoparticles by *in situ* and *ex situ* conjugation were shown to feature up to five-fold higher surface coverage compared to the functionalized nanoparticles generated by the conventional ligand exchange method.[290]

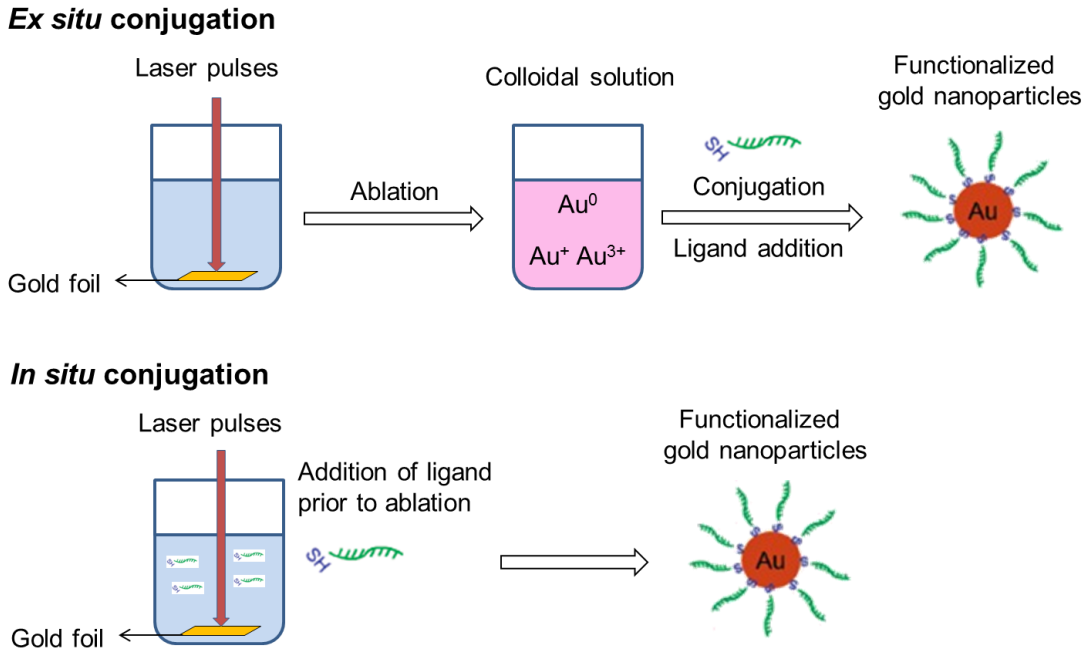

Figure 4.37 Schematic representation of the generation of functionalized gold nanoparticles by laser-based *ex situ* (*top*) and *in situ* (*bottom*) conjugation.

In this work the functionalized gold nanoparticles with peptides were prepared by laser ablation approach by our cooperation partner *Lisa Gamrad* in the working group of *Prof. Stephan Barcikowski* in the Institute of Technical Chemistry at the University of Duisburg-Essen. Laser ablation of gold nanoparticles was carried out using a picosecond laser system providing < 10 ps laser pulses at a wavelength of 1064 nm (pulse energy > 160 µJ, beam diameter: 2 mm), a power of 17 W, a repetition rate of 100 kHz and a focal length of 100 mm. The generation of the functionalized gold nanoparticles was done in two different ways depending on the types of conjugation.

For *ex situ* conjugation, the gold nanoparticles were first prepared before adding the ligands. The ablation was carried out in 0.6 mM sodium phosphate buffer at pH 8.0 using a 30 mL batch chamber in a time range of 150 seconds. The experimental set up (Figure 4.38, left) shows the laser beam focused through a quartz window on the 500 µm thick gold target (1 cm × 1.4 cm) which is fixed with a screw. In order to avoid accumulation of nanoparticles nearby the gold target, the solvent has to be stirred continuously during the ablation process. This was done with the help of an electrical driven motor which is fixed to the chamber cover and affects the movement of a Teflon stirrer blade dipping into the solvent. With the help of the software "LaserDesk", it is possible to control the scanning unity such as the geometry, the scanning speed and the number of cycles that is equivalent to the duration of the ablation. A spiral with an external diameter of 6 mm and a scanning speed of 6 mm/s was used. After the generation of nanoparticles, the big particles with diameters over 10 nm were removed via centrifugation to obtain monodispersed nanoparticles. Then a series of concentrations of the ligands (0-1500 µM) was prepared in 500 µL sodium phosphate buffer (0.6 mM, pH 6.0), followed by the addition of 1 mL monodispersed gold nanoparticles. In order to achieve one series of conjugates with the same gold concentration, the gold nanoparticles were always used from the same batch. Then the sample mixtures were adjusted to pH 6.0 and shaken for one hour to ensure the completion of the conjugation.

For *in situ* conjugation, ligands have to be added to the ablation liquid (0.6 mM sodium phosphate buffer) before nanoparticle generation. The laser ablation experiments were performed in 1.5 mL sodium phosphate buffer solution (0.6 mM, pH 6.0) in the presence of the ligands that should be conjugated to the surface of the gold nanoparticles. The experimental set up (Figure 4.38, right) consists of a standard optical glass cuvette with 2 mL volume where a gold ribbon (5.5 cm × 0.4 cm) with a thickness of 100 µm fixed on an inset can be placed. The "LaserDesk" software and the scanner were utilized for this type of ablation as well. A spiral with an external diameter of 3 mm and a scanning speed of 6 mm/s was used in this experiment. The duration of the laser ablation was 7 seconds. A series of Au NPs samples with different ligand concentrations (0-1500 µM) were prepared individually and were also shaken for one hour after the ablation.

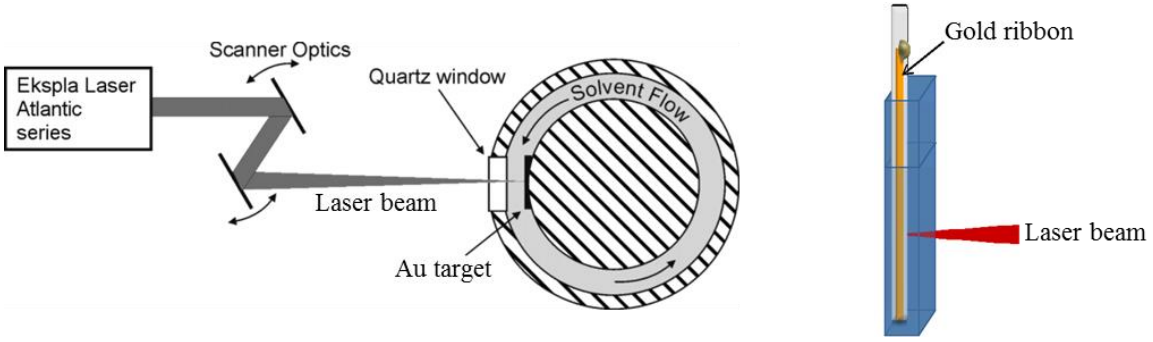

Figure 4.38 Schematic representation of the laser ablation of gold nanoparticles in liquids in absence of ligands in a batch chamber (*left*)[291] and in presence of ligands in a cuvette (*right*).

Ligand **161** containing the peptide sequence KWK(GCP) with a combination of basic and aromatic amino acids as well as the artificial GCP gtoup was first tried for the conjugation. Ligand **158** was also used as a control to adjust the surface functionalities and charges. Therefore, both monovalent and bivalent conjugations were prepared and analyzed. For the monovalent conjugation, only one type of ligand (**161**) was used during the *ex situ* or *in situ* conjugation. After the conjugation, the unbound ligands were removed from the conjugates by using ultracentrifugation and the surface coverage was tested with the help of UV/Vis spectroscopy. For the bivalent conjugation, two types of ligands (**161** and **158**) were used. Bivalent conjugation was performed as above described monovalent conjugation by adding both types of ligands to the gold colloids (*ex situ*) or the ablation liquid (*in situ*) at the same time. Figure 4.39 shows the structure overview of the monovalent conjugates (**171**) featuring the cationic ligand (**161**) and bivalent conjugates (**172**) featuring both the cationic ligand (**161**) and neutral ligand (**158**).

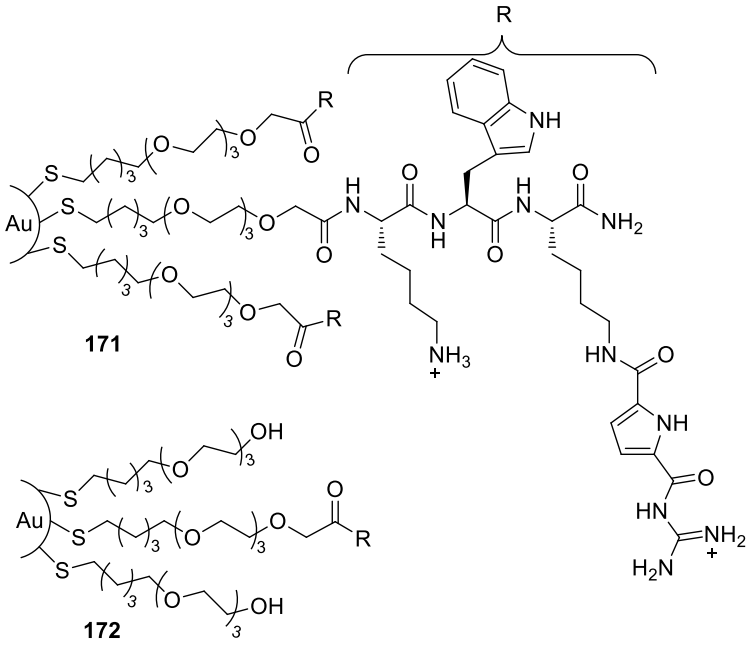

Figure 4.39 Structure features of the monovalent conjugates (**171**) and bivalent conjugates (**172**).

4.3.5 Characterization of Conjugated Gold Nanoparticles

Ex Situ Conjugation

We have used more often the *ex situ* conjugation to prepare the conjugates because the gold concentration, the particle size and the size distribution can be easily controlled. For the first test experiment, the conjugates with ligand **161** were prepared by using low ligand concentrations (0-10 μM). The polydispersed gold nanoparticles were generated by laser ablation in sodium phosphate buffer (0.6 mM, pH 8.0), to which a series of concentrations of ligand **161** (in 0.6 mM sodium phosphate buffer, pH 6.0) was added and the mixture was adjusted to pH 6.0 and subjected to 1 h conjugation. Absorption spectra of the gold colloids were recorded to determine the gold concentration, surface plasmon resonance (SPR) wavelength and primary particle index (PPI). The absorbance at 380 nm is primarily caused by the interband transition of gold, which is a good parameter for the estimation of Au NPs concentrations.[292] The gold concentration was then determined using the calibration curve of the absorbance at 380 nm (Figure 4.40) according to the *Lambert-Beer* law (A = εbc). A series of gold colloids with different gold concentrations were prepared by using different laser durations. After each laser ablation, the gold target was weighed to calculate the mass of gold in solution which was divided by the volume to obtain the mass concentration of the gold nanoparticles. The absorption spectra of these samples were measured and the calibration curve was then obtained by fitting the absorbance data at 380 nm against gold concentrations using linear regression analysis. The absorbance at 800 nm is mainly due to asymmetric aggregates. The PPI, which is a good indicator of the quality of the gold colloids, was calculated by the ratio of the absorbance at 380 nm and that at 800 nm. The SPR peaks mainly depend on the size of the gold nanoparticles.

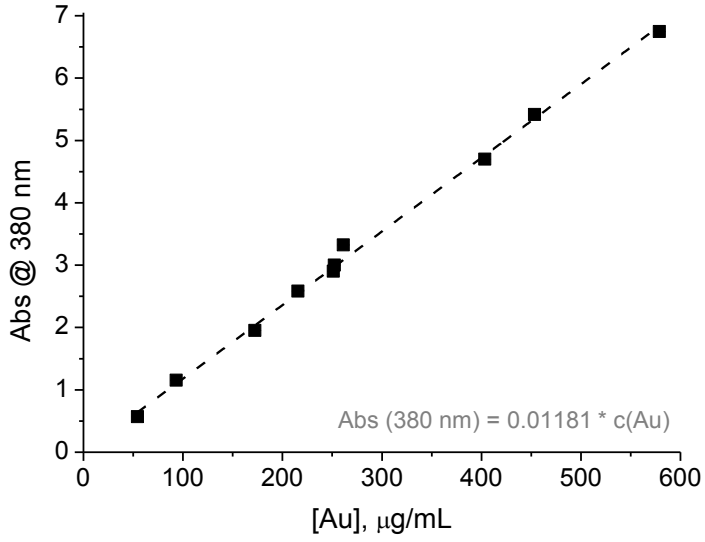

Figure 4.40 Calibration curve for determining the gold concentration.

As shown in Figure 4.41, the gold concentration initially decreased with the increase of the ligand concentration and reached a minimum value at ligand concentrations of 3-5 μM before it started increasing again. This is due to the compensation of the charges: initially the surface of the gold nanoparticles is negatively charged, when conjugated with the positively charged ligands, it reached the isoelectric point at a specific ligand concentration and formed large aggregation and the particles precipitated. With higher ligand concentration, the surface of the gold nanoparticles became positively charged and much less aggregation was observed. The red shift of the SPR peaks with the increasing ligand concentrations also revealed the aggregation of the nanoparticles. The decrease of the PPI values indicated the aggregation as well. However, after a few days, the nanoparticles were all precipitated because the amount of the positively charged ligands on the surface of Au NPs is still too low to stabilize the nanoparticles for longer time. Therefore, in order to obtain relatively stable nanoparticles, the functionalized Au NPs should be prepared with even higher ligand concentrations.

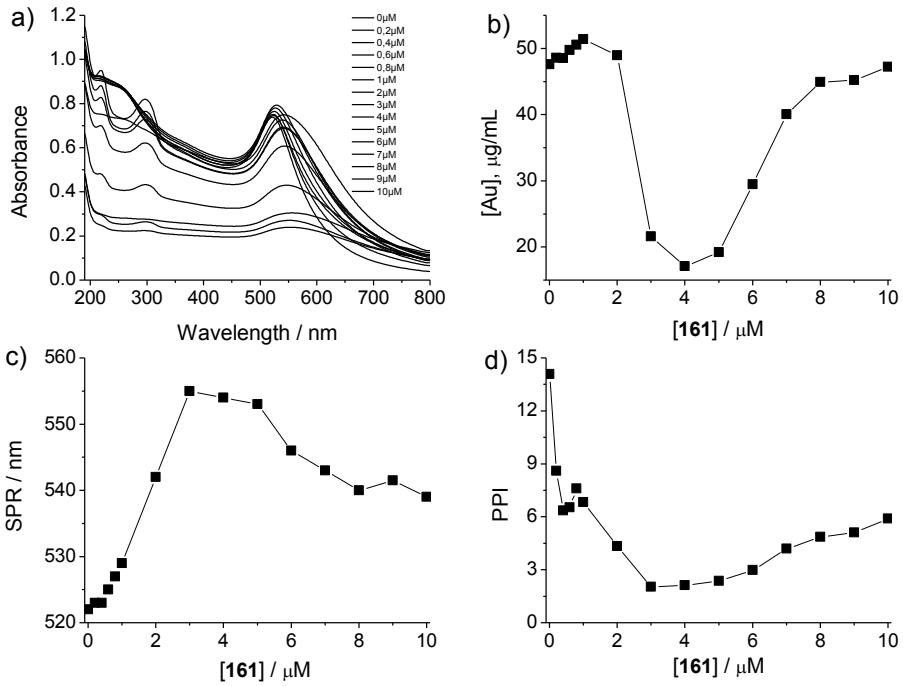

Figure 4.41 a) Absorption spectra of conjugates of Au NPs with different ligand concentrations ([**161**] = 0-10 μM) and plots of b) gold concentration, c) SPR peak, and d) PPI versus ligand concentration.

Accordingly conjugates with higher ligand concentrations (15-1000 μM) were prepared and analyzed. In order to test the long-term stability, the UV/Vis spectra were recorded after 2 hours, 11 days and 15 days respectively. As shown in Figure 4.42, no aggregation of the nanoparticles was observed at these high ligand concentrations after the conjugation. The gold nanoparticles with lower ligand concentrations (below 587 μM) started to aggregate only after some days, whereas those with higher ligand concentrations have a good long-term stability.

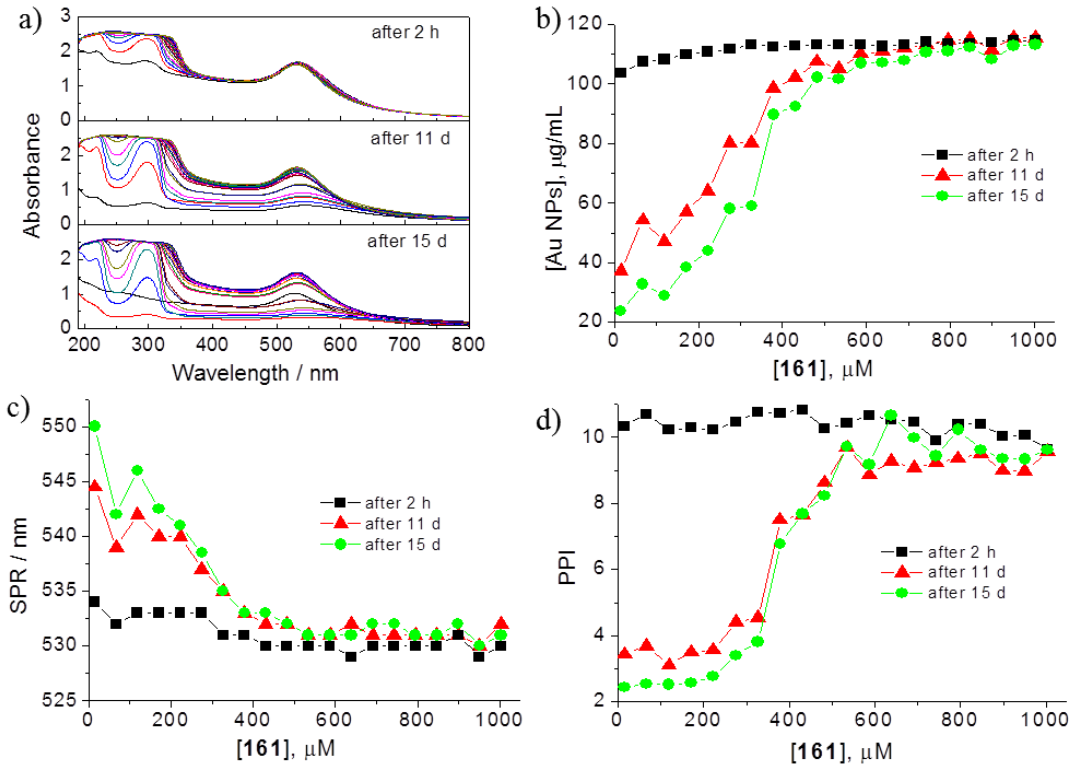

Figure 4.42 a) Absorption spectra of conjugates of Au NPs with different ligand concentrations ([**161**] = 15-1000 µM) and plots of b) gold concentration, c) SPR peak, and d) PPI versus ligand concentration.

The hydrodynamic diameters of the Au NPs were measured with the help of dynamic light scattering (DLS) measurement. The DLS is a technique that is based on the different *Rayleigh* scattering properties of particles with different sizes. It measures the fluctuation in scattering intensity of the particles with time when irradiated with monochromatic and coherent laser light. The *Brownian* motion of the particles resuts in different scattering intensity and its speed depends on the size of the particles and the viscosity of the solvent. The diffusion constant as a characteristic for the mobility of the particle depends on the hydrodynamic radius of the spherical particles with the solvent shell which can be calculated with the help of the *Stokes-Einstein* equation (12).

$$D = \frac{k_B T}{6\pi\eta r} \qquad (12)$$

Where D is the diffusion constant, k_B is Boltzmann's constant, T is temperature, η is the viscosity and r is the radius of the particles.

The intensity of scattering of a particle is proportional to the particle diameter by the power of six as large particles scatter much more light than smaller particles. Thus the intensity distribution weighs large particles much more than smaller ones. The polydispersity index (PDI) is a characteristic for defining the monodispersity of the system: the lower the PDI, the more monodisperse the system is. The intensity

distribution can be converted to a volume distribution and further to a number distribution. The hydrodynamic diameters of the conjugated Au NPs with different ligand concentrations obtained from DLS measurements are shown in Figure 4.43. The results showed that the nanoparticles with higher ligand concentrations have smaller sizes which indicated that the higher amounts of the ligands can better stabilize the nanoparticles.

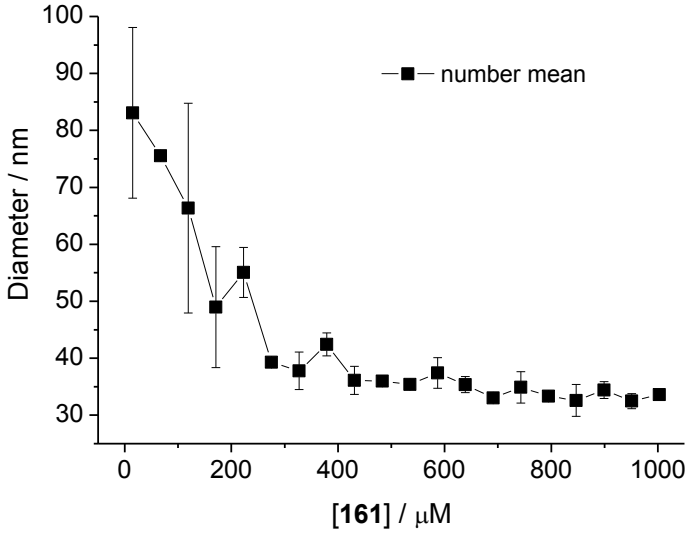

Figure 4.43 Hydrodynamic diameter of Au NPs with different ligand concentrations ([**161**] = 15-1000 μM) obtained from DLS measurements. The y error bars represent the standard deviation from at least three measurements.

The sizes of the gold nanoparticles were analyzed with analytical CPS disc centrifuge. The CPS disc centrifuge uses sedimentation to measure particle size distribution. Particles settle in a fluid according to *Stokes*' Law (equation 13).

$$v_s = \frac{2}{9} \frac{(\rho_p - \rho_f)}{\eta} gr^2 \qquad (13)$$

Where v_s is the settling velocity of the particles, ρ_p and ρ_f are the mass densities of the particles and the fluid, respectively, η is the viscosity, g is the gravitational acceleration and r is the radius of the particles.

Sedimentation velocity increases proportionally with the square of the particle diameter. Hence a small difference in particle sizes causes a significant difference in settling rates. The particles with the same size settle at the same speed and arrive at a detector beam as a thin band. The time that is needed to reach the detector is used to calculate the size of the particles. This technique allows measuring a wide range of particle sizes (5 nm-50 μm).

The size distributions of the Au NPs directly after the laser ablation as well as after the removal of big particles were analyzed by CPS disc centrifugation. As depicted in Figure 4.44, the Au NPs were monodispersed after removing big particles by ultracentrifugation.

The sizes of conjugated Au NPs with ligand **161** were determined as well using disc centrifugation. The conjugates are a bit larger due to the surface coverage by the ligands compared to the ligand-free Au NPs (Figure 4.44, right). This result further confirmed the successful conjugation of the ligands to the surface of the Au NPs. However, the sizes measured by disc centrifugation are much smaller than those obtained from the DLS measurements. This is due to the fact that DLS measures the sizes of the solvated particles. Moreover, DLS weighs big particles more because they scatter more light than smaller ones, whereas the disc centrifugation could measure the particles more separately.

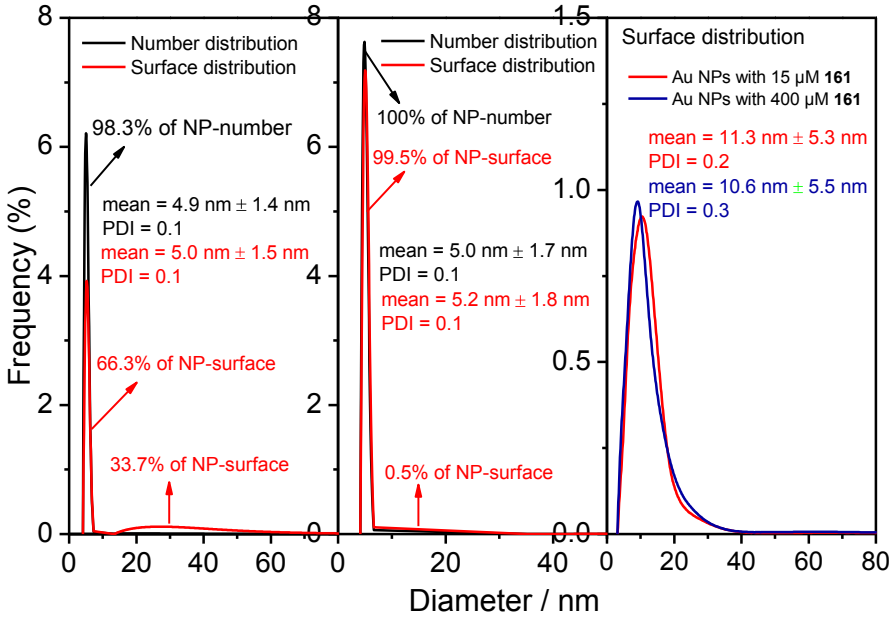

Figure 4.44 Number and surface size distribution of the gold nanoparticles before (*left*) and after (*middle*) the removal of big particles, as well as surface size distribution of the monovalent conjugated Au NPs with ligand **161** (*right*) obtained from the disc centrifugation measurements.

In addition, the size distributions of the ligand-free and the conjugated Au NPs were determined by transmission electron microscopy (TEM). The results clearly show that the Au NPs are spherical particles with diameter around 6-7 nm (Figure 4.45). This finding is in agreement with the sizes determined by disc centrifugation. The sizes of the ligand-free and the conjugated Au NPs are similar because only the gold core could be seen by TEM.

Besides monovalent conjugates with positively charged ligand (**161**) as the recognition unit for β-tryptase, bivalent conjugates with the second neutral ligand (**158**) as the surface control is also interesting. Therefore, after removing the big particles (> 10 nm) to obtain the monodispersed Au NPs, their monovalent (with ligand **161**) and bivalent (with ligands **161** and **158**) conjugates were prepared with the help of *ex situ* conjugation. For the monovalent conjugation, a series of concentrations of ligand **161** (0-725 µM) was used. For the bivalent conjugation, the same concentration series of ligand **161** (0-725 µM) was taken and respectively ligand **158** was used with two-fold concentrations (0-1450 µM).

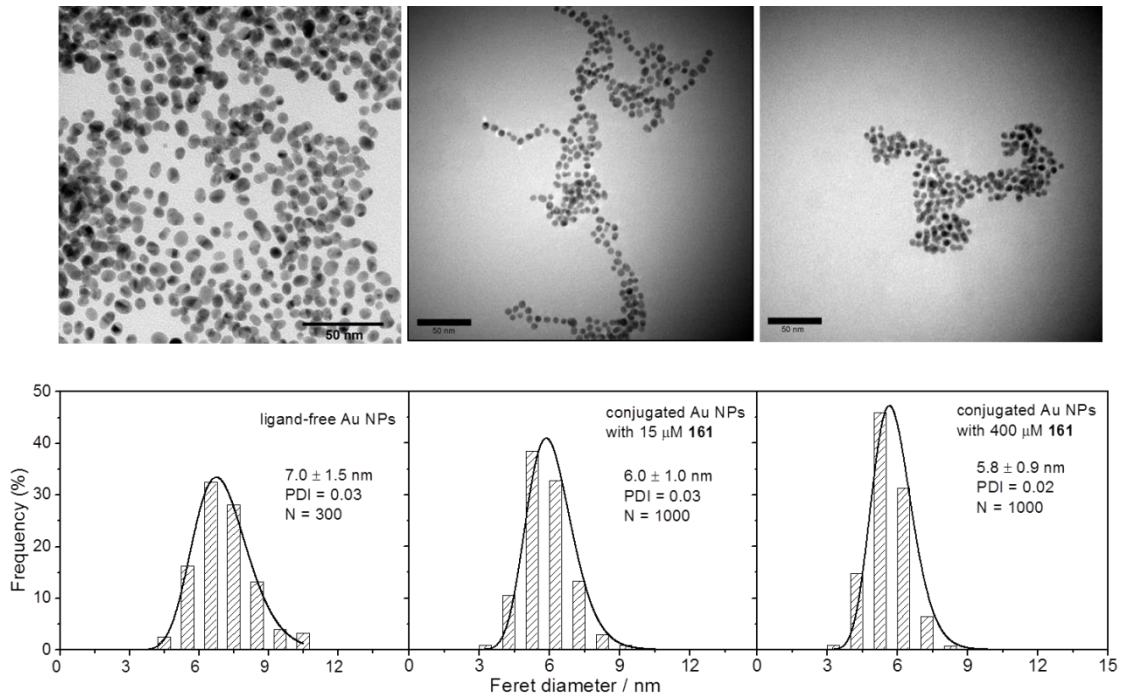

Figure 4.45 *Top*: TEM images of ligand-free Au NPs (*left*) and monovalent conjugated Au NPs with ligand (**161**) concentrations at 15 μM (*middle*) and 400 μM (*right*), respectively. *Bottom*: The corresponding surface size distributions of the ligand-free Au NPs and conjugates.

Accordingly both the monovalent and bivalent conjugations were carried out as described above. After the laser ablation and 1 h conjugation, absorbance of the gold colloids was recorded to determine the gold concentration and PPI. As shown in Figure 4.46, both of the monovalent and bivalent conjugates are stable with higher ligand concentrations.

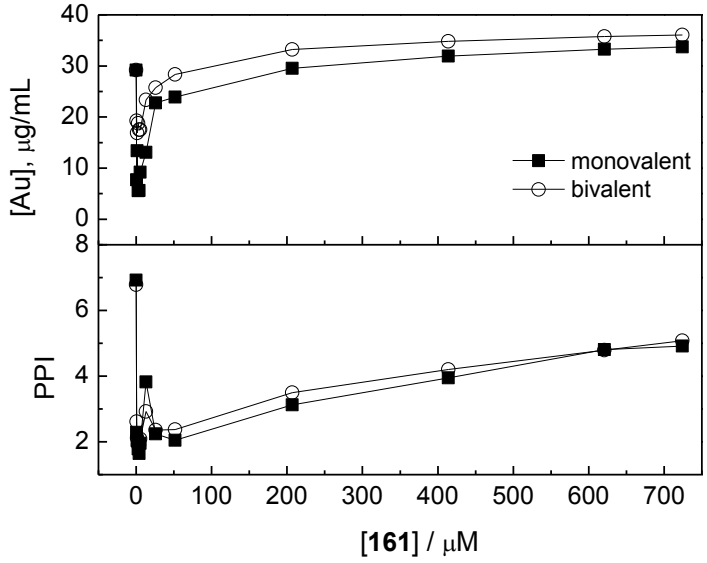

Figure 4.46 Plots of gold concentration and PPI versus different ligand (**161**) concentrations (0-725 μM) of monovalent and bivalent conjugated Au NPs obtained from *ex situ* conjugation.

The purification of the conjugates (to remove the unbound ligands) was carried out by using the ultracentrifugation. After centrifugation, the supernatant was removed and the nanoparticles were redispersed in the same volume of the buffer solution by using ultrasonication. The centrifugation and redispersion steps were repeated three times. The combined supernatants were analyzed with the help of UV/Vis spectroscopy to determine the concentration of the unbound ligands. Then the surface coverage of the gold nanoparticles was calculated from these data by subtracting the unbound ligands from the total amount of the ligands used for the conjugation. The absorbance of ligand **161** was recorded and the unbound ligand concentration was evaluated using the calibration curve of the absorbance at 296 nm (Figure 4.47) according to the *Lambert-Beer* law (A = εbc).

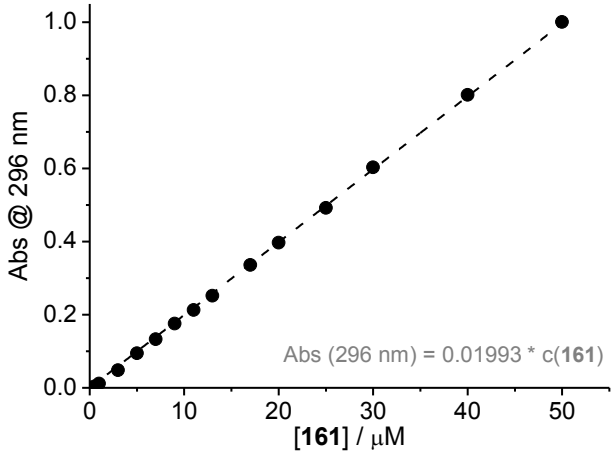

Figure 4.47 Calibration curve for determining the concentration of ligand **161**.

Figure 4.48 illustrates the absorption spectra of the monovalent conjugated Au NPs before and after centrifugation, as well as that of the supernatant. It showed clearly that it is possible to remove the unbound ligand albeit with the loss of gold as indicated by the decrease of the absorbance at 380 nm. At the same time, the formation of bigger aggregates was also evident from the increase of the absorbance at 800 nm. This is because the particles formed agglomerates and it is difficult to redisperse all the Au NPs in buffer solution after centrifugation and also some of the particles stick to the vial.

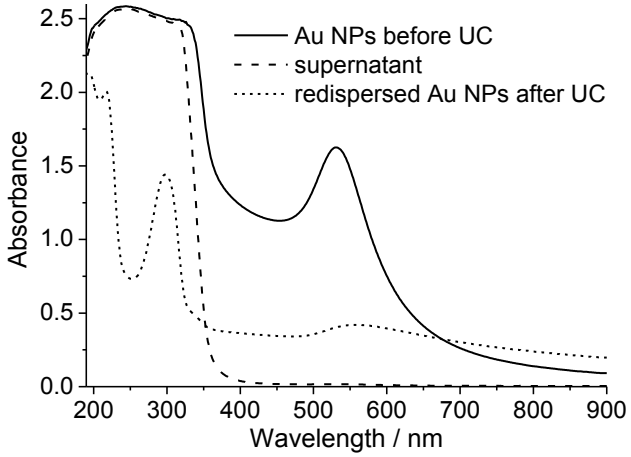

Figure 4.48 Absorption spectra of the monovalent conjugated Au NPs before and after ultracentrifugation, as well as the supernatant.

The conjugation efficiency, defined as the percentage of total amount of ligand bound to the surface of the Au NPs, can be calculated. Figure 4.49 illustrates the surface coverage and conjugation efficiency of the conjugates obtained from the *ex situ* conjugation. Because the control ligand **158** does not contain any chromophore, only ligand **161** was used to determine the surface coverage for both monovalent and bivalent conjugates. As a result the monovalent conjugates exhibited very high conjugation efficiency (> 80 %) in the concentration range of 0.5-430 μM compared to the bivalent conjugates (ca. 40-80 %). The similar conjugation efficiency both at lower and higher ligand concentrations suggests that most likely a monolayer surface is first formed at low ligand concentrations which subsequently transformed into multilayers with increasing concentration of the ligand(s).

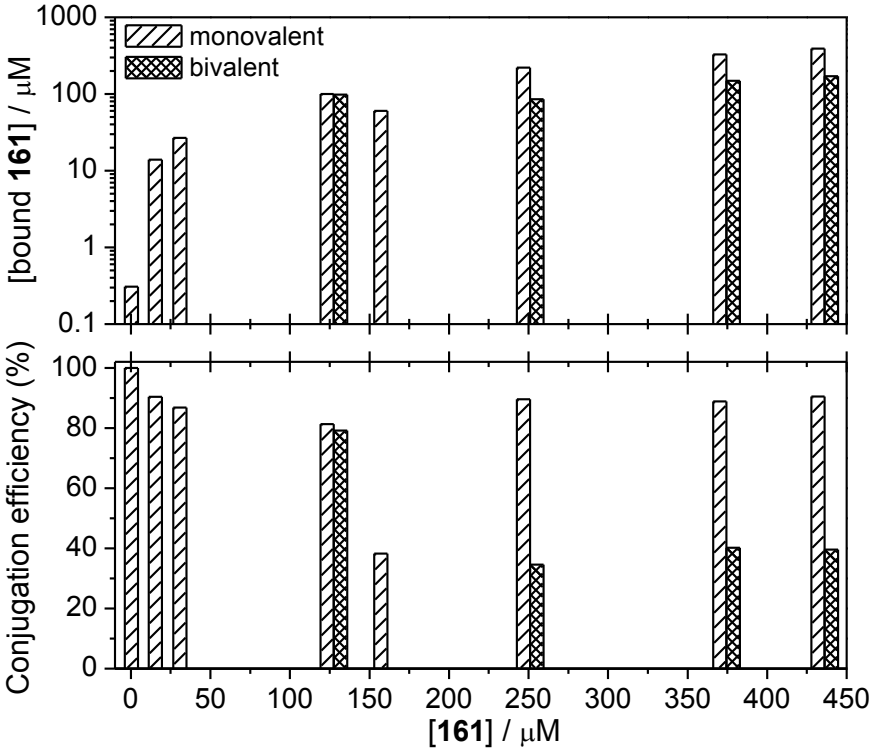

Figure 4.49 The concentration (*top*) and percentage (*bottom*) of ligand **161** conjugated to the surface of the gold nanoparticles compared to the total amount of ligand used for *ex situ* conjugation.

After the centrifugation, the redispersed conjugated Au NPs were shown to have bigger size and higher polydispersity as depicted by DLS measurements (Figure 4.50) and disc centrifugation analysis (Figure 4.51). The particles seem to be bigger due to the big agglomeration as they come closer together during the centrifugation. Moreover, the DLS weighs bigger particles more as they scatter more light than smaller ones. A significant difference in the size distribution was obtained by TEM as shown in Figure 4.52. The results showed that the individual particle sizes could be seen after the removal of the unbound ligands and the sizes are similar to the conjugates before centrifugation (see Figure 4.45). Some agglomerates could be seen but most of the particles present the

smaller sizes as obtained before centrifugation. Why the agglomeration could not be seen from TEM is unclear at the moment. The big aggregates might be already lost during the sample preparation.

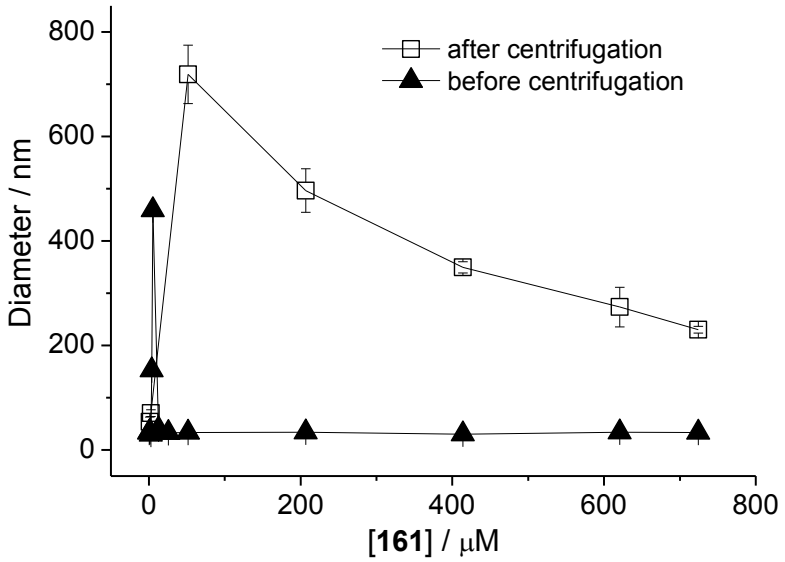

Figure 4.50 Hydrodynamic diameters (number distribution) of monovalent conjugated Au NPs before and after the removal of unbound ligand. The y error bars represent the standard deviation from at least three measurements.

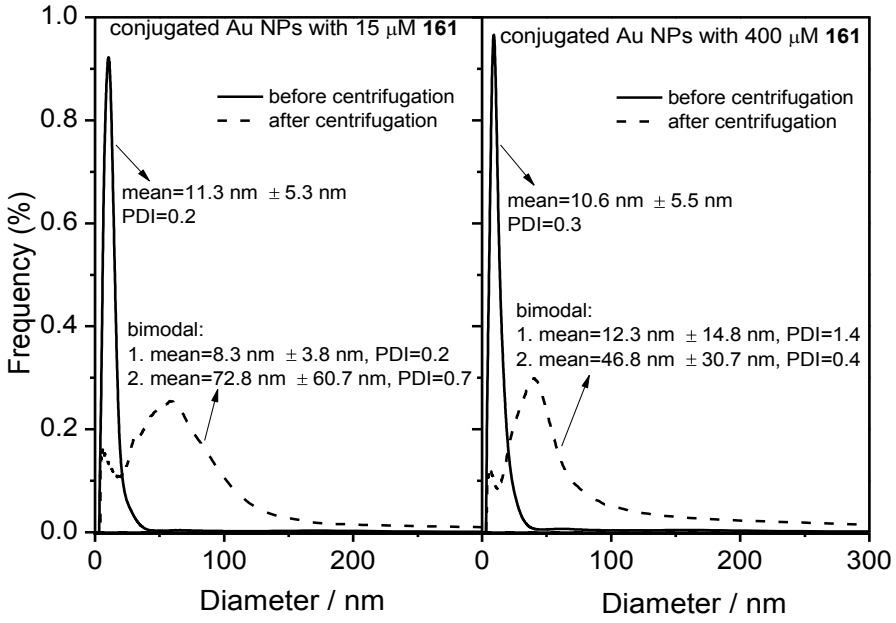

Figure 4.51 Surface size distribution of monovalent conjugated Au NPs with ligand (**161**) concentrations at 15 μM (*left*) and 400 μM (*right*) obtained from the disc centrifugation measurements before and after removal of unbound ligand.

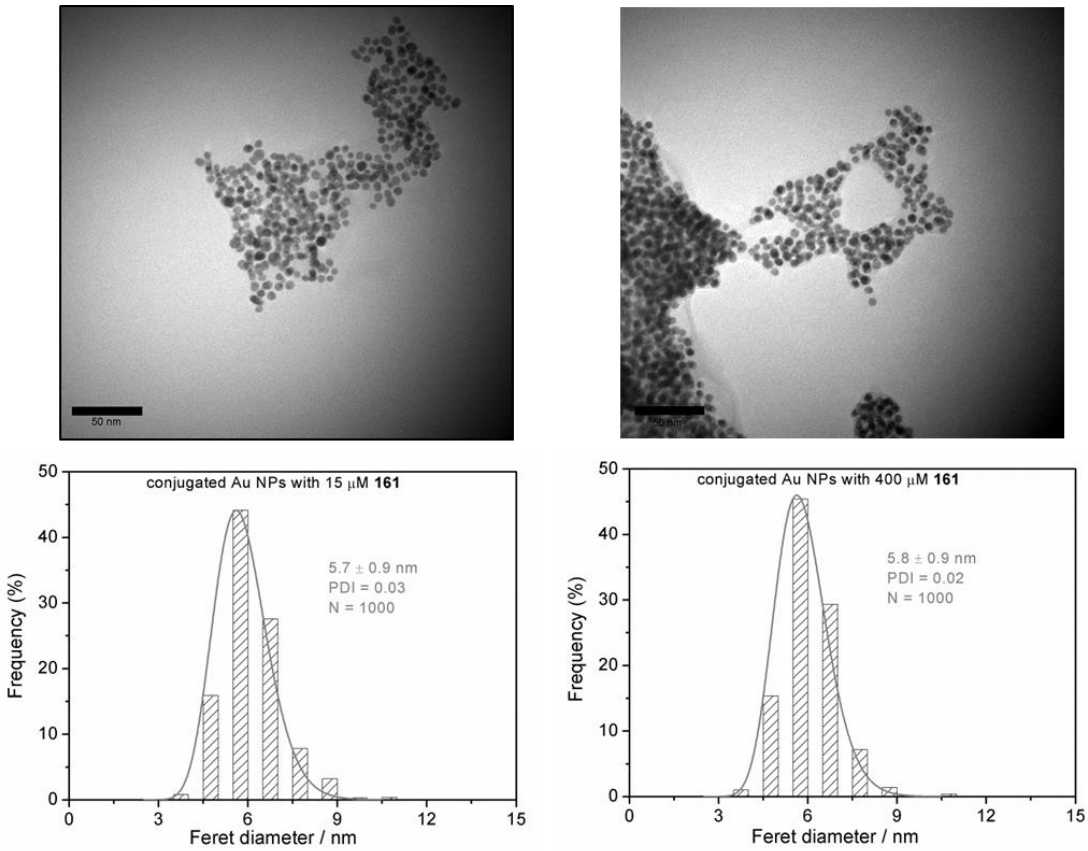

Figure 4.52 *Top*: TEM images of monovalent conjugated Au NPs with ligand (**161**) concentrations at 15 μM (*left*) and 400 μM (*right*) after the removal of unbound ligands. *Bottom*: The corresponding surface size distributions of the conjugates.

In Situ Conjugation

In situ conjugation was also tested in this work to take advantage of its high conjugation efficiency.[290] Both monovalent and bivalent conjugated Au NPs were generated. For monovalent conjugation, a series of different ligand (**161**) concentrations (0-725 μM) was prepared in 1.5 mL sodium phosphate buffer (600 μM, pH 6.0). Each sample was added in an optical glass cuvette to which a gold ribbon was placed and subjected to the laser ablation for 7 seconds. The samples were then shaken for one hour to ensure the complete conjugation. The bivalent conjugation was performed in the same way by using the same concentrations of ligand **161** (0-725 μM) as the monovalent conjugation and respectively two-fold of the control ligand **158** (0-1450 μM) as the surface blocker. The absorption spectra of conjugated Au NPs were measured and the gold concentration as well as the PPI were evaluated in the same way as above described for the *ex situ* conjugation. As shown in Figure 4.53, the isoelectric point aggregation and precipitation was observed again at low ligand concentration (3-5 μM). The conjugated Au NPs are stable with high ligand concentrations. In comparison with the monovalent conjugated gold colloids, the bivalent conjugated gold colloids have lower gold

concentration and low quality, which indicated that bivalent conjugates formed bigger aggregates than the monovalent conjugates.

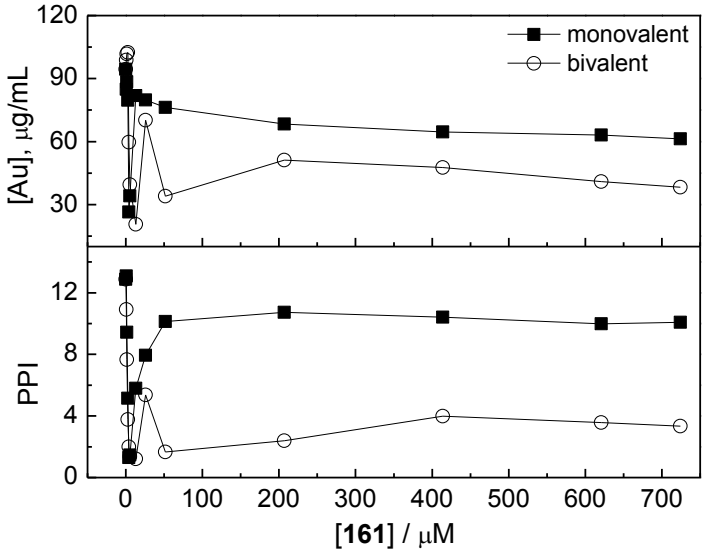

Figure 4.53 Plots of gold concentration and PPI versus different ligand (**161**) concentrations (0-725 μM) of monovalent and bivalent conjugates obtained from *in situ* conjugation.

Figure 4.54 illustrated the number-weighted mean size of the monovalent and bivalent conjugates with different ligand concentrations obtained by DLS measurements. The results showed that conjugates with low ligand concentrations have large particle sizes due to the isoelectric point aggregation and those with high ligand concentrations have smaller particles sizes. This finding is in agreement with the results obtained from the absorption spectra, which also showed that the bivalent conjugates have larger particle size and are not as stable as the monovalent conjugates.

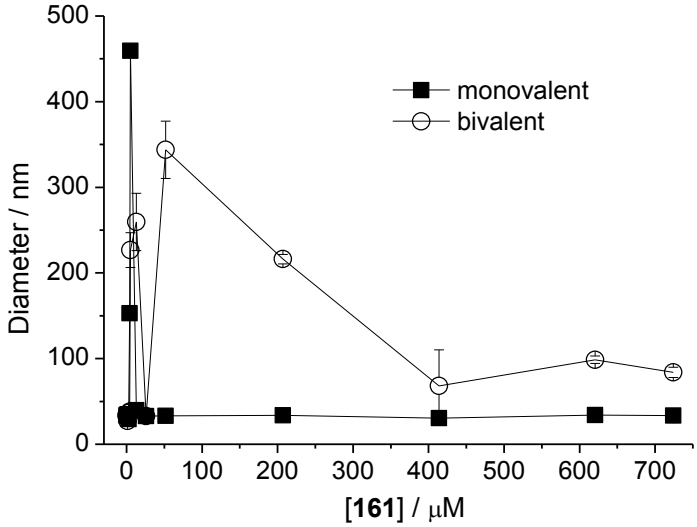

Figure 4.54 Hydrodynamic diameters of monovalent and bivalent conjugates obtained by DLS measurements. The y error bars represent the standard deviation from at least three measurements.

This result was further verified by the measurement of the zeta potential of the particles. When placing a particle with a net surface charge in the liquid, it attracts the counter ions close to its surface and results in the formation of the electrical double layer which contains the *Stern* layer and the diffuse layer. Within the diffuse layer, there is a slipping plane close to the *Stern* layer and the ions inside the slipping plane moves with the particle. Zeta potential is known as the electric potential that exists at the location of this slipping plane. It is often used to indicate the potential stability of the colloidal system. The greater the zeta potential, the more stable the suspension is. The general definition of the stable suspension is that the zeta potential should be more positive than +30 mV or more negative than -30 mV. Zeta potential of the particles can be measured using electrophoresis. By applying an electric field across the suspension, particles move towards the electrode of opposite charge with a constant velocity referred to the electrophoretic mobility (U_E). The zeta potential (ζ) related to the electrophoretic mobility can be calculated by the *Henry* equation (14).

$$U_E = \frac{2\varepsilon\zeta f(ka)}{3\eta} \tag{14}$$

Where ε is dielectric constant, η is the viscosity and *f(ka)* is *Henry*'s function. Two values 1.5 and 1.0 are generally used as approximations for *f(ka)* related to aqueous and non-aqueous medias, respectively.

As shown in Figure 4.55, the monovalent conjugates have zeta potential values of +40 mV with higher ligand concentrations (> 50 μM), whereas the bivalent conjugates have much lower zeta potential values of only +20 mV. This is because the neutral ligand (**158**) occupied some space on the particle surface and resulted in fewer amounts of the positively charged ligands (**161**) on the surface of the bivalent conjugated Au NPs. This result revealed that the bivalent conjugates have less surface charges and are not as stable as the monovalent conjugates.

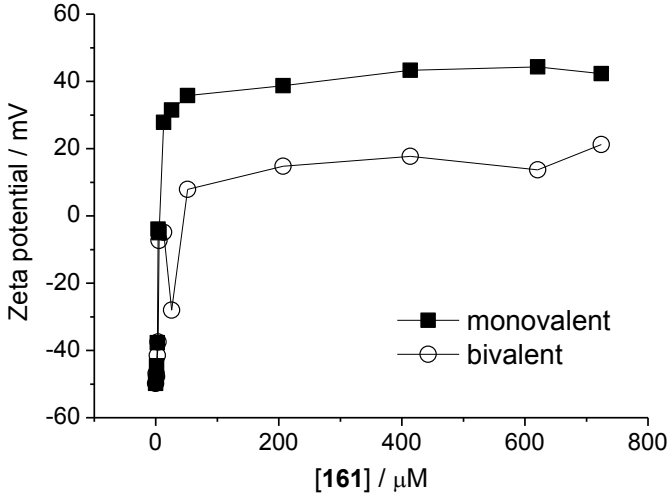

Figure 4.55 Zeta potentials of monovalent and bivalent conjugates in sodium phosphate buffer (pH 6.0).

The surface coverage of the monovalent conjugates obtained by *in situ* conjugation was evaluated as described above for the *ex situ* conjugation. Figure 4.56 illustrates the surface coverage and conjugation efficiency of the monovalent conjugates. The results demonstrated that the monovalent conjugates obtained by *in situ* conjugation have a high conjugation efficiency (> 70 %) in the whole concentration range of 0.5-720 μM as also observed previously for the *ex situ* conjugation (see Figure 4.49).

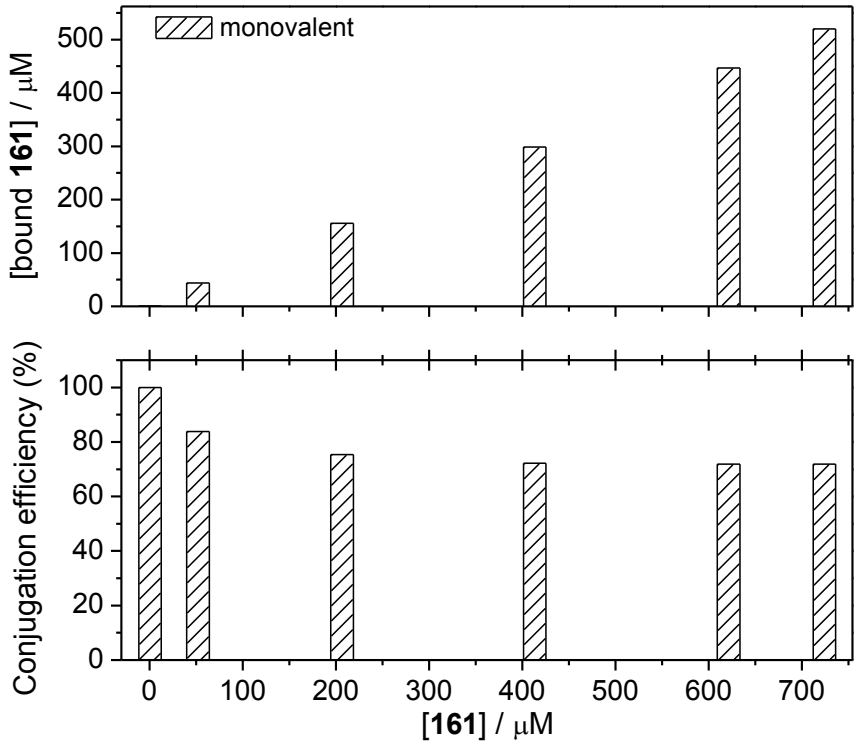

Figure 4.56 The concentration (*top*) and percentage (*bottom*) of ligand **161** conjugated to the surface of the gold nanoparticles compared to the total amount of ligand used for *in situ* conjugation.

In conclusion, monovalent and bivalent conjugated gold nanoparticles using positively charged peptide ligands can be successfully prepared by both *ex situ* and *in situ* conjugation. The *ex situ* conjugation is possible to control the gold concentration and the size distribution of the nanoparticles. Conjugates have good long-term stability but only with higher surface coverage after the removal of unbound ligands. Both of the methods showed very high conjugation efficiencies. In order to test the enzyme inhibition by the conjugates, the conjugated Au NPs with different ligand concentrations were determined for β-tryptase inhibition after removing the unbound ligands.

4.3.6 Enzyme Assay

Enzyme Inhibition Assay

The enzyme inhibition assay was performed in white 96 well microplate in 50 mM Tris-HCl buffer at pH 7.4 as described in Chapter 4.1.4. In order to measure the kinetic parameters the hydrolysis rate of substrate Tos-Gly-Pro-Arg-AMC by rhSkin β-tryptase in the presence of different concentrations of ligands and conjugates was determined at appropriate enzyme concentration and fixed substrate concentration. The kinetics of the enzymatic cleavage is monitored by measuring the increase of the fluorescence activity of the released AMC at 460 nm emission (380 nm excitation) over the time of 15 min. The assays (at 25 ^{o}C) were carried out in a final volume of 200 µL in assay buffer (165 µL) wherein the enzyme (10 µL, final concentration 0.25 nM) was incubated with various concentrations of conjugated Au NPs or free ligands (20 µL) and finally the substrate (5 µL, final concentration 50 µM) was added.

In this project, the Au NPs are used as the scaffolds to provide the multivalent interactions with the enzyme by attaching efficient ligands to their surface. In order to compare the enzyme inhibitory activity of the multivalent conjugates with the free ligands, the gold core should not interfere the inhibition results. Therefore, in order to test if the Au NPs themselves interfere the enzymatic activity, the enzyme assay in the presence of the ligand-free Au NPs was performed. A series of dilutions from the stock solution of Au NPs at a gold concentration of 313 µg/mL was prepared in 0.6 mM sodium phosphate buffer (pH 6.0) to determine their influence on the activity of β-tryptase. The enzyme inhibition results showed that in the presence of Au NPs, the rate of the product (AMC) conversion is lower compared to the sample without Au NPs, which could be due to the inhibition of the enzyme activity or the quenching fluorescence activity of the released AMC. However, whether the interference is resulted from the direct enzyme inhibition or the fluorescence quench of AMC needs to be investigated. Therefore, in order to test if the Au NPs have any influences on the fluorescence of the released product, fluorescence titration experiment of AMC with ligand-free Au NPs was carried out. The results demonstrated that the fluorescence of AMC is quenched by ligand-free Au NPs as shown in Figure 4.57. Hence, the observed decrease of fluorescence activity of AMC in the enzyme kinetic assay might be caused by the fluorescence quenching of AMC but not by the direct inhibition of the enzyme.

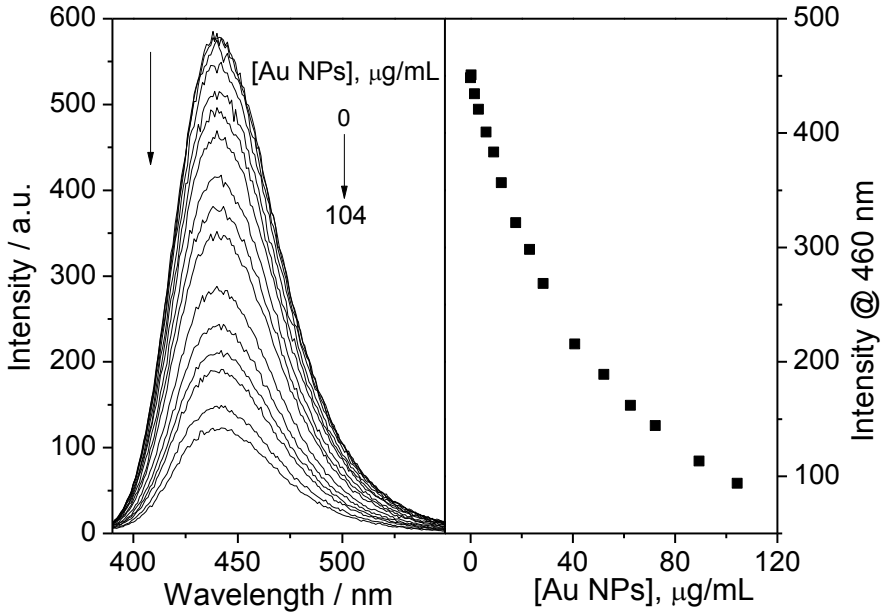

Figure 4.57 Fluorescence spectra of AMC in Tris buffer (50 mM, pH 7.4) in the presence of ligand-free Au NPs of increasing concentration (*left*) and plots of intensity at 460 nm versus Au NPs concentration (*right*).

To further demonstrate the influence of the gold core from the conjugated Au NPs in the enzyme inhibition, a more direct experiment is to determine if the Au NPs affect the IC_{50} value of a standard inhibitor. Therefore, the IC_{50} value of the standard inhibitor *p*-aminobenzamidine (pAb， **25**) was determined in the presence of ligand-free Au NPs. The result in Table 4.5 showed that the IC_{50} values of pAb in the presence of Au NPs with lower (36 μg/mL) or higher (60 μg/mL) gold concentrations are very similar to that in the absence of Au NPs, indicating that the Au NPs has no influence on the IC_{50} value of the inhibitor. Hence, the ligand-free Au NPs might influence the fluorescence activity of the enzyme assay, but if the conjugates have the same gold concentrations, they would have the same effect on the enzyme assay without interfering the IC_{50} values of the conjugates.

Table 4.5 IC_{50} values [μM] of the standard inhibitor **pAb** for β-tryptase in the presence of Au NPs or phosphate buffer.

Standard inhibitor	IC_{50} values [μM]
pAb[a]	25.45 ± 0.68
pAb with phosphate buffer[b]	23.02 ± 0.61
pAb with Au NPs (36 μg/mL)[b]	22.36 ± 1.13
pAb with Au NPs (60 μg/mL)[b]	22.03 ± 0.79

[a] IC_{50} value of pAb was measured in Tris-HCl buffer. [b] IC_{50} values of pAb were measured in Tris-HCl buffer in the presence of 20 μL phosphate buffer or Au NPs in phosphate buffer.

Then, the IC_{50} values of conjugates with different surface functionalities were determined. Due to the instability of the bivalent conjugates after the removal of the unbound ligands, only the IC_{50} values of monovalent conjugates were determined after removing the unbound ligands. The IC_{50} values of the monovalent conjugates (**171**) refer to the ligand (**161**) concentration on the surface of the Au NPs needed for the half maximal inhibition of the enzyme. In order to compare with the ligand itself, the IC_{50} values of the thiolalkylated peptide ligand (**161**) used for conjugation and the related alkylated peptide ligand (**168**) as well as the acetylated peptide ligand (**170**) as controls were also determined. The results summarized in Table 4.6 showed that the conjugates have low micromolar inhibitory affinity similar to the free ligands (**161**, **168**, **170**) featuring the same peptide sequence. It is surprising that the multivalent conjugated Au NPs are not superior to the single ligand. This might be due to the size of the Au NPs being so large that they do not fit to the entrance to the central pore of the enzyme. Moreover, the Au NPs might be not able to reach the two types of favored binding sites on the surface of β-tryptase which are situated at the monomer-monomer interfaces and around the active sites as described by the docking studies (Chapter 4.1.1) for this type of peptide ligands and thus only have moderate inhibitory activity. However, nevertheless this result demonstrated that the Au NPs at least do not disturb the enzyme inhibition and have no toxicity for this enzyme activity during the assay as often found when using NPs in the biological systems.[293] The similar IC_{50} values of ligands featuring the same alkylated TEG linker but with (**161**) or without (**168**) the terminal thiol group indicates that the thiol group does not contribute to the enzyme inhibition. Moreover, the comparison of ligand **170** without the alkylated TEG linker with ligand **161** and ligand **168** containing the alkylated TEG linker revealed that the linker has no influence in the enzyme inhibitory activity. This is also demonstrated by the neutral ligand **158** which showed no inhibition of β-tryptase even at a very high concentration of 1 mM. The single-armed ligands (**161**, **168**, **170**) containing the peptide sequence KWK with the artificial arginine analog GCP group attaching to the side chain of the C-terminal lysine have very low IC_{50} values compared to the single-armed peptide ligand RWKG (K_i = 306 μM) in *Wich*'s work[13] which contains arginine instead of lysine-derived GCP binding motif. Their IC_{50} values are also much lower than the above described standard inhibitor pAb featuring the guanidine analog amidine. These findings are in agreement with the previous results, demonstrating again that the artificial arginine analog GCP moiety can significantly improve the enzyme inhibitory activity compared to peptide ligand with just proteinogenic amino acids. However, why the single-armed ligands (**161**, **168**, **170**) have such low IC_{50} values compared to the peptide-derived hydrazide **138** (IC_{50} = 24 μM) featuring the same peptide sequence and the GCP group (see Chapter 4.2) is unclear at this moment.

Table 4.6 IC_{50} values [μM] of the monovalent conjugated Au NPs and ligands for β-tryptase.

	Inhibitors	IC_{50} values [μM]
Conjugated Au NPs	*Ex situ* conjugates (**171**)	2.12 ± 0.49
	In situ conjugates (**171**)	1.29 ± 0.22
Ligands for comparison with the conjugates	**161**	2.25 ± 0.16
	168	3.62 ± 0.10
	170	1.03 ± 0.04
	158	> 1000

In order to further investigate how these single-armed inhibitors interact with β-tryptase, the mode of enzyme inhibition was determined by measuring the enzyme reaction rate at different substrate concentrations (0-500 μM) in the presence of different inhibitor concentrations (0, 1, 5, 10, 50 μM). The inhibition mode can then be illustrated by analyzing the data with the help of nonlinear regression (Figure 4.58) and the *Lineweaver-Burk* plots (Figure 4.59). The analyses of both plots clearly show that the enzyme inhibition is competitive. The nonlinear regression shows that the reaction rates rise slowly in the presence of inhibitor but have the tendency to reach the same V_{max} at a higher substrate concentration. The half maximum reaction rate is reached at higher substrate concentration depending on the amount of the present inhibitor, which confirms that the K_m value is increased in the presence of inhibitor. All these information is a sign for competitive inhibition mode. Moreover, the double-reciprocal *Lineweaver-Burk* plots show that they have an interception on the x-axis in the presence or in the absence of inhibitor, which is also indicative for a competitive inhibition. Hence, with the help of these experiments it is possible to prove that most likely these single-armed inhibitors compete with the substrate for the same binding site and hence act as competitive inhibitors of β-tryptase.

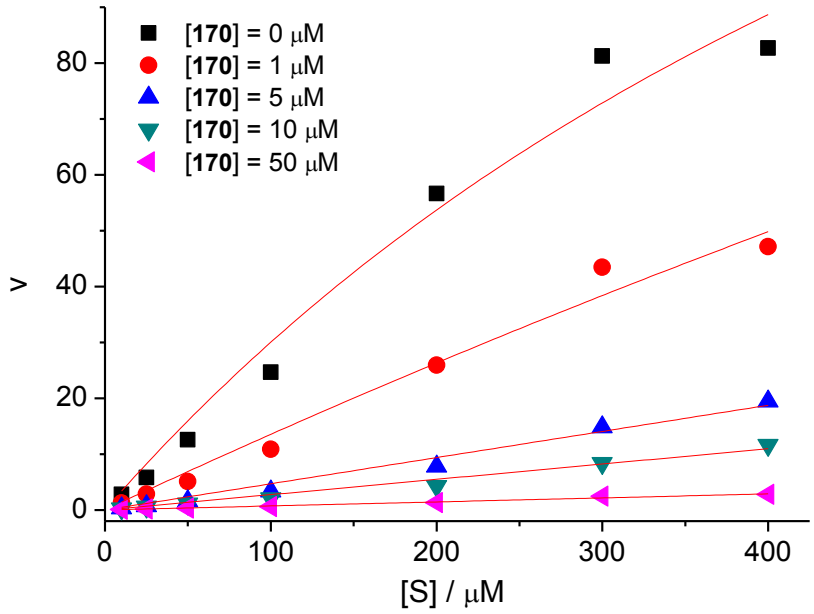

Figure 4.58 Nonlinear regression analysis of reaction velocity versus substrate concentration according to the *Michaelis-Menten* equation.

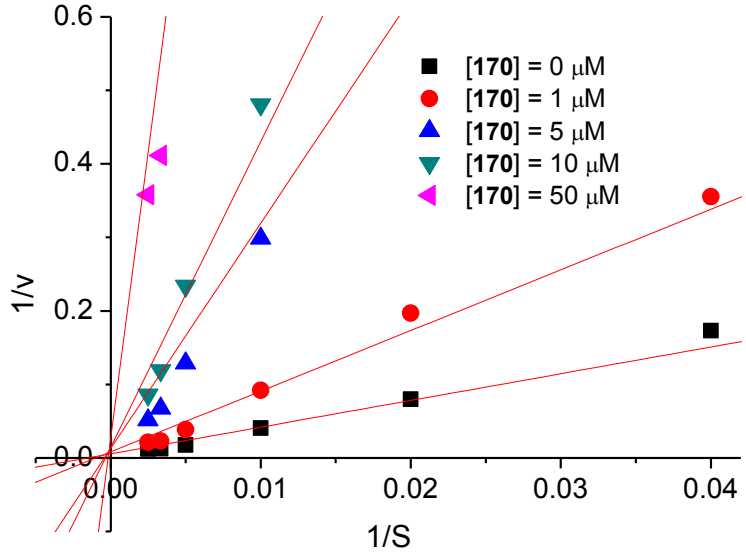

Figure 4.59 *Lineweaver-Burk* plots of 1/v against 1/[S] in the absence and in the presence of a fixed concentration of an inhibitor.

4.3.7 Molecular Modeling Studies

The investigation of the enzyme inhibition mode in the above chapter led to the conclusion that the small single-armed inhibitor binds directly to the active catalytic sites buried inside the central pore of β-tryptase. To further verify how this type of inhibitors inhibits β-tryptase, docking studies were carried out to visualize possible binding modes between the inhibitor and β-tryptase. The calculations were done by *Martin Ehlers* in our working group by using the software Schrödinger MacroModel and Glide software (Version 2012 Update 2). The ligand 3D structure was minimized with the help of the optimized potential for liquid simulation (OPLS) 2005 force field. The enzyme input is based on the reported crystal structure of β-tryptase (PDB code: 1A0L) with all water molecules and substrates removed from the binding pore of the crystal structure. Then Glide was used to generate a receptor grid file of the active catalytic centers of β-tryptase, to obtain detailed information about possible binding sites. Because the tetrameric structure of the enzyme is symmetric, it is interesting to dock the more detailed and specific parts of the enzyme. Therefore, besides the full tetrameric tryptase structure, the "long-half", "short-half", and the "quarter" protein structures were prepared as well. Grids were then prepared for all the four types of protein structure. Ligand docking was then performed in the extra precision mode with sampling of nitrogen inversions and ring confirmations. The ligand conformations were simulated without any constrains or restrictions besides a penalization in the implemented scoring function (Glide) for nonplanar amide conformations. Post-docking minimizations were performed using a rejecting threshold of 0.5 kcal/mol.

The calculations of ligand **170** and the four types of protein structures show some favored ligand conformations binding to the active site of β-tryptase. The docked binding surface area within the "short-half" structure of the enzyme is shown in Figure 4.60. It situates around one active site of the enzyme and spans over the interface of two monomers. As shown in Figure 4.61, the ligand interacts with the enzyme by binding to the active site with the GCP group and the monomer-monomer interface with the lysine side chain. A closer look with different views of the binding region reveals that the GCP moiety fits perfectly the geometry of the S1 binding pocket and is buried in this cavity.

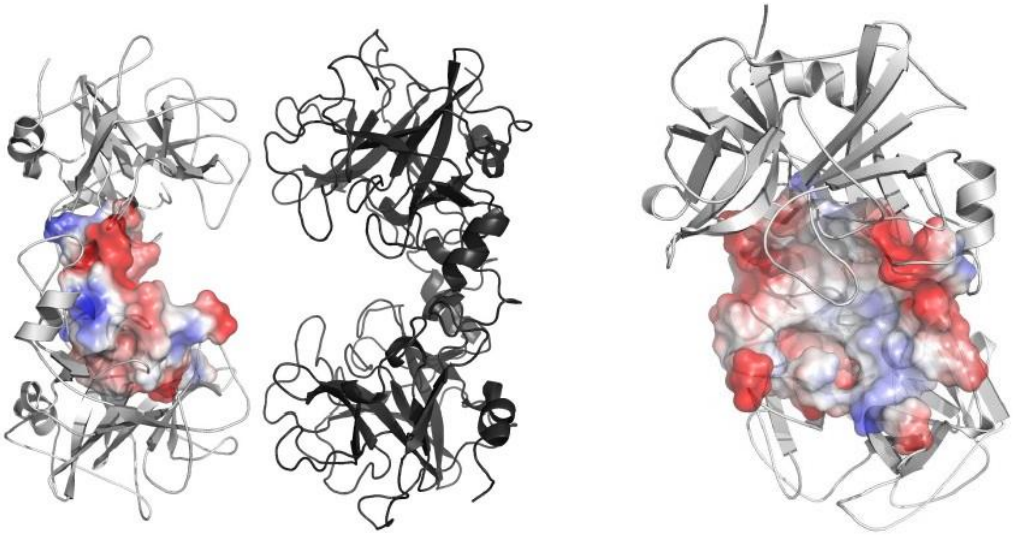

Figure 4.60 *Left*: The tetrameric structure of β-tryptase (PDB code: 1A0L); the left side ("short-half") is used for the calculations with the interaction area between the ligand and the enzyme represented as colored surface; the right, darker side (second "short-half") is excluded from the calculations. *Right*: Close-up of the concave binding surface within the "short-half" structure involved in the calculations. The surface colors represent the positive (blue) and negative (red) surface electrostatic potentials.

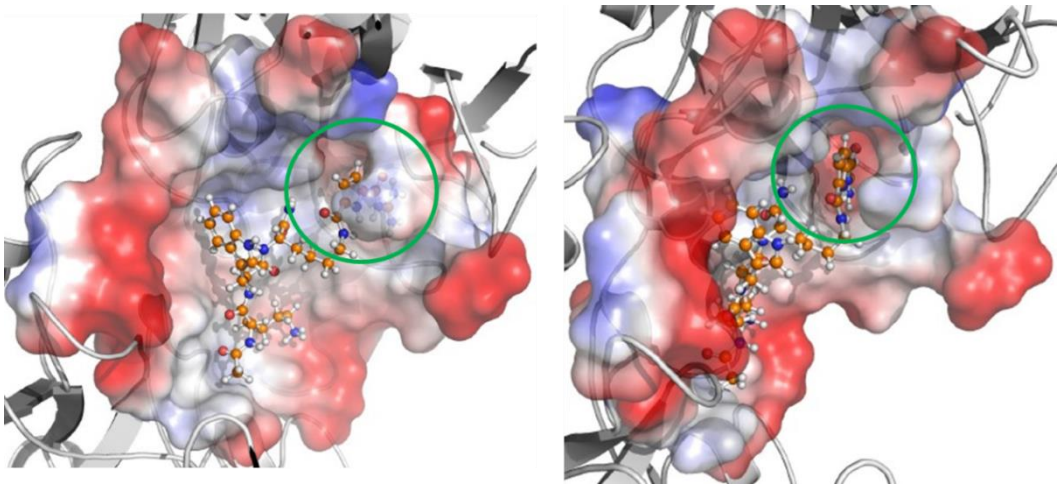

Figure 4.61 Different views of calculated images of the tripeptide ligand **170** (shown as ball and sticks) in the active site of β-tryptase. The GCP group fits perfectly in the S1 binding pocket (marked with the green circle).

Figure 4.62 illustrates the key interactions between the ligand and the protein residues. The GCP group binds to the acidic S1 pocket by forming four hydrogen bond assisted ion pairs between the guanidinio group of the GCP moiety and the protein residues ASP-189, Ser-190 and Gly-219. The lysine side chain of the ligand binds to the monomer-monomer interface through the charge interaction with the protein residue Glu-217.

A more detailed interaction diagram (Figure 4.63) shows clearly the distributions of the protein residues in a distance of 4 Å to the ligand and their possible interactions with the

ligand. The surrounding line represents the contact area featuring various surface characteristics. Besides the above described interactions of protein residues with GCP group and lysine side chain of the ligand, additional interactions are shown between the backbone of the ligand and the hydrophobic residue Ala-97, as well as the polar residues Gln-98 and Ser-214.

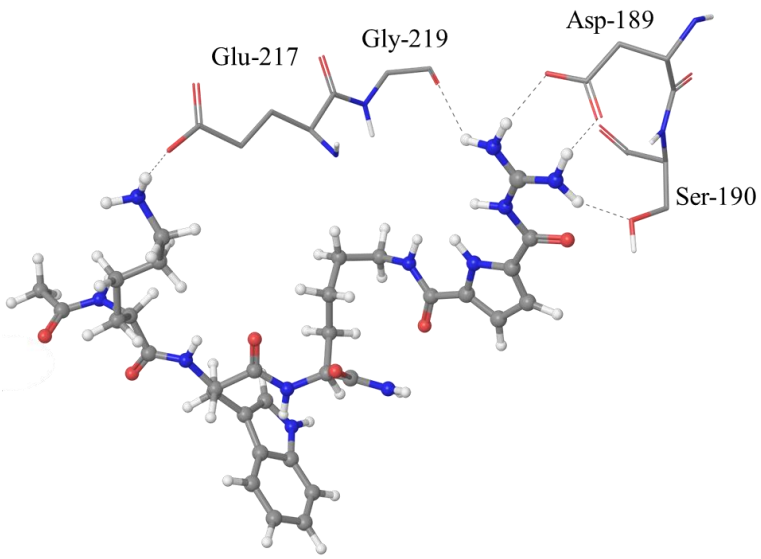

Figure 4.62 Schematic representation of the interaction between the ligand (**170**) and the protein residues. The hydrogen bonds are presented as black dashed lines.

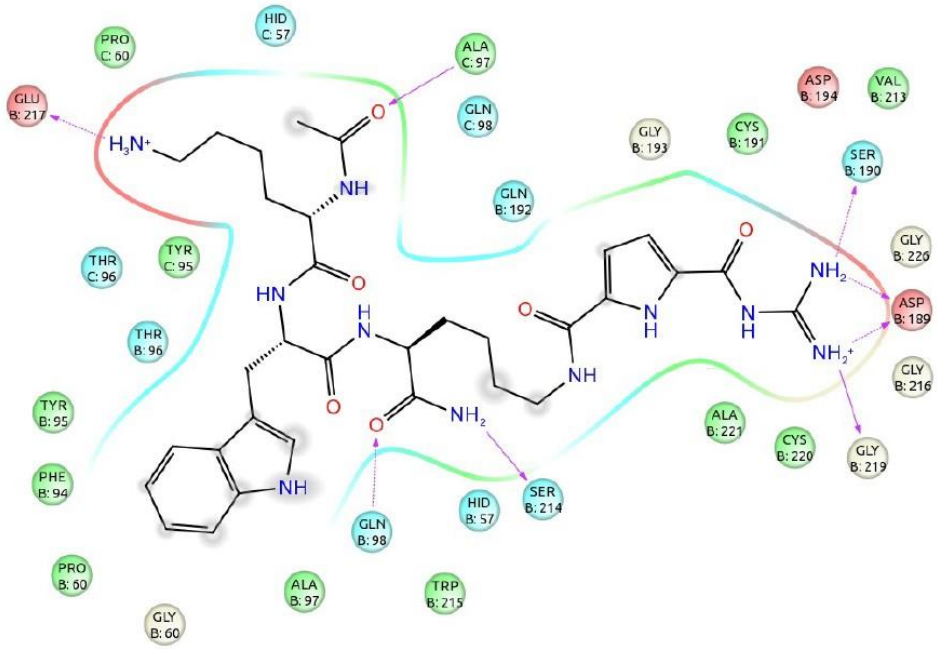

Figure 4.63 The interaction diagram of the protein residues around the ligand (**170**) within a distance of 4 Å. The hydrogen bonds are presented as arrows with solid and dashed lines, showing the interactions of the ligand with the backbones and side chains of the protein residues, respectively. The surrounding line represents the contact area with different colors indicative of different surface characteristics (red = acidic, green = hydrophobic, blue = polar). The gray surrounding of some ligand atoms indicates a solvent exposed position.

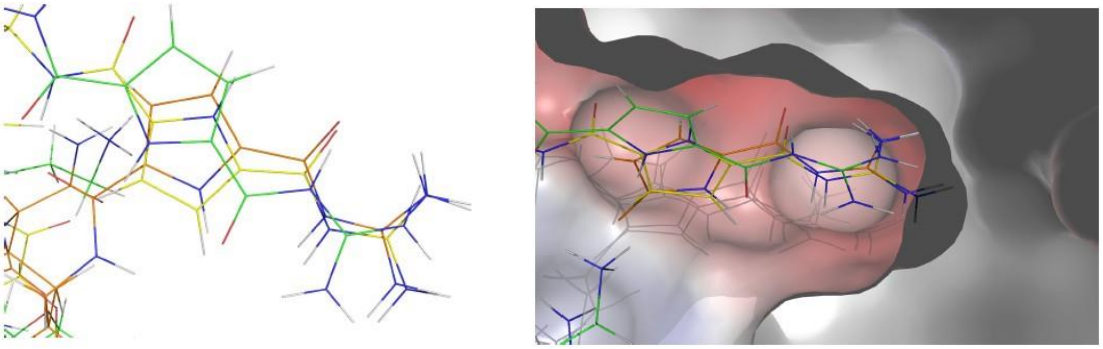

Figure 4.64 *Left*: Overlay of the conformations of GCP moieties of three calculated ligands (**161**, **168** and **170**). *Right*: The acidic S1 binding pocket of the β-tryptase is addressed by the GCP moiety of the ligands.

The docking studies were also performed with ligands featuring the same peptide sequence but containing the alkylated TEG chain with (**161**) or without (**168**) a terminal thiol group. The resulting conformations of these two ligands reveal a well-defined position of the GCP moiety but no define position of the alkylated TEG chain. As shown in Figure 4.64, the comparison of the three calculated ligands (**161**, **168** and **170**) indicates that the GCP groups have the same binding positions. The binding regions of the three conformations of different ligands demonstrate a favorite binding position of the GCP group in a deep S1 cavity of the enzyme. These results demonstrated the importance of the GCP group for the efficient inhibition of β-tryptase.

Therefore, the calculation results also confirm that most likely the ligands bind to the active site of β-tryptase and thus compete with the substrate for the same binding site. The artificial GCP group of the ligand fits perfectly to the S1 binding pocket of β-tryptase by interacting with residues ASP-189, Ser-190 and Gly-219 through four hydrogen bonds, while the lysine side chain binds to the monomer-monomer interface of the protein by interacting with the residue Glu-217. These findings are also in agreement with the docking studies described in Chapter 4.1.1. The calculations underline the importance of the GCP group for binding to the active site of the enzyme, which also explains the much more efficient inhibition of β-tryptase by this type of ligands containing the GCP group compared to other active site inhibitors such as the above described single-armed peptide ligand RWKG in *Wich*'s work[13] and the standard inhibitor pAb. Hence, this type of small ligands containing the GCP group can already efficiently bind to the active site of the enzyme. However, when they were attached to the surface of the gold nanoparticles, most likely the large size of the conjugated Au NPs might not allow it to interact with the acidic hot spots around the entrance to the central pore of the enzyme. Probably only random binding to acidic areas on the protein surface occurs. Therefore, the access of the substrate to the active site might not be completely blocked by the conjugates, thus they only show moderate inhibition affinity similar to the single-armed ligands which compete with the substrate for binding to the active site of β-tryptase.

In conclusion, it is possible to generate and evaluate the monovalent and bivalent conjugated gold nanoparticles by *ex situ* or *in situ* conjugation with the help of laser ablation. Both the *ex situ* and *in situ* conjugations have shown high conjugation efficiency. The monovalent conjugates featuring the positively charged peptide ligands containing the artificial arginine analog GCP binding motif on the surface of the nanoparticles show long-term stability and could inhibit β-tryptase with low micromolar affinity. We could demonstrate that the conjugated nanoparticles do not disturb the enzyme activity when compared with the free ligand. The single-armed ligands inhibit β-tryptase with low micromolar affinity in a competitive way. It could be demonstrated by docking studies that the inhibition is based on the binding to the S1 pocket of the enzyme and thus the inhibitors compete with the substrate for the active site. The inhibition data of the single-armed ligands show that the artificial GCP groups can significantly improve the enzyme inhibitory activity compared to the ligands with only proteinogenic amino acids. In future studies, ligands with different characteristics can be conjugated to the surface of the gold nanoparticles and test for given biological targets.

5. SUMMARY AND OUTLOOK

This thesis was focused on the discovery of novel and potent inhibitors for the serine protease β-tryptase which has a unique tetrameric structure consisting of four monomers with the A_2B_2 arrangement pointing towards to a central pore and four active sites buried inside the cavity. Not like the classical active site inhibitors of β-tryptase as mostly described in the literature, the multivalent ligands were designed by using new structures and new approaches to inhibit β-tryptase through protein surface recognition. The ligands featuring the basic residues were used to bind to the acidic hot spots around the entrance to the central pore, thus blocking the access to the active sites. Besides the proteinogenic amino acids, the artificial arginine analog GCP moiety was used as the tailor-made binding motif to improve the inhibitory affinity. The inhibitors were shown to efficiently bind to the protein surface through the electrostatic interactions and hydrogen bonding. The results are briefly summarized in the following text.

5.1 New Tetravalent Peptide Ligands with Two Different Sets of Arms for the Inhibition of β-Tryptase

The new design of tetravalent ligands in the first part of this thesis was based on the previous findings of tetravalent peptide ligands with four identical arms attached to a lysine dendrimer scaffold. Now docking studies revealed that there are at least two different kinds of binding sites on the enzyme: one at the interfaces of two monomers and one nearby the catalytic center. Hence, in order to bind to the two binding sites of the enzyme, the tetravalent peptide ligands **115**-**120** (Figure 5.1) with two different sets of arms and the artificial arginine analog GCP moiety were designed and synthesized by using standard Fmoc SPPS with an orthogonal protecting group strategy. To further test the influence of the artificial GCP moiety on the inhibition of β-tryptase, tetravalent ligands **124**-**125** with four identical arms terminating with the artificial GCP group were designed and synthesized by using microwave-assisted Fmoc SPPS.

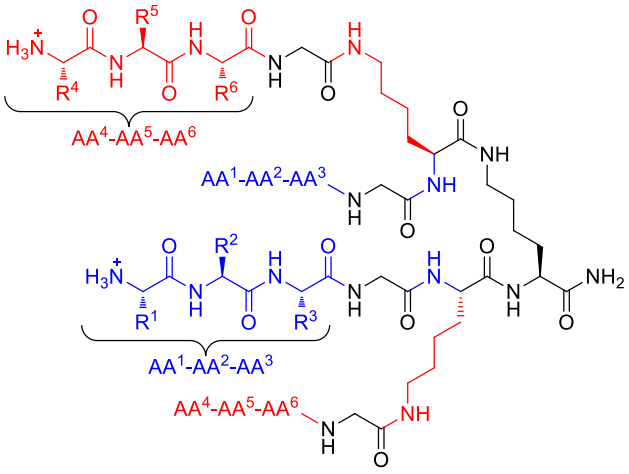

	AA^1	AA^2	AA^3	AA^4	AA^5	AA^6
115	Arg	Trp	Lys	Arg	Leu	Phe
116	Lys	Trp	Lys	Lys	Leu	Phe
117	Arg	Trp	Lys	Lys	Leu	Phe
118	Arg	Trp	Lys	Lys	Trp	Lys
119	Arg	Trp	Lys	Phe	Arg	Lys
120	Arg	Trp	Lys	GCP	Leu	Phe

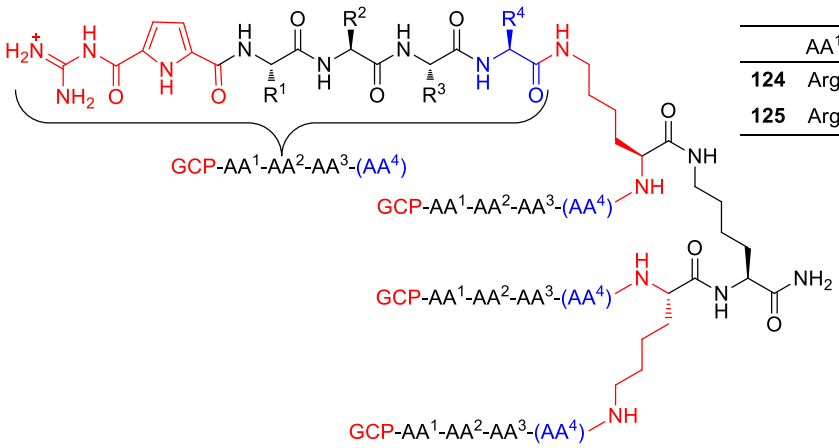

	AA^1	AA^2	AA^3	AA^4
124	Arg	Trp	Lys	Gly
125	Arg	Trp	Lys	—

Figure 5.1 Structure of tetravalent peptide ligands (**115-120**) with two different sets of arms (colored in red and blue, respectively) and tetravalent ligands (**124-125**) with four identical arms terminating with the artificial arginine analog GCP moiety.

Enzyme assays of these ligands revealed that all the ligands could efficiently inhibit β-tryptase with lower micromolar to nanomolar affinity (K_i values between 13 μM and 0.067 μM). The ligand **120** with two different sets of arms and the artificial arginine analog GCP group was shown to be the most efficient inhibitor in these series of peptide ligands. It was observed that inhibitor **120** has 60 and 200 times higher inhibitory affinity to the β-tryptase than inhibitors **115** and **117** by replacing amino acid arginine or lysine with the artificial GCP group, respectively. This finding revealed that the presence of the artificial GCP group can significantly improve the inhibitory affinity of such tetravalent peptide ligands. Furthermore, inhibitor **120** showed a biphasic inhibition mode: one with high affinity (K_i = 0.056 μM) and one with low affinity (K_i = 19.59 μM). This finding could result from the two different sets of arms binding to the two different binding sites of the enzyme with different binding affinities as identified from the docking studies. The tetravalent inhibitors **124-125** with four identical arms showed similar inhibitory affinities to β-tryptase which indicated that an additional glycine is not necessary and the peptide

arm consisting of the tripeptide and the terminal GCP group should have the appropriate length to bind to the surface of the enzyme. Furthermore, all the ligands showed no inhibition against other related serine proteases such as trypsin and α-chymotrypsin, which indicated the highly selective binding to β-tryptase.

With the help of the dialysis experiments and the replacement experiments by the addition of excess heparin which restored the enzyme activity, it could be shown that these ligands inhibit the β-tryptase in a reversible way. The further investigation of the inhibition mode with the help of the interpretation of the nonlinear regression and the *Lineweaver-Burk* plots could show that the tetravalent inhibitors inhibit the enzyme in a noncompetitive mode. This finding indicated that most likely the inhibitors bind to the surface of the enzyme and do not compete with the substrate for the active sites. This is confirmed by the computational calculations of possible binding modes between the inhibitor and β-tryptase. As illustrated in Figure 5.2, the cationic residues of inhibitor **120** bind to a cluster of acidic amino acids such as aspartic and glutamic acids that accumulate at the entrance to the central pore and around the active sites of β-tryptase, which agree very well with the findings of these two kinds of favored anionic binding sites from the docking studies. Therefore, the tetravalent inhibitors could span over the entrance to the central pore, thus limiting the access to the active sites.

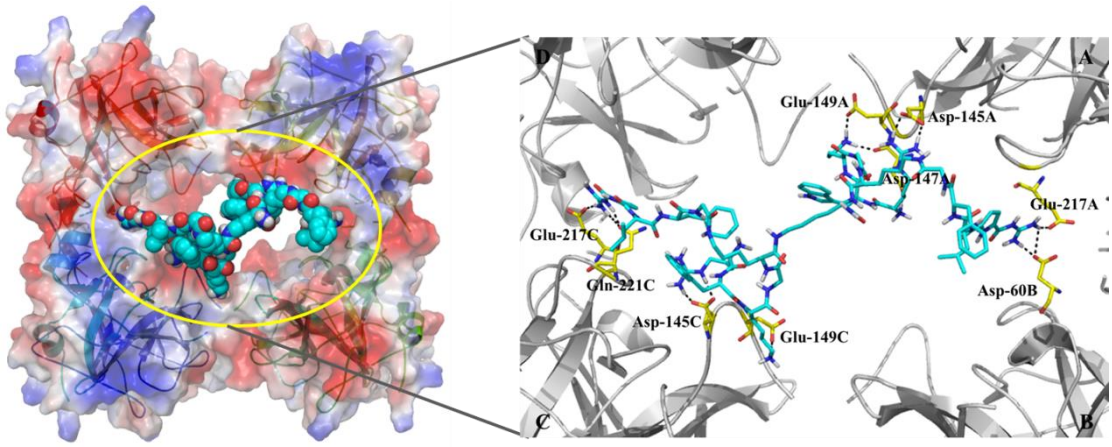

Figure 5.2 Representation of a possible binding mode of the inhibitor **120** (cyan) to the surface of β-tryptase. The cationic inhibitor could bind to the anionic residues (yellow sticks) and spread out across the central pore, thus blocking the access to the active sites.

The artificial GCP moiety as the tailor-made binding motif has been shown to improve the enzyme inhibitory affinity compared to analogous ligands with only proteinogenic amino acids. The variation of its combinatorial position within the peptide arms could be interesting for developing even more efficient inhibitors of β-tryptase. Therefore, the artificial amino acid derived GCP building block AA-GCP **173** (Figure 5.3) can be used to incorporate into different positions in the peptide arms. The synthesis of **173** has been developed in this group and it can be easily implemented in the peptide arms by using

standard Fmoc SPPS approach.[294]

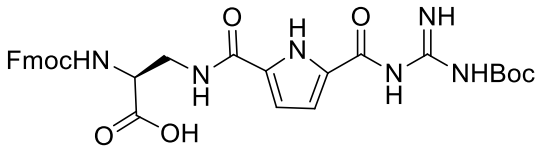

173

Figure 5.3 The amino acid guanidiniocarbonyl pyrrole binding motif (AA-GCP) **173** allows implementing the artificial arginine analog GCP units into different positions within the arms for the discovery of even more potent inhibitors of β-tryptase.

Even though efficient inhibitors have been discovered from the design of the tetravalent ligands with two different sets of arms and the artificial GCP binding motif, the peptide sequences of the two different arms are yet to be optimized. Therefore, in order to improve the inhibitory affinity, a combinatorial approach would be possible for the discovery of even more efficient inhibitors of β-tryptase. As depicted in Figure 5.4, a combinatorial library of the four-armed peptide ligands with two different sets of arms each composed of a variable tetrapeptide unit (**174**) can be generated by using split and mix approach. Six different amino acids (Lys, Arg, Trp, Phe, Glu, AA-GCP) including the basic, aromatic, acidic amino acids and the artificial AA-GCP building block can be used in each variable position to ensure a sufficient structural and chemical diversity in the library. The optimized tetravalent peptide structure from the combinatorial library could possibly show more efficient inhibitory properties for β-tryptase.

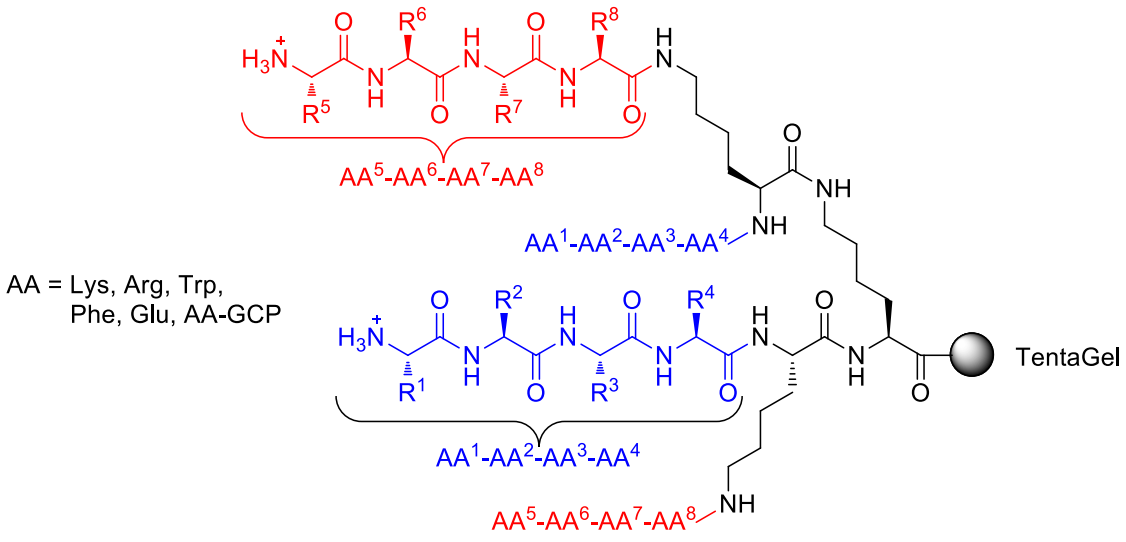

174

Figure 5.4 Combinatorial library consists of tetravalent peptide ligands with two different sets of arms each contains four combinatorial positions (Lys, Arg, Trp, Phe, Glu, AA-GCP) would allow for identifying more efficient inhibitors of β-tryptase.

5.2 New DCC Approach for the Discovery of Inhibitors of β-Tryptase

The second part of this thesis was focused on the discovery of potent inhibitors of β-tryptase by using a new dynamic combinatorial approach with the help of dynamic deconvolution strategy. The DCLs were based on reversible acyl hydrazone formation between hydrazides and aldehydes. As depicted in Figure 5.5, five peptide-derived hydrazides comprising a tetrapeptide sequence with a glycine and a variable tripeptide part featuring cationic (Lys, Arg, lysine-derived GCP), aromatic (Trp), hydrophobic (Ala) and anionic (Glu) amino acids for sufficient structure diversity. All the hydrazides were synthesized via microwave-assisted SPPS. Five different di- and tri-aldehydes with structural complexity were used as scaffolds allowing building up the multivalent inhibitors. In order to identify the active components from the library, a dynamic deconvolution protocol was utilized. The full library and ten sub-libraries in which one building block is missing were generated under acidic conditions. After the complete equilibrium of all the libraries, the resulting mixtures were subjected to investigation of inhibitory activity of β-tryptase under the required physiological conditions.

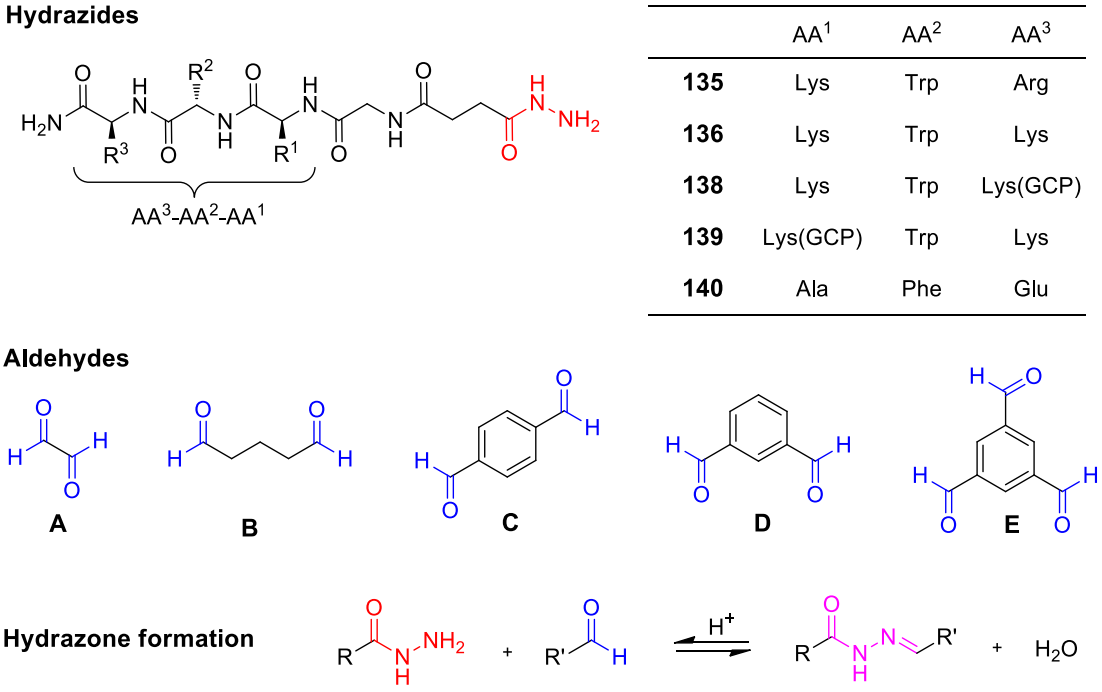

	AA^1	AA^2	AA^3
135	Lys	Trp	Arg
136	Lys	Trp	Lys
138	Lys	Trp	Lys(GCP)
139	Lys(GCP)	Trp	Lys
140	Ala	Phe	Glu

Figure 5.5 Hydrazide and aldehyde building blocks for generation of the hydrazone-based dynamic combinatorial libraries.

The screening of the libraries revealed that the positively charged hydrazides (**135**-**136**, **138**-**139**) are of importance for enzyme inhibition while the negatively charged hydrazide **140** is not necessary. This finding revealed the importance of the basic residues for the complementary electrostatic interactions with the acidic hot spots on the surface of the enzyme. Moreover, the peptide sequence and the artificial GCP group also played a key

role in binding to the enzyme. Hydrazide **138** featuring the artificial GCP group is the most active component in the library, which indicated that the GCP group can increase the inhibitory affinity. However, this effect relies on its position within the peptide arm as observed from **139** with much less activity. Further evaluation of the scaffolds by using the size-reduced libraries confirmed that the aromatic and rigid tri-aldehyde **E** and di-aldehyde **C** are the most active scaffolds in the library.

The representative library members **141**-**149** as shown in Figure 5.6 were synthesized individually containing both the homo- and hetero-meric inhibitors and their inhibitory properties were determined using standard enzyme kinetic assays. The inhibition data is in agreement with the screening of the DCLs which showed that all the positively charged two- and three-armed inhibitors can efficiently inhibit β-tryptase with K_i values in low nanomolar range (12-392 nM) while the negatively charged compound **145** showed no inhibition (K_i > 100 μM) at all. Furthermore, in direct comparison with the monovalent hydrazides, these inhibitors show three orders of magnitude increase of affinity, which clearly indicates a significant multivalency effect. Furthermore, the two most potent inhibitors **141** (K_i = 12.5 nM) and **143** (K_i = 22.5 nM) are one order of magnitude more efficient than the best tetravalent inhibitor $(RWKG)_4$ (K_i = 170 nM) from the previous combinatorial library. This finding suggests that rigid aromatic scaffolds are superior to more flexible ones. More interestingly, the five-fold difference in inhibitory affinity between **143** and **144** was illustrated with the help of computational calculations which revealed similar binding modes of them to β-tryptase but more stable intramolecular interactions in **144** than **143**, thus resulting in a less inhibitory affinity to the enzyme.

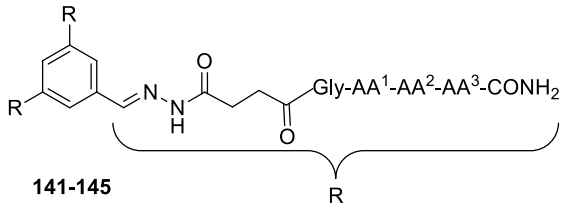

141-145

	AA^1	AA^2	AA^3
141	Lys	Trp	Arg
142	Lys	Trp	Lys
143	Lys	Trp	Lys(GCP)
144	Lys(GCP)	Trp	Lys
145	Ala	Phe	Glu

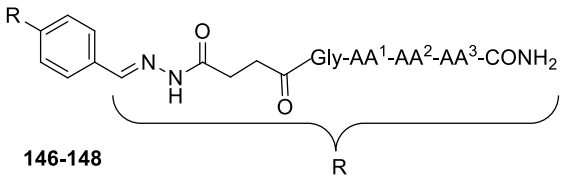

146-148

	AA^1	AA^2	AA^3
146	Lys	Trp	Arg
147	Lys	Trp	Lys
148	Lys	Trp	Lys(GCP)

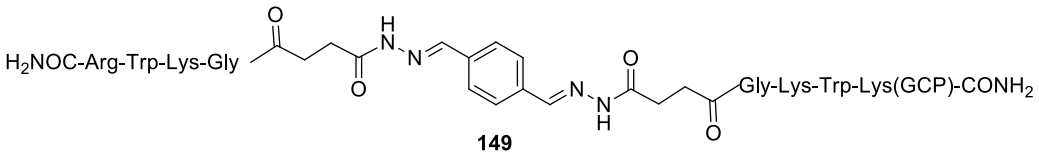

149

Figure 5.6 Acyl hydrazones derived from the tri- or di-aldehyde scaffolds and the five hydrazides.

Further experiments revealed the highly selective inhibition of β-tryptase by these inhibitors against other related serine proteases such as trypsin and α-chymotrypsin. Furthermore, the inhibition of β-tryptase by these inhibitors was demonstrated to be reversible by dialysis experiments. With the help of *Dixon* plots, it could be shown that these inhibitors feature a noncompetitive inhibition mode, suggesting most likely surface binding. The calculations confirmed that the inhibitors can indeed bind to the surface of β-tryptase blocking access to its central pore and thus shutting down the enzyme activity.

One unexpected finding of these results was that the position of the artificial GCP group is very important for the inhibitory activity of the inhibitors. Hence, the continuing work on this topic should focus on the combinatorial variations within the peptide arms by incorporating the GCP units in different positions. The GCP group can be easily implemented into different positions within the peptide arms in the form of artificial amino acid derived arginine analogs (**173**, **175**) as shown in Figure 5.7. These two building blocks with different length of side chains can be used as the normal amino acids in Fmoc SPPS with no limitations. Thus, a combinatorial approach can be utilized for optimizing the peptide sequences.

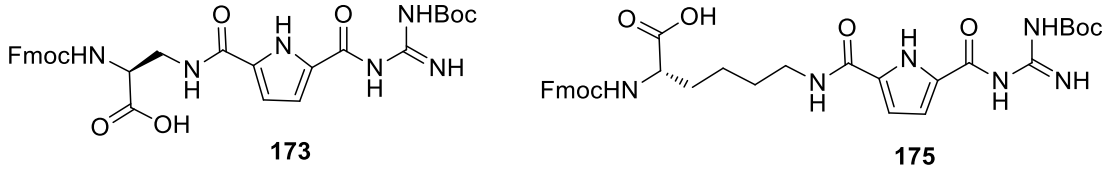

Figure 5.7 The tailor-made amino acid derived GCP binding motifs (**173**, **175**) allows a combinatorial structural optimization with the GCP units in different positions within the side chains of β-tryptase inhibitors.

Another interesting finding of these results was that the rigid aromatic scaffolds for building up the multivalent inhibitors of β-tryptase are superior to the flexible ones. Therefore, the scaffold with four or five aldehyde groups can be used for the development of even more efficient inhibitors of β-tryptase. For example, the tetra-aldehyde (**176**) or penta-aldehyde (**177**) derived from biphenyl or calix[5]arene as shown in Figure 5.8 can be used. The syntheses of these compounds are already known in the literature.[295-296]

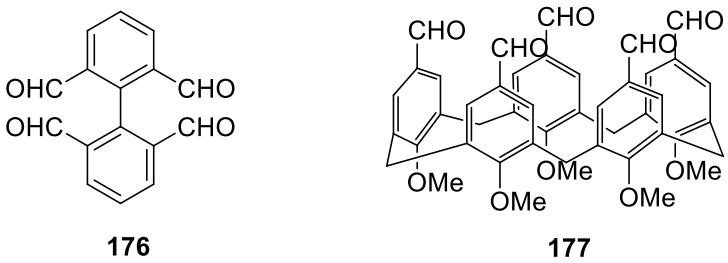

Figure 5.8 Possible rigid scaffolds with four (**176**) or five (**177**) attachment aldehyde groups for constructing more potent inhibitors of β-tryptase.

Since this approach has shown a great power for identifying efficient enzyme inhibitors, it can be extended to discovery of receptors for other biological targets such as proteins or DNA. Therefore, DCLs can be generated by using new scaffolds and suitable peptide structures with the tailor-made binding motifs for targeting a specific biological molecule by means of DCLs. Furthermore, due to the addition of aniline could accelerated the equilibration and allow generation of DCLs under near physiological conditions, the preparation of new DCLs can be carried out in the presence of aniline, allowing biological targets templation to select the best inhibitors or receptors.

5.3 Gold Nanoparticles as Scaffold for Protein Surface Binding

The last part of this thesis was concerned with the development of novel inhibitors of β-tryptase by using gold nanoparticles as scaffold based on protein surface recognition event. A series of ligands featuring thiolalkylated TEG chain terminating with different recognition motifs and the artificial arginine analog GCP were synthesized via microwave-assisted SPPS for the conjugation of gold nanoparticles. The fabrication of the gold nanoparticles by laser ablation was carried out by our cooperation partner from the working group of *Prof. Barcikowski*. The monovalent and bivalent conjugated gold nanoparticles with one or two types of ligands were prepared by *ex situ* and *in situ* conjugation. As shown in Figure 5.9, in the first studies, the positively charged peptide ligand (**161**) containing the artificial arginine analog GCP was used for the monovalent conjugates (**171**). For bivalent conjugates (**172**), the neutral ligand (**158**) was used as a surface blocker in addition to the positively charged ligand (**161**). With the help of UV/Vis spectroscopy the gold concentration could be evaluated and the quality of the obtained gold colloids could be analyzed. It could be shown that the monovalent conjugates have very good long-term stability. The surface coverage value and the conjugation efficiency could be calculated after removing the unbound ligands by using ultracentrifugation. It could be shown that the conjugation efficiency of the monovalent conjugates is over 80 % with ligand concentrations at 0.5-430 μM. The surface of the Au NPs (d = 5 nm) is already saturated at 374 ligands per NP and multilayers are suggested with higher ligand amount. It could be shown that the particle sizes are around 5-6 nm by means of disc centrifugation and TEM experiments. The hydrodynamic diameters obtained by DLS measurements are a bit larger (20-30 nm) due to the solvation and the strong signals weighed by rather bigger particles.

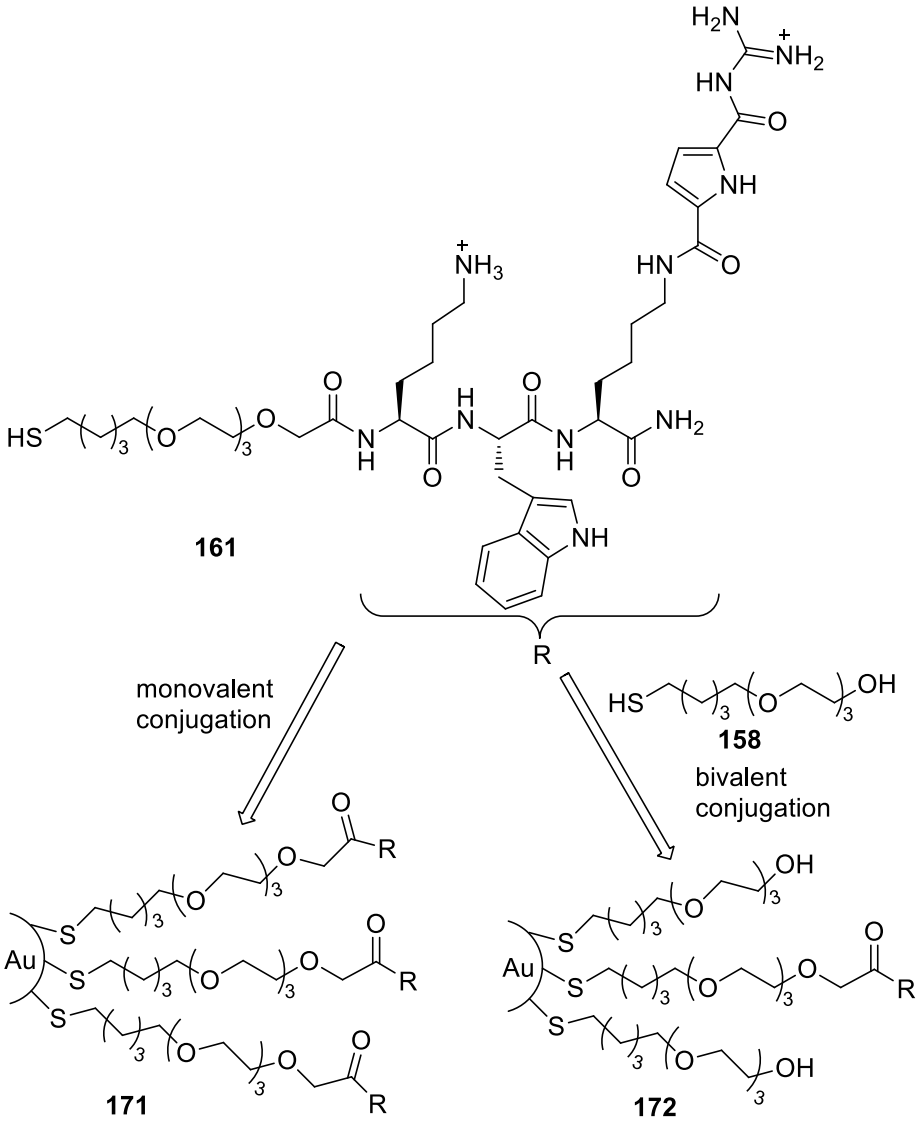

Figure 5.9 Ligands (**161**, **158**) used for the preparation of monovalent conjugates (**171**) and bivalent conjugates (**172**).

In the first preliminary enzyme inhibition studies we could demonstrate that the Au NPs themselves have no interference with the determination of the IC_{50} values. Enzyme assays of the monovalent conjugates **171** and the related free ligand **161** revealed that both the conjugates and the ligand could efficiently inhibit β-tryptase with lower micromolar (IC_{50} = 1-3 μM). Even though the conjugates are not superior to the single-armed ligand, we could demonstrate that at least the conjugated Au NPs have no influence in the activity of this enzyme. The comparison of the single-armed ligand **161** with either the peptide ligand containing only the proteinogenic amino acids, e.g. RWKG or the small standard inhibitor pAb revealed that the presence of the artificial GCP binding motif can significantly improve the inhibitory activity.

In order to further investigate the inhibitory activity of such single-armed ligand, the

ligands featuring the same peptide sequence KWK and the artificial GCP group, with (**168**) or without (**170**) the alkylated TEG chain were synthesized (Figure 5.10). The inhibition data revealed that these two ligands have similar inhibitory activities to ligand **161**. Further investigation of the inhibition mode of this type of single-armed ligands with the help of the interpretation of the nonlinear regression and the *Lineweaver-Burk* plots could show that they inhibit the β-tryptase in a competitive way. This finding revealed that the ligands bind to the active site of the enzyme. This is confirmed by docking studies of the possible binding mode between the ligand and β-tryptase. As shown in Figure 5.11, the GCP moiety fits perfectly in the S1 binding pocket through the interaction with Asp-189, Ser-190 and Gly-219. Hence, this type of ligands inhibits β-tryptase by competing with the substrate for the same active site.

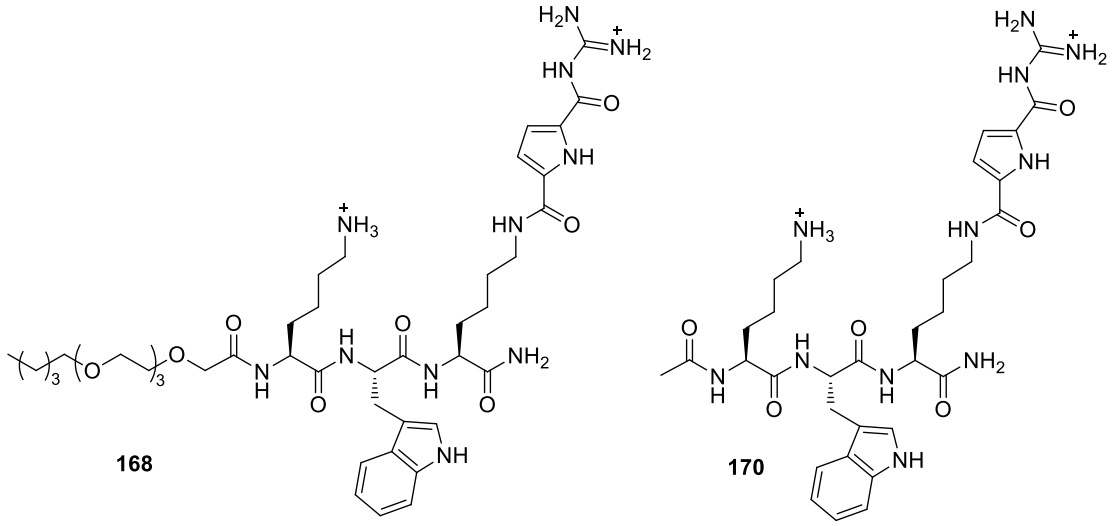

Figure 5.10 Ligands (**168**, **170**) used for comparison with ligand **171**.

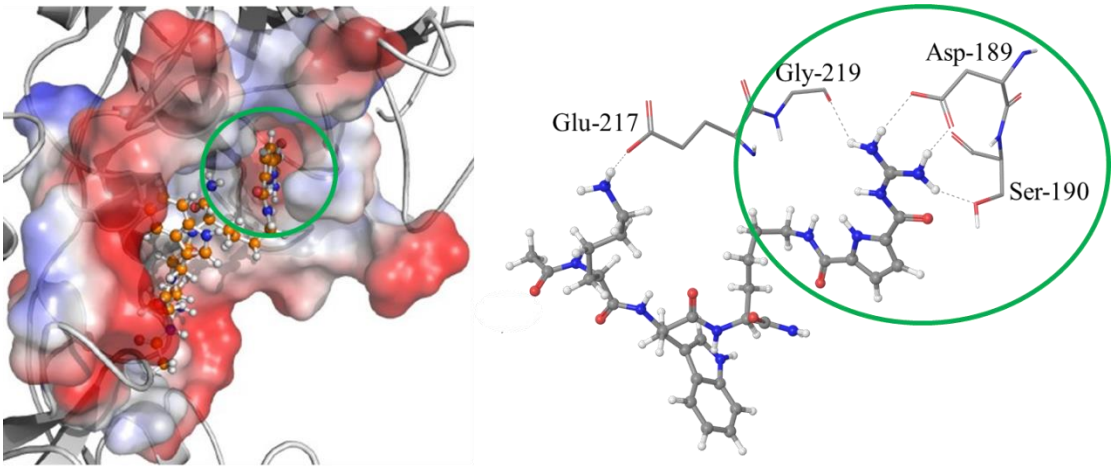

Figure 5.11 Representation of the possible binding mode of the single-armed ligand **170** to the active site of β-tryptase. The GCP group fits perfectly in the S1 binding pocket (marked with the green circle) by interacting with Asp-189, Ser-190 and Gly-219.

Therefore, although more work in this project is still on-going, the preliminary results have shown that we are able to prepare and analyze the peptide conjugated Au NPs and apply these conjugates in enzyme inhibition. Even though the conjugates are not superior to the single ligand in this work so far, this is only the first result for only one trial ligand. The next step could be the preparation of conjugates with other peptide ligands (**162**-**165**) that have been synthesized in this work. These conjugates might be attractive for the interactions with different biological targets, such as proteins featuring different characteristics or nucleotides. The positively charged peptide conjugates featuring the artificial GCP moieties could be used for DNA binding and gene delivery. The negatively charged conjugates could be very interesting for the proteins feature positive surface patches, such as α-chymotrypsin or cytochrome *c*.

6. EXPERIMENTAL SECTION

6.1 General Experimental and Analytical Methods

Solvents and Chemicals

All solvents were dried before use if necessary. Diethyl ether and THF were distilled from sodium with benzophenone as indicator. DCM was distilled from calcium hydride. DMF was distilled from calcium hydride under reduced pressure. Methanol was distilled before use. All solvents were stored under argon before use. Water for spectroscopic measurements was purified with a *TKA* MicroPure ultrapure water system. All other solvents and chemicals were used as supplied from commercial sources unless otherwise stated.

Inert Gas

Reactions under inert gas were carried out with Argon (99.998 %) from *Air Liquide* which was dried with Silica Gel Orange.

Magnetic Stirrer

Reactions were carried out by using magnetic stirring bars with the help of a MR 3001 K magnetic stirrer from *Heidolph*.

Rotary Evaporator

Distillation of solvents was performed at 40 ^{o}C under appropriate pressure with the help of a *Heidolph* Hei-VAP Advantage rotary evaporator.

Vacuum Pumps

Vacuum was generated with a *Vacuubrand* CVC3000 pump. High vacuum was generated with a RC6 *Vacuubrand* chemistry hybrid pump.

Thin layer Chromatography (TLC)

Analytical TLC was carried out to monitor reactions on silica gel precoated plates on aluminium foils ALUGRAM SIL G/UV254 and C18 SiO2 aluminium foils ALUGRAM RP-18W/UV254 from *Macherey-Nagel*. The spots were visualized by fluorescence

quenching upon irradiation with 254 nm UV light or with the help of iodine vapors.

Flash Chromatography

Flash chromatography was performed on columns packed with Silica gel 60M with a spherical size of 40-63 μm from *Macherey-Nagel*. Organic solvents used for flash chromatography were distilled prior to use and the ratio of solvent mixtures were reported in volume.

Orbital Shaker for Peptide Synthesis

The standard solid phase peptide synthesis was carried out with IKA KS 130 basic orbital shaker.

Microwave for Peptide Synthesis

Microwave assisted SPPS were performed in the CEM Discover Systems with Gas Addition Kit Accessory.

Analytical HPLC

The analytical "Medium Performance Liquid Chromatography" (HPLC) was done with *Dionex* HPLC apparatus: P680 pump, ASI-100 automated sample injector, UVD-340U UV detector, UltiMate 3000 Column Compartment. The *YMC* ODS-A RP18 column with a pore size of 12 nm and a spherical size of 5 μM was utilized. The sizes of 15 cm × 3.0 mm and 25 cm × 10 mm were used for the analytical and semi-preparative analysis, respectively. Commercially available HPLC grade solvents and ultrapure water were used as eluents and solvent mixtures were reported in volume percent.

Preparative MPLC

The preparative "High Performance Liquid Chromatography" (HPLC) was performed with an *Armen Instrument* Spot Flash Liquid Chromatography MPLC apparatus with *YMC* ODS-A columns with a pore size of 12 nm and a spherical size of 50 μM. Distilled or HPLC grade solvents and ultrapure water were used as eluents. Products were detected by means of a UV detector.

Lyophilization

Lyophilization was carried out in an Alpha 1-4 LD plus freeze drying apparatus from *Christ*.

Nuclear Magnetic Resonance (NMR)

^{1}H and ^{13}C NMR spectra in $CDCl_3$ or DMSO-d_6 were recorded with *Bruker* DMX 300, *Bruker* DRX 500 and *Bruker* Avance 700 spectrometer. The spectra were calibrated by the

residual signals of the deuterated solvents as internal standard. The chemical shifts are reported in ppm (δ value). The coupling constants are reported in Hertz. The following abbreviations for the description of the signal multiplicity are used: s = singlet, d = doublet, t = triplet, q = quartet, m = multiplet, br = broad signal.

Fourier Transform Infrared Spectroscopy (FT-IR)

The IR spectra were measured on a *Jasco* FT/IR-430 with ATR attachment spectrometer. The bands are reported in cm^{-1} and the following abbreviations are utilized for the description of the band intensities: s = strong, m = middle, w = weak, br = broad.

Mass Spectrometry (MS)

High resolution ESI mass spectra were recorded with a *Bruker* BioTOF III spectrometer.

Melting Point

Melting points were measured in open end glass capillary tubes with *Büchi* Melting Point B-540 and are quoted uncorrected.

pH Meter

The pH was determined with the *Knick* pH-Meter 766 Calimatic. The pH-meter was calibrated with commercial available buffer standards (pH = 4.00 and 7.00).

UV/Vis Spectroscopy

UV/Vis spectra were recorded with *Jasco* V-660 or *Thermo Scientific* Evolution 201 spectrometer in standard quartz microcuvettes with 1 cm width. All spectra are corrected against the background (assay buffer).

Fluorescence Spectroscopy

Fluorescence spectra were recorded in sterile Nunclon Surface 96-well plates from *Nunc* with a *Varian* Carey Eclipse Fluorescence spectrophotometer with microplate reader unit.

Picosecond Laser

Laser ablation of gold nanoparticles was carried out using an *Ekspla Atlantic* picosecond laser system providing < 10 ps laser pulses at a wavelength of 1064 nm (pulse energy > 160 µJ, beam diameter: 2 mm), a power of 17.03 W, a repetition rate of 100 kHz and a focal length of 100 mm. The generation of the functionalized gold nanoparticles was done in two different ways depending on the types of conjugation.

Dynamic Light Scattering

DLS measurements were performed with a Zetasizer Nano-ZS from *Malvern Instruments GmbH* and analyzed with the software provided from the manufacturer.

Centrifuge

Precipitates of the peptides were centrifuged with a Rotofix 32 from *Hettich*.

Ultracentrifuge

The separation of big particles > 10 nm to obtain monomodal and monodisperse gold nanoparticles was carried out with *Beckman Coulter* Optima™ MAX-XP with the conditions of 7 °C, 30000xg and 13 minutes. Purification of gold nanoparticles was done with the conditions of 7 °C, 30000xg and 31 minutes.

Disc Centrifuge

The particle sizes were determined by using a CPS Instruments analytical disc centrifuge (ADC) DC 24000 with 24000 RPM for 30 minutes. Measurements were done with 0.1 mL solution against a sucrose gradient detected by an UV/Vis detector at 400 nm.

Transmission Electron Microscopy (TEM)

The measurements were carried out using a *Phillips* CM 12 transmission electron microscope on a carbon-coated copper grid. Particle sizes were determined by counting 1000 nanoparticles and taking their average value.

Force Field Calculations

Computational force field calculations were performed with the help of *Schrödinger* MacroModel Vers. 9.9 software. The calculations were carried out based on the force field OPLS (optimized potentials for liquid simulations) 2005 by using water as solvent. The structure of the enzyme was frozen while the inhibitor was put as mobilized during the calculation. The resulting structures were obtained from the result of 1000 calculation cycles.

Docking Studies

Docking studies were done by using Schrodinger MacroModel and Glide software (Version 2012 Update 2). Ligand preparation were done by the following steps: After generation of the 2D structure, they got converted into a 3D model, which was minimized in the OPLS 2005 force field using MacroModel with 1500 iterations and a convergence threshold of 0.05. Glide was used to generate a receptor grid file of the active centers of the tryptase, to get detailed information about possible binding motifs.

6.2 General procedures for the SPPS

***Kaiser* Test**

In order to detect the free amino groups on the resin, two separate solutions of Ninhydrin (1 g) in ethanol (10 mL) and phenol (40 g) in ethanol (10 mL), respectively were prepared for the *Kaiser* test. A few resin beads were taken from the reaction and added to a mixture of the two solutions with each 0.3 mL, which was heated for 2 min at 100-110 ^{o}C. Resin beads with free amino functionalities (-NH_2) were colored dark blue or red while the resin beads without amino functions stayed white.

6.2.1 General Procedures for Standard SPPS

Standard solid phase peptide synthesis was performed in Schlenck glass vessels equipped with a frit and a stopper. The reaction mixtures were shaken on the orbital shaker under argon atmosphere. The solution was removed by filtration after the reaction and the resin beads were washed with the solvent. The solvent volume used for the coupling was chosen to fulfill the concentration of the reactants between 0.1-0.2 M, which has been demonstrated to be the most efficient concentrations for the SPPS.

Fmoc Deprotection

Fmoc protecting group was removed by treatment with 20 % piperidine in DMF two times each for 20 min. Then the resin was thoroughly washed six times with DMF each for 5 min. The completion of the Fmoc deprotection with the formation of free amino groups was monitored by a positive *Kaiser* test and repeated if necessary.

Alloc Deprotection

The removal of Alloc protecting group was achieved by treatment with $Pd(PPh_3)_4$ (0.1 eq) in the presence of $PhSiH_3$ (24 eq) in DCM two times each for 20 min. Then the resin was washed three times with DCM and three times with DMF each for 5 min. The completion of the Alloc deprotection was monitored by a positive *Kaiser* test and repeated if necessary.

Coupling Procedure

The Fmoc-protected Rink amide resin and Rink amide MBHA resin were used in this thesis. The resin was first swollen in DCM for 1-2 h. Then the Fmoc protecting group was removed by agitation in 20 % piperidine/DMF as described above. The amino acid (3 eq) was then attached to the resin (1 eq) using PyBop (3 eq) as the coupling reagent and DIPEA (6 eq) as the base in DMF under argon atmosphere at room temperature by shaking the reaction mixture for 6-12 h. Then the resin was washed with DMF for three times each for 5 min, followed by the repetition of the coupling and washing steps. The

quantitative attachment of the amino acids was monitored by a negative *Kaiser* test and repeated if necessary.

Cleavage from the Resin

After the completion of all the coupling steps and Fmoc deprotection if necessary, the resin was thoroughly washed with DCM (3 × 5 min), MeOH (3 × 5 min) and again DCM (3 × 5 min). Then the resin was dried under vacuum for 1 h. The cleavage of the product from the Rink amide resin or Rink amide MBHA resin was achieved by adding a mixture of TFA/H_2O/TIS (95:2.5:2.5) to the resin and the suspension was shaken for 3 h at room temperature and washed twice with TFA. The filtrates were combined and concentrated under vacuum to get an oily residue to which the diethyl ether was added to precipitate the peptide. The resulting suspension was centrifuged and the supernatant solvent was decanted. The solid was washed once again by diethyl ether and centrifuged again before it was dissolved in water and freeze-dried to get the crude product. The crude product was then purified by RP18-MPLC using appropriate conditions (H_2O/MeOH + 1 % TFA).

6.2.2 General Procedures for Microwave-Assisted SPPS

Microwave-assisted solid phase peptide synthesis was carried out in a microwave-transparent polyethylene tubes equipped with a frit using a CEM Discover microwave apparatus. The reaction mixtures were bubbling with argon during the reaction steps. The solution was removed by filtration after the completion of a reaction step and the resin beads were washed with the solvent. The solvent volume used for the coupling was chosen to ensure the concentration of the reactants between 0.1-0.2 M. It also depends on the volume of the reaction tubes and normally 2-20 mL was suitable.

Fmoc Deprotection

Fmoc protecting group was removed by treatment with 20 % piperidine in DMF two times for 1.5 min and 5 min, respectively under irradiation condition (20 W, T_{max} = 60 °C, $\Delta T = \pm 5$ °C). Then the resin was thoroughly washed six times with DMF each for 2 min with the help of argon bubbling. The completion of the Fmoc deprotection step was monitored by a positive *Kaiser* test and repeated if necessary.

Alloc Deprotection

The removal of Alloc protecting group was carried out by treatment with $Pd(PPh_3)_4$ (0.1 eq) in the presence of $PhSiH_3$ (24 eq) in DCM for 10 min at 20W and a maximum temperature of 30 °C. Then the resin was washed three times with DCM and three times with DMF each for 2 min with the help of argon bubbling. The completion of the Alloc deprotection was monitored by a positive *Kaiser* test and repeated if necessary.

Coupling Procedure

The Fmoc-protected Rink amide resin or Rink amide MBHA resin was first swollen in DCM for 1-2 h by shaking the reaction tube on the orbital shaker or with the help of argon bubbling. Then the Fmoc protecting group was removed by treatment with 20 % piperidine/DMF as described above. The amino acid (3 eq) was then attached to the resin (1 eq) using PyBop (3 eq) as the coupling reagent and DIPEA (6 eq) as the base in DMF under argon atmosphere by microwave irradiation (20 W, T_{max} = 60 °C, $\Delta T = \pm 5$ °C) for 20 min. The resin was then washed with DMF for three times each for 2 min with the help of argon bubbling, followed by the repetition of the coupling and washing steps. The quantitative attachment of the amino acids was monitored by a negative *Kaiser* test and repeated if necessary.

Cleavage from the Resin

Cleavage of the product from the resin was carried out without microwave irradiation. Therefore, after the completion of all the coupling steps and the final washing cycles, the resin was transferred into Schlenck glass vessels equipped with a frit and a stopper and treated with a mixture of TFA/H_2O/TIS (95:2.5:2.5) according to the procedure described in Chapter 6.2.1.

6.3 Syntheses of Tetravalent Peptide Ligands

6.3.1 SPPS of Tetravalent Ligands with Two Different Sets of Arms

Synthesis of Tetravalent Peptide Ligand $(RWKG)_2(RLFG)_2$ (115)

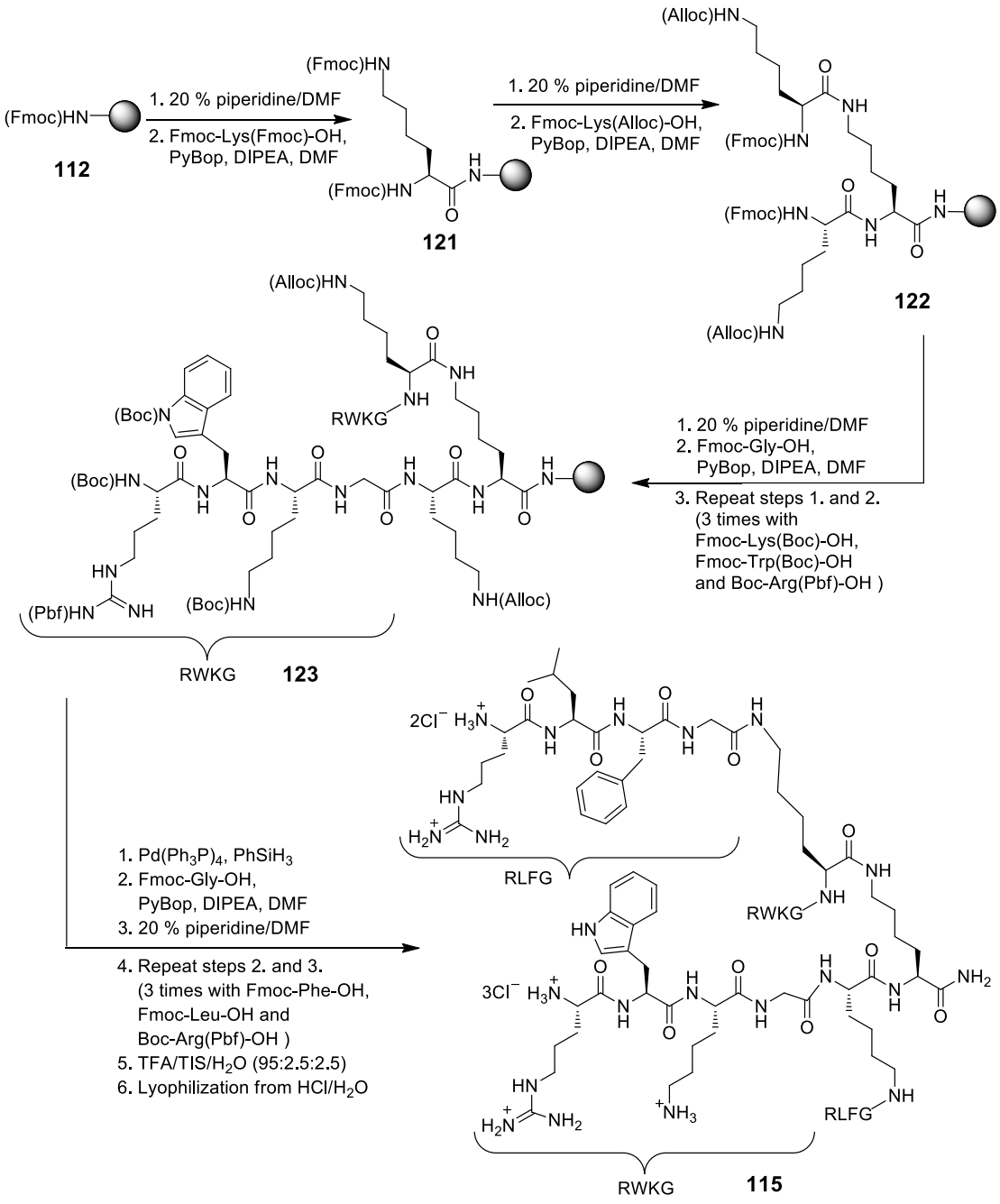

The synthesis of tetravalent ligand **115** was carried out according to standard solid phase peptide synthesis described in Chapter 6.2.1. Rink amide resin (100 mg, 0.99 mmol/g, 0.099 mmol, 1 eq) was weighed out into a glass peptide synthesis vessel and allowed to swell in DCM (10 mL) for 1 h. Then, the Fmoc protecting group was removed

with 20 % piperidine/DMF and the resin was allowed to react with Fmoc-Lys(Fmoc)-OH (147 mg, 0.248 mmol, 2.5 eq) and PyBOP (129 mg, 0.248 mmol, 2.5 eq) in 4 % DIPEA/DMF (8 mL) for 6 h to introduce the first branching. After washing with DMF, the first coupling step was repeated with another 2.5 equivalents of the reactants to assure complete conversion of all accessible amino groups on the resin. Then, all Fmoc groups were removed under standard deprotection conditions and the resin was treated with Fmoc-Lys(Alloc)-OH (292 mg, 0.495 mmol, 5 eq) and PyBOP (258 mg, 0.495 mmol, 5 eq) in 4 % DIPEA/DMF (8 mL) for 6 h to introduce the second branching. Then the Fmoc protecting group was removed, followed by the attachment of the first two arms of tetrapeptide sequences according to standard SPPS procedures: Fmoc-Gly-OH (147 mg, 0.495 mmol, 5 eq), Fmoc-Lys(Boc)-OH (232 mg, 0.495 mmol, 5 eq), Fmoc-Trp(Boc)-OH (261 mg, 0.495 mmol, 5 eq) and Boc-Arg(Pbf)-OH (261 mg, 0.495 mmol, 5 eq) were coupled with the help of PyBOP (258 mg, 0.495 mmol, 5 eq) in 4 % DIPEA/DMF (8 mL) and the Fmoc protecting groups were respectively removed after each coupling step allowing the following coupling. Then, the removal of the Alloc protecting group was achieved with $Pd(PPh_3)_4$ (11.4 mg, 9.9 µmol, 0.1 eq) in the presence of $PhSiH_3$ (292 µL, 2.38 mmol, 24 eq) in DCM. After an intensive washing cycle with DCM (3 × 8 mL) and DMF (3 × 8 mL), the second two arms of tetrapeptide sequences were attached according to standard SPPS procedures: Fmoc-Gly-OH (147 mg, 0.495 mmol, 5 eq), Fmoc-Phe-OH (192 mg, 0.495 mmol, 5 eq), Fmoc-Leu-OH (175 mg, 0.495 mmol, 5 eq) and Boc-Arg(Pbf)-OH (261 mg, 0.495 mmol, 5 eq) were coupled with the help of PyBOP (258 mg, 0.495 mmol, 5 eq) in 4 % DIPEA/DMF (8 mL) and the Fmoc protecting groups were respectively removed after each coupling step. All the *Kaiser* tests showed quantitative reactions with deprotection and coupling steps. After the final coupling and washing steps, the resin was dried under reduced pressure for one hour. Then the product was cleaved from the solid support by treatment with a 10 mL mixture of TFA/TIS/H_2O (95:2.5:2.5) for 3 h according to the standard procedure for Rink amide resin described in Chapter 6.2.1. Crude product was purified via RP18-MPLC using appropriate conditions (H_2O/MeOH + 1 % TFA). Pure product was transferred into its hydrochloride salt by dissolving the product in water with 10 % 1 M aqueous hydrochloric acid and lyophilizing three times to give **115** as white solid with 95 % purity according to analytical HPLC analysis.

$C_{114}H_{193}Cl_{10}N_{39}O_{19}$ 2600.45 g/mol

Yield 40 mg, 15.4 µmol, 16 %

Mp. > 250 °C (decomposition)

^{1}H NMR (500 MHz, DMSO-*d*$_6$): δ [ppm] = 0.83 (d, *J* = 6.3 Hz, 6 H, 2 × Leu-CH_3), 0.86 (d, *J* = 6.4 Hz, 6 H, 2 × Leu-CH_3), 1.16-1.80, 2.70-2.80 (m, 70 H, 20 × Lys-CH_2, 12 × Arg-CH_2, 2 × Leu-CH_2, 2 × Leu-CH), 2.85-3.03 (m, 8 H, 2 × Trp-CH_2, 2 × Phe-CH_2), 3.68-4.62 (m, 23 H, 4 × Gly-CH_2, 15 × CH), 6.97-8.88 (m, 78 H, 10 × Trp-CH, 10 ×

Phe-CH, 6 × NH_3^+, 22 × NH, 9 × NH_2), 10.93 (s, 2 H, 2 × Trp-NH).

^{13}C NMR (125 MHz, DMSO-*d*$_6$): δ [ppm] = 21.5, 22.0, 22.7, 23.0, 23.8, 23.9, 26.4, 27.4, 28.3, 28.7, 29.2, 31.1, 31.4, 31.9, 38.5, 40.7, 42.1 (48 C, 4 × Leu-CH_3, 20 × Lys-CH_2, 12 × Arg-CH_2, 2 × Leu-CH_2, 2 × Leu-CH, 2 × Phe-CH_2, 2 × Trp-CH_2, 4 × Gly-CH_2), 51.5, 52.6, 53.9, 64.1 (15 C, 15 × CH), 109.6, 111.3, 116.9, 118.2, 118.6, 120.9, 124.1, 124.9, 126.2, 127.2, 128.0, 129.2, 133.8, 136.1, 137.7 (28 C, 12 × Phe-C, 16 × Trp-C), 157.0 (4 C, 4 × Gua-Cq), 168.5, 171.2, 171.6, 171.8, 173.5 (19 C, 19 × CO-Cq).

HRMS (ESI): m/z calculated for $C_{114}H_{185}N_{39}O_{19}^{2+}$ $[M+2H]^{2+}$: 1202.7363; found: 1202.7422.

FT-IR (ATR): $\tilde{\nu}$ [cm^{-1}] = 3254 (br), 2971 (br), 2923 (br), 1645 (s), 1521 (s), 1456(m), 1242 (m), 1066 (m).

Synthesis of Tetravalent Peptide Ligand $(KWKG)_2(KLFG)_2$ (116)

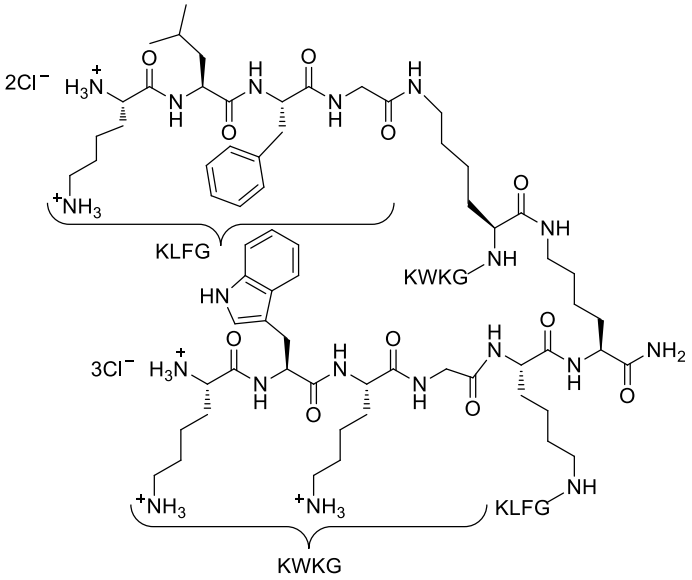

116

The tetravalent peptide ligand **116** was synthesized accordingly on Rink amide MBHA resin (100 mg, 0.67 mmol/g, 0.067 mmol, 1 eq) following the above described SPPS procedure. After attaching the orthogonal protected lysine dendrimer on the resin, the amino acids Fmoc-Gly-OH (100 mg, 0.335 mmol, 5 eq), Fmoc-Lys(Boc)-OH (157 mg, 0.335 mmol, 5 eq), Fmoc-Trp(Boc)-OH (177 mg, 0.335 mmol, 10 eq) and Boc-Lys(Boc)-OH (116 mg, 0.335 mmol, 5 eq) were attached to the first set of arms and Fmoc-Gly-OH (100 mg, 0.335 mmol, 5 eq), Fmoc-Phe-OH (130 mg, 0.335 mmol, 5 eq), Fmoc-Leu-OH (118 mg, 0.335 mmol, 10 eq) and Fmoc-Lys(Boc)-OH (157 mg, 0.335 mmol, 5 eq) to the second set of arms. After the cleavage and purification steps, the product was obtained as white solid with 95 % purity according to analytical HPLC analysis.

$C_{114}H_{193}Cl_{10}N_{31}O_{19}$ 2656.48 g/mol

Yield 26 mg, 9.8 µmol, 14 %

Mp. > 250 °C (decomposition)

^{1}H NMR (500 MHz, DMSO-d_6): δ [ppm] = 0.82 (d, J = 6.5 Hz, 6 H, 2 × Leu-CH_3), 0.85 (d, J = 6.5 Hz, 6 H, 2 × Leu-CH_3), 1.18-1.76, 2.68-2.79 (m, 78 H, 36 × Lys-CH_2, 2 × Leu-CH_2, 2 × Leu-CH), 3.02-3.05 (m, 8 H, 2 × Trp-CH_2, 2 × Phe-CH_2), 3.69-4.64 (m, 23 H, 4 × Gly-CH_2, 15 × CH), 6.96-8.86 (m, 70 H, 10 × Trp-CH, 10 × Phe-CH, 10 × NH_3^+, 18 × NH, 1 × NH_2), 10.92 (s, 2 H, 2 × Trp-NH).

^{13}C NMR (125 MHz, DMSO-d_6): δ [ppm] = 20.9, 21.0, 21.6, 23.0, 24.0, 26.3, 26.4, 27.4, 28.7, 30.4, 31.2, 37.3, 38.3, 38.4, 38.5, 40.1, 40.2, 40.7, 42.1 (52 C, 4 × Leu-CH_3, 36 × Lys-CH_2, 2 × Leu-CH_2, 2 × Leu-CH, 2 × Phe-CH_2, 2 × Trp-CH_2, 4 × Gly-CH_2), 51.6, 51.8, 52.6, 54.0 (15 C, 15 × CH), 109.7, 111.3, 118.3, 118.6, 121.0, 124.1, 126.3, 127.2, 128.1, 129.3, 136.1, 137.7 (28 C, 12 × Phe-C, 16 × Trp-C), 168.4, 168.5, 168.7, 171.2,

171.3, 171.7 (19 C, 19 × CO-Cq).

HRMS (ESI): m/z calculated for $C_{114}H_{185}N_{31}O_{19}^{2+}$ $[M+2H]^{2+}$: 1146.2201; found: 1146.7158.

FT-IR (ATR): $\tilde{\nu}$ [cm^{-1}] = 3239 (br), 3053 (br), 2923 (br), 2871 (w), 1651 (s), 1539 (s), 1456 (m), 1114 (m), 1056 (m).

Synthesis of Tetravalent Peptide Ligand $(RWKG)_2(KLFG)_2$ (117)

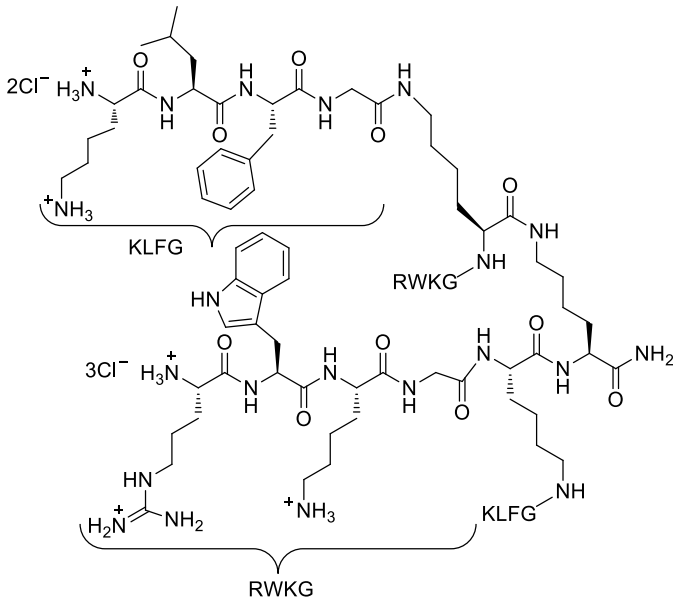

117

The tetravalent peptide ligand **117** was synthesized accordingly on Rink amide MBHA resin (100 mg, 0.67 mmol/g, 0.067 mmol, 1 eq) following the above described SPPS procedure. After attaching the orthogonal protected lysine dendrimer on the resin, the amino acids Fmoc-Gly-OH (100 mg, 0.335 mmol, 5 eq), Fmoc-Lys(Boc)-OH (157 mg, 0.335 mmol, 5 eq), Fmoc-Trp(Boc)-OH (177 mg, 0.335 mmol, 10 eq) and Boc-Arg(Pbf)-OH (176 mg, 0.335 mmol, 5 eq) were attached to the first set of arms and Fmoc-Gly-OH (100 mg, 0.335 mmol, 5 eq), Fmoc-Phe-OH (130 mg, 0.335 mmol, 5 eq), Fmoc-Leu-OH (118 mg, 0.335 mmol, 10 eq) and Fmoc-Lys(Boc)-OH (157 mg, 0.335 mmol, 5 eq) to the second set of arms. After the cleavage and purification steps, the product was obtained as white solid with 95 % purity according to analytical HPLC analysis.

$C_{114}H_{193}Cl_{10}N_{35}O_{19}$ 2712.51 g/mol

Yield 22 mg, 8.1 µmol, 12 %

Mp. > 250 °C (decomposition)

^{1}H NMR (700 MHz, DMSO-d_6): δ [ppm] = 0.82 (d, J = 5.7 Hz, 6 H, 2 × Leu-CH_3), 0.85 (d, J = 5.7 Hz, 6 H, 2 × Leu-CH_3), 1.15-1.83, 2.68-2.86 (m, 74 H, 28 × Lys-CH_2, 6 × Arg-CH_2, 2 × Leu-CH_2, 2 × Leu-CH), 2.97-3.04 (m, 8 H, 2 × Trp-CH_2, 2 × Phe-CH_2), 3.78-4.61 (m, 23 H, 4 × Gly-CH_2, 15 × CH), 6.96-8.84 (m, 74 H, 10 × Trp-CH, 10 × Phe-CH, 8 × NH_3^+, 20 × NH, 5 × NH_2), 10.91 (s, 2 H, 2 × Trp-NH).

^{13}C NMR (175 MHz, DMSO-d_6): δ [ppm] = 20.9, 21.6, 22.0, 23.0, 23.8, 23.9, 26.2, 26.4, 27.4, 28.3, 28.7, 30.3, 31.1, 31.4, 37.2, 38.2, 38.5, 40.7, 42.0 (50 C, 4 × Leu-CH_3, 28 × Lys-CH_2, 6 × Arg-CH_2, 2 × Leu-CH_2, 2 × Leu-CH, 2 × Phe-CH_2, 2 × Trp-CH_2, 4 × Gly-CH_2), 51.4, 51.8, 52.7, 53.9 (15 C, 15 × CH), 109.6, 111.3, 118.2, 118.6, 120.9, 124.1,

126.3, 127.2, 128.0, 129.2, 136.1, 137.7 (28 C, 12 × Phe-C, 16 × Trp-C), 156.9 (2 C, 2 × Gua-Cq), 168.3, 168.4, 168.5, 168.6,168.8, 171.1, 171.2, 171.3, 171.5, 171.6, 171.8, 173.7 (19 C, 19 × CO-Cq).

HRMS (ESI): m/z calculated for $C_{114}H_{185}N_{35}O_{19}^{2+}$ $[M+2H]^{2+}$: 1174.7302; found: 1174.7286.

FT-IR (ATR): $\tilde{\nu}$ [cm^{-1}] = 3216 (br), 3053 (br), 2932 (br), 1646 (s), 1521 (s), 1457 (m), 1232 (m), 1085 (m).

Synthesis of Tetravalent Peptide Ligand $(RWKG)_2(KWKG)_2$ (118)

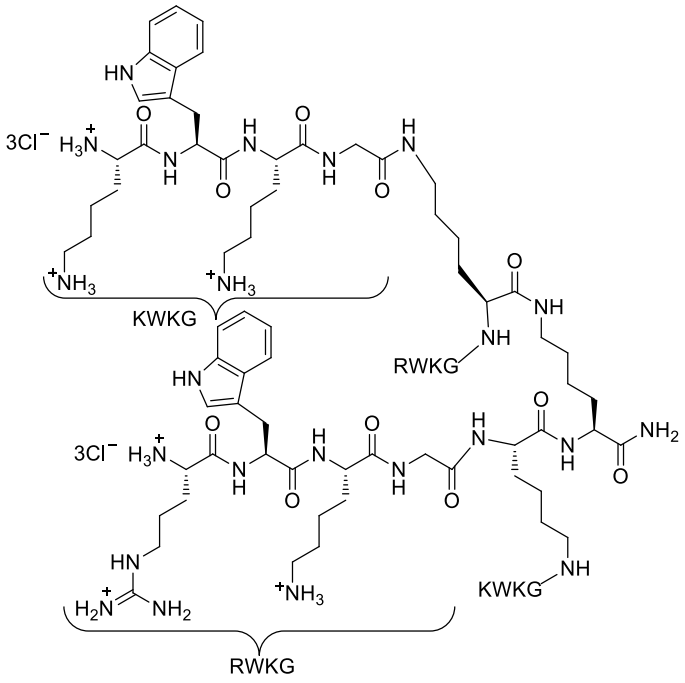

118

The tetravalent peptide ligand **118** was synthesized accordingly on Rink amide MBHA resin (100 mg, 0.67 mmol/g, 0.067 mmol, 1 eq) following the above described SPPS procedure. After attaching the orthogonal protected lysine dendrimer on the resin, the amino acids Fmoc-Gly-OH (100 mg, 0.335 mmol, 5 eq), Fmoc-Lys(Boc)-OH (157 mg, 0.335 mmol, 5 eq), Fmoc-Trp(Boc)-OH (177 mg, 0.335 mmol, 10 eq) and Boc-Arg(Pbf)-OH (176 mg, 0.335 mmol, 5 eq) were attached to the first set of arms and Fmoc-Gly-OH (100 mg, 0.335 mmol, 5 eq), Fmoc-Lys(Boc)-OH (157 mg, 0.335 mmol, 5 eq), Fmoc-Trp(Boc)-OH (177 mg, 0.335 mmol, 10 eq) and Fmoc-Lys(Boc)-OH (157 mg, 0.335 mmol, 5 eq) to the second set of arms. After the cleavage and purification steps, the product was obtained as white solid with 95 % purity according to analytical HPLC analysis.

$C_{118}H_{199}Cl_{12}N_{39}O_{19}$ 2893.53 g/mol

Yield 32 mg, 11.1 µmol, 16 %

Mp. > 250 °C (decomposition)

^{1}H NMR (700 MHz, DMSO-d_6): δ [ppm] = 1.29-1.78, 2.74-2.92 (m, 84 H, 36 × Lys-CH_2, 6 × Arg-CH_2), 3.00-3.03 (m, 8 H, 4 × Trp-CH_2), 3.67-4.61 (m, 23 H, 4 × Gly-CH_2, 15 × CH), 6.97-8.84 (m, 80 H, 20 × Trp-CH, 10 × NH_3^+, 20 × NH, 5 × NH_2), 10.91 (s, 4 H, 4 × Trp-NH).

^{13}C NMR (175 MHz, DMSO-d_6): δ [ppm] = 20.9, 22.1, 22.4, 22.9, 23.9, 26.3, 26.5, 27.5, 28.4, 28.8, 30.4, 30.8, 31.1, 38.3, 38.6, 40.0, 40.2 , 42.0 (50 C, 36 × Lys-CH_2, 6 × Arg-CH_2, 4 × Trp-CH_2, 4 × Gly-CH_2), 51.0, 51.6, 51.9, 52.7, 53.9, 54.0 (15 C, 15 × CH),

109.6, 111.3, 118.3, 118.7, 120.9, 124.2, 125.1, 127.1, 136.1 (32 C, 32 × Trp-C), 157.1 (2 C, 2 × Gua-Cq), 168.5, 168.6,168.7, 168.8, 171.2, 171.3, 171.4, 171.6, 171.8, 171.9, 173.7 (19 C, 19 × CO-Cq).

HRMS (ESI): m/z calculated for $C_{118}H_{189}N_{39}O_{19}^{2+}$ $[M+2H]^{2+}$: 1128.7519; found: 1128.7384.

FT-IR (ATR): $\tilde{\nu}$ [cm^{-1}] = 3222 (br), 3053 (br), 2932 (br), 1645 (s), 1520 (s), 1456 (m), 1233 (m).

Synthesis of Tetravalent Peptide Ligand $(RWKG)_2(FRKG)_2$ (119)

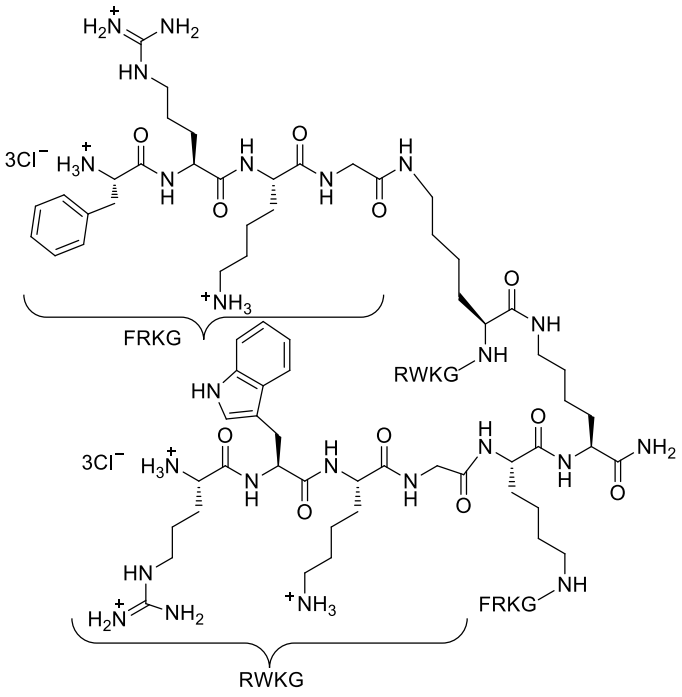

119

The tetravalent peptide ligand **119** was synthesized accordingly on Rink amide MBHA resin (100 mg, 0.67 mmol/g, 0.067 mmol, 1 eq) following the above described SPPS procedure. After attaching the orthogonal protected lysine dendrimer on the resin, the amino acids Fmoc-Gly-OH (100 mg, 0.335 mmol, 5 eq), Fmoc-Lys(Boc)-OH (157 mg, 0.335 mmol, 5 eq), Fmoc-Trp(Boc)-OH (177 mg, 0.335 mmol, 10 eq) and Boc-Arg(Pbf)-OH (176 mg, 0.335 mmol, 5 eq) were attached to the first set of arms and Fmoc-Gly-OH (100 mg, 0.335 mmol, 5 eq), Fmoc-Lys(Boc)-OH (157 mg, 0.335 mmol, 5 eq), Fmoc-Arg(Pbf)-OH (217 mg, 0.335 mmol, 5 eq) and Boc-Phe-OH (89 mg, 0.335 mmol, 5 eq) to the second set of arms. After the cleavage and purification steps, the product was obtained as white solid with 95 % purity according to analytical HPLC analysis.

$C_{114}H_{197}Cl_{12}N_{41}O_{19}$ 2871.48 g/mol

Yield 20 mg, 7.0 μmol, 10 %

Mp. > 250 °C (decomposition)

^{1}H NMR (500 MHz, DMSO-d_6): δ [ppm] = 1.19-1.77, 2.74-3.00 (m, 80 H, 28 × Lys-CH_2, 12 × Arg-CH_2), 3.10-3.15 (m, 8 H, 2 × Trp-CH_2, 2 × Phe-CH_2), 3.68-4.61 (m, 23 H, 4 × Gly-CH_2, 15 × CH), 6.96-8.95 (m, 84 H, 10 × Trp-CH, 10 × Phe-CH, 8 × NH_3^+, 22 × NH, 9 × NH_2), 10.92 (s, 2 H, 2 × Trp-NH).

^{13}C NMR (125 MHz, DMSO-d_6): δ [ppm] = 22.0, 22.1, 23.9, 24.8, 26.4, 27.4, 28.3, 28.7, 28.9, 30.9, 31.4, 36.8, 38.5, 40.3, 42.0 (48 C, 28 × Lys-CH_2, 12 × Arg-CH_2, 2 × Phe-CH_2, 2 × Trp-CH_2, 4 × Gly-CH_2), 51.5, 52.4, 52.7, 52.8, 53.3 (15 C, 15 × CH), 109.6, 111.3,

118.3, 118.6, 120.9, 124.1, 127.1, 127.2, 128.6, 129.7, 135.0, 136.1 (28 C, 12 × Phe-C, 16 × Trp-C), 157.1 (4 C, 4 × Gua-Cq), 168.0, 168.4, 168.6, 170.9, 171.2, 171.4, 171.7, 171.8, 173.1 (19 C, 19 × CO-Cq).

HRMS (ESI): m/z calculated for $C_{114}H_{187}N_{41}O_{19}^{2+}$ $[M+2H]^{2+}$: 1217.7472; found: 1217.7508.

FT-IR (ATR): $\tilde{\nu}$ [cm^{-1}] = 3209 (br), 3053 (br), 2932 (br), 2869 (w), 1644 (s), 1531 (s), 1455 (m), 1233 (m).

Synthesis of Tetravalent Peptide Ligand $(RWKG)_2(GCP\text{-}LFG)_2$ (120)

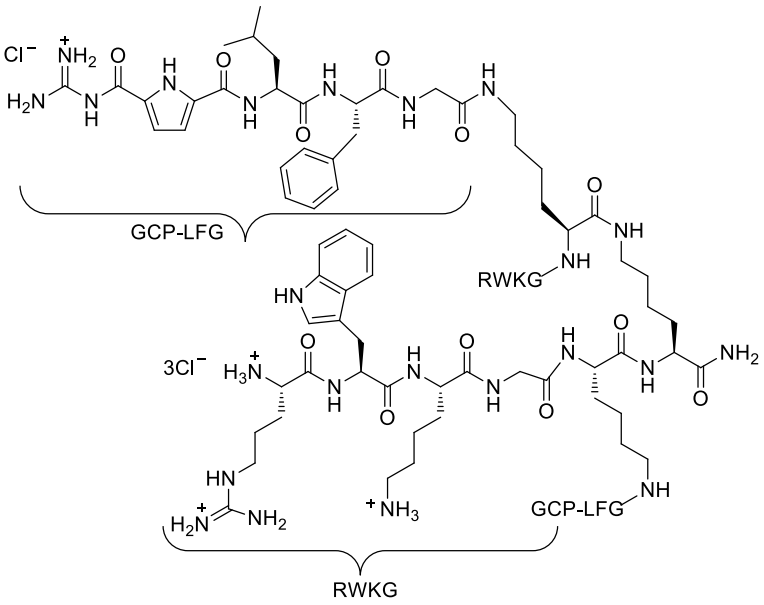

120

The tetravalent peptide ligand **120** was synthesized accordingly on Rink amide MBHA resin (100 mg, 0.67 mmol/g, 0.067 mmol, 1 eq) following the above described SPPS procedure. After attaching the orthogonal protected lysine dendrimer on the resin, the amino acids Fmoc-Gly-OH (100 mg, 0.335 mmol, 5 eq), Fmoc-Lys(Boc)-OH (157 mg, 0.335 mmol, 5 eq), Fmoc-Trp(Boc)-OH (177 mg, 0.335 mmol, 10 eq) and Boc-Arg(Pbf)-OH (176 mg, 0.335 mmol, 5 eq) were attached to the first set of arms and Fmoc-Gly-OH (100 mg, 0.335 mmol, 5 eq), Fmoc-Phe-OH (130 mg, 0.335 mmol, 5 eq), Fmoc-Leu-OH (118 mg, 0.335 mmol, 10 eq) and Boc-GCP group (**111**) (133 mg, 0.335 mmol, 5 eq) to the second set of arms. After the cleavage and purification steps, the product was obtained as white solid with 95 % purity according to analytical HPLC analysis.

$C_{116}H_{179}Cl_8N_{39}O_{21}$ 2739.54 g/mol

Yield 26 mg, 9.5 μmol, 10 %

Mp. > 250 °C (decomposition)

^{1}H NMR (500 MHz, DMSO-d_6): δ [ppm] = 0.82 (d, J = 6.4 Hz, 6 H, 2 × Leu-CH_3), 0.87 (d, J = 6.4 Hz, 6 H, 2 × Leu-CH_3), 1.24-1.79, 2.75-3.01 (m, 58 H, 20 × Lys-CH_2, 6 × Arg-CH_2, 2 × Leu-CH_2, 2 × Leu-CH), 3.16-3.20 (m, 8 H, 2 × Trp-CH_2, 2 × Phe-CH_2), 3.77-4.63 (m, 21 H, 4 × Gly-CH_2, 13 × CH), 6.90-8.82 (m, 74 H, 10 × Trp-CH, 10 × Phe-CH, 4 × GCP-CH, 4 × NH_3^+, 20 × NH, 9 × NH_2), 10.90 (s, 2 H, 2 × Trp-NH), 12.09 (s, 2 H, 2 × Gua-NH), 12.49 (s, 2 H, 2 × GCP-NH).

^{13}C NMR (125 MHz, DMSO-d_6): δ [ppm] = 21.5, 22.0, 22.9, 23.8, 24.2, 26.4, 27.5, 28.3, 28.8, 31.1, 38.5, 40.1, 42.1 (42 C, 4 × Leu-CH_3, 20 × Lys-CH_2, 6 × Arg-CH_2, 2 × Leu-CH_2, 2 × Leu-CH, 2 × Phe-CH_2, 2 × Trp-CH_2, 4 × Gly-CH_2), 51.5, 52.6, 53.9, 54.0

(13 C, 13 × CH), 109.6, 111.3, 113.6, 115.8, 116.9, 118.2, 118.6, 120.9, 124.0, 125.6, 126.2, 127.2, 128.0, 129.2, 132.3, 136.1, 137.8 (36 C, 12 × Phe-C, 16 × Trp-C, 8 × GCP-C), 155.5, 157.0, 158.9, 159.7 (4 C, 4 × Gua-Cq), 168.3, 168.5, 171.1, 171.2, 171.3, 171.9, 172.0 (21 C, 21 × CO-Cq).

HRMS (ESI): m/z calculated for $C_{116}H_{174}N_{39}O_{21}^{3+}$ $[M+3H]^{3+}$: 816.7919; found: 816.7965.

FT-IR (ATR): $\tilde{\nu}$ [cm^{-1}] = 3242 (br), 3059 (br), 2933 (br), 2863 (w), 1645 (s), 1524 (s), 1238 (m).

6.3.2 Microwave-Assisted SPPS of Tetravalent Ligands with Four Identical Arms Terminating with the GCP Moiety

Synthesis of Tetravalent Peptide Ligand (GCP-RWKG)$_4$) (124)

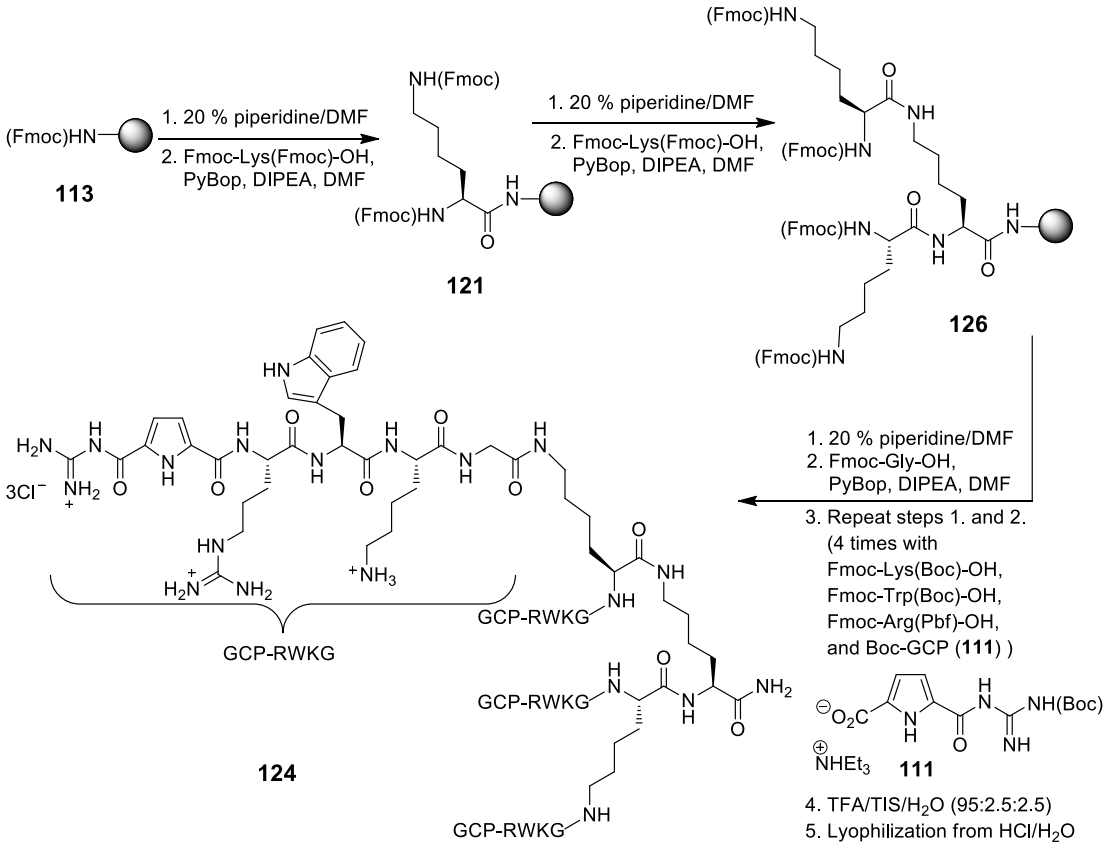

Tetravalent peptide ligand **124** with four identical arms was synthesized according to the standard microwave-assisted solid phase peptide synthesis described in Chapter 6.2.2. The Rink amide MBHA resin (200 mg, 0.67 mmol/g, 0.134 mmol, 1 eq) was allowed to swell in DCM (10 mL) for 1 h. Then, the Fmoc protecting group was removed with 20 % piperidine/DMF, followed by a *Kaiser* test to confirm the completely formation of free amino functions. Then the first amino acid Fmoc-Lys(Fmoc)-OH (198 mg, 0.335 mmol, 2.5 eq) was attached with the help of the coupling reagent PyBOP (175 mg, 0.335 mmol, 2.5 eq) in 4 % DIPEA/DMF (5 mL). The first coupling step was repeated to ensure the quantitative reaction, which was confirmed by a negative *Kaiser* test. After removal of the Fmoc protecting group and the washing step, Fmoc-Lys(Fmoc)-OH (396 mg, 0.67 mmol, 5 eq) was attached once again to the two branches with coupling reagent PyBOP (350 mg, 0.67 mmol, 5 eq) in 4 % DIPEA/DMF (5 mL) to introduce the scaffold with four identical arms. Then after removing all the Fmoc protecting groups on the four branches of the lysine scaffold, the peptide sequence of the four arms were built by using the standard microwave-assisted SPPS procedure: Fmoc-Gly-OH (398 mg, 1.34 mmol, 10 eq), Fmoc-Lys(Boc)-OH (628 mg, 1.34 mmol, 10 eq), Fmoc-Trp(Boc)-OH (706 mg, 1.34

mmol, 10 eq), and Fmoc-Arg(Pbf)-OH (869 mg, 1.34 mmol, 10 eq), as well as the Boc-protected GCP group (**111**) (533 mg, 1.34 mmol, 10 eq) were coupled similarly with the help of PyBOP (700 mg, 1.34 mmol, 10 eq) in 4 % DIPEA/DMF (5 mL) and the Fmoc protecting groups were respectively removed after each coupling step. After the last coupling step and the final washing cycle, the resin was dried and the product was cleaved from the solid support without microwave irradiation according to the general procedure (TFA/TIS/H_2O = 95:2.5:2.5) for the Rink amide MBHA resin as described in Chapter 6.2.1. Crude peptide was purified by RP18-MPLC using appropriate conditions (H_2O/MeOH + 0.05 % TFA). Pure product was transferred into its hydrochloride salt to give **124** as white solid with 95 % purity according to analytical HPLC analysis.

$C_{146}H_{223}Cl_{12}N_{59}O_{27}$ 3662.15 g/mol

Yield 10 mg, 2.7 µmol, 2 %

Mp. 245-250 °C (decomposition)

^{1}H NMR (700 MHz, DMSO-*d*$_6$): δ [ppm] = 1.15-1.76, 2.95-3.11 (m, 80 H, 12 × Arg-CH_2, 28 × Lys-CH_2), 2.68-2.77 (m, 8 H, 4 × Trp-CH_2), 3.64-4.57 (m, 23 H, 15 × CH, 4 × Gly-CH_2), 6.91-8.70 (m, 100 H, 8 × GCP-CH, 20 × Trp-CH, 26 × NH, 17 × NH_2, 4 × NH_3^+), 10.82 (s, 4 H, 4 × Trp-NH), 11.97 (s, 4 H, 4 × Gua-NH), 12.52 (s, 4 H, 4 × GCP-NH).

^{13}C NMR (175 MHz, DMSO-*d*$_6$): δ [ppm] = 22.0, 22.1, 22.7, 22.9, 25.1, 26.5, 27.2, 28.7, 28.9, 31.1, 31.2, 38.5, 38.6, 40.4, 42.0 (48 C, 28 × Lys-CH_2, 12 × Arg-CH_2, 4 × Trp-CH_2, 4 × Gly-CH_2), 52.6, 52.7, 53.6 (15 C, 15 × CH), 109.8, 127.3, 136.0 (12 C, 12 × Trp-Cq), 111.3, 118.2, 120.8, 123.7 (s, 20 C, 20 × Trp-CH), 113.7, 115.8 (8 C, 8 × GCP-CH), 125.7, 132.2 (8 C, 8 × GCP-Cq), 155.5 (s, 4 C, 4 × GCP-Gua-Cq), 156.8 (4 C, 4 × Arg-Cq), 159.1, 159.8, 168.5, 171.4, 171.5, 171.7 (27 C, 27 × CO-Cq).

HRMS (ESI): m/z calculated for $C_{146}H_{215}N_{59}O_{27}^{4+}$ $[M+4H]^{4+}$: 806.9317; found: 806.9315.

FT-IR (ATR): $\tilde{\nu}$ [cm^{-1}] = 3310 (br), 3055 (br), 2868 (w), 1643 (s), 1527 (s), 1470 (m).

Synthesis of Tetravalent Peptide Ligand (GCP-RWK)$_4$ (125)

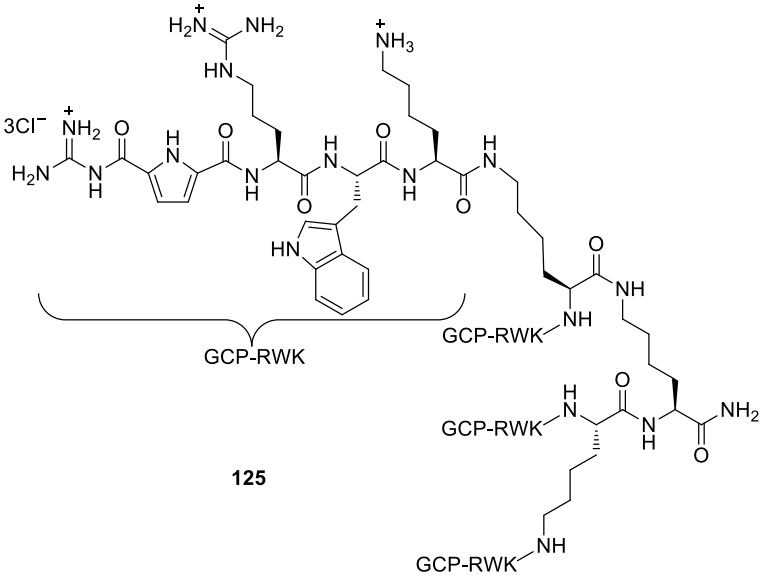

The second tetravalent peptide ligand **125** with four identical arms was synthesized accordingly on Rink amide MBHA resin (200 mg, 0.67 mmol/g, 0.134 mmol, 1 eq) following the standard microwave-assisted SPPS procedure. After attaching the lysine dendrimer on the resin, the amino acids Fmoc-Lys(Boc)-OH (628 mg, 1.34 mmol, 10 eq), Fmoc-Trp(Boc)-OH (706 mg, 1.34 mmol, 10 eq), Fmoc-Arg(Pbf)-OH (869 mg, 1.34 mmol, 10 eq), as well as the Boc-GCP group (**111**) (533 mg, 1.34 mmol, 10 eq) were coupled. After the cleavage and purification steps, the product was obtained as white solid with 95 % purity according to analytical HPLC analysis.

$C_{138}H_{211}Cl_{12}N_{55}O_{23}$ 3433.94 g/mol

Yield 17 mg, 5.0 µmol, 4 %

Mp. 230-233 °C (decomposition)

^{1}H NMR (500 MHz, DMSO-*d*$_6$): δ [ppm] = 1.18-1.77, 2.89-3.19 (m, 80 H, 12 × Arg-CH_2, 28 × Lys-CH_2), 2.68-2.78 (m, 8 H, 4 × Trp-CH_2), 4.12-4.59 (m, 15 H, 15 × CH), 6.89-8.75 (m, 96 H, 8 × GCP-CH, 20 × Trp-CH, 22 × NH, 17 × NH_2, 4 × NH_3^+), 10.86 (d, *J* = 15.1, 4 H, 4 × Trp-NH), 12.11 (s, 4 H, 4 × Gua-NH), 12.53 (s, 4 H, 4 × GCP-NH).

^{13}C NMR (125 MHz, DMSO-*d*$_6$): δ [ppm] = 22.1, 22.2, 22.8, 22.9, 25.2, 26.5, 27.3, 28.8, 28.9, 31.5, 38.6, 40.1, 40.5 (44 C, 28 × Lys-CH_2, 12 × Arg-CH_2, 4 × Trp-CH_2), 52.5, 52.7, 53.6 (15 C, 15 × CH), 109.8, 127.3, 136.0 (12 C, 12 × Trp-Cq), 111.3, 118.2, 118.4, 120.8, 123.7 (20 C, 20 × Trp-CH), 113.8, 115.9 (8 C, 8 × GCP-CH), 125.7, 132.3 (8 C, 8 × GCP-Cq), 155.6 (4 C, 4 × GCP-Gua-Cq), 156.9 (4 C, 4 × Arg-Cq), 159.1, 159.8, 171.1, 171.3, 171.4 (23 C, 23 × CO-Cq).

HRMS (ESI): m/z calculated for $C_{138}H_{202}N_{55}O_{23}^{3+}$ $[M+3H]^{3+}$: 999.5446; found: 999.5459.

FT-IR (ATR): $\tilde{\nu}$ [cm^{-1}] = 3063 (br), 2939 (w), 1634 (s), 1538 (s), 1471 (m).

6.4 Syntheses of Peptide-Derived Hydrazides

Synthesis of *tert*-butyl hydrazinecarboxylate (131)

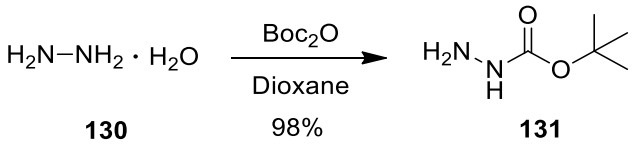

A solution of hydrazine monohydrate **130** (12.5 g, 250 mmol, 5 eq) in 50 mL dioxane was cooled to 0 °C and a cool solution of Boc_2O (10.9 g, 50 mmol, 1 eq) in dioxane (100 mL) was added dropwise under vigorous stirring. The reaction mixture was stirred at room temperature for 12 h. Then the solvent was removed, the residue was dissolved in ethyl acetate, washed with brine twice. The organic phase was dried over $MgSO_4$ and evaporated under reduced pressure to give **131** as white crystal.

$C_5H_{12}N_2O_2$ 132.16 g/mol

Yield 6.49 g, 49 mmol, 98 %

Mp. 37 °C

^{1}H NMR (300 MHz, $CDCl_3$): δ [ppm] = 1.46 (s, 9 H, 3 × CH_3), 3.26 (s, 2 H, NH_2), 5.84 (s, 1H, NH).

^{13}C NMR (75 MHz, DMSO-d_6): δ [ppm] = 28.47 (CH_3), 80.65 (C_q), 158.17 (CO).

HRMS (ESI): m/z calculated for $C_5H_{12}N_2O_2Na^+$ $[M+Na]^+$: 155.0791; found: 155.0813.

FT-IR (ATR): $\tilde{\nu}$ [cm^{-1}] = 3277 (br), 3060 (br), 3275 (w), 2932 (w), 1635 (s), 1523 (s), 1394 (w), 1280 (m), 1253 (m), 1197 (m), 1047 (w), 952 (w).

Synthesis of 4-(*N'-tert*-butoxycarbonyl-hydrazino)-4-oxo-butyric acid (132)

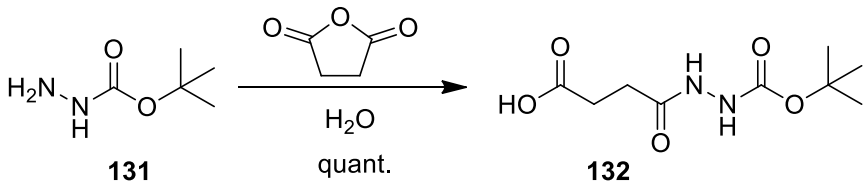

131 132

A solution of **131** (1.32 g, 10 mmol, 1 eq) and succinic anhydride (1.0 g, 10 mmol, 1 eq) in 30 mL water was stirred at room temperature for 4 h. The reaction proceeded clean, and full conversion to **132** was confirmed by ESI-MS. The reaction mixture was lyophilized to give **132** as white solid which was used in SPPS without any further purification.

$C_9H_{16}N_2O_5$ 232.23 g/mol

Yield 2.32 g, 10 mmol, quant.

Mp. 40 °C

^{1}H NMR (300 MHz, $CDCl_3$): δ [ppm] = 1.46 (s, 9 H, 3 × CH_3), 2.53 (t, J = 6.7 Hz, 2 H, CH_2), 2.66-2.74 (m, 2 H, CH_2), 7.11 (s, 1H, NH), 8.42 (s, 1H, NH).

^{13}C NMR (75 MHz, DMSO-d_6): δ [ppm] = 28.27 (CH_3), 28.47 (CH_2), 29.06 (CH_2), 82.21 (C_q), 156.30 (CO), 172.65 (CO), 176.45 (CO).

HRMS (ESI): m/z calculated for $C_9H_{15}N_2O_5^-$ $[M-H]^-$: 231.0986, found: 231.0938.

FT-IR (ATR): $\tilde{\nu}$ [cm^{-1}] = 3272 (br), 3053 (br), 2975 (w), 2931 (w), 1643 (s), 1524 (s), 1396 (w), 1252 (m), 1198 (m), 1046 (w), 954 (w).

Microwave-Assisted SPPS of Hydrazide (135)

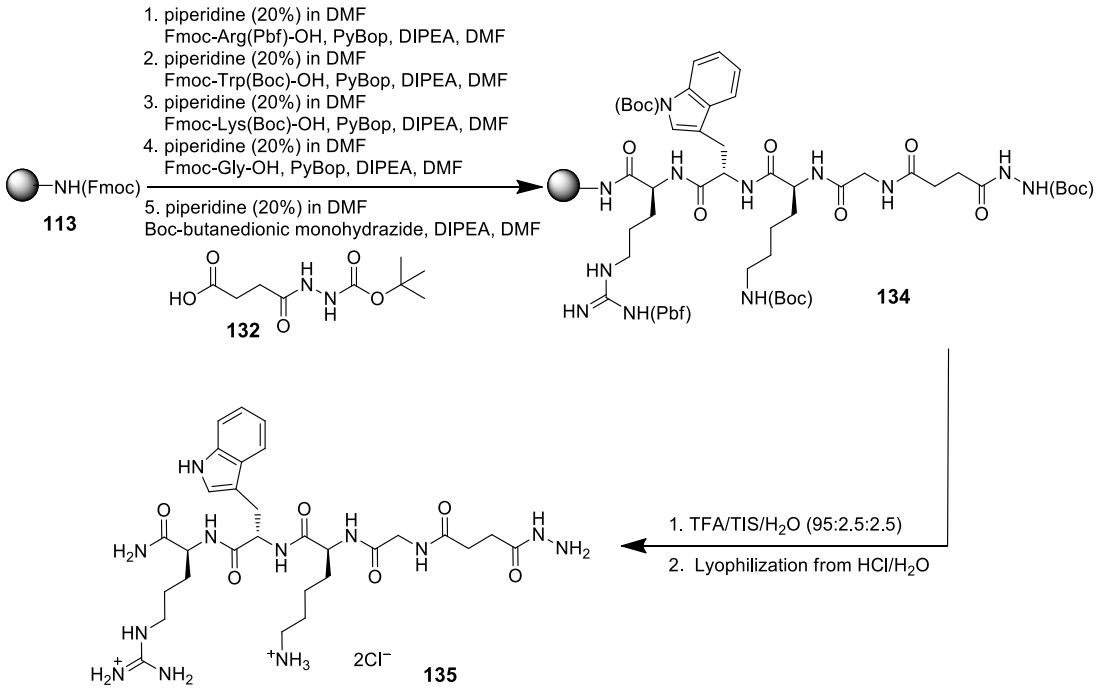

The synthesis of **135** was carried out on Rink amide MBHA resin (200 mg, 0.84 mmol/g, 0.168 mmol, 1 eq) according to the standard microwave-assisted SPPS procedure described in Chapter 6.2.2. The resin was swollen in DCM (10 mL) for 2 h, followed by the removal of Fmoc protecting group with 20 % piperidine/DMF. After a washing cycle with DMF, the first amino acid Fmoc-Arg(Pbf)-OH (327 mg, 0.504 mmol, 3 eq) was attached to the resin with the coupling reagent PyBop (262 mg, 0.504 mmol, 3 eq) and the base DIPEA (171 µL, 1.008 mmol, 6 eq) in DMF (5 mL) by microwave irradiation condition for 20 min. The coupling was repeated and the resin was washed thoroughly and the *Kaiser* test showed a negative result. Then after the Fmoc deprotection, the Fmoc-Trp(Boc)-OH (265 mg, 0.504 mmol, 3 eq), Fmoc-Lys(Boc)-OH (236 mg, 0.504 mmol, 3 eq), Fmoc-Gly-OH (150 mg, 0.504 mmol, 3 eq) and Boc-butanedionic monohydrazide (**132**) (117 mg, 0.504 mmol, 3 eq) were coupled in the same manner. After the final washing cycles, the cleavage of the product from the resin was carried out without microwave irradiation by using a mixture of TFA/H_2O/TIS (95:2.5:2.5) according to the general procedure for Rink amide MBHA resin as described in Chapter 6.2.1. The crude product was purified by RP18-MPLC using appropriate conditions (MeOH/H_2O + 0.1 % TFA). Pure product was transferred into its hydrochloride salt by dissolving in water with hydrochloric acid and lyophilizing three times to give **135** as a white solid with 99 % purity according to analytical HPLC analysis.

$C_{29}H_{48}Cl_2N_{12}O_6$ 731.67 g/mol

Yield 56 mg, 76.5 µmol, 46 %

Mp. 134 °C

^{1}H NMR (500 MHz, DMSO-*d*$_6$): δ [ppm] = 1.16-1.25 (m, 2 H, Lys-CH_2), 1.40-1.73 (m, 8 H, 2 × Lys-CH_2, 2 × Arg-CH_2), 2.46 (m, 4 H, 2 × CH_2), 2.68-2.72 (m, 2 H, Arg-CH_2), 2.99-3.19 (m, 6 H, Lys-CH_2, Trp-CH_2, NH_2), 3.70-3.71 (m, 2 H, Gly-CH_2), 4.16-4.20 (m, 2 H, Lys-CH, Arg-CH), 4.46-4.50 (m, 1 H, Trp-CH), 6.97 (t, *J* = 7.5 Hz, 1 H, Trp-CH_{ar}), 7.05 (t, *J* = 7.6 Hz, 1 H, Trp-CH_{ar}), 7.11 (s, 1 H, NH_2), 7.17 (s, 1 H, Trp-CH_{ar}), 7.31 (s, 1 H, NH_2), 7.33 (d, *J* = 8.1 Hz, 1 H, Trp-CH_{ar}), 7.57 (d, *J* = 7.8 Hz, 1 H, Trp-CH_{ar}),7.76 (t, *J* = 5.7 Hz, 1 H, NH), 7.89 (d, *J* = 8.0 Hz, 1 H, NH), 7.93 (brs, 3 H, Lys-NH_3^+), 8.09 (d, *J* = 7.6 Hz, 1 H, NH), 8.16 (d, *J* = 7.7 Hz, 1 H, NH), 8.26 (t, *J* = 5.7 Hz, 1 H, NH), 10.88 (s, 1 H, Trp-NH), 11.00 (s, 1 H, NH).

^{13}C NMR (125 MHz, DMSO-*d*$_6$): δ [ppm] = 22.10 (Lys-CH_2), 25.00 (Arg-CH_2), 26.52 (Lys-CH_2), 27.22 (Trp-CH_2), 28.11 (CH_2), 29.16 (Arg-CH_2), 29.55 (CH_2), 31.10 (Lys-CH_2), 38.54 (Lys-CH_2), 40.39 (Arg-CH_2), 42.17 (Gly-CH_2), 52.08 (Arg-CH), 52.71 (Lys-CH), 53.90 (Trp-CH), 109.94 (Trp-C_q), 111.37 (Trp-CH_{ar}), 118.33 (Trp-CH_{ar}), 118.41 (Trp-CH_{ar}), 120.91 (Trp-CH_{ar}), 123.74 (Trp-CH_{ar}), 127.26 (Trp-C_q), 136.07 (Trp-C_q), 156.92 (Gua-C_q), 169.25 (CO), 171.15 (CO), 171.35 (CO), 171.42 (CO), 171.65 (CO), 173.33 (CO).

HRMS (ESI): m/z calculated for $C_{29}H_{47}N_{12}O_6^+$ $[M+H]^+$: 659.3736; found: 659.3778.

FT-IR (ATR): $\tilde{\nu}$ [cm^{-1}] = 3138 (br), 3045 (br), 2897 (br), 1637 (s), 1522 (s), 1403 (s), 1339 (w), 1230 (m), 1092 (s), 745 (m).

Microwave-Assisted SPPS of Hydrazide (136)

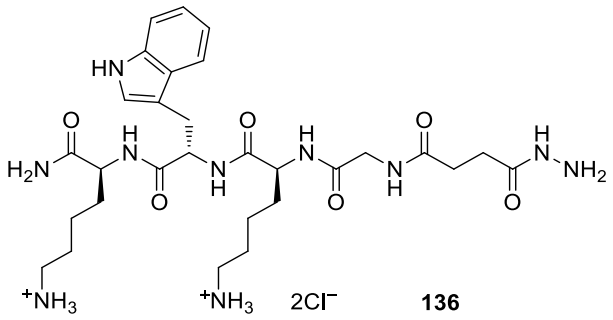

136

The peptide-derived hydrazide **136** was synthesized accordingly on Rink amide MBHA resin (200 mg, 0.84 mmol/g, 0.168 mmol, 1 eq) following the above described microwave-assisted SPPS procedure. The coupling reagent PyBop (262 mg, 0.504 mmol, 3 eq) and the base DIPEA (171 µL, 1.008 mmol, 6 eq) in DMF (5 mL) were used during the coupling steps. After Fmoc deprotection, the amino acids Fmoc-Lys(Boc)-OH (236 mg, 0.504 mmol, 3 eq), Fmoc-Trp(Boc)-OH (265 mg, 0.504 mmol, 3 eq), Fmoc-Lys(Boc)-OH (236 mg, 0.504 mmol, 3 eq), Fmoc-Gly-OH (150 mg, 0.504 mmol, 3 eq) and Boc-butanedionic monohydrazide (**132**) (117 mg, 0.504 mmol, 3 eq) were coupled. After the cleavage and purification steps, the product was obtained as a white solid with 98 % purity according to analytical HPLC analysis.

$C_{29}H_{48}Cl_2N_{10}O_6$ 703.66 g/mol

Yield 51 mg, 72.5 µmol, 43 %

Mp. 134 °C

^{1}H NMR (500 MHz, DMSO-*d*$_6$): δ [ppm] = 1.17-1.29 (m, 4 H, 2 × Lys-CH_2), 1.48-1.67 (m, 8 H, 4 × Lys-CH_2), 2.40-2.47 (m, 4 H, 2 × CH_2), 2.67-2.76 (m, 4 H, 2 × Lys-CH_2), 3.00-3.19 (m, 2 H, Trp-CH_2), 3.71-3.72 (m, 2 H, Gly-CH_2), 4.14-4.21 (m, 2 H, 2 × Lys-CH), 4.46-4.50 (m, 1 H, Trp-CH), 6.97 (t, *J* = 7.5 Hz, 1 H, Trp-CH_{ar}), 7.04-7.08 (m, 2 H, Trp-CH_{ar}, NH_2), 7.18 (s, 1 H, Trp-CH_{ar}), 7.25 (s, 1 H, NH_2), 7.33 (d, *J* = 8.1 Hz, 1 H, Trp-CH_{ar}), 7.58 (d, *J* = 7.4 Hz, 1 H, Trp-CH_{ar}), 7.85 (d, *J* = 7.4 Hz, 1 H, NH), 8.00 (brs, 6 H, 2 × Lys-NH_3^+), 8.11 (d, *J* = 6.7 Hz, 1 H, NH), 8.20 (d, *J* = 8.2 Hz, 1 H, NH), 8.28 (brs, 1 H, NH), 10.91 (s, 1 H, Trp-NH), 11.06 (s, 1 H, NH).

^{13}C NMR (125 MHz, DMSO-*d*$_6$): δ [ppm] = 22.06 (Lys-CH_2), 22.10 (Lys-CH_2), 26.49 (Lys-CH_2), 26.53 (Lys-CH_2), 27.08 (Trp-CH_2), 28.08 (CH_2), 29.53 (CH_2), 31.10 (Lys-CH_2), 31.32 (Lys-CH_2), 38.45 (Lys-CH_2), 38.54 (Lys-CH_2), 42.15 (Gly-CH_2), 52.24 (Lys-CH), 52.68 (Lys-CH), 53.85 (Trp-CH), 109.94 (Trp-C_q), 111.31 (Trp-CH_{ar}), 118.25 (Trp-CH_{ar}), 118.38 (Trp-CH_{ar}), 120.84 (Trp-CH_{ar}), 123.70 (Trp-CH_{ar}), 127.22 (Trp-C_q), 136.03 (Trp-C_q), 169.19 (CO), 171.08 (CO), 171.19 (CO), 171.32 (CO), 171.65 (CO), 173.39 (CO).

HRMS (ESI): m/z calculated for $C_{29}H_{47}N_{10}O_6^+$ $[M+H]^+$: 631.3675; found: 631.3692.

FT-IR (ATR): $\tilde{\nu}$ [cm^{-1}] = 3239 (br), 3038 (br), 2920 (br), 1642 (s), 1521 (s), 1339 (w), 1232 (m), 1160 (w), 1098 (w), 745 (m).

Microwave-Assisted SPPS of Hydrazide (138)

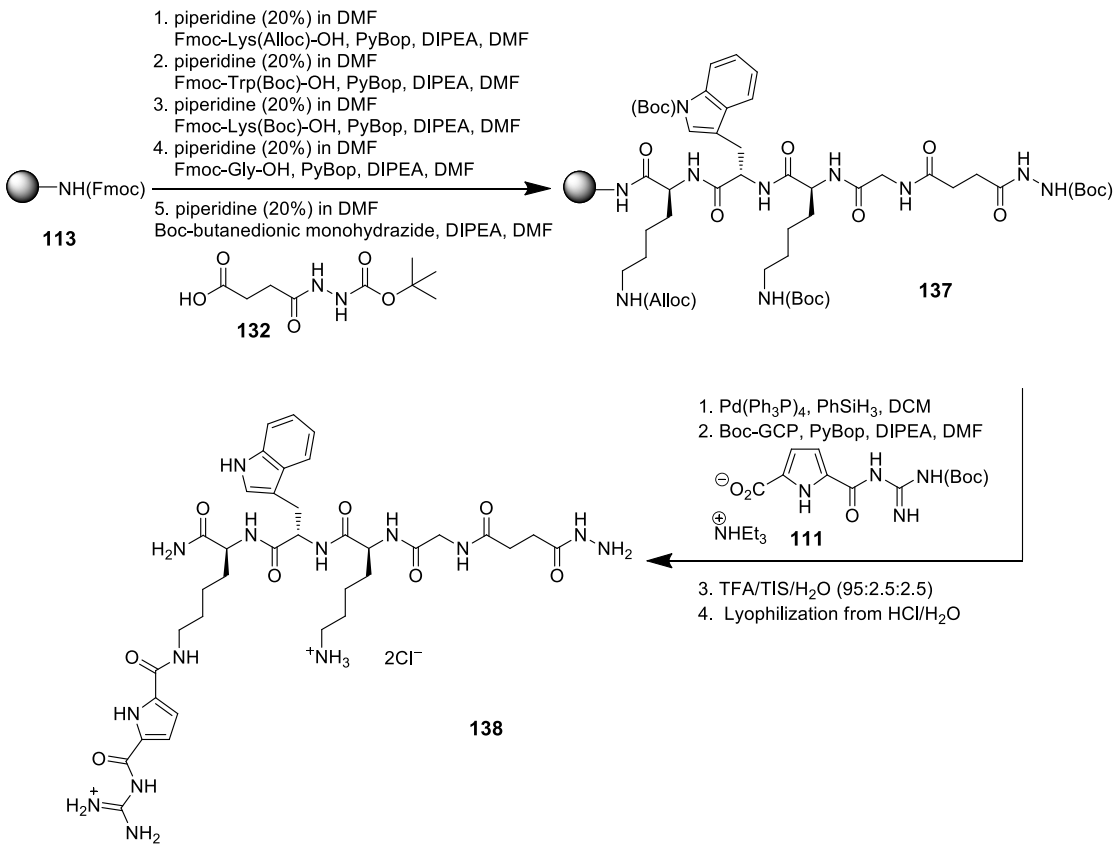

The peptide-derived hydrazide **138** was synthesized accordingly on Rink amide MBHA resin (200 mg, 0.84 mmol/g, 0.168 mmol, 1 eq) following the above described microwave-assisted SPPS procedure. The coupling reagent PyBop (262 mg, 0.504 mmol, 3 eq) and the base DIPEA (171 µL, 1.008 mmol, 6 eq) in DMF (5 mL) were used during the coupling steps. After Fmoc deprotection, the amino acids Fmoc-Lys(Alloc)-OH (228 mg, 0.504 mmol, 3 eq), Fmoc-Trp(Boc)-OH (265 mg, 0.504 mmol, 3 eq), Fmoc-Lys(Boc)-OH (236 mg, 0.504 mmol, 3 eq), Fmoc-Gly-OH (150 mg, 0.504 mmol, 3 eq) and Boc-butanedionic monohydrazide (**132**) (117 mg, 0.504 mmol, 3 eq) were coupled. After the removal of Alloc protecting group with $Pd(PPh_3)_4$ (19.4 mg, 0.0168 mmol, 0.1 eq) in the presence of $PhSiH_3$ (495 µL, 4.032 mmol, 24 eq) in DCM, the Boc-GCP group (**111**) (200 mg, 0.504 mmol, 3 eq) was coupled. After the cleavage and purification steps, the product was obtained as a white solid with 96 % purity according to analytical HPLC analysis.

$C_{36}H_{54}Cl_2N_{14}O_8$ 881.81 g/mol

Yield 52 mg, 59.0 µmol, 35 %

Mp. 176 °C

^{1}H NMR (500 MHz, DMSO-*d*$_6$): δ [ppm] = 1.20-1.33 (m, 4 H, 2 × Lys-CH_2), 1.46-1.69 (m, 8 H, 4 × Lys-CH_2), 2.37-2.47 (m, 4 H, 2 × CH_2), 2.69-2.72 (m, 2 H, Lys-CH_2),

2.97-3.02, 3.14-3.23 (m, 4 H, Lys-CH_2, Trp-CH_2), 3.69-3.71 (m, 2 H, Gly-CH_2), 4.15-4.22 (m, 2 H, 2 × Lys-CH), 4.47-4.52 (m, 1 H, Trp-CH), 6.87-6.88 (m, 1 H, GCP-CH_{ar}), 6.96 (t, *J* = 7.5 Hz, 1 H, Trp-CH_{ar}), 7.03-7.06 (m, 2 H, Trp-CH_{ar}, NH_2), 7.16 (s, 1 H, Trp-CH_{ar}), 7.25 (s, 1 H, NH_2), 7.32 (d, *J* = 8.8 Hz, 1 H, Trp-CH_{ar}), 7.54-7.57 (m, 2 H, GCP-CH_{ar}, Trp-CH_{ar}), 7.83 (d, *J* = 8.8 Hz,, 1 H, NH),7.93 (brs, 3 H, Lys-NH_3^+), 8.06 (d, *J* = 8.1 Hz,, 1 H, NH), 8.15 (d, *J* = 8.1 Hz,, 1 H, NH), 8.23 (brs, 1 H, NH), 8.50-8.68 (m, 5 H, 5 × NH), 10.87 (s, 1 H, Trp-NH), 11.03 (s, 1 H, NH), 12.06 (s, 1 H, Gua-NH), 12.34 (s, 1 H, GCP-NH).

^{13}C NMR (125 MHz, DMSO-*d*$_6$): δ [ppm] = 22.05 (Lys-CH_2), 22.74 (Lys-CH_2), 26.50 (Lys-CH_2), 27.24 (Trp-CH_2), 28.06 (CH_2), 28.72 (Lys-CH_2), 29.50 (CH_2), 31.17 (Lys-CH_2), 31.77 (Lys-CH_2), 38.50 (Lys-CH_2), 38.73 (Lys-CH_2), 42.11 (Gly-CH_2), 52.41 (Lys-CH), 52.55 (Lys-CH), 53.77 (Trp-CH), 109.92 (Trp-C_q), 111.28 (Trp-CH_{ar}), 112.45 (GCP-CH_{ar}), 115.99 (GCP-CH_{ar}), 118.24 (Trp-CH_{ar}), 118.37 (Trp-CH_{ar}), 120.82 (Trp-CH_{ar}), 123.68 (Trp-CH_{ar}), 125.33 (GCP-C_q), 127.23 (Trp-C_q), 132.95 (GCP-Cq), 136.02 (Trp-C_q), 155.54 (Gua-C_q), 159.02 (CO), 159.64 (CO), 169.06 (CO), 171.09 (CO), 171.14 (CO), 171.29 (CO), 171.50 (CO), 173.50 (CO).

HRMS (ESI): m/z calculated for $C_{36}H_{53}N_{14}O_8^+$ $[M+H]^+$: 809.4165; found: 809.4177.

FT-IR (ATR): $\tilde{\nu}$ [cm^{-1}] = 3188 (br), 3049 (br), 2926 (br), 1638 (s), 1523 (s), 1281 (s), 1195 (m), 813 (w), 745 (m).

Microwave-Assisted SPPS of Hydrazide (139)

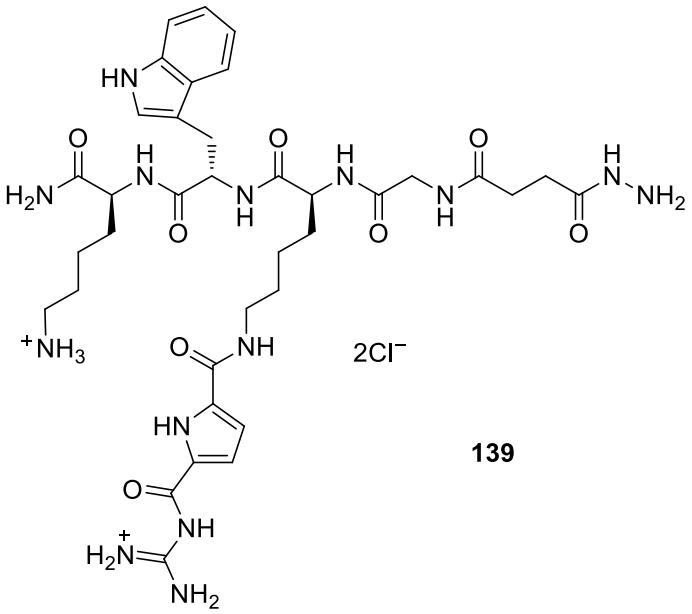

139

The peptide-derived hydrazide **139** was synthesized accordingly on Rink amide MBHA resin (200 mg, 0.84 mmol/g, 0.168 mmol, 1 eq) following the above described microwave-assisted SPPS procedure. The coupling reagent PyBop (262 mg, 0.504 mmol, 3 eq) and the base DIPEA (171 µL, 1.008 mmol, 6 eq) in DMF (5 mL) were used during the coupling steps. After Fmoc deprotection, the amino acids Fmoc-Lys(Boc)-OH (236 mg, 0.504 mmol, 3 eq), Fmoc-Trp(Boc)-OH (265 mg, 0.504 mmol, 3 eq), Fmoc-Lys(Alloc)-OH (228 mg, 0.504 mmol, 3 eq), Fmoc-Gly-OH (150 mg, 0.504 mmol, 3 eq) and Boc-butanedionic monohydrazide (**132**) (117 mg, 0.504 mmol, 3 eq) were coupled. After the removal of Alloc protecting group with $Pd(PPh_3)_4$ (19.4 mg, 0.0168 mmol, 0.1 eq) in the presence of $PhSiH_3$ (495 µL, 4.032 mmol, 24 eq) in DCM, the Boc-GCP group (**111**) (200 mg, 0.504 mmol, 3 eq) was coupled. After the cleavage and purification steps, the product was obtained as a white solid with 91 % purity according to analytical HPLC analysis.

$C_{36}H_{54}Cl_2N_{14}O_8$ 881.81 g/mol

Yield 53 mg, 60.1 µmol, 36 %

Mp. 178 °C

^{1}H NMR (500 MHz, DMSO-*d*$_6$): δ [ppm] = 1.18-1.29 (m, 4 H, 2 × Lys-CH_2), 1.42-1.70 (m, 8 H, 4 × Lys-CH_2), 2.36-2.47 (m, 4 H, 2 × CH_2), 2.71-2.76 (m, 2 H, Lys-CH_2), 2.99-3.04, 3.15-3.19 (m, 4 H, Lys-CH_2, Trp-CH_2), 3.71-3.72 (m, 2 H, Gly-CH_2), 4.13-4.21 (m, 2 H, 2 × Lys-CH), 4.46-4.50 (m, 1 H, Trp-CH), 6.87-6.88 (m, 1 H, GCP-CH_{ar}), 6.97 (t, *J* = 7.4 Hz, 1 H, Trp-CH_{ar}), 7.03-7.06 (m, 2 H, Trp-CH_{ar}, NH_2), 7.16 (s, 1 H, Trp-CH_{ar}), 7.21 (s, 1 H, NH_2), 7.32 (d, *J* = 8.2 Hz, 1 H, Trp-CH_{ar}), 7.54-7.58 (m, 2 H, GCP-CH_{ar}, Trp-CH_{ar}), 7.83 (d, *J* = 8.5 Hz,, 1 H, NH), 7.93 (brs, 3 H, Lys-NH_3^+), 8.09 (d, *J* = 7.9 Hz,, 1 H, NH), 8.13 (d, *J* = 7.8 Hz,, 1 H, NH), 8.24 (t, *J* = 6.2 Hz,, 1 H, NH), 8.49-8.68 (m, 5 H,

5 × NH), 10.87 (s, 1 H, Trp-NH), 11.01 (s, 1 H, NH), 12.07 (s, 1 H, Gua-NH), 12.33 (s, 1 H, GCP-NH).

^{13}C NMR (125 MHz, DMSO-*d*$_6$): δ [ppm] = 22.09 (Lys-CH_2), 22.79 (Lys-CH_2), 26.54 (Lys-CH_2), 27.07 (Trp-CH_2), 28.07 (CH_2), 28.74 (Lys-CH_2), 29.51 (CH_2), 31.29 (Lys-CH_2), 31.48 (Lys-CH_2), 38.58 (Lys-CH_2), 38.65 (Lys-CH_2), 42.08 (Gly-CH_2), 52.24 (Lys-CH), 52.87 (Lys-CH), 53.77 (Trp-CH), 109.93 (Trp-C_q), 111.28 (Trp-CH_{ar}), 112.42 (GCP-CH_{ar}), 116.00 (GCP-CH_{ar}), 118.23 (Trp-CH_{ar}), 118.37 (Trp-CH_{ar}), 120.83 (Trp-CH_{ar}), 123.67 (Trp-CH_{ar}), 125.33 (GCP-C_q), 127.24 (Trp-C_q), 132.96 (GCP-Cq), 136.02 (Trp-C_q), 155.53 (Gua-C_q), 159.01 (CO), 159.63 (CO), 169.17 (CO), 171.10 (CO), 171.15 (CO), 171.27 (CO), 171.81 (CO), 173.36 (CO).

HRMS (ESI): m/z calculated for $C_{36}H_{53}N_{14}O_8^+$ $[M+H]^+$: 809.4165; found: 809.4186.

FT-IR (ATR): $\tilde{\nu}$ [cm^{-1}] = 3183 (br), 3044 (br), 2925 (br), 1638 (s), 1533 (s), 1281 (s), 1195 (m), 814 (w), 745 (m).

Microwave-Assisted SPPS of Hydrazide (140)

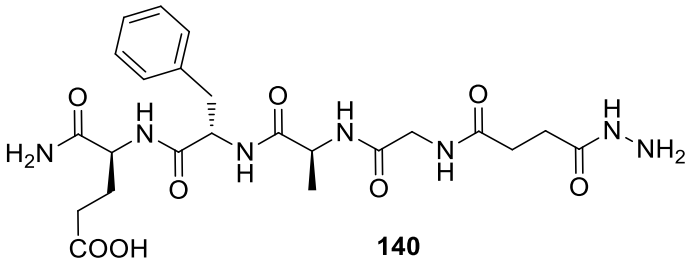

140

The peptide-derived hydrazide **140** was synthesized accordingly on Rink amide MBHA resin (200 mg, 0.84 mmol/g, 0.168 mmol, 1 eq) following the above described microwave-assisted SPPS procedure. The coupling reagent PyBop (262 mg, 0.504 mmol, 3 eq) and the base DIPEA (171 µL, 1.008 mmol, 6 eq) in DMF (5 mL) were used during the coupling steps. After Fmoc deprotection, the amino acids Fmoc-Glu(O^{t}Bu)-OH (214 mg, 0.504 mmol, 3 eq), Fmoc-Phe-OH (195 mg, 0.504 mmol, 3 eq), Fmoc-Ala-OH (157 mg, 0.504 mmol, 3 eq), Fmoc-Gly-OH (150 mg, 0.504 mmol, 3 eq) and Boc-butanedionic monohydrazide (**132**) (117 mg, 0.504 mmol, 3 eq) were coupled. After the cleavage and purification steps, the product was obtained as a white solid with 91 % purity according to analytical HPLC analysis.

$C_{23}H_{33}N_7O_8$ 535.55 g/mol

Yield 31 mg, 57.9 µmol, 34 %

Mp. > 250 °C (decomposition)

^{1}H NMR (500 MHz, DMSO-*d*$_6$): δ [ppm] = 1.10-1.18 (m, 3 H, Ala-CH_3), 1.70-1.83, 1.89-2.00 (m, 2 H, Glu-CH_2), 2.19-2.30 (m, 2 H, Glu-CH_2), 2.36-2.46 (m, 4 H, 2 × CH_2), 2.79-3.07 (m, 2 H, Phe-CH_2), 3.68-3.69 (m, 2 H, Gly-CH_2), 4.15-4.24 (m, 2 H, Glu-CH, Ala-CH), 4.41-4.50 (m, 1 H, Phe-CH), 7.09 (s, 1 H, NH_2), 7.15-7.19 (m, 2 H, 2 × Phe-CH_{ar}), 7.24-7.26 (m, 4 H, 3 × Phe-CH_{ar}, NH_2), 7.82-8.18 (m, 4 H, 4 × NH), 10.98 (s, 1 H, NH).

^{13}C NMR (125 MHz, DMSO-*d*$_6$): δ [ppm] = 18.03 (Ala-CH_3), 27.31 (Glu-CH_2), 28.03 (CH_2), 29.45 (CH_2), 30.04 (Glu-CH_2), 36.84 (Phe-CH_2), 42.01 (Gly-CH_2), 48.30 (Ala-CH), 51.80 (Glu-CH), 54.23 (Phe-CH), 126.28 (Phe-CH_{ar}), 128.03 (Phe-CH_{ar}), 128.08 (Phe-CH_{ar}), 129.18 (Phe-CH_{ar}), 129.22 (Phe-CH_{ar}), 137.80 (Phe-C_q), 170.73 (CO), 171.12 (CO), 171.19 (CO), 172.25 (CO), 172.88 (CO), 173.77 (CO), 173.94 (CO).

HRMS (ESI): m/z calculated for $C_{23}H_{34}N_7O_8^+$ $[M+H]^+$: 536.2463; found: 536.2399.

FT-IR (ATR): $\tilde{\nu}$ [cm^{-1}] = 3197 (br), 3044 (br), 2925 (br), 1640 (s), 1524 (s), 1407 (w), 1234 (m), 1197 (m), 1031 (w), 744 (m).

6.5 Syntheses of Acyl Hydrazones

The acyl hydrazones were synthesized from peptide-derived hydrazides and the tri- or di- aldehydes with slightly excess hydrazides compared to the amounts of the aldehyde groups.

Synthesis of acyl hydrazone 141

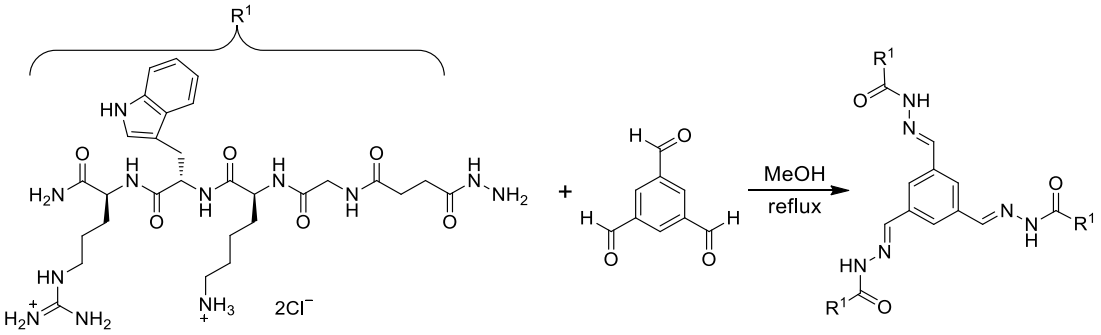

135 E 141

Tri-aldehyde **E** (1.62 mg, 0.01 mmol, 1 eq) and hydrazide **135** (25.6 mg, 0.035 mmol, 3.5 eq) were dissolved in 10 mL MeOH under argon atmosphere. Then the reaction mixture was allowed to proceed under reflux overnight. After the solvent was removed, the crude product was purified by RP18-MPLC using appropriate conditions (MeOH/H_2O + 0.1 % TFA). Pure product was transferred into its hydrochloride salt to obtain **141** as a white solid with 92 % purity according to analytical HPLC analysis.

$C_{96}H_{144}Cl_6N_{36}O_{18}$ 2303.12 g/mol

Yield 6 mg, 2.6 µmol, 26 %

Mp. 215 °C (decomposition)

^{1}H NMR (500 MHz, DMSO-*d*$_6$): δ [ppm] = 1.19-1.24 (m, 6 H, 3 × Lys-CH_2), 1.44-1.72 (m, 24 H, 6 × Lys-CH_2, 6 × Arg-CH_2), 2.69-2.72 (m, 6 H, 3 × Lys-CH_2), 2.91-3.19 (m, 12 H, 3 × Arg-CH_2, 3 × Trp-CH_2), 3.73 (s, 6 H, 3 × Gly-CH_2), 4.16-4.20 (m, 6 H, 3 × Lys-CH, 3 × Arg-CH), 4.46-4.51 (m, 3 H, 3 × Trp-CH), 6.95 (q, *J* = 7.4 Hz, 3 H, 3 × Trp-CH_{ar}), 7.03 (q, *J* = 7.2 Hz, 3 H, 3 × Trp-CH_{ar}), 7.13 (s, 3 H, NH_2), 7.17 (s, 3 H, 3 × Trp-CH_{ar}), 7.27 (s, 3 H, NH_2), 7.31 (t, *J* = 8.6 Hz, 3 H, 3 × Trp-CH_{ar}), 7.55 (t, *J* = 7.5 Hz, 3 H, 3 × Trp-CH_{ar}), 7.72 (s, 3 H, 3 × NH), 7.88 (brs, 9 H, 3 × Lys-NH_3^+), 7.93-8.05 (m, 5 H, 5 × NH), 8.07-8.17 (m, 6 H, 3 × Phe-CH_{ar}, 3 × CH=N), 8.25-8.30 (m, 4 H, 4 × NH), 10.87 (s, 3 H, 3 × Trp-NH), 11.40 (t, *J* = 10.9 Hz, 1 H, NH), 11.75 (s, 1 H, NH).

^{13}C NMR (125 MHz, DMSO-*d*$_6$): δ [ppm] = 22.09 (Lys-CH_2), 24.96 (Arg-CH_2), 26.45 (Lys-CH_2), 27.12 (Trp-CH_2), 27.42 (CH_2), 29.09 (Arg-CH_2), 29.49 (CH_2), 30.03 (Lys-CH_2), 30.88 (Lys-CH_2), 38.47 (Lys-CH_2), 40.32 (Arg-CH_2), 43.93 (Gly-CH_2), 52.06 (Arg-CH), 52.80 (Lys-CH), 53.84 (Trp-CH), 109.94 (Trp-C_q), 111.34 (Trp-CH_{ar}), 118.23 (Trp-CH_{ar}), 118.31 (Trp-CH_{ar}), 120.86 (Trp-CH_{ar}), 123.68 (Trp-CH_{ar}), 126.01 (Phe-CH_{ar}),

127.24 (Trp-C_q), 135.36 (Phe-C_q), 136.07 (Trp-C_q), 142.01 (CH=N), 156.87 (Gua-C_q), 169.48 (CO), 171.23 (CO), 171.62 (CO), 171.92 (CO), 172.24 (CO), 173.20 (CO).

HRMS (ESI): m/z calculated for $C_{96}H_{142}N_{36}O_{18}^{4+}$ $[M+4H]^{4+}$: 522.0327; found: 522.0328.

FT-IR (ATR): $\tilde{\nu}$ [cm^{-1}] = 3189 (br), 3044 (br), 2926 (br), 1647 (s), 1522 (s), 1339 (w), 1237 (m), 1161 (w), 1098 (w), 1025 (w), 955 (w), 745 (m).

Synthesis of acyl hydrazone 142

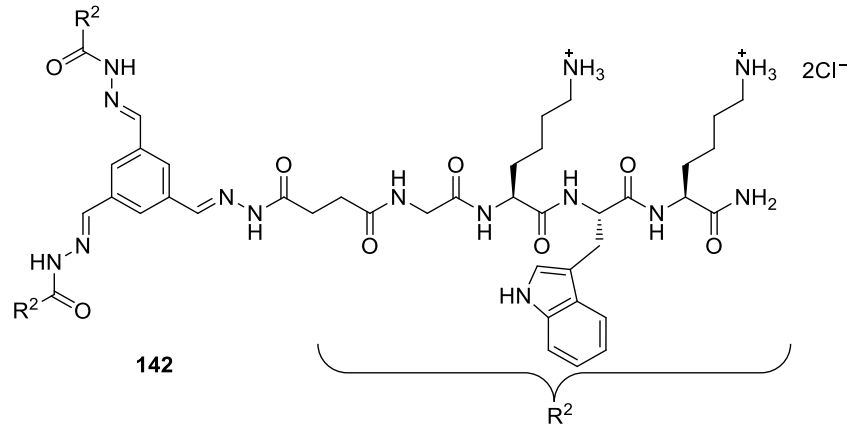

The synthesis of acyl hydrazone **142** from tri-aldehyde **E** (1.62 mg, 0.01 mmol, 1 eq) and hydrazide **136** (24.6 mg, 0.035 mmol, 3.5 eq) was carried out under analogous above described conditions. After purification steps, **142** was obtained as a white solid with 93 % purity according to analytical HPLC analysis.

$C_{96}H_{144}Cl_6N_{30}O_{18}$ 2219.08 g/mol

Yield 5 mg, 2.3 μmol, 23 %

Mp. 216 °C (decomposition)

^{1}H NMR (500 MHz, DMSO-*d*$_6$): δ [ppm] = 1.18-1.27 (m, 12 H, 6 × Lys-CH_2), 1.52-1.67 (m, 24 H, 12 × Lys-CH_2), 2.69-2.74 (m, 12 H, 6 × Lys-CH_2), 3.04-3.19 (m, 6 H, 3 × Trp-CH_2), 3.73 (s, 6 H, 3 × Gly-CH_2), 4.16 (s, 6 H, 6 × Lys-CH), 4.48 (s, 3 H, 3 × Trp-CH), 6.96 (t, *J* = 7.3 Hz, 3 H, 3 × Trp-CH_{ar}), 7.01-7.13 (m, 6 H, 3 × Trp-CH_{ar}, NH_2), 7.18-7.23 (m, 6 H, 3 × Trp-CH_{ar}, NH_2), 7.30-7.33 (m, 3 H, 3 × Trp-CH_{ar}), 7.56 (t, *J* = 8.0 Hz, 3 H, 3 × Trp-CH_{ar}), 7.81-7.88 (m, 4 H, 4 × NH), 7.87 (brs, 18 H, 6 × Lys-NH_3^+), 8.09-8.14 (m, 6 H, 3 × Phe-CH_{ar}, 3 × CH=N), 8.26-8.33 (m, 5 H, 5 × NH), 10.89 (s, 2 H, 2 × Trp-NH), 11.43 (s, 1 H, NH), 11.79 (s, 1 H, NH).

^{13}C NMR (125 MHz, DMSO-*d*$_6$): δ [ppm] = 22.09 (Lys-CH_2), 26.44 (Lys-CH_2), 26.53 (Lys-CH_2), 27.02 (Trp-CH_2), 30.88 (Lys-CH_2), 31.23 (Lys-CH_2), 38.45 (Lys-CH_2), 38.53 (Lys-CH_2), 43.90 (Gly-CH_2), 52.28 (Lys-CH), 52.80 (Lys-CH), 53.84 (Trp-CH), 109.93 (Trp-C_q), 111.26 (Trp-CH_{ar}), 118.21 (Trp-CH_{ar}), 118.30 (Trp-CH_{ar}), 120.82 (Trp-CH_{ar}), 123.65 (Trp-CH_{ar}), 127.18 (Trp-C_q), 132.54 (Phe-CH_{ar}), 135.50 (Phe-C_q), 136.04 (Trp-C_q), 169.52 (CO), 171.18 (CO), 171.65 (CO), 173.39 (CO).

HRMS (ESI): m/z calculated for $C_{96}H_{143}N_{30}O_{18}^{5+}$ $[M+5H]^{5+}$: 401.0239; found: 401.0228.

FT-IR (ATR): $\tilde{\nu}$ [cm^{-1}] = 3239 (br), 3038 (br), 2919 (br), 1646 (s), 1522 (s), 1339 (w), 1235 (m), 1159 (w), 1102 (w), 1025 (w), 954 (w), 745 (m).

Synthesis of acyl hydrazone 143

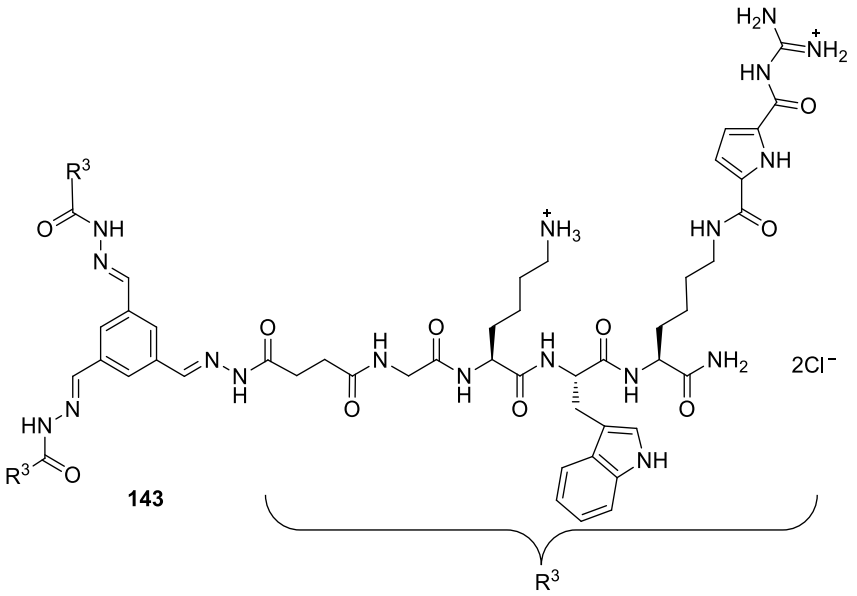

The synthesis of acyl hydrazone **143** from tri-aldehyde **E** (1.62 mg, 0.01 mmol, 1 eq) and hydrazide **138** (30.8 mg, 0.035 mmol, 3.5 eq) was carried out under analogous above described conditions. After purification steps, **143** was obtained as a white solid with 94 % purity according to analytical HPLC analysis.

$C_{117}H_{162}Cl_6N_{42}O_{24}$ 2753.52 g/mol

Yield 8 mg, 2.9 μmol, 29 %

Mp. 229 °C (decomposition)

^{1}H NMR (500 MHz, DMSO-*d*$_6$): δ [ppm] = 1.19-1.33, 1.49-1.71 (m, 36 H, 18 × Lys-CH_2), 2.71-2.76 (m, 6 H, 3 × Lys-CH_2), 2.92-3.02 (m, 6 H, 3 × Trp-CH_2), 3.16-3.25 (m, 6 H, 3 × Lys-CH_2), 3.69-3.76 (m, 6 H, 3 × Gly-CH_2), 4.16-4.22 (m, 6 H, 6 × Lys-CH), 4.49-4.52 (m, 3 H, 3 × Trp-CH), 6.87 (s, 3 H, 3 × GCP-CH_{ar}), 6.94-6.97 (m, 3 H, 3 × Trp-CH_{ar}), 7.02-7.09 (m, 6 H, 3 × Trp-CH_{ar}, NH_2), 7.15-7.16 (m, 3 H, 3 × Trp-CH_{ar}), 7.23 (s, 3 H, NH_2), 7.30-7.33 (m, 3 H, 3 × Trp-CH_{ar}), 7.45 (s, 3 H, 3 × GCP-CH_{ar}), 7.55 (t, *J* = 8.7 Hz, 3 H, 3 × Trp-CH_{ar}), 7.80 (brs, 9 H, 3 × Lys-NH_3^+), 7.84-8.01 (m, 6 H, 6 × NH), 8.06-8.07 (m, 6 H, 6 × NH), 8.21-8.25 (m, 6 H, 3 × Phe-CH_{ar}, 3 × CH=N), 8.41-8.57 (m, 13 H, 13 × NH), 10.81, 10.82 (s, 3 H, 3 × Trp-NH), 11.37(t, *J* = 18.1 Hz, 1 H, NH), 11.66 (t, *J* = 9.5 Hz, 1 H, NH), 11.87 (s, 3 H, 3 × Gua-NH), 12.31 (s, 3 H, 3 × GCP-NH).

^{13}C NMR (125 MHz, DMSO-*d*$_6$): δ [ppm] = 22.09 (Lys-CH_2), 22.75 (Lys-CH_2), 26.50 (Lys-CH_2), 27.22 (Trp-CH_2), 28.73 (Lys-CH_2), 29.45 (CH_2), 30.02 (CH_2), 31.04 (Lys-CH_2), 31.73 (Lys-CH_2), 34.26 (Lys-CH_2), 38.60 (Lys-CH_2), 38.74 (Lys-CH_2), 42.29 (Gly-CH_2), 52.45 (Lys-CH), 52.56 (Lys-CH), 53.74 (Trp-CH), 109.89 (Trp-C_q), 111.27 (Trp-CH_{ar}), 112.36 (GCP-CH_{ar}), 115.89 (GCP-CH_{ar}), 118.23 (Trp-CH_{ar}), 118.33 (Trp-CH_{ar}), 120.82 (Trp-CH_{ar}), 123.64 (Trp-CH_{ar}), 125.33 (GCP-C_q), 127.21 (Trp-C_q), 132.91 (GCP-Cq), 135.31 (Phe-CH_{ar}), 135.48 (Phe-C_q), 136.00 (Trp-C_q), 144.78

(CH=N), 155.43 (Gua-C_q), 159.05 (CO), 159.62 (CO), 168.34 (CO), 169.23 (CO), 169.34 (CO), 171.14 (CO), 171.54 (CO), 171.92 (CO), 172.27 (CO), 173.54 (CO).

HRMS (ESI): m/z calculated for $C_{117}H_{160}N_{42}O_{24}^{4+}$ $[M+4H]^{4+}$: 634.5649; found: 634.5649.

FT-IR (ATR): $\tilde{\nu}$ [cm^{-1}] = 3272 (br), 3047 (br), 2940 (br), 1645 (s), 1541 (s), 1284 (s), 1199 (m), 815 (w), 746 (m).

Synthesis of acyl hydrazone 144

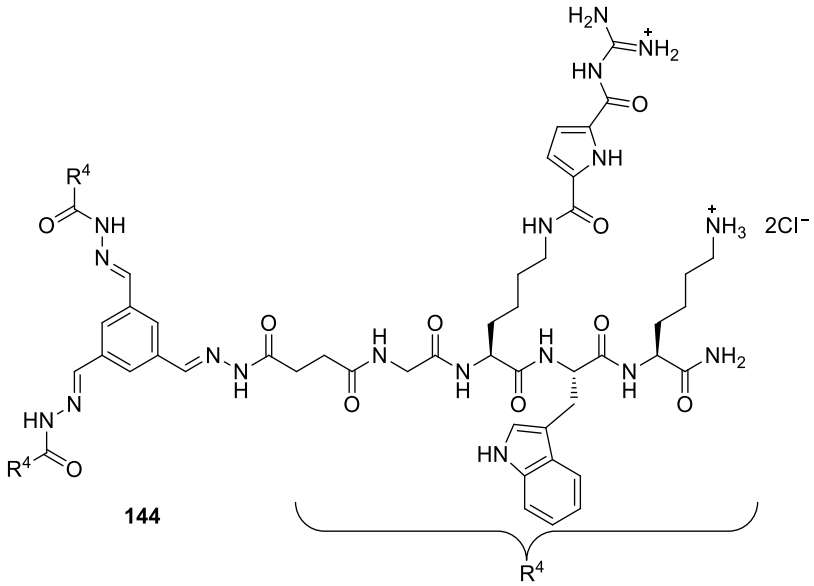

144

The synthesis of acyl hydrazone **144** from tri-aldehyde **E** (1.62 mg, 0.01 mmol, 1 eq) and hydrazide **139** (30.8 mg, 0.035 mmol, 3.5 eq) was carried out under analogous above described conditions. After purification steps, **144** was obtained as a white solid with 96 % purity according to analytical HPLC analysis.

$C_{117}H_{162}Cl_6N_{42}O_{24}$ 2753.52 g/mol

Yield 10 mg, 3.6 μmol, 36 %

Mp. 231 °C (decomposition)

^{1}H NMR (500 MHz, DMSO-*d*$_6$): δ [ppm] = 1.19-1.29, 1.45-1.68 (m, 36 H, 18 × Lys-CH_2), 2.74-2.75 (m, 6 H, 3 × Lys-CH_2), 2.91-3.04 (m, 6 H, 3 × Trp-CH_2), 3.15-3.19 (m, 6 H, 3 × Lys-CH_2), 3.73 (s, 6 H, 3 × Gly-CH_2), 4.14-4.17 (m, 6 H, 6 × Lys-CH), 4.45-4.49 (m, 3 H, 3 × Trp-CH), 6.86 (s, 3 H, 3 × GCP-CH_{ar}), 6.92-6.97 (m, 3 H, 3 × Trp-CH_{ar}), 7.00-7.09 (m, 6 H, 3 × Trp-CH_{ar}, NH_2), 7.16-7.20 (m, 6 H, 3 × Trp-CH_{ar}, NH_2), 7.30 (t, *J* = 9.8 Hz, 3 H, 3 × Trp-CH_{ar}), 7.49 (s, 3 H, 3 × GCP-CH_{ar}), 7.55 (t, *J* = 9.1 Hz,, 3 H, 3 × Trp-CH_{ar}), 7.85 (brs, 9 H, 3 × Lys-NH_3^+), 7.79-7.80, 7.91-7.92 (m, 6 H, 6 × NH), 8.04-8.07 (m, 6 H, 6 × NH), 8.11-8.30 (m, 7 H, NH, 3 × Phe-CH_{ar}, 3 × CH=N), 8.43-8.62 (m, 15 H, 15 × NH), 10.81, 10.84 (s, 3 H, 3 × Trp-NH), 11.35 (t, *J* = 13.8 Hz, 1 H, NH), 11.67 (s, 1 H, NH), 11.97 (s, 3 H, 3 × Gua-NH), 12.30 (s, 3 H, 3 × GCP-NH).

^{13}C NMR (125 MHz, DMSO-*d*$_6$): δ [ppm] = 22.09 (Lys-CH_2), 22.83 (Lys-CH_2), 26.55 (Lys-CH_2), 27.01 (Trp-CH_2), 28.70 (Lys-CH_2), 29.47 (CH_2), 31.23 (Lys-CH_2), 38.61 (Lys-CH_2), 43.95 (Gly-CH_2), 52.26 (Lys-CH), 52.99 (Lys-CH), 53.77 (Trp-CH), 109.90 (Trp-C_q), 111.26 (Trp-CH_{ar}), 112.35 (GCP-CH_{ar}), 115.91 (GCP-CH_{ar}), 118.20 (Trp-CH_{ar}), 118.30 (Trp-CH_{ar}), 120.81 (Trp-CH_{ar}), 123.58 (Trp-CH_{ar}), 123.63 (Trp-CH_{ar}), 125.31 (GCP-C_q), 127.18 (Trp-C_q), 132.91 (GCP-Cq), 135.25 (Phe-CH_{ar}), 135.43 (Phe-C_q), 136.00 (Trp-C_q), 144.56 (CH=N), 155.45 (Gua-Cq), 158.97 (CO), 159.59 (CO), 168.26

(CO), 169.39 (CO), 171.15 (CO), 171.84 (CO), 173.35 (CO).

HRMS (ESI): m/z calculated for $C_{117}H_{160}N_{42}O_{24}^{4+}$ $[M+4H]^{4+}$: 634.5649; found: 634.5650.

FT-IR (ATR): $\tilde{\nu}$ [cm^{-1}] = 3232 (br), 3049 (br), 2921 (br), 1648 (s), 1541 (s), 1284 (m), 1252 (m), 1201 (w), 1098 (w), 1025 (w), 955 (w), 748 (m).

Synthesis of acyl hydrazone 145

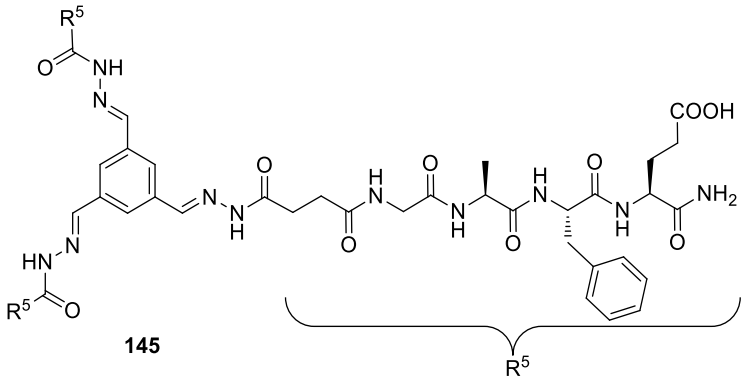

The synthesis of acyl hydrazone **145** from tri-aldehyde **E** (1.62 mg, 0.01 mmol, 1 eq) and hydrazide **140** (18.7 mg, 0.035 mmol, 3.5 eq) was carried out under analogous above described conditions. After purification steps, **145** was obtained as a white solid with 90 % purity according to analytical HPLC analysis.

$C_{78}H_{99}N_{21}O_{24}$ 1714.75 g/mol

Yield 4 mg, 2.3 μmol, 23 %

Mp. 149 °C (decomposition)

^{1}H NMR (500 MHz, DMSO-*d*$_6$): δ [ppm] = 1.14-1.19 (m, 9 H, 3 × Ala-CH_3), 1.72-1.78, 1.91-1.96 (m, 6 H, 3 × Glu-CH_2), 2.19-2.22 (m, 6 H, 3 × Glu-CH_2), 2.82-2.91 (m, 6 H, 3 × Phe-CH_2), 3.70 (s, 6 H, 3 × Gly-CH_2), 4.14-4.22 (m, 6 H, 3 × Glu-CH, 3 × Ala-CH), 4.42 (s, 3 H, 3 × Phe-CH), 7.09-7.26 (m, 21 H, 15 × Phe-CH_{ar}, 3 × NH_2), 7.78-8.23 (m, 18 H, 12 × NH, 3 × CH=N, 3 × CH_{ar}), 11.36 (t, *J* = 12.1 Hz, 1 H, NH) 11.56 (t, *J* = 10.5 Hz, 1 H, NH).

^{13}C NMR (125 MHz, DMSO-*d*$_6$): δ [ppm] = 17.73 (Ala-CH_3), 27.23 (Glu-CH_2), 29.47 (CH_2), 30.05 (Glu-CH_2), 34.32 (CH_2), 36.80 (Phe-CH_2), 44.21 (Gly-CH_2), 48.53 (Ala-CH), 51.84 (Glu-CH), 54.25 (Phe-CH), 126.26 (Phe-CH_{ar}), 126.28 (Phe-CH_{ar}), 128.07 (Phe-CH_{ar}), 128.09 (Phe-CH_{ar}), 129.09 (Phe-CH_{ar}), 129.13 (Phe-CH_{ar}), 137.76 (Phe-C_q), 137.79 (Phe-C_q), 169.21 (CO), 170.75 (CO), 172.31 (CO), 172.36 (CO), 172.90 (CO), 173.97 (CO).

HRMS (ESI): m/z calculated for $C_{78}H_{96}N_{21}O_{24}^{3-}$ $[M-3H]^{3-}$: 570.2318; found: 570.2401.

FT-IR (ATR): $\tilde{\nu}$ [cm^{-1}] = 3264 (br), 3060 (br), 2930 (br), 1636 (s), 1531 (s), 1407 (w), 1254 (m), 1198 (m), 1130 (m), 953 (w), 800 (w), 745 (m).

Synthesis of acyl hydrazone 146

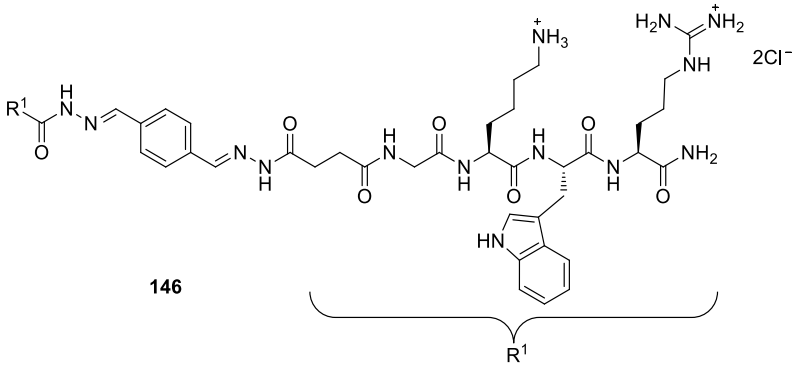

The synthesis of acyl hydrazone **146** from di-aldehyde **C** (1.34 mg, 0.01 mmol, 1 eq) and hydrazide **135** (18.3 mg, 0.025 mmol, 2.5 eq) was carried out under analogous above described conditions. After purification steps, **146** was obtained as a white solid with 98 % purity according to analytical HPLC analysis.

$C_{66}H_{98}Cl_4N_{24}O_{12}$ 1561.45 g/mol

Yield 6 mg, 3.8 μmol, 38 %

Mp. 220 °C (decomposition)

^{1}H NMR (500 MHz, DMSO-*d*$_6$): δ [ppm] = 1.18-1.24 (m, 4 H, 2 × Lys-CH_2), 1.44-1.71 (m, 16 H, 4 × Lys-CH_2, 4 × Arg-CH_2), 2.63-2.74 (m, 4 H, 2 × Lys-CH_2), 2.89-3.20 (m, 8 H, 2 × Arg-CH_2, 2 × Trp-CH_2), 3.71-3.72 (m, 4 H, 2 × Gly-CH_2), 4.16-4.20 (m, 4 H, 2 × Lys-CH, 2 × Arg-CH), 4.46-4.51 (m, 2 H, 2 × Trp-CH), 6.94-6.98 (m, 2 H, 2 × Trp-CH_{ar}), 7.04 (t, *J* = 7.3 Hz, 2 H, 2 × Trp-CH_{ar}), 7.12 (s, 2 H, NH_2), 7.16 (s, 2 H, 2 × Trp-CH_{ar}), 7.25-7.26 (m, 2 H, NH_2), 7.31-7.33 (m, 2 H, 2 × Trp-CH_{ar}), 7.54-7.57 (m, 2 H, 2 × Trp-CH_{ar}), 7.62-7.70 (m, 6 H, 6 H, 4 × Phe-CH_{ar}, 2 × NH), 7.86 (brs, 6 H, 2 × Lys-NH_3^+), 8.00-8.17 (m, 6 H, 2 × CH=N, 4 × NH), 8.25-8.30 (m, 2 H, 2 × NH), 10.85 (s, 2 H, 2 × Trp-NH), 11.36 (s, 1 H, NH), 11.64 (s, 1 H, NH).

^{13}C NMR (125 MHz, DMSO-*d*$_6$): δ [ppm] = 22.08 (Lys-CH_2), 24.94 (Arg-CH_2), 26.48 (Lys-CH_2), 27.11 (Trp-CH_2), 27.50 (CH_2), 29.09 (Arg-CH_2), 30.88 (Lys-CH_2), 38.48 (Lys-CH_2), 40.34 (Arg-CH_2), 42.35 (Gly-CH_2), 52.06 (Arg-CH), 52.72 (Lys-CH), 53.82 (Trp-CH), 109.91 (Trp-C_q), 111.26 (Trp-CH_{ar}), 118.23 (Trp-CH_{ar}), 118.29 (Trp-CH_{ar}), 120.84 (Trp-CH_{ar}), 123.61 (Trp-CH_{ar}), 126.99 (Phe-CH_{ar}), 127.18 (Trp-C_q), 135.50 (Phe-C_q), 136.03 (Trp-C_q), 142.19 (CH=N), 156.80 (Gua-C_q), 169.57 (CO), 171.23 (CO), 171.62 (CO), 171.94 (CO), 172.29 (CO), 173.21 (CO), 173.63 (CO).

HRMS (ESI): m/z calculated for $C_{66}H_{97}N_{24}O_{12}^{3+}$ $[M+3H]^{3+}$: 472.5900; found: 472.5863.

FT-IR (ATR): $\tilde{\nu}$ [cm^{-1}] = 3171 (br), 3048 (br), 2925 (br), 1638 (s), 1523 (s), 1231 (w), 1167 (w), 1096 (w), 1024 (w), 952 (w), 745 (m).

Synthesis of acyl hydrazone 147

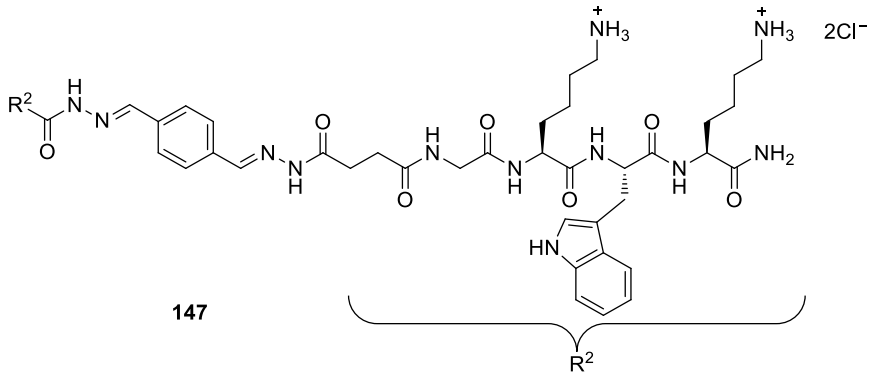

147

The synthesis of acyl hydrazone **147** from di-aldehyde **C** (1.34 mg, 0.01 mmol, 1 eq) and hydrazide **136** (17.6 mg, 0.025 mmol, 2.5 eq) was carried out under analogous above described conditions. After purification steps, **147** was obtained as a white solid with 97 % purity according to analytical HPLC analysis.

$C_{66}H_{98}Cl_4N_{20}O_{12}$ 1505.42 g/mol

Yield 13 mg, 8.6 µmol, 86 %

Mp. 182 °C (decomposition)

^{1}H NMR (500 MHz, DMSO-*d*$_6$): δ [ppm] = 1.17-1.29 (m, 8 H, 4 × Lys-CH_2), 1.48-1.70 (m, 16 H, 8 × Lys-CH_2), 2.69-2.74 (m, 8 H, 4 × Lys-CH_2), 3.04-3.09 (m, 4 H, 2 × Trp-CH_2), 3.72 (s, 4 H, 2 × Gly-CH_2), 4.12-4.21 (m, 4 H, 4 × Lys-CH), 4.47 (s, 2 H, 2 × Trp-CH), 6.94-6.99 (m, 2 H, 2 × Trp-CH_{ar}), 7.03-7.07 (m, 4 H, 2 × Trp-CH_{ar}, NH_2), 7.17-7.20 (m, 4 H, 2 × Trp-CH_{ar}, NH_2), 7.31-7.33 (m, 2 H, 2 × Trp-CH_{ar}), 7.54-7.57 (m, 2 H, 2 × Trp-CH_{ar}), 7.61 (s, 1 H, Phe-CH_{ar}), 7.66 (s, 1 H, Phe-CH_{ar}), 7.70 (s, 1 H, Phe-CH_{ar}), 7.78-7.82 (m, 2 H, 2 × NH), 7.89 (brs, 12 H, 4 × Lys-NH_3^+), 8.00-8.02 (m, 2 H, 2 × CH=N), 8.07-8.34 (m, 6 H, 6 × NH), 10.86 (s, 2 H, 2 × Trp-NH), 11.36 (s, 1 H, NH), 11.65 (s, 1 H, NH).

^{13}C NMR (125 MHz, DMSO-*d*$_6$): δ [ppm] = 22.11 (Lys-CH_2), 26.49 (Lys-CH_2), 26.56 (Lys-CH_2), 27.06 (Trp-CH_2), 27.49 (CH_2), 29.28 (CH_2), 30.02 (CH_2), 30.88 (Lys-CH_2), 31.27 (Lys-CH_2), 38.53 (Lys-CH_2), 38.60 (Lys-CH_2), 42.35 (Gly-CH_2), 52.28 (Lys-CH), 52.78 (Lys-CH), 53.80 (Trp-CH), 109.93 (Trp-C_q), 111.27 (Trp-CH_{ar}), 118.22 (Trp-CH_{ar}), 118.33 (Trp-CH_{ar}), 118.51 (Trp-CH_{ar}), 120.84 (Trp-CH_{ar}), 123.66 (Trp-CH_{ar}), 126.98 (Phe-CH_{ar}), 127.22 (Trp-C_q), 136.03 (Trp-C_q), 142.21 (CH=N), 169.37 (CO), 169.60 (CO), 171.17 (CO), 171.65 (CO), 171.94 (CO), 172.30 (CO), 173.37 (CO), 173.64 (CO).

HRMS (ESI): m/z calculated for $C_{66}H_{97}N_{20}O_{12}^{3+}$ $[M+3H]^{3+}$: 453.9193; found: 453.9185.

FT-IR (ATR): $\tilde{\nu}$ [cm^{-1}] = 3176 (br), 3047 (br), 2925 (br), 1637 (s), 1523 (s), 1340 (w), 1200 (m), 1174 (m), 1128 (m), 1026 (w), 954 (w), 835 (w), 798 (w), 744 (m).

Synthesis of acyl hydrazone 148

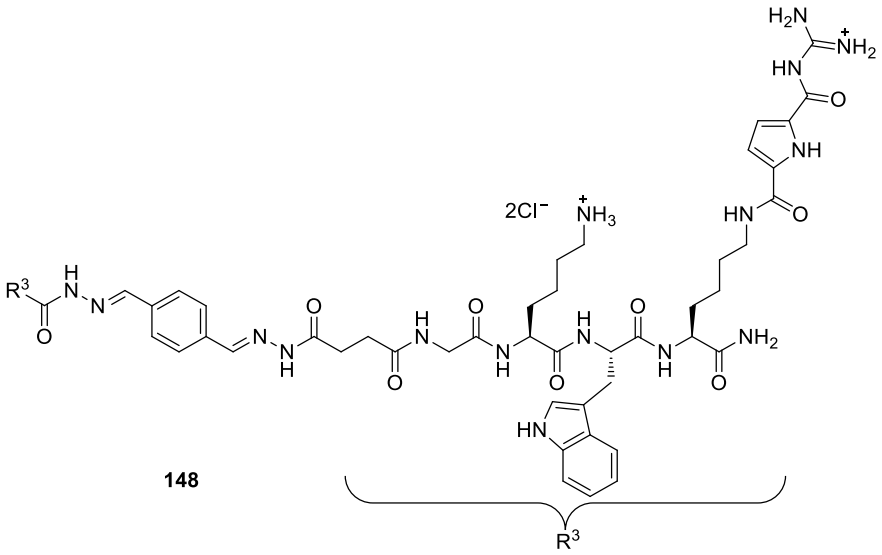

148

The synthesis of acyl hydrazone **148** from di-aldehyde **C** (1.34 mg, 0.01 mmol, 1 eq) and hydrazide **138** (22 mg, 0.025 mmol, 2.5 eq) was carried out under analogous above described conditions. After purification steps, **148** was obtained as a white solid with 93 % purity according to analytical HPLC analysis.

$C_{80}H_{110}Cl_4N_{28}O_{16}$ 1861.72 g/mol

Yield 12 mg, 6.4 μmol, 64 %

Mp. 214 °C (decomposition)

^{1}H NMR (500 MHz, DMSO-*d*$_6$): δ [ppm] = 1.19-1.33 (m, 8 H, 4 × Lys-CH_2), 1.47-1.68 (m, 16 H, 8 × Lys-CH_2), 2.69-2.71 (m, 4 H, 2 × Lys-CH_2), 2.89-3.04(m, 4 H, 2 × Trp-CH_2), 3.16-3.23 (m, 4 H, 2 × Lys-CH_2), 3.71 (s, 4 H, 2 × Gly-CH_2), 4.15-4.19 (m, 4 H, 4 × Lys-CH), 4.48-4.49 (m, 2 H, 2 × Trp-CH), 6.87 (s, 2 H, 2 × GCP-CH_{ar}), 6.95 (t, *J* = 7.5 Hz, 2 H, 2 × Trp-CH_{ar}), 7.02-7.06 (m, 4 H, 2 × Trp-CH_{ar}, NH_2), 7.16 (s, 2 H, 2 × Trp-CH_{ar}), 7.21-7.23 (m, 2 H, NH_2), 7.30-7.32 (m, 2 H, 2 × Trp-CH_{ar}), 7.51 (s, 2 H, 2 × GCP-CH_{ar}), 7.54-7.55 (m, 2 H, 2 × Trp-CH_{ar}), 7.60 (s, 1 H, Phe-CH_{ar}), 7.65 (s, 2 H, 2 × Phe-CH_{ar}), 7.69 (s, 1 H, Phe-CH_{ar}), 7.77-7.81 (m, 2 H, 2 × NH), 7.86 (brs, 6 H, 2 × Lys-NH_3^+), 7.99-8.18 (m, 6 H, 6 × NH), 8.26-8.30 (m, 2 H, 2 × CH=N), 8.46-8.64 (m, 8 H, 8 × NH), 10.84 (s, 2 H, 2 × Trp-NH), 11.35 (s, 1 H, NH), 11.63 (s, 1 H, NH), 12.00 (s, 2 H, 2 × Gua-NH), 12.32 (s, 2 H, 2 × GCP-NH).

^{13}C NMR (125 MHz, DMSO-*d*$_6$): δ [ppm] = 22.09 (Lys-CH_2), 22.75 (Lys-CH_2), 26.48 (Lys-CH_2), 27.19 (Lys-CH_2), 27.52 (Trp-CH_2), 28.71 (Lys-CH_2), 29.30 (CH_2), 30.03 (CH_2), 30.93 (Lys-CH_2), 31.71 (Lys-CH_2), 38.54 (Lys-CH_2), 38.73 (Lys-CH_2), 42.25 (Gly-CH_2), 42.37 (Gly-CH_2), 52.46 (Lys-CH), 52.58 (Lys-CH), 52.69 (Lys-CH), 53.84 (Trp-CH), 109.93 (Trp-C_q), 111.26 (Trp-CH_{ar}), 112.41 (GCP-CH_{ar}), 115.95 (GCP-CH_{ar}), 118.22 (Trp-CH_{ar}), 118.30 (Trp-CH_{ar}), 120.80 (Trp-CH_{ar}), 123.62 (Trp-CH_{ar}), 125.31

(GCP-C_q), 126.96 (Phe-CH_{ar}), 127.21 (Trp-C_q), 132.93 (GCP-Cq), 135.28 (Phe-C_q), 136.01 (Trp-C_q), 142.17 (CH=N), 155.48 (Gua-C_q), 158.99 (CO), 159.62 (CO), 168.22 (CO), 169.23 (CO), 169.44 (CO), 171.14 (CO), 171.57 (CO), 171.90 (CO), 172.27 (CO), 173.49 (CO), 173.63 (CO).

HRMS (ESI): m/z calculated for $C_{80}H_{109}N_{28}O_{16}^{3+}$ $[M+3H]^{3+}$: 572.6187; found: 572.6192.

FT-IR (ATR): $\tilde{\nu}$ [cm^{-1}] = 3273 (br), 3055 (br), 2930 (br), 1643 (s), 1540 (s), 1282 (s), 1197 (m), 953 (w), 815 (w), 746 (m).

Synthesis of acyl hydrazone 149

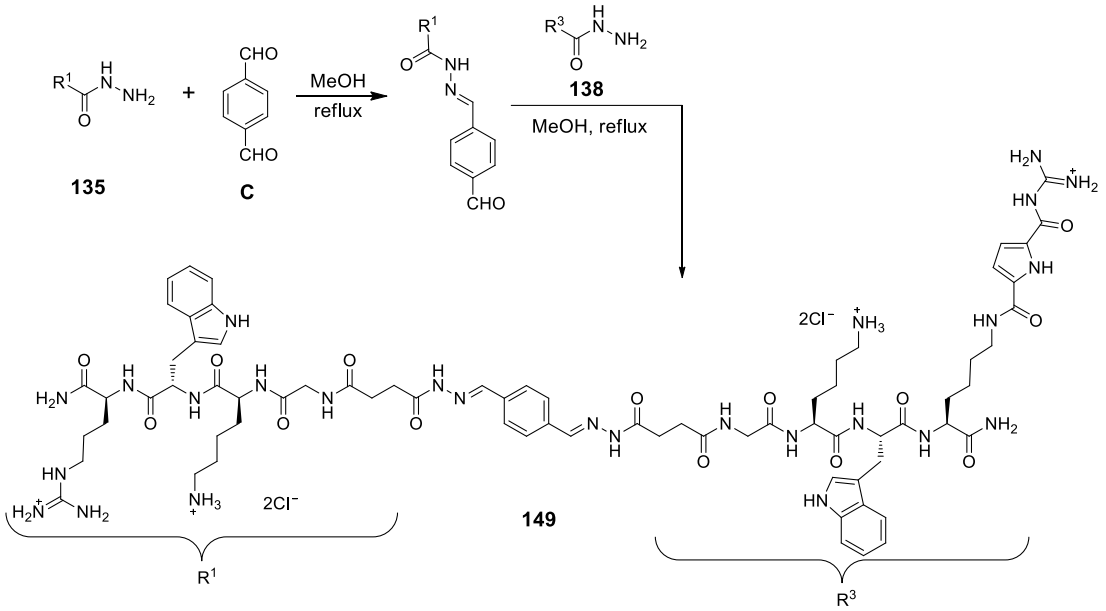

Di-aldehyde **C** (67 mg, 0.5 mmol, 10 eq) and hydrazide **135** (36.6 mg, 0.05 mmol, 1 eq) were dissolved in 10 mL MeOH under argon atmosphere. Then the reaction mixture was refluxed overnight. After the purification by RP18-MPLC, the product of mono-hydrazone with one aldehyde group was obtained, which was then subjected to react with hydrazide **138** by using equimolar amount in 10 mL MeOH under argon atmosphere. The reaction mixture was refluxed overnight and the crude product was purified by RP18-MPLC using appropriate conditions (MeOH/H_2O + 0.1 % TFA). Pure product was transferred into its hydrochloride salt to give **149** as a white solid with 91 % purity according to analytical HPLC analysis.

$C_{73}H_{104}Cl_4N_{26}O_{14}$ 1711.58 g/mol

Yield 3 mg, 1.8 μmol, 18 %

Mp. 210 °C (decomposition)

^{1}H NMR (700 MHz, DMSO-*d*$_6$): δ [ppm] = 1.19-1.30 (m, 6 H, 3 × Lys-CH_2), 1.42-1.71 (m, 16 H, 6 × Lys-CH_2, 2 × Arg-CH_2), 2.69-2.71 (m, 4 H, 2 × Lys-CH_2), 2.91-3.22 (m, 8 H, Lys-CH_2, Arg-CH_2, 2 × Trp-CH_2), 3.72 (s, 4 H, 2 × Gly-CH_2), 4.15-4.23 (m, 4 H, 3 × Lys-CH, Arg-CH), 4.47-4.52 (m, 2 H, 2 × Trp-CH), 6.86 (s, 1 H, GCP-CH_{ar}), 6.95-6.98 (m, 2 H, 2 × Trp-CH_{ar}), 7.02-7.07 (m, 3 H, 2 × Trp-CH_{ar}, NH_2), 7.12 (s, 2 H, NH_2), 7.16-7.17 (m, 2 H, 2 × Trp-CH_{ar}), 7.20-7.26 (m, 2 H, NH_2), 7.31-7.34 (m, 2 H, 2 × Trp-CH_{ar}), 7.47 (s, 1 H, GCP-CH_{ar}), 7.54-7.56 (m, 2 H, 2 × Trp-CH_{ar}), 7.62 (s, 1 H, Phe-CH_{ar}), 7.67-7.71 (m, 3 H, 3 × Phe-CH_{ar}), 7.77-7.91 (m, 8 H, 2 × NH, 2 × Lys-NH_3^+), 7.95-8.19 (m, 6 H, 6 × NH), 8.24-8.33 (m, 2 H, 2 × CH=N), 8.42-8.64 (m, 5 H, 5 × NH), 10.83, (s, 1 H, Trp-NH), 10.85 (s, 1 H, Trp-NH), 11.35 (s, 1 H, NH), 11.62 (d, *J* = 19.7 Hz, 1 H, NH), 11.93 (s, 1 H, Gua-NH), 12.32 (s, 1 H, GCP-NH).

^{13}C NMR (175 MHz, DMSO-*d*$_6$): δ [ppm] = 22.07 (Lys-CH_2), 22.74 (Lys-CH_2), 24.93 (Arg-CH_2), 26.48 (Lys-CH_2), 27.14 (Trp-CH_2), 27.47 (CH_2), 28.71 (Lys-CH_2), 29.05 (Arg-CH_2), 29.27 (CH_2), 30.00 (CH_2), 30.94 (Lys-CH_2), 31.69 (Lys-CH_2), 38.50 (Lys-CH_2), 38.56 (Lys-CH_2), 38.70 (Lys-CH_2), 40.34 (Arg-CH_2), 42.36 (Gly-CH_2), 52.05 (Arg-CH), 52.43 (Lys-CH), 52.60 (Lys-CH), 52.76 (Lys-CH), 53.78 (Trp-CH), 109.92 (Trp-C_q), 111.27 (Trp-CH_{ar}), 112.33 (GCP-CH_{ar}), 115.90 (GCP-CH_{ar}), 118.21 (Trp-CH_{ar}), 118.30 (Trp-CH_{ar}), 120.82 (Trp-CH_{ar}), 123.61 (Trp-CH_{ar}), 125.31 (GCP-C_q), 126.96 (Phe-CH_{ar}), 127.22 (Trp-C_q), 129.91 (Phe-CH_{ar}), 132.99 (GCP-Cq), 135.26 (Phe-C_q), 136.03 (Trp-C_q), 142.17 (CH=N), 156.83 (Gua-C_q), 159.02 (CO), 168.22 (CO), 169.39 (CO), 169.58 (CO), 171.11 (CO), 171.23 (CO), 171.49 (CO), 171.54 (CO), 171.85 (CO), 172.24 (CO), 173.19 (CO), 173.45 (CO), 173.61 (CO).

HRMS (ESI): m/z calculated for $C_{73}H_{103}N_{26}O_{14}^{3+}$ $[M+3H]^{3+}$: 522.6044; found: 522.6066.

FT-IR (ATR): $\tilde{\nu}$ [cm^{-1}] = 3175 (br), 3048 (br), 2930 (br), 1637 (s), 1523 (s), 1232 (w), 1165 (w), 1095 (w), 1011 (w), 952 (w), 744 (m).

6.6 Syntheses of Ligands for Au Nanoparticles

6.6.1 Synthesis of the thioalkylated TEG linker as Precursor for SPPS

Synthesis of Pent-1-en-5-yltriethylene glycol (151)

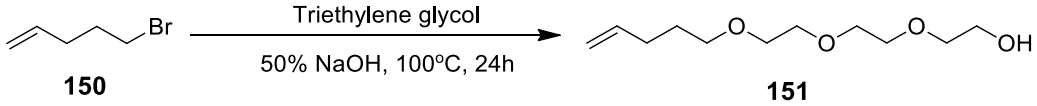

150 **151**

A mixture of 4 ml of 50 % aqueous NaOH (2 g, 50 mmol, 1 eq) and triethylene glycol (75 g, 500 mmol, 10 eq) was stirred for 30 min in an oil bath at 100 °C under an argon atmosphere, and then 5-bromopent-1-ene (**150**) (7.45 g, 50 mmol, 1 eq) was added. The reaction mixture was heated at 100 °C for 24 h. The reaction mixture was cooled and adjusted pH to 7 by using 1 M HCl, diluted with 50mL brine, extracted four times with ethyl acetate. The combined organic layer was dried over $MgSO_4$ and concentrated by rotary evaporation under reduced pressure to give yellow oil containing a mixture of mono- and di-ethers. Purification of the oil by flash chromatography on silica gel (cyclohexane/ethyl acetate = 1/4) to obtain **151** as a clear oil.

$C_{11}H_{22}O_4$ 218.29 g/mol

Yield 7.68 g, 35.2 mmol, 70 %

^{1}H NMR (300 MHz, $CDCl_3$): δ [ppm] = 1.61-1.71 (m, 2 H, CH_2), 2.05-2.12 (m, 2 H, CH_2), 2.63 (br s, 1 H, OH), 3.45 (t, J = 6.6 Hz, 2 H, CH_2), 3.54-3.71 (m, 12 H, 6 × CH_2), 4.91-5.03 (m, 2 H, CH_2), 5.72-5.86 (m, 1 H, CH).

^{13}C NMR (75 MHz, $CDCl_3$): δ [ppm] = 28.83 (CH_2), 30.30 (CH_2), 61.83 (CH_2), 70.17 (CH_2), 70.48 (CH_2), 70.70 (CH_2), 70.74 (CH_2), 70.83 (CH_2), 72.60 (CH_2), 114.79 (CH_2), 138.35 (CH).

HRMS (ESI): m/z calculated for m/z calculated for $C_{11}H_{22}O_4Na^+$ $[M+Na]^+$: 241.1410; found: 241.1425.

FT-IR (ATR): $\tilde{\nu}$ [cm^{-1}] = 3440 (br), 2865 (br), 1100 (s), 1066 (s), 911 (m).

Synthesis of Pent-1-en-5-yltriethylene glycol-acetic acid ethyl ester (152)

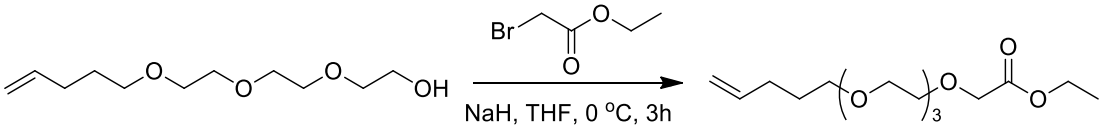

151 **152**

A solution of **151** (4.36 g, 20 mmol, 1 eq), KI (0.66 g, 4 mmol, 0.2 eq) and NaH (50 %, 0.96 g, 20 mmol, 1 eq) in dry THF (30 mL) was stirred at room temperature under argon atmosphere for 30 min and then cooled down to 0 °C. Then ethyl bromoacetate (4.5 mL, 40 mmol, 2 eq) was added and the reaction mixture was stirred for 3 h at 0 °C. The reaction mixture was then adjusted pH to 7.0 by 5 % citric acid aqueous solution and extracted with ethyl acetate (3 × 50 mL). The combined organic layers were dried over $MgSO_4$ and concentrated with a rotatory evaporator under reduced pressure. The brown oil was purified by flash chromatography on silica gel (cyclohexane/ethyl acetate = 2/1) to give **152** as a clear oil.

$C_{15}H_{28}O_6$ 304.38 g/mol

Yield 4.47 g, 14.7 mmol, 73 %

^{1}H NMR (300 MHz, $CDCl_3$): δ [ppm] = 1.25 (t, J = 7.1 Hz, 3 H, CH_3),1.60-1.69 (m, 2 H, CH_2), 2.01-2.12 (m, 2 H, CH_2), 3.44 (t, J = 6.6 Hz, 2 H, CH_2), 3.53-3.72 (m, 12 H, 6 × CH_2), 4.12 (s, 2 H, CH_2), 4.18 (q, J = 7.1 Hz, 2 H, CH_2), 4.89-5.02 (m, 2 H, CH_2), 5.71-5.85 (m, 1 H, CH).

^{13}C NMR (75 MHz, $CDCl_3$): δ [ppm] = 14.27 (CH_3), 28.87 (CH_2), 30.30 (CH_2), 60.83 (CH_2), 68.81 (CH_2), 70.19 (CH_2), 70.67 (CH_2), 70.70 (CH_2), 70.72 (CH_2), 70.77 (CH_2), 70.97 (CH_2), 114.74 (CH_2), 138.35 (CH), 170.52 (CO).

HRMS (ESI): m/z calculated for m/z calculated for $C_{15}H_{28}O_6Na^+$ $[M+Na]^+$: 327.1778; found: 327.1861.

FT-IR (ATR): $\tilde{\nu}$ [cm^{-1}] = 2866 (br), 1752 (m), 1201 (m), 1107 (s), 1030 (m), 912 (m).

Synthesis of Thioacetate (153)

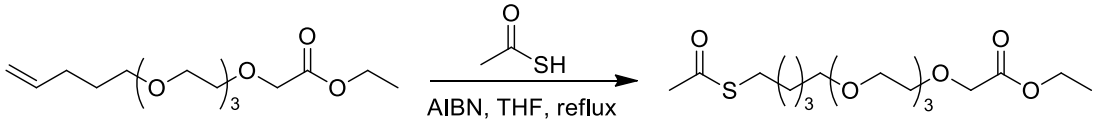

152 **153**

A solutions of **152** (5.33 g, 17.5 mmol, 1 eq) and a catalytic amount of AIBN (863 mg, 5.25 mmol, 0.3 eq) in dry THF (45 mL) was purged with argon for 10 min and heated to reflux, then thioacetic acid (3.12 mL, 43.8 mmol, 2.5 eq) was rapidly added to the reaction mixture and the mixture was kept stirring under reflux overnight. The disappearance of the signal of double bonds (multi peaks at 5-6 ppm) and the appearance of a new single peak of methyl group (at around 2.3 ppm) monitored by ^{1}H NMR indicated the complete reaction. Then the reaction mixture was concentrated under reduced pressure and purified by flash chromatography on silica gel (cyclohexane/ethyl acetate = 2/1) to afford **153** as a colorless oil.

$C_{17}H_{32}O_7S$ 380.50 g/mol

Yield 5.76 g, 15.1 mmol, 86 %

^{1}H NMR (300 MHz, $CDCl_3$): δ [ppm] = 1.28 (t, J = 7.3 Hz, 3 H, CH_3), 1.37-1.45 (m, 2 H, CH_2), 1.53-1.61 (m, 4 H, 2 × CH_2), 2.31 (s, 3 H, CH_3), 2.86 (t, J = 7.2 Hz, 2 H, CH_2), 3.44 (t, J = 6.5 Hz, 2 H, CH_2), 3.54-3.75 (m, 12 H, 6 × CH_2), 4.14 (s, 2 H, CH_2), 4.21 (q, J = 7.1 Hz, 2 H, CH_2).

^{13}C NMR (75 MHz, $CDCl_3$): δ [ppm] = 14.35 (CH_3), 25.52 (CH_2), 29.18 (CH_2), 29.26 (CH_2), 29.50 (CH_2), 30.76 (CH_3), 60.93 (CH_2), 68.88 (CH_2), 70.25 (CH_2), 70.73 (CH_2), 70.77 (CH_2), 71.05 (CH_2), 71.26 (CH_2), 170.61 (CO), 196.08 (CO).

HRMS (ESI): m/z calculated for m/z calculated for $C_{17}H_{32}O_7SNa^+$ $[M+Na]^+$: 403.1761; found: 403.1838.

FT-IR (ATR): $\tilde{\nu}$ [cm^{-1}] = 2864 (br), 1752 (m), 1687 (s), 1201 (m), 1104 (s), 1030 (m), 952 (m).

Synthesis of Thiol (154)

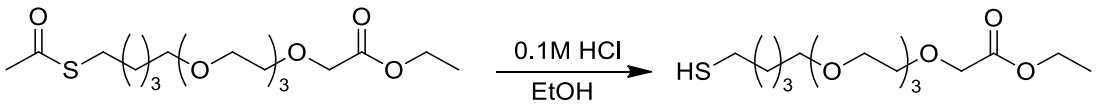

153 **154**

To a solution of **153** (3.8 g, 10 mmol, 1 eq) in absolute ethanol (40 mL) was added an aqueous solution of concentrated HCl (4.0 mL) and the resulting mixture was heated to reflux for 12 h. The ^{1}H NMR of the reaction mixture showed that the single peak of methyl group (at around 2.3 ppm) was disappeared and a new quartet peak (at around 2.5 ppm) was appeared, indicating the completion of the reaction. Then the mixture was cool down to room temperature and adjusted pH to 6 using 1 M NaOH. The solution was partially concentrated, diluted with brine (30 mL) and extracted with dichloromethane (5 × 30 mL). The combined organic layer was dried with $MgSO_4$ and concentrated with a rotatory evaporator under reduced pressure to get pale yellow oil. This product was used immediately to the next step without purification.

Synthesis of Trityl thioether (155)

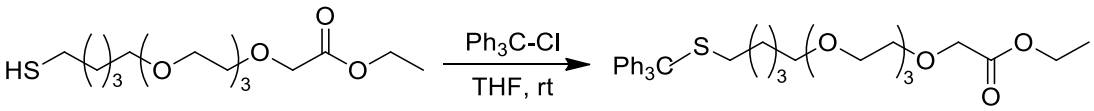

154 **155**

To a solution of **154** (3.38 g, 10 mmol, 1eq) in dry THF (15 mL) was added trityl chloride (8.64 g, 30 mmol, 3eq) under argon atmosphere. The reaction mixture was stirred at room temperature (2-4 days) until complete disappearance of **154** as monitored by ^{1}H NMR (quartet peaks at 2.5 ppm). If necessary, 2 eq of trityl chloride was added and the mixture was stirred for another two days to complete the reaction. Then the reaction mixture was concentrated with a rotatory evaporator under reduced pressure and purified by flash chromatography on silica gel (cyclohexane/ethyl acetate = 2/1) to give **155** as a clear oil.

$C_{34}H_{44}O_6S$ 580.77 g/mol

Yield 4.1 g, 7 mmol, 70 % (over last two steps)

^{1}H NMR (300 MHz, $CDCl_3$): δ [ppm] = 1.27 (t, *J* = 7.1 Hz, 3 H, CH_3), 1.34-1.47 (m, 6 H, 3 × CH_2), 2.13 (t, *J* = 7.2 Hz, 2 H, CH_2), 3.35 (t, *J* = 6.5 Hz, 2 H, CH_2), 3.51-3.72 (m, 12 H, 6 × CH_2), 4.13 (s, 2 H, CH_2), 4.20 (q, *J* = 7.1 Hz, 2 H, CH_2), 7.15-7.30 (m, 10 H, 10 × CH_{ar}), 7.37-7.41 (m, 5 H, 5 × CH_{ar}).

^{13}C NMR (75 MHz, $CDCl_3$): δ [ppm] = 14.36 (CH_3), 25.74 (CH_2), 28.60 (CH_2), 29.35 (CH_2), 32.07 (CH_2), 60.92 (CH_2), 66.54 (C_q), 68.90 (CH_2), 70.22 (CH_2), 70.73 (CH_2), 70.77 (CH_2), 70.79 (CH_2), 71.05 (CH_2), 71.32 (CH_2), 126.65 (CH_{ar}), 127.94 (CH_{ar}), 129.74 (CH_{ar}), 145.19 (C_q), 170.60 (CO).

HRMS (ESI): m/z calculated for m/z calculated for $C_{34}H_{44}O_6SNa^+$ $[M+Na]^+$: 603.2751; found: 603.2799.

FT-IR (ATR): $\tilde{\nu}$ [cm^{-1}] = 2862 (br), 1751 (m), 1444 (m), 1202 (m), 1108 (s), 1032 (m), 742 (s), 699 (s).

Synthesis of Trityl-protected thioalkylated TEG acetic acid (156)

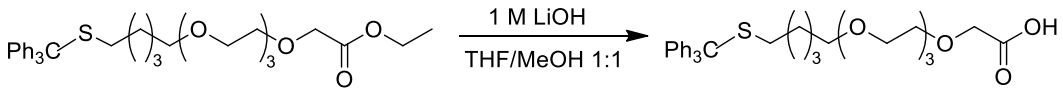

155 **156**

To a solution of **155** (2.9 g, 5 mmol, 1 eq) in 1:1 THF/MeOH (50 mL) was added aqueous solution of lithium hydroxide (240 mg, 10 mmol in 10 mL H_2O). The reaction mixture was stirred at room temperature for 12 h. The solution was acidified to pH 1 with 1 M HCl, diluted with brine (20 mL) and extracted with dichloromethane (4 × 30 mL). The combined organic layers were washed with brine (20 mL), dried over $MgSO_4$ and concentrated with a rotatory evaporator under reduced pressure to afford **156** as a pale yellow oil.

$C_{32}H_{40}O_6S$ 552.72 g/mol

Yield 2.7 g, 4.9 mmol, 98 %

^{1}H NMR (300 MHz, $CDCl_3$): δ [ppm] = 1.22-1.47 (m, 6 H, 3 × CH_2), 2.12 (t, J = 7.2 Hz, 2 H, CH_2), 3.37 (t, J = 6.6 Hz, 2 H, CH_2), 3.54-3.74 (m, 12 H, 6 × CH_2), 4.12 (s, 2 H, CH_2), 7.16-7.28 (m, 10 H, 10 × CH_{ar}), 7.37-7.41 (m, 5 H, 5 × CH_{ar}).

^{13}C NMR (75 MHz, $CDCl_3$): δ [ppm] = 25.66 (CH_2), 28.56 (CH_2), 29.18 (CH_2), 32.06 (CH_2), 66.54 (C_q), 69.26 (CH_2), 70.27 (CH_2), 70.48 (CH_2), 70.56 (CH_2), 70.83 (CH_2), 71.35 (CH_2), 71.76 (CH_2), 126.65 (CH_{ar}), 127.94 (CH_{ar}), 129.73 (CH_{ar}), 145.18 (C_q), 172.03 (CO).

HRMS (ESI): m/z calculated for m/z calculated for $C_{32}H_{40}O_6SNa^+$ $[M+Na]^+$: 575.2438; found: 575.2537.

FT-IR (ATR): $\tilde{\nu}$ [cm^{-1}] = 2862 (br), 1736 (m), 1443 (m), 1105 (s), 1032 (m), 741 (s), 699 (s).

6.6.2 Synthesis of the thioalkylated TEG ligand

Synthesis of Alkylated thioacetate (157)

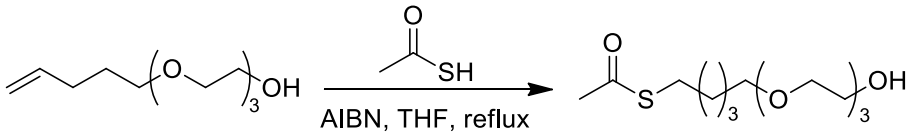

151 **157**

A solutions of **151** (650 mg, 3 mmol, 1 eq) and a catalytic amount of AIBN (148 mg, 0. 9 mmol, 0.3 eq) in dry THF (20 mL) was heated to reflux, then thioacetic acid (535 µL, 7.5 mmol, 2.5 eq) was added to the reaction mixture and the mixture was refluxed overnight. The reaction mixture was concentrated with a rotatory evaporator under reduced pressure and purified by flash chromatography on silica gel (cyclohexane/ethyl acetate = 1/1) to afford **157** as a clear oil.

$C_{13}H_{26}O_5S$ 294.41 g/mol

Yield 640 mg, 2.17 mmol, 72 %

^{1}H NMR (300 MHz, $CDCl_3$): δ [ppm] = 1.33-1.44 (m, 2 H, CH_2), 1.51-1.62 (m, 4 H, 2 × CH_2), 2.29 (s, 3 H, CH_3), 2.59 (br s, 1 H, OH), 2.84 (t, J = 7.3 Hz, 2 H, CH_2), 3.42 (t, J = 6.6 Hz, 2 H, CH_2), 3.54-3.71 (m, 12 H, 6 × CH_2).

^{13}C NMR (75 MHz, $CDCl_3$): δ [ppm] = 25.01 (CH_2), 28.68 (CH_2), 28.73 (CH_2), 29.01 (CH_2), 30.28 (CH_3), 61.40 (CH_2), 69.74 (CH_2), 70.04 (CH_2), 70.26 (CH_2), 70.30 (CH_2), 70.80 (CH_2), 72.17 (CH_2), 195.61 (CO).

HRMS (ESI): m/z calculated for m/z calculated for $C_{13}H_{26}O_5SNa^+$ $[M+Na]^+$: 317.1393; found: 317.1429.

FT-IR (ATR): $\tilde{\nu}$ [cm^{-1}] = 2928 (br), 2864 (br), 1752 (m), 1687 (s), 1201 (m), 1104 (s), 1030 (m), 952 (m).

Synthesis of Alkylated thiol (158)

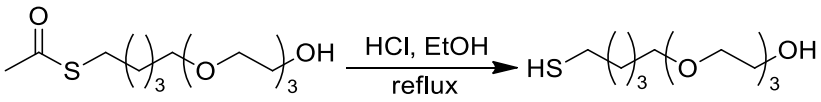

157 **158**

A solution of **157** (640 mg, 2.17 mmol, 1 eq) in methanol (20 mL) was purged with argon for 10 min, then an aqueous solution of concentrated HCl (2 mL) was added to the solution and the resulting mixture was heated to reflux overnight. Then the reaction mixture was cooled to room temperature and adjusted pH to 6 using 1 M NaOH. The solution was diluted with brine (20 mL) and extracted with dichloromethane (3 × 30 mL). The combined organic phases were dried over $MgSO_4$ and concentrated was concentrated with a rotatory evaporator under reduced pressure and purified by flash chromatography on silica gel (cyclohexane/ethyl acetate = 1/1) to afford **158** as a clear oil.

$C_{11}H_{24}O_4S$ 252.37 g/mol

Yield 450 mg, 1.78 mmol, 82 %

^{1}H NMR (300 MHz, $CDCl_3$): δ [ppm] = 1.33 (t, *J* = 7.8 Hz, 1 H, SH), 1.40-1.48 (m, 2 H, CH_2), 1.54-1.67 (m, 4 H, 2 × CH_2), 2.52 (q, *J* = 7.3 Hz, 2 H, CH_2), 3.45 (t, *J* = 6.5 Hz, 2 H, CH_2), 3.56-3.72 (m, 12 H, 6 × CH_2).

^{13}C NMR (75 MHz, $CDCl_3$): δ [ppm] = 24.66 (CH_2), 25.04 (CH_2), 29.15 (CH_2), 33.95 (CH_2), 61.90 (CH_2), 70.22 (CH_2), 70.51 (CH_2), 70.75 (CH_2), 70.77 (CH_2), 71.34 (CH_2), 72.60 (CH_2).

HRMS (ESI): m/z calculated for m/z calculated for $C_{11}H_{24}O_4SNa^+$ $[M+Na]^+$: 275.1288; found: 275.1315.

FT-IR (ATR): $\tilde{\nu}$ [cm^{-1}] = 2930 (br), 2861 (br), 1455 (w), 1350 (w), 1289 (w), 1247 (w), 1097 (s), 1066 (s), 933 (w), 885 (w).

6.6.3 Microwave-Assited SPPS of Thiolalkylated Peptide Ligands

Synthesis of Thiolalkylated Peptide Ligand (161)

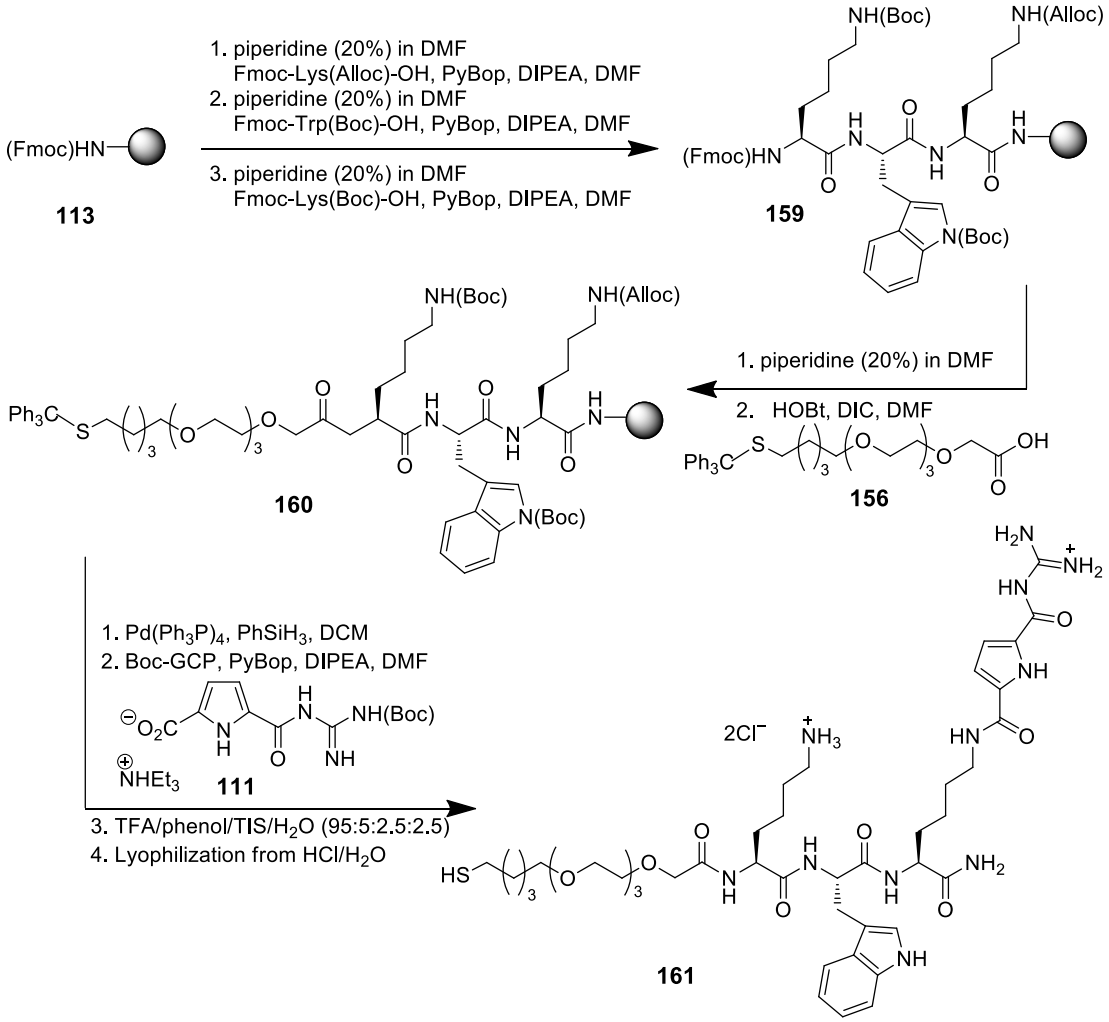

The synthesis of **161** was carried out on Rink amide MBHA resin (200 mg, 0.84 mmol/g, 0.168 mmol, 1 eq) according to the standard microwave-assisted SPPS procedure described in Chapter 6.2.2. The resin was swollen in DCM (10 mL) for 2 h, followed by the removal of Fmoc protecting group with 20 % piperidine/DMF. After a washing cycle with DMF, the first amino acid Fmoc-Lys(Alloc)-OH (228 mg, 0.504 mmol, 3 eq) was attached to the resin with the coupling reagent PyBop (262 mg, 0.504 mmol, 3 eq) and the base DIPEA (171 µL, 1.008 mmol, 6 eq) in DMF (5 mL) by microwave irradiation for 20 min. The coupling was repeated and a negative *Kaiser* test confirmed the complete reaction. After the Fmoc deprotection, the Fmoc-Trp(Boc)-OH (265 mg, 0.504 mmol, 3 eq) and Fmoc-Lys(Boc)-OH (236 mg, 0.504 mmol, 3 eq) were coupled in the same manner. Then, after the Fmoc deprotection, the thiolalkylated TEG linker (**156**) (278 mg, 0.504 mmol, 3 eq) was coupled to the resin with the help of DIC (95 µL, 0.605 mmol, 3.6 eq) and HOBt (102 mg, 0.756 mmol, 4.5 eq) in DMF. After the removal of Alloc protecting group with $Pd(PPh_3)_4$ (19.4 mg, 0.0168 mmol, 0.1 eq) in the presence of $PhSiH_3$ (495 µL,

4.032 mmol, 24 eq) in DCM, the Boc-GCP group (**111**) (200 mg, 0.504 mmol, 3 eq) was coupled. After the final washing cycles, the cleavage of the product from the resin was carried out without microwave irradiation by using a mixture of TFA/phenol/H_2O/TIS (95:5:2.5:2.5) according to the general procedure for Rink amide MBHA resin. The crude product was purified by RP18-MPLC using appropriate conditions (MeOH/H_2O + 0.1 % TFA). Pure product was transferred into its hydrochloride salt by dissolving in water with hydrochloric acid and lyophilizing three times to give **161** as a white solid with 95 % purity according to analytical HPLC analysis.

$C_{43}H_{69}Cl_2N_{11}O_{10}S$ 1003.05 g/mol

Yield 49 mg, 48.8 μmol, 29 %

Mp. 146 °C

^{1}H NMR (500 MHz, DMSO-*d*$_6$): δ [ppm] = 1.13-1.38 (m, 6 H, 2 × Lys-CH_2, CH_2), 1.46-1.70 (m, 12 H, 4 × Lys-CH_2, 2 × CH_2), 2.46-2.48 (m, 2 H, CH_2), 2.66-2.76 (m, 2 H, Lys-CH_2), 2.95-2.99, 3.14-3.23 (m, 4 H, Lys-CH_2, Trp-CH_2), 3.34 (t, *J* = 6.3 Hz, 2 H, CH_2), 3.43-3.54 (m, 12 H, 6 × CH_2), 3.88 (s, 2 H, CH_2), 4.16-4.21 (m, 1 H, Lys-CH), 4.28-4.32 (m, 1 H, Lys-CH), 4.53-4.57 (m, 1 H, Trp-CH), 6.86-6.87 (m, 1 H, Pyr-CH_{ar}), 6.95 (t, *J* = 7.4 Hz, 1 H, Trp-CH_{ar}), 7.03-7.05 (m, 2 H, Trp-CH_{ar}, NH_2), 7.13 (s, 1 H, Trp-CH_{ar}), 7.28 (s, 1 H, NH_2), 7.31 (d, *J* = 8.2 Hz, 1 H, Trp-CH_{ar}), 7.51-7.62 (m, 3 H, GCP-CH_{ar}, Trp-CH_{ar}, NH), 7.84 (brs, 3 H, Lys-NH_3^+), 7.90 (d, *J* = 8.1 Hz,, 1 H, NH), 8.22 (d, *J* = 7.8 Hz,, 1 H, NH), 8.45-8.65 (m, 5 H, 5 × NH), 10.84 (s, 1 H, Trp-NH), 12.01 (s, 1 H, Gua-NH), 12.32 (s, 1 H, Pyr-NH).

^{13}C NMR (125 MHz, DMSO-*d*$_6$): δ [ppm] = 22.03 (Lys-CH_2), 22.71 (Lys-CH_2), 25.26 (CH_2), 26.59 (Lys-CH_2), 27.37 (Trp-CH_2), 27.52 (CH_2), 28.72 (Lys-CH_2), 28.80 (CH_2), 29.28 (CH_2), 31.66 (Lys-CH_2), 31.83 (Lys-CH_2), 38.59 (Lys-CH_2), 38.73 (Lys-CH_2), 51.70 (Lys-CH), 52.34 (Lys-CH), 53.53 (Trp-CH), 69.42 (CH_2), 69.50 (CH_2), 69.73 (CH_2), 70.17 (CH_2), 70.22 (CH_2), 109.86 (Trp-C_q), 111.22 (Trp-CH_{ar}), 112.38 (Pyr-CH_{ar}), 115.95 (Pyr-CH_{ar}), 118.18 (Trp-CH_{ar}), 118.39 (Trp-CH_{ar}), 120.79 (Trp-CH_{ar}), 123.55 (Trp-CH_{ar}), 125.29 (Pyr-C_q), 127.25 (Trp-C_q), 132.93 (Pyr-Cq), 136.00 (Trp-C_q), 155.46 (Gua-C_q), 158.97 (CO), 159.62 (CO), 169.05 (CO), 171.06 (CO), 171.10 (CO), 173.41 (CO).

HRMS (ESI): m/z calculated for $C_{43}H_{68}N_{11}O_{10}S^+$ $[M+H]^+$: 930.4866; found: 930.4952.

FT-IR (ATR): $\tilde{\nu}$ [cm^{-1}] = 3172 (br), 3056 (br), 2925 (br), 2865 (br), 1645 (s), 1523 (m), 1456 (w), 1346 (w), 1235 (w), 1088 (s), 742 (m).

Synthesis of Thiolalkylated Peptide Ligand (162)

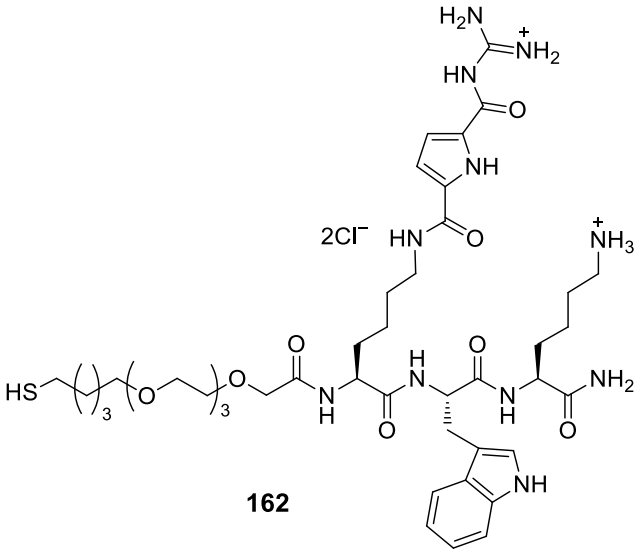

162

The peptide ligand **162** was synthesized accordingly on Rink amide MBHA resin (200 mg, 0.84 mmol/g, 0.168 mmol, 1 eq) following the above described microwave-assisted SPPS procedure. The coupling reagent PyBop (262 mg, 0.504 mmol, 3 eq) and the base DIPEA (171 µL, 1.008 mmol, 6 eq) in DMF (5 mL) were used for coupling the amino acids, whereas DIC (95 µL, 0.605 mmol, 3.6 eq) and HOBt (102 mg, 0.756 mmol, 4.5 eq) were used for the attachment of the thiolalkylated TEG linker (**156**). After Fmoc deprotection, the amino acids Fmoc-Lys(Boc)-OH (236 mg, 0.504 mmol, 3 eq), Fmoc-Trp(Boc)-OH (265 mg, 0.504 mmol, 3 eq), Fmoc-Lys(Alloc)-OH (228 mg, 0.504 mmol, 3 eq) and thiolalkylated TEG linker (**156**) (278 mg, 0.504 mmol, 3 eq) were coupled. After the removal of Alloc protecting group with $Pd(PPh_3)_4$ (19.4 mg, 0.0168 mmol, 0.1 eq) in the presence of $PhSiH_3$ (495 µL, 4.032 mmol, 24 eq) in DCM, the Boc-GCP group (**111**) (200 mg, 0.504 mmol, 3 eq) was coupled. After the cleavage and purification steps, the product was obtained as a white solid with 91 % purity according to analytical HPLC analysis.

$C_{43}H_{69}Cl_2N_{11}O_{10}S$	1003.05 g/mol
Yield	47 mg, 46.8 µmol, 28 %
Mp.	148 °C

^{1}H NMR (500 MHz, DMSO-d_6): δ [ppm] = 1.12-1.38 (m, 6 H, 2 × Lys-CH_2, CH_2), 1.45-1.71 (m, 12 H, 4 × Lys-CH_2, 2 × CH_2), 2.48 (t, J = 7.3 Hz, 2 H, CH_2), 2.72-2.77 (m, 2 H, Lys-CH_2), 2.97-3.02, 3.14-3.21 (m, 4 H, Lys-CH_2, Trp-CH_2), 3.34 (t, J = 6.5 Hz, 2 H, CH_2), 3.44-3.55 (m, 12 H, 6 × CH_2), 3.89 (s, 2 H, CH_2), 4.16-4.20 (m, 1 H, Lys-CH), 4.28-4.32 (m, 1 H, Lys-CH), 4.52-4.56 (m, 1 H, Trp-CH), 6.86-6.87 (m, 1 H, Pyr-CH_{ar}), 6.96 (t, J = 7.4 Hz, 1 H, Trp-CH_{ar}), 7.03-7.07 (m, 2 H, Trp-CH_{ar}, NH_2), 7.15 (s, 1 H, Trp-CH_{ar}), 7.25 (s, 1 H, NH_2), 7.31 (d, J = 8.1 Hz, 1 H, Trp-CH_{ar}), 7.54-7.55 (m, 1 H,

Pyr-CH_{ar}), 7.58 (d, *J* = 8.0 Hz, 1 H, Trp-CH_{ar}), 7.63 (d, *J* = 8.3 Hz, 1 H, NH), 7.87 (brs, 3 H, Lys-NH_3^+), 7.92 (d, *J* = 8.2 Hz,, 1 H, NH), 8.19 (d, *J* = 7.8 Hz,, 1 H, NH), 8.47-8.67 (m, 5 H, 5 × NH), 10.85 (s, 1 H, Trp-NH), 12.06 (s, 1 H, Gua-NH), 12.33 (s, 1 H, Pyr-NH).

^{13}C NMR (125 MHz, DMSO-*d*$_6$): δ [ppm] = 22.07 (Lys-CH_2), 22.72 (Lys-CH_2), 25.26 (CH_2), 26.57 (Lys-CH_2), 27.26 (Trp-CH_2), 27.52 (CH_2), 28.71 (Lys-CH_2), 28.79 (CH_2), 29.28 (CH_2), 31.39 (Lys-CH_2), 31.84 (Lys-CH_2), 38.59 (Lys-CH_2), 38.66 (Lys-CH_2), 52.01 (Lys-CH), 52.15 (Lys-CH), 53.49 (Trp-CH), 69.42 (CH_2), 69.48 (CH_2), 69.67 (CH_2), 69.71 (CH_2), 69.73 (CH_2), 70.17 (CH_2), 109.85 (Trp-C_q), 111.23 (Trp-CH_{ar}), 112.36 (Pyr-CH_{ar}), 115.97 (Pyr-CH_{ar}), 118.17 (Trp-CH_{ar}), 118.40 (Trp-CH_{ar}), 120.80 (Trp-CH_{ar}), 123.56 (Trp-CH_{ar}), 125.29 (Pyr-C_q), 127.27 (Trp-C_q), 132.95 (Pyr-Cq), 136.00 (Trp-C_q), 155.49 (Gua-C_q), 158.95 (CO), 159.63 (CO), 169.15 (CO), 171.06 (CO), 171.36 (CO), 173.27 (CO).

HRMS (ESI): m/z calculated for $C_{43}H_{68}N_{11}O_{10}S^+$ $[M+H]^+$: 930.4866; found: 930.4730.

FT-IR (ATR): $\tilde{\nu}$ [cm^{-1}] = 3169 (br), 3051 (br), 2918 (br), 2860 (br), 1645 (s), 1525 (m), 1456 (w), 1347 (w), 1234 (w), 1090 (s), 743 (m).

Synthesis of Thiolalkylated Peptide Ligand (163)

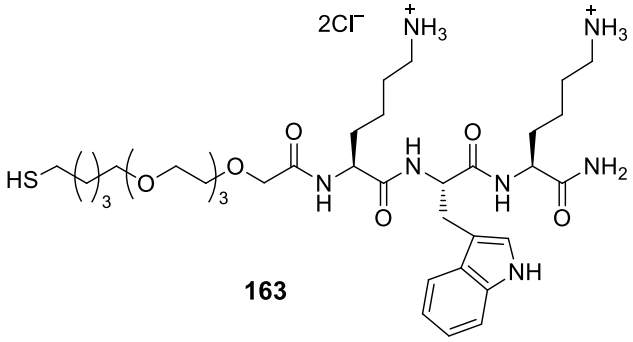

163

The peptide ligand **163** was synthesized accordingly on Rink amide MBHA resin (200 mg, 0.84 mmol/g, 0.168 mmol, 1 eq) following the above described microwave-assisted SPPS procedure. The coupling reagent PyBop (262 mg, 0.504 mmol, 3 eq) and the base DIPEA (171 µL, 1.008 mmol, 6 eq) in DMF (5 mL) were used for coupling the amino acids, whereas DIC (95 µL, 0.605 mmol, 3.6 eq) and HOBt (102 mg, 0.756 mmol, 4.5 eq) were used for the attachment of the thiolalkylated TEG linker (**156**). After Fmoc deprotection, the amino acids Fmoc-Lys(Boc)-OH (236 mg, 0.504 mmol, 3 eq), Fmoc-Trp(Boc)-OH (265 mg, 0.504 mmol, 3 eq), Fmoc-Lys(Boc)-OH (236 mg, 0.504 mmol, 3 eq) and thiolalkylated TEG linker (**156**) (278 mg, 0.504 mmol, 3 eq) were coupled. After the cleavage and purification steps, the product was obtained as a white solid with 94 % purity according to analytical HPLC analysis.

$C_{36}H_{63}Cl_2N_7O_8S$ 824.90 g/mol

Yield 62 mg, 75.2 µmol, 45 %

Mp. 92 °C

^{1}H NMR (500 MHz, DMSO-*d*$_6$): δ [ppm] = 1.13-1.70 (m, 18 H, 6 × Lys-CH_2, 3 × CH_2), 2.47-2.48 (m, 2 H, CH_2), 2.67-2.77 (m, 4 H, 2 × Lys-CH_2) 2.97-3.02, 3.14-3.18 (m, 2 H, Trp-CH_2), 3.35 (t, *J* = 6.6 Hz, 2 H, CH_2), 3.44-3.55 (m, 12 H, 6 × CH_2), 3.90 (s, 2 H, CH_2), 4.16-4.20 (m, 1 H, Lys-CH), 4.27-4.31 (m, 1 H, Lys-CH), 4.52-4.56 (m, 1 H, Trp-CH), 6.96 (t, *J* = 7.5 Hz, 1 H, Trp-CH_{ar}), 7.03-7.07 (m, 2 H, Trp-CH_{ar}, NH_2), 7.15 (s, 1 H, Trp-CH_{ar}), 7.30-7.32 (m, 2 H, Trp-CH_{ar}, NH_2), 7.58 (d, *J* = 7.9 Hz, 1 H, Trp-CH_{ar}), 7.65 (d, *J* = 8.2 Hz, 1 H, NH), 7.93 (d, *J* = 8.2 Hz, 1 H, NH), 7.98 (brs, 6 H, 2 × Lys-NH_3^+), 8.28 (d, *J* = 7.9 Hz,, 1 H, NH), 10.88 (s, 1 H, Trp-NH).

^{13}C NMR (125 MHz, DMSO-*d*$_6$): δ [ppm] = 22.04 (Lys-CH_2), 22.07 (Lys-CH_2), 25.27 (CH_2), 26.54 (Lys-CH_2), 26.56 (Lys-CH_2), 27.28 (Trp-CH_2), 27.52 (CH_2), 28.80 (CH_2), 29.28 (CH_2), 31.40 (Lys-CH_2), 31.61 (Lys-CH_2), 38.49 (Lys-CH_2), 38.51 (Lys-CH_2), 51.82 (Lys-CH), 52.14 (Lys-CH), 53.60 (Trp-CH), 69.43 (CH_2), 69.50 (CH_2), 69.69 (CH_2), 69.73 (CH_2), 70.17 (CH_2), 70.19 (CH_2), 109.86 (Trp-C_q), 111.23 (Trp-CH_{ar}), 118.17 (Trp-CH_{ar}), 118.40 (Trp-CH_{ar}), 120.80 (Trp-CH_{ar}), 123.56 (Trp-CH_{ar}), 127.24 (Trp-C_q), 136.00 (Trp-C_q), 169.10 (CO), 171.09 (CO), 171.17 (CO), 173.29 (CO).

HRMS (ESI): m/z calculated for $C_{36}H_{62}N_7O_8S^+$ $[M+H]^+$: 752.4375; found: 752.4376.

FT-IR (ATR): $\tilde{\nu}$ [cm^{-1}] = 3172 (br), 3051 (br), 2924 (br), 2860 (br), 1644 (s), 1525 (m), 1456 (w), 1346 (w), 1234 (w), 1088 (s), 743 (m).

Synthesis of Thiolalkylated Peptide Ligand (164)

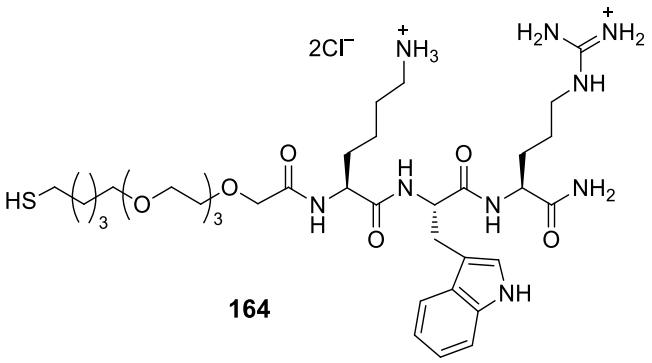

164

The peptide ligand **164** was synthesized accordingly on Rink amide MBHA resin (200 mg, 0.84 mmol/g, 0.168 mmol, 1 eq) following the above described microwave-assisted SPPS procedure. The coupling reagent PyBop (262 mg, 0.504 mmol, 3 eq) and the base DIPEA (171 µL, 1.008 mmol, 6 eq) in DMF (5 mL) were used for coupling the amino acids, whereas DIC (95 µL, 0.605 mmol, 3.6 eq) and HOBt (102 mg, 0.756 mmol, 4.5 eq) were used for the attachment of the thiolalkylated TEG linker (**156**). After Fmoc deprotection, the amino acids Fmoc-Arg(pbf)-OH (327 mg, 0.504 mmol, 3 eq), Fmoc-Trp(Boc)-OH (265 mg, 0.504 mmol, 3 eq), Fmoc-Lys(Boc)-OH (236 mg, 0.504 mmol, 3 eq) and thiolalkylated TEG linker (**156**) (278 mg, 0.504 mmol, 3 eq) were coupled. After the cleavage and purification steps, the product was obtained as a white solid with 95 % purity according to analytical HPLC analysis.

$C_{36}H_{63}Cl_2N_9O_8S$ 852.91 g/mol

Yield 34 mg, 40 µmol, 24 %

Mp. 93 °C

^{1}H NMR (500 MHz, DMSO-*d*$_6$): δ [ppm] = 1.16-1.73 (m, 16 H, 3 × Lys-CH_2, 2 × Arg-CH_2, 3 × CH_2), 2.67-2.73 (m, 4 H, CH_2, Lys-CH_2), 2.97-3.18 (m, 4 H, Arg-CH_2, Trp-CH_2), 3.35-3.37 (m, 2 H, CH_2), 3.44-3.56 (m, 12 H, 6 × CH_2), 3.89 (s, 2 H, CH_2), 4.19-4.23 (m, 1 H, Lys-CH), 4.26-4.31 (m, 1 H, Arg-CH), 4.52-4.56 (m, 1 H, Trp-CH), 6.96 (t, *J* = 7.5 Hz, 1 H, Trp-CH_{ar}), 7.04 (t, *J* = 7.5 Hz, 1 H, Trp-CH_{ar}), 7.12-7.15 (m, 2 H, Trp-CH_{ar}, NH_2), 7.31 (d, *J* = 8.0 Hz, 1 H, Trp-CH_{ar}), 7.37 (s, 1 H, NH_2), 7.58 (d, *J* = 7.8 Hz, 1 H, Trp-CH_{ar}), 7.63 (d, *J* = 8.0 Hz, 1 H, NH), 7.79 (t, *J* = 5.6 Hz, 1 H, NH), 7.95-7.98 (m, 4 H, Lys-NH_3^+, NH), 8.27 (d, *J* = 8.1 Hz,, 1 H, NH), 10.88 (s, 1 H, Trp-NH).

^{13}C NMR (125 MHz, DMSO-*d*$_6$): δ [ppm] =δ [ppm] = 22.03 (Lys-CH_2), 24.49 (CH_2), 24.92 (Arg-CH_2), 26.54 (Lys-CH_2), 27.37 (Trp-CH_2), 28.36 (CH_2), 28.75 (CH_2), 29.21 (Arg-CH_2), 31.57 (Lys-CH_2), 37.72 (Lys-CH_2), 38.50 (Arg-CH_2), 51.81 (Lys-CH), 51.90 (Arg-CH), 53.65 (Trp-CH), 69.43 (CH_2), 69.50 (CH_2), 69.68 (CH_2), 69.73 (CH_2), 70.12 (CH_2), 70.19 (CH_2), 109.83 (Trp-C_q), 111.25 (Trp-CH_{ar}), 118.20 (Trp-CH_{ar}), 118.38 (Trp-CH_{ar}), 120.80 (Trp-CH_{ar}), 123.57 (Trp-CH_{ar}), 127.24 (Trp-C_q), 136.00 (Trp-C_q),

156.89 (Gua-C_q), 169.10 (CO), 171.18 (CO), 173.16 (CO).

HRMS (ESI): m/z calculated for $C_{72}H_{122}N_{18}O_{16}S_2^{2+}$ $[M+H]^{2+}$: 779.4358; found: 779.4366 (disulfide).

FT-IR (ATR): $\tilde{\nu}$ [cm^{-1}] = 3173 (br), 3051 (br), 2918 (br), 2865 (br), 1647 (s), 1525 (m), 1456 (w), 1345 (w), 1240 (w), 1085 (s), 744 (m).

Synthesis of Thiolalkylated Peptide Ligand (165)

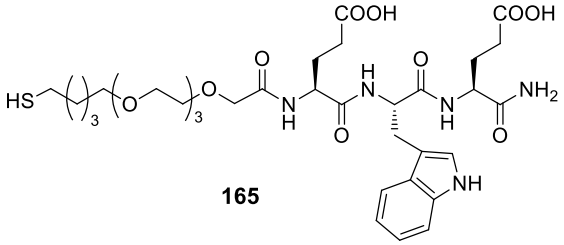

165

The peptide ligand **165** was synthesized accordingly on Rink amide MBHA resin (200 mg, 0.84 mmol/g, 0.168 mmol, 1 eq) following the above described microwave-assisted SPPS procedure. The coupling reagent PyBop (262 mg, 0.504 mmol, 3 eq) and the base DIPEA (171 µL, 1.008 mmol, 6 eq) in DMF (5 mL) were used for coupling the amino acids, whereas DIC (95 µL, 0.605 mmol, 3.6 eq) and HOBt (102 mg, 0.756 mmol, 4.5 eq) were used for the attachment of the thiolalkylated TEG linker (**156**). After Fmoc deprotection, the amino acids Fmoc-Glu(O^{t}Bu)-OH (214 mg, 0.504 mmol, 3 eq), Fmoc-Trp(Boc)-OH (265 mg, 0.504 mmol, 3 eq), Fmoc-Glu(O^{t}Bu)-OH (214 mg, 0.504 mmol, 3 eq) and thiolalkylated TEG linker (**156**) (278 mg, 0.504 mmol, 3 eq) were coupled. After the cleavage and purification steps, the product was obtained as a white solid with 92 % purity according to analytical HPLC analysis.

$C_{34}H_{51}N_5O_{12}S$ 753.86 g/mol

Yield 25 mg, 33 µmol, 20 %

Mp. 60 °C

^{1}H NMR (500 MHz, DMSO-*d*$_6$): δ [ppm] = 1.32-1.39 (m, 2 H, CH_2), 1.45-1.51 (m, 4 H, 2 × CH_2), 1.70-1.78 (m, 2 H, Glu-CH_2), 1.86-1.94 (m, 2 H, Glu-CH_2), 2.16-2.21 (m, 4 H, 2 × Glu-CH_2), 2.46-2.48 (m, 2 H, CH_2), 2.93-2.98, 3.13-3.17 (m, 2 H, Trp-CH_2), 3.35 (t, *J* = 6.6 Hz, 2 H, CH_2), 3.43-3.54 (m, 12 H, 6 × CH_2), 3.87 (s, 2 H, CH_2), 4.16-4.20 (m, 1 H, Glu-CH), 4.30-4.34 (m, 1 H, Glu-CH), 4.50-4.55 (m, 1 H, Trp-CH), 6.96 (t, *J* = 7.5 Hz, 1 H, Trp-CH_{ar}), 7.03-7.06 (m, 2 H, Trp-CH_{ar}, NH_2), 7.13 (s, 1 H, Trp-CH_{ar}), 7.16 (s, 1 H, NH_2), 7.30 (d, *J* = 8.1 Hz, 1 H, Trp-CH_{ar}), 7.58 (d, *J* = 8.0 Hz, 1 H, Trp-CH_{ar}), 7.64 (d, *J* = 8.1 Hz,, 1 H, NH), 8.03 (d, *J* = 8.0 Hz,, 1 H, NH), 8.11 (d, *J* = 7.7 Hz, 1 H, NH), 10.79 (s, 1 H, Trp-NH), 12.09 (s, 1 H, COOH).

^{13}C NMR (125 MHz, DMSO-*d*$_6$): δ [ppm] = 25.27 (CH_2), 27.29 (Trp-CH_2), 27.46 (Glu-CH_2), 27.51 (CH_2), 28.79 (CH_2), 29.28 (CH_2), 30.06 (Glu-CH_2), 30.20 (Glu-CH_2), 51.26 (Glu-CH), 51.91 (Glu-CH), 53.47 (Trp-CH), 69.41 (CH_2), 69.50 (CH_2), 69.64 (CH_2), 69.73 (CH_2), 70.16 (CH_2), 70.22 (CH_2), 109.83 (Trp-C_q), 111.22 (Trp-CH_{ar}), 118.16 (Trp-CH_{ar}), 118.38 (Trp-CH_{ar}), 120.80 (Trp-CH_{ar}), 123.54 (Trp-CH_{ar}), 127.23 (Trp-C_q), 136.00 (Trp-C_q), 169.20 (CO), 170.82 (CO), 171.15 (CO), 172.96 (CO), 173.95 (CO), 173.98 (CO).

FT-IR (ATR): $\tilde{\nu}$ [cm^{-1}] = 3174 (br), 3051 (br), 2923 (br), 2866 (br), 1645 (s), 1525 (m), 1457 (w), 1347 (w), 1233 (w), 1090 (s), 744 (m).

6.6.4 Syntheses of Alkylated Peptide Ligands

Synthesis of Ethyl alkylated TEG acetate (166)

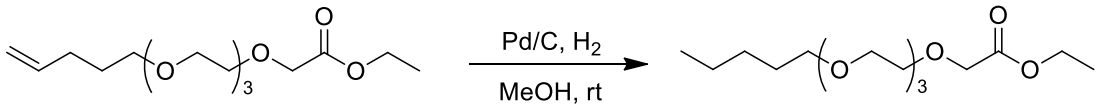

152 **166**

A mixture of the **152** (640 mg, 2.1 mmol, 1 eq), a catalytic amount of Pd/C (≈ 50 mg) in methanol (30 ml) was vigorously stirred at room temperature for 4 h under hydrogen atmosphere. The resulting solution was filtered through a celite pad which was washed two times with methanol. The solvent was evaporated under reduced pressure to yield **166** as a clear oil.

$C_{15}H_{30}O_6$ 306.40 g/mol

Yield 621 mg, 2 mmol, 95 %

^{1}H NMR (300 MHz, $CDCl_3$): δ [ppm] = 0.89 (t, J = 6.9 Hz, 3 H, CH_3), 1.26-1.33 (m, 7 H, CH_3, 2 × CH_2), 1.53-1.62 (m, 2 H, CH_2), 3.44 (t, J = 6.8 Hz, 2 H, CH_2), 3.57-3.75 (m, 12 H, 6 × CH_2), 4.14 (s, 2 H, CH_2), 4.21 (q, J = 7.6 Hz, 2 H, CH_2).

^{13}C NMR (75 MHz, $CDCl_3$): δ [ppm] = 14.17 (CH_3), 14.35 (CH_3), 22.67 (CH_2), 28.41 (CH_2), 29.47 (CH_2), 60.93 (CH_2), 68.81 (CH_2), 68.91 (CH_2), 70.21 (CH_2), 70.52 (CH_2), 70.75 (CH_2), 70.80 (CH_2), 71.06 (CH_2), 71.67 (CH_2), 170.62 (CO).

HRMS (ESI): m/z calculated for $C_{15}H_{30}O_6Na^+$ $[M+Na]^+$: 329.1935; found: 329.1911.

Synthesis of alkylated TEG acetic acid (167)

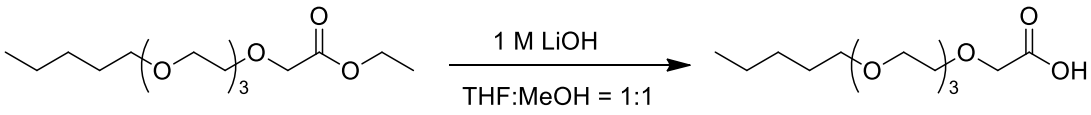

166 **167**

To a solution of **166** (621 mg, 2 mmol) in 1:1 THF/MeOH (20 mL) was added 1 M aqueous solution of lithium hydroxide. The solution was purged with argon for 10 min and stirred at room temperature for 12 h. The solution was acidified to pH 1 with 1 M HCl, diluted with brine (20 mL) and extracted with dichloromethane (4 × 20 mL). The combined organic layers were washed with brine (20 mL), dried over $MgSO_4$ and concentrated under reduced pressure to afford **167** as pale yellow oil.

$C_{13}H_{26}O_6$ 278.34 g/mol

Yield 548 mg, 1.97 mmol, 98 %

^{1}H NMR (300 MHz, $CDCl_3$): δ [ppm] = 0.89 (t, J = 6.9 Hz, 3 H, CH_3), 1.28-1.33 (m, 4 H, 2 × CH_2), 1.55-1.64 (m, 2 H, CH_2), 3.47 (t, J = 6.9 Hz, 2 H, CH_2), 3.58-3.78 (m, 12 H, 6 × CH_2), 4.15 (s, 2 H, CH_2).

^{13}C NMR (75 MHz, $CDCl_3$): δ [ppm] = 14.16 (CH_3), 22.63 (CH_2), 28.34 (CH_2), 29.28 (CH_2), 69.34 (CH_2), 70.27 (CH_2), 70.49 (CH_2), 70.53 (CH_2), 70.59 (CH_2), 70.84 (CH_2), 71.75 (CH_2), 71.79 (CH_2), 171.94 (CO).

HRMS (ESI): m/z calculated for $C_{13}H_{26}O_6Na^+$ $[M+Na]^+$: 301.1622; found: 301.1598.

Synthesis of Alkane Peptide Ligand (168)

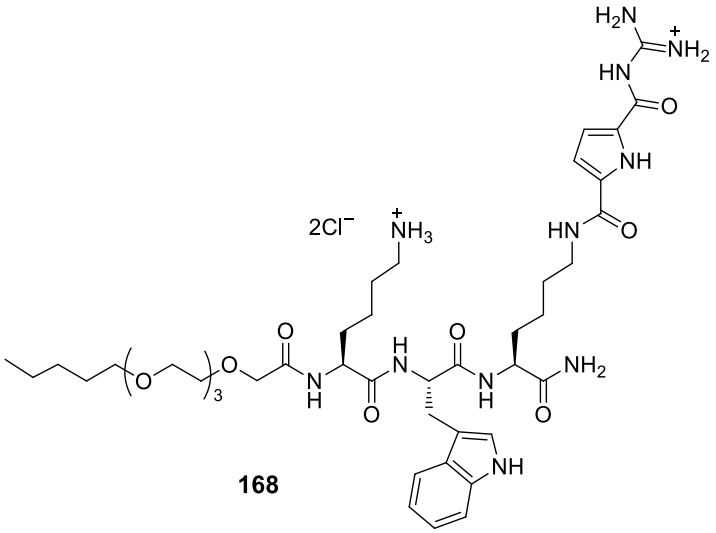

168

The peptide ligand **168** was synthesized accordingly on Rink amide MBHA resin (200 mg, 0.84 mmol/g, 0.168 mmol, 1 eq) following the above described microwave-assisted SPPS procedure. The coupling reagent PyBop (262 mg, 0.504 mmol, 3 eq) and the base DIPEA (171 µL, 1.008 mmol, 6 eq) in DMF (5 mL) were used for coupling the amino acids, whereas DIC (95 µL, 0.605 mmol, 3.6 eq) and HOBt (102 mg, 0.756 mmol, 4.5 eq) were used for the attachment of the alkylated TEG linker (**167**). After Fmoc deprotection, the amino acids Fmoc-Lys(Boc)-OH (236 mg, 0.504 mmol, 3 eq), Fmoc-Trp(Boc)-OH (265 mg, 0.504 mmol, 3 eq), Fmoc-Lys(Alloc)-OH (228 mg, 0.504 mmol, 3 eq) and alkylated TEG linker (**167**) (140 mg, 0.504 mmol, 3 eq) were coupled. After the removal of Alloc protecting group with $Pd(PPh_3)_4$ (19.4 mg, 0.0168 mmol, 0.1 eq) in the presence of $PhSiH_3$ (495 µL, 4.032 mmol, 24 eq) in DCM, the Boc-GCP group (**111**) (200 mg, 0.504 mmol, 3 eq) was coupled. After the cleavage and purification steps, the product was obtained as a white solid with 95 % purity according to analytical HPLC analysis.

$C_{43}H_{69}Cl_2N_{11}O_{10}$ 970.98 g/mol

Yield 70 mg, 72.1 µmol, 43 %

Mp. 153 °C

^{1}H NMR (500 MHz, DMSO-*d*$_6$): δ [ppm] = 0.85 (t, J = 7.0 Hz, 3 H, CH_3), 1.16-1.33 (m, 8 H, 2 × CH_2, 2 × Lys-CH_2), 1.43-1.53 (m, 8 H, CH_2, 3 × Lys-CH_2), 1.61-1.72 (m, 2 H, Lys-CH_2), 2.68-2.74 (m, 2 H, Lys-CH_2), 2.97 (dd, 1 H, J_1 = 14.8 Hz, J_2 = 9.0 Hz, Trp-CH_2), 3.15 (dd, J_1 = 19.4 Hz, J_2 = 4.8 Hz, 1 H, Trp-CH_2), 3.21 (q, J = 6.8 Hz, 2 H, Lys-CH_2), 3.34 (t, J = 6.6 Hz, 2 H, CH_2), 3.42-3.56 (m, 12 H, 6 × CH_2), 3.88 (s, 2 H, CH_2), 4.16-4.20 (m, 1 H, Lys-CH), 4.27-4.32 (m, 1 H, Lys-CH), 4.52-4.57 (m, 1 H, Trp-CH), 6.87 (dd, J_1 = 4.1 Hz, J_2 = 2.4 Hz, 1 H, Pyr-CH_{ar}), 6.95 (t, J = 7.5 Hz, 1 H, Trp-CH_{ar}), 7.02-7.05 (m, 2 H, Trp-CH_{ar}, NH_2), 7.13 (s, 1 H, Trp-CH_{ar}), 7.29 (s, 1 H, NH_2), 7.31 (d, J = 8.0 Hz, 1 H, Trp-CH_{ar}), 7.54 (dd, J_1 = 4.1 Hz, J_2 = 2.5 Hz, 1 H, Pyr-CH_{ar}), 7.57 (d, J =

7.9 Hz, 1 H, Trp-CH_{ar}), 7.61 (d, *J* = 8.2 Hz, 1 H, NH), 7.88-7.91 (m, 4 H, Lys-NH_3^+, NH), 8.24 (d, *J* = 8.0 Hz,, 1 H, NH), 8.55 (t, *J* = 5.5 Hz,, 1 H, NH), 8.48, 8.67 (brs, 4 H, Gua × NH_4^+), 10.85 (s, 1 H, Trp-NH), 12.05 (s, 1 H, Gua-NH), 12.33 (s, 1 H, Pyr-NH).

^{13}C NMR (125 MHz, DMSO-*d*$_6$): δ [ppm] = 13.93 (CH_3), 21.93 (CH_2), 22.04 (Lys-CH_2), 22.71 (Lys-CH_2), 26.58 (Lys-CH_2), 27.37 (Trp-CH_2), 27.83 (CH_2), 28.72 (Lys-CH_2), 28.85 (CH_2), 31.66 (Lys-CH_2), 31.83 (Lys-CH_2), 38.57 (Lys-CH_2), 38.72 (Lys-CH_2), 51.73 (Lys-CH), 52.35 (Lys-CH), 53.56 (Trp-CH), 69.42 (CH_2), 69.50 (CH_2), 69.69 (CH_2), 69.73 (CH_2), 69.75 (CH_2), 70.22 (CH_2), 70.27 (CH_2), 109.87 (Trp-C_q), 111.23 (Trp-CH_{ar}), 112.41 (Pyr-CH_{ar}), 115.97 (Pyr-CH_{ar}), 118.18 (Trp-CH_{ar}), 118.39 (Trp-CH_{ar}), 120.79 (Trp-CH_{ar}), 123.56 (Trp-CH_{ar}), 125.30 (Pyr-C_q), 127.25 (Trp-C_q), 132.95 (Pyr-Cq), 136.00 (Trp-C_q), 155.52 (Gua-C_q), 158.97 (CO), 159.63 (CO), 169.06 (CO), 171.07 (CO), 171.11 (CO), 173.43 (CO).

HRMS (ESI): m/z calculated for $C_{43}H_{69}N_{11}O_{10}^+$ $[M+2H]^{2+}$: 449.7609; found: 449.7580.

FT-IR (ATR): $\tilde{\nu}$ [cm^{-1}] = 3235 (br), 2928 (br), 2866 (br), 1652 (s), 1541 (s), 1457 (w), 1282 (s), 1196 (w), 1096 (s), 744 (m).

Synthesis of Peptide Ligand (170)

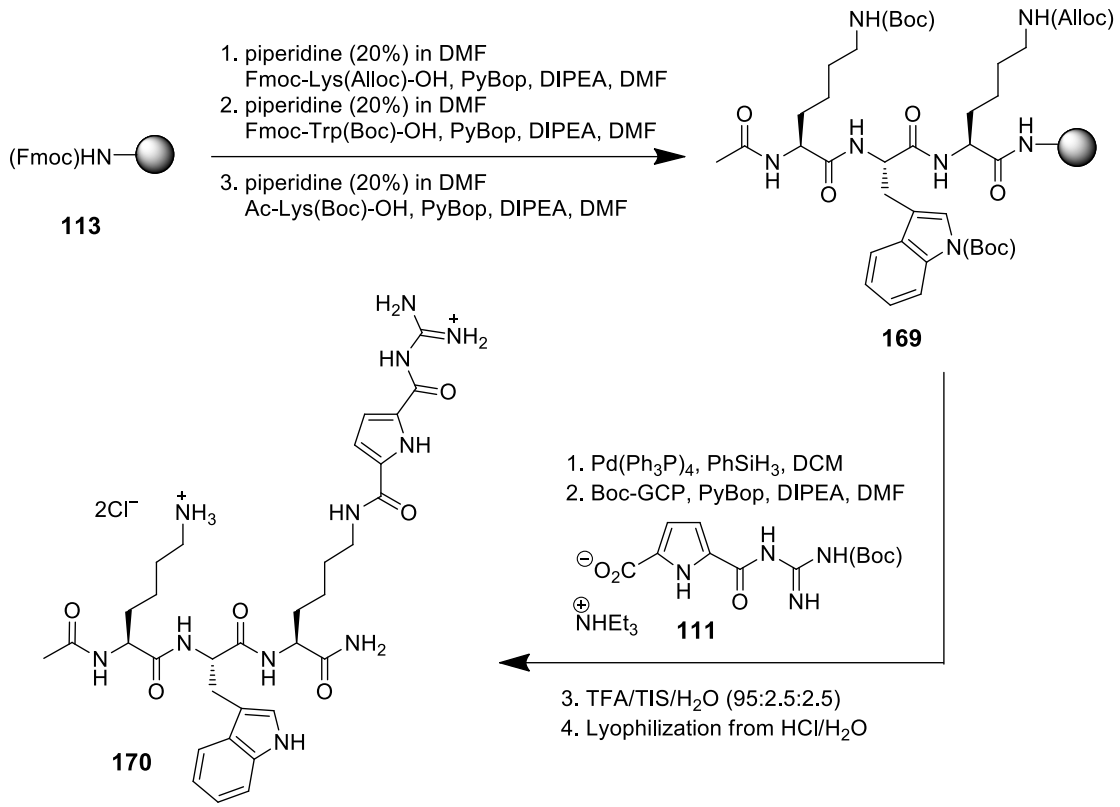

The peptide ligand **170** was synthesized accordingly on Rink amide MBHA resin (200 mg, 0.84 mmol/g, 0.168 mmol, 1 eq) following the above described microwave-assisted SPPS procedure. The coupling reagent PyBop (262 mg, 0.504 mmol, 3 eq) and the base DIPEA (171 µL, 1.008 mmol, 6 eq) in DMF (5 mL) were used during the coupling steps. After Fmoc deprotection, the amino acids Fmoc-Lys(Alloc)-OH (228 mg, 0.504 mmol, 3 eq), Fmoc-Trp(Boc)-OH (265 mg, 0.504 mmol, 3 eq) and Ac-Lys(Boc)-OH (145 mg, 0.504 mmol, 3 eq) were coupled. After the removal of Alloc protecting group with $Pd(PPh_3)_4$ (19.4 mg, 0.0168 mmol, 0.1 eq) in the presence of $PhSiH_3$ (495 µL, 4.032 mmol, 24 eq) in DCM, the Boc-GCP group (**111**) (200 mg, 0.504 mmol, 3 eq) was coupled. After the cleavage and purification steps, the product was obtained as a white solid with 93 % purity according to analytical HPLC analysis.

$C_{32}H_{47}Cl_2N_{11}O_6$ 752.69 g/mol

Yield 40 mg, 53.1 µmol, 32 %

Mp. 186 °C

^{1}H NMR (500 MHz, DMSO-d_6): δ [ppm] = 1.16-1.33 (m, 4 H, 2 × Lys-CH_2), 1.40-1.71 (m, 8 H, 4 × Lys-CH_2), 2.68-2.73 (m, 2 H, Lys-CH_2), 2.99 (dd, 1 H, J_1 = 14.8 Hz, J_2 = 8.9 Hz, Trp-CH_2), 3.16 (dd, J_1 = 15.1 Hz, J_2 = 4.7 Hz, 1 H, Trp-CH_2), 3.21 (q, J = 6.5 Hz, 2 H, Lys-CH_2), 4.47-4.52 (m, 1 H, Trp-CH), 6.86 (dd, J_1 = 4.0 Hz, J_2 = 2.4 Hz, 1 H, Pyr-CH_{ar}), 6.96 (t, J = 7.4 Hz, 1 H, Trp-CH_{ar}), 7.02-7.05 (m, 2 H, Trp-CH_{ar}, NH_2), 7.13 (s, 1 H,

Trp-CH_{ar}), 7.24 (s, 1 H, NH_2), 7.31 (d, *J* = 8.1 Hz, 1 H, Trp-CH_{ar}), 7.53-7.55 (m, 2 H, Pyr-CH_{ar}, Trp-CH_{ar}), 7.80 (d, *J* = 8.1 Hz, 1 H, NH), 7.90 (brs, 3 H, Lys-NH_3^+), 8.03 (d, *J* = 7.9 Hz,, 1 H, NH), 8.07 (d, *J* = 7.5 Hz,, 1 H, NH), 8.54 (d, *J* = 5.5 Hz,, 1 H, NH), 8.49, 8.67 (brs, 4 H, Gua × NH_4^+), 10.88 (s, 1 H, Trp-NH), 12.05 (s, 1 H, Gua-NH), 12.33 (s, 1 H, Pyr-NH).

^{13}C NMR (125 MHz, DMSO-*d*$_6$): δ [ppm] = 21.21 (Lys-CH_2), 22.45 (CH_3), 22.73 (Lys-CH_2), 26.58 (Lys-CH_2), 27.13 (Trp-CH_2), 28.73 (Lys-CH_2), 31.07 (Lys-CH_2), 31.73 (Lys-CH_2), 38.50 (Lys-CH_2), 38.73 (Lys-CH_2), 52.43 (Lys-CH), 52.76 (Lys-CH), 53.55 (Trp-CH), 109.86 (Trp-C_q), 111.23 (Trp-CH_{ar}), 112.42 (Pyr-CH_{ar}), 115.97 (Pyr-CH_{ar}), 118.21 (Trp-CH_{ar}), 118.34 (Trp-CH_{ar}), 120.79 (Trp-CH_{ar}), 123.56 (Trp-CH_{ar}), 125.30 (Pyr-C_q), 127.27 (Trp-C_q), 132.96 (Pyr-Cq), 136.00 (Trp-C_q), 155.52 (Gua-C_q), 158.97 (CO), 159.63 (CO), 169.62 (CO), 171.10 (CO), 171.75 (CO), 173.49 (CO).

HRMS (ESI): m/z calculated for $C_{32}H_{47}N_{11}O_6^+$ $[M+2H]^{2+}$: 340.6850; found: 340.6855.

FT-IR (ATR): $\tilde{\nu}$ [cm^{-1}] = 3184 (br), 3050 (br), 2934 (br), 1651 (s), 1547 (s), 1283 (s), 1196 (m), 745 (m).

6.7 Preparation of the Functionalized Gold Nanoparticles

Preparation of monovalent conjugates (171)

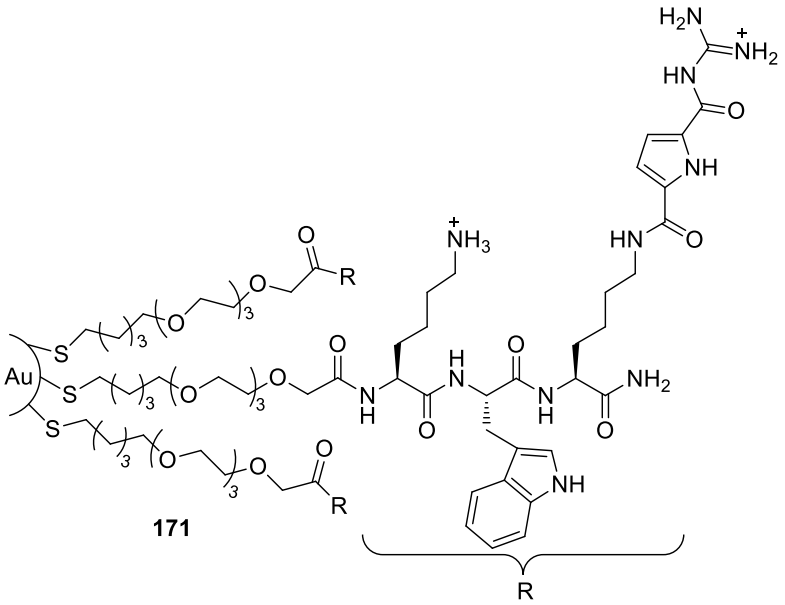

Monovalent conjugated Au NPs **171** was carried out by attaching ligand **161** to the surface of Au NPs via *ex situ* or *in situ* conjugation. For *ex situ* conjugation, the gold nanoparticles were first prepared in the absence of ligand in 30 mL sodium phosphate buffer (0.6 mM, pH 6.0) by laser ablation for 150 s. Then the big particles (d > 10 nm) were removed by ultracentrifugation to get the monodispersed nanoparticles. In order to get the conjugated Au NPs with different surface density, a series of concentrations of the ligand in sodium phosphate buffer (each in 0.5 mL) resulting in the following final concentrations: 0 µM, 0.5 µM, 1.3 µM, 2.6 µM, 3.9 µM, 5.2 µM, 12.9 µM, 25.9 µM, 51.7 µM, 206.9 µM, 413.8 µM, 620.7 µM, 724.2 µM were prepared. For the first try, higher ligand concentrations: 795 µM, 847 µM, 900 µM, 950 µM and 1000 µM were also prepared. Then to each solution of the ligand 1 mL of gold nanoparticles was added and the mixtures were shaken for 1 h. For *in situ* conjugation, the gold nanoparticles were prepared in the presence of the ligands. A series of concentrations of the ligand in sodium phosphate buffer (each in 1.5 mL) resulting in the following final concentrations: 0 µM, 0.5 µM, 1.3 µM, 2.6 µM, 3.9 µM, 5.2 µM, 12.9 µM, 25.9 µM, 51.7 µM, 206.9 µM, 413.8 µM, 620.7 µM, 724.2 µM were prepared. The laser ablation was performed in a cuvette where the solution and a gold ribbon were placed inside. For each ligand concentration, the laser ablation was carried out for 7 seconds. Afterwards, the Au NPs samples were shaken for 1 h to ensure the complete conjugation. After the conjugation, the unbound ligands were removed from the conjugates by using ultracentrifugation and the surface coverage was determined with the help of UV/Vis spectroscopy.

Preparation of bivalent conjugates (172)

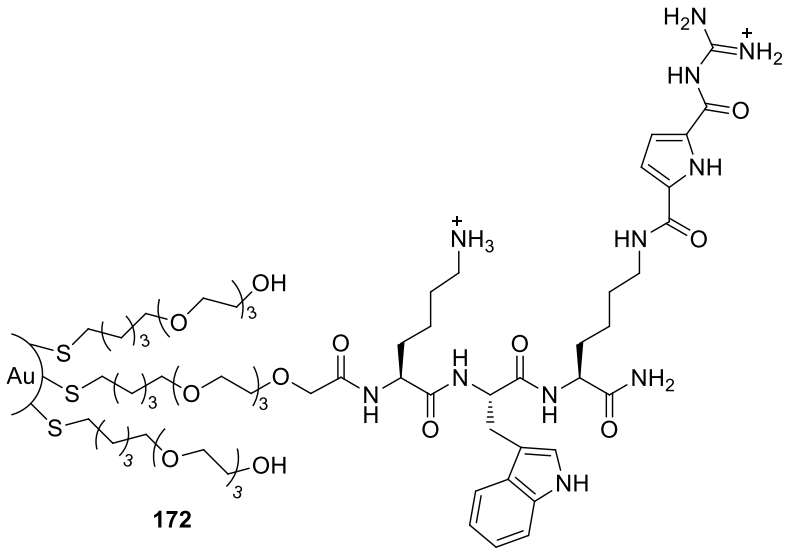

172

Bivalent conjugated Au NPs **172** was carried out by attaching the positively charged ligand **161** and the neutral ligand **158** to the surface of Au NPs via *ex situ* or *in situ* conjugation. It was prepared following the above described procedures by using two types of different ligands (**161** and **158**) instead of only using one type of ligand (**161**) for monovalent conjugation. In order to obtain different surface density, a series of concentrations of the ligand **161** in sodium phosphate buffer resulting in the following final concentrations: 0 µM, 0.5 µM, 1.3 µM, 2.6 µM, 3.9 µM, 5.2 µM, 12.9 µM, 25.9 µM, 51.7 µM, 206.9 µM, 413.8 µM, 620.7 µM, 724.2 µM were prepared. Ligand **158** was used as the surface blocker with respectively double amount. For both *ex situ* and *in situ* conjugation, the Au NPs samples were shaken for 1 h to ensure the complete conjugation after the laser ablation. After the conjugation, the unbound ligands were removed from the conjugates by using ultracentrifugation and the surface coverage was determined with the help of UV/Vis spectroscopy.

6.8 Generation of the Dynamic Combinatorial Libraries

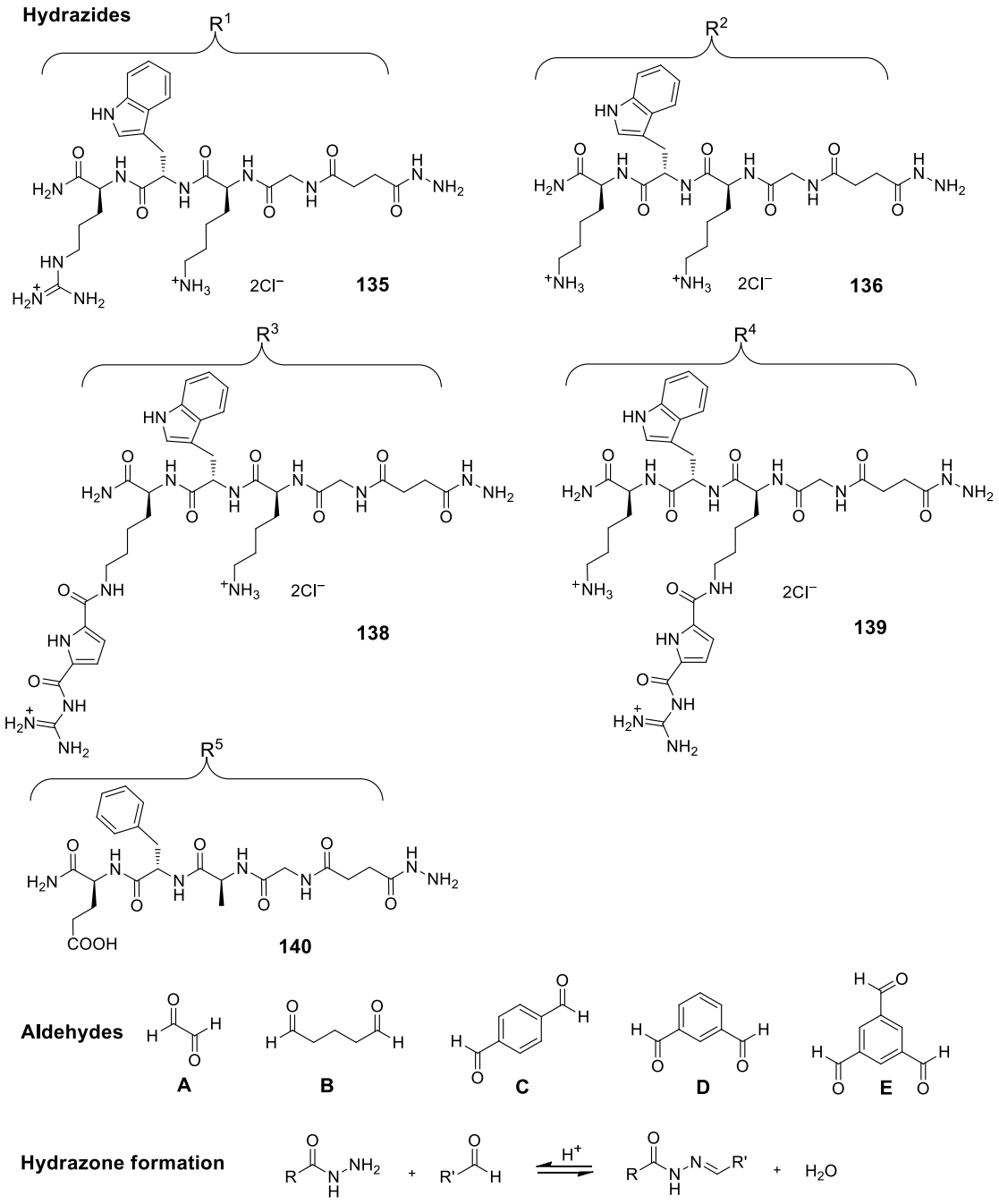

The dynamic combinatorial libraries can be easily generated in 100 mM sodium acetate buffer solutions at pH 4.0 containing 10 % DMSO (v/v) to help dissolve the aromatic aldehydes and the acyl hydrazones, upon gently agitation for three days. The full library was prepared by mixing all the ten building blocks (five hydrazides and five aldehydes) together in an aqueous acetate buffer solution at room temperature. At the same time, ten sub-libraries were generated under the same conditions by mixing all components except one specific building block was omitted and replaced by the blank

acetate buffer solution containing 10 % DMSO. Equilibration of all the libraries was carried out in the absence of the enzyme. The concentrations of the hydrazide groups or aldehyde groups of each building block were kept the same. For example, the stock solutions of mono-hydrazides **135**-**136**, **138**-**140** (1 mM), di-aldehydes **A**-**D** (0.5 mM) and tri-aldehyde **E** (0.33 mM) were prepared in sodium acetate buffer (100 mM, pH = 4.0, containing 10 % DMSO, v/v). Then, the full library was generated by adding all the five hydrazides and five aldehydes (each 10 μL) to sodium acetate buffer (100 mM, pH = 4.0, containing 10 % DMSO, v/v). The ten sub-libraries were performed under the same conditions except the building block to be removed was exchanged by sodium acetate buffer (100 mM, pH = 4.0, containing 10 % DMSO, v/v). The final concentration of the libraries amounted to 0.5 mM in total for both hydrazide and aldehyde groups. Together with a reference sample (acetate buffer containing 10 % DMSO) without any building blocks, this series of 12 samples was sufficient to screening the complete 95-membered library (not counting partially formed species). The mixtures of all the libraries were allowed to equilibrate at room temperature with shaking for 3 days to ensure a complete equilibrium and the resulting acyl hydrazones were adjusted to physiological conditions (pH 7.4) freezing-out the library composition and subsequently tested for inhibitory activity in the presence of β-tryptase. The second size-reduced library containing all the five aldehydes but only hydrazide **138**, as well as the corresponding six sub-libraries were generated and analyzed in the same way. The full library was generated by adding hydrazide **138** (50 μL) and five aldehydes (each 10 μL) to sodium acetate buffer. The six sub-libraries were performed under the same conditions except the building block to be removed was exchanged by sodium acetate buffer. The final concentration of the libraries amounted to 0.5 mM in total for both hydrazide and aldehyde groups.

6.9 Enzyme Assay

6.9.1 General Remarks

The heparin-stabilized recombinant human rhSkin β-tryptase (134 kDa) used in this thesis was purchased from *Promega* (Catalog No. G7061) and delivered in a vial of 0.5 mL aqueous solution at a mass concentration of 200 μg/mL. The β-tryptase is supplied in 10 mM 2-(*N*-morpholino) ethanesulfonic acid (MES) buffer (pH 6.1), containing 10 % glycerol, 200 mM NaCl and 0.5 mg/mL heparin. For easier use it was separated into aliquots in 50 vials, so that it was available in single vials each containing 2 μg of the enzyme in 10 μL solution at the same concentration of 200 μg/mL. The fluorogenic substrate Tos-Gly-Pro-Arg-AMC used for β-tryptase was purchased from *Bachem* (Catalog No. I-1365).

The other two related serine proteases trypsin (23 kDa) and α-chymotrypsin (25 kDa) from bovine pancreas used for selectivity assay were purchased from *Merck* (Catalog No. 6502 and 230832, respectively) and delivered as white solids. The fluorogenic substrates Z-Phe-Arg-AMC and Suc-Leu-Tyr-AMC used for trypsin and α-chymotrypsin respectively were purchased from *Bachem* (Catalog No. I-1160 and I-1355, respectively).

The cleavage of the fluorogenic substrates by the enzymes results in a strong increase of fluorescence emission at 460 nm (380 nm excitation) due to the release of the free AMC, which can be used to monitor the kinetics of the enzymatic cleavage. Therefore, in order to measure the kinetic parameters for the hydrolysis of the substrate by enzyme, the experiments were performed in a high throughput kinetic assay using a fluorescence spectrophotometer with a microplate reader unit and white 96 well plates by monitoring the fluorescence at 460 nm over the time of 15 min. The following fluorescence spectrometer settings were used for all enzyme assays.

Spectrophotometer parameters

Ex. wavelength	380 nm
Em. wavelength	460 nm
Ex. slit	10 nm
Em. slit	20 nm
Temperature	25 ^{o}C
Detector	Manual (450 V)
Sampling interval	One measurement per minute

The Tris-HCl buffers with different compositions and pH values were used as the assay buffers for the three enzymes which were prepared with the following components for a total volume of 100 mL. The required pH values were adjusted by using 1 M aqueous HCl

solution.

β-Tryptase (pH 7.4)

Reagent	Concentration	Amount
Tris	50 mM	0.606 g
NaCl	100 mM	0.584 g
Heparin	50 μg/mL	5 mg
Triton-X	0.02 %	20 μL
H_2O		100 mL

Trypsin and α-Chymotrypsin (pH 8.0)

Reagent	Concentration	Amount
Tris	50 mM	0.606 g
NaCl	100 mM	0.584 g
EDTA	5 mM	146 mg
H_2O		100 mL

6.9.2 Enzyme Inhibition Assay

Inhibition Assay for β-Tryptase

Before the enzyme inhibition experiment, the enzyme was diluted in assay buffer and the final concentration of the enzyme had to be determined prior the tests in order to find appropriate concentration to make the slope of the linear graph between 15 and 30 in the absence of inhibitor. The stock solution of substrate was prepared in DMSO at a concentration of 2 mM. The enzyme kinetic assay was performed in a total volume of 200 µL of analyte solution, containing the assay buffer, the enzyme, the solvent that used for preparation of the inhibitors and the substrate which were added to the white well plate in the following order. The mixture was thoroughly mixed and fluorescence activity at 460 nm was measured over the time of 15 min.

Addition order for enzyme concentration assay

Assay buffer	165 µL
Enzyme	10 µL
DMSO or H_2O	20 µL
Substrate	5 µL, c(final) = 50 µM

After finding the appropriate concentration of the enzyme (normally the final concentrations at 0.25 nM for DMSO and 0.1 nM for water depending on the different solvents for dissolving the inhibitor), the screening of the inhibitors was carried out in the Tris-HCl assay buffer. The kinetic assays were carried out in a final volume of 200 µL in assay buffer (165 µL) wherein the enzyme (10 µL) was incubated with DMSO (as a reference) or inhibitors (20 µL) and finally the substrate (5 µL, final concentration 50 µM) was added in the following order. All the solutions were thoroughly mixed and finally the increase of fluorescence activity was measured over the time of 15 min. All the inhibitors were first prepared as a stock solution of 1 mM in DMSO. The inhibitory activities (in %) of all the inhibitors was then first determined three-fold at an inhibitor concentration of 100 µM to investigate their potential as potent inhibitors of β-tryptase. If the inhibition was higher than 80 % also the half maximal inhibitory concentration (IC_{50}) and the absolute inhibition constant (K_i) was determined at various inhibitor concentrations.

Addition order for enzyme inhibition assay

Assay buffer	165 µL
Enzyme	10 µL, c(final) = 0.25 nM
DMSO or Inhibitor	20 µL
Substrate	5 µL, c(final) = 50 µM

To determine the IC_{50} and K_i values, a series of the stock solution of inhibitors in DMSO resulting in the following final concentrations: 100 μM, 80 μM, 60 μM, 40 μM, 20 μM, 10 μM, 8 μM, 6 μM, 4 μM, 2 μM, 1 μM, 0.1 μM were measured. Depending on the inhibitory activity, sometimes bigger and smaller concentrations were prepared (1000-0.01 μM). The resulting data of the residual enzyme activity (in %) compared to the reference sample were processed with the GraFit program by using the 4-parameter equation (9) as shown in Chapter 4.1.4 to calculate the IC_{50} values of the inhibitors. The K_i values were calculated from the IC_{50} values depending on the inhibition modes (see Chapter 2.1.2). For the noncompetitive inhibitors, the K_i values are independent of the substrate concentrations and equal to the IC_{50} values

Selectivity Assay against Trypsin and *α*-Chymotrypsin

Trypsin and *α*-chymotrypsin were chosen to check the enzyme selectivity. The assays were performed in a 50 mM Tris-HCl buffer at pH 8.0, containing 5 mM EDTA and 100 mM NaCl. Fluorogenic substrates Z-Phe-Arg-AMC and Suc-Leu-Tyr-AMC were used for trypsin and *α*-chymotrypsin respectively. The stock solution of substrate was prepared in DMSO at a concentration of 2 mM. All the inhibitors were prepared as a stock solution of 1 mM in DMSO. The kinetic assays (at 25 ^{o}C) were carried out in a final volume of 200 μL by adding the enzyme (10 μL) to Tris-HCl buffer (pH 8.0, 165 μL) and then the addition of inhibitor (20 μL, final concentration 100 μM) and finally the substrate (5 μL, final concentration 50 μM) was added. All the solutions were thoroughly mixed and finally the increase of fluorescence activity was measured at 460 nm emission (380 nm excitation) over the time of 15 min.

Reversibility of β-Tryptase Inhibition

The first test on reversibility of β-tryptase inhibition was performed in a dialysis experiment. The Float-A-Lyzer G2 dialysis separation tubes (20 kDa) in which a mixture (total volume of 1000 μL) of assay buffer (Tris-HCl, 50 mM, pH 7.4, 750 μL), β-tryptase (50 μL, final concentration 0.5 nM) and inhibitor (200 μL, final concentration 200 μM) in buffer (containing 10 % DMSO) or pure buffer (containing 10 % DMSO, 200 μL) without inhibitor as the reference were contained. The dialysis tubes were floated vertically in the dialysate reservoir containing a stir bar to adjust the stirring rate to form a gentle rotating current. The samples were dialyzed at room temperature and with 4 complete buffer changes (every 12-24 h). The tests were done from time to time by taking a 100 μL sample from the dialysis tube, adding 95 μL assay buffer and the substrate (5 μL, final concentration 50 μM) before the mixtures were submitted to determine the residual activity of the enzyme using a fluorescence assay.

In the second experiment to test the reversibility of enzyme inhibition, the enzyme (10 μL) was incubated with the inhibitor (20 μL, final concentration 100 μM) or blank DMSO

(20 μL) in assay buffer (155 μL) for 5 minutes. Then either heparin in buffer (10 μL, final concentration 1 mg/mL) or buffer without heparin (10 μL) was added to the vials. All the mixtures were incubated for another 5 minutes, followed by the addition of substrate (5 μL, final concentration 50 μM) and the fluorescence readout. The higher enzyme activity in the vial with heparin compared to the vial with buffer indicates a reversibility binding of the inhibitor to the enzyme.

Mode of β-Tryptase Inhibition

The inhibition mechanism was characterized with the interpretation of nonlinear regression fits and *Lineweaver-Burk* plots, as well as *Dixon* plots. In order to construct nonlinear regression fits and *Lineweaver-Burk* plots, the rate of the enzyme reaction was measured at different substrate concentrations (10-600 μM) but always with a fixed enzyme concentration for different inhibitor concentrations (0, 5, 10 and 100 μM). For *Dixon* plots, the rate of the enzyme reaction was determined at different inhibitor concentrations for different substrate concentrations (25, 50, 75, 150 and 200 μM).

Screening of the Dynamic Combinatorial Libraries

All screening measurements of DCLs were performed under similar conditions as above described. In the enzyme screening measurement (at 25 ^{o}C), 10 μL of β-tryptase was added to 180 μL Tris-HCl buffer, in which the enzyme was incubated with various equilibrated library mixtures (5 μL) in sodium acetate buffer (100 mM, pH 4.0, containing 10 % DMSO, v/v) and finally the substrate (5 μL, final concentration 50 μM) was added in the following order. The solutions were thoroughly mixed and the rate of hydrolysis of the AMC substrate was determined by monitoring the fluorescence change at 460 nm for 15 min.

Addition order for DCLs screening

Assay buffer	180 μL
Enzyme	10 μL, c(final) = 0.125 nM
Acetate buffer or DCLs	5 μL
Substrate	5 μL, c(final) = 50 μM

6.10 Molecular Mechanics Calculations

Molecular modeling calculations were performed with the help of Schrödinger MacroModel Vers. 9.9 software. The enzyme input is based on the reported crystal structure of β-tryptase (PDB code: 1A0L). All water molecules and substrates of the PDB crystal structure were removed from the binding pore. The calculations were carried out based on the force field OPLS (optimized potentials for liquid simulations) 2005 by using water as solvent to visualize the possible three dimensional structures of the interactions between the inhibitors and the enzyme. The structure of the enzyme was fixed while the inhibitor was put as mobilized during the calculation. So the calculations began at the potential energy of the start conformation and by simulating new conformations a minimal potential was searched. The resulting structures were obtained from the result of 1000 calculation cycles.

Docking studies were done by using Schrodinger MacroModel and Glide software (Version 2012 Update 2). Ligand preparation were done by the following steps: After generation of the 2D structure, they got converted into a 3D model, which was minimized in the OPLS 2005 force field using MacroModel with 1500 iterations and a convergence threshold of 0.05. Before starting the docking study on β-tryptase (PDB code: 1A0L), the ligand and water molecules within the crystal structure were deleted, followed by the preparation of protein structure with the protein preparation wizzard assigning bond orders, adding hydrogens and disulfides. After this basic preparation of ligand and protein structure files Glide was used to generate a receptor grid file of the active centers of the tryptase, to get detailed information about possible binding motifs. The long- and short-half, a quarter and the full tetrameric tryptase structures were prepared. Grids were prepared for all four versions of the protein structure. Ligand docking was done in the extra precision mode with sampling of nitrogen inversions and ring confirmations. The ligand conformations were simulated without any constrains or restrictions beside a penalization in the implemented scoring function (Glide) for nonplanar amid conformations. Post-docking minimizations were performed using a rejecting threshold of 0.5 kcal/mol.

7. APPENDIX

7.1 List of Abbreviations

δ	chemical shift
^{o}C	Celsius
λ	wavelength
μ	micro
ε	extinction coefficient
η	viscosity
ζ	zeta potential
Å	Ångstrom
A	alanine
AA	amino acid
abs	absolute
Ac	acetyl
AFM	atomic force microscopy
AIBN	azobis(isobutyronitrile)
Ala	alanine
Alloc	allyloxycarbonyl
AMC	7-amino-4-methyl-cumarine
Ar	argon
Arg	arginine
Asp	aspartic acid
Au	gold
Au NPs	gold nanoparticles
Bn	benzyl
Boc	*tert*-butyloxycarbonyl
*t*Bu	*tert*-butyl
br	broad
c	concentration

ca.	circa
$CDCl_3$	deuterated chloroform
cm	centimeter
d	doublet / diameter / day (s)
D	diffusion constant
Da	dalton
DCL	dynamic combinatorial library
DCM	dichloromethane
DIC	*N,N'*-diisopropylcarbodiimide
DIPEA	*N,N´*-diisopropylethyl amine
DLS	dynamic light scattering
DMF	*N,N´*-dimethyl formamide
DMSO	dimethyl sulfoxide
DMSO-d_6	deuterated dimethyl sulfoxide
E	glutamic acid / enzyme
e.g.	for example
eq	equivalent
ES	enzyme-substrate complex
ESI	electrospray ionization
ESI-MS	electrospray ionization mass spectrometry
F	phenylalanine
Fmoc	9-fluorenylmethyloxycarbonyl
FRET	fluorescence resonance energy transfer
FT-IR	fourier-transform infrared
g	gram
G	glycine
Gln	glutamine
Glu	glutamic acid
Gly	glycine
GCP	guanidiniocarbonyl pyrrole
h	hour (s)
His	histidine
HOBt	1-hydroxybenzotriazole
HPLC	high performance liquid chromatography
HRMS	high resolution mass spectrometry
Hz	Hertz
I	inhibitor
IC_{50}	half maximal inhibitory concentration

IR	infrared
ITC	isothermal titration calorimetry
K	lysine
K_i	dissociation (inhibition) constant
kJ	kilo Joule
K_m	*Michaelis* constant
L	liter / leucine / loading value
Leu	leucine
Lys	lysine
m	milli / medium / multiplett / meter
M	mol/L
m/z	mass per charge
max	maximum
MBHA	*p*-methylbenzhydrylamine
Me	methyl
MeOH	methanol
MHz	megahertz
min	minute (s)
µM	micromolar
mM	millimolar
Mp.	melting point
MPLC	medium performance liquid chromatography
MS	mass spectrometry
n	nano
nm	nanometer
nM	nanomolar
NMM	*N*-methylmorpholin
NMR	nuclear magnetic resonance
NPs	nanoparticles
p	para
Pbf	2,2,4,6,7-pentamethyldihydrobenzofuran-5-sulfonyl
Pd	palladium
Pd/C	palladium on charcoal
PDI	polydispersity index
pH	pondus hydrogenii
Phe	phenylalanine
PI	isoelectric point
PPI	primary particle index

ppm	parts per million
Pro	proline
PyBOP	benzotriazol-1-yl-N-oxy-tris(pyrrolidino)phosphonium hexafluorophosphate
q	quadruplet
r	radius
R	arginine
RP	reversed phase
rt	room temperature
s	singulett / strong / second (s)
S	substrate
Ser	serine
SPPS	solid phase peptide synthesis
SPR	surface plasmon resonance
t	time
t_R	retention time
T	temperature
TEG	triethylene glycol
TEM	transmission electron microscopy
TFA	trifluoroacetic acid
THF	tetrahydrofuran
TIS	triisopropylsilane
Tos	tosyl
Trt	trityl
Trp	tryptophan
Tyr	tyrosine
U_E	Electrophoretic mobility
UV	ultraviolet
UV/Vis	ultraviolet/visible
V	volume / valine
v	velocity
v_0	initial reaction rate
V_{max}	maximum reaction velocity
Val	valine
w	weak
W	tryptophan

7.2 Supplementary Experimental Data

7.2.1 HPLC Data

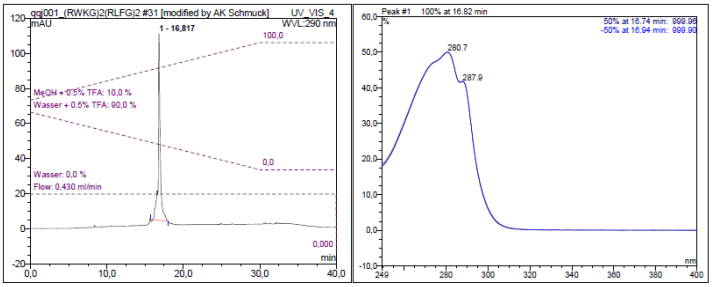

Figure 7.1 Analytical HPLC run of four-armed peptide ligand **115** with 95 % purity, solvent: 10 % to 100 % MeOH/H_2O (0.05 % TFA) in 30 min, flow rate: 0.43 ml/min, retention time t_R = 16.8 min; the peak integration is based on detection at 290 nm.

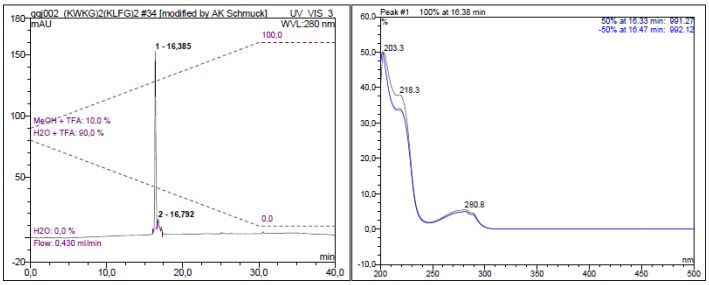

Figure 7.2 Analytical HPLC run of four-armed peptide ligand **116** with 95 % purity, solvent: 10 % to 100 % MeOH/H_2O (0.05 % TFA) in 30 min, flow rate: 0.43 ml/min, retention time t_R = 16.4 min; the peak integration is based on detection at 280 nm.

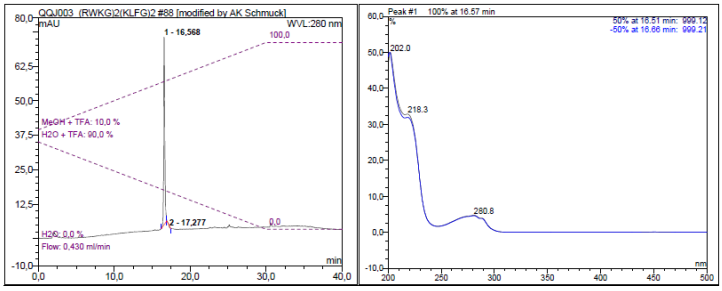

Figure 7.3 Analytical HPLC run of four-armed peptide ligand **117** with 95 % purity, solvent: 10 % to 100 % MeOH/H_2O (0.05 % TFA) in 30 min, flow rate: 0.43 ml/min, retention time t_R = 16.6 min; the peak integration is based on detection at 280 nm.

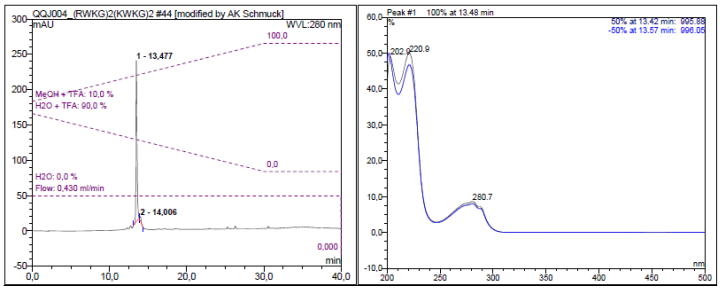

Figure 7.4 Analytical HPLC run of four-armed peptide ligand **118** with 95 % purity, solvent: 10 % to 100 % MeOH/H_2O (0.05 % TFA) in 30 min, flow rate: 0.43 ml/min, retention time t_R = 13.5 min; the peak integration is based on detection at 280 nm.

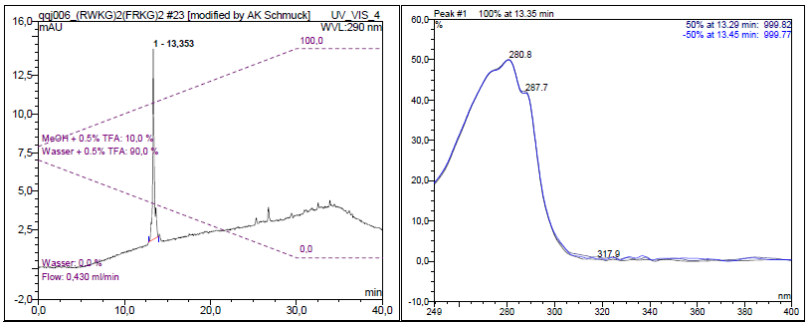

Figure 7.5 Analytical HPLC run of four-armed peptide ligand **119** with 95 % purity, solvent: 10 % to 100 % MeOH/H_2O (0.05 % TFA) in 30 min, flow rate: 0.43 ml/min, retention time t_R = 13.4 min; the peak integration is based on detection at 290 nm.

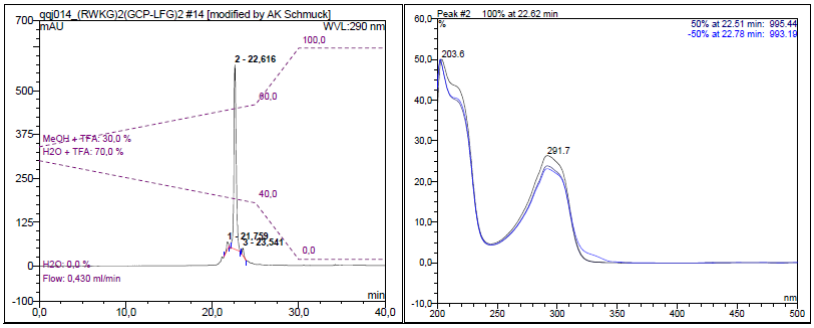

Figure 7.6 Analytical HPLC run of four-armed peptide ligand **120** with 95 % purity, solvent: 30 % to 60 % MeOH/H_2O (0.05 % TFA) in 25 min, flow rate: 0.43 ml/min, retention time t_R = 22.6 min; the peak integration is based on detection at 290 nm.

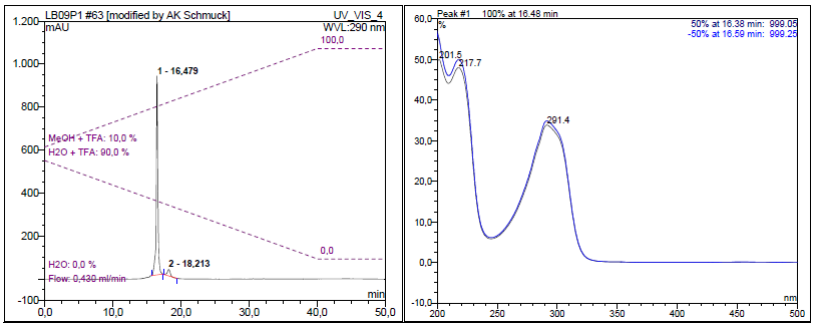

Figure 7.7 Analytical HPLC run of four-armed peptide ligand **124** with 95 % purity, solvent: 10 % to 100 % MeOH/H_2O (0.05 % TFA) in 30 min, flow rate: 0.43 ml/min, retention time t_R = 16.5 min; the peak integration is based on detection at 290 nm.

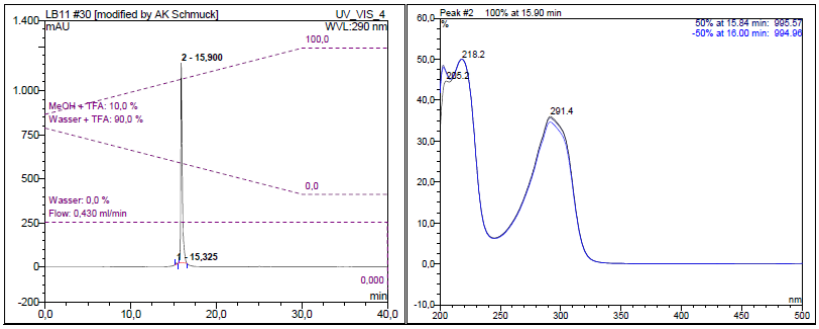

Figure 7.8 Analytical HPLC run of four-armed peptide ligand **125** with 95 % purity, solvent: 10 % to 100 % MeOH/H_2O (0.05 % TFA) in 30 min, flow rate: 0.43 ml/min, retention time t_R = 15.9 min; the peak integration is based on detection at 290 nm.

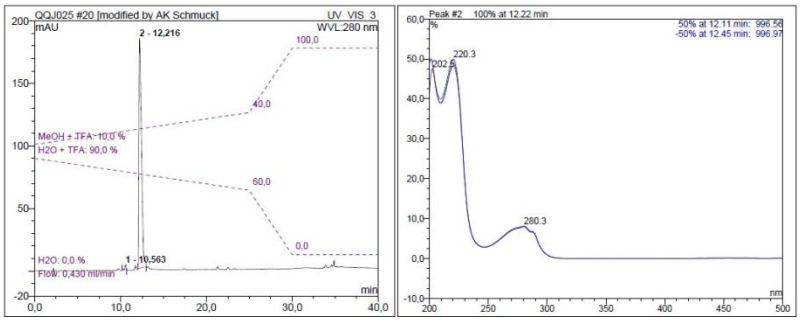

Figure 7.9 Analytical HPLC run of peptide-derived hydrazide **135** with 99 % purity, solvent: 10 % to 40 % MeOH/H_2O (0.05 % TFA) in 25 min, flow rate: 0.43 ml/min, retention time t_R = 12.2 min; the peak integration is based on detection at 280 nm.

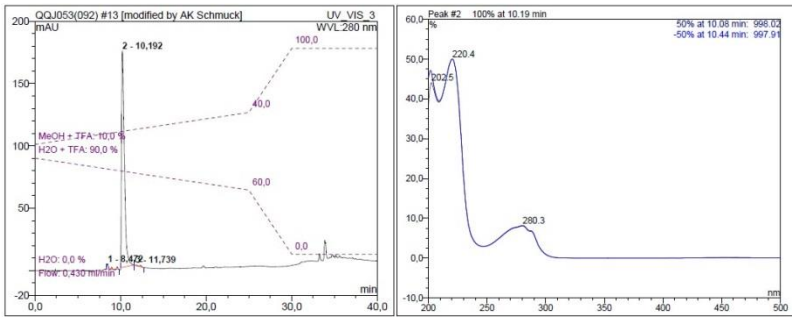

Figure 7.10 Analytical HPLC run of peptide-derived hydrazide **136** with 98 % purity, solvent: 10 % to 40 % MeOH/H_2O (0.05 % TFA) in 25 min, flow rate: 0.43 ml/min, retention time t_R = 10.2 min; the peak integration is based on detection at 280 nm.

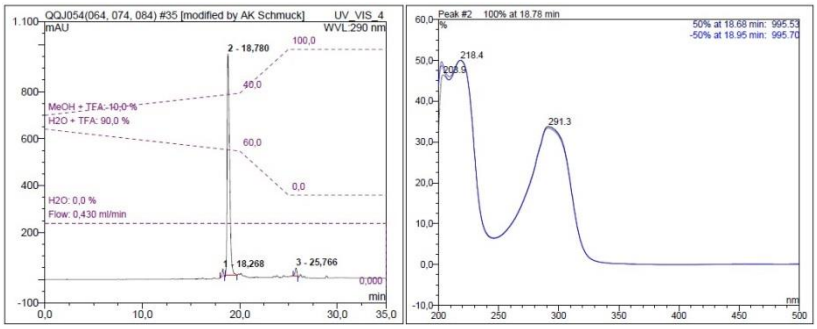

Figure 7.11 Analytical HPLC run of peptide-derived hydrazide **138** with 96 % purity, solvent: 10 % to 40 % MeOH/H_2O (0.05 % TFA) in 20 min, flow rate: 0.43 ml/min, retention time t_R = 18.8 min; the peak integration is based on detection at 290 nm.

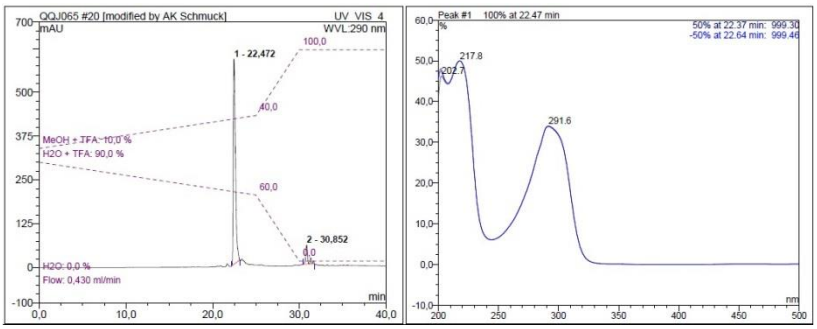

Figure 7.12 Analytical HPLC run of peptide-derived hydrazide **139** with 91 % purity, solvent: 10 % to 40 % MeOH/H_2O (0.05 % TFA) in 25 min, flow rate: 0.43 ml/min, retention time t_R = 22.5 min; the peak integration is based on detection at 290 nm.

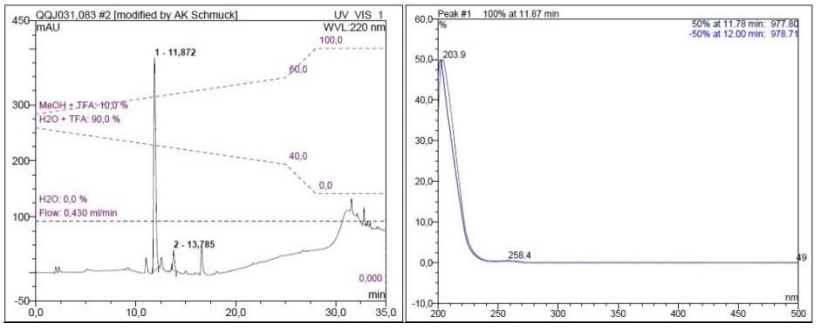

Figure 7.13 Analytical HPLC run of peptide-derived hydrazide **140** with 91 % purity, solvent: 10 % to 60 % MeOH/H_2O (0.05 % TFA) in 25 min, flow rate: 0.43 ml/min, retention time t_R = 11.9 min; the peak integration is based on detection at 220 nm.

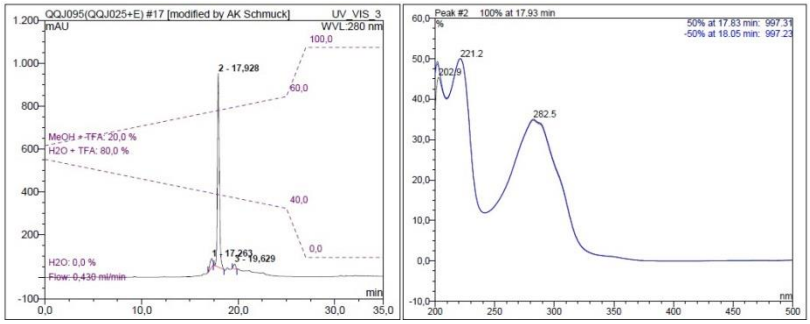

Figure 7.14 Analytical HPLC run of acyl hydrazone **141** with 92 % purity, solvent: 20 % to 60 % MeOH/H_2O (0.05 % TFA) in 25 min, flow rate: 0.43 ml/min, retention time t_R = 17.9 min; the peak integration is based on detection at 280 nm.

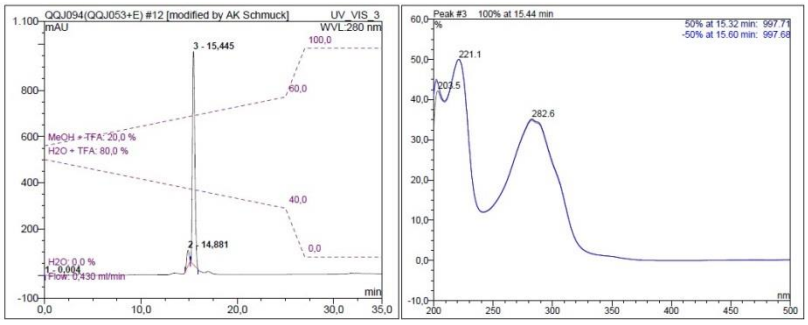

Figure 7.15 Analytical HPLC run of acyl hydrazone **142** with 93 % purity, solvent: 20 % to 60 % MeOH/H_2O (0.05 % TFA) in 25 min, flow rate: 0.43 ml/min, retention time t_R = 15.4 min; the peak integration is based on detection at 280 nm.

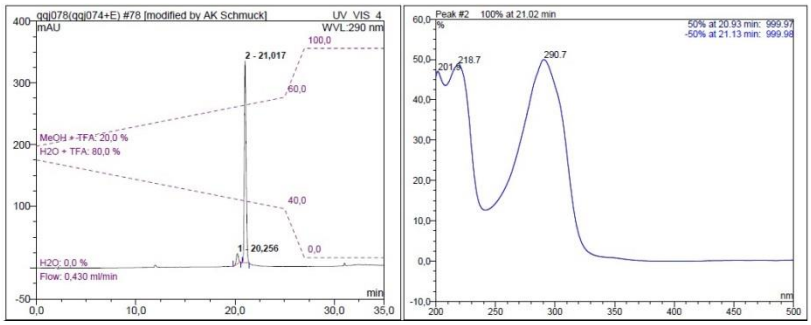

Figure 7.16 Analytical HPLC run of acyl hydrazone **143** with 94 % purity, solvent: 20 % to 60 % MeOH/H_2O (0.05 % TFA) in 25 min, flow rate: 0.43 ml/min, retention time t_R = 21.0 min; the peak integration is based on detection at 290 nm.

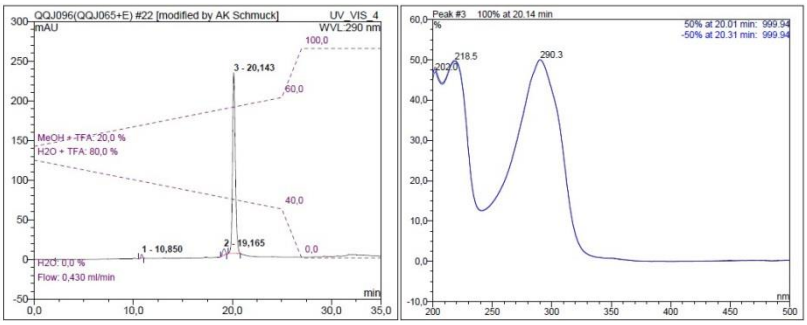

Figure 7.17 Analytical HPLC run of acyl hydrazone **144** with 96 % purity, solvent: 20 % to 60 % MeOH/H_2O (0.05 % TFA) in 25 min, flow rate: 0.43 ml/min, retention time t_R = 20.1 min; the peak integration is based on detection at 290 nm.

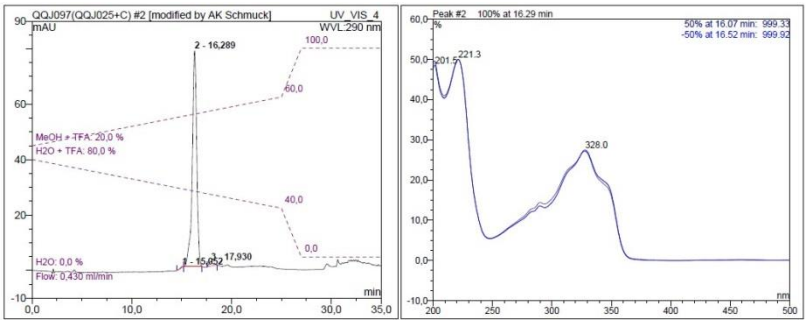

Figure 7.18 Analytical HPLC run of acyl hydrazone **146** with 98 % purity, solvent: 20 % to 60 % MeOH/H_2O (0.05 % TFA) in 25 min, flow rate: 0.43 ml/min, retention time t_R = 16.3 min; the peak integration is based on detection at 290 nm.

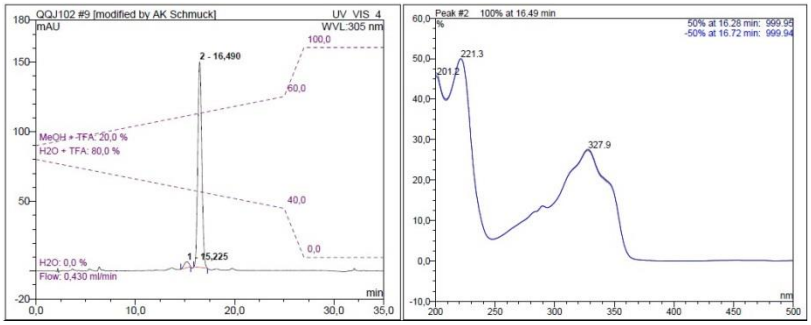

Figure 7.19 Analytical HPLC run of acyl hydrazone **147** with 97 % purity, solvent: 20 % to 60 % MeOH/H_2O (0.05 % TFA) in 25 min, flow rate: 0.43 ml/min, retention time t_R = 16.5 min; the peak integration is based on detection at 305 nm.

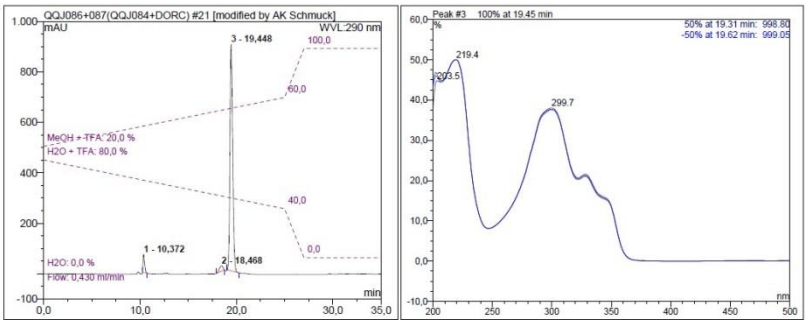

Figure 7.20 Analytical HPLC run of acyl hydrazone **148** with 93 % purity, solvent: 20 % to 60 % MeOH/H_2O (0.05 % TFA) in 25 min, flow rate: 0.43 ml/min, retention time t_R = 19.5 min; the peak integration is based on detection at 290 nm.

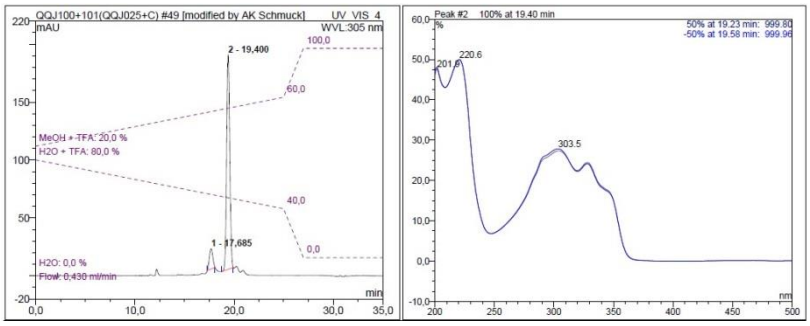

Figure 7.21 Analytical HPLC run of acyl hydrazone **149** with 91 % purity, solvent: 20 % to 60 % MeOH/H_2O (0.05 % TFA) in 25 min, flow rate: 0.43 ml/min, retention time t_R = 19.4 min; the peak integration is based on detection at 305 nm.

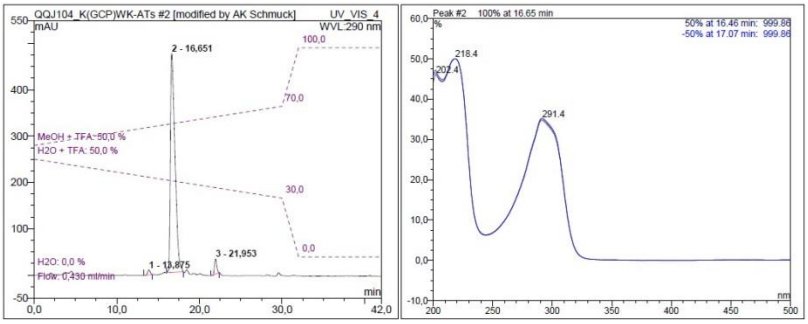

Figure 7.22 Analytical HPLC run of ligand **161** with 95 % purity, solvent: 50 % to 70 % MeOH/H_2O (0.05 % TFA) in 30 min, flow rate: 0.43 ml/min, retention time t_R = 16.7 min; the peak integration is based on detection at 290 nm.

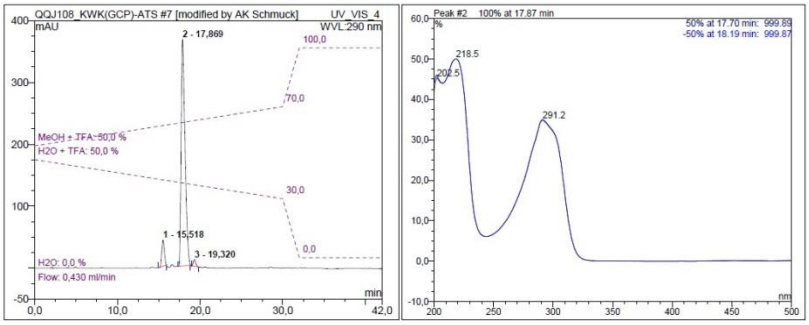

Figure 7.23 Analytical HPLC run of ligand **162** with 91 % purity, solvent: 50 % to 70 % MeOH/H_2O (0.05 % TFA) in 30 min, flow rate: 0.43 ml/min, retention time t_R = 17.9 min; the peak integration is based on detection at 290 nm.

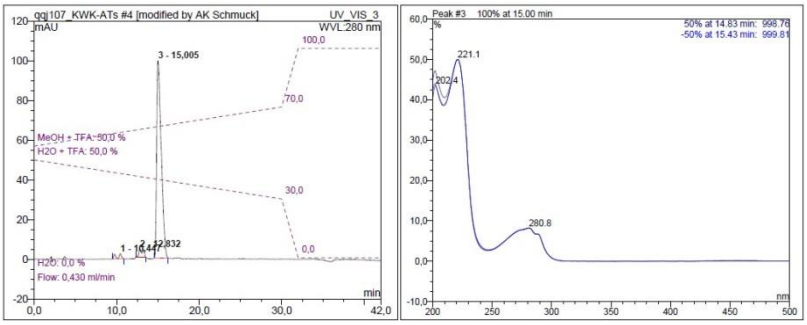

Figure 7.24 Analytical HPLC run of ligand **163** with 94 % purity, solvent: 50 % to 70 % MeOH/H_2O (0.05 % TFA) in 30 min, flow rate: 0.43 ml/min, retention time t_R = 15.0 min; the peak integration is based on detection at 280 nm.

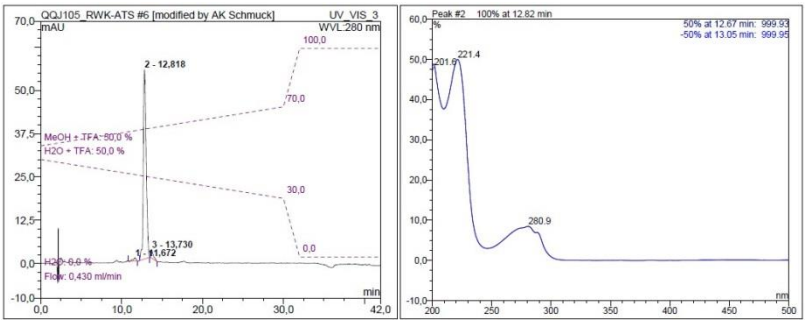

Figure 7.25 Analytical HPLC run of ligand **164** with 95 % purity, solvent: 50 % to 70 % MeOH/H_2O (0.05 % TFA) in 30 min, flow rate: 0.43 ml/min, retention time t_R = 12.8 min; the peak integration is based on detection at 280 nm.

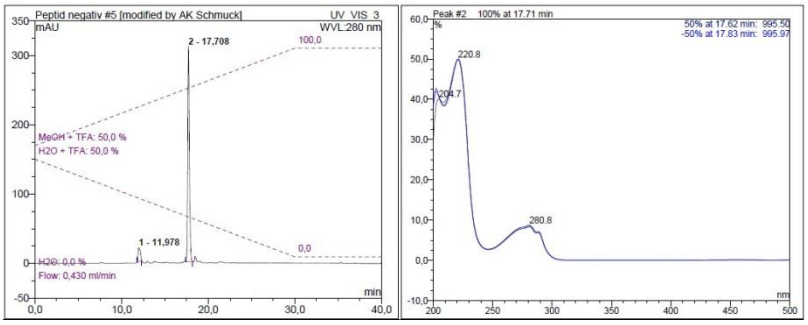

Figure 7.26 Analytical HPLC run of ligand **165** with 92 % purity, solvent: 50 % to 100 % MeOH/H_2O (0.05 % TFA) in 30 min, flow rate: 0.43 ml/min, retention time t_R = 17.7 min; the peak integration is based on detection at 280 nm.

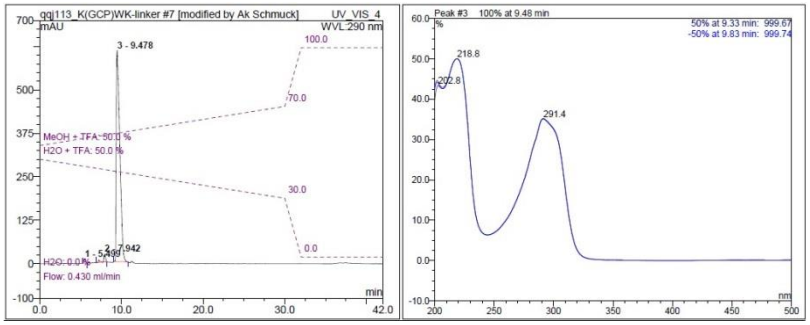

Figure 7.27 Analytical HPLC run of ligand **168** with 95 % purity, solvent: 50 % to 70 % MeOH/H_2O (0.05 % TFA) in 30 min, flow rate: 0.43 ml/min, retention time t_R = 9.5 min; the peak integration is based on detection at 290 nm.

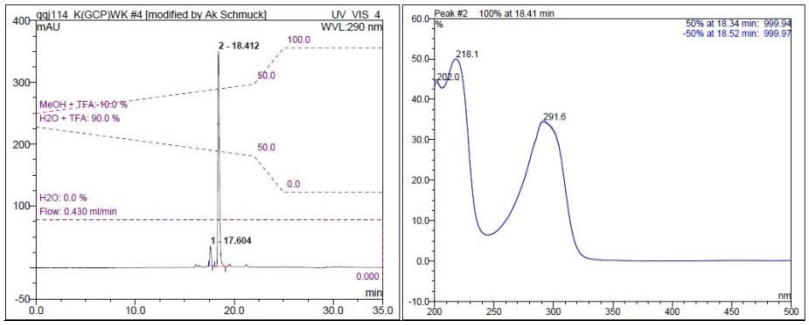

Figure 7.28 Analytical HPLC run of ligand **170** with 93 % purity, solvent: 10 % to 50 % MeOH/H_2O (0.05 % TFA) in 22 min, flow rate: 0.43 ml/min, retention time t_R = 18.4 min; the peak integration is based on detection at 290 nm.

7.2.2 Enzyme Inhibition Data

The following data is based on the β-tryptase inhibition assays for all the inhibitors. All the measurements were done in triplicate with the substrate concentration at 50 μM. The average value of the residual enzyme activity (in %) at different inhibitor concentrations were listed in the following tables. The IC_{50} values were calculated from these data with the help of GraFit program on the basis of nonlinear regression.

Four-armed peptide ligand $(RWKG)_2(RLFG)_2$ (115)

[**115**], μM	Enzyme activity, %
100	6.19
80	7.79
60	9.52
40	14.97
20	27.61
10	32.68
8	36.95
6	39.62
4	45.88
2	56.86
1	71.40
0.1	91.63

$IC_{50} = 4.04 \pm 0.81$ μM

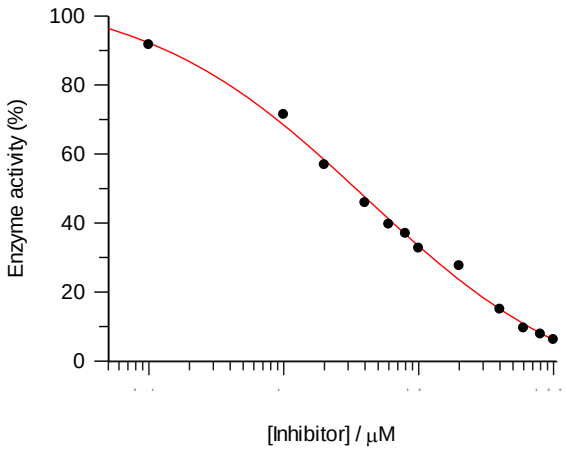

Four-armed peptide ligand $(KWKG)_2(KLFG)_2$ (116)

[**116**], μM	Enzyme activity, %
100	5.83
80	6.44
60	7.81
40	10.23
20	32.86
10	43.76
6	55.54
4	60.21
2	67.16
1	79.44
0.1	87.99

$IC_{50} = 12.77 \pm 3.77$ μM

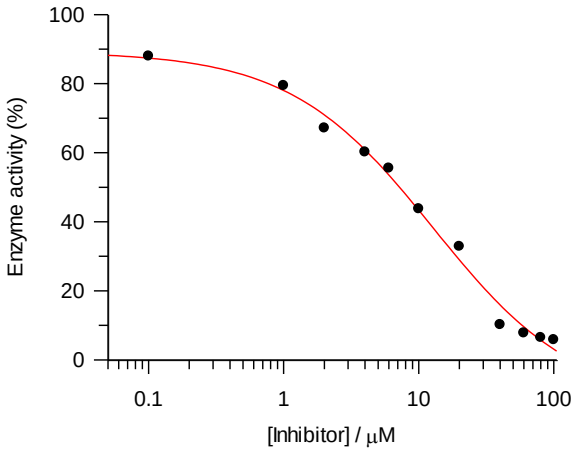

Four-armed peptide ligand $(RWKG)_2(KLFG)_2$ (117)

[**117**], μM	Enzyme activity, %
100	3.10
80	3.47
60	4.71
40	12.70
20	29.20
10	53.10
8	59.96
6	61.87
4	69.32
2	80.79
1	87.83
0.1	99.69

IC_{50} = 13.37 ± 2.45 μM

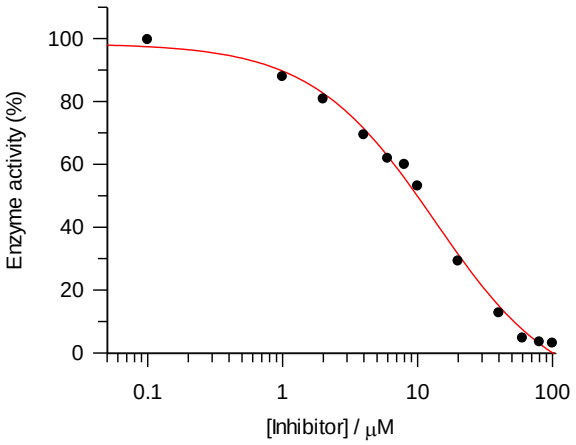

Four-armed peptide ligand $(RWKG)_2(KWKG)_2$ (118)

[**118**], μM	Enzyme activity, %
100	2.16
80	2.74
60	3.37
40	3.83
20	22.61
10	47.41
8	55.81
6	59.17
4	66.53
2	74.77
1	88.88
0.1	97.70

IC_{50} = 10.37 ± 1.64 μM

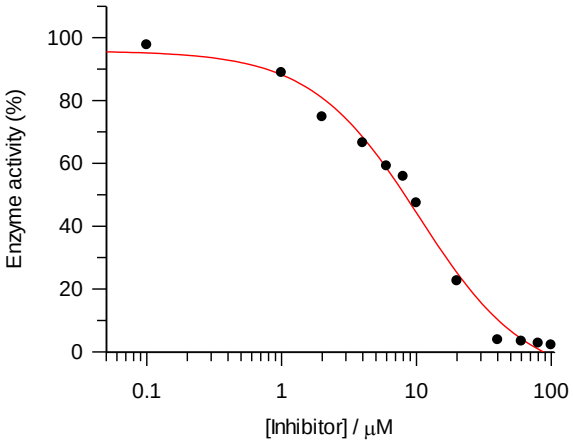

Four-armed peptide ligand $(RWKG)_2(FRKG)_2$ (119)

[**119**], μM	Enzyme activity, %
100	2.16
80	2.27
60	2.35
40	2.53
20	17.71
10	41.56
8	47.99
6	57.93
4	61.06
2	76.08
1	84.46
0.1	99.99

IC_{50} = 8.16 ± 1.14 μM

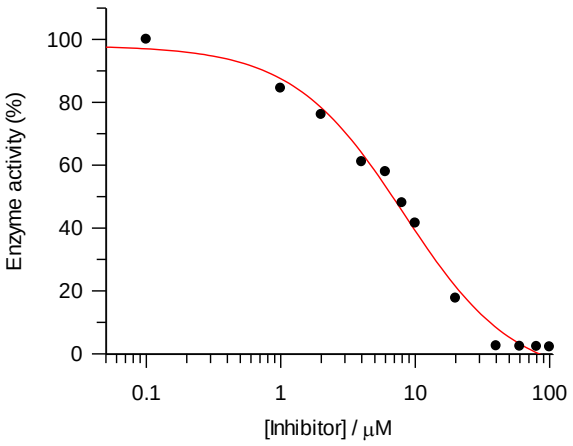

Four-armed peptide ligand $(RWKG)_2(GCP\text{-}LFG)_2$ (120)

[**120**], μM	Enzyme activity, %
100	4.26
80	6.00
60	5.87
40	10.06
20	21.79
10	29.76
8	31.64
4	35.73
2	40.08
1	41.40
0.8	44.87
0.6	44.21
0.4	52.52
0.2	61.43
0.01	99.00

I: $IC_{50} = 0.056 \pm 0.026$ μM
II: $IC_{50} = 19.59 \pm 2.63$ μM

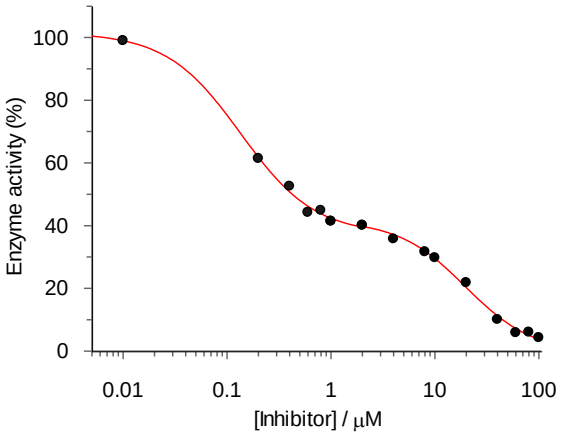

Four-armed peptide ligand $(GCP\text{-}RWKG)_4$ (124)

[**124**], μM	Enzyme activity, %
100	2.51
80	2.51
60	3.13
40	3.07
20	15.53
10	30.20
8	41.93
6	44.14
4	53.44
2	59.14
1	81.39
0.1	99.27

$IC_{50} = 4.93 \pm 0.96$ μM

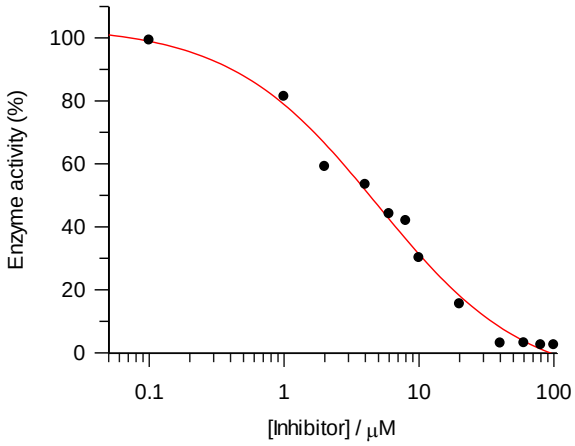

Four-armed peptide ligand $(GCP\text{-}RWK)_4$ (125)

[**125**], μM	Enzyme activity, %
100	5.73
80	6.23
60	6.52
40	9.37
20	28.35
10	52.67
8	52.69
6	60.17
4	68.85
2	75.04
1	90.22
0.1	99.99

$IC_{50} = 10.67 \pm 2.27$ μM

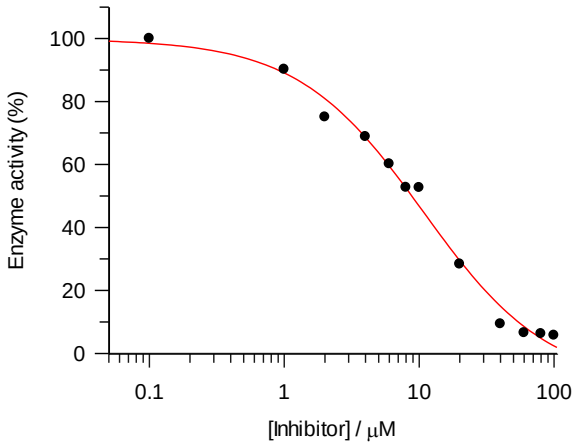

Peptide-derived hydrazide 135

[**135**], μM	Enzyme activity, %
800	3.39
600	4.12
400	4.36
200	6.71
100	11.83
80	13.45
60	16.78
40	21.99
20	34.71
10	54.13
6	68.12
3	88.07
1	95.40

IC_{50} = 12.65 ± 0.61 μM

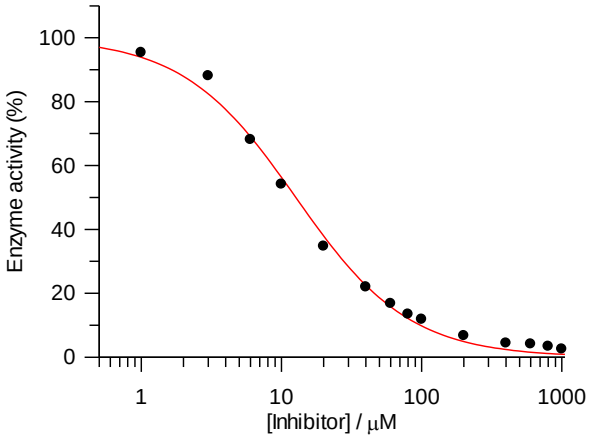

Peptide-derived hydrazide 136

[**136**], μM	Enzyme activity, %
1000	7.91
800	11.14
600	12.32
400	15.78
200	25.01
100	40.76
80	45.87
60	49.63
40	58.91
20	66.61
10	79.66
6	95.99
3	99.00
1	99.99

IC_{50} = 61.05 ± 3.97 μM

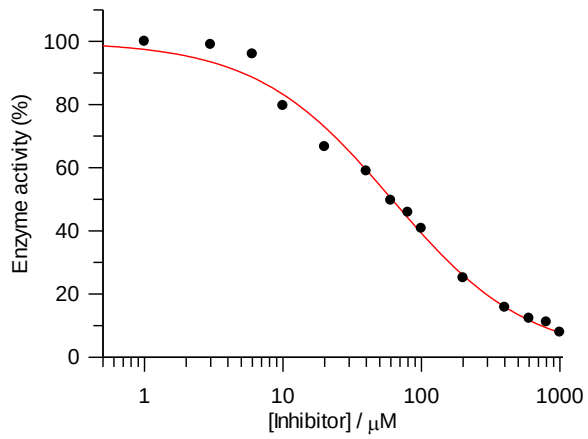

Peptide-derived hydrazide 138

[**138**], μM	Enzyme activity, %
1000	6.14
800	6.74
600	6.50
400	9.54
200	12.77
100	20.96
80	25.24
60	28.87
40	35.17
20	53.39
10	66.89
6	77.62
3	92.52
1	97.62

IC_{50} = 23.58 ± 1.17 μM

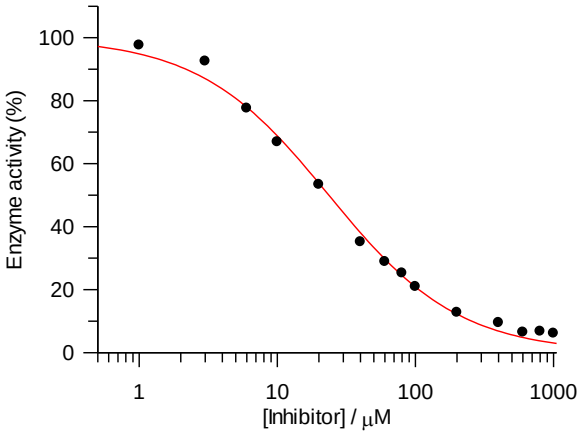

Peptide-derived hydrazide 139

[**139**], μM	Enzyme activity, %
1000	11.75
800	12.85
600	12.45
400	15.84
200	19.12
100	24.68
80	25.78
60	27.52
40	36.05
20	49.36
10	64.13
6	81.24
3	92.15
1	97.77

IC_{50} = 24.50 ± 2.87 μM

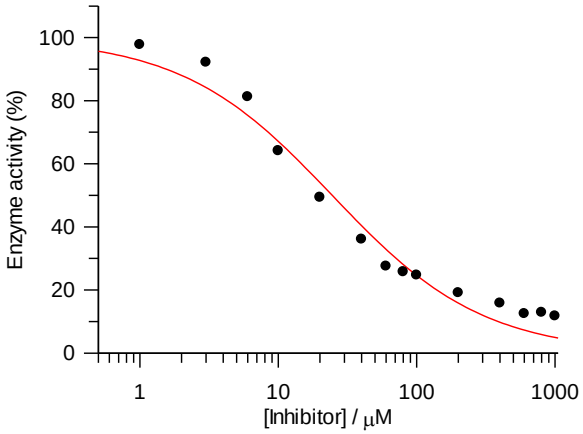

Acyl hydrazone 141

[**141**], μM	Enzyme activity, %
10	6.17
5	8.27
1	10.15
0.8	9.78
0.6	11.18
0.4	13.26
0.2	13.46
0.1	14.34
0.08	15.18
0.06	18.65
0.04	28.04
0.02	44.39
0.01	65.94
0.001	105.28

IC_{50} = 0.0125 ± 0.0008 μM

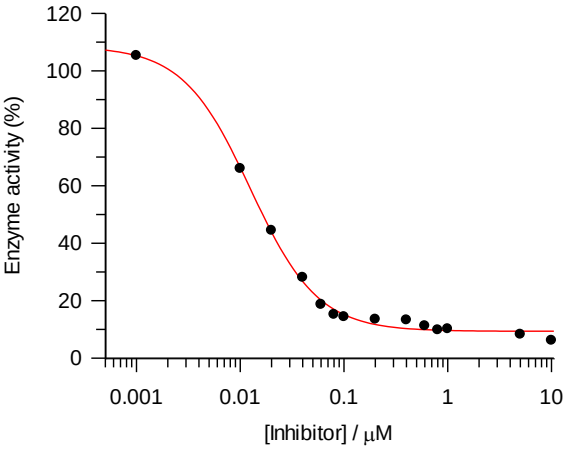

Acyl hydrazone 142

[**142**], μM	Enzyme activity, %
10	7.98
5	10.74
1	17.50
0.8	23.53
0.6	33.36
0.4	42.85
0.1	50.38
0.08	55.45
0.06	63.31
0.04	71.51
0.02	87.12
0.01	92.10
0.001	100.11

IC_{50} = 0.1049 ± 0.0310 μM

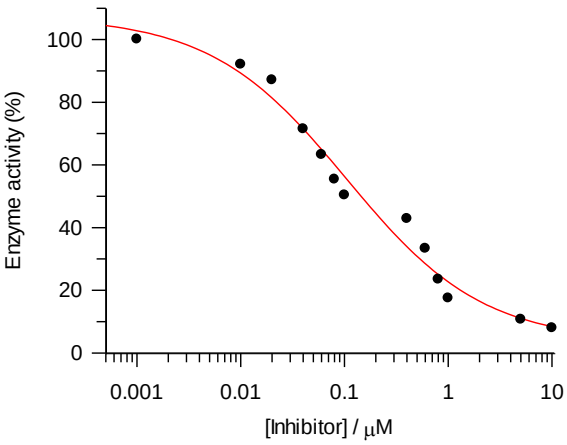

Acyl hydrazone 143

[**143**], μM	Enzyme activity, %
10	11.07
5	11.72
1	14.47
0.8	15.88
0.6	17.89
0.4	19.37
0.2	23.36
0.1	24.53
0.08	29.33
0.04	39.57
0.02	63.32
0.01	79.51
0.001	99.90

IC_{50} = 0.0225 ± 0.0021 μM

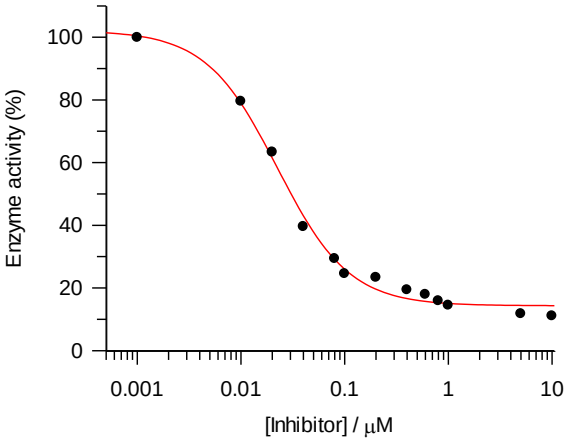

Acyl hydrazone 144

[**144**], μM	Enzyme activity, %
100	3.65
80	4.79
60	5.58
40	12.27
32	34.23
30	19.54
28	36.81
26	42.33
25	38.35
22	48.41
20	48.82
10	56.06
6	59.78
4	63.90
2	65.77
1	64.74
0.8	65.33
0.6	69.84
0.4	73.88
0.2	77.66
0.1	87.80
0.01	99.00

I: IC_{50} = 0.1140 ± 0.0193 μM

II: IC_{50} = 29.93 ± 1.44 μM

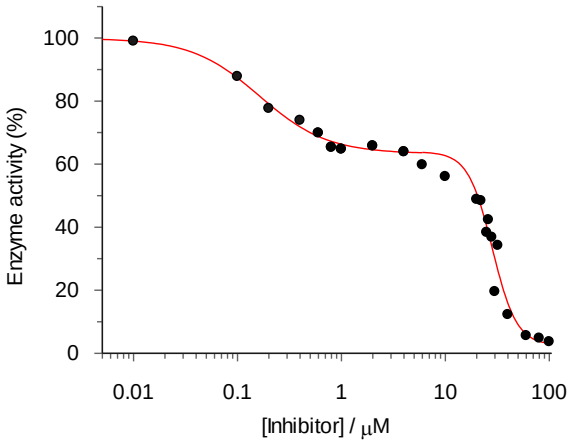

Acyl hydrazone 146

[**146**], μM	Enzyme activity, %
10	12.50
5	13.89
1	16.85
0.8	18.24
0.6	20.83
0.4	24.29
0.2	31.19
0.1	45.90
0.08	51.80
0.06	60.30
0.04	69.21
0.02	86.52
0.01	92.91
0.001	99.99

IC_{50} = 0.0656 ± 0.0023 μM

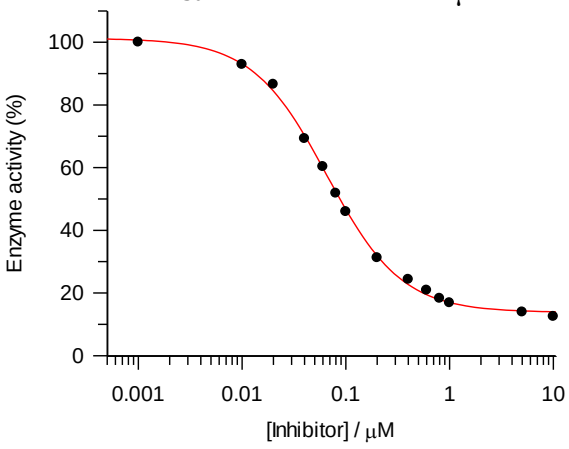

Acyl hydrazone 147

[**147**], μM	Enzyme activity, %
10	6.60
2	18.03
1	29.01
0.8	32.78
0.6	40.76
0.4	52.74
0.2	74.45
0.1	87.83
0.06	89.71
0.04	98.89
0.02	99.99

IC_{50} = 0.3918 ± 0.0244 μM

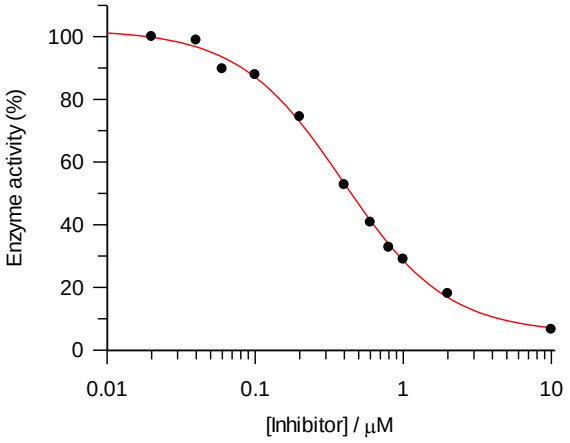

Acyl hydrazone 148

[**148**], μM	Enzyme activity, %
10	4.71
5	4.28
1	8.63
0.8	11.40
0.6	13.18
0.4	18.47
0.2	31.33
0.15	36.63
0.1	43.66
0.08	55.35
0.06	62.64
0.04	73.33
0.01	95.86
0.001	104.34

IC_{50} = 0.0780 ± 0.0031 μM

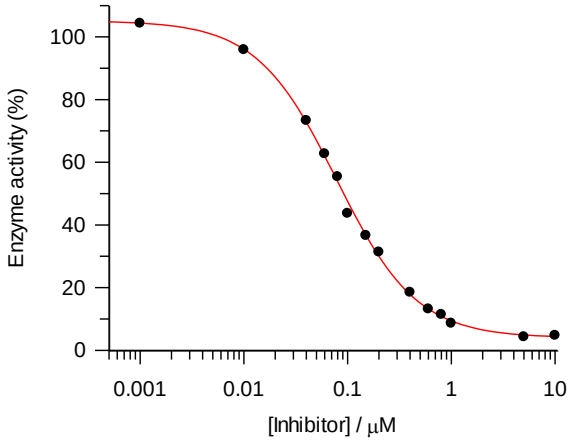

Acyl hydrazone 149

[**149**], μM	Enzyme activity, %
10	12.67
5	13.44
1	18.7
0.8	20.53
0.6	23.12
0.4	28.49
0.2	42.51
0.1	60.69
0.08	70.86
0.06	75.02
0.04	85.09
0.02	92.85
0.01	99
0.001	99.99

IC_{50} = 0.1208 ± 0.0039 μM

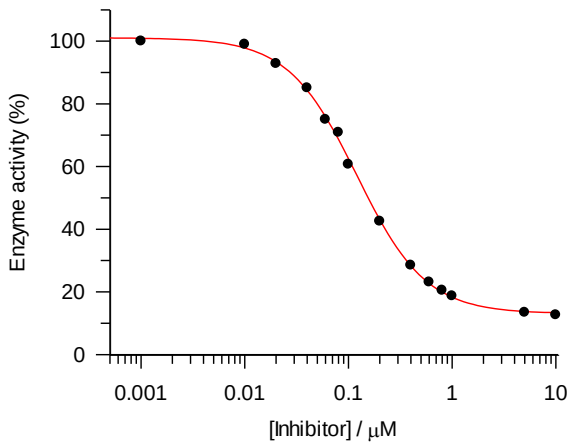

Thiolalkylated ligand 161

[**161**], μM	Enzyme activity, %
20	22.71
10	30.66
8	34.41
6	38.92
4	45.19
2	61.03
1	80.94
0.5	91.64
0.1	99
0.01	99.99

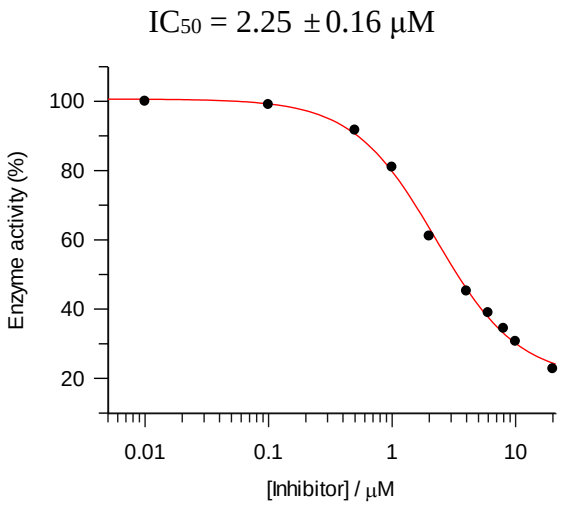

Thiolalkylated ligand 162

[**162**], μM	Enzyme activity, %
1000	25.12
800	30.83
600	39.15
400	50.13
200	71.8
100	86.65
10	90.47

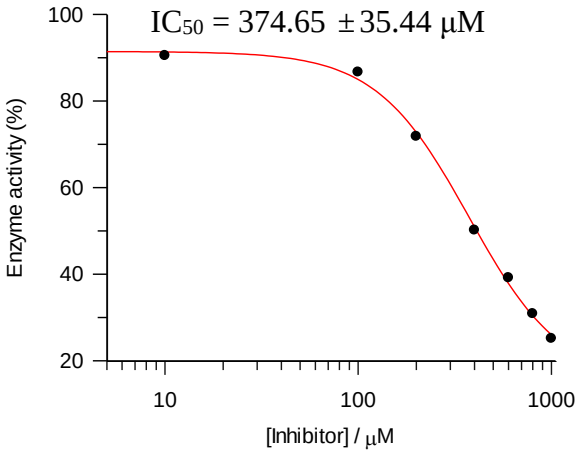

Thiolalkylated ligand 163

[**163**], μM	Enzyme activity, %
100	33.02
80	33.5
60	33.99
40	37.36
20	42.02
10	51.71
8	58.18
6	61.74
4	71.18
2	82.98
1	96.59
0.5	99.99

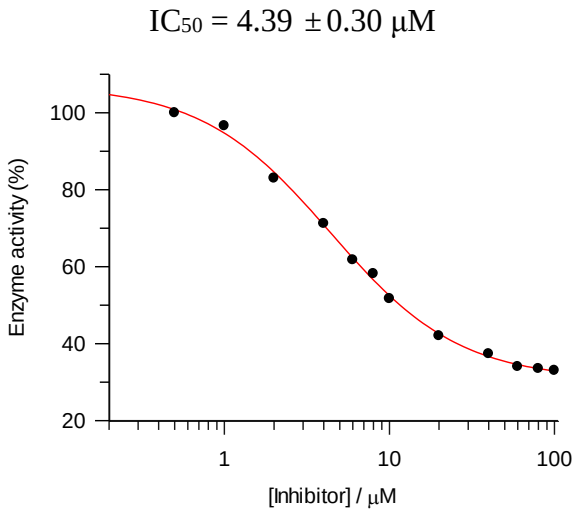

Thiolalkylated ligand 164

[**164**], μM	Enzyme activity, %
10	18.67
8	18.44
6	18.04
4	19.71
2	18.65
1	19.28
0.1	63.58
1	18.91
0.8	22.73
0.6	24.69
0.4	31.99
0.2	44.01
0.1	63.61
0.1	63.04
0.08	70.82
0.06	74.67
0.04	78.68
0.02	89.48
0.01	93.22
0.001	97.47

IC_{50} = 0.1271 ±0.0052 μM

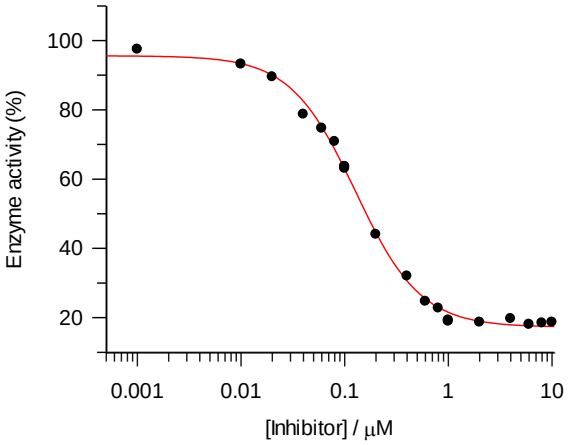

Alkylated ligand 168

[**168**], μM	Enzyme activity, %
100	7.37
80	8.87
60	9.55
40	11.99
20	18.29
10	29.79
8	34.51
6	40.03
4	48.94
2	68.9
1	83.1
0.1	99.00

IC_{50} = 3.62 ±0.10 μM

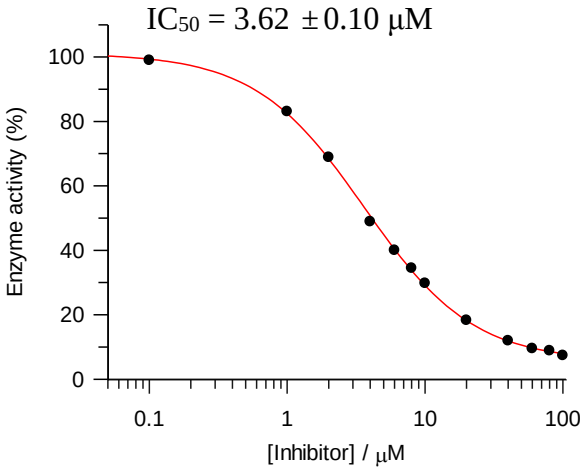

Tripeptide ligand 170

[**170**], μM	Enzyme activity, %
100	2.75
80	1.93
60	3.44
40	3.38
20	5.06
10	8.91
8	10.38
6	13.34
4	18.09
2	35.82
1	53.71
0.1	99

IC_{50} = 1.03 ±0.04 μM

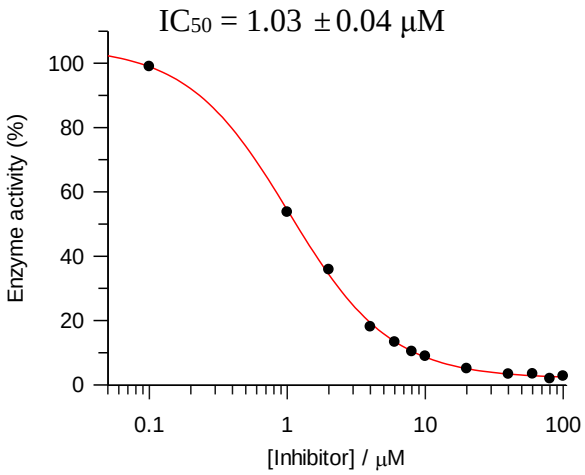

***Ex situ* conjugates 171**

[**161**], μM	Enzyme activity, %
8.74	18.35
4.37	30.51
4.11	31.16
2.06	47.99
1.75	53.10
1.18	64.84
0.87	64.72
0.41	79.39
0.24	87.34
0	72.02

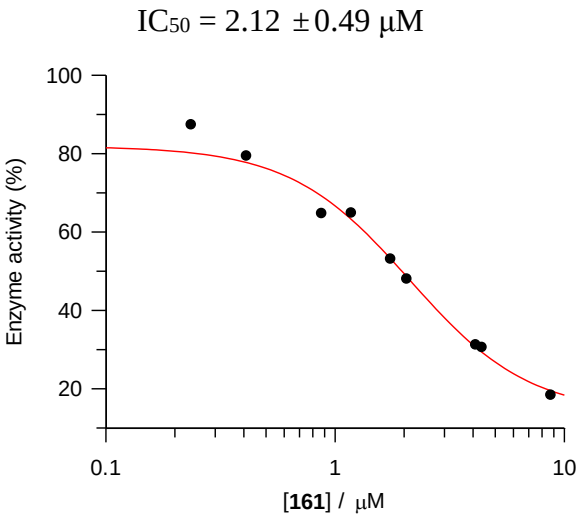

***In situ* conjugates 172**

[**161**], μM	Enzyme activity, %
61.56	51.19
25.13	51.70
0.26	71.79
0.05	74.78
0	75.87

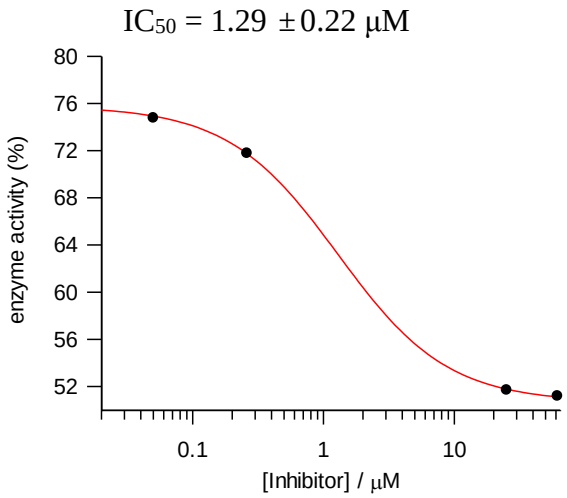

7.2.3 Screening of DCLs

The following data were based on the enzyme screening data of the full library and sub-libraries. The relative activities of sub-libraries compared to the full library, as well as the normalized activity related to the full library were listed in the following tables. The name of the sub-libraries represents the lacking specific building blocks.

Table 7.1 Relative and normalized activity of sub-libraries compared to the full library (inhibitory activity: 62 %).

Sub-libraries	Relative activity, %	Normalized activity, %
135	13.28	21.41935
136	15.10333	24.36022
138	29.55667	47.67204
139	8.19667	13.22043
140	-3.93667	-6.34946
A	0.39	0.62903
B	5.87	9.46774
C	5.06	8.16129
D	2.74667	4.43011
E	11.08	17.87097

Table 7.2 Relative and normalized activity of sub-libraries compared to the size-reduced full library (inhibitory activity: 52 %).

Sub-libraries	Relative activity, %	Normalized activity, %
138	52.16667	99.99994
A	1.9	3.64217
B	1.03667	1.98722
C	8.43	16.15973
D	0.26333	0.50479
E	15.86	30.40254

7.2.4 Determination of Enzyme Inhibition Modes

The following data were based on the determination of enzyme inhibition modes by different kinds of inhibitors.

Table 7.3 Nonlinear analysis of enzyme inhibition mode of four-armed peptide ligand $(RWKG)_2(GCP\text{-}LFG)_2$ (**120**).

Nonlinear analysis				
	[**120**] = 0 μM	[**120**] = 5 μM	[**120**] = 10 μM	[**120**] = 100 μM
[S], μM	*v*	*v*	*v*	*v*
600	127.47	61.755	33.835	6.54
400	107.92	53.4	38.58	4.315
300	57.50667	20.16	18.29	2.335
200	27.31333	8.35	7.34	1.125
100	12.79333	3.87	3.595	0.715
50	2.80667	0.585	0.715	0.07
10	81.425	38.725	30.32	3.1

Table 7.4 Determination of enzyme inhibition mode of four-armed peptide ligand $(RWKG)_2(GCP\text{-}LFG)_2$ (**120**) with the help of *Lineweaver-Burk* plots.

Lineweaver-Burk				
	[**120**] = 0 μM	[**120**] = 5 μM	[**120**] = 10 μM	[**120**] = 100 μM
1/[S]	1/*v*	1/*v*	1/*v*	1/*v*
0.00167	0.00784	–	–	0.15291
0.0025	0.00927	0.01873	0.02592	0.23175
0.00333	0.01228	0.02582	0.03298	0.32258
0.005	0.01739	0.0496	0.05467	0.42827
0.01	0.03661	0.11976	0.13624	0.88889
0.02	0.07817	0.2584	0.27816	1.3986
0.025	0.10204	0.3876	0.42735	–
0.05	0.20747	0.86207	0.88496	–
0.1	0.35629	1.26582	1.3986	–

Table 7.5 Determination of enzyme inhibition mode of acyl hydrazone (**141**) with the help of *Dixon* plots.

Dixon						
	[S] = 25 μM	[S] = 50 μM	[S] = 75 μM	[S] = 100 μM	[S] = 150 μM	[S] = 200 μM
[**141**], μM	1/*v*	1/*v*	1/*v*	1/*v*	1/*v*	1/*v*
0.1	0.7266	0.33762	0.22597	0.19017	0.10815	0.06772
0.08	0.66231	–	0.19897	0.14076	0.08418	0.05424
0.06	0.55846	–	0.16071	0.11025	0.0686	0.04353
0.04	0.3747	0.15339	0.11546	0.07569	0.04572	0.02961
0.02	0.21583	0.09654	0.06531	0.04568	0.02737	0.01912
0.01	0.14911	0.0722	0.05047	0.03561	0.02264	0.01585
0.001	0.11322	0.05245	0.03591	0.02587	0.01658	0.01185

Table 7.6 Nonlinear analysis of enzyme inhibition mode of single-armed ligand (**170**).

Nonlinear analysis					
	[**170**] = 0 μM	[**170**] = 1 μM	[**170**] = 5 μM	[**170**] = 10 μM	[**170**] = 50 μM
[S], μM	*v*	*v*	*v*	*v*	*v*
400	82.68557	47.15248	19.43252	11.64199	2.79383
300	81.27196	43.4512	14.82594	8.38411	2.42982
200	56.64116	25.89424	7.77569	4.273	1.27449
100	24.65435	10.87509	3.35119	2.07963	0.58519
50	12.53852	5.08	1.54533	1.15346	0.29905
25	5.78335	2.81226	0.69612	0.60259	0.16302
10	2.7752	1.21561	0.33383	0.24	0.07634

Table 7.7 Determination of enzyme inhibition mode of single-armed ligand (**170**) with the help of *Lineweaver-Burk* plots.

Lineweaver-Burk					
	[**170**] = 0 μM	[**170**] = 1 μM	[**170**] = 5 μM	[**170**] = 10 μM	[**170**] = 50 μM
1/[S]	1/*v*	1/*v*	1/*v*	1/*v*	1/*v*
0.0025	0.01209	0.02121	0.05146	0.0859	0.35793
0.00333	0.0123	0.02301	0.06745	0.11927	0.41155
0.005	0.01766	0.03862	0.12861	0.23403	0.78463
0.01	0.04056	0.09195	0.2984	0.48085	1.70885
0.02	0.07975	0.19685	0.64711	0.86695	3.34387
0.04	0.17291	0.35559	1.43653	1.65952	6.13423
0.1	0.36033	0.82263	2.99556	4.16667	–

7.3 Curriculum Vitae

The CV is not included in this online version of the thesis for reasons of data protection.

7.4 List of Publications

Journal

Qian-Qian Jiang, Lina Bartsch, Wilhelm Sicking, Peter R. Wich, Dominik Heider, Daniel Hoffmann, Carsten Schmuck;

A New Approach to Inhibit Human β-Tryptase by Protein Surface Binding of Four-Armed Peptide Ligands with Two Different Sets of Arms;

Org. Biomol. Chem., **2013**, *11*, 1631–1639. Selected as "hot paper".

Poster Presentation

Qian-Qian Jiang, Carsten Schmuck;

Design of Multivalent Peptides as Potent Inhibitors for β-Tryptase;

3rd European Chemistry Congress, Nürnberg, Germany, 29th Aug-2nd Sep **2010**.

Symposium in Supramolecular Chemistry, Essen, Germany, 24th-25th Feb **2011**.

Junges Chemie Symposium Ruhr, Essen, Germany, 22nd Sep **2011**.

Qian-Qian Jiang, Carsten Schmuck;

Discovery of Potent Inhibitors of Human β-Tryptase from Dynamic Combinatorial Library;

Forschungstag der Medizinischen Fakultät, Essen, Germany, 23rd Nov **2012**.

8. BIBLIOGRAPHY

[1] Malcolm Dixon, E. C. Webb, *Enzymes*, third ed., Academic Press Inc., New York, **1979**.

[2] H. John Smith, C. Simons, *Enzymes and their inhibition: drug development*, CRC Press, **2005**.

[3] C. Seife, Blunting nature's Swiss army knife. *Science* **1997**, *277*, 1602-1603.

[4] B. Turk, Targeting proteases: successes, failures and future prospects. *Nat. Rev. Drug Discov.* **2006**, *5*, 785-799.

[5] G. Abbenante, D. P. Fairlie, Protease inhibitors in the clinic. *Med. Chem.* **2005**, *1*, 71-104.

[6] M. Cuccioloni, M. Mozzicafreddo, L. Bonfili, V. Cecarini, A. M. Eleuteri, M. Angeletti, Natural Occurring Polyphenols as Template for Drug Design. Focus on Serine Proteases. *Chem. Biol. Drug Des.* **2009**, *74*, 1-15.

[7] L. Hedstrom, Serine protease mechanism and specificity. *Chem. Rev.* **2002**, *102*, 4501-4523.

[8] B. E. Maryanoff, Inhibitors of serine proteases as potential therapeutic agents: The road from thrombin to tryptase to cathepsin G. *J. Med. Chem.* **2004**, *47*, 769-787.

[9] J. M. Clark, W. M. Abraham, C. E. Fishman, R. Forteza, A. Ahmed, A. Cortes, R. L. Warne, W. R. Moore, R. D. Tanaka, Tryptase Inhibitors Block Allergen-Induced Airway and Inflammatory Responses in Allergic Sheep. *Am. J. Respir. Crit. Care. Med.* **1995**, *152*, 2076-2083.

[10] J. F. Molinari, M. Scuri, W. R. Moore, J. Clark, R. Tanaka, W. M. Abraham, Inhaled tryptase causes bronchoconstriction in sheep via histamine release. *Am. J. Respir. Crit. Care. Med.* **1996**, *154*, 649-653.

[11] J. M. Clark, W. R. Moore, R. D.Tanaka, Tryptase inhibitors: a new class of antiinflammatory drug. *Drugs Future* **1996**, *21*, 811-816.

[12] P. J. B. Pereira, A. Bergner, S. Macedo-Ribeiro, R. Huber, G. Matschiner, H. Fritz, C. P. Sommerhoff, W. Bode, Human beta-tryptase is a ring-like tetramer with active sites facing a central pore. *Nature* **1998**, *392*, 306-311.

[13] P. R. Wich, C. Schmuck, Reversible and Noncompetitive Inhibition of beta-Tryptase by Protein Surface Binding of Tetravalent Peptide Ligands Identified from a Combinatorial Split-Mix Library. *Angew. Chem. Int. Ed.* **2010**, *49*, 4113-4116.

[14] C. Schmuck, Carboxylate binding by 2-(guanidiniocarbonyl)pyrrole receptors in aqueous solvents: Improving the binding properties of guanidinium cations through additional hydrogen bonds. *Chem. Eur. J.* **2000**, *6*, 709-718.

[15] C. Schmuck, M. Heil, J. Scheiber, K. Baumann, Charge interactions do the job: A combined statistical and combinatorial approach to finding artificial receptors for binding tetrapeptides in water. *Angew. Chem. Int. Ed.* **2005**, *44*, 7208-7212.

[16] V. Henri, *Lois Générales de l'Action des Diastases*, Librairie Scientifique A. Hermann, Paris, **1903**.

[17] L. Michaelis, M. L. Menten, Die Kinetik der Invertinwirkung. *Biochem. Z.* **1913**, *49*, 333-369.

[18] I. H. Segel, *Enzyme kinetics*, John Wiley & Sons, Inc., **1975**.

[19] M. E. Jones, Analysis of Algebraic Weighted Least-Squares Estimators for Enzyme Parameters. *Biochem. J.* **1992**, *288*, 533-538.

[20] W. X. Tian, C. L. Tsou, Determination of the Rate-Constant of Enzyme Modification by Measuring the Substrate Reaction in the Presence of the Modifier. *Biochemistry* **1982**, *21*, 1028-1032.

[21] R. Kitz, I. B. Wilson, Esters of Methanesulfonic Acid as Irreversible Inhibitors of Acetylcholinesterase. *J. Biol. Chem.* **1962**, *237*, 3245-3249.

[22] M. Dixon, The Determination of Enzyme Inhibitor Constants. *Biochem. J.* **1953**, *55*, 170-171.

[23] A. Cornish-Bowden, A simple graphical method for determining the inhibition constants of mixed, uncompetitive and non-competitive inhibitors. *Biochem. J.* **1974**, *137*, 143-144.

[24] J. L. Reymond, V. S. Fluxa, N. Maillard, Enzyme assays. *Chem. Commun.* **2009**, 34-46.

[25] C. Oberthur, H. Graf, M. Hamburger, The content of indigo precursors in Isatis tinctoria leaves - a comparative study of selected accessions and post-harvest treatments. *Phytochemistry* **2004**, *65*, 3261-3268.

[26] J. B. Kempton, S. G. Withers, Mechanism of Agrobacterium Beta-Glucosidase: Kinetic Studies. *Biochemistry* **1992**, *31*, 9961-9969.

[27] J. Yang, Y. Koga, H. Nakano, T. Yamane, Modifying the chain-length selectivity of the lipase from Burkholderia cepacia KWI-56 through in vitro combinatorial mutagenesis in the substrate-binding site. *Protein Eng.* **2002**, *15*, 147-152.

[28] E. T. Farinas, U. Schwaneberg, A. Glieder, F. H. Arnold, Directed evolution of a cytochrome P450 monooxygenase for alkane oxidation. *Adv. Synth. Catal.* **2001**, *343*, 601-606.

[29] A. Celik, G. A. Roberts, J. H. White, S. K. Chapman, N. J. Turner, S. L. Flitsch, Probing the substrate specificity of the catalytically self-sufficient cytochrome P450RhF from a Rhodococcus sp. *Chem. Commun.* **2006**, 4492-4494.

[30] Z. Q. Wang, J. F. Liao, Z. J. Diwu, N-DEVD-N '-morpholinecarbonyl-rhodamine 110: novel caspase-3 fluorogenic substrates for cell-based apoptosis assay. *Bioorg. Med. Chem. Lett.* **2005**, *15*, 2335-2338.

[31] F. Badalassi, D. Wahler, G. Klein, P. Crotti, J. L. Reymond, A versatile periodate-coupled fluorogenic assay for hydrolytic enzymes. *Angew. Chem. Int. Ed.* **2000**, *39*, 4067-4070.

[32] L. Cai, N. Friedman, X. S. Xie, Stochastic protein expression in individual cells at the single molecule level. *Nature* **2006**, *440*, 358-362.

[33] C. Kimchi-Sarfaty, J. M. Oh, I. W. Kim, Z. E. Sauna, A. M. Calcagno, S. V. Ambudkar, M. M. Gottesman, A "silent" polymorphism in the MDR1 gene changes substrate specificity. *Science* **2007**, *315*, 525-528.

[34] A. Hennig, D. Roth, T. Enderle, W. M. Nau, Nanosecond time-resolved fluorescence protease assays. *ChemBioChem* **2006**, *7*, 733-737.

[35] H. Sahoo, W. M. Nau, Phosphorylation-induced conformational changes in short peptides probed by fluorescence resonance energy transfer in the 10A domain. *ChemBioChem* **2007**, *8*, 567-573.

[36] H. Takakusa, K. Kikuchi, Y. Urano, S. Sakamoto, K. Yamaguchi, T. Nagano, Design and synthesis of an enzyme-cleavable sensor molecule for phosphodiesterase activity based on fluorescence resonance energy transfer. *J. Am. Chem. Soc.* **2002**, *124*, 1653-1657.

[37] Y. Kawanishi, K. Kikuchi, H. Takakusa, S. Mizukami, Y. Urano, T. Higuchi, T. Nagano, Design and synthesis of intramolecular resonance-energy transfer probes for use in ratiometric

measurements in aqueous solution. *Angew. Chem. Int. Ed.* **2000**, *39*, 3438-3440.

[38] H. Takakusa, K. Kikuchi, Y. Urano, H. Kojima, T. Nagano, A novel design method of ratiometric fluorescent probes based on fluorescence resonance energy transfer switching by spectral overlap integral. *Chem. Eur. J.* **2003**, *9*, 1479-1485.

[39] E. D. Matayoshi, G. T. Wang, G. A. Krafft, J. Erickson, Novel Fluorogenic Substrates for Assaying Retroviral Proteases by Resonance Energy-Transfer. *Science* **1990**, *247*, 954-958.

[40] T. Kohl, K. G. Heinze, R. Kuhlemann, A. Koltermann, P. Schwille, A protease assay for two-photon crosscorrelation and FRET analysis based solely on fluorescent proteins. *Proc. Natl. Acad. Sci. USA* **2002**, *99*, 12161-12166.

[41] R. Warfield, P. Bardelang, H. Saunders, W. C. Chan, C. Penfold, R. James, N. R. Thomas, Internally quenched peptides for the study of lysostaphin: an antimicrobial protease that kills Staphylococcus aureus. *Org. Biomol. Chem.* **2006**, *4*, 3626-3638.

[42] Y. Z. Yang, P. Babiak, J. L. Reymond, Low background FRET-substrates for lipases and esterases suitable for high-throughput screening under basic (pH 11) conditions. *Org. Biomol. Chem.* **2006**, *4*, 1746-1754.

[43] H. E. Muller, Abts Peroxidase Medium as a Highly Sensitive Plate Assay for Detection of Hydrogen-Peroxide Production in Bacteria. *J. Microbiol. Methods* **1984**, *2*, 101-102.

[44] M. D. Truppo, F. Escalettes, N. J. Turner, Rapid determination of both the activity and enantioselectivity of ketoreductases. *Angew. Chem. Int. Ed.* **2008**, *47*, 2639-2641.

[45] R. G. Whittaker, M. K. Manthey, D. S. Lebrocque, P. J. Hayes, A Microtiter Plate Assay for the Characterization of Serine Proteases by Their Esterase-Activity. *Anal. Biochem.* **1994**, *220*, 238-243.

[46] L. E. Janes, R. J. Kazlauskas, Quick E. A fast spectrophotometric method to measure the enantioselectivity of hydrolases. *J. Org. Chem.* **1997**, *62*, 4560-4561.

[47] L. E. Janes, A. C. Lowendahl, R. J. Kazlauskas, Quantitative screening of hydrolase libraries using pH indicators: Identifying active and enantioselective hydrolases. *Chem. Eur. J.* **1998**, *4*, 2324-2331.

[48] K. E. S. Dean, G. Klein, O. Renaudet, J. L. Reymond, A green fluorescent chemosensor for amino acids provides a versatile high-throughput screening (HTS) assay for proteases. *Bioorg. Med. Chem. Lett.* **2003**, *13*, 1653-1656.

[49] J. L. Reymond, D. Wahler, Substrate arrays as enzyme fingerprinting tools. *ChemBioChem* **2002**, *3*, 701-708.

[50] J. Grognux, J. L. Reymond, Classifying enzymes from selectivity fingerprints. *ChemBioChem* **2004**, *5*, 826-831.

[51] Y. Z. Yang, P. Babiak, J. L. Reymond, New monofunctionalized fluorescein derivatives for the efficient high-throughput screening of lipases and esterases in aqueous media. *Helv. Chim. Acta* **2006**, *89*, 404-415.

[52] J. Kofoed, J. L. Reymond, Identification of protease substrates by combinatorial profiling on TentaGel beads. *Chem. Commun.* **2007**, 4453-4455.

[53] A. Furka, F. Sebestyen, M. Asgedom, G. Dibo, General-Method for Rapid Synthesis of Multicomponent Peptide Mixtures. *Int. J. Pept. Protein Res.* **1991**, *37*, 487-493.

[54] K. S. Lam, M. Lebl, V. Krchnak, The "one-bead-one-compound" combinatorial library method. *Chem. Rev.* **1997**, *97*, 411-448.

[55] K. S. Lam, S. E. Salmon, E. M. Hersh, V. J. Hruby, W. M. Kazmierski, R. J. Knapp, A New Type of

Synthetic Peptide Library for Identifying Ligand-Binding Activity. *Nature* **1991**, *354*, 82-84.

[56] K. Braeckmans, S. C. De Smedt, M. Leblans, R. Pauwels, J. Demeester, Encoding microcarriers: Present and future technologies. *Nat. Rev. Drug Discov.* **2002**, *1*, 447-456.

[57] G. Lowe, R. Quarrell, Screening Peptide Bead Libraries for Enzyme Inhibitors. *Methods: A Companion to Methods in Enzymology* **1994**, *6*, 411-416.

[58] K. S. Lam, M. Lebl, Selective Technology: Bead-Binding Screening. *Methods: A Companion to Methods in Enzymology* **1994**, *6*, 372-380.

[59] J. Z. Wu, Q. Y. N. Ma, K. S. Lam, Identifying Substrate Motifs of Protein-Kinases by a Random Library Approach. *Biochemistry* **1994**, *33*, 14825-14833.

[60] M. Meldal, I. Svendsen, K. Breddam, F. I. Auzanneau, Portion-Mixing Peptide Libraries of Quenched Fluorogenic Substrates for Complete Subsite Mapping of Endoprotease Specificity. *Proc. Natl. Acad. Sci. USA* **1994**, *91*, 3314-3318.

[61] M. Meldal, Pega - a Flow Stable Polyethylene-Glycol Dimethyl Acrylamide Copolymer for Solid-Phase Synthesis. *Tetrahedron Lett.* **1992**, *33*, 3077-3080.

[62] M. Meldal, I. Svendsen, Direct Visualization of Enzyme-Inhibitors Using a Portion Mixing Inhibitor Library Containing a Quenched Fluorogenic Peptide Substrate .1. Inhibitors for Subtilisin Carlsberg. *J. Chem. Soc., Perkin Trans. 1* **1995**, 1591-1596.

[63] M. Renil, M. Ferreras, J. M. Delaisse, N. T. Foged, M. Meldal, PEGA supports for combinatorial peptide synthesis and solid-phase enzymatic library assays. *J. Pept. Sci.* **1998**, *4*, 195-210.

[64] J. J. Perona, C. S. Craik, Evolutionary divergence of substrate specificity within the chymotrypsin-like serine protease fold. *J. Biol. Chem.* **1997**, *272*, 29987-29990.

[65] P. K. Madala, J. D. A. Tyndall, T. Nall, D. P. Fairlie, Update 1 of: Proteases Universally Recognize Beta Strands In Their Active Sites. *Chem. Rev.* **2010**, *110*, Pr1-Pr31.

[66] T. Tanaka, B. J. Mcrae, K. Cho, R. Cook, J. E. Fraki, D. A. Johnson, J. C. Powers, Mammalian Tissue Trypsin-Like Enzymes - Comparative Reactivities of Human-Skin Tryptase, Human-Lung Tryptase, and Bovine Trypsin with Peptide 4-Nitroanilide and Thioester Substrates. *J. Biol. Chem.* **1983**, *258*, 3552-3557.

[67] I. Schechter, A. Berger, On the size of the active site in proteases. I. Papain. *Biochem. Biophys. Res. Commun.* **1967**, *27*, 157-162.

[68] E. Erez, D. Fass, E. Bibi, How intramembrane proteases bury hydrolytic reactions in the membrane. *Nature* **2009**, *459*, 371-378.

[69] G. G. Glenner, L. A. Cohen, Histochemical Demonstration of a Species-Specific Trypsin-Like Enzyme in Mast Cells. *Nature* **1960**, *185*, 846-847.

[70] L. B. Schwartz, A. M. A. Irani, K. Roller, M. C. Castells, N. M. Schechter, Quantitation of Histamine, Tryptase, and Chymase in Dispersed Human T-Mast and Tc-Mast Cells. *J. Immunol.* **1987**, *138*, 2611-2615.

[71] L. B. Schwartz, R. A. Lewis, K. F. Austen, Tryptase from Human Pulmonary Mast-Cells - Purification and Characterization. *J. Biol. Chem.* **1981**, *256*, 1939-1943.

[72] J. S. Miller, G. Moxley, L. B. Schwartz, Cloning and characterization of a second complementary DNA for human tryptase. *J. Clin. Invest.* **1990**, *86*, 864-870.

[73] P. Vanderslice, S. M. Ballinger, E. K. Tam, S. M. Goldstein, C. S. Craik, G. H. Caughey, Human mast cell tryptase: multiple cDNAs and genes reveal a multigene serine protease family. *Proc. Natl. Acad. Sci. USA* **1990**, *87*, 3811-3815.

[74] H. Z. Xia, C. L. Kepley, K. Sakai, J. Chelliah, A. M. A. Irani, L. B. Schwartz, Quantitation of

Tryptase, Chymase, Fc-Epsilon-Ri-Alpha and Fc-Epsilon-Ri-Gamma Messenger-Rnas in Human Mast-Cells and Basophils by Competitive Reverse Transcription-Polymerase Chain-Reaction. *J. Immunol.* **1995**, *154*, 5472-5480.

[75] C. Prussin, D. D. Metcalfe, 4. IgE, mast cells, basophils, and eosinophils. *J. Allergy. Clin. Immunol.* **2003**, *111*, S486-494.

[76] V. Payne, P. C. A. Kam, Mast cell tryptase: a review of its physiology and clinical significance. *Anaesthesia* **2004**, *59*, 695-703.

[77] D. MacGlashan, IgE receptor and signal transduction in mast cells and basophils. *Curr. Opin. Immunol.* **2008**, *20*, 717-723.

[78] G. H. Caughey, Tryptase genetics and anaphylaxis. *J. Allergy Clin. Immun.* **2006**, *117*, 1411-1414.

[79] F. E. R. Simons, A. J. Frew, I. J. Ansotegui, B. S. Bochner, D. B. K. Golden, F. D. Finkelman, D. Y. M. Leung, J. Lotvall, G. Marone, D. D. Metcalfe, U. Muller, L. J. Rosenwasser, H. A. Sampson, L. B. Schwartz, M. van Hage, A. F. Walls, Risk assessment in anaphylaxis: Current and future approaches. *J. Allergy Clin. Immun.* **2007**, *120*, S2-S24.

[80] G. T. Desanctis, M. Merchant, D. R. Beier, R. D. Dredge, J. K. Grobholz, T. R. Martin, E. S. Lander, J. M. Drazen, Quantitative Locus Analysis of Airway Hyperresponsiveness in a/J and C57bl/6j Mice. *Nat. Genet.* **1995**, *11*, 150-154.

[81] R. Forteza, Y. Botvinnikova, A. Ahmed, A. Cortes, R. H. Gundel, A. Wanner, W. M. Abraham, The interaction of alpha(1)-proteinase inhibitor and tissue kallikrein in controlling allergic ovine airway hyperresponsiveness. *Am. J. Respir. Crit. Care. Med.* **1996**, *154*, 36-42.

[82] J. E. Hunt, R. L. Stevens, K. F. Austen, J. Zhang, Z. N. Xia, N. Ghildyal, Natural disruption of the mouse mast cell protease 7 gene in the C57BL/6 mouse. *J. Biol. Chem.* **1996**, *271*, 2851-2855.

[83] W. M. Abraham, Tryptase: potential role in airway inflammation and remodeling. *Am. J. Physiol. Lung Cell. Mol. Physiol.* **2002**, *282*, L193-L196.

[84] D. Proud, E. S. Siekierski, G. S. Bailey, Identification of Human-Lung Mast-Cell Kininogenase as Tryptase and Relevance of Tryptase Kininogenase Activity. *Biochem. Pharmacol.* **1988**, *37*, 1473-1480.

[85] A. Kozik, R. B. Moore, J. Potempa, T. Imamura, M. Rapala-Kozik, J. Travis, A novel mechanism for bradykinin production at inflammatory sites - Diverse effects of a mixture of neutrophil elastase and mast cell tryptase versus tissue and plasma kallikreins on native and oxidized kininogens. *J. Biol. Chem.* **1998**, *273*, 33224-33229.

[86] C. P. Sommerhoff, W. Bode, G. Matschiner, A. Bergner, H. Fritz, The human mast cell tryptase tetramer: a fascinating riddle solved by structure. *Biochim. Biophys. Acta* **2000**, *1477*, 75-89.

[87] P. Berger, D. W. Perng, H. Thabrew, S. J. Compton, J. A. Cairns, A. R. McEuen, R. Marthan, J. M. T. De Lara, A. F. Walls, Tryptase and agonists of PAR-2 induce the proliferation of human airway smooth muscle cells. *J. Appl. Physiol.* **2001**, *91*, 1372-1379.

[88] C. P. Sommerhoff, C. Sollner, R. Mentele, G. P. Piechottka, E. A. Auerswald, H. Fritz, A Kazal-Type Inhibitor of Human Mast-Cell Tryptase - Isolation from the Medical Leech Hirudo-Medicinalis, Characterization, and Sequence-Analysis. *Biol. Chem. Hoppe-Seyler* **1994**, *375*, 685-694.

[89] G. C. Paesen, C. Siebold, K. Harlos, M. F. Peacey, P. A. Nuttall, D. I. Stuart, A tick protein with a modified Kunitz fold inhibits human tryptase. *J. Mol. Biol.* **2007**, *368*, 1172-1186.

[90] C. P. Sommerhoff, W. Bode, P. J. B. Pereira, M. T. Stubbs, J. Sturzebecher, G. P. Piechottka, G. Matschiner, A. Bergner, The structure of the human beta II-tryptase tetramer: Fo(u)r better or worse.

Proc. Natl. Acad. Sci. USA **1999**, *96*, 10984-10991.

[91] N. Schaschke, A. Dominik, G. Matschiner, C. P. Sommerhoff, Bivalent inhibition of beta-tryptase: Distance scan of neighboring subunits by dibasic inhibitors. *Bioorg. Med. Chem. Lett.* **2002**, *12*, 985-988.

[92] N. Schaschke, G. Matschiner, F. Zettl, U. Marquardt, A. Bergner, W. Bode, C. P. Sommerhoff, L. Moroder, Bivalent inhibition of human beta-tryptase. *Chem. Biol.* **2001**, *8*, 313-327.

[93] S. C. Alter, D. D. Metcalfe, T. R. Bradford, L. B. Schwartz, Regulation of Human Mast-Cell Tryptase - Effects of Enzyme Concentration, Ionic-Strength and the Structure and Negative Charge-Density of Polysaccharides. *Biochem. J.* **1987**, *248*, 821-827.

[94] S. C. Alter, J. A. Kramps, A. Janoff, L. B. Schwartz, Interactions of Human Mast-Cell Tryptase with Biological Protease Inhibitors. *Arch. Biochem. Biophys.* **1990**, *276*, 26-31.

[95] K. C. Elrod, W. R. Moore, W. M. Abraham, R. D. Tanaka, Lactoferrin, a potent tryptase inhibitor, abolishes late-phase airway responses in allergic sheep. *Am. J. Respir. Crit. Care. Med.* **1997**, *156*, 375-381.

[96] L. Cregar, K. C. Elrod, D. Putnam, W. R. Moore, Neutrophil myeloperoxidase is a potent and selective inhibitor of mast cell tryptase. *Arch. Biochem. Biophys.* **1999**, *366*, 125-130.

[97] J. Hallgren, S. Estrada, U. Karlson, K. Alving, G. Pejler, Heparin antagonists are potent inhibitors of mast cell tryptase. *Biochemistry* **2001**, *40*, 7342-7349.

[98] T. Mecca, G. M. L. Consoli, C. Geraci, R. La Spina, F. Cunsolo, Polycationic calix[8]arenes able to recognize and neutralize heparin. *Org. Biomol. Chem.* **2006**, *4*, 3763-3768.

[99] P. Thongyoo, C. Bonomelli, R. J. Leatherbarrow, E. W. Tate, Potent Inhibitors of beta-Tryptase and Human Leukocyte Elastase Based on the MCoTI-II Scaffold. *J. Med. Chem.* **2009**, *52*, 6197-6200.

[100] C. P. Sommerhoff, O. Avrutina, H. U. Schmoldt, D. Gabrijelcic-Geiger, U. Diederichsen, H. Kolmar, Engineered Cystine Knot Miniproteins as Potent Inhibitors of Human Mast Cell Tryptase beta. *J. Mol. Biol.* **2010**, *395*, 167-175.

[101] J. Hallgren, G. Pejler, Biology of mast cell tryptase - An inflammatory mediator. *FEBS J.* **2006**, *273*, 1871-1895.

[102] M. T. Krishna, A. Chauhan, L. Little, K. Sampson, R. Hawksworth, T. Mant, R. Djukanovic, T. Lee, S. Holgate, Inhibition of mast cell tryptase by inhaled APC 366 attenuates allergen-induced late-phase airway obstruction in asthma. *J. Allergy Clin. Immun.* **2001**, *107*, 1039-1045.

[103] M. J. Costanzo, S. C. Yabut, H. R. Almond, P. Andrade-Gordon, T. W. Corcoran, L. de Garavilla, J. A. Kauffman, W. M. Abraham, R. Recacha, D. Chattopadhyay, B. E. Maryanoff, Potent, small-molecule inhibitors of human mast cell tryptase. Antiasthmatic action of a dipeptide-based transition-state analogue containing a benzothiazole ketone. *J. Med. Chem.* **2003**, *46*, 3865-3876.

[104] B. A. Katz, J. M. Clark, J. S. Finer-Moore, T. E. Jenkins, C. R. Johnson, M. J. Ross, C. Luong, W. R. Moore, R. M. Stroud, Design of potent selective zinc-mediated serine protease inhibitors. *Nature* **1998**, *391*, 608-612.

[105] T. Selwood, H. Smolensky, D. R. McCaslin, N. M. Schechter, The interaction of human tryptase-beta with small molecule inhibitors provides new insights into the unusual functional instability and quaternary structure of the protease. *Biochemistry* **2005**, *44*, 3580-3590.

[106] J. M. Dener, K. D. Rice, W. S. Newcomb, V. R. Wang, W. B. Young, A. R. Gangloff, E. Y. L. Kuo, L. Cregar, D. Putnam, M. Wong, Dibasic inhibitors of human mast cell tryptase. Part 3: Identification of a series of potent and selective inhibitors containing the benzamidine functionality. *Bioorg. Med. Chem. Lett.* **2001**, *11*, 1629-1633.

[107] K. D. Rice, A. R. Gangloff, E. Y. L. Kuo, J. M. Dener, V. R. Wang, R. Lum, W. S. Newcomb, C. Havel, D. Putnam, L. Cregar, M. Wong, R. L. Warne, Dibasic inhibitors of human mast cell tryptase. Part 1: Synthesis and optimization of a novel class of inhibitors. *Bioorg. Med. Chem. Lett.* **2000**, *10*, 2357-2360.

[108] K. D. Rice, V. R. Wang, A. R. Gangloff, E. Y. L. Kuo, J. M. Dener, W. S. Newcomb, W. B. Young, D. Putnam, L. Cregar, M. Wong, P. J. Simpson, Dibasic inhibitors of human mast cell tryptase. Part 2: Structure-activity relationships and requirements for potent activity. *Bioorg. Med. Chem. Lett.* **2000**, *10*, 2361-2366.

[109] C. D. Wright, A. M. Havill, S. C. Middleton, M. A. Kashem, D. J. Dripps, W. M. Abraham, D. S. Thomson, L. E. Burgess, Inhibition of allergen-induced pulmonary responses by the selective tryptase inhibitor 1,5-bis-{4-[(3-carbamimidoyl-benzenesulfonylamino)-methyl]phenoxy}-pentane (AMG-126737). *Biochem. Pharmacol.* **1999**, *58*, 1989-1996.

[110] L. E. Burgess, B. J. Newhouse, P. Ibrahim, J. Rizzi, M. A. Kashem, A. Hartman, B. J. Brandhuber, C. D. Wright, D. S. Thomson, G. P. A. Vigers, K. Koch, Potent selective nonpeptidic inhibitors of human lung tryptase. *Proc. Natl. Acad. Sci. USA* **1999**, *96*, 8348-8352.

[111] W. J. Tremaine, A. Brzezinski, J. A. Katz, D. C. Wolf, T. J. Fleming, J. Mordenti, L. C. Strenkoski-Nix, M. C. Kurth, A. U. C. S. Grp, Treatment of mildly to moderately active ulcerative colitis with a tryptase inhibitor (APC 2059): an open-label pilot study. *Aliment. Pharm. Therap.* **2002**, *16*, 407-413.

[112] S. W. Oh, C. I. Pae, D. K. Lee, F. Jones, G. K. S. Chiang, H. O. Kim, S. H. Moon, B. L. Cao, C. Ogbu, K. W. Jeong, G. Kozu, H. Nakanishi, M. Kahn, E. Y. Chi, W. R. Henderson, Tryptase inhibition blocks airway inflammation in a mouse asthma model. *J. Immunol.* **2002**, *168*, 1992-2000.

[113] M. del Fresno, D. B. Fernandez-Forner, M. Miralpeix, V. Segarra, H. Ryder, M. Royo, F. Albericio, Combinatorial approaches towards the discovery of new tryptase inhibitors. *Bioorg. Med. Chem. Lett.* **2005**, *15*, 1659-1664.

[114] D. Scarpi, J. D. McBride, R. J. Leatherbarrow, Inhibition of human beta-tryptase by Bowman-Birk inhibitor derived peptides: creation of a new tri-functional inhibitor. *Bioorg. Med. Chem.* **2004**, *12*, 6045-6052.

[115] N. Schaschke, C. P. Sommerhoff, Upgrading a Natural Product: Inhibition of Human beta-Tryptase by Cyclotheonamide Analogues. *ChemMedChem* **2010**, *5*, 367-370.

[116] D. Janke, C. P. Sommerhoff, N. Schaschke, The arginine mimicking beta-amino acid beta(3)hPhe(3-H2N-CH2) as S1 ligand in cyclotheonamide-based beta-tryptase inhibitors. *Bioorg. Med. Chem.* **2011**, *19*, 7236-7243.

[117] W. C. Lumma, K. M. Witherup, T. J. Tucker, S. F. Brady, J. T. Sisko, A. M. Naylor-Olsen, S. D. Lewis, B. J. Lucas, J. P. Vacca, Design of novel, potent, noncovalent inhibitors of thrombin with nonbasic P-1 substructures: Rapid structure-activity studies by solid-phase synthesis. *J. Med. Chem.* **1998**, *41*, 1011-1013.

[118] S. Roehrig, A. Straub, J. Pohlmann, T. Lampe, J. Pernerstorfer, K. H. Schlemmer, P. Reinemer, E. Perzborn, Discovery of the novel antithrombotic agent 5-chloro-N-({(5S)-2-oxo-3[4-(3-oxomorpholin-4-yl)phenyl]-1,3-oxazolidin-5-yl}methyl)thiophene-2-carboxamide (BAY 59-7939): An oral, direct factor Xa inhibitor. *J. Med. Chem.* **2005**, *48*, 5900-5908.

[119] G. Y. Liang, Y. M. Choi-Sledeski, X. Chen, Y. Gong, E. W. MacMillan, J. Tsay, K. Sides, J. Cairns, B. Kulitzscher, D. J. Aldous, I. Morize, H. W. Pauls, Dimerization of beta-tryptase inhibitors, does

it work for both basic and neutral P1 groups? *Bioorg. Med. Chem. Lett.* **2012**, *22*, 3370-3376.

[120] T. Mecca, G. M. L. Consoli, C. Geraci, F. Cunsolo, Designed calix[8]arene-based ligands for selective tryptase surface recognition. *Bioorg. Med. Chem.* **2004**, *12*, 5057-5062.

[121] M. W. Peczuh, A. D. Hamilton, Peptide and protein recognition by designed molecules. *Chem. Rev.* **2000**, *100*, 2479-2493.

[122] A. A. Bogan, K. S. Thorn, Anatomy of hot spots in protein interfaces. *J. Mol. Biol.* **1998**, *280*, 1-9.

[123] T. Schrader, S. Koch, Artificial protein sensors. *Mol. Biosyst.* **2007**, *3*, 241-248.

[124] S. Fletcher, A. D. Hamilton, Protein surface recognition and proteomimetics: mimics of protein surface structure and function. *Curr. Opin. Chem. Biol.* **2005**, *9*, 632-638.

[125] R. Jain, J. T. Ernst, O. Kutzki, H. S. Park, A. D. Hamilton, Protein recognition using synthetic surface-targeted agents. *Mol. Divers.* **2004**, *8*, 89-100.

[126] P. Wich, Universität Würzburg (Würzburg), **2009**.

[127] M. R. Arkin, J. A. Wells, Small-molecule inhibitors of protein-protein interactions: Progressing towards the dream. *Nat. Rev. Drug Discov.* **2004**, *3*, 301-317.

[128] W. E. Stites, Protein-protein interactions: Interface structure, binding thermodynamics, and mutational analysis. *Chem. Rev.* **1997**, *97*, 1233-1250.

[129] A. G. Cochran, Protein-protein interfaces: mimics and inhibitors. *Curr. Opin. Chem. Biol.* **2001**, *5*, 654-659.

[130] H. Pelletier, J. Kraut, Crystal Structure of a Complex between Electron Transfer Partners, Cytochrome c Peroxidase and Cytochrome c. *Science* **1992**, *258*, 1748-1755.

[131] A. N. Volkov, J. A. R. Worrall, E. Holtzmann, M. Ubbink, Solution structure and dynamics of the complex between cytochrome c and cytochrome c peroxidase determined by paramagnetic NMR. *Proc. Natl. Acad. Sci. USA* **2006**, *103*, 18945-18950.

[132] G. C. Kresheck, L. B. Vitello, J. E. Erman, Calorimetric Studies on the Interaction of Horse Ferricytochrome-C and Yeast Cytochrome-C Peroxidase. *Biochemistry* **1995**, *34*, 8398-8405.

[133] X. W. Wu, J. H. Bayle, D. Olson, A. J. Levine, The P53 Mdm-2 Autoregulatory Feedback Loop. *Gene Dev.* **1993**, *7*, 1126-1132.

[134] P. H. Kussie, S. Gorina, V. Marechal, B. Elenbaas, J. Moreau, A. J. Levine, N. P. Pavletich, Structure of the MDM2 oncoprotein bound to the p53 tumor suppressor transactivation domain. *Science* **1996**, *274*, 948-953.

[135] A. J. Wilson, Inhibition of protein-protein interactions using designed molecules. *Chem. Soc. Rev.* **2009**, *38*, 3289-3300.

[136] H. Yin, A. D. Hamilton, Strategies for targeting protein-protein interactions with synthetic agents. *Angew. Chem. Int. Ed.* **2005**, *44*, 4130-4163.

[137] V. Martos, P. Castreno, J. Valero, J. de Mendoza, Binding to protein surfaces by supramolecular multivalent scaffolds. *Curr. Opin. Chem. Biol.* **2008**, *12*, 698-706.

[138] T. Oshima, Y. Baba, Recognition of exterior protein surfaces using artificial ligands based on calixarenes, crown ethers, and tetraphenylporphyrins. *J. Incl. Phenom. Macro. Chem.* **2012**, *73*, 17-32.

[139] V. Bohmer, Calixarenes, Macrocycles with (Almost) Unlimited Possibilities. *Angew. Chem. Int. Ed.* **1995**, *34*, 713-745.

[140] S. Shinkai, Calixarenes - the 3rd-Generation of Supramolecules. *Tetrahedron* **1993**, *49*, 8933-8968.

[141] L. Baldini, A. Casnati, F. Sansone, R. Ungaro, Calixarene-based multivalent ligands. *Chem. Soc. Rev.* **2007**, *36*, 254-266.

[142] A. W. Coleman, F. Perret, A. Moussa, M. Dupin, Y. Gu, H. Perron, Calix[n]arenes as protein sensors. *Top. Curr. Chem.* **2007**, *277*, 31-88.

[143] C. S. Greenberg, P. J. Birckbichler, R. H. Rice, Transglutaminases - Multifunctional Cross-Linking Enzymes That Stabilize Tissues. *FASEB J.* **1991**, *5*, 3071-3077.

[144] S. Francese, A. Cozzolino, L. Caputo, C. Esposito, M. Martino, C. Gaeta, F. Troisi, P. Neri, Transglutaminase surface recognition by peptidocalix[4]arene diversomers. *Tetrahedron Lett.* **2005**, *46*, 1611-1615.

[145] M. G. Chini, S. Terracciano, R. Riccio, G. Bifulco, R. Ciao, C. Gaeta, F. Troisi, P. Neri, Conformationally Locked Calixarene-Based Histone Deacetylase Inhibitors. *Org. Lett.* **2010**, *12*, 5382-5385.

[146] H. S. Park, Q. Lin, A. D. Hamilton, Protein surface recognition by synthetic receptors: A route to novel submicromolar inhibitors for alpha-chymotrypsin. *J. Am. Chem. Soc.* **1999**, *121*, 8-13.

[147] H. S. Park, Q. Lin, A. D. Hamilton, Modulation of protein-protein interactions by synthetic receptors: Design of molecules that disrupt serine protease-proteinaceous inhibitor interaction. *Proc. Natl. Acad. Sci. USA* **2002**, *99*, 5105-5109.

[148] Y. Hamuro, M. C. Calama, H. S. Park, A. D. Hamilton, A calixarene with four peptide loops: An antibody mimic for recognition of protein surfaces. *Angew. Chem. Int. Ed.* **1997**, *36*, 2680-2683.

[149] Y. Wei, G. L. McLendon, A. D. Hamilton, M. A. Case, C. B. Purring, Q. Lin, H. S. Park, C. S. Lee, T. N. Yu, Disruption of protein-protein interactions: design of a synthetic receptor that blocks the binding of cytochrome c to cytochrome c peroxidase. *Chem. Commun.* **2001**, 1580-1581.

[150] S. Gordo, V. Martos, E. Santos, M. Menendez, C. Bo, E. Giralt, J. de Mendoza, Stability and structural recovery of the tetramerization domain of p53-R337H mutant induced by a designed templating ligand. *Proc. Natl. Acad. Sci. USA* **2008**, *105*, 16426-16431.

[151] R. E. McGovern, H. Fernandes, A. R. Khan, N. P. Power, P. B. Crowley, Protein camouflage in cytochrome c-calixarene complexes. *Nat. Chem.* **2012**, *4*, 527-533.

[152] R. K. Jain, A. D. Hamilton, Protein surface recognition by synthetic receptors based on a tetraphenylporphyrin scaffold. *Org. Lett.* **2000**, *2*, 1721-1723.

[153] A. J. Wilson, K. Groves, R. K. Jain, H. S. Park, A. D. Hamilton, Directed denaturation: Room temperature and stoichiometric unfolding of cytochrome c by a metalloporphyrin dimer. *J. Am. Chem. Soc.* **2003**, *125*, 4420-4421.

[154] K. Groves, A. J. Wilson, A. D. Hamilton, Catalytic unfolding and proteolysis of cytochrome c induced by synthetic binding agents. *J. Am. Chem. Soc.* **2004**, *126*, 12833-12842.

[155] L. Baldini, A. J. Wilson, J. Hong, A. D. Hamilton, Pattern-based detection of different proteins using an array of fluorescent protein surface receptors. *J. Am. Chem. Soc.* **2004**, *126*, 5656-5657.

[156] H. C. Zhou, L. Baldini, J. Hong, A. J. Wilson, A. D. Hamilton, Pattern recognition of proteins based on an array of functionalized porphyrins. *J. Am. Chem. Soc.* **2006**, *128*, 2421-2425.

[157] K. Kano, Y. Ishida, Supramolecular complex of cytochrome c with a polyanionic beta-cyclodextrin. *Angew. Chem. Int. Ed.* **2007**, *46*, 727-730.

[158] A. J. Wilson, J. Hong, S. Fletcher, A. D. Hamilton, Recognition of solvent exposed protein surfaces using anthracene derived receptors. *Org. Biomol. Chem.* **2007**, *5*, 276-285.

[159] D. M. Tagore, K. I. Sprinz, S. Fletcher, J. Jayawickramarajah, A. D. Hamilton, Protein recognition and denaturation by self-assembling fragments on a DNA quadruplex scaffold. *Angew. Chem. Int. Ed.* **2007**, *46*, 223-225.

[160] J. F. Cai, B. A. Rosenzweig, A. D. Hamilton, Inhibition of Chymotrypsin by a Self-Assembled

DNA Quadruplex Functionalized with Cyclic Peptide Binding Fragments. *Chem. Eur. J.* **2009**, *15*, 328-332.

[161] C. Renner, J. Piehler, T. Schrader, Arginine- and lysine-specific polymers for protein recognition and immobilization. *J. Am. Chem. Soc.* **2006**, *128*, 620-628.

[162] J. Muldoon, A. E. Ashcroft, A. J. Wilson, Selective Protein-Surface Sensing Using Ruthenium(II) Tris(bipyridine) Complexes. *Chem. Eur. J.* **2010**, *16*, 100-103.

[163] M. H. Filby, J. Muldoon, S. Dabb, N. C. Fletcher, A. E. Ashcroft, A. J. Wilson, Protein surface recognition using geometrically pure Ru(II) tris(bipyridine) derivatives. *Chem. Commun.* **2011**, *47*, 559-561.

[164] R. Shenhar, V. M. Rotello, Nanoparticles: Scaffolds and building blocks. *Acc. Chem. Res.* **2003**, *36*, 549-561.

[165] M. J. Hostetler, J. E. Wingate, C. J. Zhong, J. E. Harris, R. W. Vachet, M. R. Clark, J. D. Londono, S. J. Green, J. J. Stokes, G. D. Wignall, G. L. Glish, M. D. Porter, N. D. Evans, R. W. Murray, Alkanethiolate gold cluster molecules with core diameters from 1.5 to 5.2 nm: Core and monolayer properties as a function of core size. *Langmuir* **1998**, *14*, 17-30.

[166] A. C. Templeton, M. P. Wuelfing, R. W. Murray, Monolayer protected cluster molecules. *Acc. Chem. Res.* **2000**, *33*, 27-36.

[167] A. K. Boal, V. M. Rotello, Fabrication and self-optimization of multivalent receptors on nanoparticle scaffolds. *J. Am. Chem. Soc.* **2000**, *122*, 734-735.

[168] M. C. Daniel, D. Astruc, Gold nanoparticles: Assembly, supramolecular chemistry, quantum-size-related properties, and applications toward biology, catalysis, and nanotechnology. *Chem. Rev.* **2004**, *104*, 293-346.

[169] C. C. You, A. Verma, V. M. Rotello, Engineering the nanoparticle-biomacromolecule interface. *Soft Matter* **2006**, *2*, 190-204.

[170] M. De, P. S. Ghosh, V. M. Rotello, Applications of Nanoparticles in Biology. *Adv. Mater.* **2008**, *20*, 4225-4241.

[171] K. Saha, S. S. Agasti, C. Kim, X. N. Li, V. M. Rotello, Gold Nanoparticles in Chemical and Biological Sensing. *Chem. Rev.* **2012**, *112*, 2739-2779.

[172] A. Verma, V. M. Rotello, Surface recognition of biomacromolecules using nanoparticle receptors. *Chem. Commun.* **2005**, 303-312.

[173] N. O. Fischer, C. M. McIntosh, J. M. Simard, V. M. Rotello, Inhibition of chymotrypsin through surface binding using nanoparticle-based receptors. *Proc. Natl. Acad. Sci. USA* **2002**, *99*, 5018-5023.

[174] L. M. Demers, C. A. Mirkin, R. C. Mucic, R. A. Reynolds, R. L. Letsinger, R. Elghanian, G. Viswanadham, A fluorescence-based method for determining the surface coverage and hybridization efficiency of thiol-capped oligonucleotides bound to gold thin films and nanoparticles. *Anal. Chem.* **2000**, *72*, 5535-5541.

[175] A. Verma, J. M. Simard, V. M. Rotello, Effect of ionic strength on the binding of alpha-chymotrypsin to nanoparticle receptors. *Langmuir* **2004**, *20*, 4178-4181.

[176] N. O. Fischer, A. Verma, C. M. Goodman, J. M. Simard, V. M. Rotello, Reversible "irreversible" inhibition of chymotrypsin using nanoparticle receptors. *J. Am. Chem. Soc.* **2003**, *125*, 13387-13391.

[177] J. C. Love, L. A. Estroff, J. K. Kriebel, R. G. Nuzzo, G. M. Whitesides, Self-assembled monolayers of thiolates on metals as a form of nanotechnology. *Chem. Rev.* **2005**, *105*, 1103-1169.

[178] R. Hong, N. O. Fischer, A. Verma, C. M. Goodman, T. Emrick, V. M. Rotello, Control of protein structure and function through surface recognition by tailored nanoparticle scaffolds. *J. Am. Chem. Soc.* **2004**, *126*, 739-743.

[179] H. Bayraktar, P. S. Ghosh, V. M. Rotello, M. J. Knapp, Disruption of protein-protein interactions using nanoparticles: inhibition of cytochrome c peroxidase. *Chem. Commun.* **2006**, 1390-1392.

[180] C. C. You, M. De, G. Han, V. M. Rotello, Tunable inhibition and denaturation of alpha-chymotrypsin with amino acid-functionalized gold nanoparticles. *J. Am. Chem. Soc.* **2005**, *127*, 12873-12881.

[181] M. De, C. C. You, S. Srivastava, V. M. Rotello, Biomimetic interactions of proteins with functionalized nanoparticles: A thermodynamic study. *J. Am. Chem. Soc.* **2007**, *129*, 10747-10753.

[182] C. C. You, O. R. Miranda, B. Gider, P. S. Ghosh, I. B. Kim, B. Erdogan, S. A. Krovi, U. H. F. Bunz, V. M. Rotello, Detection and identification of proteins using nanoparticle-fluorescent polymer 'chemical nose' sensors. *Nat. Nanotechnol.* **2007**, *2*, 318-323.

[183] M. De, S. Rana, H. Akpinar, O. R. Miranda, R. R. Arvizo, U. H. F. Bunz, V. M. Rotello, Sensing of proteins in human serum using conjugates of nanoparticles and green fluorescent protein. *Nat. Chem.* **2009**, *1*, 461-465.

[184] O. R. Miranda, H. T. Chen, C. C. You, D. E. Mortenson, X. C. Yang, U. H. F. Bunz, V. M. Rotello, Enzyme-Amplified Array Sensing of Proteins in Solution and in Biofluids. *J. Am. Chem. Soc.* **2010**, *132*, 5285-5289.

[185] O. R. Miranda, X. N. Li, L. Garcia-Gonzalez, Z. J. Zhu, B. Yan, U. H. F. Bunz, V. M. Rotello, Colorimetric Bacteria Sensing Using a Supramolecular Enzyme-Nanoparticle Biosensor. *J. Am. Chem. Soc.* **2011**, *133*, 9650-9653.

[186] P. A. Brady, R. P. BonarLaw, S. J. Rowan, C. J. Suckling, J. K. M. Sanders, 'Living' macrolactonisation: Thermodynamically-controlled cyclisation and interconversion of oligocholates. *Chem. Commun.* **1996**, 319-320.

[187] P. A. Brady, J. K. M. Sanders, Thermodynamically-controlled cyclisation and interconversion of oligocholates: metal ion templated 'living' macrolactonisation. *J. Chem. Soc., Perkin Trans. 1* **1997**, 3237-3253.

[188] B. Hasenknopf, J. M. Lehn, N. Boumediene, A. DupontGervais, A. VanDorsselaer, B. Kneisel, D. Fenske, Self-assembly of tetra- and hexanuclear circular helicates. *J. Am. Chem. Soc.* **1997**, *119*, 10956-10962.

[189] I. Huc, J. M. Lehn, Virtual combinatorial libraries: Dynamic generation of molecular and supramolecular diversity by self-assembly. *Proc. Natl. Acad. Sci. USA* **1997**, *94*, 2106-2110.

[190] S. J. Rowan, S. J. Cantrill, G. R. Cousins, J. K. Sanders, J. F. Stoddart, Dynamic covalent chemistry. *Angew. Chem. Int. Ed.* **2002**, *41*, 898-952.

[191] P. T. Corbett, J. Leclaire, L. Vial, K. R. West, J. L. Wietor, J. K. M. Sanders, S. Otto, Dynamic combinatorial chemistry. *Chem. Rev.* **2006**, *106*, 3652-3711.

[192] J. M. Lehn, Dynamic combinatorial chemistry and virtual combinatorial libraries. *Chem. Eur. J.* **1999**, *5*, 2455-2463.

[193] S. Otto, R. L. E. Furlan, J. K. M. Sanders, Dynamic combinatorial chemistry. *Drug Discovery Today* **2002**, *7*, 117-125.

[194] J. M. Lehn, From supramolecular chemistry towards constitutional dynamic chemistry and adaptive chemistry. *Chem. Soc. Rev.* **2007**, *36*, 151-160.

[195] S. Otto, K. Severin, Dynamic Combinatorial Libraries for the Development of Synthetic Receptors

and Sensors. *Top. Curr. Chem.* **2007**, *277*, 267-288.

[196] O. Ramstrom, J. M. Lehn, Drug discovery by dynamic combinatorial libraries. *Nat. Rev. Drug. Discov.* **2002**, *1*, 26-36.

[197] F. B. Cougnon, J. K. Sanders, Evolution of dynamic combinatorial chemistry. *Acc. Chem. Res.* **2012**, *45*, 2211-2221.

[198] S. Ladame, Dynamic combinatorial chemistry: on the road to fulfilling the promise. *Org. Biomol. Chem.* **2008**, *6*, 219-226.

[199] E. Moulin, G. Cormos, N. Giuseppone, Dynamic combinatorial chemistry as a tool for the design of functional materials and devices. *Chem. Soc. Rev.* **2012**, *41*, 1031-1049.

[200] S. Otto, Dynamic molecular networks: from synthetic receptors to self-replicators. *Acc. Chem. Res.* **2012**, *45*, 2200-2210.

[201] H. F. Gilbert, Protein disulfide isomerase and assisted protein folding. *J. Biol. Chem.* **1997**, *272*, 29399-29402.

[202] H. F. Gilbert, Thiol/Disulfide Exchange Equilibria and Disulfide Bond Stability. *Methods Enzymol.* **1995**, *251*, 8-28.

[203] P. A. Fernandes, M. J. Ramos, Theoretical insights into the mechanism for thiol/disulfide exchange. *Chem. Eur. J.* **2004**, *10*, 257-266.

[204] S. Otto, R. L. E. Furlan, J. K. M. Sanders, Dynamic combinatorial libraries of macrocyclic disulfides in water. *J. Am. Chem. Soc.* **2000**, *122*, 12063-12064.

[205] S. M. Ngola, P. C. Kearney, S. Mecozzi, K. Russell, D. A. Dougherty, A selective receptor for arginine derivatives in aqueous media. Energetic consequences of salt bridges that are highly exposed to water. *J. Am. Chem. Soc.* **1999**, *121*, 1192-1201.

[206] S. Otto, R. L. E. Furlan, J. K. M. Sanders, Selection and amplification of hosts from dynamic combinatorial libraries of macrocyclic disulfides. *Science* **2002**, *297*, 590-593.

[207] P. T. Corbett, L. H. Tong, J. K. M. Sanders, S. Otto, Diastereoselective amplification of an induced-fit receptor from a dynamic combinatorial library. *J. Am. Chem. Soc.* **2005**, *127*, 8902-8903.

[208] B. de Bruin, P. Hauwert, J. N. Reek, Dynamic combinatorial chemistry: the unexpected choice of receptors by guest molecules. *Angew. Chem. Int. Ed.* **2006**, *45*, 2660-2663.

[209] B. Brisig, J. K. M. Sanders, S. Otto, Selection and amplification of a catalyst from a dynamic combinatorial library. *Angew. Chem. Int. Ed.* **2003**, *42*, 1270-1273.

[210] L. Vial, J. K. M. Sanders, S. Otto, A catalyst for an acetal hydrolysis reaction from a dynamic combinatorial library. *New J. Chem.* **2005**, *29*, 1001-1003.

[211] M. Rauschenberg, S. Bomke, U. Karst, B. J. Ravoo, Dynamic Peptides as Biomimetic Carbohydrate Receptors. *Angew. Chem. Int. Ed.* **2010**, *49*, 7340-7345.

[212] A. M. Whitney, S. Ladame, S. Balasubramanian, Templated ligand assembly by using G-quadruplex DNA and dynamic covalent chemistry. *Angew. Chem. Int. Ed.* **2004**, *43*, 1143-1146.

[213] S. Ladame, A. M. Whitney, S. Balasubramanian, Targeting nucleic acid secondary structures with polyamides using an optimized dynamic combinatorial approach. *Angew. Chem. Int. Ed.* **2005**, *44*, 5736-5739.

[214] K. Jantos, R. Rodriguez, S. Ladame, P. S. Shirude, S. Balasubramanian, Oxazole-based peptide macrocycles: A new class of G-quadruplex binding ligands. *J. Am. Chem. Soc.* **2006**, *128*, 13662-13663.

[215] A. Bugaut, K. Jantos, J. L. Wietor, R. Rodriguez, J. K. M. Sanders, S. Balasubramanian, Exploring

the differential recognition of DNA G-quadruplex targets by small molecules using dynamic combinatorial chemistry. *Angew. Chem. Int. Ed.* **2008**, *47*, 2677-2680.

[216] P. T. Corbett, S. Otto, J. K. M. Sanders, What are the limits to the size of effective dynamic combinatorial libraries? *Org. Lett.* **2004**, *6*, 1825-1827.

[217] H. Schiff, Eine neue Reihe organischer Basen. *Ann. Chem. Pharm.* **1864**, *131*, 118-119.

[218] A. Herrmann, Dynamic mixtures and combinatorial libraries: imines as probes for molecular evolution at the interface between chemistry and biology. *Org. Biomol. Chem.* **2009**, *7*, 3195-3204.

[219] C. D. Meyer, C. S. Joiner, J. F. Stoddart, Template-directed synthesis employing reversible imine bond formation. *Chem. Soc. Rev.* **2007**, *36*, 1705-1723.

[220] S. Zameo, B. Vauzeilles, J. M. Beau, Dynamic combinatorial chemistry: Lysozyme selects an aromatic motif that mimics a carbohydrate residue. *Angew. Chem. Int. Ed.* **2005**, *44*, 965-969.

[221] R. L. E. Furlan, Y. F. Ng, S. Otto, J. K. M. Sanders, A new cyclic pseudopeptide receptor for Li+ from a dynamic combinatorial library. *J. Am. Chem. Soc.* **2001**, *123*, 8876-8877.

[222] S. L. Roberts, R. L. E. Furlan, S. Otto, J. K. M. Sanders, Metal-ion induced amplification of three receptors from dynamic combinatorial libraries of peptide-hydrazones. *Org. Biomol. Chem.* **2003**, *1*, 1625-1633.

[223] R. T. S. Lam, A. Belenguer, S. L. Roberts, C. Naumann, T. Jarrosson, S. Otto, J. K. M. Sanders, Amplification of acetylcholine-binding catenanes from dynamic combinatorial libraries. *Science* **2005**, *308*, 667-669.

[224] T. J. Hubin, D. H. Busch, Template routes to interlocked molecular structures and orderly molecular entanglements. *Coord. Chem. Rev.* **2000**, *200*, 5-52.

[225] T. Bunyapaiboonsri, O. Ramstrom, S. Lohmann, J. M. Lehn, L. Peng, M. Goeldner, Dynamic deconvolution of a pre-equilibrated dynamic combinatorial library of acetylcholinesterase inhibitors. *ChemBioChem* **2001**, *2*, 438-444.

[226] T. Bunyapaiboonsri, H. Ramstrom, O. Ramstrom, J. Haiech, J. M. Lehn, Generation of Bis-cationic heterocyclic inhibitors of Bacillus subtilis HPr kinase/phosphatase from a ditopic dynamic combinatorial library. *J. Med. Chem.* **2003**, *46*, 5803-5811.

[227] O. Ramstrom, S. Lohmann, T. Bunyapaiboonsri, J. M. Lehn, Dynamic combinatorial carbohydrate libraries: Probing the binding site of the concanavalin A lectin. *Chem. Eur. J.* **2004**, *10*, 1711-1715.

[228] A. Dirksen, S. Dirksen, T. M. Hackeng, P. E. Dawson, Nucleophilic catalysis of hydrazone formation and transimination: implications for dynamic covalent chemistry. *J. Am. Chem. Soc.* **2006**, *128*, 15602-15603.

[229] A. Dirksen, T. M. Hackeng, P. E. Dawson, Nucleophilic catalysis of oxime ligation. *Angew. Chem. Int. Ed.* **2006**, *45*, 7581-7584.

[230] V. T. Bhat, A. M. Caniard, T. Luksch, R. Brenk, D. J. Campopiano, M. F. Greaney, Nucleophilic catalysis of acylhydrazone equilibration for protein-directed dynamic covalent chemistry. *Nat. Chem.* **2010**, *2*, 490-497.

[231] A. J. Clipson, V. T. Bhat, I. McNae, A. M. Caniard, D. J. Campopiano, M. F. Greaney, Bivalent Enzyme Inhibitors Discovered Using Dynamic Covalent Chemistry. *Chem. Eur. J.* **2012**, *18*, 10562-10570.

[232] Z. Grote, R. Scopelliti, K. Severin, Adaptive behavior of dynamic combinatorial libraries generated by assembly of different building blocks. *Angew. Chem. Int. Ed.* **2003**, *42*, 3821-3825.

[233] K. Severin, The advantage of being virtual-target-induced adaptation and selection in dynamic combinatorial libraries. *Chem. Eur. J.* **2004**, *10*, 2565-2580.

[234] P. T. Corbett, S. Otto, J. K. M. Sanders, Correlation between host-guest binding and host amplification in simulated dynamic combinatorial libraries. *Chem. Eur. J.* **2004**, *10*, 3139-3143.

[235] P. T. Corbett, J. K. M. Sanders, S. Otto, Competition between receptors in dynamic combinatorial libraries: Amplification of the fittest? *J. Am. Chem. Soc.* **2005**, *127*, 9390-9392.

[236] R. C. Benyon, J. A. Enciso, A. D. Befus, Analysis of Human Skin Mast-Cell Proteins by 2-Dimensional Gel-Electrophoresis - Identification of Tryptase as a Sialylated Glycoprotein. *J. Immunol.* **1993**, *151*, 2699-2706.

[237] J. Kyte, R. F. Doolittle, A Simple Method for Displaying the Hydropathic Character of a Protein. *J. Mol. Biol.* **1982**, *157*, 105-132.

[238] R. Ihaka, R. Gentleman, R: A Language for Data Analysis and Graphics. *J. Comput. Graph. Stat.* **1996**, *5*, 299-314.

[239] D. Heider, D. Hoffmann, Interpol: An R package for preprocessing of protein sequences. *BioData Mining* **2011**, *4*, 16.

[240] L. Breiman, Random forests. *Machine Learning* **2001**, *45*, 5-32.

[241] E. Krieger, G. Vriend, Models@Home: distributed computing in bioinformatics using a screensaver based approach. *Bioinformatics* **2002**, *18*, 315-318.

[242] G. Vriend, What If - a Molecular Modeling and Drug Design Program. *J. Mol. Graphics.* **1990**, *8*, 52-56.

[243] O. Trott, A. J. Olson, Software News and Update AutoDock Vina: Improving the Speed and Accuracy of Docking with a New Scoring Function, Efficient Optimization, and Multithreading. *J. Comput. Chem.* **2010**, *31*, 455-461.

[244] W. C. Chan, P. D. White, *Fmoc solid phase peptide synthesis – a practical approach*, Oxford University Press, New York, **2000**.

[245] M. Amblard, J. A. Fehrentz, J. Martinez, G. Subra, Methods and Protocols of modern solid phase peptide synthesis. *Mol. Biotechnol.* **2006**, *33*, 239-254.

[246] I. Coin, M. Beyermann, M. Bienert, Solid-phase peptide synthesis: from standard procedures to the synthesis of difficult sequences. *Nat. Protoc.* **2007**, *2*, 3247-3256.

[247] A. Isidro-Llobet, M. Alvarez, F. Albericio, Amino Acid-Protecting Groups. *Chem. Rev.* **2009**, *109*, 2455-2504.

[248] H. Rink, Solid-Phase Synthesis of Protected Peptide-Fragments Using a Trialkoxy-Diphenyl-Methylester Resin. *Tetrahedron Lett.* **1987**, *28*, 3787-3790.

[249] F. Albericio, N. Kneibcordonier, S. Biancalana, L. Gera, R. I. Masada, D. Hudson, G. Barany, Preparation and Application of the 5-(4-(9-Fluorenylmethyloxycarbonyl)Aminomethyl-3,5-Dimethoxyphenoxy)Valeric Acid (Pal) Handle for the Solid-Phase Synthesis of C-Terminal Peptide Amides under Mild Conditions. *J. Org. Chem.* **1990**, *55*, 3730-3743.

[250] M. S. Bernatowicz, S. B. Daniels, H. Koster, A Comparison of Acid Labile Linkage Agents for the Synthesis of Peptide C-Terminal Amides. *Tetrahedron Lett.* **1989**, *30*, 4645-4648.

[251] S. K. Shannon, G. Barany, 4-(9-fluorenylmethyloxycarbonyl)phenylhydrazine (FmPH): A new chromophoric reagent for quantitative monitoring of solid-phase aldehydes. *J. Org. Chem.* **2004**, *69*, 4586-4594.

[252] M. Dessolin, M. G. Guillerez, N. Thieriet, F. Guibe, A. Loffet, New Allyl Group Acceptors for Palladium-Catalyzed Removal of Allylic Protections and Transacylation of Allyl Carbamates. *Tetrahedron Lett.* **1995**, *36*, 5741-5744.

[253] N. Thieriet, J. Alsina, E. Giralt, F. Guibe, F. Albericio, Use of Alloc-amino acids in solid-phase

peptide synthesis. Tandem deprotection-coupling reactions using neutral conditions. *Tetrahedron Lett.* **1997**, *38*, 7275-7278.

[254] E. Kaiser, Colescot.Rl, Bossinge.Cd, P. I. Cook, Color Test for Detection of Free Terminal Amino Groups in Solid-Phase Synthesis of Peptides. *Anal. Biochem.* **1970**, *34*, 595-598.

[255] D. A. Pearson, M. Blanchette, M. L. Baker, C. A. Guindon, Trialkylsilanes as Scavengers for the Trifluoroacetic-Acid Deblocking of Protecting Groups in Peptide-Synthesis. *Tetrahedron Lett.* **1989**, *30*, 2739-2742.

[256] Y. X. Han, F. Albericio, G. Barany, Occurrence and minimization of cysteine racemization during stepwise solid-phase peptide synthesis. *J. Org. Chem.* **1997**, *62*, 4307-4312.

[257] A. Stadler, C. O. Kappe, High-speed couplings and cleavages in microwave-heated, solid-phase reactions at high temperatures. *Eur. J. Org. Chem.* **2001**, 919-925.

[258] S. A. Palasek, Z. J. Cox, J. M. Collins, Limiting racemization and aspartimide formation in microwave-enhanced Fmoc solid phase peptide synthesis. *J. Pept. Sci.* **2007**, *13*, 143-148.

[259] B. Bacsa, K. Horvati, S. Bosze, F. Andreae, C. O. Kappe, Solid-phase synthesis of difficult peptide sequences at elevated temperatures: A critical comparison of microwave and conventional heating technologies. *J. Org. Chem.* **2008**, *73*, 7532-7542.

[260] H. Y. Kuchelmeister, Universität Duisburg-Essen (Essen), **2011**.

[261] R. B. Brandt, J. E. Laux, S. W. Yates, Calculation of Inhibitor Ki and Inhibitor Type from the Concentration of Inhibitor for 50-Percent Inhibition for Michaelis-Menten Enzymes. *Biochem. Med. Metab. Biol.* **1987**, *37*, 344-349.

[262] F. McTaggart, G. R. Brown, R. G. Davidson, S. Freeman, G. A. Holdgate, K. B. Mallion, D. J. Mirrlees, G. J. Smith, W. H. J. Ward, Inhibition of squalene synthase of rat liver by novel 3' substituted quinuclidines. *Biochem. Pharmacol.* **1996**, *51*, 1477-1487.

[263] T. C. Mou, N. Masada, D. M. F. Cooper, S. R. Sprang, Structural Basis for Inhibition of Mammalian Adenylyl Cyclase by Calcium. *Biochemistry* **2009**, *48*, 3387-3397.

[264] S. Cha, Tight-Binding Inhibitors .1. Kinetic-Behavior. *Biochem. Pharmacol.* **1975**, *24*, 2177-2185.

[265] J. F. Morrison, Kinetics of the reversible inhibition of enzyme-catalysed reactions by tight-binding inhibitors. *Biochim. Biophys. Acta* **1969**, *185*, 269-286.

[266] A. Lundequist, M. A. Juliano, L. Juliano, G. Pejler, Polycationic peptides as inhibitors of mast cell serine proteases. *Biochem. Pharmacol.* **2003**, *65*, 1171-1180.

[267] A. Dirksen, S. Dirksen, T. M. Hackeng, P. E. Dawson, Nucleophilic catalysis of hydrazone formation and transimination: Implications for dynamic covalent chemistry. *J. Am. Chem. Soc.* **2006**, *128*, 15602-15603.

[268] A. Bredihhin, U. Maeorg, Effective strategy for the systematic synthesis of hydrazine derivatives. *Tetrahedron* **2008**, *64*, 6788-6793.

[269] C. Palegrosdemange, E. S. Simon, K. L. Prime, G. M. Whitesides, Formation of Self-Assembled Monolayers by Chemisorption of Derivatives of Oligo(Ethylene Glycol) of Structure Hs(Ch2)11(Och2ch2)Meta-Oh on Gold. *J. Am. Chem. Soc.* **1991**, *113*, 12-20.

[270] B. T. Houseman, M. Mrksich, Efficient solid-phase synthesis of peptide-substituted alkanethiols for the preparation of substrates that support the adhesion of cells. *J. Org. Chem.* **1998**, *63*, 7552-7555.

[271] B. P. Orner, R. Derda, R. L. Lewis, J. A. Thomson, L. L. Kiessling, Arrays for the combinatorial exploration of cell adhesion. *J. Am. Chem. Soc.* **2004**, *126*, 10808-10809.

[272] M. Brust, J. Fink, D. Bethell, D. J. Schiffrin, C. Kiely, Synthesis and Reactions of Functionalized Gold Nanoparticles. *J. Chem. Soc., Chem. Commun.* **1995**, 1655-1656.

[273] M. Brust, M. Walker, D. Bethell, D. J. Schiffrin, R. Whyman, Synthesis of Thiol-Derivatized Gold Nanoparticles in a 2-Phase Liquid-Liquid System. *J. Chem. Soc., Chem. Commun.* **1994**, 801-802.

[274] M. J. Hostetler, A. C. Templeton, R. W. Murray, Dynamics of place-exchange reactions on monolayer-protected gold cluster molecules. *Langmuir* **1999**, *15*, 3782-3789.

[275] V. Amendola, M. Meneghetti, Laser ablation synthesis in solution and size manipulation of noble metal nanoparticles. *Phys. Chem. Chem. Phys.* **2009**, *11*, 3805-3821.

[276] V. Amendola, M. Meneghetti, What controls the composition and the structure of nanomaterials generated by laser ablation in liquid solution? *Phys. Chem. Chem. Phys.* **2013**, *15*, 3027-3046.

[277] J. P. Sylvestre, S. Poulin, A. V. Kabashin, E. Sacher, M. Meunier, J. H. T. Luong, Surface chemistry of gold nanoparticles produced by laser ablation in aqueous media. *J. Phys. Chem. B* **2004**, *108*, 16864-16869.

[278] H. Muto, K. Yamada, K. Miyajima, F. Mafune, Estimation of surface oxide on surfactant-free gold nanoparticles laser-ablated in water. *J. Phys. Chem. C* **2007**, *111*, 17221-17226.

[279] L. K. Ono, B. R. Cuenya, Formation and thermal stability of Au2O3 on gold nanoparticles: Size and support effects. *J. Phys. Chem. C* **2008**, *112*, 4676-4686.

[280] S. Barcikowski, G. Compagnini, Advanced nanoparticle generation and excitation by lasers in liquids. *Phys. Chem. Chem. Phys.* **2013**, *15*, 3022-3026.

[281] S. Barcikowski, F. Mafune, Trends and Current Topics in the Field of Laser Ablation and Nanoparticle Generation in Liquids. *J. Phys. Chem. C* **2011**, *115*, 4985-4985.

[282] F. Mafune, J. Kohno, Y. Takeda, T. Kondow, Dissociation and aggregation of gold nanoparticles under laser irradiation. *J. Phys. Chem. B* **2001**, *105*, 9050-9056.

[283] V. Amendola, M. Meneghetti, Controlled size manipulation of free gold nanoparticles by laser irradiation and their facile bioconjugation. *J. Mater. Chem.* **2007**, *17*, 4705-4710.

[284] F. Mafune, J. Kohno, Y. Takeda, T. Kondow, H. Sawabe, Formation of gold nanoparticles by laser ablation in aqueous solution of surfactant. *J. Phys. Chem. B* **2001**, *105*, 5114-5120.

[285] A. V. Kabashin, M. Meunier, C. Kingston, J. H. T. Luong, Fabrication and characterization of gold nanoparticles by femtosecond laser ablation in an aqueous solution of cyclodextrins. *J. Phys. Chem. B* **2003**, *107*, 4527-4531.

[286] J. P. Sylvestre, A. V. Kabashin, E. Sacher, M. Meunier, J. H. T. Luong, Stabilization and size control of gold nanoparticles during laser ablation in aqueous cyclodextrins. *J. Am. Chem. Soc.* **2004**, *126*, 7176-7177.

[287] S. Petersen, S. Barcikowski, In Situ Bioconjugation: Single Step Approach to Tailored Nanoparticle-Bioconjugates by Ultrashort Pulsed Laser Ablation. *Adv. Funct. Mater.* **2009**, *19*, 1167-1172.

[288] S. Petersen, J. Jakobi, S. Barcikowski, In situ bioconjugation-Novel laser based approach to pure nanoparticle-conjugates. *Appl. Surf. Sci.* **2009**, *255*, 5435-5438.

[289] J. G. Walter, S. Petersen, F. Stahl, T. Scheper, S. Barcikowski, Laser ablation-based one-step generation and bio-functionalization of gold nanoparticles conjugated with aptamers. *J. Nanobiotechnol.* **2010**, *8*, 21.

[290] S. Petersen, S. Barcikowski, Conjugation Efficiency of Laser-Based Bioconjugation of Gold Nanoparticles with Nucleic Acids. *J. Phys. Chem. C* **2009**, *113*, 19830-19835.

[291] P. Nachev, D. D. van 'T Zand, V. Coger, P. Wagener, K. Reimers, P. M. Vogt, S. Barcikowski, A. Pich, Synthesis of hybrid microgels by coupling of laser ablation and polymerization in aqueous medium. *J. Laser Appl.* **2012**, *24*, 042012-042011-042017.

[292] S. Petersen, A. Barchanski, U. Taylor, S. Klein, D. Rath, S. Barcikowski, Penetratin-Conjugated Gold Nanoparticles - Design of Cell-Penetrating Nanomarkers by Femtosecond Laser Ablation. *J. Phys. Chem. C* **2011**, *115*, 5152-5159.

[293] S. Sharifi, S. Behzadi, S. Laurent, M. L. Forrest, P. Stroeve, M. Mahmoudi, Toxicity of nanomaterials. *Chem. Soc. Rev.* **2012**, *41*, 2323-2343.

[294] C. Schmuck, L. Geiger, Design and synthesis of a new class of arginine analogues with an improved anion binding site in the side chain. *Chem. Commun.* **2005**, 772-774.

[295] S. C. Agarwal, B. L. Vanduuren, Synthesis of Diepoxides and Diphenol Ethers of Pyrene and Dibenz[a,H]Anthracene. *J. Org. Chem.* **1975**, *40*, 2307-2313.

[296] J. Garcia-Hartjes, S. Bernardi, C. A. Weijers, T. Wennekes, M. Gilbert, F. Sansone, A. Casnati, H. Zuilhof, Picomolar inhibition of cholera toxin by a pentavalent ganglioside GM1os-calix[5]arene. *Org. Biomol. Chem.* **2013**, *11*, 4340-4349.